The University Of Sheffield.

Modelling, optimisation and control of Stirling engine based low-carbon decentralised energy systems

Godfrey Toochukwu Udeh

A thesis submitted in fulfilment of the requirements for the degree of *Doctor of Philosophy*

The University of Sheffield
Faculty of Engineering
Department of Mechanical Engineering

November, 2021

Declarations

The candidate confirms that the work submitted is his own and that appropriate credit has been given where reference has been made to the work of others.

Aknowledgement

This research would not have been possible without the full funding provided by the Petroleum Technology Development Fund, an agency of the Ministry of Petroleum Resources, in Nigeria.

I am sincerely grateful to my supervisors; Professors Mohamed Pourkashanian, Derek Ingham and Lin Ma and Dr. Kevin Hughes for their invaluable contributions, support and guidance that were pivotal to the success of my Ph.D. I also want to thank Dr. Stavros for his support with several aspects of my modelling and documentation of the findings from this research and for providing very useful ideas and comments that helped in refining the work.

Special thanks to all my colleagues and wonderful friends in the Energy 2050 research group and in the department of Mechanical Engineering. I am particularly, grateful to my colleagues in the Energy Systems research group, Dr. Oscar, Ali, Mohammed, Bashar, Celal, Ismail, Maria and all the newcomers, for the helpful feedback and informative presentations in a range of topics during the weekly meetings.

I also want to thank other wonderful friends that contributed in one way or the other to the success of this programme. Hannah, Wayne, Divine, Dr. Kelachi, Dr. Fodio, Peter, Joe, Della, Agnes, and many others, thank you for your support.

To my lovely family, Dad and Mum and my siblings, I am grateful for your unceasing prayers, love, patience, and other moral supports rendered in the course of my PhD journey. I love you all.

Finally, I am immensely thankful to God for keeping me and my family in good health all through this period particularly, in the pandemic and for the deep insights and wisdom that sustained this project.

Abstract

Energy has been linked to economic growth and will play a vital role in the recovery of the global economy in this post-COVID era. The world's population has risen to about eight billion, and is driving the mounting demand for energy. This is an issue of great concern that is worsening the energy trilemma of affordability, sustainability, and reliability. To this end, several ingenious attempts are being made to advance the technologies for energy generation some of which have been tested and deployed across the globe. Among these technologies, decentralised energy systems (DES) are becoming popular due to their prospects for minimising energy wastage and ability to utilise local available clean fuels to drive the energy conversion processes in the system.

In this PhD thesis, three new configurations of DES are modelled, optimised, simulated, and analysed. The global aim is to enhance the efficiency and reliability as well as minimise the cost and pollutant emissions of contemporary DES, by shifting from the heavy reliance on fossil fuel to clean energy based solutions. First, a multi-carrier DES that comprises a combined cycle Stirling engine (ST) and organic Rankine cycle (ORC) prime mover, biomass drier and combustor, single effect absorption chiller and waste heat boiler has been proposed and will be powered by woodchips. The proposed DES can produce cooling, heating, electric power and dry woodchips, simultaneously. A comprehensive thermal model of the ST prime mover has been developed to predict accurate results of the engine's performance at its operational speeds. The enhanced model predicts the thermal efficiency and brake power of the prototype engine with relative errors of +0.3% and -4.02%, respectively. Based on the developed model, overall primary energy savings and carbon emissions reductions of the multi-carrier DES have been examined and are 51% and 40%, respectively compared to a fossil fuel based separate cooling, heating, and power system. This is an improvement of 42.2% and 9.45%, respectively, compared to a multi-carrier system utilising sole ST prime mover.

Further, another DES solution has been proposed to overcome the challenge of heavy dependence on diesel generators (DG) to augment the reliability of renewable

energy systems. The proposed DES concept consists of wind turbine, solar photovoltaic, and battery storage and will deploy wood chips biomass powered split ST or combined ST and ORC as the back-up to fulfill the electricity demand. The optimal number and types of the components of the energy system that simultaneously minimises the loss of power supply probability (LPSP), levelised cost of energy (LCOE) and dumped power have been found using the genetic algorithm. Obtained results show that the deployment of combined ST+ORC back-up in load following mode yields 60.70% and 33.71% reductions in the LCOE and CO_2 emissions, respectively compared to the DG back-up system but with slightly higher LPSP. While 61.4%, 33% and 24.47% reductions in the LCOE, CO_2 emissions and LPSP have been observed with the deployment of split ST in circuit charging mode.

The final DES proposed integrates the multi-carrier DES and the hybrid system and deploys the ST+ORC as back-up and prime mover in the system. Some modified rule-based energy management strategies (EMS) are proposed to effectively coordinate the simultaneous generation of energy vectors, while the optimal number of system components and the best control strategy are found by deploying a bi-level optimisation. Results indicate the best control strategy and system configuration achieve slight reductions in dumped power and CO_2 emissions but increases the number of start-ups of the back-up by 36%. However, it demonstrates additional capabilities in handling complex systems by doubling the generation of heating and increasing the rate of cooling generation.

The results obtained highlight the capabilities of decentralised multi-carrier energy systems in reducing primary energy consumption, energy cost and pollutant emissions as well as in improving system reliability. Increasing cases of flooding and other environmental issues linked to global warming and the mounting energy costs are compelling arguments that favour their deployment, particularly in the remote locations of developing countries.

Research Outcomes

- Udeh GT, Michailos S, Ingham D, Hughes KJ, Ma L, Pourkashanian M. A new non-ideal second-order thermal model with additional loss effects for simulating beta Stirling engines. Energy Convers Manag 2020; 206:112493. doi:10.1016/j.enconman.2020.112493.
- Udeh GT, Michailos S, Ingham D, Hughes KJ, Ma L, Pourkashanian M. A techno-enviro-economic assessment of a biomass fuelled micro-CCHP driven by a hybrid Stirling and ORC engine. Energy Convers Manag 2021;227:113601. doi:10.1016/j.enconman.2020.113601.
- Udeh GT, Michailos S, Ingham D, Hughes KJ, Ma L, Pourkashanian M. Multi-objective optimal sizing of a biomass fueled hybrid Stirling engine coupled with an ORC decentralised micro-CCHP system. International conference on Applied Energy, Dec 1- 10, 2020, Bangkok, Thailand.
- Udeh GT, Michailos S, Ingham D, Hughes KJ, Ma L, Pourkashanian M. Optimal sizing of a hybrid PV-WT-battery storage system: effects of split-ST and combined ST+ORC back-ups in circuit charging and load following. Energy Convers Manag. 2022;256:115370. doi:10.1016/j.enconman.2022.115370
- Udeh GT, Michailos S, Ingham D, Hughes KJ, Ma L, Pourkashanian M. A modified rule-based energy management scheme for optimal operation of a hybrid solar PV-wind power integrated multi-carrier energy system. Applied Energy. 2022;312:118763.doi:10.1016/j.apenergy.2022.118763.
- B. Shboul, I. Al-Arfi, S. Michailos, D. Ingham, GT udeh, L. Ma, K.J. Hughes, and M. Poukashanian, “Multi-objective Optimal Performance of a Hybrid CPSD-SE/HWT System for Microgrid Power Generation,” Applications of Nature-Inspired Computing in Renewable Energy Systems, M.A. Mellal, Eds. Pennsylvania, USA:IGI Global Publisher of Timely Knowledge, 2022, doi:10.4018/978-1-7998-8561-0.

Nomenclature

$\tilde{c}$	Unit cost ($\frac{\$}{kg} or\ \$/l$)
g	Acceleration due to gravity (ms^{-2})
h	Specific flow enthalpy (J/kg)
k	Boltzmann's constant
k_{T}	Power temperature coefficient (%/°C)
$m, \dot{m}$	Mass of working fluid (kg) and mass flowrate (kg/s)
n, n	Diode ideal factor, component life (years)
q	Quantity of charges conveyed by an electron (Coulombs)
t	Time (s)
v	Specific volume (m^3/kg) or velocity (m/s)
A_{PVg}	Generation area of PV module (m^2)
ATC	Annual total cost ($)
ATE	Artificial thermal efficiency (-)
C	Capacity (Ah), cost ($)
C_{pg}	Isobaric specific heat capacity (J/kgK)
C_{vg}	Isochoric specific heat capacity (J/kgK)
CR	Cooling ratio $(-)$
D	Euclidean distance $(-)$
DOD	Depth of discharge $(-)$
DPSP	Defficiency of power supply probability $(-)$
E	Internal energy (J)
E_{GO}	Band gap energy of the semi-conductor used in the cell
F_{dirt}	Factor compensating for losses due to dirt, wires, module mismatch on PV surface

FUE	Fuel utilisation efficiency $(-)$
G	Solar irradiance $\left(\frac{W}{m^2}\right)$
H, h	Flow enthalpy (J), specific flow enthalpy (J/kg)
HV	Heating value $(\mathrm{J/kg})$
I	PV cell current (A)
I_{o}	Cell reverse current (A)
K_{i}	Short circuit current temperature coefficient
LCC	Life cycle cost ($)
LCOE	Levelised cost of energy ($/kWh)
LPSP	Loss of power supply probability $(-)$
$N_{\mathrm{p}}, N_{\mathrm{s}}$	Number of PV cells in parallel and series, respectively
NOCT	Nominal operating cell temperature (°C)
NPC	Net present cost ($)
P	Pressure (Pa), Power (W)
PES	Primary energy savings $(-)$
Q	Heat transfer (J)
R	Blade radius (m) and Resistance (ohms)
R_{g}	Specific gas constant (J/kgK)
RI	Ranking index $(-)$
T	Temperature (K)
V	Voltage (volts) or volume of the heat exchanger spaces (m^3)
W	Work (J)
Z	Elevation (m)

Subscripts

amb	Ambient

Ann	Annualised
ave	Average
Bat	Battery
c, C	Compression (cold) space, scale index; cell
ch	Charge
con	Condenser
$disch$	Discharge
$diss$	Dissipation
e	Expansion (hot) space
evap	Evaporator
exp	Expander
f, F	Fuel or refrigerant; Cut-out
FC	Fuel consumption
gen	Generation
h, h	Heater space, hot; horizontal
hub_h	Hub height
$I\&A$	Installation and acquisition
inf	Inflation
int	Interest
k, k	Cooler; shape factor
l	Load
m	Mechanical
max	Maximum
min	Minimum
o	Surface
$o\&m$	Operation and maintenance
ph	Phase

pc	Power conditioning
r, r	Regenerator, rate
ref	Reference
refp	Refrigerant pump
rep	Replacement
rs	Reverse saturation
sc	Short circuit
sh	Shunt

Greek Letters

α	Temperature coefficient $(\%/°\mathrm{C})$
σ	Standard deviation $(-)$
$\bar{x}$	Mean $(-)$
χ	Emission factor $(kgGHG/kgfuel)$
γ	Specific heat ratio $(-)$
φ	Crank angle (degrees)
ϕ	Phase angle (degrees)
$\mathbb{Z}$	Stroke of the piston or displacer (m)
ξ	Coefficient of performance
ω	Rotational speed (rad/s)
β	Temperature coefficient $(°\mathrm{C}^{-1})$
ρ	Density of gas (kg/m^3)
ϕ	Porosity in wire mesh $(-)$
ω	Angular speed (rad/s)
η	Efficiency $(-)$
ξ	Coefficient of performance $(-)$
Δ	Change in quantity
ε	Heat exchanger effectiveness $(-)$

μ	Dynamic viscosity (Ns/m^2)

Abbreviations

ARS	Absorption refrigeration system
BMC	Biomass combustor
BMD	Biomass drier
BSS	Battery storage system
CC	Circuit charging
CCHP	Combined cooling, heating and power
CCP	Combined cooling and power
CERTS	Consortium for electric reliability technology solution
CHP	Combined heating and power
CSP	Concentrated solar power
DES	Decentralised energy system
DG	Diesel generator
DWH	Domestic water heater
EMS	Energy management strategy
FST	Finite speed thermodynamics
FTT	Finite time thermodynamics
G	Generation
GHG	Greenhouse gas
GT	Gas turbine
HDI	Human development index
HRES	Hybrid renewable energy system
ICE	Internal combustion engines
ICPC	International panel on climate change
IRENA	International renewable energy agency

JC	Job creation
LF	Load following
LINMAP	Linear programming technique for multi-dimensional analysis of preference
RE	Renewable energy
REA	Rural electrification agency
MCFC	Molten carbonate fuel cell
MOEA	Multi-objective evolutionary algorithm
MOPSO	Multi-objective particle swarm optimisation
MOSaDE	Multi-objective self-adaptive differential evolution
MT	Micro turbine
NDC	Naturally determined contribution
NIS	Negative ideal solution
NSGA II	Non-dominated sorting genetic algorithm
ORC	Organic Rankine cycle
PEM	Proton exchange membrane
PES	Primary energy saving
PIS	Positive ideal solution
PV	Photovoltaic
SCHP	Separate cooling, heating and power
SOC	State of charge
SOFC	Solid-oxide fuel cell
ST	Stirling engine
STC	Standard test condition
TOPSIS	Technique for order of preference by similarity to ideal solution
UC	Unit commitment
WT	Wind turbine

Table of Contents

List of Figures

List of Tables

Chapter 1 Introduction

Growing population, worsening climate change challenges, and increasing energy poverty are some of the motivations for exploring ways to improve energy efficiency that have been central to the discussions in this chapter. This chapter discusses the trends in global energy consumption and production particularly, the drivers of the increasing penetration of renewable energy technologies into the global energy mix. It undertakes an audit of technological issues affecting the reliability, modelling and control of contemporary decentralised energy systems. Through this pathway, a strong case has been built to support the work that is presented in the thesis. Finally, it outlines the research aim and main objectives and the thesis structure.

1.1. Transition in the global energy mix

Energy is the foundation for the growth of any economy and its sufficiency and efficient utilisation are acceptable standards for measuring the well-being and prosperity of people [1]. The world's population is growing and it is estimated that there are around eight billion people living on this planet today [2]. Correspondingly, global electricity production and consumption have been increasing in recent years as can be observed in Fig. 1-1. It was estimated that the global electricity production for 2012 will be about 22,000 TWh [3]–[5]. Nearly a decade after, global electricity production has risen by over 22%, while the electricity demand has been growing by 2% on an annual basis [6], [7], and it is projected to expand by 37% around 2040 [8].

Despite these projections, primary energy consumption fell by 4.5% in 2020 and this can be attributed to the devastating impact of COVID-19 on the global economy. This period also recorded a steep decline in energy consumption per capita, while electricity generation diminished marginally by 0.9% [9] (see, Fig. 1-1). The decline in electricity production in 2020 was driven by the fall in the consumption of crude oil, due to travel restrictions and general lockdown of most countries. Interestingly, electricity generation from renewable resources, particularly solar, expanded in 2020 [10]. In spite of this, renewable energy (RE) sources contribute only 26% of the global electricity production, while combustible fuels contribute about 67% of the total production [10].

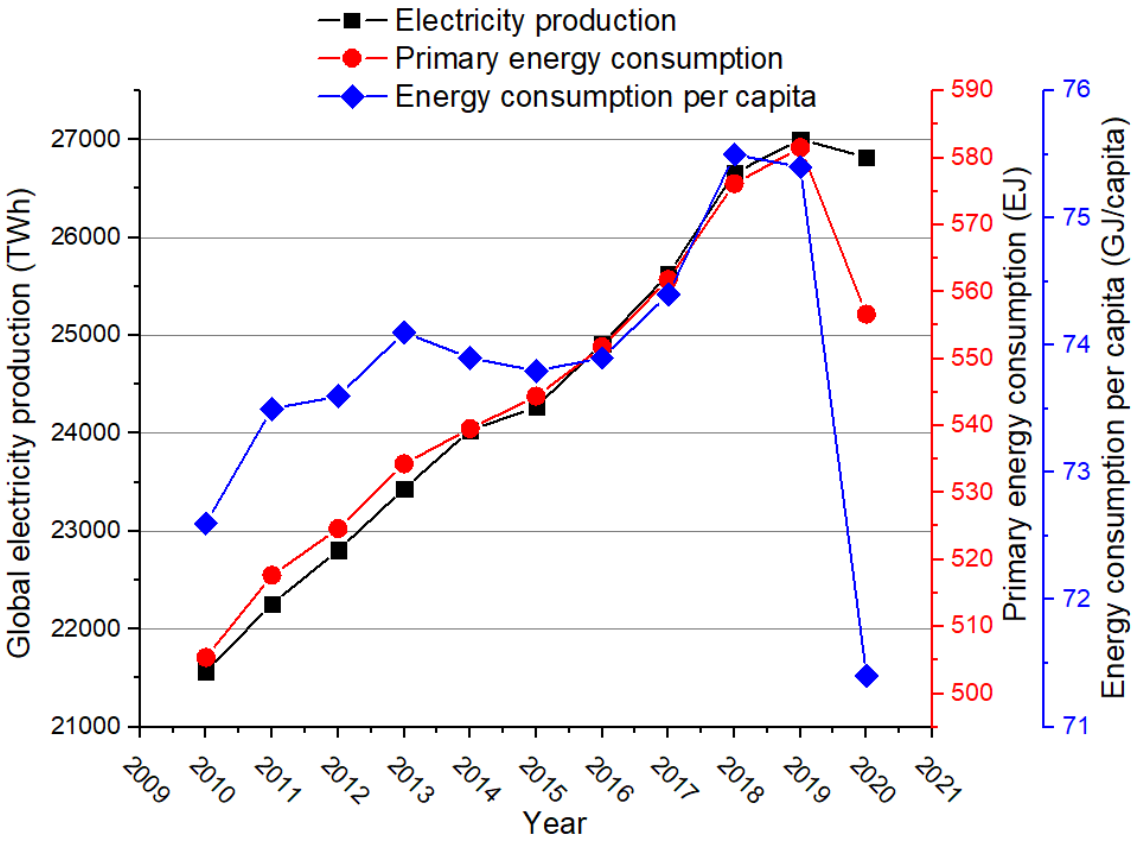

Fig. 1-1. Global energy production and consumption (source: BP Energy outlook report, 2021 [9], [11]).

Nevertheless, the last decade or so has recorded a surge in the use of RE technologies for electricity generation [12]. The consumption of RE based solutions has continued to rise on a yearly basis, with projections that it may contribute about 18% of the total global energy consumption by 2035 [8]. Most of the observed increase in the penetration of RE is catalysed by the rapidly declining costs of onshore wind and solar power. The cost of onshore wind and solar power has reduced remarkably by 40% and 55%, respectively since 2016 [9],[13], [14]. The other reasons for the expanding share of renewables in the global energy mix include, the intensifying climate change challenges [15], increasing attempts to provide electricity to the rural settlements [16], [13], government support and energy security issues [17]. Some of these drivers are discussed in detail in the next section.

1.1.1. Pathways to expanding energy security

It has been reported that about 2.5 billion people globally are grappling with unreliable electricity supply [18], while over 1.1 billion people are in total darkness,

with about 80% of this figure residing in Africa and Southern Asia [19]–[21]. Meanwhile, 63.7% of the global population live in countries with average energy demand per capita of less than 100 GJ/head [9]. While North America has the highest energy consumption per capita of 217 GJ/head, Africa is at the bottom of the ladder with only 14 GJ/head [9]. The increasing transition to RE based technologies could help to close this wide gap in energy security. Therefore, the procurement of renewable electricity to off-grid locations is considered a vital prerequisite for the triumph of RE technologies essentially, to meet the electricity demand of the locations without access to electricity.

To this end, the recent drive of the United Nations Sustainable Development Goals (Goal 7) [24], is to provide electricity to developing countries – small islands, developing states and land-locked developing countries – with the help of sustainable energy systems. In turn, this policy framework triggers an increase in the utilisation of RE based solutions. According to the United Nations [24], the use of solar lanterns and stand-alone solar home systems is incapable of meeting the electricity needs of these locations. It has been argued that over 30% of the energy demand of most of the remote regions would be met if off-grid energy systems are vigorously developed, not only to power homes, but to unlock their economic potentials [22]–[24].

1.1.2. Carbon emissions reduction pathways

According to the International Renewable Energy Agency (IRENA), about two-thirds of the global carbon emissions are emitted from the energy sector. In the last fifty years, global CO_2 emissions have grown from 320 ppm to 350 ppm [8], with the last decade recording an annual growth of 2 ppm [25]. However, the global carbon emissions fell sharply by 6.3% in 2020, due to COVID 19 travel restrictions and general reductions in industrial activities [9]. While the observed decline in carbon emissions is commendable, there are worrying concerns that it may be reversed as the lockdowns are lifted and the global economy recovers [9]. The greenhouse effect – remotely caused by the rise in the global temperatures with growing carbon emissions – has been cranking up ecological problems such as, flooding, acid rain, increased volcanic activities, deforestation, and wildfires. In the Paris agreement, the

target is to limit the growth in the global average temperature to below 2°C by aggressively reducing carbon emissions. The massive deployment of renewable energy solutions is one of the key components of the naturally determined contributions (NDC) reached in the Paris agreement, which has the prospects of achieving this ambitious goal [10].

The GHG protocol has categorised carbon emissions into three scopes, by mapping the sources of the emissions. This protocol has placed a responsibility on companies to report the scope 1 and 2 emissions, while scope 3 emissions that are difficult to monitor still enjoy some flexibility [10]. Scope 1 emissions are largely direct emissions from the combustion of fuels for the production of energy vectors and for firing automobiles, leakages from greenhouse gases and other emissions from industrial processes. On the otherhand, scope 2 emissions are derived from the consumption of grid electricity, while scope 3 emissions are indirect emissions that occur in the value chain of a company. Based on the scope of the emissions, sustainability tools such as carbon offsetting, renewable energy certificates and corporate power purchase agreements are now being deployed to minimise emissions [10]. These tools promote increased penetration of renewable energy into the global energy mix [26]. According to the estimates made by IRENA, if NDC is implemented judiciously, global renewable power capacity would hit 3.5 TW by 2030 [10]. This is about 50% of the targeted output of the Paris agreement and it is a significant contribution that will check the expected rise in the global carbon emissions, especially in this post-COVID era.

1.1.3. Nigerian energy mix and future direction

Nigeria has a population of over 180 million people and about 80 million people are unconnected to the electricity grid [23], [27]. Sadly, most of the people without access to electricity in Nigeria reside in remote locations that are located miles away from the urban settlements and are in large part, characterised by poor access roads, difficult terrains, and dispersed pattern of settlements. These locations are facing harrowing developmental challenges that affect the well-being of the people and impede their prosperity.

As is the case anywhere in the world, the burning issues in the electricity industry in Nigeria are: reliability of supply; affordability of energy; and environmental protection – the trio is the so-called energy trilemma [28]. More recently, a fourth dimension – that concerns energy justice – has been added, leading to the energy quadrilemma [29]. The grid electricity has an installed capacity of over 10 GW, and about 2 GW is generated from base load power plants that are mainly hydro-powerplants, while the rest are produced from thermal power plants [30]. However, the grid transmission capacity stands at 7 GW, and provides an average supply reliability of about 40%, a consequence of the weak power transmission infrastructure [30]. Due to the low grid reliability, a sizable majority of the population resort to the use of small-scale internal combustion engines (ICE) currently producing about 12 GW, to guarantee their energy security [16] [23], [31]. Consequently, inefficient generation of electricity with ICEs to augment the grid reliability cost the nation over $14 billion annually [16].

On a positive note, Nigeria receives abundant supply of solar irradiation and has good biomass potentials that can be deployed to solve some of these energy challenges. In spite of this, the total installed RE capacity in Nigeria based on 2020 estimates is 40 MW, with solar contributing about two-thirds of the total [10]. However, the RE based solutions are increasingly being deployed into the Nigerian energy mix and has increased by more than six folds since 2011. Nevertheless, this is still insignificant compared to South Africa with the highest RE share in Africa [10]. Nigeria has committed to increasing her share of RE power by 13 GW as a contribution to the global drive to transition to net zero emissions. This goal will be realised by aggressively deploying solar photovoltaic (PV) for rural electrification. Hence, the significant increase in the installed capacity of RE power, particularly solar PV.

Unfortunately, most of the contemporary solar based energy solutions that are deployed in Nigeria consist of PV, battery storage and DG back-up systems [23]. Hybrid solar PV and battery systems notably present high energy costs, augmented emissions and low reliability and may not support economic activities in the remote locations [32]–[34]. Moreover, energy systems that can produce more than one energy vector, save primary energy and perform better than the hybrid systems.

These energy systems are already making strong inroads into the European energy market [35], [36]. Unfortunately, there is no evidence of the deployment of similar energy models into the Nigerian energy mix. The deployment of energy solutions generating multiple vectors into the Nigerian energy mix, particularly in the remote locations with huge agro-based commercial activities is pivotal to the realisation of some of the goals of the government, including the mitigation of the soaring rural-urban migration and improved access to quality healthcare. These emerging energy system models will lead the discussions in the next section.

1.2. Challenges facing decentralised energy systems

Decentralised energy system (DES) concepts are gaining popularity nowadays, for matching the energy needs of customers especially in remote off-grid locations. A DES has the potential of producing only one energy vector or multiple energy vectors and other goods. Several DES concepts have been developed in the literature and are being deployed to meet the energy needs of customers in different locations across the globe. The popular DES concepts are the hybrid renewable systems (HRES), combined heating and power (CHP), combined cooling and power (CCP), combined cooling, heating, and power (CCHP) and multi-carrier systems [35].

Multi-carrier energy systems are energy systems that integrate several components or subsystems to produce different energy vectors and other useful goods. The products of these energy systems include, cooling, heating, hot water, electricity, clean water, ice block, hydrogen gas and wood chips [37]. Unlike conventional energy systems, DES are installed close to the energy consumers, thereby reducing the power transmission losses that are incurred when electricity is transmitted over long distances via the grid [38], [39]. In addition, primary energy is conserved in these systems by recovering the waste heat to provide other useful goods. Moreover, DES can utilise a variety of locally available fuel in their operation.

Despite the numerous breakthroughs in deploying DES concepts, the contemporary models still present many challenges. They are faced with the issue of low reliability, high energy cost and emissions. In addition, regarding the design of the system, accurate models of the system components are pivotal to the improved

understanding of their behaviour. Moreover, these models are required for the optimisation of the system, which is undertaken either at the design stage; to select the optimum system configuration or at the operational level; to find the best system operating regime. Additional issues arise from the effective management of the flow of energy vectors in the various units of the system. These issues are elaborately discussed in this section with the view to proffering some plausible solutions.

1.2.1. Improving decentralised energy system concepts

Although solar and wind resources are abundant and mature [40], [41], they are characterised by periodic and stochastic behaviour, respectively [6], [42], and are generally not correlated with the electricity demand [43], necessitating the deployment of diesel generators (DG) as a back-up to augment their reliability [44]–[48]. Unfortunately, the utilisation of DG as a back-up in HRES results in additional carbon emissions and augmented costs. In addition, fossil fuels are often unavailable in remote regions, due to logistic constraints. Moreover, the expected depletion of fossil fuels cannot provide a long-term solution. The enumerated challenges of increased emissions and high energy cost from the deployment of DG as back-up in HRES can be minimised by utilising programmable back-ups fired by low-carbon energy sources such as biomass fuel. To this end, biomass powered back-ups are now being deployed in improving the reliability of HRES [49][50].

However, notwithstanding the numerous interesting features of the Stirling engine (ST) [51]–[53], only a few studies utilised biomass driven ST as the back-up in HRES configurations. This may be a consequence of their low electrical efficiency, particularly at the micro-power scale [54], [55]. Thankfully, this problem can be solved by incorporating another heat engine to recover the waste heat from the engine and produce additional power [8]. That way, the global efficiency of the combined system is improved. It is plausible that the deployment of the proposed back-up to fulfill the electric load could reduce the cost of energy of a HRES and minimise the carbon emissions. So far, this opportunity has not been fully explored in the literature.

Similarly, several sole ST driven CCHP systems have been studied and remarkable savings in primary energy and emissions reductions were observed compared to

conventional separate cooling, heating and power systems [56] [57]. However, the low efficiency of the ST affects the energy utilisation of the system. Therefore, dual prime movers have been proposed and several combined cycles driven CCHP were investigated. Korlu et al. [58] and Entezari et al. [59] proposed a combined gas turbine (GT) and ST bottoming cycle to improve the electrical efficiency of the CCHP system and observed significant improvements compared to GT only driven CCHP. Chitsaz et al. [60] proposed a fuel cell with ST bottoming cycle and observed 24.61% increase in the electrical efficiency of the standalone fuel cell. Although Bahrami et al. [61] reported that combining the ST and the ORC could yield 4-8% increase in the electrical efficiency of sole ST, there is scant information on studies that examined a CCHP system driven by combined ST and ORC prime mover. Meanwhile, further enhancements in the energy utilisation can be achieved by advanced waste heat recovery to produce additional goods in a multi-carrier energy system. While some multi-carrier energy system concepts have been proposed to enhance the DES fuel utilisation, most of these studies only considered producing other goods such as clean water [62].

For DES driven by biomass fuels, the regulation of the quality of the biomass fuel is very imperative, particularly for systems deployed in tropical remote regions [63]. One traditional way of controlling the quality of the woodchips fuel is by undertaking in-situ drying of the feedstock with the waste heat obtained from the combustion flue. The incorporation of drying may scavenge the available thermal energy and limit its potential to produce other useful energy vectors and goods. Therefore, it is important to investigate the performance of a multi-carrier DES concept that will be fired by wood chips powered combined ST and ORC, to co-produce cooling, heating, power, and dry woodchips. Finally, a system that leverages on the strengths of the proposed HRES and multi-carrier energy system, by deploying the ST+ORC to simultaneously serve as back-up to the HRES and drive the multi-carrier system could offer further improvements in system performance. This DES configuration has not been investigated before and is being proposed in this study.

1.2.2. Modelling challenges and optimisation of DES components

Second-order thermal models of the ST offer the perfect balance between model accuracy and computational speed and are suitable for the dynamic simulation of the engine's performance [64]. Since Urieli and Berchowitz [65] implemented the numerical solutions of the original Finkelstein second-order adiabatic model [66], several other notable efforts have been made to improve on the accuracy of the simple adiabatic model. Babaelahi and Sayyaadi [67] replaced the adiabatic processes assumed in the simple analysis with polytropic processes and accounted for several losses in the engine. They reported errors as a difference of 14.34% and 3.14% in the power output and thermal efficiency of the experimental engine, respectively. Li et al. [68] also assumed polytropic processes, and considered the shuttle heat loss and mass leakage through the gap between the displacer and the cylinder wall in the formulation of the governing equations of the engine. This model predicts the brake power and thermal efficiency of the experimental engine with a relative error of – 2.6% and + 3.78%, respectively. However, in most of the previous works, the losses in the engine were decoupled from the governing equations of the engine. Unfortunately, the losses in the engine interact with the conditions of the engine fluid, necessitating their direct coupling to its basic equations to accurately determine the flow conditions in the engine. Therefore, in this study, an attempt will be made to develop a computer simulation tool for the study of the behaviour of the ST based on an advanced modelling effort that comprehensively couples several irreversibilities in the engine to the adiabatic model, to improve its prediction accuracy.

On the other hand, the optimisation of DES is necessary to determine the optimal configuration of the system components and the best operating regime [8]. Shengjun et al. [69] obtained the optimal points of different ORC working fluids and cycles by implementing a parametric optimisation. Boyaghchi and Safari [70] achieved 3.27 and 4.9 times improvements in the total avoidable exergy destruction and cost rates, respectively, of a geothermal energy based multi-carrier DES by undertaking the system's parametric optimisation. So far, the parametric optimisation of the multi-carrier energy system proposed in Section 1.2.1 has not been performed to find its optimal operating regime.

In addition, power curtailment characterises HRES concepts, and this is done to minimise excessive dumping of power. Unfortunately, the curtailment of power from the renewable generators lead to the over reliance of the system on fossil fuel powered DG back-up [71]. Therefore, more emissions are produced, and the energy cost increases because of the use of high pollutant emitting and expensive fossil fuels. It is clear that there is a conflict between the system reliability and cost or carbon emissions [72]. This problem can be tackled at the design stage by conducting multi-objective sizing optimisation of the hybrid system and by simultaneously considering the emissions, cost, dumped power and reliability of the system as the objective functions. Thus far, the optimal sizing optimisation of the HRES proposing ST based back-ups described in Section 1.2.1 has not been performed.

1.2.3. Energy management challenges in decentralised systems

The effective management of the flow of energy in the numerous generation and storage units that comprise a decentralised energy system is crucial to reduce system operational cost, improve efficiency and reliability [37], [73]. In the literature, heuristic, fuzzy-logic, unit commitment (UC) problem-based and smart tools have been proposed as energy management strategy (EMS) approaches for different energy system configurations [73], [74].

While the traditional heuristic approaches including, the load following (LF), circuit charging (CC) and peak shaving and the fuzzy logic are popular for managing HRES [75]–[77], the scheduling approach has been deployed to manage the operation of DES generating more than one energy vector [37][78][79]. Unfortunately, the traditional heuristic approaches present some challenges. The deployment of the back-up to follow the load in the LF mode results in the engine operating below its rated conditions. Thus more fuel is consumed and this leads to higher emissions and operating cost [76]. On the other hand, the CC mode is characterised by the excessive dumping of power [75], [76] and the frequent charging and discharging of the batteries that is inimical to the component's life [77], [80]. While the peak shaving presents a problem of over sizing of the system leading to excessive dumping of power [81]. There have been attempts to solve these challenges by proposing a hybrid of the LF and CC [82] and the deployment of several small capacity back-ups

in CC [83]. Ayodele et al. [83] deployed 3-split DG as back-up in circuit charging. They compared the results to a single DG back-up system and found 46%, 28%, 82%, and 94% reductions in life cycle cost, cost of energy, CO_2 emissions, and dumped power, respectively.

The scheduling EMS approaches rely on the forecast of the future production of renewable generators and the consumers' energy demand, and this is a setback, because of the high prediction errors associated with the forecast of these data. Besides, with the increasing complexity of the system, the computational time will increase prolonging the response time of the system. This is even made worse as the length of the prediction horizon increases [78]. The rule-based approach on the other hand is subjective and prone to errors because the rules are made based on the experience of the designer.

Consequently, an energy management approach that can minimise the errors in the contemporary approaches is needed. Therefore, rule-based energy management strategies that leverages on the strengths of the LF and CC EMS by deploying combined cycle and split back-up to ensure the uninterrupted operation of a multi-carrier system have been proposed. While the deployment of split back-ups has been established to minimise the dumped power and emissions in a HRES and improve the system's reliability, it is not clear how it will impact the performance of the battery storage. Further, as the number of splits of the back-up increases, the frequency of start-ups of the back-up may increase and this could increase the operational cost of the system. Unfortunately, there is limited knowledge of the global impact of split back-ups on the cost of energy of the system with or without the inclusion of batteries. Finally, for a multi-carrier energy system generating other energy vectors apart from electricity, it will be insightful to investigate the impact of the combined inclusion of batteries and split back-up on the generation of these other energy vectors.

1.3. Aim and objectives of the present study

This study, therefore, proposes the concept development, modelling, optimisation and control of new configurations of integrated green fuel-based decentralised energy systems, designed to generate 230 kW of electric power, cooling, hot water

and dry wood chips, to meet the energy needs of a test location. Hence, the following are the specific objectives:

a) To propose new configurations of decentralised energy systems including:
   (i) Hybrid renewable energy system that deploys a wood chips powered combined Stirling and ORC or split Stirling as a back-up;
   (ii) A multi-carrier system that is driven by Stirling and ORC to simultaneously produce cooling, heating, power, and dry wood chips and;
   (iii) An integrated decentralised energy system concept that deploys Stirling and ORC to back-up the HRES and drive the multi-carrier system in parallel.
b) To develop a computer simulation tool based on the comprehensive coupling of several loss effects to the adiabatic model of the Stirling engine for the simulation of the dynamic performance of Stirling engines based decentralised energy systems and to perform robust validation of the developed model against experimental data and other model results.
c) To conduct parametric analysis of a new configuration of multi-carrier system that deploys a dual Stirling+ORC prime mover powered by wood chips fuel to produce cooling, heating, and electric power and dry wood chips and study the impact of cooling ratio, speed of the main prime mover, and quality of the biomass fuel on its performance.
d) To perform parametric optimisation of the proposed multi-carrier system from a multi-objective perspective and obtain the optimal operating parameters of the multi-carrier decentralised energy system from the Pareto set of optimal solutions, by deploying a modified decision-making tool.
e) To determine the optimal configuration of the novel HRES that simultaneously minimises the carbon emissions, reliability, cost, and dumped power by implementing a memetic algorithm and a decision-making tool and compare the results of the different test cases with the diesel generator base case, from the perspectives of reliability, cost, compactness and sustainability.
f) To propose novel rule-based energy managing strategies for managing the continuous operation of the hybrid system integrated multi-carrier system and investigate the impact of the proposed dispatch strategies on the battery utilisation, start-ups of the back-up, dumped power and generation of other

energy vectors, by implementing bi-level optimisation and dynamic simulation of the optimal system.

1.4. Thesis outline

The overall structure of this thesis reflects the sequence of events leading to the realisation of the global objectives. The remaining part of the thesis is structured as follows:

Chapter 2 presents the audit of contemporary decentralised energy system concepts that have been proposed in the literature. Additionally, it focuses on the review of the existing knowledge on the modelling, optimisation, and energy management of these systems. This is intended to draw new insights into the topics and identify the gaps in the literature. Finally, the chapter outlines the identified gaps in the literature.

Chapter 3 introduces the new decentralised energy systems configurations formulated and proposed in this study. The chapter presents the process and thermodynamic diagrams of the formulated systems and describes the energy conversion processes. Finally, it describes the characteristics of the test location and assesses the local weather data and available energy resources of the location.

Chapter 4 describes the general principles of the second-order modelling of the kinematic Stirling engine. This chapter outlines the assumptions that define the scope of the modelling efforts for the adiabatic model and highlights the updated assumptions for the proposed model. It undertakes the development of the proposed enhanced second-order thermal model. Finally, the chapter presents the solution approach for implementing the model solutions.

Chapter 5 implements the solutions of the developed thermal model with the data of an experimental engine and presents the robust validation of the model predicted results against experimental data and other theoretical models. In addition, it discusses the results investigating the model performance in predicting the dynamic simulation of the engine and deploys the enhanced model to study the impact of key engine parameters on its performance.

Chapter 6 details the steps taken to model and validate the components of the new multi-carrier system configuration. It also undertakes the integration of the subsystems of the energy system and provides the performance metrics for assessing the system and implementing the parametric optimisation. This chapter discusses the simulated results for the parametric analysis of the system and compares it to that of fossil fuel-based systems and other similar systems. Finally, it undertakes the parametric optimisation of the system and evaluates the results.

Chapter 7 undertakes the multi-objective sizing optimisation of new configuration of hybrid renewable energy system. It formulates the mathematical models for predicting the energy generation from the system components and describes the strategies for dispatching the energy generated. Additionally, it formulates the optimisation problem and implements the solution. This chapter compares different hybrid system cases to the base case. Also, it simulates the effect of seasonal variations on the dynamic performance of the optimal system and undertakes sensitivity analysis to examine its response to variation in some key parameters.

Chapter 8 proposes novel energy management strategies for the control of the operation of the integrated multi-carrier energy system. This chapter implements bi-level system sizing optimisation to obtain the optimal system configuration. It discusses the results of the optimal system configurations obtained from the proposed control strategies. The final part of this chapter examines the impact of the proposed EMS on the battery performance, frequency of operation of the back-up, and generation of other energy vectors in the optimal system.

Chapter 9 summarises the key results obtained and highlights the original contributions to knowledge in this study. Finally, it recommends some future work to expand the frontier of knowledge in this thematic area.

Chapter 2 Decentralised Energy Systems

This chapter presents the review of the relevant literature on the trend in the concept development of decentralised energy systems. It also reviews the mathematical models deployed to study the behaviour of the components and evaluate the system performance. The chapter undertakes further reviews on the design and parametric optimisation of the components and subsystems of different configurations of the energy system. Additionally, it surveys previous research efforts on the management of the flow of energy from the various units of the system. The review undertaken in this chapter has provided new insights into the hot topics in the concept development, modelling, optimisation and energy management of decentralised energy systems. Finally, it outlines the knowledge gaps in the literature on these topics and this will be central to the works that will be undertaken in this thesis.

2.1. Introduction

With the growing need to pursue energy efficiency and minimise losses in the transmission of energy from the generation stations to the point of consumption, the concept of decentralised energy systems was originated. Decentralised energy systems (DES) are simply energy networks that integrate several energy generating and storage units, often localised at the point of consumption. This concept, which is used interchangeably in the literature as micro-grids, was introduced by the consortium for electric reliability technology solutions (CERTS) in 2002 [84], [85]. However, unlike micro-grid systems which could operate in grid-connected or off-grid modes [84], the definition of DES in this thesis precludes energy systems that operate in grid-connected mode.

Several concepts of DES have been formulated in the literature. They include energy systems designed to supply only one energy vector and those that supply two or more energy vectors. In the first category, hybrid renewable energy systems (HRES) are popularly being deployed to match the electricity demand particularly in off-grid remote locations. While in the second category of DES, combined heating and power (CHP), combined cooling and power (CCP), combined heating, cooling and power (CCHP) and multi-carrier energy systems have been deployed to generate two or

more useful energy products. The more recent DES concept that has been attracting the attention of researchers is the integrated DES concept, where a hybrid renewable energy system (HRES) is integrated to the second DES category.

The formulation of the DES configuration is the first step in the system design [39]. Thereafter, models of the components are developed to study the system and predict its performance. These models are the basis for undertaking the sizing optimisation of DES systems that have been extensively undertaken in the literature. Since DES deploys many units to meet the energy demand of the consumers, it is important to formulate an approach to manage the operation of the system. It has been reported that the energy management strategy deployed to coordinate the operation of a DES affects the size and performance of the system [73]. Hence, most authors have integrated the system sizing optimisation and the energy management strategy in order to obtain the optimal system configuration.

The other aspect of DES design that has been receiving considerable attention from researchers is the dynamic simulation of the system to reveal its real-time behaviour. The hourly simulation of the operation of a DES provides useful insights on the performance of the components of the system, while matching the load and this is vital for decision making. All of these aspects of the design of DES shall be the kernel of the discussions in the subsequent sections.

2.2. Trend in micro-decentralised energy system concepts

Here, the several concepts of decentralised energy systems that have been formulated in recent times are presented. As has been mentioned, the popular concepts of DES found in the literature include the HRES, CHP, CCP, CCHP, multi-carrier and HRES integrated CHP/CCP/CCHP energy systems. In these energy system concepts, internal and external combustion engines such as Stirling engines (ST), diesel generators (DG), micro-turbines (MT), organic Rankine cycles (ORC) and fuel cells [55], [86] serve as the prime movers. On the other hand, in HRES, these heat engines serve as the back-up to augment the power supply and ensure the reliability of the system. A very important aspect of the design of a DES is the selection of the suitable prime mover to drive the energy generation of the system. The prime mover selected in a DES design is determined by the ease of maintenance,

cost, energy demand, local pollution, in-situ available fuel and electrical efficiency [87].

A review of prime movers for small scale DES, particularly biomass powered CCHP systems was performed in [88] and the ST was recommended for driving micro-CCHP systems. The ST has some fascinating features. Similar to the ORC, it can utilise multiple clean energy sources of low, medium and high grade quality [89]. ST however, have good part load performance and high heat sink temperatures [90]. In addition, they produce less noise in operation, low vibration and are easier to maintain [91]. Consequently, ST have become the subject of intense studies in recent times for deployment in DES. Nevertheless, in order to provide a comprehensive review of recent studies on DES concepts, this survey of the literature will focus on studies that deployed all of the aforementioned prime movers.

Further, the prime movers deployed in DES indicate low electrical efficiencies when delivering electrical power at small and micro-scale, 12 – 35% [88], [92] and 9.2 – 33% [54], [55], respectively. Regrettably, about 60% of the total fuel energy in an internal combustion engine is lost in the exhaust [93]–[97]. For a gas turbine, just about a third of the input energy is utilised for power generation [97]; the rest is lost in the exhaust. The fuel consumption of IC engines could be reduced by 10%, if 6% of the energy in the exhaust can be recovered [98], [99]. In addition to the proclivity of enhancing the performance of IC engines by re-using the waste heat from its exhaust, the level of emissions produced from these engines can be minimised [100].

Therefore, the untapped energy in the exhaust flue of the prime mover of DES can be recovered to drive another engine; this concept is known as topping and bottoming cycle integration. That way, the overall electrical efficiency of the prime mover could be enhanced. The use of combined cycles is an established way of improving the performance of any heat engine, by maximising the fuel utilisation of the system [101]. Several authors have deployed this concept to improve the electrical efficiency of subsystems of DES in the literature [93], [100]. In this critical review of the available literature on DES concepts, additional emphasis will be placed on the configuration of the prime mover deployed.

2.2.1. Hybrid renewable energy systems

Green energy solutions hybridising many clean energy resources are becoming more competitive for meeting the energy demand at off-grid locations, mainly because of the steady decline in the cost of system components and improving efficiencies. Fig. 2-1 illustrates a simple hybrid renewable energy system (HRES) concept comprising solar photovoltaic (PV) modules, wind turbines (WT), battery storage system (BSS) and diesel generator (DG) back-up, to match the electric load of the consumers.

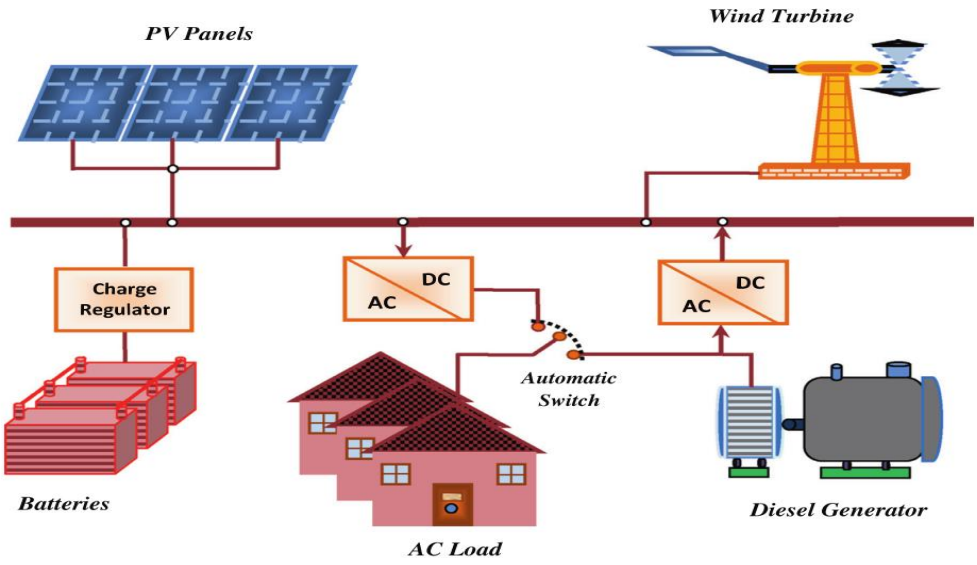

Fig. 2-1. Schematic diagram of a standalone micro-grid system [102].

The energy sources constituting a HRES are mainly determined by the locally availabile resources in the design location and the intended application, among other factors. DES deploying the HRES concept are characterised by high efficiencies, low transmission losses, low voltage [103], and ability to manage and coordinate the subsystems in a more decentralised manner [104]. However, some endogenous challenges, such as high storage costs, less usable energy during the year, intermittent energy generation, lack of protection, and environmental/safety concerns [105], set commercialisation barriers.

The earlier concepts of renewable energy systems utilised a single renewable energy resource to fulfil the electricity demand of the targeted consumers [106]–[108]. Unfortunately, most renewable energy resources, particularly solar and wind, are

spasmodic in nature. Hence, the reliability of the system is not guaranteed and can only be augmented by deploying large storage facilities, thereby resulting in increased energy cost [32]–[34]. Nonetheless, these types of DES systems are easier to design and manage, but the hybrid systems are more attractive because of their numerous advantages. The pros and cons of hybrid systems have been summarised and presented in Table 2-1.

Table 2-1. Pros and cons of hybrid renewable energy systems [109].

Pros	Cons
Complementarity of the RE sources helping to overcome individual weaknesses	Depends strongly on local weather conditions
Can utilise local grid networks, minimising cost of grid expansion	Increased complexity of the system with the increasing number of the sub-systems
More stable and can reliably match load demand	Lack of adequate knowledge for managing the system's operation

As can be seen in Table 2-1, HRES integrating more than one complementary renewable energy resources are more reliable and less costly, when compared to the earlier single renewable resource systems [110], [111]. Therefore, recent DES designs deploy a hybrid of green energy sources to match the electric load at the design location. Notwithstanding the improved reliability of HRES, back-ups are still required to minimise the mismatch between the electricity generation from these stochastic resources and the demand [105], [112]. Internal combustion engines (ICE), such as the DG, have been popularly deployed as the back-up in HRES and are in some designs combined with battery storage. There are also HRES configurations that deploy external combustion engines including the ST, ORC and MT or even fuel cells, as the back-up. Most HRES present different unique configurations depending on the available local resources [113].

Olatomiwa et al. [33] investigated different HRES concepts proposed to fulfil the electricity demands of some locations in Nigeria. They compared the net present

cost (NPC), cost of energy (COE) and renewable fraction (RF) obtained by deploying a stand-alone DG system, hybrid PV-DG system with and without battery and PV-WT-DG system with and without battery. It was remarked that the PV-DG-battery concept is the best HRES configuration for the location. Olatomiwa et al. [34] studied different HRES concepts to supply the electric load in some rural hospitals in Nigeria and reported that the PV-WT-DG-battery is the best configuration for most of the locations. Efunbote and Adeleke [114] proposed a hybrid wind and solar system for some locations in Nigeria. They reported that 86% of the total electricity demand was met by the solar PV, while the WT supplied the remainder. Diemuodeke et al. [27] compared the cost of electricity from different HRES concepts deployed to meet the electricity demand of some coastal communities in southern Nigeria and observed higher energy cost when a single resource (solar PV only and BSS) was deployed.

Several other deployments of different concepts of HRES have been presented for remote locations across the globe. Diaf et al. [15] proposed a hybrid solar and wind power system designed to handle a 3 kWh/day load requirement on the island of Corsica and observed that large storage capacity contributed to the increase in the levelised cost of the system. Kaabeche et al. [102] investigated a hybrid of PV, WT and BSS to match the electric load for a residential household in Bouzareah, Algeria. They observed cheaper energy costs with a reduction in the storage capacity of the battery. Belfkira et al. [47] proposed a hybrid WT-PV-DG and BSS configuration to match the 15 kW peak electric load demand of a location in Dakar, Senegal. It was found that the inclusion of battery storage resulted in a reduction in the total cost of the system, lower fuel consumption, and reduced DG operating hours compared to the configuration without battery storage. Bhakta et al. [115] designed a 1 kW hybrid WT and solar PV for an isolated hamlet of Northeast India. It was reported that the COE of this HRES ranges from 0.271 – 0.510 $/kWh and for these figures, the cost effectiveness can be achieved for such remote locations.

Bhaktar and Mukherjee [116] evaluated a solar PV only system with fixed tilt and two-axes tracking system intended for similar locations in India. Adaramola et al. [117] modelled a HRES that is comprised of solar PV-WT-DG and BSS for some locations in Ghana and found a COE of 0.281 $/kWh. Kraa et al. [118] proposed a HRES that

consists of WT, solar PV and battery storage systems. Maleki et al. [119] performed the cost optimisation of a grid integrated HRES comprising solar PV, WT, solar thermal collector and fuel cells and found the optimal system configuration. Xu et al. [120] proposed a stand-alone HRES that integrates solar, wind, hydro-power as the energy sources and determined the optimum system configuration. Anwari et al. [121] studied the design of hybrid solar PV and DG for locations in Malaysia. They concluded that the micro-grid system contributed to the reduction in the total emissions when compared to the base case (diesel generator only system).

Other notable HRES concepts are: Ismail et al. [40] that employed a MT as a back-up source for their energy system designed for a remote community in Palestine; Nfah and Ngundam [122] that modelled wind and solar hybrid system for a location in Cameroon; Giannoulis and Haralambopoulos [41] that studied the impact of introducing micro-grid systems to provide electric power to the Lesvos island in Greece; Patel and Singal [123] that proposed deploying a generator fired by biomass fuel from wheat straw, mustard stalks and fuel wood and biogas from animal dungs as the back-up in a WT-PV HRES concept designed for a village settlement in India; and Ghaem Sigharchian et al. [124] that investigated the feasibility of deploying biogas driven gas engine as a back-up for a solar PV-WT system designed for the Garissa community in Kenya.

2.2.2. Cogeneration decentralised energy systems

One of the simplest DES concepts that has been widely studied and deployed to meet local energy demand is the cogeneration of heating and power in a combined heating and power system (CHP). The other concept that is not so popular is the cogeneration of cooling and electricity in a combined cooling and power system (CCP). These cogeneration energy systems (CHP or CCP) utilise a single source of fuel to co-produce useful energy vectors in the form of electricity and cooling or heating, simultaneously. They deploy different prime movers to generate electricity and integrate a water boiler (or a thermal chiller) fired by the waste heat from the prime mover to produce hot water (or cooling). With the deployment of CHPs, global efficiency typically in the range of 40-50% or even higher can be attained in a DES [89]. The other environmental and economic benefits of CHPs deployment are

reductions in emissions and primary energy utilisation. These types of DES are making strong inroads into the European energy mix in recent times [35], [36].

2.2.2.1. Single prime mover cogeneration systems

Several authors have deployed sole prime movers to drive the power and cooling or heating generation from cogeneration DES. Fig. 2-2 is an example of a CHP system driven by ST. It is seen that flue gas is produced from the combustion of fuel in the combustor. It then supplies the thermal energy needed in the ST, before driving the production of hot water in a boiler. This is the traditional and ubiquitous cogeneration concept in the literature.

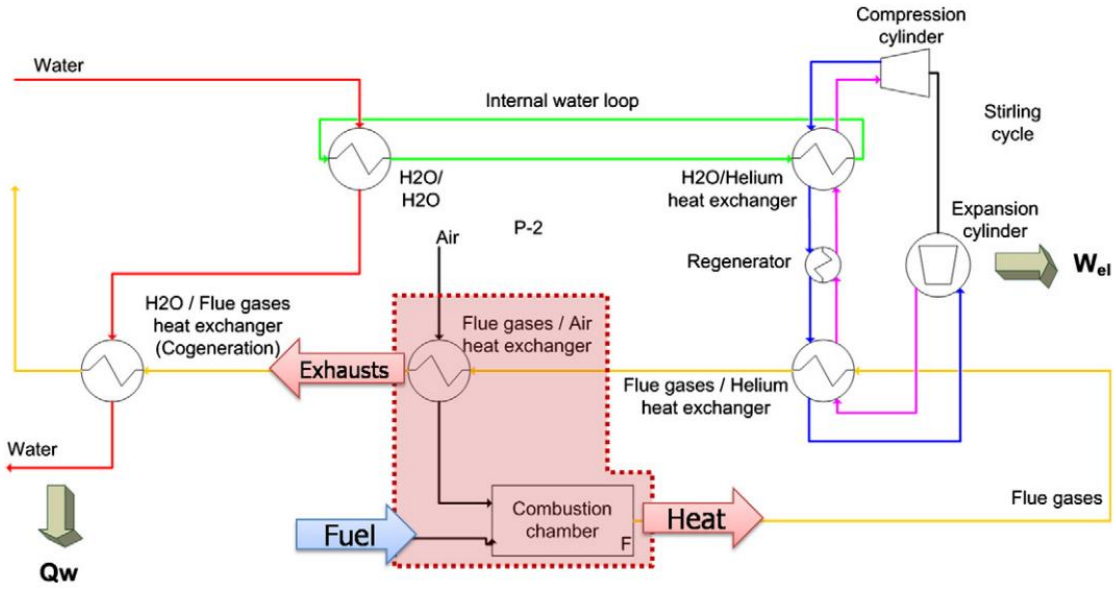

Fig. 2-2. Schematic of a Stirling engine driven combined heating and power system [54].

Parente et al. [54] experimentally investigated the ST driven micro-CHP system configured in Fig. 2-2, that is powered by a flameless combustion technology. These authors focused mainly on the burner flame characterisation with the change in the concentration of hydrogen in the fuel, in order to understand the operating temperature regime of the system.

Renzi and Bradoni [36] proposed a biogas fuel powered micro-CHP driven by a regenerative ST. The authors recuperated the waste flue gas to preheat the combustion air and achieved a raise in the electrical efficiency of the prime mover to 22.5%. Ghaebi et al. [125] examined the design and optimisation of a novel CCP

system deploying the Kalina cycle to produce power while cold energy is produced by the ejector refrigeration cycle. The authors found the optimum design parameters of the system by simultaneously optimising the energy and exergy efficiencies and the sum unit cost of the product and reported optimum results of 20.4%, 16.69% and 2466.35 $/MWh, respectively.

Gonzalez et al. [90] modelled a ST based micro-CHP to supply the electricity and hot water demand of a residential house in three locations in Spain. Asaee et al. [126] proposed an ICE driven micro-CHP for deployment in Canadian houses and observed 10% reductions in greenhouse gas (GHG) emissions and 20% savings in the primary energy. Similarly, Abbassi [127] developed a joint numerical and technical model for predicting the performance of an ICE driven micro-CHP. Ferreira et al. [128] designed a CHP system driven by solar-powered ST for small scale applications. The authors found the optimal configuration of the system by optimising its annual worth.

Some research efforts have been focused on biomass powered CHPs for small scale application. The deployment of biomass could help reduce GHG emissions from the system and maximise the utilisation of the onsite available energy. Therefore, some researchers examined the effect of different biomass feedstocks on the performance of micro-CHPs. Cardozo and Malmquist [129] investigated the impact of fouling of the heater on the performance of a ST driven micro-CHP plant that is fired by bagasse and wood chips. They found that the system produced comparable power outputs for both biomass fuels, although lower CHP efficiency is observed with bagasse pellets compared with woodchips, because of the higher ash content of the former. Damirchiet al. [130] experimentally examined the technical viability of using bagasse, pruned wood, poplar, switchgrass and sawdust to fire a gamma-type ST driven micro-CHP plant. It was remarked that saw dust produced the most electrical power because of its high calorific value, while pruned wood offered the least power.

2.2.2.2. Multiple prime mover cogeneration systems

The utilisation of two or more prime movers to supply the electric power in a cogeneration DES has been undertaken. In this concept, one of the prime movers

serves as the main driver (topping cycle), while the other prime mover(s) is the bottoming cycle that is driven by recovered waste heat from the former. Fig. 2-3 depicts a dual-prime mover CHP, where solid-oxide fuel cell (SOFC) serves as the topping cycle and ST the bottoming cycle. As Fig. 2-3 illustrates, waste heat from the SOFC is recovered to fire the ST and produce additional power, while the heat rejected from the ST serves as the thermal energy for the direct heating of the room. This concept helps to improve the electrical efficiency of the system [58] and has been receiving some attention in the literature.

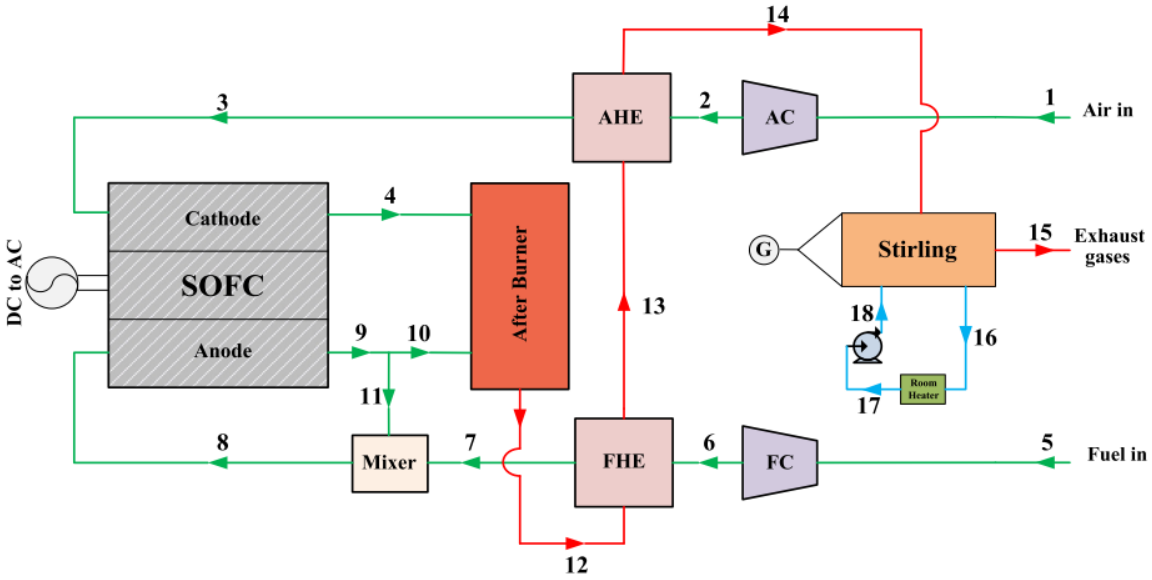

Fig. 2-3. Schematic of the SOFC-ST dual prime mover combined heating and power system [60].

Chitsaz et al. [60] proposed the system described in Fig. 2-3. They remarked that the deployment of the ST as the bottoming cycle to the FC, raised the thermal efficiency of the SOFC by 24.61%. Balakheli et al. [131] proposed a CHP driven by a combined cycle of DG and ST bottoming cycle, and powered by the waste heat recovered from the former.

Rokni [132] deployed a SOFC in combined power mode with a ST to fire a micro-CHP system designed to supply electric power and hot water to an average family home. It was found that the electrical efficiency of the stand-alone SOFC improved by 10% with the recovery of the waste heat in the ST bottoming cycle. Similarly, Rokni [133] examined the performance of a small scale CHP system driven by a combined cycle

comprised of municipal solid waste (MSW) powered SOFC topping cycle and ST bottoming cycle and realised 50% increase in the electrical power.

Mehrpooya and Sharifzadeh [134] investigated a cogeneration concept where a combined electric power is generated from a SOFC, CO_2 oxy-fuel cycle and steam turbine, while liquiefied natural gas (LNG) is vaporised to provide the cold energy. It was observed that the efficiency of the system improved significantly with the deployment of LNG as the cold energy and the cold source. Mahmoudi et al. [135] proposed a CCP comprising a hydrogen fed SOFC, a gas turbine and a thermal chiller and conducted an energy and exergy audit of the system. The authors found the exergy efficiency of the system improved by 6.5% compared with a stand-alone SOFC system.

Diomudeke et al. [136] proposed a DES concept that integrates a gas turbine, steam turbine, SOFC, ORC and absorption chiller to simultaneously produce power and cooling from agro-wastes, in a farm settlement. The authors performed a 4E (energy, exergy, economic and environmental) analysis of the plant based on thermodynamic models and obtained energy and exergy efficiencies of 63.62% and 58.48%, respectively. Saneye and Katebi [137] evaluated the energy, exergy, economic and environmental performance of a small scale CHP that is fired by a micro-turbine integrated to a SOFC bottoming cycle. They obtained the optimal system configuration by conducting a multi-objective optimisation of the exergy efficiency and total system cost. Although numerous cogeneration DES concepts utilising single and multiple prime movers have been extensively proposed by previous researchers, the primary energy utilisation of this DES concept could be enhanced if the waste heat is recovered to produce additional energy vectors such as cooling.

2.2.3. Tri-generation decentralised energy system

In a more complex concept of DES, several energy system components are integrated to simultaneously generate cooling, heating, and power. The tri-generation of energy vectors is achieved in a combined cooling, heating and power (CCHP) system. Here, a fraction of the waste heat from the prime mover is deployed to fire a waste heat boiler to produce hot water and the remainder is sent to a

thermal chiller, to produce cooling. By this arrangement, technical, economic and environmental benefits are realised in the form of improved energy and exergy efficiencies, savings in primary energy and reductions in emission, respectively [88]. Several CCHP system concepts have been proposed in the literature which are driven by different prime movers.

2.2.3.1. Single prime mover tri-generation system

The initial efforts to develop a tri-generation system mainly focused on systems deploying one prime mover to drive the simultaneous generation of cooling, heating and power as depicted in Fig. 2-4. It is seen that an ICE serves as the sole prime mover in this tri-generation concept to provide electric power. Also, waste heat is recovered from the exhaust gas to produce cooling in an ejector refrigeration system, while additional waste heat is extracted from the water jacket of the engine to produce domestic hot water. The review of the studies of tri-generation systems formulated based on this concept is presented. Javan et al. [138] analysed the performance of the micro-CCHP proposed in Fig. 2-4. Also, they tested different working fluids for the operation of the ORC and found R-11 as the best refrigerant.

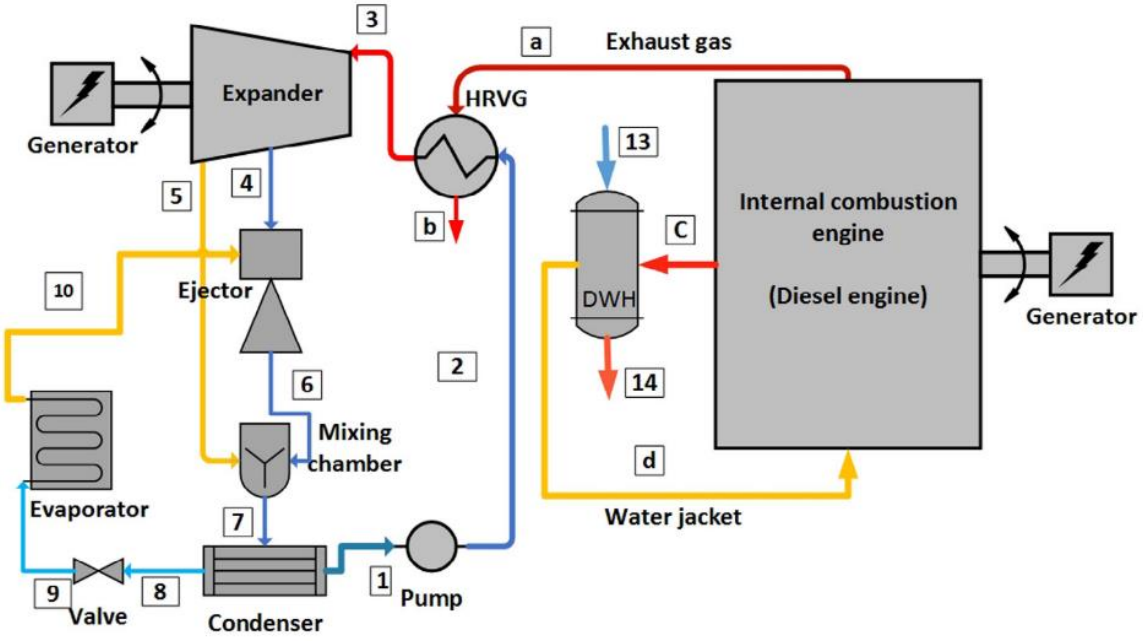

Fig. 2-4. Schematic of a tri-generation system driven by an internal combustion engine to co-produce cooling, heating and power [138].

Chahartaghi and Sheykhi [56] compared the energy, exergy, environmental and economic performance of a Stirling engine driven CCHP system working with hydrogen and helium gases. They formulated models to assess the primary energy savings (PES), CO_2 emissions reduction (CO_2ER) and fuel consumption reduction of the system compared with traditional separate cooling, heating, and power (SCHP) systems. It was observed that the proposed CCHP performed better than the conventional separate cooling, heating, and power systems especially at low and medium speeds of rotation of the prime mover and for the engine working with hydrogen gas.

Rokni [139] evaluated the feasibility of deploying municipal solid waste (MSW) to power a tri-generation system. In this system configuration, syngas is produced from the gasification of the MSW to drive the generation of electricity in the SOFC plant. Also, the waste heat from the SOFC is recovered for cooling generation in a thermal chiller and for domestic heating. The authors obtained an efficiency of 74.5% for the base case and 86.8% for the optimised system. Additional results show that the electrical efficiency of the proposed system increases by increasing the moisture content of the MSW fuel.

Similarly, Chahartaghi et al. [57] modelled a CCHP energy system comprising two beta-type ST, a single effect absorption chiller and a domestic water heater. They investigated the PES and CO_2 ER of the system as a function of some of the operating and geometrical parameters of the engine. It was observed that PES and CO_2 ER were enhanced by 29.47% and 36.22%, respectively compared with the conventional separate energy generation systems.

Braimakis and Karellas [140] investigated the performance of an ORC driven DES that switches from tri-generation mode in winter to cogeneration mode in summer. In addition, the DES utilises a combination of biomass boiler and parabolic trough collector (PTC) as the primary energy for powering the prime mover. The authors examined the impact of the waste heat recuperation and superheating of the working fluid on the performance of the system and noted that it does not yield a significant increase in the system's efficiency. Karami and Sayyaadi [141] evaluated the techno-enviro-economic performance of a Stirling engine driven CCHP system

in four different locations with distinct climatic conditions. They disclosed cost savings in most locations using the proposed system, with the exception of one location characterised by extremely hot and humid weather.

Ebrahimi and Derakshan [142] presented a CCHP energy system concept that utilised the proton exchange membrane fuel cell (PEM FC) as the prime mover. The waste heat from the PEM FC is recovered by a heat recovery boiler and thermo-electric cooler to improve the primary energy utilisation. They conducted energy and exergy audit of the system and obtained overall efficiency and PES of 76.94% and 43.25%, respectively. Also, it was found that exergy is destroyed predominantly in the fuel cell and system exergy efficiency of 53.86% was reported.

Charhartaghi and Kharkashi [143] modelled a micro-CCHP that deployed a PEM FC as the prime mover. Further, an absorption chiller and water heater were deployed for combined generation of cooling and heating, respectively. The authors obtained energy, exergy and fuel energy saving ratios of 81.55%, 54.55% and 45%, respectively from the numerical investigation. Kaldehi et al. [144] modelled an alpha-type ST driven small scale CCHP system for residential sectors of different climates. Also, the authors determined the optimum size of the system in the electrical and thermal load following modes and based on the overall efficiency. They obtained overall efficiency of 54% from the tri-generation system and 40% reduction in CO_2 emissions.

Mago [145] investigated the performance of a biomass fuel energised CCHP driven by a ST operating at constant efficiency, and meeting constant thermal heat load. It was reported that about 50% cost savings could be achieved with the system when using wood chips compared with using natural gas. Ebrahimi [146] examined the potentials in deploying a natural gas fired GT for combined production of cooling, heating, and power and realised more than 30% savings in the primary energy compared with a GT only system.

2.2.3.2. Multiple prime movers tri-generation system

In the recent designs of tri-generation DES, two or more prime movers have been deployed to increase the power generation and consequently, improve the electrical efficiency of the system. Here, the waste heat from the topping cycle is recovered

to power the bottoming cycle. Fig. 2-5 depicts a tri-generation system that runs on a single primary energy to produce combined power from a molten-carbonate fuel cell (MCFC), ST and GT. As Fig. 2-5 indicates, natural gas is the input fuel to this energy system. It is steam-cracked to produce the hydrogen fuel required in the MCFC, while the other by-products are combusted in the combustor with the oxygen produced from the cathode of the MCFC, to produce the flue that drives the GT. The waste heat produced from the MCFC powers the heater of the ST, whereas additional waste heat is recovered from the ST cooler to produce cooling in a thermal chiller. Finally, steam is produced for domestic heating from the waste flue before going to stack. This tri-generation concept has been modelled by a few authors in the literature.

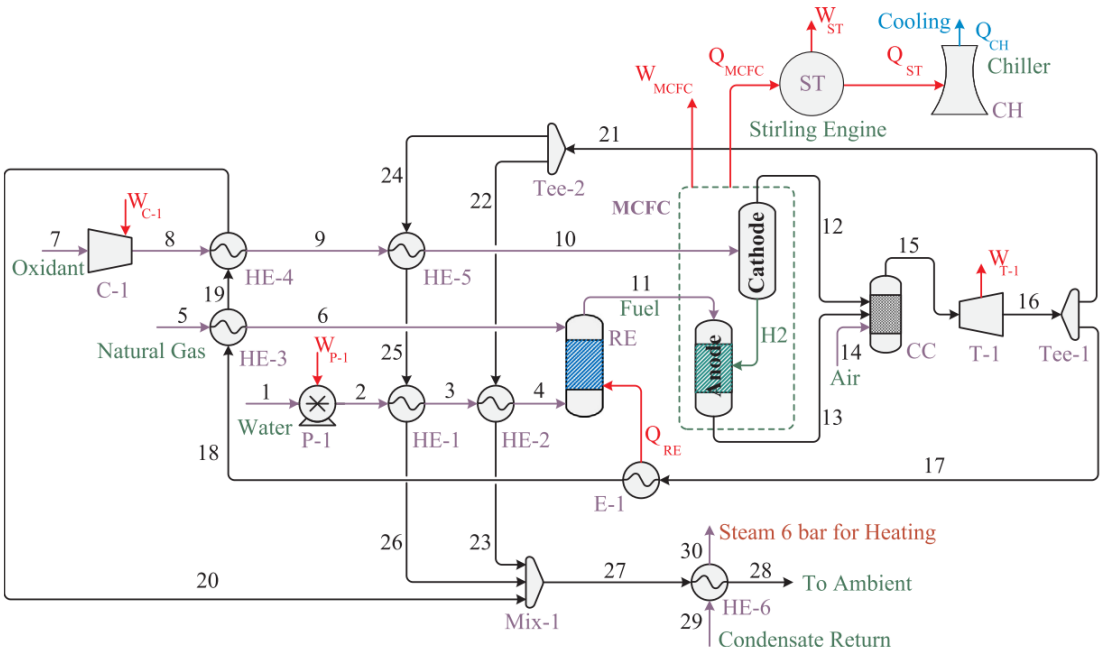

Fig. 2-5. Schematic of a typical tri-generation system deploying multiple prime movers to produce cooling, heating and power [147].

Mehrpooya and Ansarinasab [147] performed the exergy audit of the novel CCHP system shown in Fig. 2-5. The authors found the CCHP components' contribution to the avoidable and unavoidable exergy destruction and recommended three strategies to decrease the system inefficient cost rate.

Al-sulaiman et al. [148] performed an exergy-based analysis of a dual prime mover fired micro-CCHP system. This study deployed the SOFC as the main prime mover

of the DES, whereas the ORC powered by recovered waste heat serves as a bottoming cycle. Additional waste heat is recovered from the ORC to drive the heating and cooling systems. It was found that an overall efficiency of 74% can be achieved in this tri-generation system compared with an electrical efficiency of 46% obtained for the combined SOFC and ORC system. Mehrpooya et al. [149] conducted an energy and exergy audit of a CCHP system powered by a MCFC in combined power generation with a ST bottoming cycle. It was reported that the highest exergy destruction was observed in the combustor, while electrical and overall efficiencies of 42.28% and 71.71%, respectively were recorded.

It is clear that significant improvements in the technical, economic and environmental metrics are achieved with this DES concept. Nonetheless, the obtained results particularly of the exergy efficiency suggest that further improvements in the system performance is plausible, and this could be realised by minimising the avoidable exergy destruction.

2.2.4. Multi-carrier decentralised energy system

The latest trend in decentralised energy systems is the concept of a multi-carrier energy system. This emerging energy system concept that is capable of producing many energy vectors and other useful goods has been defined in Section 1.2. Fig. 2-6 represents a multi-carrier DES that utilises solar energy to produce cooling, heating, power, hydrogen, fresh water and hot water [150]. As Fig. 2-6 illustrates, a combination of solar PV/T and solar collectors were deployed to harvest the thermal energy to deployed to drive the production of electricity and cooling on one hand, and on the other hand, the production of electricity, fresh water, hot water and hydrogen. Multi-carrier energy systems unarguably, further enhances the utilisation of the available energy and would result in reduced exergy destruction. Similar DES system concepts have been previously studied and are presented herein.

Ahmadi et al. [150] proposed the multi-carrier DES system concept described in Fig. 2-6 and developed thermodynamic models of the subsystems of the DES to conduct its energy and exergy audits. They also conducted the design optimisation of the system and found a maximum exergy efficiency of 60%.

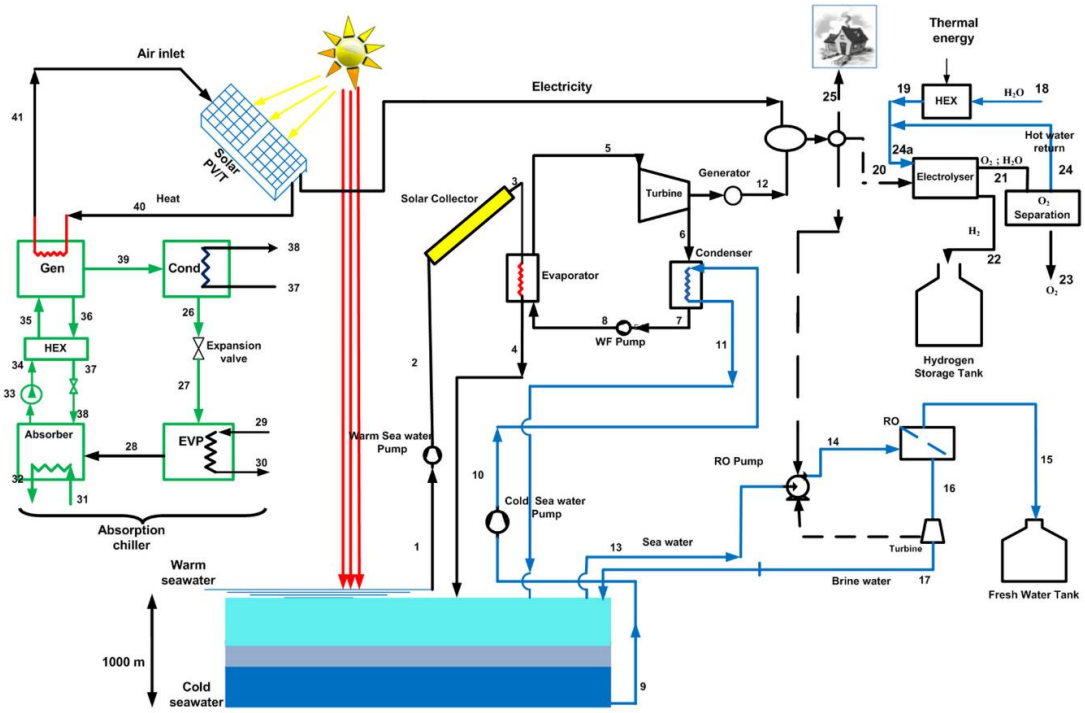

Fig. 2-6. Schematic of renewable-based multi-carrier energy system for generating heating, cooling, power, hydrogen, fresh water and hot water [150].

Mehrpooya and Mohammadi [151] proposed a multi-carrier DES that extracts thermal energy from a geothermal source, to drive a steam turbine. The expanded steam supplies the heat input to the vapour generator of the Kalina cycle; to co-produce power and cold energy and to the hot water boiler. The proposed system integrates a reverse osmosis water desalinator. They conducted parametric studies of the system and observed that higher temperature difference in the vapour generator raises the exergy efficiency of the system.

Boyaghchi and Safari [70] formulated a new DES concept that deploys a geothermal source and LNG as the heat and cold energy sources, respectively, to produce cooling, heating, power and hydrogen. An ORC serves as the prime mover in this multi-carrier system design to produce electricity, while a PEM electrolyser will produce hydrogen and the cooling is produced from the LNG. They conducted multi-objective optimisation of the system to improve its performance and observed improvements in the avoidable cost rate by 17.4% compared to the base case.

Ahmadi et al. [152] carried out an energy, exergy and environment based multi-objective optimisation of an integrated DES. This study integrated a micro-turbine, PEM electrolyser, ejector refrigeration cycle, absorption chiller, dual pressure heat

recovery steam generator and domestic water boiler to produce power, heating, cooling, hot water and hydrogen. The authors also performed parametric studies to investigate the effect of key parameters on the systems performance and found that an increase in the steam turbine isentropic efficiency, results in a corresponding increase in the exergy efficiency.

Agnew et al. [62] developed a new multi-carrier DES concept that utilises a solar PTC powered ORC to produce cooling, heating, power and fresh water. In the absence of solar power, a biomass burner is deployed to supply the heat input to the ORC, while the working fluid of the ORC powers the absorption chiller and desalination plant in a condenser/evaporator arrangement. They formulated thermodynamic models to conduct the energy and exergy analyses of the proposed system. It was found that the proposed system configuration yields an exergy efficiency of 41.7%, while additional results highlight that the solar collectors are the most inefficient energy components in the system.

Nonetheless, while significant improvements in the technical and economic performance of multi-carrier energy systems are noticeable, the fact that some of these systems deploy fossil fuel powered prime movers affect their environmental performance. Hence, the need to formulate new system concepts that will reduce the emissions from the aforementioned DES configurations.

2.2.5. HRES integrated decentralised energy systems

The other concept being deployed to achieve a remarkable reduction in the GHG emissions of DES is the utilisation of HRES to supply primarily the electricity need of the consumers. Then, a back-up driven by thermal energy from green energy sources or fossil fuel is deployed to produce the complementary energy vectors and other useful goods. This energy system is called a HRES integrated DES and could be a HRES-CCHP, HRES-CCP or HRES-CHP DES concept [101]. It is expected that by this integration, the need to deploy fossil fuels to augment the reliability of DES will be minimised. However, the unpredictability of most renewable energy resources may pose new challenges in the control and management of the system.

Fig. 2-7 represents a hybrid wind and solar system integrated into a CHP plant and designed to produce energy vectors such as cooling, heating and power and other

goods such as clean water, wood chips and ice blocks. Mazzola et al. [37] proposed the multi-good DES concept that is illustrated in Fig. 2-7. They formulated mathematical models to optimise the operation of this complex integrated DES and conducted hourly simulation of the operation of the system.

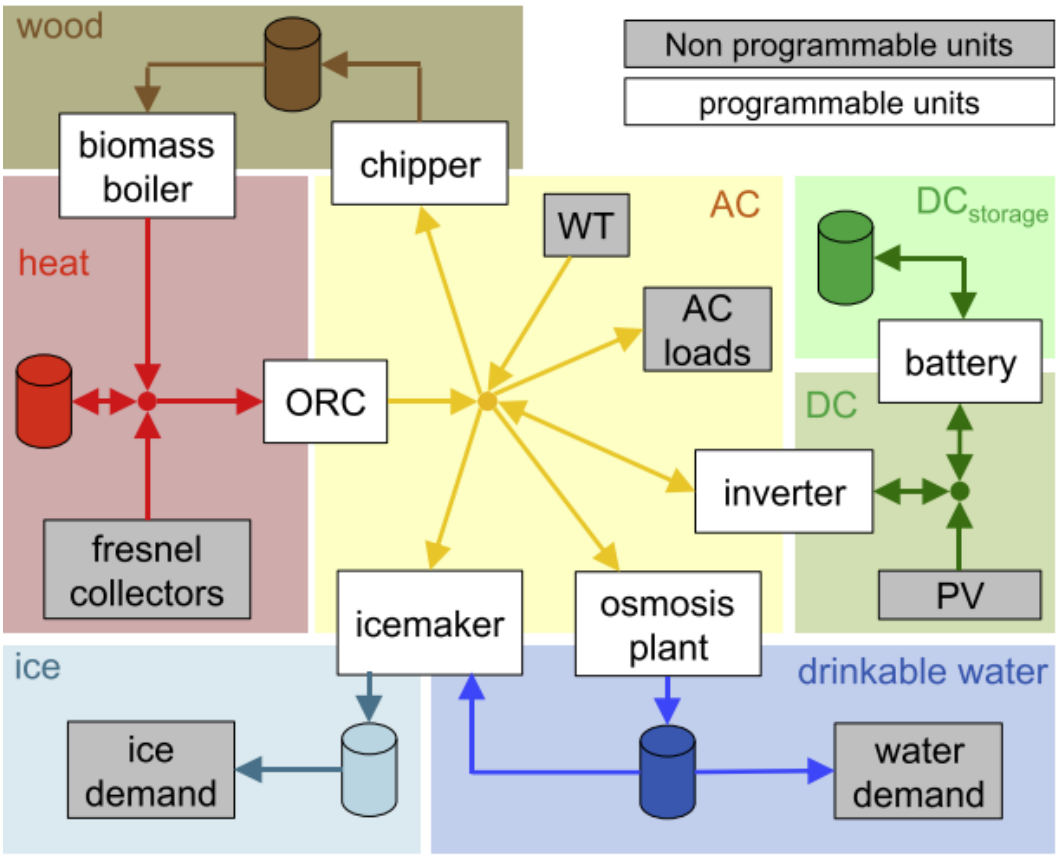

Fig. 2-7. Schematic of HRES integrated decentralised energy systems producing many different goods [37] .

Bracco et al. [153] formulated mathematical models to optimise the real-time operation of a HRES integrated DES comprising PV, CSP driven ST, MT, absorption chiller, electric vehicles and many forms of energy storage devices. They also built a test-bed in the university of Genova Savona campus in Spain to validate the developed models and study the behaviour of the DES. It was observed that the emissions and operational costs of the HRES integrated DES reduced after its optimisation. The authors recommended further works on the decentralisation of the control architecture of the DES. However, HRES integrated DES concepts have only been proposed by a few researchers and will require further studies to obtain deeper insights into its technical, economic and environmental performance.

2.3. Modelling and simulation of decentralised energy systems

The modelling of decentralised energy systems is pivotal to the design and optimisation of the system. Modelling supports the detailed understanding of the behaviour of energy systems and components when in operation and is an important tool in decision making [39]. However, a modelling effort is rated by the accuracy of the model and the amount of resources it consumes, which is an estimation of the complexity of the model. It is, therefore, important to ensure a reasonable trade-off in the accuracy and complexity of a developed model. Several efforts have been made to develop accurate models to predict the performance of the components of DES in the literature. These efforts are either experimental or theoretical and have been useful in understanding the characteristics of system components and studying their behaviour. In the following subsections, a review of modelling efforts undertaken on HRES components, prime movers, and other subsystems of DES are presented.

2.3.1. Hybrid renewable energy systems modelling

Several models have been developed to simulate the performance of renewable energy generators in literature. Bhandari et al. [39] reviewed the mathematical modelling of HRES systems and presented models for simulating the generation and storage of power in the WT, PV and battery storage. By treating the PV array as a single-diode and double-diode containing several cells connected in series and parallel, the authors formulated a model for predicting the characteristics of a PV module. The ambient temperature and solar irradiation are the main input variables required by this model. Fig. 2-8 presents the predicted results from the PV model developed in this work and it shows the variation of the PV cell current, voltage and power for different solar irradiation.

Also, the authors presented a model based on the rated power of a wind turbine that can be used to simulate its power generation. This model depends on the cut-in speed, cut-out speed and rated speed of the turbine as well as the wind speed and Weibull shape factor in the test location to simulate the turbine power. Finally, they presented models of the battery required to determine its storage capacity, charging and discharging time and predict the available energy in the battery.

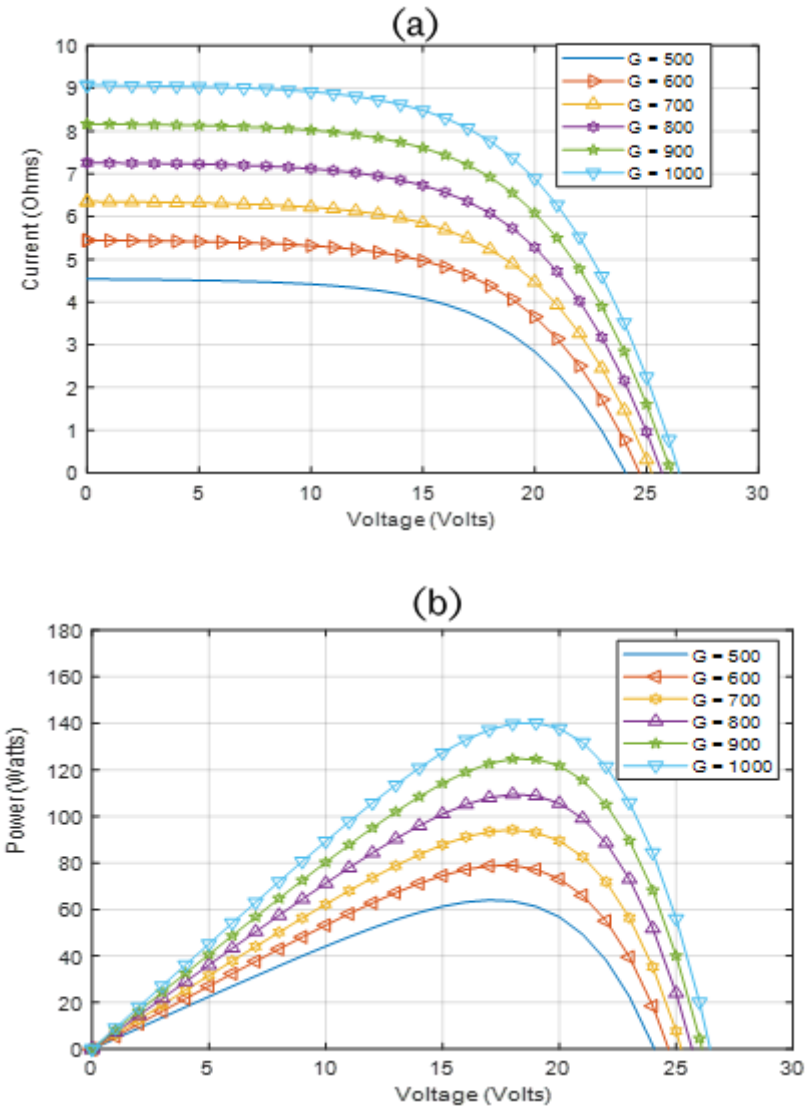

Fig. 2-8. Solar cell model predicted results of (a) current against voltage and (b) power against voltage.

Dufo-lopez et al. [80] compared different models deployed in HRES simulations for predicting the life of a lead-acid battery. In this study, the weighted Ah (Ampere hour), Schiffer, KiBaM and simplified Copetti models which estimate the voltage and state of charge (SOC) of batteries were compared. Additionally, three battery ageing models were compared and they found that the Schiffer weighted Ah model predicts the battery life more accurately. Dufo-lopez et al. [154] improved the prediction accuracy of the Ah battery ageing model by coupling the battery stress factor based on the operational environment into the original model. With this model, the effects of degradation and corrosion on battery capacity over the battery life can be evaluated accurately.

2.3.2. Modelling of prime movers of decentralised energy systems

In Section 2.2, the prime movers that have been deployed to drive DES were discussed. Considering the technological readiness level (TRL), emissions reduction, safety issues and the temperature of the heat sink, the ST and ORC are the most promising prime movers for application in DES. Therefore, this review will focus on the efforts made to model the ST and ORC in the literature.

2.3.2.1. Thermodynamic modelling of the Stirling engine

Although the invention of the Stirling engine occurred in 1816 by Robert Stirling [155], the study and subsequent unveiling of the thermodynamic principles guiding its operation was undertaken several decades later [51]. Fig. 2-9 represents the working cycle of the ST reported by Poruba and Podesva [156]. As Fig. 2-9 indicates, the main components of the engine are the regenerator, cooler, heater, transfer piston, power (working) piston, compression and expansion cylinders, and the drive mechanism. This engine is similar to the Carnot engine, as it operates between two heat sources: a heat source and a heat sink.

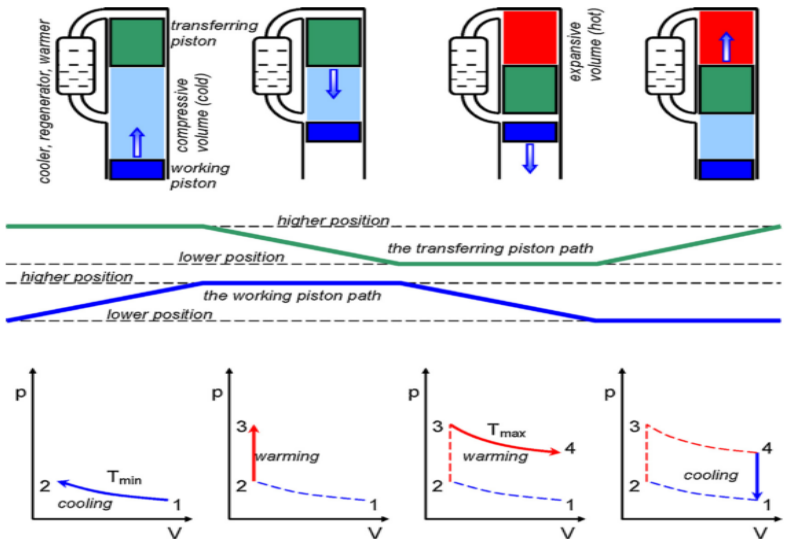

Fig. 2-9. Working cycles of an ideal Stirling engine presented on a thermodynamic plane [156].

In theory, an ideal ST is expected to deliver the maximum possible thermodynamic efficiency for a heat engine [51]–[53], [157]. However, this feat is impracticable due to design imperfections and other irreversibilities. By comparison to the Diesel and

Otto engines, the ST is an external combustion engine, and as a result, has the advantage of being able to utilise many energy sources including biomass, fossil fuels, solar energy, and geothermal sources [36], [51]–[53].

Wang et al. [158] reviewed ST for recovering low and moderate temperature heat energy. According to these authors, ST are classified based on the arrangement of the pistons and the drive systems. Based on the arrangement of pistons, they can be alpha, beta or gamma-types ST. On the other hand, based on the drive system, ST are broadly classified as kinematic, thermo-acoustic, free piston and liquid piston types. Kinematic ST are driven by kinetic drive systems such as the crank-slider mechanism (see the examples in Fig. 2-10), while thermo-acoustic types operate based on the principle of wave motion and are also called acoustic wave drive system ST [158]. Free piston and liquid piston ST are driven by piston-spring mechanisms and liquid columns, respectively. It was recommended to utilise the low temperature difference (LTD) beta-type ST with a kinematic drive mechanism for harvesting electrical energy from biomass sources.

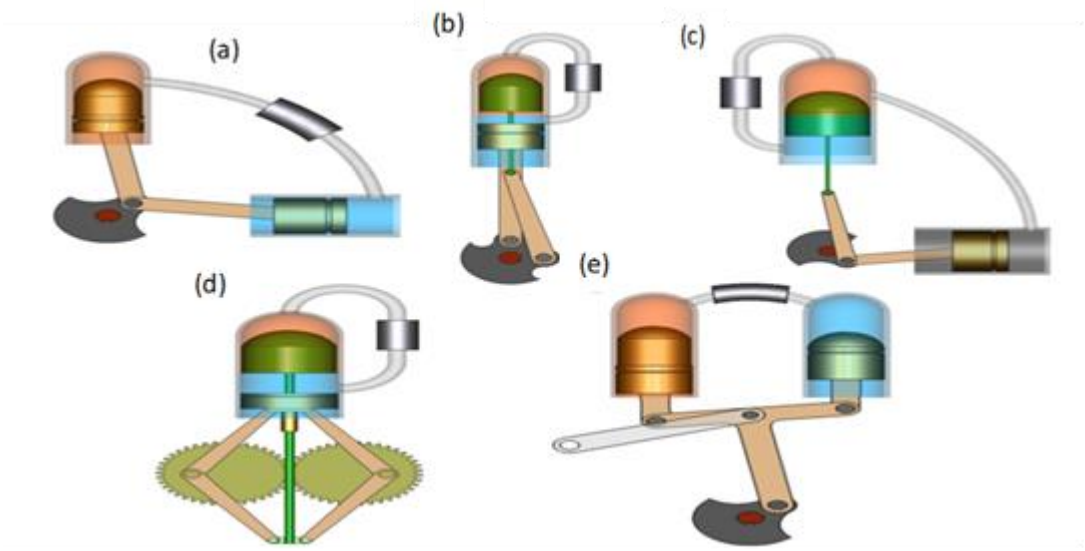

Fig. 2-10. The Stirling engine configurations (a) α – type with crank drive (b) β – type with crank drive (c) γ – type with crank drive (d) β – type with rhombic drive and (e) α – type with Ross yoke drive [159].

Prior to the design of a ST, the thermal model capable of predicting its performance must be developed. So far, the thermal analysis of ST has been undertaken using empirical, analytical and numerical models [160]. Furthermore, based on the depth

of the analysis, the models deployed to predict the engine's performance are classified as zero-order, first-order, second-order, third-order and fourth-order models [161]–[163]. In the zero-order modelling of the ST, the engine performance is determined empirically by considering the overall size of the engine, whilst the first-order models are mainly closed form analytical models [162]. The second, third and fourth-order models on the other hand, are numerical models with increasing level of accuracy respectively, but requiring much computing time [163].

Since the first attempt was made to develop a first-order model to predict the performance of the ST by Schmidt in 1871 [155], several other endeavours have been explored to improve on Schmidt's model. So far, most of the models developed are majorly of the second-order, where pressure drop, thermal losses, hysteresis losses and shuttle losses in the engine components are accounted for, whilst treating the thermodynamic processes as ideal processes [157].

2.3.2.1.1. Zero-order Stirling engine models

The preliminary design of ST has been undertaken using zero-order models. Wongwises and Kongtragool [164] compared the correlations for determining the power produced by the gamma-type low temperature differential (LTD) ST. They concluded that the Schmidt's and West formula are difficult to use when compared to the combination of the Beale number and mean pressure formula. The authors recommended the mean pressure formula for the quick design of the gamma type ST, to determine its power output. In the literature, several other zero-order models of the ST have been presented [159], [164]–[167]. These authors deployed dimensionless numbers [165], and other empirical correlations to predict the performance of ST, mainly as a function of some of the operating variables of the engine including, cycle mean pressure, piston displacement volume, temperature ratio and the speed of the engine.

The predicted results were useful in estimating the power output and first Law (thermal) efficiency of the experimental engine, for the range of operating parameters defined in developing the models. Regardless, the zero-order models developed in the literature over-predicts the performance of the experimental engine. Hence, these models are only suitable for the quick design of ST [164]. Other

limitations of the zero-order models are its inability to describe the detailed processes occurring in the engine, and relate the geometrical parameters of the engine to its performance.

2.3.2.1.2. First-order Stirling engine models

Several analytical models have been developed in the literature to predict the performance of ST. Schmidt [168] pioneered the formulation of analytical models for simulating the behaviour of the ST, based on isothermal analysis. He assumed isothermal conditions for the thermodynamic work processes in the engine. The Schmidt model could reveal the overall pressure in the main components of the engine. Nonetheless, it overestimated the performance of the prototype engine (by 30 – 60%), since isothermal processes can only be achieved in practice using an infinite heat transfer surface.

Martini [169] improved on the Schmidt model by coupling the internal irreversibilities in the regenerator and other heat exchangers, to the isothermal model. This model accounted for the imperfect regeneration and some of the heat losses in the engine. Other researchers deployed modelling tools based on classical thermodynamics, such as the finite-time thermodynamics (FTT) [170], [171] and the finite-speed thermodynamics (FST) [172]–[176] to model the time-invariant performance of ST. The FST modelling approach gave better results than the FTT approach and this is because both internal and external irreversibilities were considered in the former while the latter only considered external irreversibilities.

Although analytical models for predicting the performance of ST are usually easy to implement, reducing the complexity and the computational costs associated with higher order models [177], these models accuracy are limited because of the assumed isothermal processes. In addition, analytical models do not relate the engine's main design parameters to its thermal performance metrics.

2.3.2.1.3. Non-ideal Stirling engine second-order models

Second-order modelling approach of ST was deployed for the first time by Finkelstein [66], based on isentropic work processes in the compression and expansion spaces of the engine. Urieli and Berchowitz [65] pioneered the development of a computer based code to implement the numerical solutions of the

Finkelstein adiabatic model. They further improved on the Finkelstein model by accounting for some irreversibilities in the engine, in what is called the Simple analysis. They divided the engine into five main control volumes (see, Fig. 2-11 and Fig. 2-12) and conducted a mass and energy balance at the ingress and egress of these control volumes. The resulting differential equations, linking the engine's geometrical parameters and the physical properties of the internal gas to its thermal performance indicators, were solved using the fourth-order Runge-Kutta numerical scheme.

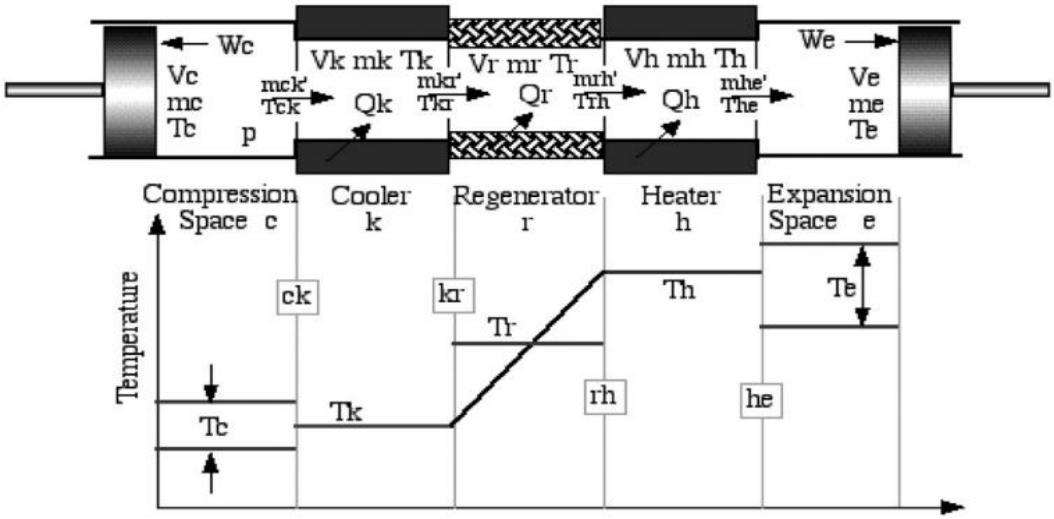

Fig. 2-11. Stirling engine control volumes [157].

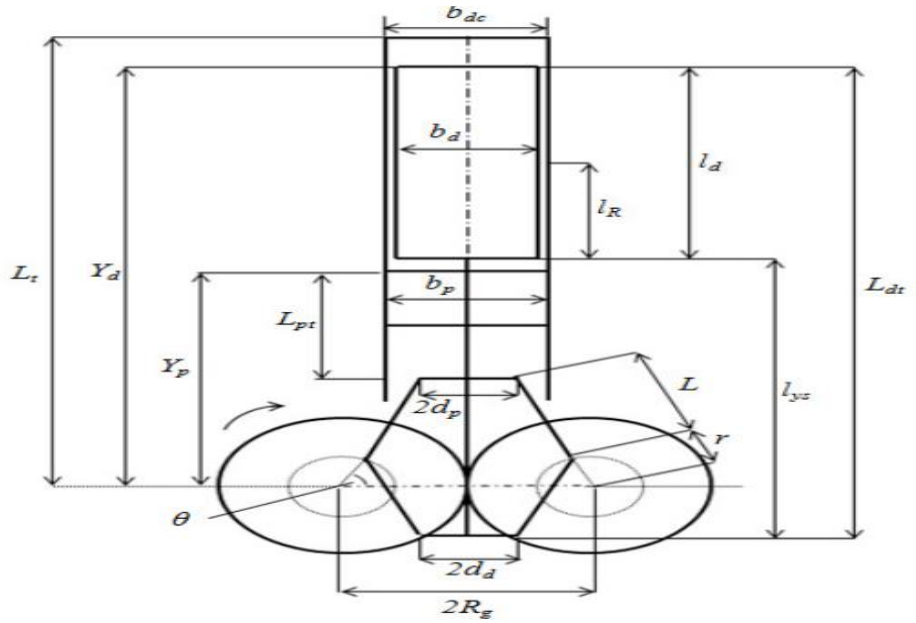

Fig. 2-12. Schematic diagram of the beta-type Stirling engine with rhombic drive mechanism [157].

Table 2-2. Improved second-order models of the Stirling engine.

Author(s)	Model type	Losses considered		Experimental engine	Key findings
		Heat losses	Work losses		
Timoumi et al. [178]	Adiabatic	Considered losses due to energy dissipation, external and internal conduction, shuttle effect.	Spring hysteresis losses.	3 kW beta-type GPU-3 engine.	Model prediction accuracy of engine thermal efficiency improved by 39.5% compared to Ref. [65] but over predicted experimental data by 35 %.
Cheng et al. [179]	Numerical	Heat loss due to imperfect regeneration.	Work loss due to pressure drop in the heat exchangers and forced shaft work.	0.3 kW beta-type engine	Numerical model predicted the engine's shaft power by 12–20% more than the experimental results, whilst the thermal efficiency of the engine obtained from the numerical model was 4.2%

					higher than that of the latter.
Alfarawi et al. [180]	Non-adiabatic	Considered losses due to shuttle effect, conduction in the heat exchangers, and imperfect regeneration.	Accounted for pressure drop and forced work in the piston losses.	Gamma-type engine.	Model over predicted the engine's power and efficiency by 15%, although this value varied, as expected with the hot end (heater) temperature
Babaelahi and Sayyaadi [181]	Non-adiabatic	Coupled the shuttle heat loss and longitudinal conduction through the wall of the regenerator into the thermal model and were accounted for at the end of each cycle.	Considered work losses due to mass leakage into the buffer space, variation in the working pressure around the piston and mechanical friction.	3 kW beta-type GPU-3 engine.	Model predicts output power and efficiency of the experimental engine as a difference of 20.7% and 7.1%, respectively.
Babaelahi and Sayyaadi [67]	Polytropic	Considered the effect of heat leakage from expansion to compression	Finite speed losses in the piston, pressure drop in the heat	3 kW beta-type GPU-3 engine.	Reported errors as a difference of 14.34% and 3.14% in predicting the

		spaces, shuttle heat losses and non-ideal heat recovery of the regenerator.	exchangers and mass leakage from the working space to the buffer space.		power output and the energetic efficiency of the experimental engine, respectively.
Babaelahi and Sayyaadi [182]	Polytropic	In addition to the losses considered in [67], the polytropic heat losses from the expansion and compression spaces were coupled to the energy balance equations of those spaces.	Finite speed losses in the piston, pressure drop in the heat exchangers and mass leakage from the working space to the buffer space.	3 kW beta-type GPU-3 engine.	Prediction errors of 3.42% and 8.30% were obtained from the model for the thermal efficiency and power, respectively.
Sayyadi and Ghasemi [183]	Polytropic	Coupled losses due to non-ideal regeneration to the thermal model.	Effect of inertia losses, finite speed losses, pressure drop in heat exchangers, and mechanical friction losses.	3 kW beta-type GPU-3 engine.	-4.03% and -14.88% prediction errors in the thermal efficiency and indicated power is obtained.

Araoz et al. [184]	Adiabatic	Accounted for losses due to axial conduction, shuttle heat transfer and imperfect heat regeneration.	Pressure drop in the flow processes and forced compression and expansion losses.	7.5 kW GPU-3 Stirling engine.	Found that at higher temperatures, intermediate and low pressure levels, the model predicted better results than the fourth order LeRC model.
Li et al. [68]	Polytropic	Coupled shuttle heat loss into the thermal model and accounted for regenerator imperfection and conduction losses at every time step.	Coupled work loss due to mass leakage into the buffer space to the thermal model and accounted for finite speed loss of piston, mechanical friction loss, and spring hysteresis loss at every time step.	3 kW beta-type GPU-3 engine	Model predicts the thermal efficiency and indicated power of the engine to an accuracy of -2.6% and 3.78%, respectively.

Some remarkable efforts have been made to improve on the prediction accuracy of the Urieli and Berchowitz [65] model by accounting for additional losses in the engine [67], [68], [178]–[184]. Table 2-2 presents some of the recently improved models developed to predict the performance of different ST types. However, in most of these models, the losses in the engine were accounted for at the end of the numerical integration. Unfortunately, the losses in the engine affect the conditions of the working fuild and need to be coupled to the governing equations in an interactive manner. By so doing, the model would accurately reveal the working conditions of the fluid in the engine and this may lead to the improvement in its prediction accuracy. Therefore, a comprehensive modelling effort is required to couple first and second category loss effects to the mass and energy conservation equations applied to the main working volumes of the engine.

2.3.2.1.4. Third and fourth-order Stirling models

The second-order ST model is suitable for conducting parametric studies on the engine; however they do not give detailed information of the thermal and flow fields in the engine. In particular, these models do not reveal the velocity, temperature, density and pressure profiles of the working fluid, at a discrete level in the control volumes of the engine [64].

To fully understand the flow behaviour in the working spaces of the engine, third and fourth-order modelling approaches are usually deployed. Third-order modelling involves formulating the partial differential equations that govern the operation of the engine, based on mass, momentum, and energy balances of the different control volumes [162]. Toghyani et al. [185] deployed a third-order model to determine the optimal heat source temperature, frequency, engine stroke and mean effective pressure of the GPU-3 ST, that would yield the maximum power output and thermal efficiency. They found the best results from the Pareto set by deploying the fuzzy logic decision making method. This model, however, did not yield better results than the existing adiabatic models. This is because the authors oversimplified the complex processes in the engine to optimise the computing speed.

On the other hand, fourth-order modelling involves deploying a 3-D CFD technique to solve the complex flow problems taking place in the engine at every node of the

mesh generated. Marek and Jan [186] deployed a dynamic mesh to map the various volumes of the ST in a 3-D CFD modelling study. The authors compared the results of the adiabatic models to that obtained from the fourth-order modelling approach. It was concluded that the second-order models are better for the design and optimisation of the engine because of the shorter computational time.

Mohammadi and Jafarian [187] deployed an open source CFD software (OpenFoam), to investigate the impact of hydrodynamic losses, on the performance of the ST. They reported an error of 15.15% in predicting the experimental engine's power output. Mokheilmer et al. [188] performed CFD modelling of a beta-type ST without a regenerator (to simplify the flow problem) and compared the performance of three different working fluids for the engine. It was found that the engine working with hydrogen performs better than the other working fluids based on the power generation and thermal efficiency.

Similarly, Ben-Mansour and Abuelyamen [189] conducted CFD modelling of alpha-type, beta-type and gamma-type ST without a regenerator. The authors also compared the thermal efficiency and power produced from each of these ST types. They validated the predicted results against experimental data and observed a prediction error of 8.1% in the indicated engine power. Further results reveal the gamma-type ST has the best performance. Several other recent studies, where the thermal modelling of different configurations of ST using the 3-D CFD approach were implemented have been reported [190]–[192].

Although the 3-D CFD analysis provides more insight about the flow fields in the engine, and the distribution of the losses, results obtained from this approach were not significantly better than that of existing second-order models. This was attributed to the difficulty in representing the complex processes in the ST, in a CFD model. Moreover, CFD analyses consume so much computing time compared to second-order numerical analyses.

2.3.3. Modelling the organic Rankine cycle engine

The ORC has become an incredibly attractive technology for harvesting waste heat. Some of the factors responsible for the increased utilisation of the ORC engines for waste heat recovery include, its simplicity, improved efficiency, ease of adopting

already existing components used in similar cycles in its operation and the wide choice of operating conditions, cycles, heat source and working fluids [93], [94], [97], [99], [100], [193], [194]. Unlike the Rankine steam cycle, the ORC utilises organic fluids with lower thermal retention capacity as its working fluid, making it ideal for low grade waste heat recovery. While the ORC plants have been in use for a long time, the first practical attempt to fire an ORC using the exhaust waste heat from an IC engine only began after the energy crisis in 1970s [96], [193], [194].

The ORC has similar components and thermodynamic cycles as the well-developed steam Rankine cycle. However, it operates at much lower temperatures typically between 373 K and 673 K, in contrast to the Rankine steam cycle that operates at temperatures above 673 K [195]. Its main components include the evaporator, condenser, refrigerant pump and expander while the thermodynamic processes are two isobaric processes of heat addition and rejection in the heat exchangers and two isentropic work processes as seen in Fig. 2-13.

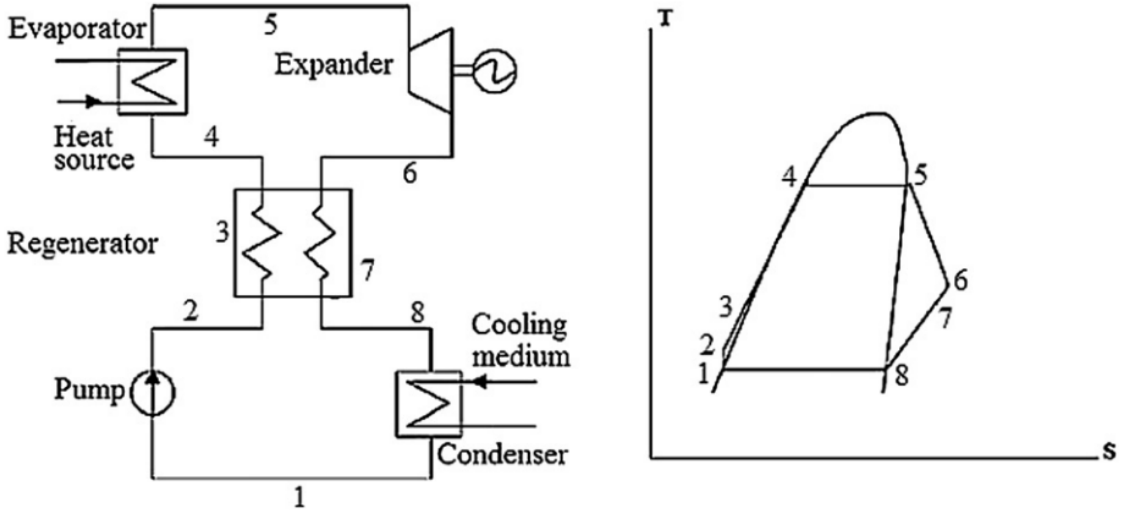

Fig. 2-13. Schematic of a typical organic Rankine cycle and its T- s (temperature-entropy) diagram [195].

The analytical models of the engine are developed based on the first and second laws of thermodynamics [93], [196]. In this case, energy and exergy audits are conducted at the inlet and outlet of each of the main components, to determine the work rate and the efficiencies. Numerical modelling of the ORC using 3-D CFD analysis has been undertaken. Some pilot scale ORCs have been built to undertake

experimental studies aimed at revealing the system's behaviour and to evaluate its performance [193], [197]. However, for detailed design analysis, heat, mass and hydrodynamic principles are employed to model the components of the engine [93], [194], [198]. Several studies in the literature have been dedicated to a range of aspects of the design of ORC engines based on the developed models such as, the selection of a suitable working fluid, parametric optimisation and cycle modification.

The choice of working fluids for application in an ORC engine is a very important topic that has been attracting significant attention from researchers. As it appears there is no consensus on a specific refrigerant suitable for all design and operating conditions of an ORC, studies are still being undertaken to compare the performance of several working fluids. Generally speaking, an ideal working fluid should meet the following conditions: (i) high thermodynamic performance; (ii) environmentally benign; (iii) safe; and (iv) be chemically stable [100]. The working fluids used in ORC are mainly categorised based on their state after the expansion process as dry, isentropic and wet, or by the cycle it is employed, as supercritical, critical and subcritical [99].

Kolsch and Radulovic [99] compared the performance of a DG exhaust gas fired ORC using toluene (dry), methanol (wet) and solkatherm (mixed) as working fluids. The power output, efficiency and heat exchanger surface area were compared for all the working fluids considered. Toluene has been reported to give better results for the power output at the operating temperatures and pressures of the system, whereas methanol yielded higher efficiencies and lower surface area [99]. On the other hand, solkatherm performed poorly in most cases, although its performance was independent of the temperature, making it a good choice for systems where the heat load is prone to variation. They recommended methanol because of its high performance and relative stability. However, methanol is a wet refrigerant and can be highly combustible. It is also inimical to the expansion device, as the production of wet fluid after its expansion in the expander, may lead to the corrosion of this vital component.

Shu et al. [193] conducted an experimental study to compare the performance of R123 and R245fa in the operation of an ORC fired by heavy duty DG. The thermal oil

cycle working with di-benzyl - toluene (DBT) is employed to stabilise the exhaust temperature from the heavy duty IC engine. They remarked that R245fa has a high heat retention capability compared to R123, and may be suitable for low-and-medium grade heat source whereas the latter will suffice at a high grade heat source. In addition, they concluded that R245fa is a stable refrigerant capable of yielding very high efficiencies at a heat source temperature below 150°C.

As a consequence of the good performance of R245fa revealed from these comparative studies, and its interesting physical and chemical properties, it has been adopted as the suitable working fluid of the ORC, by many researchers [197], [199]–[202]. Unfortunately, R245fa has two major limitations: low decomposition temperature (167°C) and high global warming potential (GWP ~1000). This has been triggering studies to find alternative refrigerants with similar performance characteristics as R245fa, but with low to moderate GWP. One of such alternatives is R1233zd, studied by Shengyun et al. [69] in their design of a dual-loop regenerative CNG engine exhaust fired ORC plant. The numerical results suggest that the performance of R245fa and R1233zd were comparable, although R245fa is slightly more efficient while R1233zd has exceptionally low GWP. So far, the use of R1233zd as working fluid has not received so much attention in the literature, notwithstanding its very promising thermo-environmental characteristics.

2.4. Optimisation of decentralised energy systems

Generally speaking, two approaches have been adopted in the optimisation of decentralised energy systems in the literature. The first approach involves the design optimisation of components and subsystems of the DES, while the other is the parametric optimisation of the operation of the energy system [78]. A review of the recent studies focusing on these aspects of DES optimisation has been carried-out and is presented in the next subsections.

2.4.1. Design optimisation of components and subsystems of DES

Design optimisation is undertaken at the design stage of the components and subsystems of a DES, to determine the optimum configuration of the system. It helps to determine the optimum geometrical size, shape, number or arrangement of the

components to guarantee the best performance [78]. A considerable amount of literature has been published on sizing of components and subsystems of DES. The review of these studies are presented here.

2.4.1.1. Sizing optimisation of hybrid renewable energy systems

It has been mentioned in Section 2.2.1 that the HRES integrate a few green energy conversion technologies to generate electricity for fulfilling the local load demand. Consequently, it is necessary to optimally determine the best HRES configuration considering the available local resources, the weather data, the control strategies and the load characteristics of the intended users. Historically, two generic optimisation approaches have been extensively employed in the design of HRES and they are the traditional and artificial intelligence techniques [19]. The former is suitable for the design of HRES, where weather data collected for a long-term for the design location can be easily assessed [105]. On the other hand, the latter is deployed where it is difficult to collect weather data over a long-term for a given location, because of inaccessibility issues [105]. Traditional optimisation methods employed in micro-grids design are: graphical methods; linear programming; iterative approach; and the least square method [203].

In recent times, mimetic algorithms such as Genetic Algorithm (GA), Particle Swarm Optimisation (PSO), Ant Colony Optimisation (ACO), Biogeography Based Optimisation (BBO), Fruit Fly Optimisation (FFO), Grasshopper Optimisation Algorithm (GOA), Multi-Objective Self-adaptive Differential Evolution (MOSaDE), Artificial Bee Algorithm (ABC), and other heuristic techniques including simulating annealing, Artificial Neural Networks (ANN), have been deployed to size the configuration of HRES [14], [15], [19], [34], [114], [204], [205]. Further, the sizing of HRES has been performed in the literature using single and multi-objective optimisation approaches that are formulated based on technical, economic, environmental and social considerations. Several sizing optimisations of HRES using single objective functions have been studied [50], [118], [119]. Most single objective optimisation of HRES involve the minimisation of the net present cost of the system and have been performed in the literature with HOMER [206].

Nonetheless, single objective optimisation of HRES can lead to the oversizing of the system, high cost of energy, excessive dumping, low reliability and renewable energy penetration, and inefficient utilisation of the available resources [207]. Therefore, multi-objective optimisation of HRES is promising and guarantees that an optimum system configuration that is reliable, cheap and produces reduced emissions is found. Several objective functions based on economic, reliability and environmental view-points have been formulated to conduct multi-objective optimisation of HRES [75], [208]–[213]. They are the loss of power supply probability (LPSP), deficiency in power supply probability (DPSP), cost of energy (COE), life cycle cost (LCC), annual total cost (ATC), levelised cost of energy (LCOE), net present cost (NPC), human development index (HDI) and job creation (JC). Due to the complexity, non-convex nature and non-linearity of the mathematical models used to predict the performance of HRES components, and the many plausible combinations of components and strategies, evolutionary algorithms have popularly been deployed to size them [214], [215].

Multi-objective optimisation problems produce a set of non-dominated optimal solutions called the Pareto frontier. Perera et al. [216] pioneered the integration of multi-objective optimisation and multi-criterion decision making in the design of HRES. With this integration, the best solution can be selected from the Pareto set, based on the criteria set by the designer. Most authors have deployed multi-criteria decision making tools such as the technique for order preference by similarity to the ideal solution (TOPSIS) [216], linear programming technique for multi-dimensional analysis of preference (LINMAP)[217] and fuzzy logic [218] in selecting the best solution from the Pareto optimal set.

Table 2-3 presents a summary of some recent studies on the multi-objective sizing optimisation of HRES performed in the literature. As Table 2-3 shows, several objective functions and decision variables have been considered in the sizing of HRES comprising different components. Additionally, it is evident that a combination of evolutionary algorithms and decision making tools have been deployed in these studies to obtain the best optimal HRES configuration. However, there are no records of sizing optimisation of a hybrid WT-PV and battery storage with split ST or combined ST+ORC back-up undertaken in the literature by simultaneously mini-

Table 2-3. Some recent studies on multi-objective optimisation of HRES.

Author	Optimisation tool	Decision making tool	Objective function	Decision variable
Bukar et al. [219]	GOA		COE and DPSP	Number of WT, PV in parallel and autonomous days
Xu et al. [120]	MOPSO		LCOE and LPSP	Number of PV and WT in parallel, reservoir storage capacity, hydro-turbine power
Belouda et al. [220]	MOPSO		Cost of system and LPSP	Number of PV and battery in parallel and WT
Sadeghi et al. [221]	MOPSO		LPSP and LCC	Number of PV and battery in parallel and WT
Barakat et al. [222]	MOPSO		LPSP and COE	Number of PV and battery in parallel and WT
Wu et al. [71]	MOPSO	TOPSIS	COE and pollutions emissions	Number of WT and battery in parallel
Gonzalez et al. [49]	MOGA		NPC and environmental impact	Number of WT and PV area

Zhao et al. [72]	Fruit fly		ATC and pollutant emissions	Number of PV and battery in parallel and WT
Dufo-lopez et al. [205]	MOEA	Truncation technique	System cost, HDI and JC	Number of PV, WT and battery in parallel and types of PV, WT, battery, inverter and diesel generator
Ramli et al. [223]	MOSaDE		LPSP, renewable fraction and COE	Number of PV in parallel and WT and hour of operation of biogas generator
Al-masri et al. [77]	Grey wolf	TOPSIS	LPSP, Total current cost and GHG emissions	Number of PV and battery in parallel and WT
Sun [224]	MOPSO	TOPSIS	COE and pollutant emissions	Number of PV and battery in parallel and WT
Rathish et al. [225]	GA		NPC, unmet load, CO_2 emissions	Number of PV, WT and battery in parallel and types of PV, WT, battery, inverter and diesel generator

-mising the LPSP, LCOE and dumped power. Although previous studies have considered the number and types of components as the decision variables for the HRES sizing optimisation, there is need for a comprehensive study that will include the number of split of the ST and control strategy as some of the decision variables.

2.4.1.2. Design optimisation of other DES components

There have been some attempts in the literature to improve on the performance of the Stirling engine, by optimising the engine's parameters. Togyani et al. [53] determined the optimum heat source temperature, stroke, mean effective pressure and frequency of a beta-type ST that will yield improved efficiency, power output and reduced pressure drop. Also, they employed the improved non-dominated sorting Pareto front GA (NSGA-II) to conduct the design optimisation of the engine and selected the best solution from the Pareto front by deploying TOPSIS, LINMAP and Fuzzy logic decision making tools. It was found that the best optimal configuration from the fuzzy logic tool selected a solution that increased the power output and thermal efficiency of the engine by 600 W and 5.7%, respectively.

Hooshang et al. [226] employed the so-called multi-layer perceptron (MLP) neural networks to the multi-objective design optimisation of the ST and considered power output and efficiency as the objective functions. The decision varaiables selected in this study are the phase angle, displacer stroke and working frequency of the engine. Timoumi et al. [178] recorded improvements in the thermal efficiency of the GPU-3 ST from 39% to 51% after optimising the geometric properties of the engine.

Ahmadi et al. [52] optimised the power output, thermal efficiency and pressure loss of a solar powered ST based on eleven decision variables. By deploying the MOEA and three multi-criteria decision making (MCDM) tools: fuzzy Bellman-Zadeh; LINMAP and TOPSIS, the best optimum configuration was obtained. The optimised engine doubles the power output and improves the efficiency marginally compared to the original engine. They formulated a correlation for predicting the performance of the optimised engine based on the Pareto optimal solution.

Duan et al. [51] optimised the power out, thermal efficiency and cycle irreversibility of the ST. Also, ten of the engine's geometric parameters were selected as the

decision variables and MOPSO was deployed to implement the optimisation. Further, the solution that is closest to the ideal solution from the Pareto front was selected using the LINMAP decision making procedure. The optimal results improve the engine power output and thermal efficiency by 15% and 20%, respectively.

Patel et al. [227] conducted a many-objective thermodynamic optimisation of a ST by employing the Multi-objective Heat Transfer Search (MOHTS) algorithm. They proposed a four-objective function thermodynamic optimisation of the system that considered the maximisation of the power output, system efficiency, ecological function, and exergy efficiency. Also, the results obtained from four-objective optimisation has been compared to that of two-objective optimisation and the former case presented better results. It was concluded that the optimum system configuration selected from the LINMAP and TOPSIS methods were comparable.

Luo et al. [191] deployed a CFD model of the rhombic drive beta-type ST to simultaneously maximise its thermal efficiency, power and minimise flow resistance power. They selected the heat exchangers diameter and length, generator matrix mesh and wire diameter as the engine parameters to be optimised. The differential evolution, GA and adaptive simulated annealing were deployed in parallel, to implement the solution to the optimisation problem. While three decision making tools were explored to select the best solution from the optimal solution set. The optimised results show the dead volume in the engine reduces with the optimisation of the geometry of the heat exchangers. Hence, the thermal efficiency of the original engine rose by 2% and power output by 80 W.

Hulin et al [228] optimised the operating and geometric parameters of the GPU-3 beta-ST including the temperature ratio, regenerator porosity, swept volume ratio, expansion phase angle advance, engine speed and pressure. They adopted a quasi-flow approach to analyse the flow processes in the heat exchangers of the engine. An optimal regenerator porosity of 0.759 was obtained which is significantly higher than the 0.697 regenerator porosity of the experimental engine.

2.4.2. Parametric optimisation of decentralised energy systems

Unlike design optimisation, parametric optimisation of a DES is conducted to optimise the operating conditions of the system [78]. In the literature, parametric optimisation of subsystems and components of the DES have been undertaken. A review of these studies is presented in this section.

2.4.2.1. Parametric optimisation of the ORC engine

The determination of optimal operating conditions for the operation of an ORC can be conducted by optimising the system design and has been receiving significant attention from researchers. Yang et al. [96] performed thermo-economic optimisation of an IC engine exhaust gas fired ORC using MOEA. First, they performed a parametric study to highlight the impact of the evaporation pressure, superheat degree, condensation temperature and the exhaust temperature at the evaporator outlet on the engine's techno-economic performance. Also, based on the developed models, they optimised these variables by deploying the GA and found the optimum evaporation pressure to be in the range of 1.1 - 2.1 MPa. It was concluded that the operating conditions of the DG has a strong impact on the optimal performance regime of the bottoming cycle.

Delgado-Torres and Garcia-Rodriguez [229] optimised the design of a regenerative ORC engine powered by thermal energy from a solar collector. This study minimised the aperture area of the solar collector while some operating conditions of the engine as well as the types of working fluid selected served as the decision variables. It was reported that the wet organic fluids yield higher values of the aperture area compared to the dry fluids.

Shengjun et al. [69] optimised the thermal efficiency, exergy efficiency, recovery efficiency, heat exchanger area per unit power output and the levelised energy cost of the sub and trans-critical ORC using different working fluids. They found different optimal points for the working fluids and ORC operating cycles. In the sub-critical cycle, the optimised thermal and exergy efficiencies are 11.1 % and 54.1%, respectively and is obtained for R123. It was concluded that R125 showed excellent economic and environmental performance in the trans-critical cycle.

2.4.2.2. Parametric optimisation of other decentralised energy systems

A considerable number of studies have been dedicated to the parametric optimisation of different DES configurations. Ahmadi et al. [152] deployed the NSGA-II to optimise the total cost rate and exergy efficiency of a multi-generation system. The mathematical models for predicting the system performance were developed based on the first and second laws of thermodynamics, while fifteen decision variables were selected for the system optimisation. Also, a sensitivity analysis was performed in this study to investigate the impact of the operating conditions of the system on the optimal results. Based on the results obtained, it was concluded that the heat recovery steam generator pressure has a positive impact on the system exergy efficiency but affects the total cost rate negatively.

Fereira et al [128] optimised the geometrical and operational parameters of a solar powered ST for micro-cogeneration of power and electricity with the pattern search optimisation tool. These authors maximised the annual total worth of the system and selected eight decision variables including the mean effective pressure of the ST and its total volume. The optimal system configuration produces 3.65 kW of electric power and 11.06 kW of thermal power and has an annual worth of 740 $/year.

Ahmadi et al. [150] performed the multi-objective optimisation of a solar-based multi-generation DES system using NSGA-II. This study optimised the total cost rate and the exergy efficiency of the system and selected nine decision variables including the warm surface mass flow rate and evaporator pitch point temperature difference. They obtained a maximum system exergy of 60% and cost rate of 154 $/h and remarked that an increase in the pinch point results in a decrease in the exergy efficiency and a reduction in the cost rate.

Boyaghchi and Safari [70] optimised the total avoidable exergy destruction rate, cost rate and investment cost rate of a geothermal energy based quadruple energy vector system. Also, seven decision variables including the geothermal mass flowrate and turbine inlet pressure were selected. This study solved the optimisation problem with the NSGA-II and selected the best solution from the Pareto set by deploying the LINMAP decision making tool. Results show an improvement in the

total avoidable exergy destruction rate and exergy cost rate of 3.27 and 4.9 times the base case, while the investment cost rate is improved by 17.4 % compared to the base case.

Ghaebi et al [125] deployed GA to optimise the thermal efficiency, exergy efficiency and sum unit cost of the product (SUCP) of a Kalina cycle integrated ejector refrigerator CCP energy system. Further, they selected the evaporator pressure, condenser pinch point, vapour generator pressure, heat source temperature, ammonia concentration and expansion ratio as the decision variables. The optimal results reveal that the thermal efficiency and SUCP can be improved by 8.16% and 4.7 %, respectively, while the exergy efficiency is nearly doubled compared to the base case.

2.5. Management of decentralised energy systems

Most decentralised energy systems integrate a number of dispatchable and non-dispatchable energy generating and storage units to fulfill the load demand of the consumers. Consequently, an energy management system (EMS) is required to efficiently coordinate the flow of energy through the generation and storage units and its subsequent dispatch to satisfy the loads [73]. EMS are mainly deployed to ensure the continuous supply of energy to the load, maximise the renewable energy penetration, minimise the cost of energy, ensure components protection due to overloading of the system and increase the stability of the energy system [73]. In the literature, heuristic, fuzzy-logic based, evolution algorithm, unit commitment (UC) problem based and smart tools have been proposed as EMS approaches for micro-grids [73], [74].

2.5.1. Heuristic energy management strategies

Traditionally, the load following (LF), circuit charging (CC) and peak shaving are the popular heuristic energy management schemes deployed in dispatching power from a hybrid renewable energy system (HRES) [34], [74], [81]. These dispatch strategies have been deployed extensively to manage the energy being produced by a HRES in the literature [50], [75]–[77]. The LF is characterised by the operation of a dispatchable back-up power unit to follow the unmet load in a DES. Thus, ensuring that the back-up operates below its rated capacity sometimes and that the battery

is under-utilised [50]. The CC strategy on the other hand, ensures the back-up is operated at its rated capacity while meeting the unmet power in the system and that the excess power produced is utilised in charging the battery. This strategy; however, could lead to the frequent charging and discharging of the battery that is inimical to the life of the battery [80] and even excessive dumping of power [76]. While the peak shaving strategy deploys the back-up to match the unmet power and the battery is introduced to meet the transient load which could lead to over design and excessive dumping of power [81].

Several attempts have been made to improve on the accuracy of the traditional heuristic approaches of managing a DES. Das and Zaman [82] proposed utilising the LF or CC based on the minimum operational cost at the time of deployment to match the energy demand of a remote community in Bangladesh with the power generated from a hybrid PV-battery and DG energy system. They found a reduction in the cost of energy by deploying the combined dispatch strategy compared with the traditional LF or CC modes. In another attempt, Ayodele et al. [83] modified the CC mode by deploying 3-split diesel generators to back-up a HRES and found reductions in dumped power and the cost of energy of the system.

2.5.2. Unit commitment problem based energy management

Other attempts have been made to optimise the energy management of a DES by treating it as a unit commitment problem and employing several ingenious techniques to solve the resulting scheduling problem. Moradi et al. [210] deployed the advanced dynamic programming (ADP) to solve the energy management problem based on two dispatch policies for a DES that hybridises WT-PV-DG-MT and FC. The objective is to minimise the operational and emission costs of the system, for a day ahead operation. The results show the system's total cost and emissions reduced drastically with the deployment of battery storage systems. Similarly, Parpergiougio and Silvente [230] examined the management of a DES that is generating electricity and heating to meet the demands of a household in the form of UC scheduling problem. Also, they formulated a mixed integer linear programming (MILP) model to minimise the system operational cost. It was found

that the proposed EMS contributed about 5% savings in the operational cost of the system and resulted in a reduction in power purchases from the grid.

Mazzola et al. [37] applied the receding horizon optimisation to solve the MILP formulated to manage the energy of a multi-good system, by minimising the cost of operation of the system, based on the forecasted weather and demand data. The obtained results reveal that 8.5% savings in operational cost could be achieved with this approach compared with the CC approach. It was remarked that the observed cost reductions in the proposed EMS approach becomes less significant with the increase in the errors in the weather forecast. Parisio et al. [104] formulated an MILP with a day ahead forecast of the energy generation and demand to minimise the operating cost of a DES.

However, most of these studies considered only the energy management of the DES without determining the optimal configuration of the system. The optimal system configuration of a HRES in particular is strongly dependent on the energy management system deployed and should be prioritised. Hence, Roshandel and Forough [78] independently sized the components of a HRES that integrates PV, WT, battery storage and DG, by minimising the total life cost of the system. Then, they applied the receding horizon to minimise the real time cost of operation of the optimal system configuration. It was found that by increasing the length of the prediction horizon, the penetration of renewable energy resources increases, and as a consequence, the reliance on diesel generators reduce. Although this approach is an improvement over the previous studies, it is still lacking because the system's energy management is not coupled to the sizing optimisation.

Thus, bi-level optimisation that couples the sizing optimisation and the system's energy management has been proposed. Li et al. [231] found the optimal configuration and control strategy of a HRES that utilises battery and hydrogen storage, by deploying a bi-level optimisation of the system. The GA has been deployed to undertake the sizing of the components of the HRES in the outer-loop, by minimising the cost of the system. Then, the operational cost of each candidate optimal solution from the outer-loop, which serves as the objective function for the MILP scheduling problem is minimised in the inner-loop by the receding horizon

approach. This study compares the results obtained from the bi-level optimisation to a rule-based system that prioritises dispatching hydrogen storage before the BSS. The results indicate that the optimal system obtained from the MILP approach lowers the energy cost compared to the rule-based system. Similarly, Rullo et al. [79] proposed a bi-level sizing and energy management of a HRES. However, in this study, both economic and reliability functions were simultaneously considered in the HRES sizing optimisation performed in the outer-loop.

It is clear from the available literature that the unit commitment approach of DES energy flow control and management is very promising and yields reduced operational costs compared to the traditional rule-based approaches. However, it consumes a lot of computational time and this may result in prolonged response time of the system, consequently limiting its reliability. Further, the RHO approach applied in the inner-loop in these studies to optimise the EMS, requires an estimation of future production from the renewable energy resources. Thus, it is difficult to implement in real-time operations especially for a multi-carrier DES, because of the limitation of existing forecasting models to predict accurate long term weather and energy demand data.

2.5.3. Fuzzy logic-based energy management

The fuzzy logic otherwise called rule-based EMS consumes less computational time and is easier to implement than the UC approaches. They rely on the formulation of some set of rules based on if-then constructs that do not require complex mathematical modelling to manage the system. Several studies have integrated the rule-based EMS with the optimal sizing of the components of a HRES. In these studies, some rules are formulated based on the experience of the designer to manage the system, while key system control variables are optimised by deploying memetic algorithms.

Dufo-lopez et al. [110] optimised the minimum state of charge of the battery, minimum power output and critical power of the DG using GA for a HRES comprising PV, WT, DG and BSS. Bukar et al. [219] proposed a rule-based strategy that deployed four operational modes to coordinate the power generation from a standalone HRES and match it with the energy consumption. Sun et al. [224] initiated a

methodology that operates by matching the charging time with the time of use of the energy, to coordinate the charging of electric vehicles with grid power or power generated from a HRES. Rouholamini and Mohammadian [232] implemented the energy management of a grid-tied WT-PV-FC-electrolyser energy system with water boiler and hydrogen storage in the form of a non-linear and constrained optimisation problem and deployed well-known heuristic techniques to solve the resulting problem.

Lu et al. [84] proposed two rule-based operational modes in the optimisation of the dispatch of the energy generated from a WT-PV-DG-MT and vehicle to grid (V2G) micro-grid. They minimised the operational cost and environmental protective costs and found the optimum system configuration. Boukettaya and Kritchen [233] formulated a dynamic management strategy for a HRES based on grid power peak limiting theory, where the grid load consumption must not exceed a previously defined limit. This limit is determined based on the consumption history of the customer and the variation in the electricity cost. Ayad et al. [118] optimised the design and energy management of a standalone WT and PV energy system by deploying the so-called differential flatness approach.

Bracco et al. [153] developed a mathematical model to minimise the daily operational cost of a smart micro-grid that will simultaneously supply electric power, cooling and heating loads and charge even electric vehicles in a university campus in Spain. The smart poly-generation micro-grid (SPM) is composed of CSP plants, MT, absorption chillers, boilers, roof mounted PV and battery storage. Bhatti and Salam [234] proposed a rule-based energy management scheme to optimise the cost of charging electric vehicles with power generated by a PV-battery system or supplied by the grid with the goal to achieve a fixed energy price during the peak hours. Ramadesigan and Bonkole [235] developed a rule-based EMS to manage the energy generated in a hybrid PV and battery storage system by deploying the maximum power point tracking (MPPT) and SOC of the battery to regulate the power generation and discharge from these sources. Nasri et al. [236] deployed the energy storage and energy recovery modes to manage the energy generation, consumption and storage in a HRES comprising solar PV, FC, electrolyser, hydrogen storage and battery banks.

2.6. Summary of the literature review and knowledge gap

From the review of the literature, several very interesting insights on the concept development, modelling, optimisation, and control of decentralised energy systems have been revealed. Firstly, there is a consensus in the literature that models (experimental or theoretical) are essential to understand the characteristics of the components and subsystems of the DES and for their design and optimisation. However, the need to ensure a good trade-off in the prediction accuracy of a model and its computational speed has been highlighted. In particular, the literature obtains that although third and fourth-order models of the ST provide detailed and accurate information on the hydro-thermal field in the engine, their implementation consume too much computational resources.

Therefore, second-order thermal models of the ST with good prediction accuracy and reasonable computational speed have been recommended for the design and optimisation of the engine. Consequently, numerous studies have explored ways to improve the prediction accuracy of the adiabatic models. However, in most of the past studies, the losses in the engine were decoupled from the theoretical equations describing the processes in the engine. Unfortunately, the losses in the engine interact with the conditions of the fluid, necessitating their direct coupling to the governing equations of the engine. Thus, in this study, a new approach that couples the mass and heat leakages in the engine to the governing differential equations and considers additional loss effects has been explored, to develop a prediction tool with improved accuracy for simulating the performance of the engine.

Also, there are numerous studies on the sizing optimisation of HRES conducted in the literature. In most of these studies, power curtailment and the use of fossil fuel powered back-ups are some of the main issues affecting the cost, emissions and reliability of the system. Nonetheless, the deployment of split DG appears to be promising to minimise the emissions, dumped power and cost of HRES with DG back-up. The other plausible solution is the deployment of combined cycle back-up to minimise fuel consumption and consequently reduce costs and emissions from the system. Although a few studies deployed split DG to reduce the dumped power and emissions from a HRES, there are no records of studies where a renewable split solution, such as the split ST has been deployed as back-up in a HRES. Moreover, the

issue of excessive power dumping, especially for standalone HRES can be mitigated at the design stage of the system, by including dumped power as one of the objective functions. Further, there are no records of studies that proposed the deployment of a biomass powered ST+ORC back-up to augment the reliability of a HRES and overcome the challenges associated with sole prime mover back-ups.

The parametric analysis and optimisation of different DES concepts are interesting topics that have been extensively researched. While there are numerous records of studies where dual prime movers of ST and FC or GT were deployed to improve the electrical efficiency of the system, studies on DES concepts that deployed ST and ORC are limited. More so, to reduce GHG emissions, solar and biomass powered DES have been explored. For the biomass fired system, the quality of the biomass fuel is an issue of great concern especially in remote tropical regions with a fair share of rainy and dry seasons. High moisture content is undesirable in woodchips fuel as it could lead to the reduction of the adiabatic combustion temperature of the fuel, the increase in the residence time in the combustion chamber and consequently, a rise in the emissions [63].

One traditional way of controlling the quality of the woodchips fuel is by undertaking in-situ drying of the feedstock with the unutilised combustion flue. The incorporation of drying may scavenge the available thermal energy and limit its potential to produce other useful energy vectors and goods. Therefore, parametric studies are required to reveal the global impact of undertaking biomass drying on the system's performance. This study has not received significant attention in the literature, particularly for the proposed CCHP configuration that deploys combined ST and ORC prime movers. It is also important to determine the optimal operating regime of this DES system to ensure its optimal performance. Unfortunately, there are no evidence of studies undertaken to find the optimal operating conditions of a biomass powered micro-CCHP driven by a hybrid ST and ORC.

The literature further reveals that the control and management of the flow of energy in DES is a hot topic that has been receiving significant attention from researchers. There is a consensus that the traditional heuristic energy management strategies cannot adequately handle the dispatch of energy in these systems. There have been

attempts to overcome some of the operational challenges of the rule-based system by deploying split prime movers in CC approach to minimise dumped power and a hybrid of CC and LF to reduce the system operational cost. Nonetheless, these solutions are still lacking and were mainly employed in managing only electricity generation. Consequently, the deployment of the MILP approach that treats the energy management of the DES as a unit commitment problem was proposed and has been extensively studied. This approach however, is lacking in two ways.

First, most of the authors have deployed the receding horizon approach to solve the MILP formulated for the unit commitment problem of managing the energy of DES. The receding horizon method consumes computational efforts, especially with the increase in the length of the prediction horizon. As a result, the response time of the system is prolonged which would affect its reliability. Secondly, MILP requires the forecast of the energy generation and consumption from the different units of the system in order to implement the energy management. This process introduces significant forecasting errors that may negatively impact the accuracy of the solution and pose some challenges in the implementation.

For these reasons, rule-based energy management of DES is gaining popularity because it deploys simple if-then constructs that are easy to implement and do not require the forecasting of future energy generation and demand data that are prone to errors. However, they are subjective because the rules are formulated based on the experience of the designer. The deployment of a hybrid of the modified heuristic approaches and the rule-based approach looks promising to achieve reductions in dumped power, operational cost and minimise the errors due to the lack of experience of the designer. However, there is no evidence of studies where a hybrid of rule-based energy management and the modified heuristic approaches were deployed in DES energy management. Moreover, the rule-based systems have only been utilised in managing the operation of HRES. There is insufficient evidence of its application to manage the generation, storage and dispatch of energy in an integrated multi-carrier energy system.

In summary, from the reviewed literature on the modelling, control and optimisation of DES, the following are the knowledge gaps that have been identified:

i) Absence of studies that performed advanced coupling of the mass leakage into the crankcase, mass leakage into the cold space from the hot space and the shuttle heat loss to the basic governing equations of the Stirling engine in the working spaces of the engine as well as considered several heat and work losses, to adequately reflect the interactions in the engine and improve the model's prediction accuracy.

ii) Lack of record of studies that proposed the deployment of a dual ST+ORC driven multi-carrier DES based on biomass combustion, to produce cooling, heating, electric power, and dry wood chips fuel and conducts robust parametric analysis to study the influence of variation in cooling ratio, engine frequency and drying of the woodchips fuel on the primary energy savings, exergy efficiency, fuel utilisation and emissions reduction of the system.

iii) Scant knowledge of the parametric optimisation of the proposed system from a multi-objective perspective by simultaneously maximising the primary energy savings, energy utilisation efficiency, exergy efficiency and artificial efficiency and considering the frequency and cooling ratio as the decision variables to obtain the optimal operating regime of the energy system that will guarantee maximum performance.

iv) Absence of studies that proposed the deployment of a biomass fired split ST or ST+ORC in CC or LF mode, respectively as the back-ups of a hybrid WT, PV and battery storage system and determine the optimal number of components by simultaneously considering technical, economic, and environmental objective functions as well as compare the optimal system to a DG base case.

v) Limited research on the deployment of novel rule-based energy management strategies to coordinate the continuous generation, storage and dispatch of cooling, heating and electricity from a hybrid renewable energy integrated multi-carrier system and implements a bi-level optimisation that integrates the system sizing and the energy management to obtain the optimal system configurations and robustly examines the impact of the proposed EMS on the battery utilisation, start-ups of the back-up, and generation of other energy vectors.

Chapter 3 Proposed Decentralised Energy System Concepts

This chapter presents the new configurations of decentralised energy systems that have been proposed in this thesis. Section 3.1 illustrates the process diagram and describes the mode of operation of the formulated HRES configurations. Additionally, it explains the schematic diagram of the new multi-carrier decentralised energy system configuration and discusses the operational modes. Further, this section analyses the process diagram and mode of operation of the emerging DES concepts that integrate HRES based DES and the multi-carrier system. Section 3.2 describes the test location for the new DES configurations being proposed in this thesis and evaluates the energy demand and weather data of the location. Finally, Section 3.3 outlines the summary of the key points of the chapter.

3.1. Introduction

As a sequel to the critical review of the literature on the decentralised energy system (DES) concepts proposed by previous researchers, three new cofigurations of integrated DES have been proposed in this thesis. First, a new HRES configuration that hybridised solar-wind-battery energy storage system and deploys a split Stirling engine (ST)+organic Rankine cycle (ORC) as the back-up has been proposed. In contrast to previous HRES concepts in the literature, the main interesting new feature of this concept is the deployment of combined cycle back-up (ST+ORC) to overcome the performance deterioration of the traditional single back-up, when operated outside its rated conditions. In addition, split ST is deployed in the proposed energy system concept to minimise the excessive consumption of fuel, emissions and dumping of power that characterise the use of single back-up.

Secondly, a new multi-carrier energy system configuration that deploys a dual prime mover of ST and ORC bottoming cycle to drive the simultaneous production of cooling, heating, electric power and dry wood chips has been proposed. To the best of the author's knowledge, this is the first DES configuration that integrates the aforementioned components and proposes in-situ drying of the wood chips fuel with the waste heat recovered from the combustion flue gas, aimed at regulating the moisture content of the woodchips.

Finally, this work proposes a new configuration of the emerging DES that integrates a HRES to a multi-carrier energy system, which has received very limited attention in the literature. In this DES concept, the split ST+ORC back-up will play two vital roles. One, to augment the power generation by the HRES and secondly, to drive the production of other energy vectors and useful goods from the multi-carrier DES system. The schematic diagram and operational modes of these DES concepts are presented in the subsequent sections.

3.1.1. Proposed configuration hybrid renewable energy system

The HRES configuration proposed in this thesis comprises the wind turbine (WT), solar photovoltaic panel (PV), battery storage system (BSS) and split Stirling engine (ST) and organic Rankine cycle (ORC) back-ups. Fig. 3-1 represents the schematic diagram of the HRES that is designed to fulfill the electric load of the customers in the test location. As Fig. 3-1 illustrates, the hybrid wind and solar energy resources are deployed as the primary energy sources to match the electricity demand. The deficit electric power at any time of the day will be fulfilled by discharging the power stored in the battery storage system, $P_{\mathrm{Bat}}\ (\mathrm{i})$ or by deploying n-number of ST, $P_{\mathrm{ST}}\ (\mathrm{i})$ or combined cycle ST and ORC, $P_{\mathrm{ST+ORC}}\ (\mathrm{i})$. As previously explained, the deployment of the combined power cycle where the waste heat from the main back-up is recovered to energise the bottoming cycle is an established way of improving the low electrical efficiency of a heat engine.

Here, the battery is the first priority to match the positive net load in the system, while the split ST+ORC will only be deployed when the battery power is fully discharged to the set safe limits. It is assumed that the proposed system will only feed the alternating current (AC) loads of the consumers. Hence, the power generated by the WT, $P_{\mathrm{WT}}\ (\mathrm{i})$ is fed directly into the AC load bus. On the contrary, the direct current (DC) power generated by the solar PV, $P_{\mathrm{PV}}\ (\mathrm{i})$ will be fed through the DC-AC inverter into the AC bus. Therefore, the DC-AC inverter is one of the power electronics that has been deployed in this HRES configuration to convert all the DC power to AC power. The other power conditioning components are the rectifier and the charge controller.

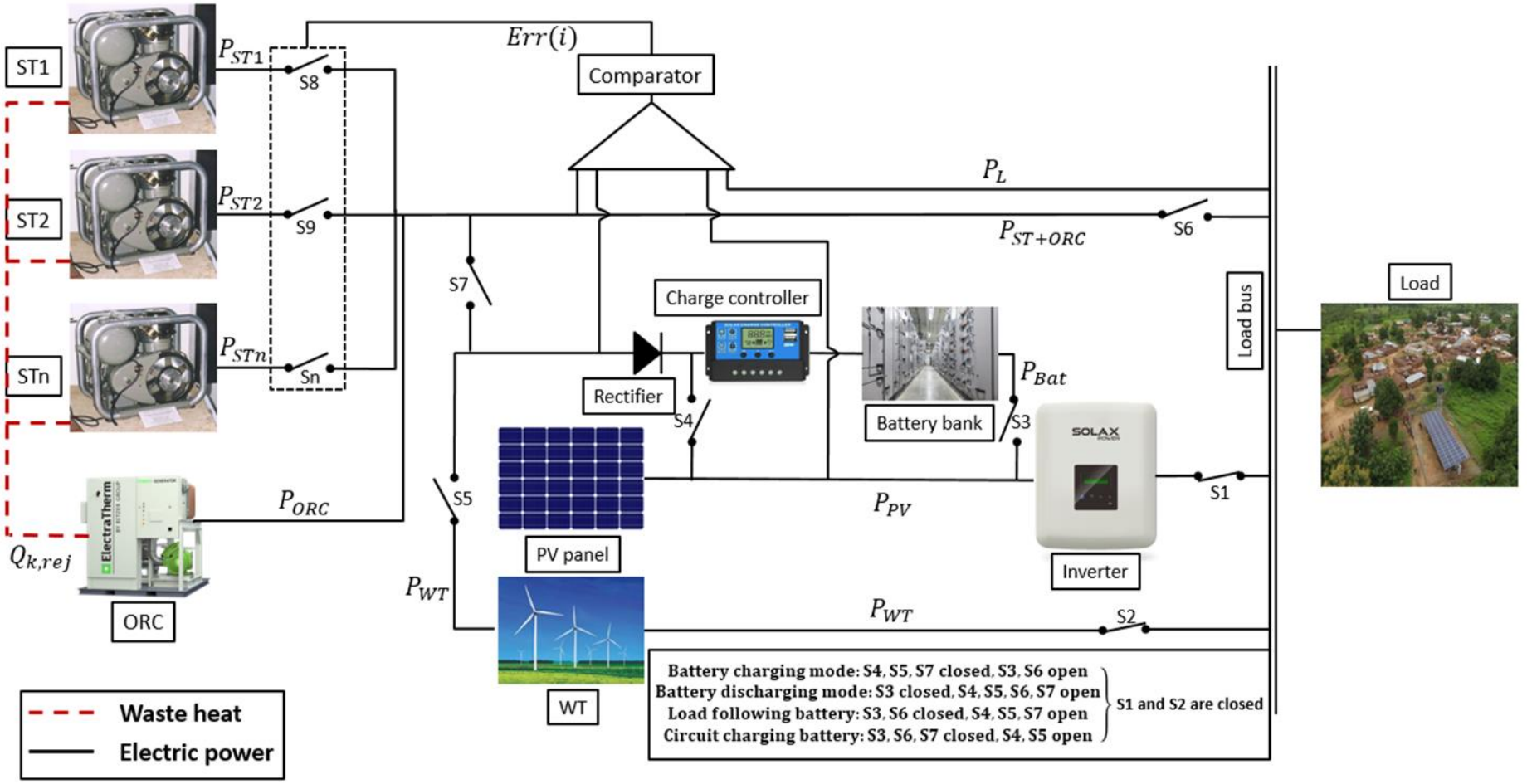

Fig. 3-1. Schematic of hybrid WT-PV-battery storage and split ST+ORC back-up energy system.

The rectifier converts the excess AC power being generated by the WT or the split ST+ORC into DC power, before feeding it to the BSS via the charge controller. On the other hand, the charge controller regulates the state of charge (SOC) of the BSS and ensures that the charging limits set on them are not exceeded. So, any excess power generated by the PV, WT or the ST+ORC is deployed to charge the BSS (depending on the control strategy being deployed) or is dumped via resistive loads where the battery charging limits have been met.

The number of ST deployed to augment the power supply when the BSS is at its low SOC is determined by two factors: the amount of net positive load in the system and the energy dispatch strategy being deployed to regulate the flow of energy from the system. A comparator has been employed to assess the amount of deficit power in the system, $P_{\mathrm{net}}\ (\mathrm{i})$ at every time step and pass the signal to the central controller. The central controller will decide the number of ST to switch ON based on the control strategy, the $SOC\ (\mathrm{i})$ and $P_{\mathrm{net}}\ (\mathrm{i})$.

Further, to prevent wet expansion in the expander of the ORC due to low refrigerant temperature at the evaporator outlet, a limit has been set on the deployment of ORC when the main ST back-up is utilising the split mode or following the load. Note that the ORC is fired by the waste heat, $Q_{\mathrm{k,rej}}\ (\mathrm{i})$ produced from the cooler of the ST. The proposed system is expected to satisfactorily match the electric load demand in the test location, with the local available wood chips fuel and other renewable resources.

3.1.2. Proposed configuration of multi-carrier energy system

The multi-carrier energy system that has been proposed in this study is driven by the ST in combined power cycle mode with an ORC that is powered by the waste heat recovered from the cooler of the ST. The direct combustion of wood chips provides the thermal energy that drives the ST, the drying of the wood chips fuel, the production of cooling from a single effect absorption refrigeration system (ARS) and hot water in a domestic water heater (DWH). Fig. 3-2 depicts the schematic diagram of the novel multi-carrier DES concept. As it is evident in Fig. 3-2 (a), wood chips are admitted into the biomass drier (BMD) at point 1 and dried using recovered waste flue exiting the ST heater (point 7). At the end of the drying process, the resulting dry woodchips, now at state 3, are fed into the biomass

combustor (BMC), where it mixes with inducted air, at state 5 and is combusted. Note that the drying process here has been achieved with two components: a dry reactor and a flash separator.

The flue produced after combustion at state 6, is sent to a solid separator to remove the solid combustion products, such as ash and carbon soot, that could result in the fouling of the heat exchangers (state 6A). The remaining flue gas at state 6B is piped in counter flow to the ST heater, to heat up the working fluid in the tubes of the ST heater and exit the heater at state 7. Meanwhile, the waste heat rejected by the ST cooler during the engine's isothermal process is readily absorbed by the organic working fluid of the ORC, in a cooler/evaporator configuration. This waste heat is utilised to vaporise the working fluid of the ORC (state 12), which then drives the blades of the turbine to produce additional electric power and leaves at state 13. It passes through a recuperator where the hot refrigerant helps to preheat the working fluid that is sent to the evaporator (state 11) by the pump (state 16), while becoming subcooled (state 14) before going into the condenser to become saturated liquid at state 15.

The integration of the ST and ORC yields a combined power cycle that is intended to enhance the fuel utilisation of the sole ST prime mover and raise the electrical power and efficiency of the prime mover over its operating speeds. Fig. 3-3 shows the temperature-entropy diagram of the combined power generation from the ST topping cycle and the ORC bottoming cycle. As Fig. 3-3 illustrates, the bottoming ORC cycle operates between the condenser and evaporator pressures, P_{cond} and P_{evap}, respectively, while the topping ST cycle operates between the heater and cooler temperatures, T_{h} and T_{k}, respectively. $Q_{\mathrm{actual,k}}$ represents the thermal exchange between the cooler of the ST and the evaporator of the ORC. Also, ΔT_{pp} is the pinch point temperature difference between the combustion flue gas, T_{flue} and the heater wall temperature, T_{wh}. The low-quality waste heat after the drying process at state 8 is piped to the desorber of the ARS to heat up the weak lithium bromide-water solution and lose some thermal energy, Q_7, thereby dropping to state 9A (see Fig. 3-2 (b)). Then the water vapour refrigerant produced from the desorber at state 23,

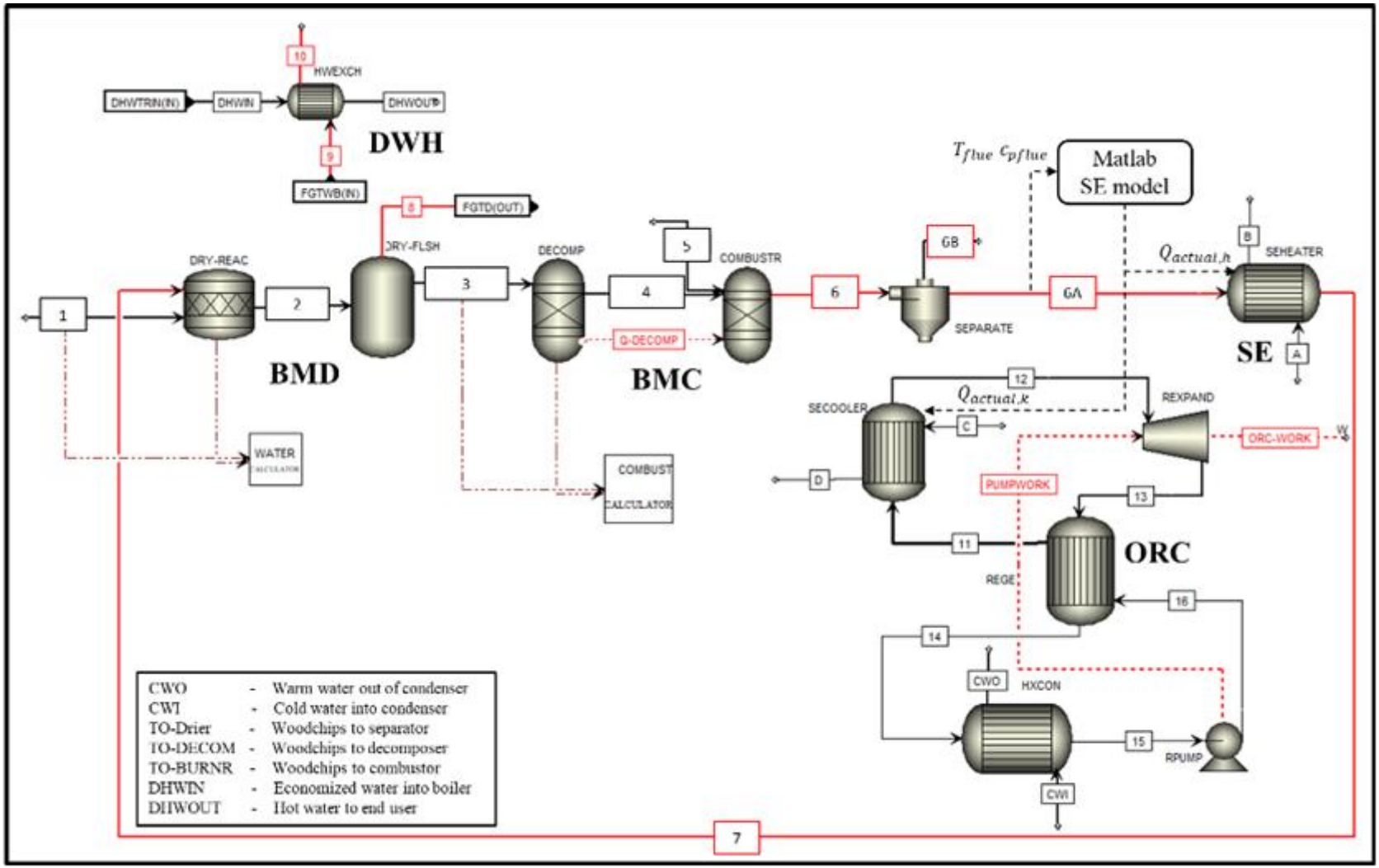
10
HWEXCH
DHWTRIN(IN)
DHWIN
DHWOUT
DWH
9
FGTWB(IN)
8
FGTD(OUT)
DRY-REAC
DRY-FLSH
DECOMP
5
COMBUSTR
GB
T_{flue} c_{pflue}
Matlab
SE model
$Q_{actuat,h}$
SEHEATER
1
2
3
4
6
GA
SEPARATE
BMD
BMC
Q-DECOMP
SE
B
A
12
$Q_{actuat,R}$
SECOOLER
REXPAND
C
D
ORC-WORK
W
WATER
COMBUST
CALCULATOR
PUMPWORK
13
11
ORC
REGE
16
14
CWO
HXCON
15
RPUMP
CWI
7
CWO - Warm water out of condenser
CWI - Cold water into condenser
TO-Drier - Woodchips to separator
TO-DECOM - Woodchips to decomposer
TO-BURNR - Woodchips to combustor
DHWIN - Economized water into boiler
DHWOUT - Hot water to end user

(a)

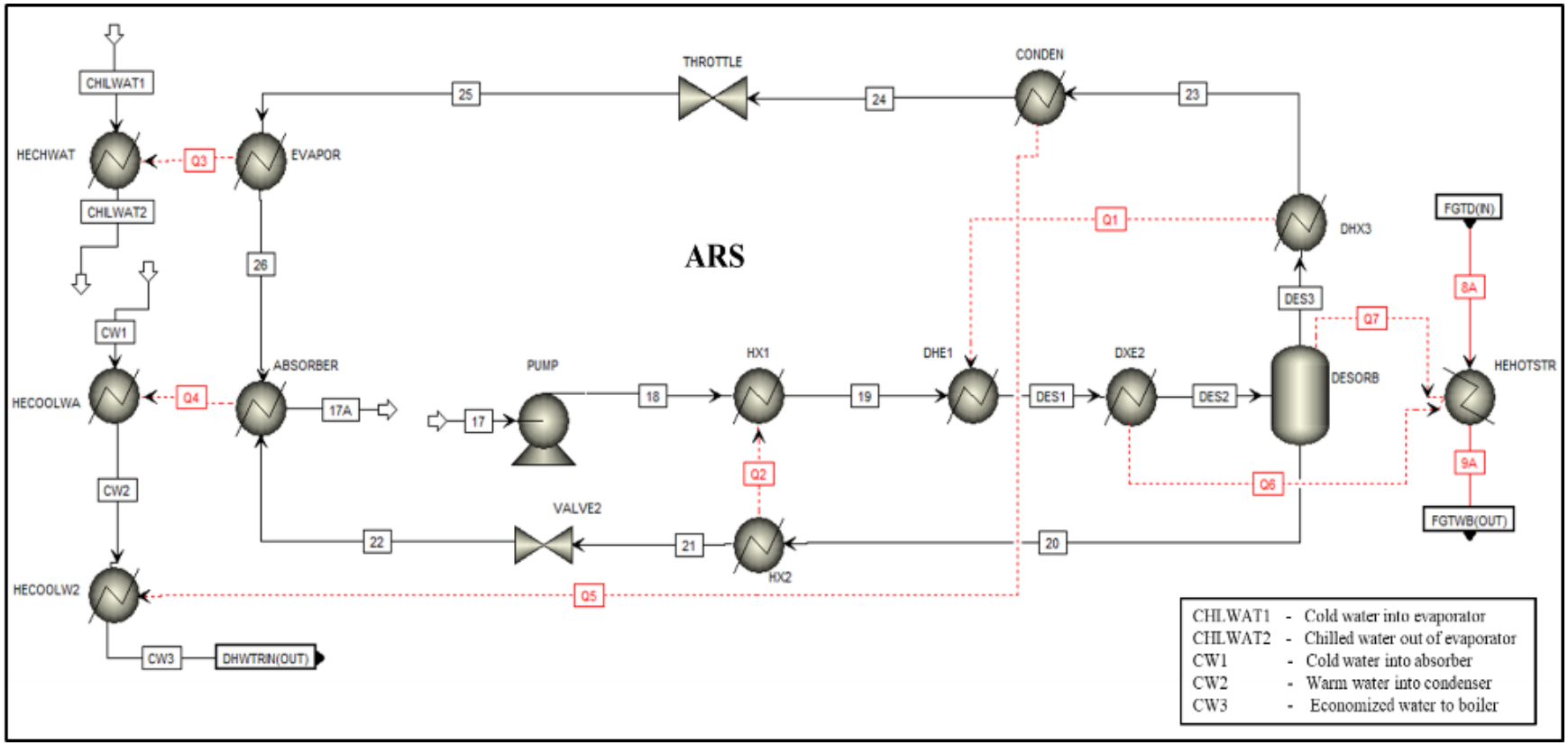

(b)

Fig. 3-2. Proposed multi-carrier decentralised energy system driven by Stirling engine with several stages of waste heat recovery (a) the woodchips drying and combustion, domestic hot water production and combined power and (b) absorption chiller.

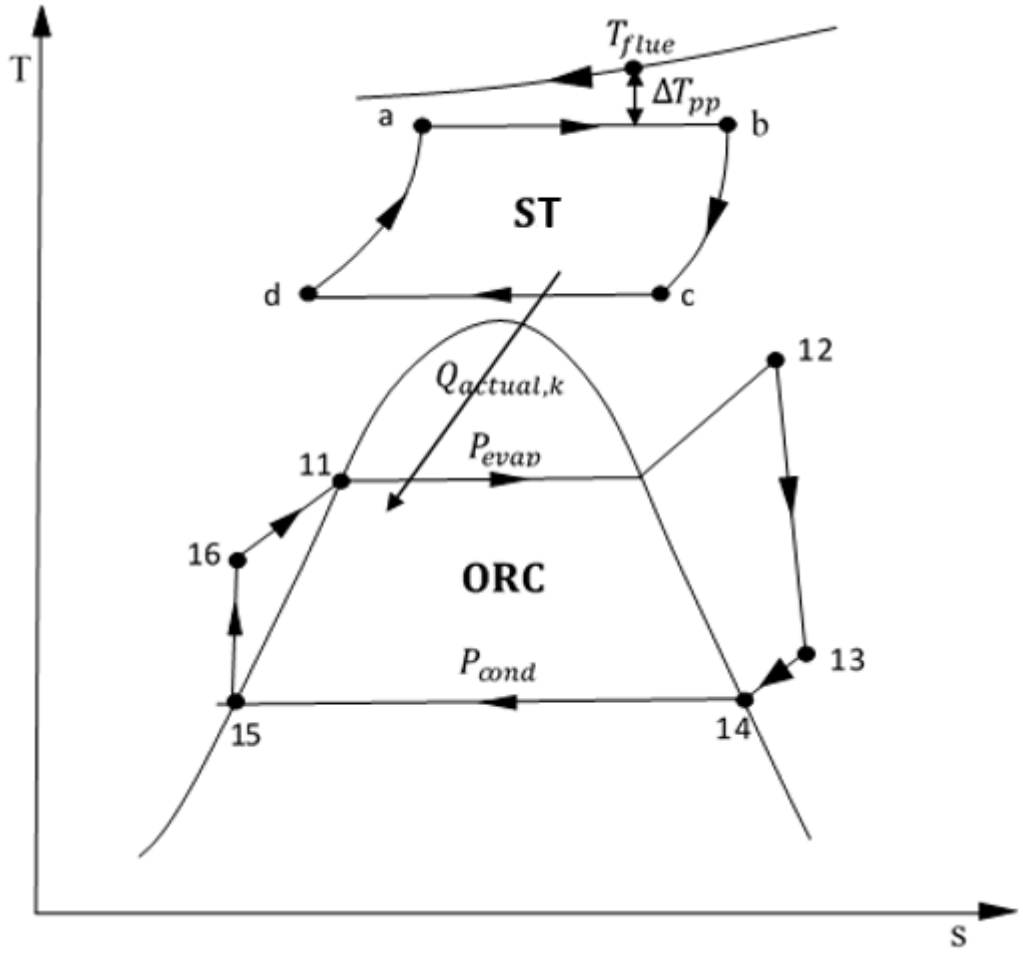

Fig. 3-3. T-s diagram of the theoretical hybrid Stirling and ORC engine cycle.

goes through the condenser and expansion valve becoming saturated liquid at the evaporator pressure giving off its latent heat, state 25. At this point, it will readily absorb heat from the utility, Q_3 (the refrigerating effect) and vaporise to be reabsorbed in the absorber by the strong lithium-bromide water solution that was released from the generator (state 20) through the valve to the absorber (state 22). The resulting weak solution, state 17 is pumped back to the generator at state 18 to repeat the process. Finally, the low grade waste heat is sent to heat water in the DWH at state 9A before going to stack at state 10. In this design, the water sent to the DWH is preheated by picking up the waste heat from the absorber, Q_4 and condenser, Q_5 of the ARS, which serve as economisers. The system described so far deploys several layers of waste heat recovery to minimise the loss of useful exergy in the system. Hence, it could yield improved thermodynamic, economic and environmental benefits.

3.1.3. Proposed HRES integrated multi-carrier energy system

The final DES configuration that is proposed in this thesis integrates the proposed HRES to the multi-carrier energy system discussed in Section 3.1.2. Fig. 3-4 is the schematic of the integrated DES concept showing the integration of the subsystems and components in Fig. 3-1 and Fig. 3-2, with the exception of the BMD. In addition, a central controller has been included here to control the flow of energy from all the generation, storage and consumption units of the integrated DES. As Fig. 3-4 shows, dry woodchips (assumed to have been dried by the flue gas as previously described) is sent into the combustor where it is combusted. The combustion flue that contains some internal energy, Q_{flue} is piped to the heater of the ST, then to the ARS, before it is sent to the DWH to drive the energy conversion processes in these energy systems.

Further, it is seen that the WT and PV supply the electric load in the location, while the split ST+ORC and the battery storage are deployed to fulfil the electricity supply in the test location if the green generators are unavailable. On the other hand, the cooling load at the test location is fed by the single effect absorption chiller, which is driven by thermal energy from the combustion flue gas. Also, the hot water needs of the test location is supplied by the waste heat boiler that derives its energy input partly, from the waste heat rejected in the absorber and condenser of the thermal chiller and the low grade combustion flue.

Due to the numerous components and subsystems integrated in this DES concept, the deployment of a central controller to coordinate the flow of energy in all the system units is essential. So, a central controller has been deployed and it is fed with the signal of the SOC (t) of the battery, net load, $\mathrm{P_{net}(t)} = \left(\mathrm{P_L(t)} - \mathrm{P_{PV}(t)} - \mathrm{P_{WT}(t)}\right)$ i.e., the difference between the load and the power generated from the PV and WT systems and the electric load, $P_{\mathrm{L}}(\mathrm{t})$ of the consumers, at every time step. Based on these signals, it controls the dispatch of the BSS and the split-ST+ORC back-up. The central controller also regulates the production of cooling and hot water, which in this design is fully dependent on the operation of the ST back-up.

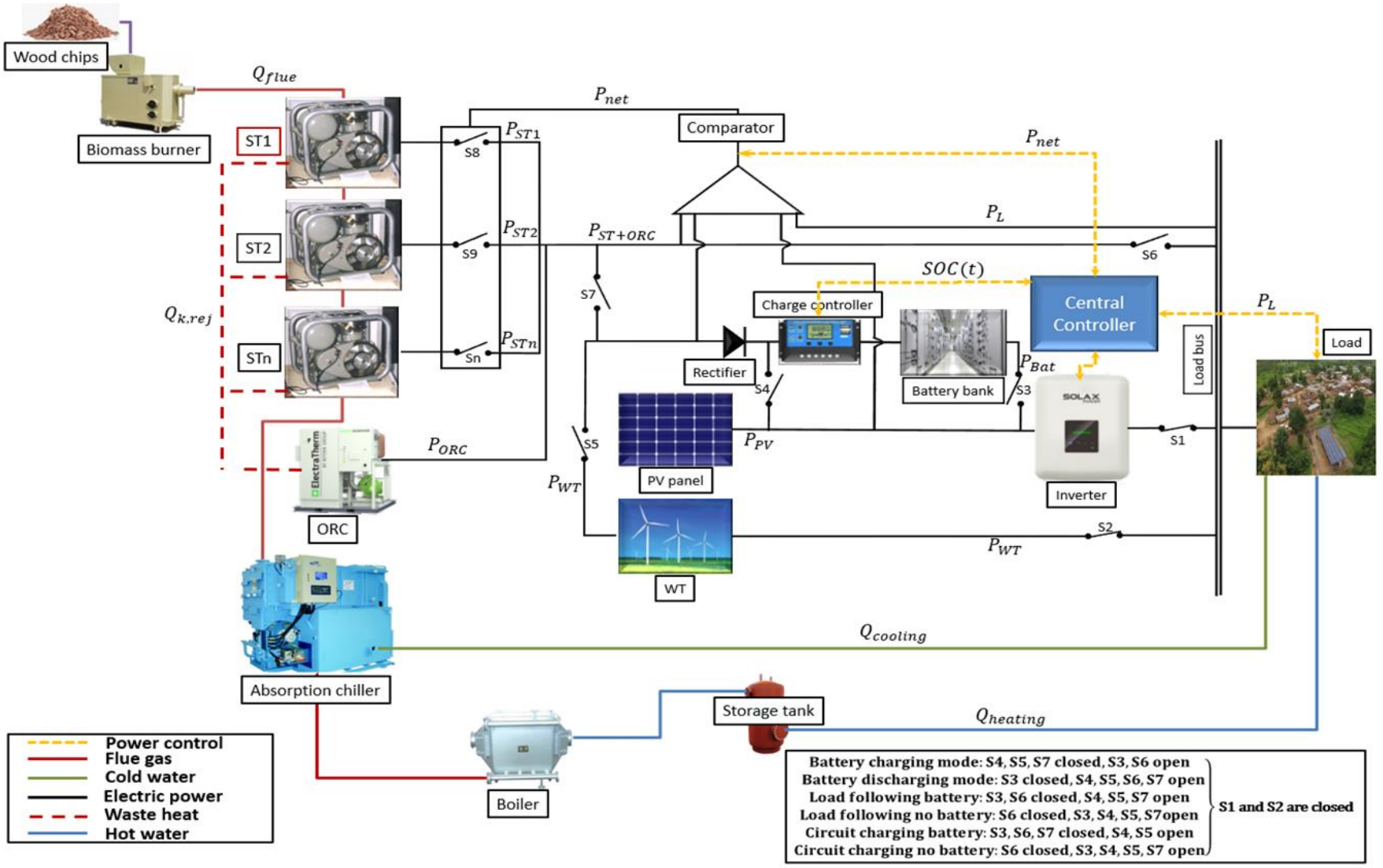

Fig. 3-4. Proposed HRES integrated multi-carrier energy system driven by the Stirling engine in combined power mode with the ORC.

With the deployment of the HRES, the reliance on the biomass powered ST+ORC prime mover in the multi-carrier energy system to supply the electric load in the test location will be minimised. This is anticipated to yield a reduction in the cost of the energy. Moreover, compared to the HRES system, the integrated multi-carrier system is capable of suppling other energy vectors just as the multi-carrier system. It therefore leverages on the strengths of the HRES and the multi-carrier energy system and is a promising energy solution to supply cheap, reliable and clean energy solutions.

3.2. Energy resource assessment

This section presents the description of the test location for the implementation of the proposed energy solutions and evaluates the energy demand and renewable resources in the test location. This is intended to assess the potentials of the local resources to drive the proposed energy system concepts and meet the demand of the consumers. These subjects are presented and elaborately discussed in the next subsections.

3.2.1. Description of the test location

In Nigeria, over 50% of the households in the remote locations do not have access to electricity [33]. To fill this gap, more than 99,450 homes and business centres have been powered by HRES based DES solutions constructed and deployed in recent times by the government, through the rural electrification agency (REA) [23]. However, there are still many remote locations without access to electricity that are being powered by unsustainable energy solutions such as DG. According to the REA, Nigeria has over $9.2 billion per year market opportunities for investments in micro-grid systems and energy consumers could save over $4.4 billion per year with these energy models compared with the alternative energy solutions [23]. Consequently, the REA has conducted field studies in some of the prospective sites for the construction of HRES and is inviting willing investors into the nation's energy sector, to build sustainable energy solutions.

One of these prospective sites earmarked for new energy solutions is the Onye-Okpan community; a coastal community in southern Nigeria (latitude: 5.98° N and longitude: 8.47° E) with 500 households, and situated seven kilometres from the nearest

electrified town. Fig. 3-5 represents the test location on a solar map and indicates the average global solar irradiance. This location is notable for medium scale commercial activities involving the processing and trading of agricultural products (yam, cassava and cocoa beans), welding and fabrication of farm implements, and other artisan related activities [23]. It requires 230 kW (60 kW for households and 170 kW for commercial activities and total daily consumption of 2.952 MWh/day) to meet their daily electricity requirements, and would be a good site for a DES that will utilise the agricultural by-products to generate multiple energy vectors and other useful goods.

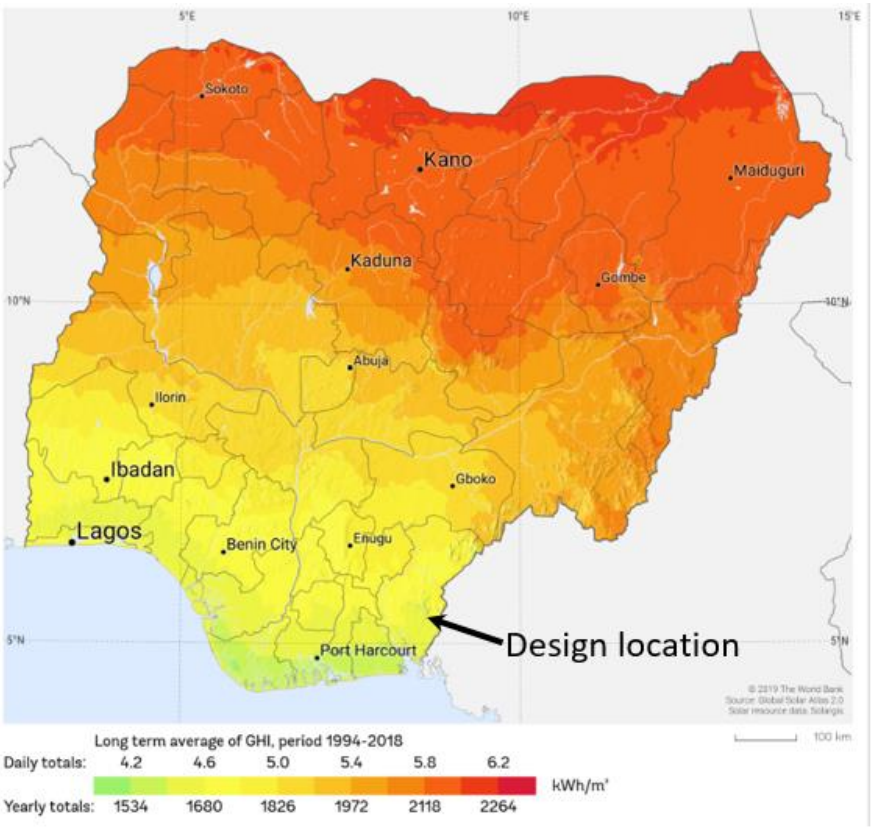

Fig. 3-5. Solar map of Nigeria showing the long term average global solar irradiance in the test location [237].

3.2.1. Weather and load data of the design location

The hourly load data for this location is presented in Fig. 3-6 and it demonstrates the electricity consumption for one representative day. As it is seen from the data, the daily energy consumption is 2.952 MWh/day with a peak load of 219.19 kW recorded at 21:00 hours. At the beginning of the day, the electricity consumption is about 20 kW, it starts to increase from dawn and reaches the first peak at 11:00 hours. Subsequently,

the electricity consumption fluctuates around this value with increased productive activities.

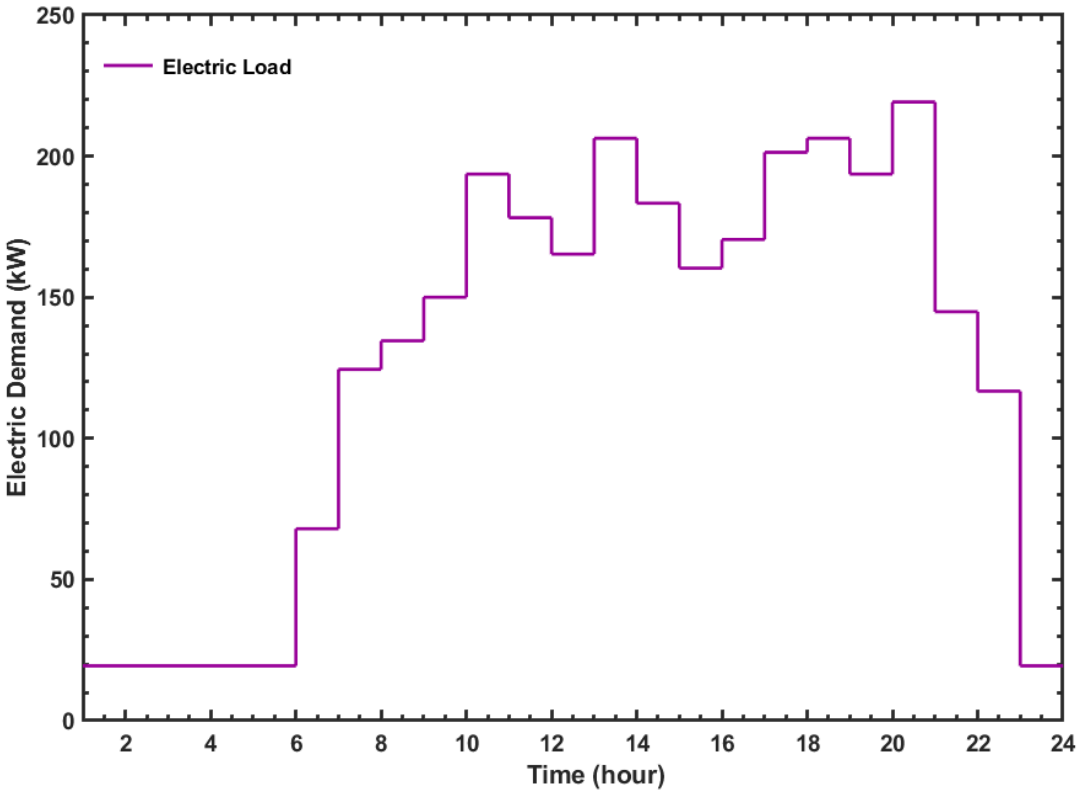

Fig. 3-6. Hourly electricity consumption at the design location [23].

In Fig. 3-7, the global solar irradiance of the location is depicted for a typical meteorological year. The daily solar irradiance for a typical day in the dry and wet seasons that are characterised by bright weather with a clear sky and stormy weather have been highlighted in Fig. 3-7 as A and B, respectively. It can be seen that, the solar insolation at the location records a high value of about 900 W/m^2 on a bright day, while the peak insolation on a typical stormy day with poor weather is about 330 W/m^2. Furthermore, this location enjoys a daily average sunshine of 7 hours with an average solar insolation of 4.52 kWh/m^2. This amount of solar insolation is sufficient to support a stand-alone hybrid renewable energy system [33].

Fig. 3-8 depicts the hourly average solar insolation per square area of the PV surface that is recorded in a period of one year, in the test location. As it is evident in Fig. 3-8, high hourly average solar insolation between 500-800 W/m^2 is experienced in the mid-day hours from late October to early March, which is the dry season months. It is seen

that in the rainy season (April – October), the average hourly solar insolation reduces in intensity as expected, due to stormy weather.

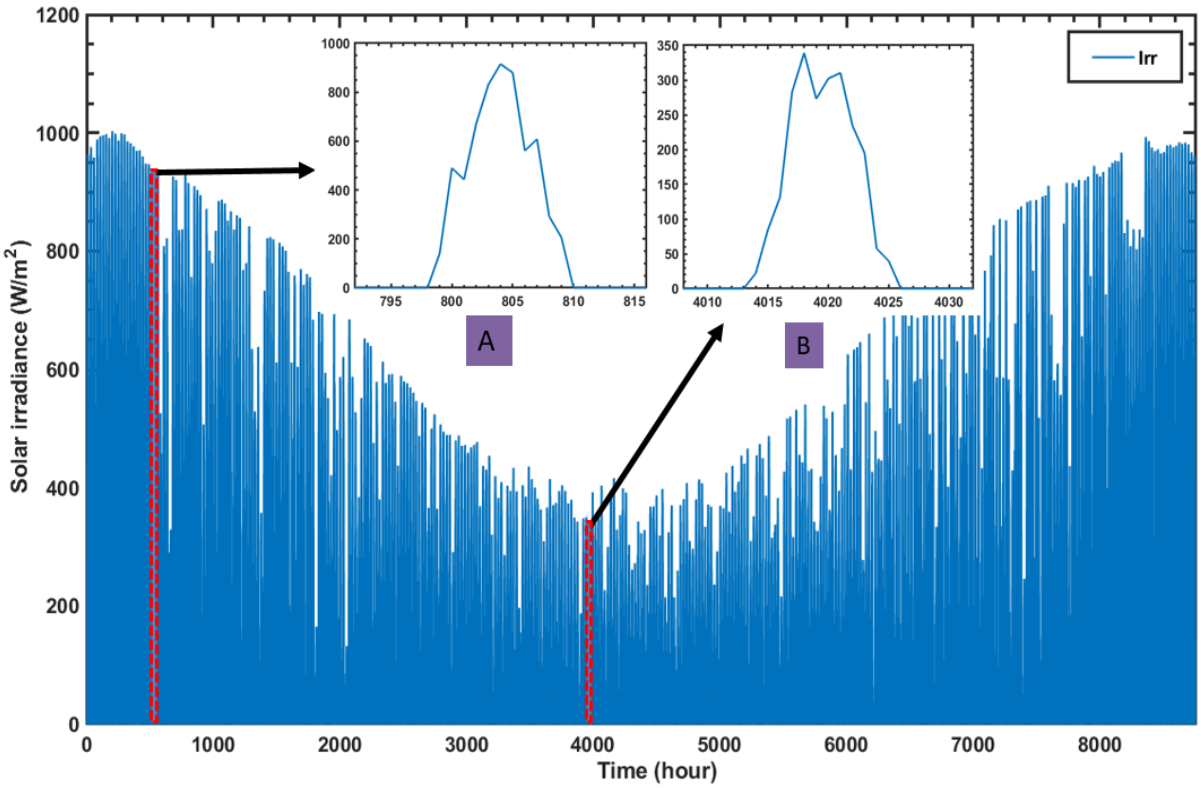

Fig. 3-7. Hourly solar irradiation at the design location [238].

Similarly, in Fig. 3-9 that shows the average hourly ambient temperature at the test location, the ambient temperature starts to increase just towards the end of the rainy season. It is seen to attain a peak of 31 °C in December, before it starts to drop albeit, slowly. Relative stability in the ambient temperature is notable from late January to early May. It is also evident that the rainy season is characterised by low ambient temperature due to cloud cover, which explains the low solar insolation for the months experiencing this season.

Conversely, Fig. 3-10 depicts the annual hourly wind speed at the test location measured at 50m hub height. As seen in Fig. 3-10, sharp variations in the wind speed at the test location is evident all year round, although not as intense as in the case of the solar insolation. From the seasonal perspective, high wind speed is notable in the rainy season where some months recorded hourly wind speeds of 6 m/s.

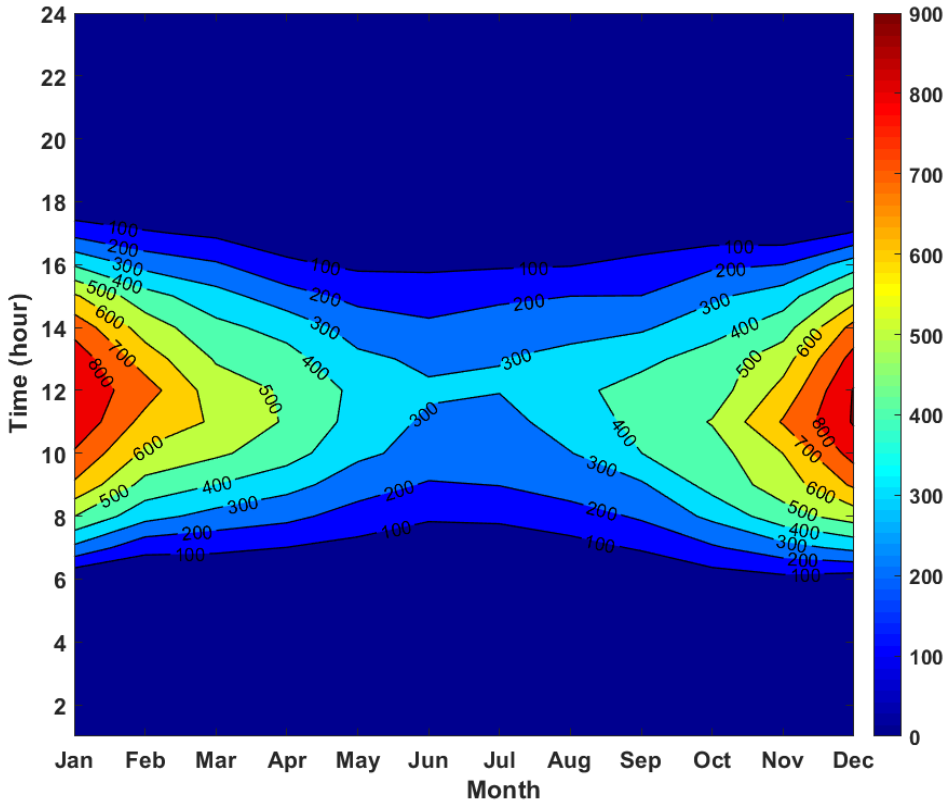

Fig. 3-8. Heat map of average solar irradiance, G_o (W/m^2) at the test location.

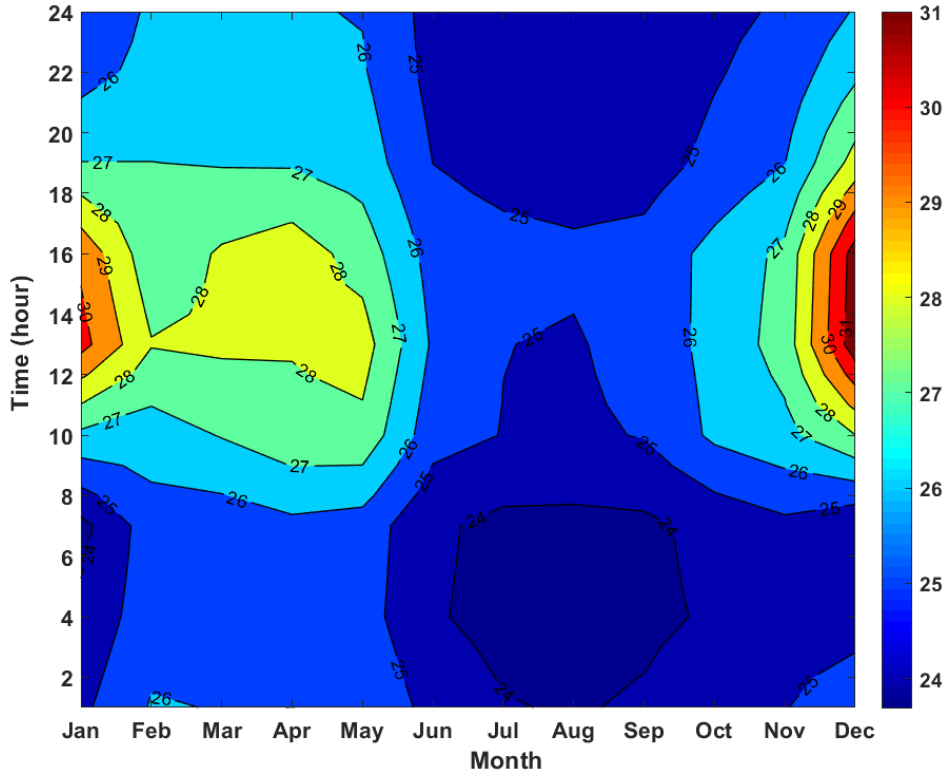

Fig. 3-9. Heat map of average daily hourly ambient temperature, T_a (°C) at the test location.

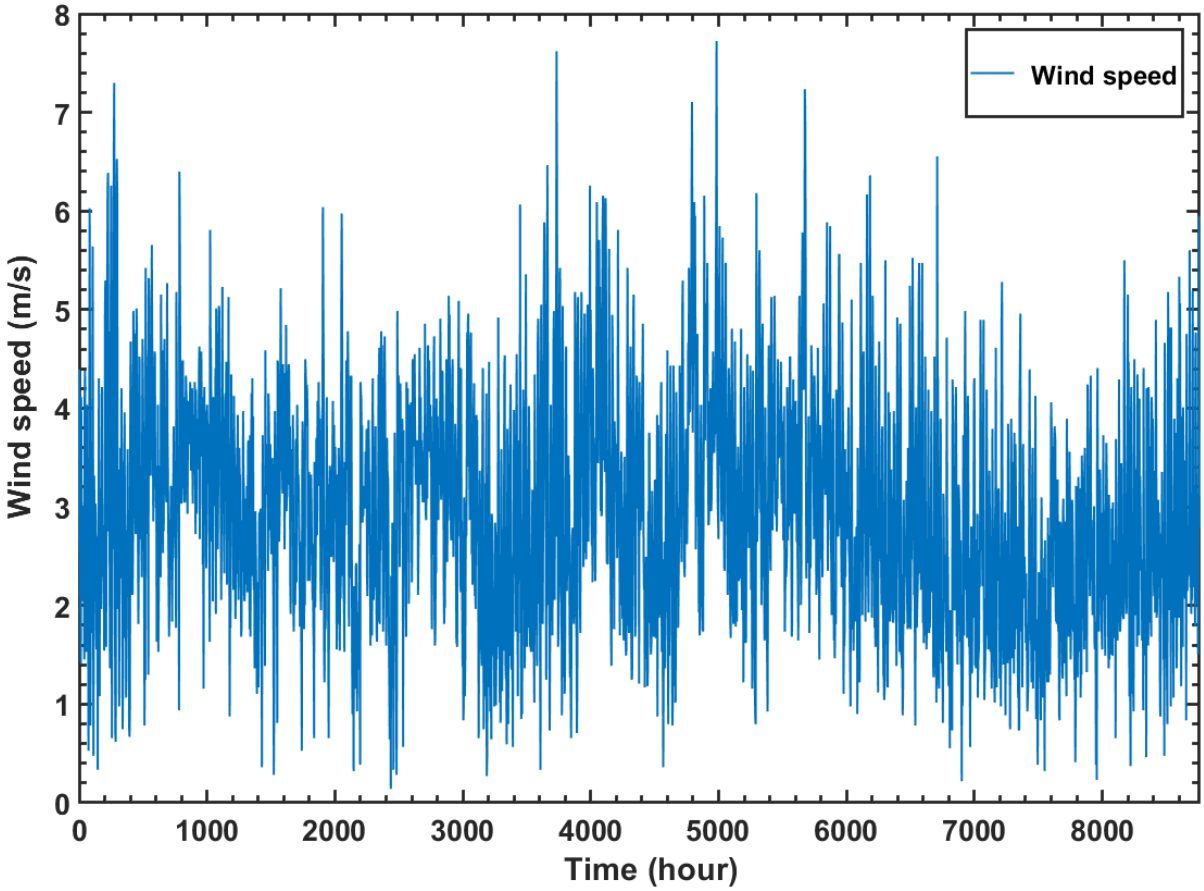

Fig. 3-10. Hourly wind speed at the design location [238].

Regarding the stochastic nature of wind, the Weibull probability density function (PDF) has been deployed to evaluate the frequency of the wind speed in the test location based on the presented historical data and it is given as [210]:

$$PDF_w = \left(\frac{k}{\varsigma}\right)\left(\frac{v}{\varsigma}\right)^{k-1} exp\left(-\left(\frac{v}{\varsigma}\right)^{k}\right) \tag{3-1}$$

The Weibull shape factor, k can be obtained from the following expression:

$$k = \left(\frac{\sigma(v)}{\bar{x}(v)}\right)^{-1.086} \tag{3-2}$$

And the wind scale index, ς is given as:

$$\frac{\varsigma}{\bar{x}(v)} = \left(0.568 + \frac{0.433}{k}\right)^{-1/k} \tag{3-3}$$

where $\sigma(v)$ is the standard deviation and $\bar{x}(v)$ mean wind speed in the test location.

If $k = 2$ is substituted in Eq. 3-1, a Rayleigh function is obtained as:

$$PDF_r = \frac{2v}{\varsigma^2} exp\left(-\left(\frac{v}{\varsigma}\right)^2\right) \tag{3-4}$$

In this case, the Rayleigh scale index can be estimated from [210]:

$$\varsigma = \frac{2}{\sqrt{\pi}} v_{ave} \approx 1.18 v_{ave} \tag{3-5}$$

The Weibull distribution of the wind velocity at the test location is shown in Fig. 3-11 for different hub heights. It is seen in Fig. 3-11 that wind speed of 3.0 m/s has the highest frequency of occurrence in the year and this is observed for a hub height of 50 m. With the decrease in the hub height, the peak Weibull frequency increases, while the average wind speed decreases. Meanwhile, wind speed, $v > 3.5$ m/s is observed for more than 65% of the curve at the design hub height of 50 m.

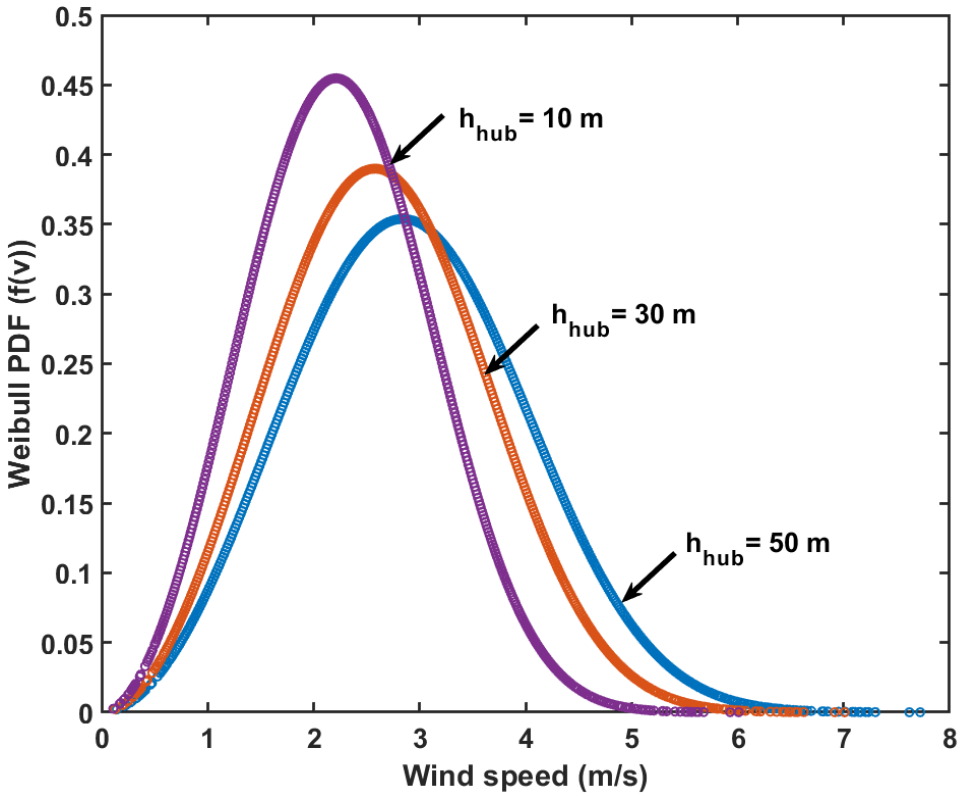

Fig. 3-11. Weibull distribution of wind speed probability at the test location for one year.

Fig. 3-12 is the hourly average wind speed in the location for the different months in a year. It is observed in this figure that there are two peak wind speed periods between

May – June and August – September with an hourly average wind speed of about 3.5 - 4 m/s. On the other hand, an average wind speed of 3.0 m/s is noticeable at the test location and pervades all the months of the year. Generally, high wind speeds are seen to occur between 14:00 – 20:00 hrs, in the day.

The high wind speed periods experienced during the rainy season which doubles as the period in the year with poor solar insolation, highlights the complementarity that exists between wind and solar energy resources; hence the motivation for their hybridisation. Finally, the test location has a reasonable share of solar and wind energy resources to support the siting of a HRES.

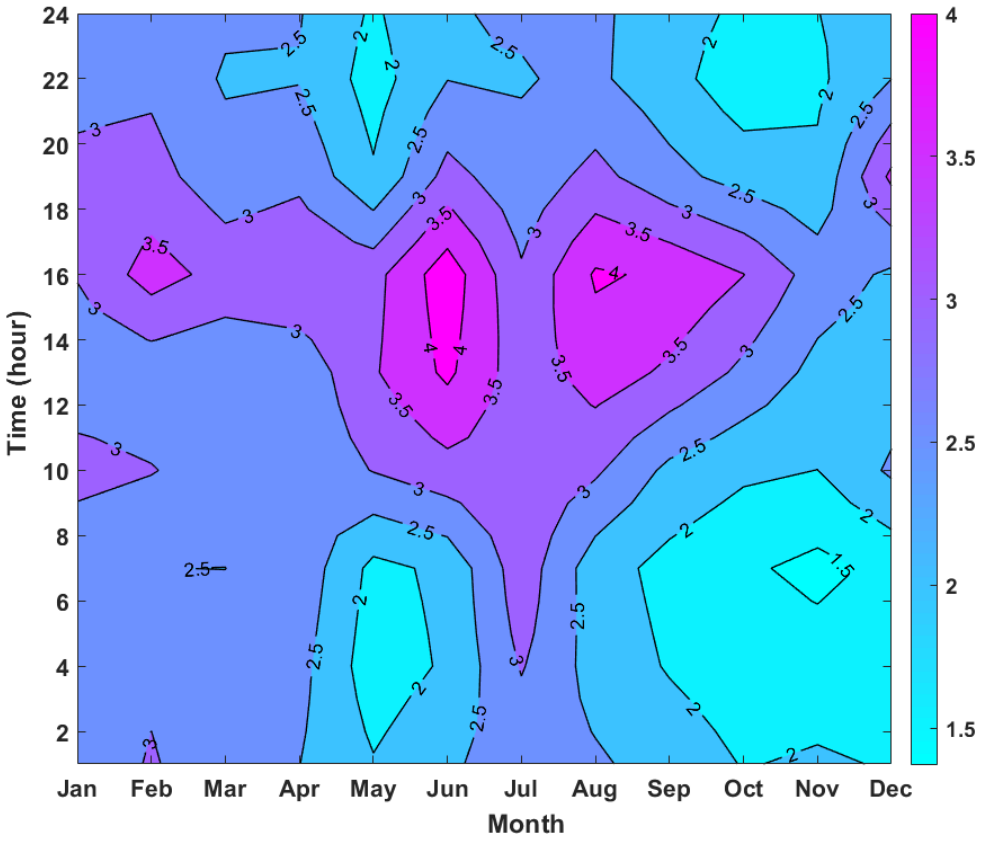

Fig. 3-12. Heat map of the average daily hourly wind speed at 50m hub height at the test location.

The estimate of biomass resources for locations in Nigeria is presented in Fig. 3-13. As it is evident in Fig. 3-13, over 70% of the total biomass resource in Nigeria is derived from wood, while nearly 20% is obtained from agricultural waste and the rest from municipal solid waste (MSW) and saw dust [239]. A plausible estimate of over 500 GJ of energy can be derived from wood biomass sources, followed closely by agricultural

waste that contains latent energy of approximately 150 GJ. It therefore follows that the intended location for the proposed novel HRES system, has sufficient biomass resource to support the deployment of wood chips fuel powered ST+ORC back-up to augment the power supply of the HRES and in parallel serve as the prime mover for the multi-carrier system, if properly harnessed.

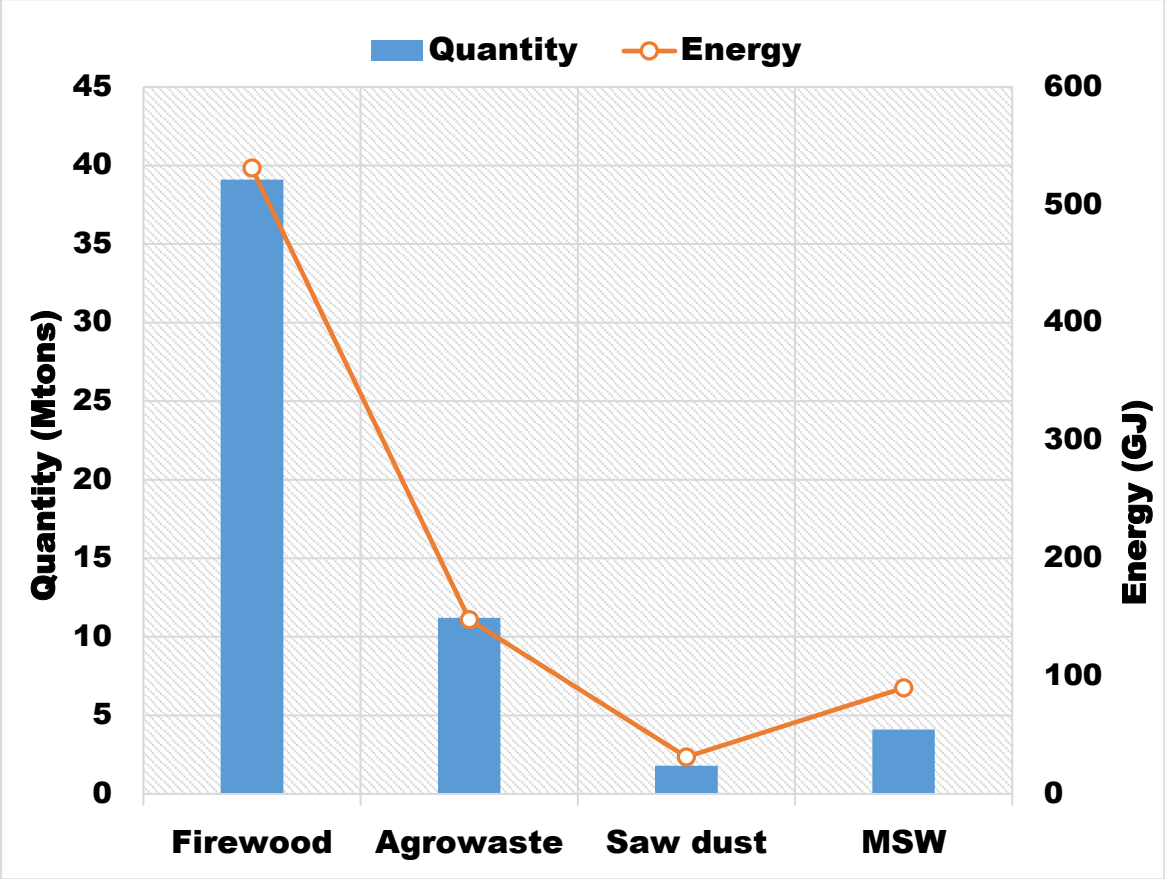

Fig. 3-13. Estimates from different sources of biomass in Nigeria [239].

3.3. Summary of the chapter

This chapter has focused on the new configurations of decentralised energy system (DES) that have been proposed to meet the energy and other goods requirements of the test location. Also, the hourly energy requirement of the test location has been assessed as well as the available local clean energy resources to meet the daily hourly energy demand. From the perspective of the concepts development, three new energy system configurations were proposed. The first concept is a hybrid renewable energy system (HRES) DES that has an interesting feature of deploying biomass fired combined Stirling engine (ST) and organic Rankine cycle (ORC), to augment the power

supply of a hybrid wind, solar and battery system. The second concept deploys several layers of waste heat recovery to drive a multi-carrier DES capable of simultaneously producing cooling, heating, power and dry woodchips. While the third concept is a hybrid of the first and second, that leverages on their respective strengths to minimise emissions, improve primary energy utilisation, cost of energy and guarantee system reliability.

Furthermore, the evaluation of the test location shows there are 500 households in this location that consume 2.952 MWh of energy daily and rely mostly on a diesel generator to meet their energy needs. The weather data assessment reveals that the average daily solar insolation in the test location is 4.52 kWh/m^2 and that the dry season months, as expected, experience high global solar irradiance and ambient temperatures. In contrast, the rainy season months record high wind speeds of an hourly average of 3.5 m/s. This highlights the complementarity between solar and wind and supports the need for hybrid systems. Also, wood constitutes more than 70% of the biomass resources in Nigeria, where the test location is derived, and has been estimated to have energy potentials of about 500 GJ. Hence, wood chips are promising fuel to drive the prime mover proposed for these energy solutions. Finally, these conclusions support the need to conduct the new modelling, optimisation, and control of the proposed energy system concepts that is presented in the subsequent chapters.

Chapter 4 Second-order Thermal Modelling of the Stirling Engine

In this chapter, the formulation of the second-order thermal models governing the operation of the Stirling engine is presented. As has been revealed from the review of the relevant literature, most previous second-order models did not consider the directing coupling of the losses in the engine to its governing equations in an interactive manner, to reflect its impact on the flow conditions. Consequently, a comprehensive coupling of the losses in the working parts of the engine to the governing equations is being explored, to improve the model's prediction accuracy. Section 4.1 presents the model developed based on a simple adiabatic analysis [65]. Section 4.2 describes the formulation of the non-ideal thermal model proposed in this thesis. Section 4.3 discusses the algorithm for implementing the solution to the formulated model and the final section summarises the work done in this chapter. The model formulation and solution approach described in this chapter form part of the author's paper published in a peer reviewed journal.

4.1. Simple adiabatic model

In the Simple analysis [65], Urieli and Berchowitz divided the Stirling engine into five main control volumes, namely: heater, cooler, compression space, expansion space, and regenerator. They assumed that the thermodynamic work processes in the engine occurred adiabatically. The other assumptions made in the Simple adiabatic analysis are as follows:

(i) The thermodynamic processes in the engine attained steady state at the end of each cycle of its operation.
(ii) The engine is running at a constant speed.
(iii) A uniform instantaneous pressure in the working spaces of the engine.
(iv) The working fluid is treated as a perfect gas and obeys the ideal gas law.
(v) The potential and kinetic energy of the working fluid exerts the same influence at the inlet and outlet of a control volume.

(vi) The total mass of the working fluid in the engine is invariant.

(vii) There is no mass leakage into the compression space from the working space via the cylinder wall-displacer gap.

(viii) There are no changes in the energy of the working fluid as a result of heat leakages between the working spaces or to the environment.

(ix) The heater and cooler are maintained at a constant temperature as it exchanges heat with the working fluid.

Urieli and Berchowitz [65] assigned single suffixes, *c, k, r, h, e* to represent the compression (cold) space, cooler, regenerator, heater and expansion (hot) space, respectively, while double suffices, *ck, kr, rh, he* represent the interfaces between the cold space – cooler, cooler – regenerator, regenerator – heater and heater – hot space, respectively as depicted in Fig. 4-1. The system of governing equations in the Simple analysis were derived by employing the equation of state of an ideal gas and the mass and energy conservation principles to each of the control volumes (CV). This set of ordinary differential equations that govern the operation of the Stirling engine are summarised and presented in Table 4-1.

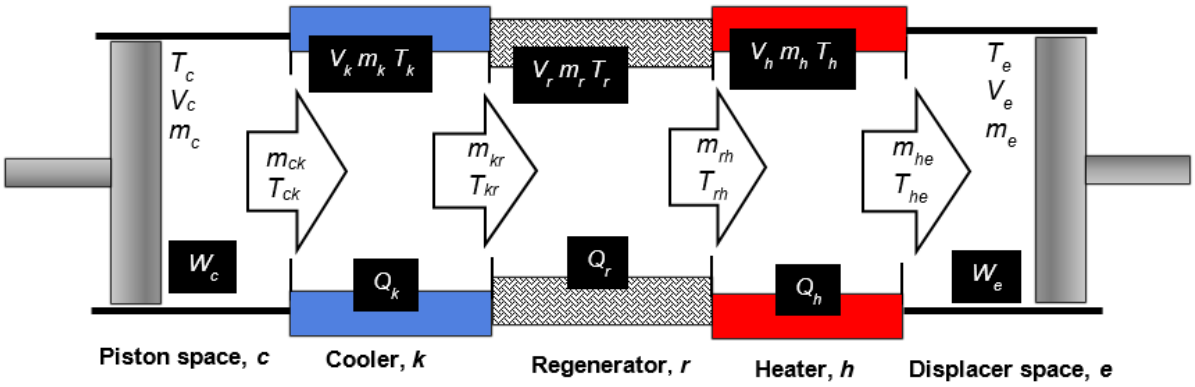

Fig. 4-1. Schematic diagram of the control volumes of the Stirling engine [65].

Table 4-1. Mass and energy balance equations of the Urieli adiabatic model [65].

$P = \frac{m_t R_g}{\left[\frac{V_c}{T_c}+\left(\frac{V_k}{T_k}+\frac{V_r}{T_r}+\frac{V_h}{T_h}\right)+\frac{V_e}{T_e}\right]}$	Pressure of the working fluid in the engine
$dP = \frac{-\gamma P\left(\frac{dV_c}{T_{ck}}+\frac{dV_e}{T_{he}}\right)}{\left[\frac{V_c}{T_c}+\gamma\left(\frac{V_k}{T_k}+\frac{V_r}{T_r}+\frac{V_h}{T_h}\right)+\frac{V_e}{T_e}\right]}$	Variation of pressure in the engine
$m_i = \frac{PV_i}{R_g T_i}, (i = c, k, r, h, e)$	Mass of working fluid in the engine's components
$dm_c = \frac{\left(PdV_c+\frac{V_c dp}{\gamma}\right)}{R_g T_{ck}}$	Change in the mass of working fluid
$dm_e = \frac{\left(PdV_e+\frac{V_e dp}{\gamma}\right)}{R_g T_{he}}$	
$dm_i = m_i \frac{dP}{P}, (i = c, k, r, h, e)$	
$dm_c = -m_{ck}$	Mass flow of working fluid
$dm_k = m_{ck} - m_{kr}$	
$dm_r = m_{kr} - m_{rh}$	
$dm_h = m_{rh} - m_{he}$	
$dm_e = m_{he}$	
$if\ m_{ck} > 0, T_{ck} = T_k; else\ T_{ck} = T_c$	Conditional temperature variation
$if\ m_{he} > 0, T_{he} = T_h; else\ T_{he} = T_e$	
$dT_i = T_i\left(\frac{dV_i}{V_i}+\frac{dP}{P}-\frac{dm_i}{m_i}\right), (i = c\ , e\ )$	Temperature variation in working spaces
$\partial Q_k = \frac{C_{vg}}{R_g} V_k\, dP + \left(C_{pg} T_{kr} dm_{kr} - C_{pg} T_{ck} dm_{ck}\right)$	Heat lost from cooler
$\partial Q_r = \frac{C_{vg}}{R_g} V_r\, dP + \left(C_{pg} T_{rh} dm_{rh} - C_{pg} T_{kr} dm_{kr}\right)$	Heat flux through the regenerator
$\partial Q_h = \frac{C_{vg}}{R_g} V_h\, dP + \left(C_{pg} T_{he} dm_{he} - C_{pg} T_{rh} dm_{rh}\right)$	Heat gained in heater
$\partial W_e = p\, dV_e$	Expansion work done by displacer
$\partial W_c = p\, dV_c$	Compression work done by piston

4.2. New non-ideal thermal model with various losses

The proposed enhanced non-ideal thermal model of the Stirling engine (ST), with various losses, has been developed in order to improve on the existing second-order models deployed for the thermal analysis of the engine. Thus, the displacer shuttle heat loss has been coupled to the energy flow equations of the hot and cold CVs in the engine, thereby invalidating the adiabatic conditions assumed in the work processes in these CVs, and made in the traditional model [65]. In addition, the mass leakage into the crankcase and the mass leakage into the cold CV were coupled to the mass conservation equations of the engine developed in [65], by considering the mass leakages across the boundaries of the CVs. These heat and mass losses that are coupled into the traditional equations form the first category losses [67], [161], [181]. With these modifications, the proposed model has been made more comprehensive in contrast to Ref. [67], [181], [182], where only the mass leakage into the crankcase and shuttle conduction loss were coupled to the traditional equations. Also, compared with Ref. [68] where only the mass leakage into the cold CV via the displacer gap and the shuttle heat loss were integrated into the traditional equations, the proposed model is more detailed. The resulting modified differential equations of the ST were solved using a fourth-order Runge-Kutta numerical scheme, at each time step in every cycle.

In addition, the pressure drop in the heat exchangers of the engine was evaluated using empirical correlations and has been used to modify the instantaneous pressure and temperature of the working fluid in all of the components of the engine. At the end of each cycle, the second and third category loss effects were introduced into the already obtained numerical results to improve the results. The second category loss effects considered in this study, which are mainly thermal losses are: losses due to regenerator imperfection, conduction losses, dissipation losses and enthalpy leakages to the buffer space. While the third category losses considered herein are work losses such as, pressure losses due to finite speed of the piston, mechanical frictional losses, spring hysteresis losses and losses due to pressure drop in the engine. The FST principle has been deployed to model the pressure and mechanical frictional losses in the piston, with the assumption that the compression speed is equal to the expansion

speed. Finally, the heater and cooler temperatures were corrected by conducting an energy balance of the components, based on the assumption that the temperature of the heat source and sink are invariant.

In order to formulate the enhanced non-ideal thermal model then several of the assumptions in the ideal analysis have been discarded. The updated assumptions of the newly enhanced non-ideal thermal model with various losses do not include the assumptions (iii), (vi), (vii) and (viii) of the Simple analysis [65], as presented in Section 4.1.

4.2.1. Formulating the modified non-ideal thermal model

The enhanced thermal model has been formulated by including additional compartments or control volumes (CV) to those presented in Fig. 4-1. Also, the following are the assumptions considered in developing the present non-ideal thermal model of the Stirling engine:

(i) The thermodynamic processes in the engine attained steady state at the end of a cycle of its operation.
(ii) The engine is operating at a fixed speed.
(iii) The working fluid is treated as a perfect gas and obeys the ideal gas law.
(iv) The potential and kinetic energy of the working fluid exerts the same influence at the inlet and outlet of a control volume.
(v) The heater and cooler are maintained at a constant temperature as it exchanges heat with the working fluid.

Fig. 4-2 is the updated CVs in the ST, and represents the loss of working fluid from the hot space to the cold space and from the compression space into the buffer/crankcase. This is via the gap between the cylinder wall and the displacer and the annular gap around the connecting rod into the crankcase, respectively as shown in Fig. 4-3. The interface between the hot CV and the cold CV has been assigned suffix, *ce*, while *leak*, stands for the interface between the connecting rod and the crankcase. The governing differential equations of the engine, which are derivatives of the

variables controlling the operation of the engine with respect to the crank angle, were developed by conducting mass and energy balances of the CVs in the engine.

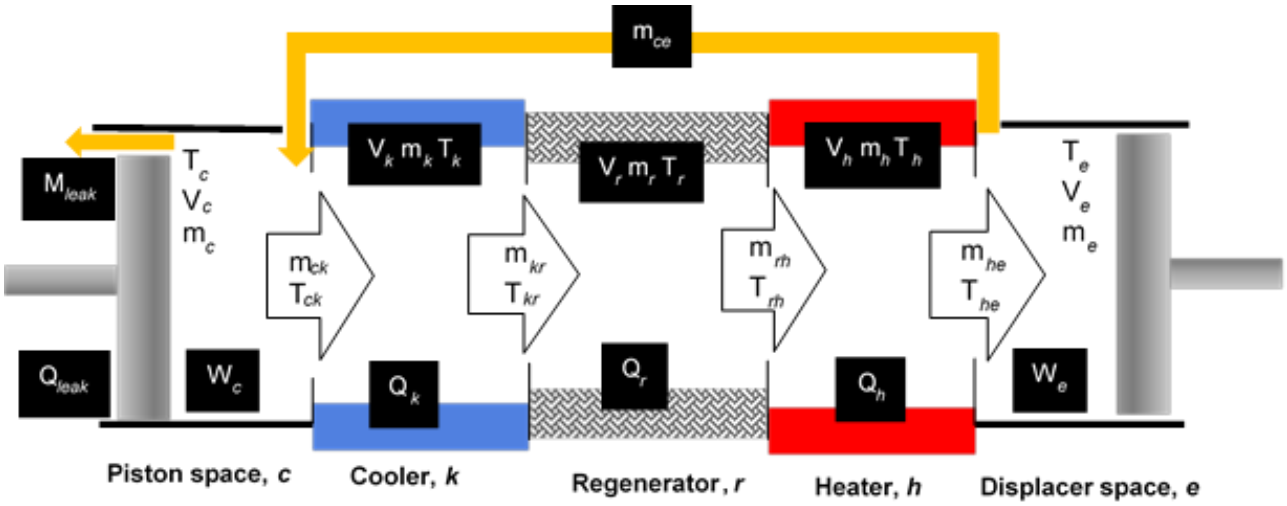

Fig. 4-2. Schematic diagram of the control volumes of a non-ideal Stirling engine [65].

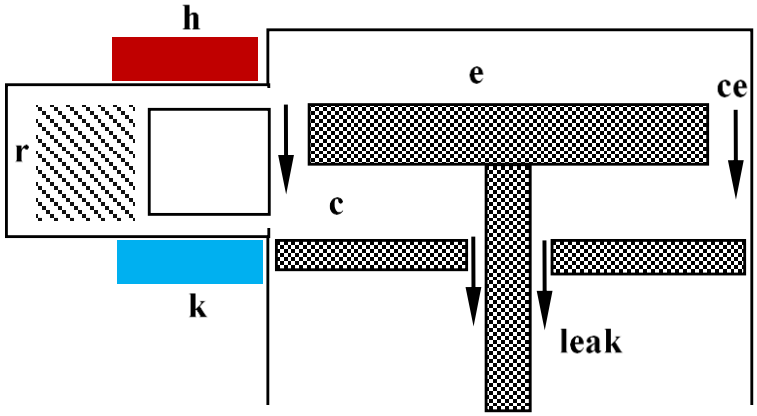

Fig. 4-3. Representation of the gaps for the leakages of the engine fluid [68].

Neglecting the difference in the potential and kinetic heads in the flow energy equation (FEE), the generalised energy equation applicable to any of the CVs can be expressed as:

$$\begin{aligned}\{\delta Q_{\text{ideal,j}} - \delta Q_{\text{sh}} - \delta Q_{\text{disp}} - \delta Q_{\text{cond}} - \delta Q_{\text{r,non-ideal}} - \delta Q_{\text{leak}}\} \\ = \{(\dot{m}_{\text{i}} c_{p,\text{i}} T_{\text{i}} - \dot{m}_{\text{o}} c_{p,\text{o}} T_{\text{o}}) + \delta W_{\text{ideal,j}} - \delta W_{\text{mech.fric.}} \\ - \delta W_{\text{FST}} - \delta W_{\text{hyst.}} - \delta W_{\text{pdrop}} + c_v d(mT)\}\end{aligned} \quad (4\text{-}1)$$

where $\delta Q_{\mathrm{ideal,j}}$ (W) is the ideal heat gained or lost and $\delta W_{\mathrm{ideal,j}}$ (W) the ideal work rate of the system (engine fluid) in any CV. The first and final terms on the right-hand side of Eq. (4-1) model the change in the energy content of the system in the CVs and its internal energy, with subscripts *i* and *o* standing for flow ingress and egress from the CV. Here, δQ_{sh} (J), δQ_{disp} (W), δQ_{cond} (W), $\delta Q_{\mathrm{r,non-ideal}}$ (W), and δQ_{leak} (W) are the additional terms to the traditional steady FEE namely the heat losses via the displacer shuttle, the energy dissipation, the conduction through the regenerator walls, the regenerator imperfection and the enthalpy leakage into the crankcase, respectively. In addition, $\delta W_{\mathrm{mech.fric.}}$ (W), δW_{FST} (W), $\delta W_{\mathrm{hyst.}}$ (W), and $\delta W_{\mathrm{pdrop}}$ (W) model the work loss rates via mechanical friction, the finite speed of the piston, the spring hysteresis and the pressure drop, respectively. c_{p} $\left(\frac{\mathrm{J}}{\mathrm{kg.K}}\right)$ and c_{v} $\left(\frac{\mathrm{J}}{\mathrm{kg.K}}\right)$ are the isobaric and isochoric specific heat capacities of the fluid, respectively.

As the displacer travels from the cold CV to the hot CV, both maintained at two different temperature levels, there is some form of thermal communication between the displacer and the host volume in this process. The heat gained or lost by the displacer in the course of its movement between these two volumes is called the shuttle heat loss, and the instantaneous rate given by $\delta \mathrm{Q}_{\mathrm{sh}}$, has been modelled as [169], [178]:

$$\delta Q_{\mathrm{sh}} = \frac{0.4 {Z_{\mathrm{d}}}^2 k_{\mathrm{d}} D_{\mathrm{d}}}{J_{\mathrm{d}} L_{\mathrm{d}}} (T_{\mathrm{e}} - T_{\mathrm{c}}) \tag{4-2}$$

where Z_{d} (m), k_{d} $(\frac{\mathrm{W}}{\mathrm{mk}})$, D_{d} (m), L_{d} (m), and J_{d} (m) are the displacer's stroke, thermal conductivity, diameter, length and annular gap between the displacer and the cylinder wall, respectively.

If only the shuttle heat loss and enthalpy leakage through the displacer clearance gap are considered in Eq. (4-1), the energy balance of the compression CV and expansion CV will reduce to:

$$\delta Q_{\mathrm{c}} = -\delta Q_{\mathrm{sh}} + \frac{c_p}{R_{\mathrm{g}}} p dV_{\mathrm{c}} + \frac{c_v}{R_{\mathrm{g}}} V_{\mathrm{c}} dp + c_p T_{\mathrm{ck}} dm_{\mathrm{ck}} + c_p T_{\mathrm{ce}} dm_{\mathrm{ce}} \tag{4-3}$$

$$\delta Q_{\mathrm{e}} = \delta Q_{\mathrm{sh}} + \frac{c_p}{R_{\mathrm{g}}} p dV_e + \frac{c_v}{R_{\mathrm{g}}} V_{\mathrm{e}} dp - c_p T_{\mathrm{he}} dm_{\mathrm{he}} - c_p T_{\mathrm{ce}} dm_{\mathrm{ce}} \qquad (4\text{-}4)$$

where R_{g} $\left(\frac{\mathrm{J}}{\mathrm{kg.K}}\right)$ is the gas constant of the working fluid.

Eq. (4-3) and (4-4) were derived by noting that the shuttle heat is lost by the displacer (piston) in the compression volume and gained in the expansion volume. This is in line with the temperature gradient in these CVs. The last terms on the right hand side of these equations model the loss of enthalpy due to the mass leakage. As it can be seen, there would be a drop in the enthalpy in the hot CV and this is due to the mass leakage via the displacer gap which leads to a corresponding gain in enthalpy in the cold CV. Meanwhile, the mass of the working fluid that can escape from the expansion CV into the compression CV at any given time in the engine could be determined from the following expression [68], [240]:

$$\dot{m}_{\mathrm{ce}} = \pi D_{\mathrm{d}} \frac{P}{4 R_{\mathrm{g}} T_{\mathrm{ce}}} \left(U_{\mathrm{d}} J_{\mathrm{d}} - \frac{J_{\mathrm{d}}^3}{6 \mu_{\mathrm{g}}} \frac{\Delta P_{\mathrm{ce}}}{L_{\mathrm{d}}} \right) \qquad (4\text{-}5)$$

where T_{ce} (K), U_{d} $(\frac{\mathrm{m}}{\mathrm{s}})$, μ_{g} $(\frac{\mathrm{Ns}}{\mathrm{m}^2})$, and ΔP_{ce} (Pa) are the temperature of the fluid escaping through the displacer gap, velocity of the displacer, dynamic viscosity of the fluid and difference in pressure between the hot and the cold CVs, respectively.

4.2.1.1. Mass conservation in the engine

The mass conservation principle has been applied to the spaces to obtain the rate of flow of the working fluid through each of the CVs and are given below:

$$dm_{\mathrm{ck}} = -dm_{\mathrm{c}} - dm_{\mathrm{ce}} \qquad (4\text{-}6a)$$

$$dm_{\mathrm{kr}} = dm_{\mathrm{ck}} - dm_{\mathrm{k}} \qquad (4\text{-}6b)$$

$$dm_{\mathrm{he}} = dm_{\mathrm{e}} - dm_{\mathrm{ce}} \qquad (4\text{-}6c)$$

$$dm_{\mathrm{rh}} = dm_{\mathrm{he}} + dm_{\mathrm{h}} \qquad (4\text{-}6d)$$

If Eq. (4-3), (4-4), (4-6a) and (4-6c) are combined and factorised, and noting that the compression and expansion processes are adiabatic, i.e., heat added (or lost) is zero, the rate of change of the mass of the working fluid in the cold and hot CVs is obtained as:

$$dm_{\mathrm{c}} = -\frac{\delta Q_{\mathrm{sh}} - \frac{c_p}{R_{\mathrm{g}}} p dV_{\mathrm{c}} - \frac{c_v}{R_{\mathrm{g}}} V_{\mathrm{c}} dp - c_p T_{\mathrm{ce}} dm_{\mathrm{ce}}}{c_p T_{ck}} - dm_{\mathrm{ce}} \tag{4-7}$$

$$dm_{\mathrm{e}} = \frac{\delta Q_{\mathrm{sh}} + \frac{c_p}{R_{\mathrm{g}}} p dV_e + \frac{c_v}{R_{\mathrm{g}}} V_{\mathrm{e}} dp - c_p T_{\mathrm{ce}} dm_{\mathrm{ce}}}{c_p T_{\mathrm{he}}} + dm_{\mathrm{ce}} \tag{4-8}$$

From the perfect gas equation, the instantaneous mass variation of the working fluid in the remaining CVs can be obtained from the following expression:

$$dm_{\mathrm{i}} = \frac{V_{\mathrm{i}}}{R_{\mathrm{g}} T_{\mathrm{i}}} dP, (\mathrm{i} = \mathrm{k}, \mathrm{r}, \mathrm{h}) \tag{4-9}$$

The instantaneous total amount of the working fluid in the engine is not expected to be constant because of the partial leakage of the engine gas into the crankcase. Thus, the amount of working fluid in the engine can be determined from the following expression:

$$m_{\mathrm{t}} = m_{\mathrm{c}} + m_{\mathrm{k}} + m_{\mathrm{r}} + m_{\mathrm{h}} + m_{\mathrm{e}} - m_{\mathrm{leak}} \tag{4-10}$$

where m_{leak} (kg) is the amount of the working fluid being lost from the cold CV of the engine into the crankcase.

The instantaneous amount of working fluid lost from the engine into the crankcase is expressed as [65]:

$$\dot{m}_{\mathrm{leak}} = \pi D_{\mathrm{p}} \frac{P + P_{\mathrm{buffer}}}{4 R_{\mathrm{g}} T_{\mathrm{g}}} \left(U_{\mathrm{p}} J_{\mathrm{p}} - \frac{J_{\mathrm{p}}^3}{6 \mu_{\mathrm{g}}} \frac{P - P_{\mathrm{buffer}}}{L_{\mathrm{p}}} \right) \tag{4-11}$$

where U_{p} ($\frac{\mathrm{m}}{\mathrm{s}}$), p_{buffer} (Pa), D_{p} (m), L_{p} (m), and J_{p} (m) are the linear velocity of the piston, buffer pressure, piston diameter, length of piston and annular gap of the piston and the cylinder wall, respectively.

By differentiating Eq. (4-10) and substituting Eq. (4-7), (4-8) and (4-9) into the resulting expression, the variation in the pressure of the working fluid is obtained as:

$$dP = \frac{\frac{\delta Q_{\mathrm{sh}} - \frac{c_p}{R_{\mathrm{g}}} P dV_{\mathrm{c}} - c_p T_{\mathrm{ce}} dm_{\mathrm{ce}}}{c_p T_{\mathrm{ck}}} - \frac{\delta Q_{\mathrm{sh}} + \frac{c_p}{R_{\mathrm{g}}} P dV_{\mathrm{e}} - c_p T_{\mathrm{ce}} dm_{\mathrm{ce}}}{c_p T_{\mathrm{he}}} + dm_{\mathrm{leak}}}{\frac{V_{\mathrm{c}}}{\gamma T_{\mathrm{ck}}} + \frac{V_{\mathrm{k}}}{T_{\mathrm{k}}} + \frac{V_{\mathrm{r}}}{T_{\mathrm{r}}} + \frac{V_{\mathrm{h}}}{T_{\mathrm{h}}} + \frac{V_{\mathrm{e}}}{\gamma T_{\mathrm{he}}}} R_{\mathrm{g}} \tag{4-12}$$

In addition, by coupling the mass leakage into the crankcase, the mass leakage through the annular displacer gap and the shuttle loss into the traditional differential equations of the Stirling engine, the Eq. (4-12) has been formulated. In fact, Eq. (4-12) encompasses the comprehensive modifications that have been made to the traditional model aiming to improve on its accuracy. Meanwhile, the instantaneous change in the temperature of the working fluid in the hot and cold CVs has been obtained from the ideal gas equation as follows:

$$dT_{\mathrm{i}} = T_{\mathrm{i}} \left(\frac{dV_{\mathrm{i}}}{V_{\mathrm{i}}} + \frac{dP}{P} - \frac{dm_{\mathrm{i}}}{m_{\mathrm{i}}} \right), \qquad \mathrm{i} = \mathrm{c}, \mathrm{e} \tag{4-13}$$

4.2.1.2. Energy conservation in the engine

Also, by conducting the energy balance of the heat exchangers in the Stirling engine using Eq. (4-1), the quasi-ideal thermal energy exchange in the mentioned CVs was determined as:

$$\begin{aligned} \delta Q_{\mathrm{quasi-ideal,k}} = {} & \frac{c_v}{R_{\mathrm{g}}} V_{\mathrm{k}} dP \\ & + c_p \left(T_{\mathrm{ck}} (dm_{\mathrm{c}} + dm_{\mathrm{ce}}) - T_{\mathrm{kr}} (dm_{\mathrm{c}} + dm_{\mathrm{ce}} + dm_{\mathrm{k}}) \right) \end{aligned} \tag{4-14}$$

$$\begin{aligned} \delta Q_{\mathrm{quasi-ideal,r}} = {} & \frac{c_v}{R_{\mathrm{g}}} V_{\mathrm{r}} dP \\ & + c_p T_{\mathrm{kr}} \big((dm_{\mathrm{c}} + dm_{\mathrm{ce}} + dm_{\mathrm{k}}) \\ & - T_{\mathrm{rh}} (dm_{\mathrm{c}} + dm_{\mathrm{ce}} + dm_{\mathrm{k}} + dm_{\mathrm{h}}) \big) \end{aligned} \tag{4-15}$$

$$\delta Q_{\text{quasi-ideal,h}} = \frac{c_v}{R_\text{g}} V_\text{h} dP + c_p\left(T_\text{rh}(dm_\text{c} + dm_\text{ce} + dm_\text{k} + dm_\text{h}) - T_\text{he}(-dm_\text{e})\right) \quad (4\text{-}16)$$

The interfacial temperatures of the working fluid at the interfaces of the CVs have been determined by considering the direction of the fluid flow. In this study, the interfacial temperatures of the fluid can be determined from the following expressions [68]:

$$if\ \dot{m}_\text{ck} > 0, T_\text{ck} = T_\text{k}$$
$$else, T_\text{ck} = T_\text{c} \quad (4\text{-}17)$$

$$if\ \dot{m}_\text{ce} > 0, T_\text{ce} = T_\text{c}$$
$$else, T_\text{ce} = T_\text{e} \quad (4\text{-}18)$$

$$if\ \dot{m}_\text{kr} > 0, T_\text{kr} = T_\text{k}$$
$$else, T_\text{kr} = T_\text{k} + (1 - \varepsilon_\text{r})(T_\text{h} - T_\text{k}) \quad (4\text{-}19)$$

$$if\ m_\text{rh} > 0, T_\text{rh} = T_\text{h} - (1 - \varepsilon_\text{r})(T_\text{h} - T_\text{k})$$
$$else, T_\text{rh} = T_\text{h} \quad (4\text{-}20)$$

$$if\ \dot{m}_\text{he} > 0, T_\text{he} = T_\text{h}$$
$$else, T_\text{he} = T_\text{e} \quad (4\text{-}21)$$

The other modifications made to the Simple adiabatic analysis model in this study, to improve on those of Ref. [68], [182], is to implement the variation of pressure in the CVs of the engine using the magnitudes of the pressure drops in the heat exchangers. As in [178], the cold CV has been chosen as the reference pressure and assigned the value of the instantaneous pressure in the engine at a given time step. Subsequently, the pressure in the other components in a particular time step was determined incrementally by utilising the information of the pressure drops in the heat exchangers in the previous time step and the direction of flow of the fluid, as follows:

$$if\ \dot{m}_{\mathrm{ck}} > 0, P_{\mathrm{k(i)}} = P_{\mathrm{c(i)}} + \frac{\Delta P_{\mathrm{k(i-1)}}}{2}$$

$$else, P_{\mathrm{k(i)}} = P_{\mathrm{c(i)}} - \frac{\Delta P_{\mathrm{k(i-1)}}}{2} \quad (4\text{-}22)$$

$$if\ \dot{m}_{\mathrm{kr}} > 0, P_{\mathrm{r(i)}} = P_{\mathrm{k(i)}} + \frac{\left(\Delta P_{\mathrm{k(i-1)}} + \Delta P_{\mathrm{r(i-1)}}\right)}{2}$$

$$else, P_{\mathrm{r(i)}} = P_{\mathrm{k(i)}} - \frac{\left(\Delta P_{\mathrm{k(i-1)}} + \Delta P_{\mathrm{r(i-1)}}\right)}{2} \quad (4\text{-}23)$$

$$if\ m_{\mathrm{rh}} > 0, P_{\mathrm{h(i)}} = P_{\mathrm{r(i)}} + \frac{\left(\Delta P_{\mathrm{r(i-1)}} + \Delta P_{\mathrm{h(i-1)}}\right)}{2}$$

$$else, P_{\mathrm{h(i)}} = P_{\mathrm{r(i)}} - \frac{\left(\Delta P_{\mathrm{r(i-1)}} + \Delta P_{\mathrm{h(i-1)}}\right)}{2} \quad (4\text{-}24)$$

$$if\ \dot{m}_{\mathrm{he}} > 0, P_{\mathrm{e(i)}} = P_{\mathrm{h(i)}} + \frac{\Delta P_{\mathrm{h(i-1)}}}{2}$$

$$else, P_{\mathrm{e(i)}} = P_{\mathrm{h(i)}} - \frac{\Delta P_{h(i-1)}}{2} \quad (4\text{-}25)$$

With the knowledge of the pressure of the fluid in each CV provided by Eq. (4-22) - (4-25), the temperature of the fluid in these CVs is updated in each time step by applying the following expression:

$$T_{\mathrm{i}} = \frac{P_{\mathrm{i}} V_{\mathrm{i}}}{R_{\mathrm{g}} m_{\mathrm{i}}}, (\mathrm{i} = \mathrm{c, k, r, h, e}) \quad (4\text{-}26)$$

These set of independent differential equations formulated for the analysis of Stirling engines can be presented as an initial value problem as follows:

$$\dot{y} = F(t, y), \qquad with\ initial\ conditions, y\left(t_{(0)}\right) = y_{(0)} \quad (4\text{-}27)$$

where the array $\mathrm{y} \equiv \mathrm{V_c, V_e, T_c, T_e, P, W_c, W_e}$, etc. denotes the unknown functions.

4.2.2. Modelling the second and third category losses in the engine

As stated in Section 4.2, the second and third category losses of ST are accounted for in the enhanced non-ideal thermal model presented in this work at the end of each cycle of the numerical iterations. The second and third category losses defined in Section 4.2.1 have been incorporated into Eq. (4-1). This section presents the principles and methods deployed in the evaluation of these losses.

4.2.2.1. Thermal losses in the enhanced Stirling second-order model

The second category losses of the engine are mainly thermal losses. The thermal losses considered in this new model are as follows:

a) Dissipation Losses:

The flow of the working fluid over the walls of the heat exchangers of the ST creates a thermal boundary layer. This, in turn, induces heat dissipation, which results in thermal losses in the engine. This loss has been modelled by expressing it as a function of the pressure drops in the heat exchangers [65], [178]:

$$Q_{\mathrm{diss,i}} = -\frac{\Delta P_{\mathrm{i}} m_{\mathrm{i}}}{\rho_{\mathrm{g}}}, (\mathrm{i} = \mathrm{k}, \mathrm{r}, \mathrm{h}) \qquad (4\text{-}28)$$

where ΔP_{i} (Pa) is the pressure drop in each heat exchanger and ρ_{g} $(\frac{\mathrm{m}^3}{\mathrm{kg}})$ is the density of the internal gas of the engine.

b) Conduction Losses:

The regenerative thermal engine utilises several heat exchangers, resulting in a variation in the temperature field across the engine. Some of the CVs are maintained at high temperatures, while others operate at very low temperatures. This obvious temperature differential can induce loss of thermal energy by internal conduction. In particular, a considerable amount of heat can be lost between the heater and the cooler - the units of the engine that operate at the extreme temperatures - as well as through the walls of the regenerator. This heat loss by internal conduction through the walls of the regenerator has been expressed as [184]:

$$Q_{\text{cond}} = R_{\text{cond}}(T_{\text{wh}} - T_{\text{wk}}) \quad (4\text{-}29)$$

where $R_{\text{cond}}\left(\frac{\text{kJ}}{\text{K}}\right)$ is the conductive thermal resistance of the walls of the regenerator, T_{wh} (K) is the temperature of the heater wall and T_{wk} (K) is the temperature of the cooler wall.

c) Heat leakage to the buffer space:

The mass leakage into the crankcase could induce some thermal energy losses in the engine. Thess losses affect the performance of the engine. In Section 4.2.1, a model was presented to determine the mass of the compressed gas escaping into the buffer space. The enthalpy loss as a result of the mass leakage has been obtained as follows:

$$Q_{\text{leak}} = m_{\text{leak}} c_p T_{\text{c}} \quad (4\text{-}30)$$

d) Non-ideal heat transfer losses:

It has been established in literature that the introduction of the regenerator in the ST could reduce the thermal energy requirement of the engine significantly. The regenerator is designed to absorb heat contained in the working fluid and to release ideally the same amount of heat when it is needed. Nevertheless, because of its thermal imperfections, it is impracticable to recover all of the heat absorbed. Hence, the performance of the regenerator is usually evaluated by its effectiveness, which simply expresses the fraction of the heat absorbed from the regenerator that could be recovered for a given regenerator design and operating conditions.

An effectiveness of 1.0 is the best case and implies complete heat recovery while an effectiveness of 0.0 is the worst case, indicating that no heat was recovered from the regenerator. It is unlikely to have an effectiveness of 1.0 in the regenerator, suggesting that the temperature of the working fluid exiting the regenerator is lower than the heater temperature. As a result, additional heat is supplied from the heater so as to make-up for the inefficiency of the regenerator and raise the fluid temperature to the required heater temperature. This however, comes at a cost; the reduction in the thermal efficiency of the engine. In this thesis, the effectiveness of the regenerator was

obtained using the number of transfer units (NTU) approach, with the help of empirical correlations. Thus, the effectiveness of the regenerator is taken herein as:

$$\varepsilon_{\mathrm{r}} = \frac{NTU}{NTU + 1} \tag{4-31}$$

The NTU is expressed as a function of the Nusselt number (Nu) of the matrix over which the fluid is flowing, and is expressed as [180]:

$$NTU = \left(\frac{4Nu}{RePr}\right)\frac{l_{\mathrm{r}}}{d_{\mathrm{hr}}} \tag{4-32}$$

where l_{r} (m), d_{hr} (m), Re (-) and Pr (-) are the length of the regenerator, hydraulic diameter of the regenerator, Reynolds and Prandtl numbers, respectively. The hydraulic diameter, $\mathrm{d_{hr}}$ which expresses the ratio of the void volume to that of the wetted area in the regenerator is given as:

$$d_{\mathrm{hr}} = \frac{4V_{\mathrm{void,r}}}{A_{\mathrm{wetted,r}}} \tag{4-33}$$

Geodon and Wood [166] studied the oscillating flows through the regenerator matrix and proposed the following expression for the estimation of the Nusselt number:

$$Nu = (1 + 0.99(RePr)^{0.66})\phi^{1.79} \tag{4-34}$$

where ϕ (-) is the porosity in the wire meshes contained in the regenerator and it can be expressed as [228]:

$$\phi = \frac{1 - (n_{\mathrm{mr}}\pi d_{\mathrm{wr}})}{4} \tag{4-35}$$

where d_{wr} (m), and n_{mr} $(\frac{1}{\mathrm{m}})$ are the regenerator mesh wire diameter and the number of meshes per meter, respectively.

Thus, the additional heat supplied by the heater to compensate for the regenerator imperfection has been obtained from:

$$Q_{\mathrm{r,non-ideal}} = Q_{\mathrm{r,ideal}}(1 - \varepsilon_{\mathrm{r}}) \tag{4-36}$$

The actual thermal loads of the heater and the cooler have been obtained by incorporating the thermal losses modelled so far into their energy balance equations. These loads can, therefore, be obtained from the following expressions:

$$Q_{\text{actual,k}} = Q_{\text{quasi-ideal,k}} + Q_{\text{cond}} - Q_{\text{r,non-ideal}} + Q_{\text{leak}} + Q_{\text{diss,total}} \quad (4\text{-}37)$$

$$Q_{\text{actual,h}} = Q_{\text{quasi-ideal,h}} - Q_{\text{cond}} + Q_{\text{r,non-ideal}} - Q_{\text{leak}} - Q_{\text{diss,total}} \quad (4\text{-}38)$$

Then, Eq. (4-37) and (4-38) have been used to update the temperature of the cooler and the heater, at the end of each cycle, by deploying the Newton's law of cooling/heating, as expressed in the following relations [67]:

$$T_{\text{h}} = T_{\text{wh}} - \frac{\text{Q}_{\text{actual,h}} Freq}{h_{\text{h}} A_{wh}} \quad (4\text{-}39)$$

$$T_{\text{k}} = T_{\text{wk}} - \frac{Q_{\text{actual,k}} Freq}{h_{\text{k}} A_{\text{wk}}} \quad (4\text{-}40)$$

where h_{h} $(\frac{\text{W}}{\text{m}^2\text{K}})$, h_{k} $(\frac{\text{W}}{\text{m}^2\text{K}})$, $Freq$ (Hz), A_{wh} (m^2), and A_{wk} (m^2) are the heat transfer coefficients in the heater and cooler, the frequency of the engine, the area of the heater wall and the area of the cooler wall, respectively.

The heat transfer coefficients of the heater and cooler have been obtained from correlations in the literature [68] as:

$$h_{\text{i}} = \frac{0.0791 \mu_{\text{i}} c_p {Re_{\text{i}}}^{0.75}}{2 D_{\text{i}} Pr_{\text{i}}}, (\text{i} = \text{k, h}) \quad (4\text{-}41)$$

4.2.2.2. Work transfer losses in the enhanced Stirling engine model

The work transfer losses have been described as third category losses in the Stirling engine [67], [181], which inadvertently reduce the actual power generated by the engine. These losses are:

a) Loss of work due to drop in pressure in the exchangers:

The internal gas flowing through the cooler, heater and regenerator of the engine is in direct contact with the walls. Thanks to no slip condition at the fluid-wall interface,

there is variation in the flow velocity, and by extension the pressure of the working fluid. The change in the pressure of the working fluid in the line of flow is responsible for the pressure loss in the heat exchangers of the ST, which contributes to its performance deterioriation. Thus, the pressure loss in the heat exchangers of the engine have been obtained in this study as:

$$\Delta P_{\mathrm{i}} = \frac{2 f_{\mathrm{i}} \mu_{\mathrm{i}} u_{\mathrm{i}} V_{\mathrm{i}}}{d_{\mathrm{hi}}^2 A_{\mathrm{i}}}, (\mathrm{i} = \mathrm{k}, \mathrm{h}, \mathrm{r}) \tag{4-42}$$

where u $(\frac{\mathrm{m}}{\mathrm{s}})$, A (m^2), and f (-) are the flow velocity, area of the heat exchanger and friction factor, respectively.

The frictional factor used in this study has been obtained from empirical correlations, based on the flow regime of the flowing fluid in the heat exchangers and can be expressed as [65]:

$$f_{\mathrm{i}} = \begin{cases} 16 & Re < 2000 \\ 7.343 \times 10^{-4} Re^{1.3142} & 2000 < Re < 4000 \\ 0.0791 Re^{0.75} & Re > 4000 \end{cases}, (\mathrm{i} = \mathrm{k}, \mathrm{h}) \tag{4-43}$$

While the friction factor of the regenerator has been evaluated from the correlations given by Kay and Londons [241] as:

$$f_{\mathrm{r}} = 54 + 1.43 Re^{0.78} \tag{4-44}$$

The work loss as a result of the pressure drop in the aforementioned heat exchangers can be obtained from the following expression:

$$W_{\mathrm{pdrop}} = \oint \sum_{\mathrm{i=k,r,h}} \Delta P_{\mathrm{i}} \, dV_{\mathrm{e}} \tag{4-45}$$

Finally, the pressure difference between the hot and the cold CVs of the ST required to model the mass leakage through the annular gap, is described in Eq. 4-46 and it is given as the sum of the pressure drops in the heat exchangers of the engine [68]:

$$\Delta P_{\mathrm{ce}} = P_{\mathrm{e}} - P_{\mathrm{c}} = \sum_{\mathrm{i=k,r,h}} \Delta P_{\mathrm{i}} \tag{4-46}$$

b) Frictional work loss in the engine:

As the displacer compresses the internal gas of the engine, the pressure of the fluid around the displacer grows to a value higher than the average pressure of the working fluid in the engine. The opposite effect is observed in the expansion process. Consequently, more compression work is generated in the actual engine's operation than the computed ideal compression work. Likewise, in the expansion process of the prototype engine, less work is produced compared with the ideal expansion work because of the lower pressure around the piston during this process. Hence, the net-work output of the prototype engine would be less than that of the theoretical engine. This loss of work in the engine, by reason of the finite motion of the piston, has been modelled by the principle of finite speed thermodynamics formulated by Petrescu [175].

On the other hand, there would be mechanical losses in the bearings and other mechanical joints of the engine. The combined finite speed and mechanical losses from the Stirling engine were obtained from the following expression [175]:

$$W_{\text{FST \& mech fric}} = \int P_{\text{cylinder}} \left(\pm \frac{\sqrt{3\gamma} u_{\text{p}}}{c} \pm \frac{\Delta p_{\text{f}}}{P_{\text{cylinder}}} \right) dV \qquad (4\text{-}47)$$

where c ($\frac{\text{m}}{\text{s}}$), Δp_{f} (Pa), and u_{p} ($\frac{\text{m}}{\text{s}}$) are the speed of the wave induced in the working fluid by the motion of the piston, the pressure drop as a result of mechanical friction and piston speed, respectively. It is important to note that the sign (+) was used in the compression process and (-) in the expansion process.

The following expressions have been used to obtain the values of c and $\Delta \text{p}_{\text{f}}$ [181]:

$$c = \sqrt{\gamma R_{\text{g}} T} \qquad (4\text{-}48)$$

$$\Delta p_{\text{f}} = 0.97 + 0.15 \frac{N_{\text{r}}}{1000} \qquad (4\text{-}49)$$

where N_{r} (rpm) is the rotational speed of the engine.

c) Work loss due to gas spring hysteresis caused by the motion of the displacer:
As the displacer compresses and expands the internal gas of the engine, it is likely that the gas could act as a spring. This unusual behaviour of the working fluid may induce the dissipation of the internal energy of the fluid. The dissipation loss, as a result of the gas spring hysteresis, has been modelled using the following expression [65]:

$$\dot{W}_{\mathrm{Hyst}} = \sqrt{\frac{1}{32}\omega\gamma^3(\gamma-1)T_{\mathrm{w}}p_{\mathrm{mean}}k_{\mathrm{g}}}\left(\frac{V_{\mathrm{d}}}{2V_{\mathrm{T}}}\right)^2 A_{wetted} \tag{4-50}$$

where ω $(\frac{\mathrm{rad}}{\mathrm{s}})$, k_{g} $(\frac{\mathrm{W}}{\mathrm{mk}})$, V_{d} (m^3), V_{T} (m^3), A_{wetted} (m^2) are the angular speed of the piston, the thermal conductivity of the gas, the instantaneous swept volume of the displacer, the total volume in the working volumes of the engine and the wetted area in the working space, respectively.

Thus, the brake power of the engine has been obtained by subtracting the work losses from the ideal work:

$$\dot{W}_{\mathrm{actual}} = \left\{\left\{\oint(p_{\mathrm{e}}dV_{\mathrm{e}} + p_{\mathrm{c}}dV_{\mathrm{c}})\right\} - W_{\mathrm{FST\ \&\ mech\ fric}} - W_{\mathrm{pdrop}}\right\} Freq - W_{\mathrm{Hyst}} \tag{4-51}$$

Thus, the actual thermal efficiency of the Stirling engine is, given as:

$$\eta_{\mathrm{Stirling}} = \frac{\dot{W}_{\mathrm{actual}}}{Q_{\mathrm{actual,h}}.freq} \tag{4-52}$$

4.3. Model solution algorithm

In this section, an algorithm was developed to describe the steps for implementing the solutions of the set of governing differential equations formulated in Section 4.2. Fig. 4-4 describes the algorithm developed to implement the model solutions. As it has been mentioned previously, the fourth-order Runge-Kutta numerical scheme has been deployed in solving the modified differential equations of the Stirling engine formulated in this work. Prior to deploying the numerical scheme, as it is seen from

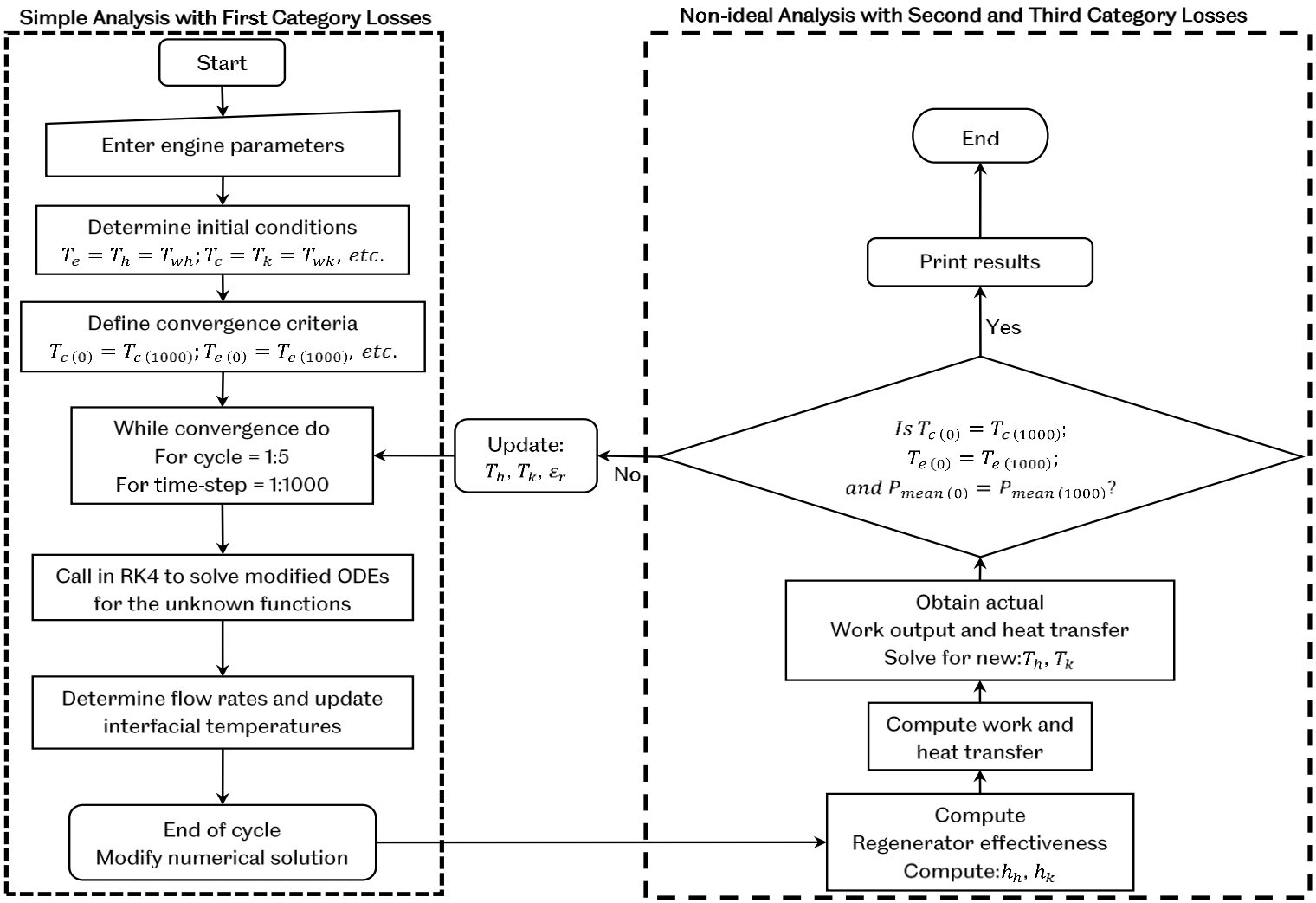

Fig. 4-4. Solution algorithm deployed for implementing the solution of the developed enhanced thermal model of the Stirling engine.

the algorithm, analytical models based on the driving mechanism and engine configuration have been used to obtain the magnitudes of the volumes of the engine gas in the working spaces and its derivatives, V_c, V_e, dV_c, and dV_e as a function of crank angle (or time of operation of the engine) in one cycle of operation, which is expected to span from $\theta = 0^\circ$ to $\theta = 360^\circ$.

Other design parameters of the engine, such as the volumes of the cooler, heater, and regenerator, V_k, V_h, and V_r, respectively, were obtained using physical measurements of the geometry of the prototype engine. Initial conditions of the temperatures of the working fluid in the heater and cooler were specified, while the gas temperature in the regenerator has been obtained as the effective mean of the heater and cooler temperatures [65]. Furthermore, initial conditions of the mass of the fluid were assumed, while Schmidt's model has been deployed to obtain the initial mass of the fluid in the CVs of the engine. The fluid in the hot and cold CVs have been assigned the magnitudes of the heater and the cooler temperatures, respectively, at time, $t_{(0)}$. In addition, ten boundary conditions of the interfacial temperatures of the CVs were specified. In this solution approach, with the exception of variables used to determine constants and other engine geometrical properties, the size of the vector y denoting the unknown functions is 44, and these compose of the analytical variables and derivatives.

The magnitudes of seven of these variables (Q_k, Q_h, Q_r, W_c, W_e, T_c, and T_e) have been obtained by numerical integration, using the fourth-order Runge-Kutta scheme, while the remaining were determined analytically. This initial value problem was solved at each time step up to the maximum time step (in this case 1000), completing one cycle of operation of the engine, before it was tested for convergence. The convergence criteria specified require that the magnitudes of the temperature of the fluid in the cold and hot CVs in conjunction with the mean pressure of the engine at the beginning of the cycle, $t_{(0)}$ $(\text{or } \theta = 0^\circ)$ should be equal to that at the end of the cycle, $t_{(1000)}$ $(\text{or } \theta = 360^\circ)$. Until this condition is met, which implies that the system had attained steady state, the differential equations were solved over repeated cycles, and the numerical results for each variable were logged in each time step. The solutions to the unknown functions, y, provided in this step have the form of a 2-dimensional array of size (44×1000). The processes described so far in this step is similar to that

employed in the Simple analysis [65], except for the fact that the traditional differential equations of the Stirling engine cited in Table 4-1 have been modified as described in Section 4.2.

At the completion of each cycle, the numerical results were modified by accounting for the thermal and the work transfer loss effects in the engine, as discussed in Section 4.2.2, to obtain the actual work and the heat interactions in the engine, and compute its thermal efficiency. Subsequently, the magnitudes of the temperature of the internal gas of the engine in the heater and cooler were modified, as described in Section 4.2.2.1, using the computed heat transfer rate in the referenced engine spaces. Finally, the updated values of the temperature of the internal gas of the engine in the heater and the cooler were transferred to the next cycle to repeat the steps described until steady state is attained.

4.4. Summary of the Chapter

A new thermal model has been developed in this chapter based on the modifications of the traditional adiabatic model of the Stirling engine. Therefore, for the first time the mass leakage from the expansion volume into the compression volume, the mass leakage from the working volume into the crankcase and the displacer shuttle loss were coupled into the governing differential equations of the simple adiabatic models of the Stirling engine. Similar to previous thermal models, second and third category losses, such as piston finite speed losses, mechanical friction losses, spring hysteresis losses, regenerator imperfection losses, heat conduction losses, enthalpy leakage losses and dissipation losses were also considered in developing the present thermal model. Conversely, in the Present Model, the instantaneous pressure in the control volumes of the engine were determined with the computed hydraulic losses in the engine, and the value used to update the temperatures in the control volumes for each time step. Finally, an algorithm for implementing the solution to the developed model that will be carried-out in the next chapter has been presented.

Chapter 5 Simulation of a Kinematic Stirling Engine Performance Based on an Enhanced Thermal Model

This chapter presents the results of the simulation of a beta-type Stirling engine with a rhombic drive mechanism. The engine's performance is simulated based on the enhanced non-ideal second-order thermal model developed in Chapter 4. Section 5.1 implements the solution of the second-order model and undertakes a robust validation of the model predicted results against experimental data, to reveal its accuracy in predicting the performance of the experimental engine. It also compares the model predicted results to the results predicted by other second-order thermal models. Section 5.2 analyses the results of the numerical simulation of the working processes of the experimental engine. Section 5.3 conducts the audit of the energy flow in the engine. Section 5.4 investigates the effect of some key engine geometric and operating parameters on its performance and the summary of the chapter is presented in the final section. The findings of this chapter have been published in the author's paper published in a peer reviewed journal.

5.1. Enhanced model validation

The enhanced thermal model of the Stirling engine developed in Chapter 4 was evaluated with geometric and operating data of a 3-kW beta-type Stirling engine known as the GPU-3 Stirling engine and designed by General Motors. The specifications of the geometrical design of the prototype engine are presented in Table 5-1. The testing of the GPU-3 Stirling engine was conducted in the NASA Lewis Research Centre and the test results of the engine's performance was presented in [169]. MATLAB codes have been developed to implement the numerical solution of the governing ordinary differential equations of the engine as described in Section 4.3 and Fig. 4-4, and are presented in Appendix A. Subsequently, the enhanced model formulated in this study was validated against the test data from the GPU-3 Stirling engine and compared with predicted results from other second-order models [65], [67], [68], [176], [181], [242].

Table 5-1. Design parameters of the prototype 3 kW Stirling engine [169].

Quantity	Value	Quantity	Value
General		**Heater**	
Working fluid	Helium	Mean tube length	245.30 mm
Piston stroke	31.20 mm	Tube outside diameter	4.83 mm
Internal diameter of cylinder	69.90 mm	Tube inside diameter	3.02 mm
Frequency	41.70 Hz	Number of tubes per cylinder	40
Mean Pressure	4.13 MPa	Dead volume of heater	70.88 mm^3
Phase angle	90	**Cooler**	
Heater temperature	977 K	Mean tube length	46.10 mm
Cooler temperature	286 K	Tube external diameter	1.59 mm
Number of cylinder	1	Tube internal diameter	1.09 mm
Regenerator		Number of tubes per cylinder	312
Regenerator length	226 mm	Dead volume of cooler	13.80 mm^3
Regenerator external diameter	80 mm	**Others**	
Regenerator internal diameter	22.60 mm	Clearance volume of the piston	28.68 mm^3
Number of regenerator	8	Clearance volume of the displacer	30.52 mm^3
Dead volume of regenerator	50.55 mm^3	Diameter of displacer	69.9 mm
Material	Stainless steel wire	Diameter of displacer rod	9.52 mm
No. of wires per cm	79 × 79	Diameter of piston rod	22.2 mm
Wire diameter	0.04 mm	Displacer clearance	0.028 mm
No of layers	308	Piston clearance	0.15 mm
Porosity of the regenerator matrix	0.69	Eccentricity	20.80 mm

In Fig. 5-1 and Table 5-2, the results obtained from the enhanced model, referred hereinafter as the 'Present Model', have been compared to the results obtained from the models developed by: Urieli and Berchowitdtz [65], referred to as 'Simple'; Babaelahi and Sayyaadi [181], referred to as 'Simple II'; Sayyaadi and Hosseinzade [242], referred to as 'CAFS'; Hosseinzade et al. [176], referred to as 'PFST'; Babaelahi and Sayyaadi [67], referred to as 'PSVL'; and Li et al. [68], thereafter referred to as 'PSML'. These models are second-order numerical models apart from the 'PFST' that is a closed-form model.

As it is evident in Fig. 5-1 and Table 5-2, the enhanced model predicts the thermal efficiency and brake power of the prototype engine at the referenced design point to a high level of accuracy with relative errors of + 0.3% and - 4.02%, respectively. The high level of accuracy of the present model is a result of a deliberate effort to minimise the assumptions made in developing the model; hence, creating a more practical scenario. In contrast to the previous models, the Present Model predicted superior results for both the brake power and the thermal efficiency at the design point of the test engine compared with the previous models.

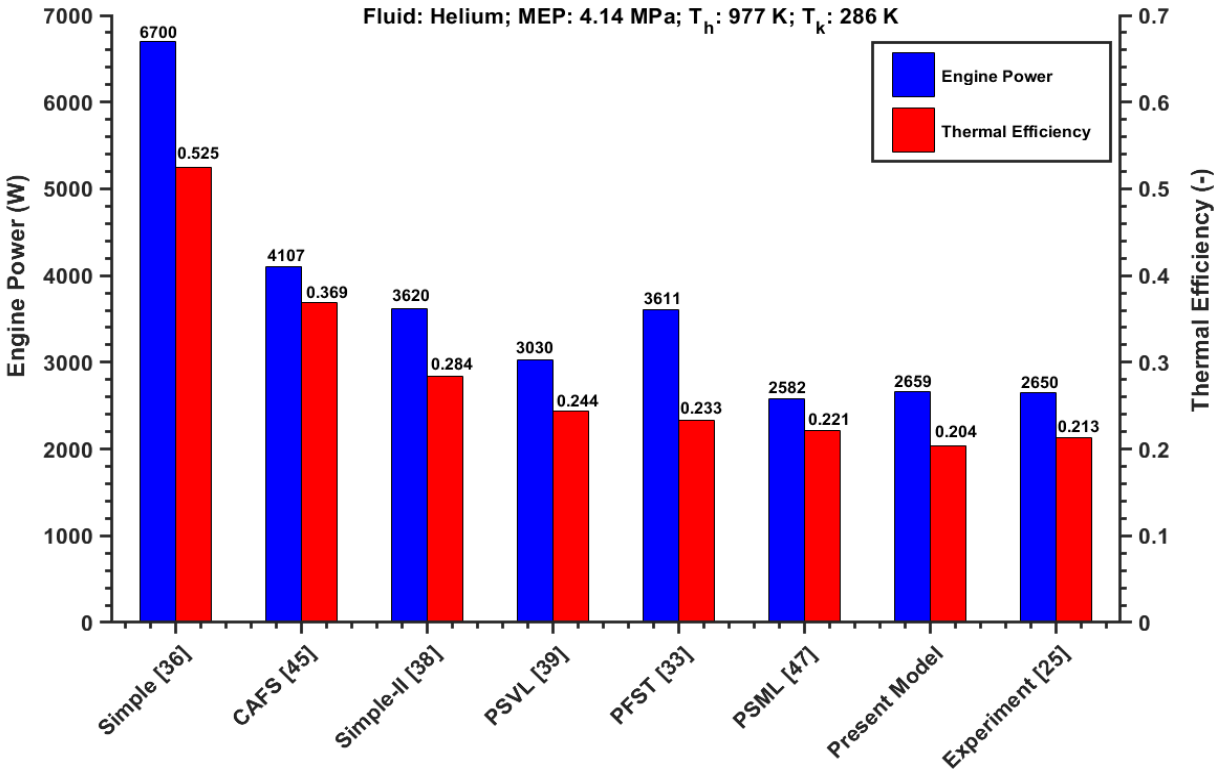

Fig. 5-1. Evaluating the prediction accuracy of the Present Model by comparing it with the experimental data and other numerical models' prediction.

Therefore, it can be concluded that the Present Model is evidently better than the referenced previous models because of the improvements made in the traditional adiabatic model, by accounting for the mass leakage into the cold CV, mass leakage into the crankcase and shuttle heat loss in the engine. In addition, unlike in the previous models, modelling the instantaneous pressure of the working fluid in the CVs of the engine for each time step in the numerical process may have contributed to improving the accuracy of the Present Model.

In particular, in the Simple model [65], which is an adiabatic model, several assumptions were made to simplify the complexity of the involved processes in the engine. This, in turn, resulted in predicting performance results that are much different to the actual engine performance results and yielding relative errors of over 100% (see, Table 5-2). On the other hand, the CAFS [242] and the Simple II [181] models (both adiabatic) did not consider the mass leakage through the displacer gap, which contributed significantly to the work losses in the engine, even though they discarded some of the assumptions made in the Simple model [65]. Further improvements were accomplished in the predicted thermal efficiency and the power output in the PSVL [67] and the PFST [176] models, by replacing the adiabatic with polytropic processes. Despite the improvements made using this approach, the failure of the authors to account for the leakage of the mass of the working fluid into the compression space has limited the accuracy of the models.

In the PSML [68], an updated model built on the principle of polytropic processes in the cold and hot CVs and consequently, improving the model accuracy, prediction errors of – 2.6% and +3.78% in the brake power and thermal efficiency, respectively have been found. Additionally, the high accuracy of the PSML model can be attributed to the coupling of the mass leakage into the compression space, to the ideal model. Even so, the Present Model predicted the engine brake power more accurately than the PSML [68], this is because both the leakage into the compression space and the mass leakage into the crankcase have been simultaneously considered. In contrast, the PSML [68] model predicted slightly better engine efficiency compared to the Present Model. This is because the PSML model appreciates the polytropic losses of the engine, while the Present Model did not. Nevertheless, the reliance on experimental data to

Table 5-2. Relative error in the prototype engine performance data predicted by the Present Model and other thermal models (T_{htr} = 977 K; T_k = 286 K; P_{mean} = 4.14 MPa; *Freq* = 41.67 Hz).

	Simple	CAFS	Simple-II	PSVL	PFST	PSML	Present model
Source	[65]	[242]	[181]	[67]	[176]	[68]	This study
Relative error in brake power (%)	+ 152.8	+ 55.0	+ 36.6	+ 14.3	+ 36.3	- 2.6	+ 0.3
Relative error in efficiency (%)	+ 146.48	+ 73.24	+ 33.33	+ 14.55	+ 9.39	+ 3.78	- 4.02

estimate the polytropic exponents in the compression and expansion processes of the engine using the PSML [68] model may limit its application and accuracy.

Fig. 5-2 (a) and (b) evaluates the performance of the Present Model in predicting the experimental data (labelled 'Exp' in the legends) of the brake power of the GPU-3 engine at various engine frequencies to that of other theoretical models. This is undertaken for engine heater temperature of 922 K, cooler temperature of 286 K and for mean engine pressures of 4.14 MPa and 2.76 MPa, respectively. It is evident that the brake power predicted by the Present Model approximates the experimental data at all the investigated frequencies. In addition, a similar trend for the brake power is observed in the experimental results, the Present model, the PFST [176] and the PSML [68], i.e., an initial increase with the increasing frequency of the engine before attaining a peak value at a frequency of 41.67 Hz. Subsequently, an appreciable decrease in the brake power is recorded as the frequency of the engine increases beyond this value, especially when the engine is operating with a mean pressure of 4.14 MPa (Fig. 5-2 (a)).

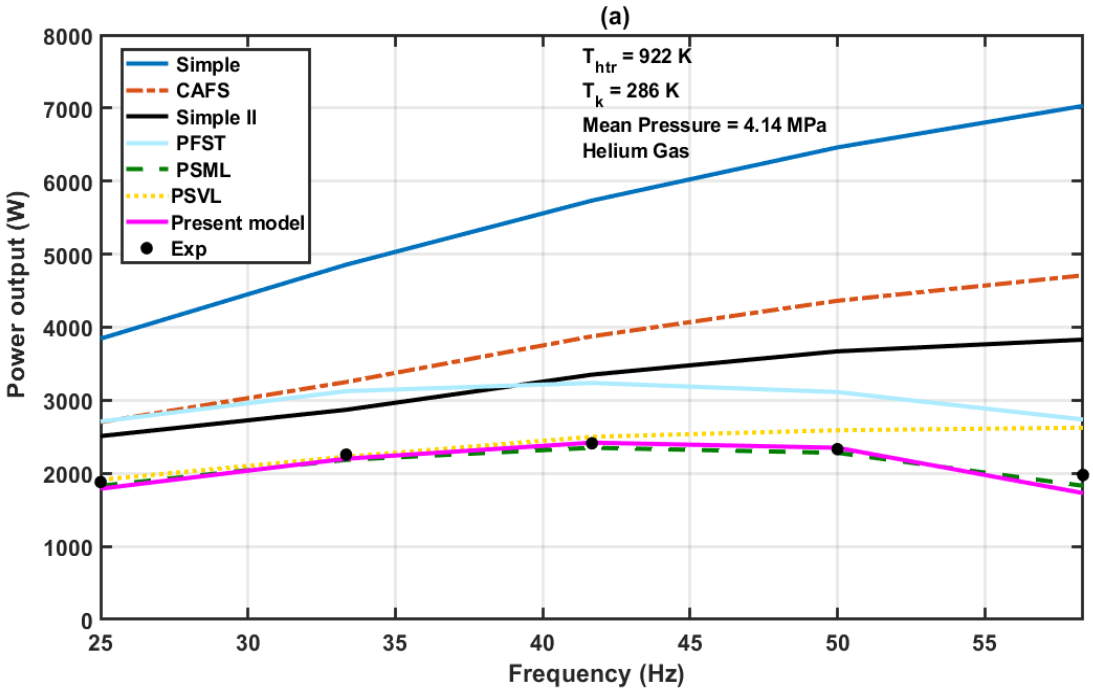

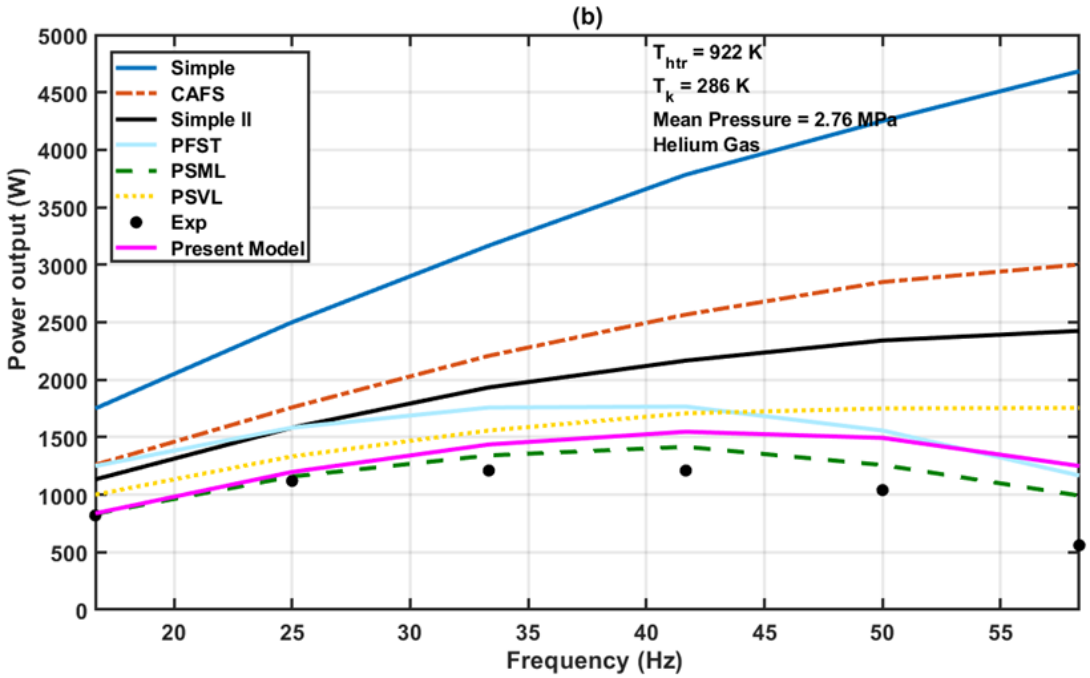

Fig. 5-2. The performance of the Present Model in estimating the brake power of the Prototype engine at various engine frequencies and comparing it to other thermal models (Simple [65], Simple II [181], CAFS [242], PSVL [67], PFST [176] , PSML [68]), and experimental data [169], at T_{htr} = 922 K, T_k = 286 K and MEPs of (a) 4.14 MPa, and (b) 2.76 MPa.

This trend could be as a result of the increase in the internal and external irreversibility in the engine, due to the increase in the frequency of the rotation of the engine. Technically, at higher frequencies the flowrate of the engine fluid would increase and consequently the ideal power will also increase, since the ideal work from the engine does not change. However, this increase in the flowrate of the engine fluid could lead to an increase in the losses due to mechanical friction in the engine, FST of the displacer, pressure drop in the heat exchangers and even the spring hysteresis. The increased losses in the engine at high engine frequencies offset the observed gain in the ideal power, leading to a decline in the brake power derived from the engine.

It is noticeable in Fig. 5-2 (a) that when comparing the prediction accuracy of the Present Model to that of other models, the Present Model predicted the experimental engine's brake power more accurately for the entire engine frequencies investigated, compared with the Simple [65], Simple II [181], CAFS [242], PSVL [67], and PFST [176] models. On the other hand, compared with the PSML

model, the Present Model predicted more superior results of the brake power of the GPU-3 engine for engine frequencies of 33 Hz – 54 Hz, while the PSML model predicted slightly better results for engine frequencies above 54 Hz.

Similarly, based on Fig. 5-2 (b), the Present Model predicted superior results of the brake power for all engine frequencies investigated when compared with the Simple [65], Simple II [181], CAFS [242], PSVL [67], and PFST [176] models, except for frequencies above 53 Hz where the PFST [176] model predicted slightly better results than the Present Model. Conversely, except for frequencies between 16.67 Hz – 25 Hz where the predicted brake power between the Present Model and PSML model were comparable, the PSML model predicted the engine brake power more accurately than the Present Model for a mean effective pressure of 2.76 MPa.

Fig. 5-3 (a) and (b) depict the relative errors recorded in estimating the brake power of the prototype engine by the Present Model for MEP of 4.14 MPa and 2.76 MPa, respectively. As can be noticed, the prediction error was less than 15% (based on Fig. 5-3 (a)) and 40% (based on Fig. 5-3 (b)) for all the engine frequencies investigated, except for the unprecedented rise in the relative error at an engine frequency of 58.33 Hz for the second case.

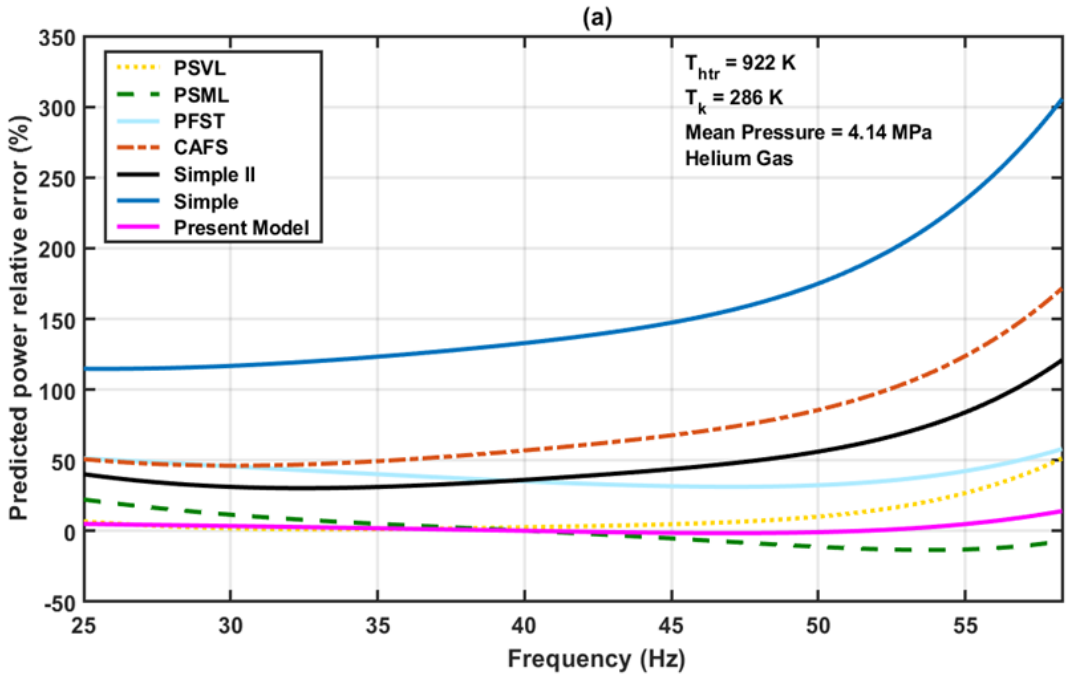

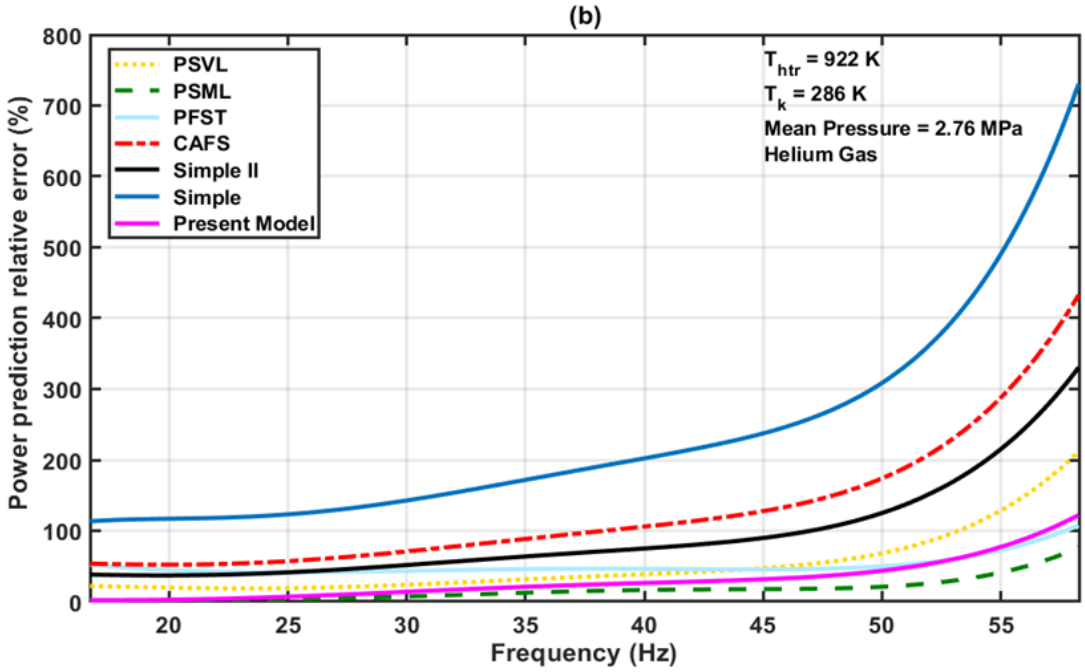

Fig. 5-3. Comparing the relative error in the predicted brake power of the Present Model at different engine frequencies with other models (Simple [65], Simple II [181], CAFS [242], PSVL [67], PFST [176], PSML [68]) at T_{htr} = 922 K, T_k = 286 K and MEPs of (a) 4.14 MPa, and (b) 2.76 MPa.

Meanwhile, compared with the Simple [65], Simple II [181], CAFS [242] and the PFST [176] models, the relative errors recorded by the Present Model were significantly lower at all the engine frequencies investigated for the two MEPs, with the exception of the PSVL [67] model where the relative errors were comparable for engine frequencies between 25 Hz and 41.67 Hz and for a MEP of 4.14 MPa. As for the more recent PSML [68] model, the Present Model recorded lower relative errors, for engine frequencies between 25 Hz and 41.67 Hz (as seen in Fig. 5-3 (a)), while the PSML [68] model produced lower relative errors at all the engine frequencies investigated except between 16.67 Hz and 25 Hz (as seen in Fig. 5-3 (b)).

It can be concluded then that the Present Model can predict superior results for the brake power of the GPU-3 engine than all the other thermal models examined in this study, at the design mean effective pressure of the engine (MEP = 4.14 MPa). However, the PSML [68] model predicted better results at the off-design conditions (MEP of 2.76 MPa). This could be because this study considered the mass leakage into the crankcase, which is estimated with the buffer pressure in the crankcase. Unfortunately, due to the paucity of data in the literature on the measured buffer

pressure in the crankcase in off-design conditions of the engine, the same buffer pressure has been assumed for the design and off-design MEP cases; an assumption that may not be realistic in practice. High buffer pressures would imply low pressure differentials between the compression space and the crankcase, leading to reduced leakage of gas into the crankcase [183]. Hence, the predicted brake power especially at high engine frequencies when the fluid is more mobile would be more than the actual power from the engine; similar to the trend observed in Fig. 5-3 (b).

Fig. 5-4 (a) and (b) show the predicted thermal efficiency of the Present Model at various engine speeds compared with the predictions of other theoretical models, for the experimental engine operating at a heater temperature of 922 K, cooler temperature of 286 K and mean effective pressure of 4.14 MPa and 2.76 MPa, respectively. It is clear that the trend in the engine thermal efficiencies predicted by the Present Model is consistent with the experimental results for the full range of engine frequencies, and the mean effective pressures investigated. On the other hand, the other models predicted linear trends that do not coincide with the experimental dataset.

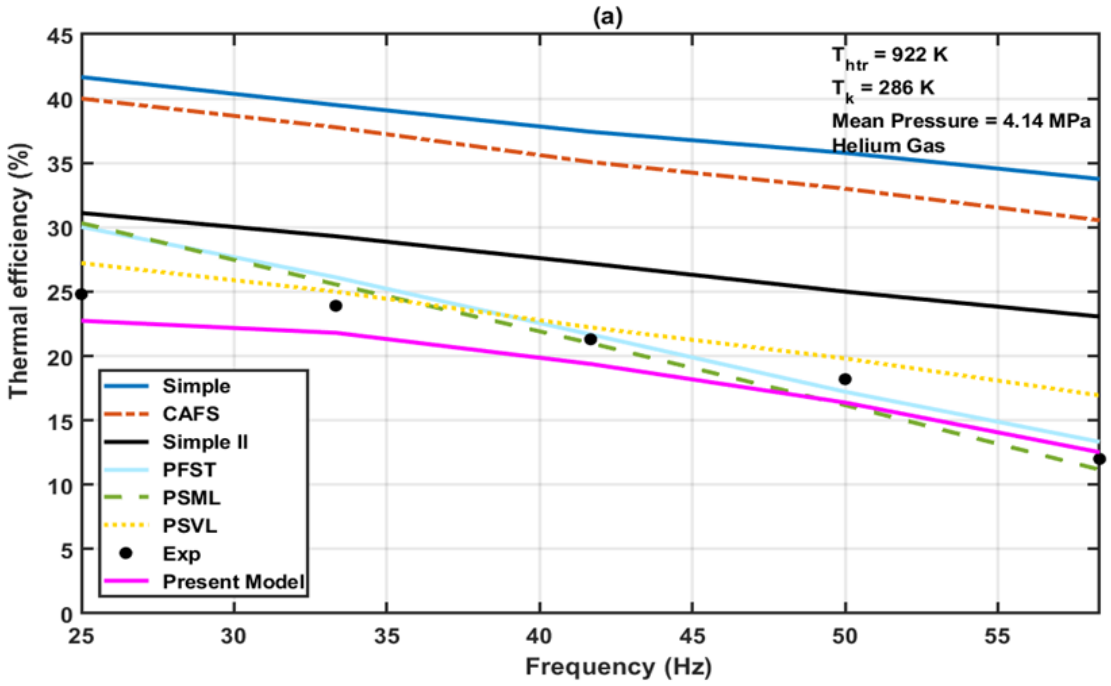

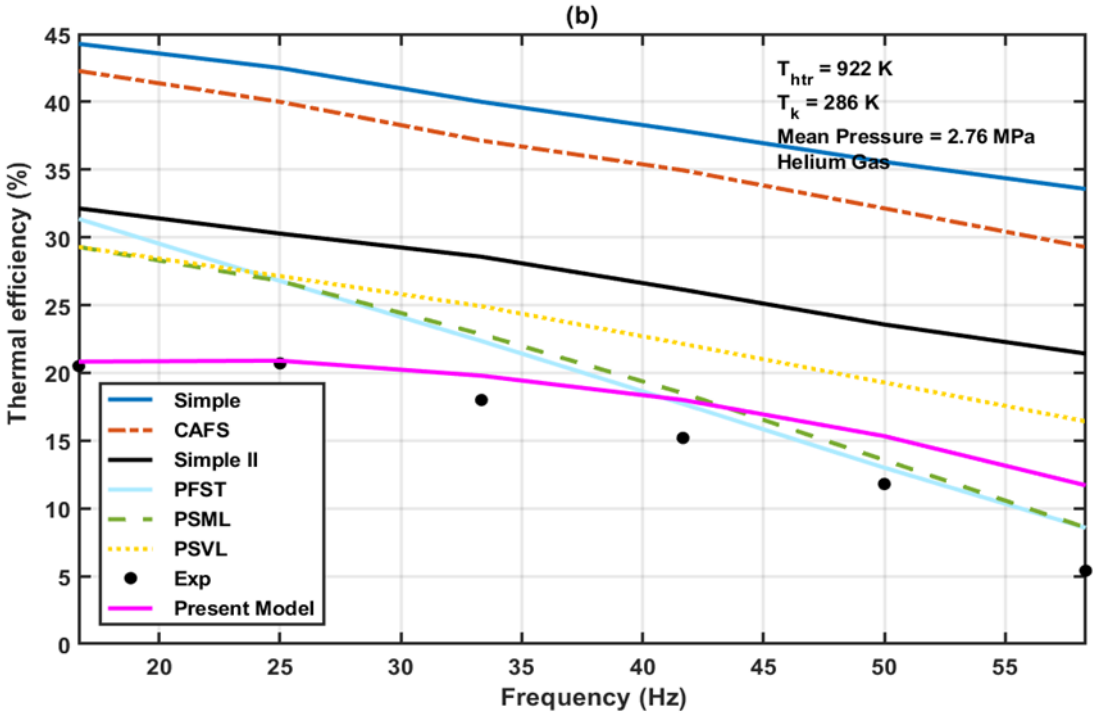

Fig. 5-4. The precision of the Present Model in estimating the thermal efficiency of the prototype Stirling engine at different engine frequencies and comparing it to previous models (Simple [65], Simple II [181], CAFS [242], PSVL [67], PFST [176], PSML [68]) and experimental data [169], at T_{htr} = 922 K, T_k = 286 K and MEPs of (a) 4.14 MPa, and (b) 2.76 MPa.

Meanwhile, the predicted efficiencies of the Present Model are seen to have remained unchanged for engine frequencies between 25 Hz and 33.33 Hz for a MEP of 4.14 MPa or slightly increased for frequencies between 16.67 Hz and 25 Hz and remained the same until 33.33 Hz for a MEP of 2.76 MPa, before decreasing appreciably in both cases. This is expected because the brake power output of the engine declines just after peaking at a frequency of 41.67 Hz. In addition, at higher engine frequencies, the dissipation of the thermal energy in the regenerative engine becomes more intense, especially in the regenerator that contributes most of the losses in the engine. It has been mentioned in Section 4.2.2.1 that additional heat will be required to compensate for the imperfect regeneration, but at the cost of a decline in the thermal efficiency of the engine as is the case in Fig. 5-4 (a) and (b).

As can be noticed from Fig. 5-4 (a), the thermal efficiencies predicted by the Present Model at MEP of 4.14 MPa were more accurate than the other models for all the engine frequencies investigated, except for the mid-range frequencies (33.33 Hz –

45 Hz) where the PSVL [67], and PFST [176], and PSML [68] models exhibit greater accuracy. Nevertheless, the consistency of the Present Model in estimating the engine's thermal efficiency, makes it superior compared to the other models. At an MEP of 2.76 MPa (Fig. 5-4 (b)), the Present Model predicted superior results for engine frequencies ranging from 16.67 Hz to 41.67 Hz. However, between frequencies of 41.67 Hz and 58.33 Hz, the PSML and PFST feature higher accuracy.

Fig. 5-5 (a) and (b) show the relative errors recorded in estimating the thermal efficiency of the prototype Stirling engine by the Present Model for MEP of 4.14 MPa and 2.76 MPa, respectively. It is seen that an average prediction error of -10% (based on Fig. 5-5 (a)) and 25% (based on Fig. 5-5 (b)) were obtained for all the engine frequencies investigated. The Present model yields lower prediction errors than all the previous models for the entire range of frequencies with the exception of the PSVL [67], PFST [176] and the PSML [68], that generate lower relative errors at the mid-range frequencies and at the design MEP of 4.14 MPa. While for the off-design MEP of 2.76 MPa (Fig. 5-5 (b)) only the PFST [176] and the PSML [68] predict the thermal efficiency of the engine with lower relative errors, for engine frequencies above 41.67 Hz. This observed trend further validates the initial assertion that the Present Model is more superior to the previous models in predicting the performance of the engine at the design MEP of 4.14 MPa.

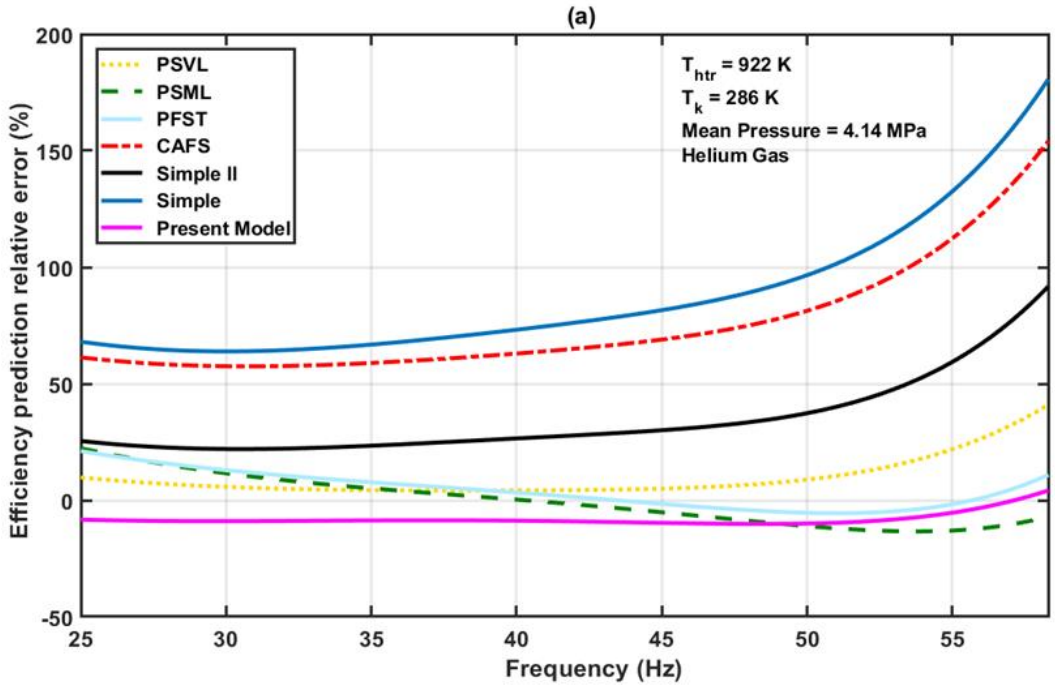

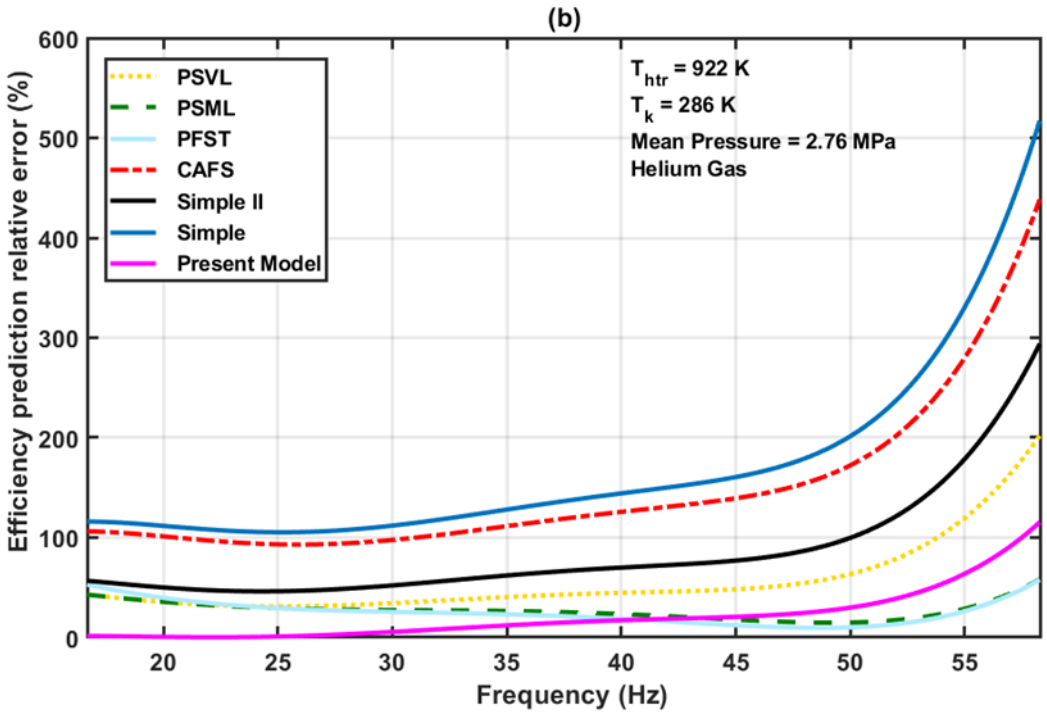

Fig. 5-5. The relative error incurred by the Present Model in estimating the thermal efficiency of the prototype Stirling engine at different engine operating frequencies, with previous models (Simple [65], Simple II [181], CAFS [242], PSVL [67], PFST [176], PSML [68]) at T_{htr} = 922 K, T_k = 286 K and MEPs of (a) 4.14 MPa, and (b) 2.76 MPa.

Finally, the relative consistency of the developed enhanced model in predicting the brake power and thermal efficiency of the GPU-3 Stirling engine, at low, medium and high engine frequencies, especially at the design point of the engine, makes it suitable and superior to previous thermal models for deployment in studies involving the dynamic operation of the engine.

5.2. Model predicted results of engine dynamic performance

So far, the validation of the model has been focused on comparing the predicted brake power and thermal efficiency to the experimental data and the results from other models. Nonetheless, additional insights may be drawn by undertaking a broader evaluation of other results predicted by the model in order to highlight its accuracy [184]. To this end, this section presents additional results showing the dynamic flow of material and energy in the components of the engine predicted by the model, at various angular speeds of the engine.

5.2.1. Simulation of change in the mass and volume of the engine fluid

Fig. 5-6 represents the variation of the mass of the working fluid in the CVs of the engine obtained in one cycle of operation from the developed model. It is evident that the mass of the working fluid in the engine varied in a sinusoidal way in the hot and cold CVs. At the beginning of the cycle, the mass of the working fluid in the cold space starts to increase remarkably from a crank angle, $\theta = 8°$ and attains a peak value at $\theta = 196°$, while it increases from $\theta = 0°$ to $\theta = 72°$ in the hot space before starting to decrease to a minimum value at $\theta = 270°$, similar to the observed trend in Ref. [184]. After the plateau phase, the mass of the working fluid in the cold and hot spaces of the engine decreases and increases appreciably, respectively.

Correspondingly, the variation in the mass of the working fluid reflects the compression, expansion, heating and cooling cyclic processes the engine fluid undergoes in these components. By contrast, the heat exchangers present less variation in the mass of the working fluid, because of the absence of moving parts like the piston and displacer to alter the volume as it is the case in the cold and hot spaces. It is seen that the cooler and regenerator noticeably handle low quantity of the engine fluid. Consequently, this may lead to poor heat transfer in these CVs.

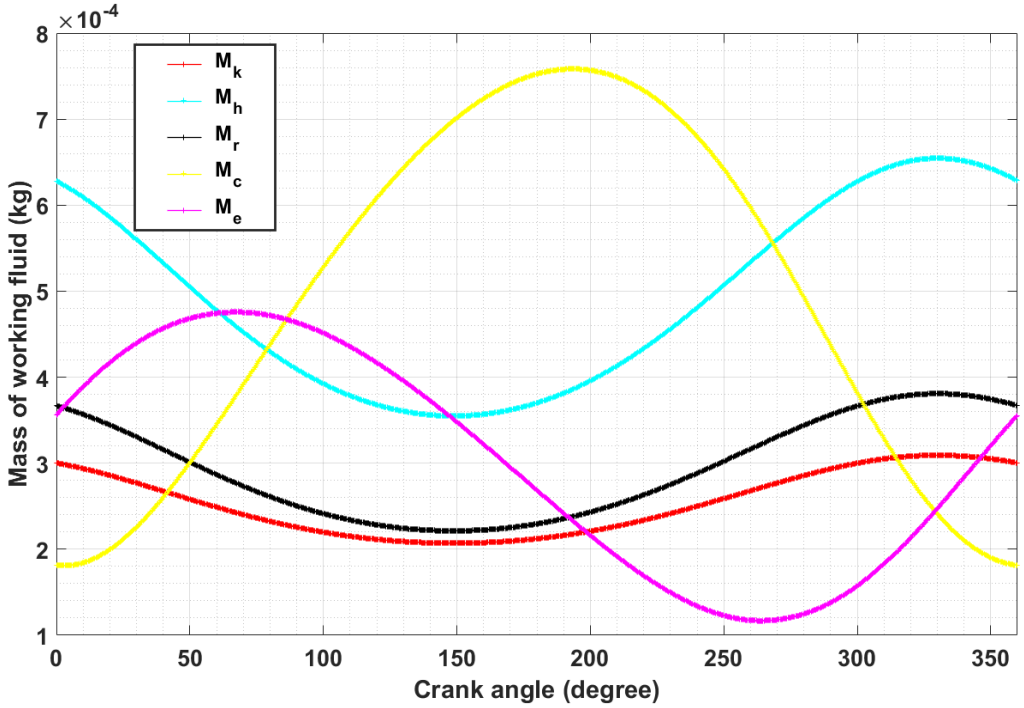

Fig. 5-6. Variation in the mass of the working fluid in the main components of the engine.

Fig. 5-7 illustrates the sinusoidal variation in the engine volume and pressure in the cold and hot spaces and for the entire engine. It is evident that the volume variations in the hot and cold spaces correspond with the mass variation predicted by the model in Fig. 5-6, as expected. Therefore, the volume of the working fluid in these spaces increases and decreases as the mass of the working fluid increases and decreases. However, the maximum and minimum volumes are attained at $\theta = 90°$ and $\theta = 270°$, respectively in the hot space, while the maximum value is attained at $\theta = 180°$ in the cold space.

On the other hand, the total pressure of the engine fluid decreases with the increase in the volume of the fluid in the hot and cold spaces at the beginning of the cycle. This decrease continues to be driven by the steep increase in volume in the cold space despite the reducing volume in the hot space, until a minimum value is attained at $\theta = 150°$. Then, the pressure starts to increase steeply with the pronounced decrease in the volume of the fluid in the hot and cold spaces of the engine. It reaches its peak at $\theta = 330°$ before starting to decline again with the appreciable increase in the volume of the fluid in the hot space.

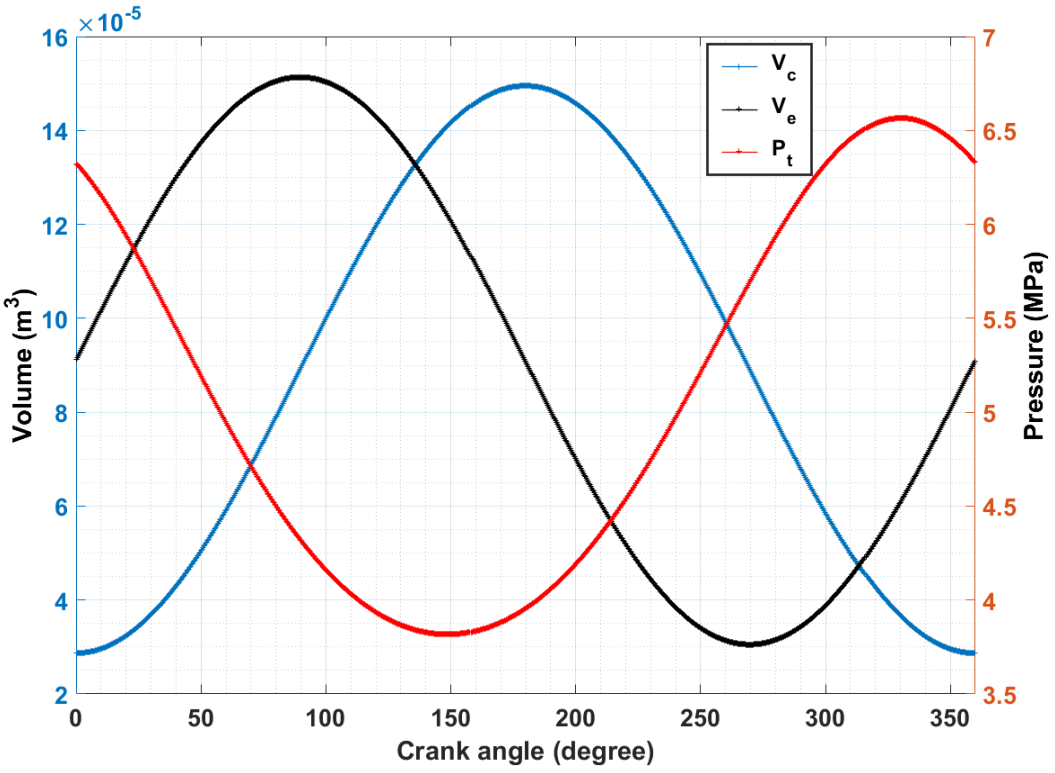

Fig. 5-7. Variation in the volume and pressure of the working fluid with the crank angle.

5.2.2. Simulation of the dynamic variation of energy in the engine

Fig. 5-8 depicts the pressure drop in the heat exchangers of the Stirling engine while Fig. 5-9 represents the energy flow in a cycle of its operation, at the various angles of rotation of the engine. As Fig. 5-8 shows, the regenerator contributes most of the pressure drop in the engine. The pressure drop in the regenerator is seen to rise steadily to a maximum of 0.2 MPa with the increase in the angle of rotation of the crankshaft from $\theta = 0°$ to $\theta = 96°$. This is the case during the transfer process after the compressed engine fluid is sent at high velocity to the hot space from the cold space; hence, the observed positive pressure drop. It is seen in Fig. 5-9 that the net cycle work and heater heat flow increase within this region, while heat is lost in the regenerator to heat up the fluid. Note that to ensure isothermal expansion in the Stirling engine, the engine fluid is heated up during the expansion process to prevent a reduction in its temperature.

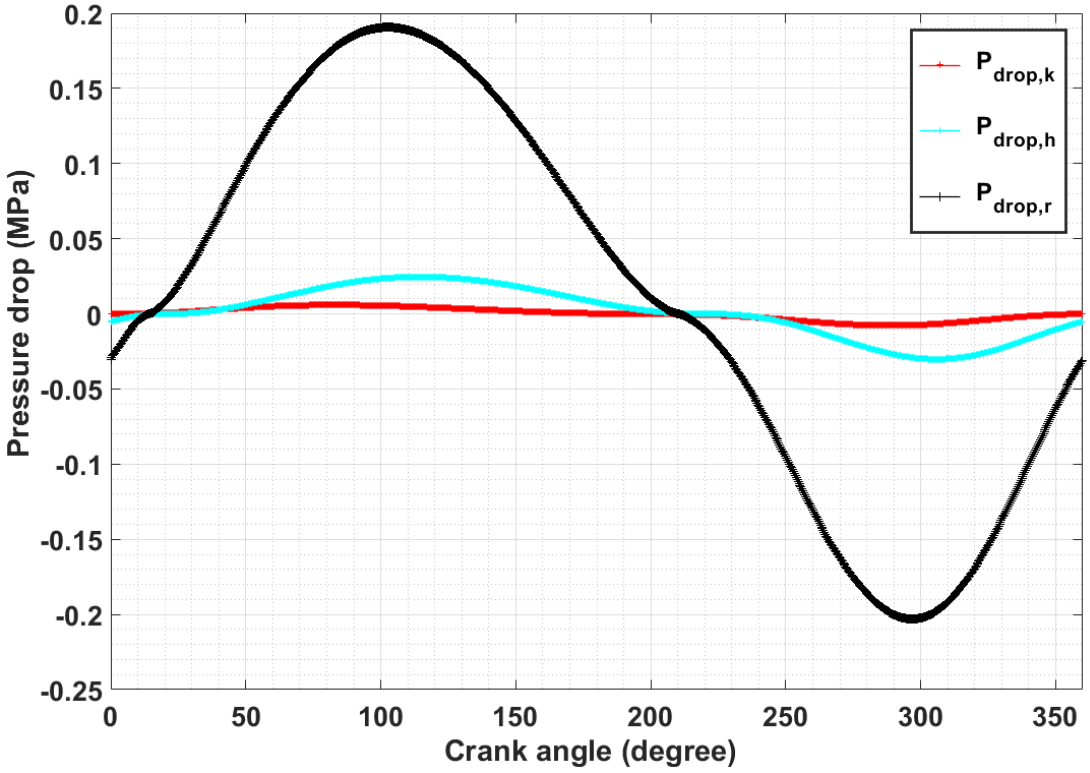

Fig. 5-8. Pressure drop in the heat exchangers of the Stirling engine.

Thereafter, the pressure drop in the regenerator decreases significantly to a minimum of -0.2 MPa at a crank angle, $\theta = 300°$ and then increases again until the end of the cycle. The other phase of negative change in pressure drop occurs when

the expanded engine fluid is being sent to the cold space from the hot space. This process is also marked with the storage of the thermal energy in the engine fluid in the wire meshes of the regenerator. Expectedly, the net cycle work decreases to a minimum value at $\theta = 300°$ and starts to increase again until the end of the cycle (see, Fig. 5-9). Therefore, the regenerator is seen to have handled most of the thermal energy transfer in the engine and is a vital component in its design. In particular, the regenerator of the Stirling engine helps to minimise the thermal energy input of a conventional heat engine by about 80% [180]. By comparison, the cooler records a very small drop in the pressure of the working fluid, which could be as a result of the low velocity of the fluid in this component, thanks to the compression work. Conversely, appreciable level of pressure drop compared with that of the cooler is seen in the heater, but far less compared with the pressure drop in the regenerator [184], [228].

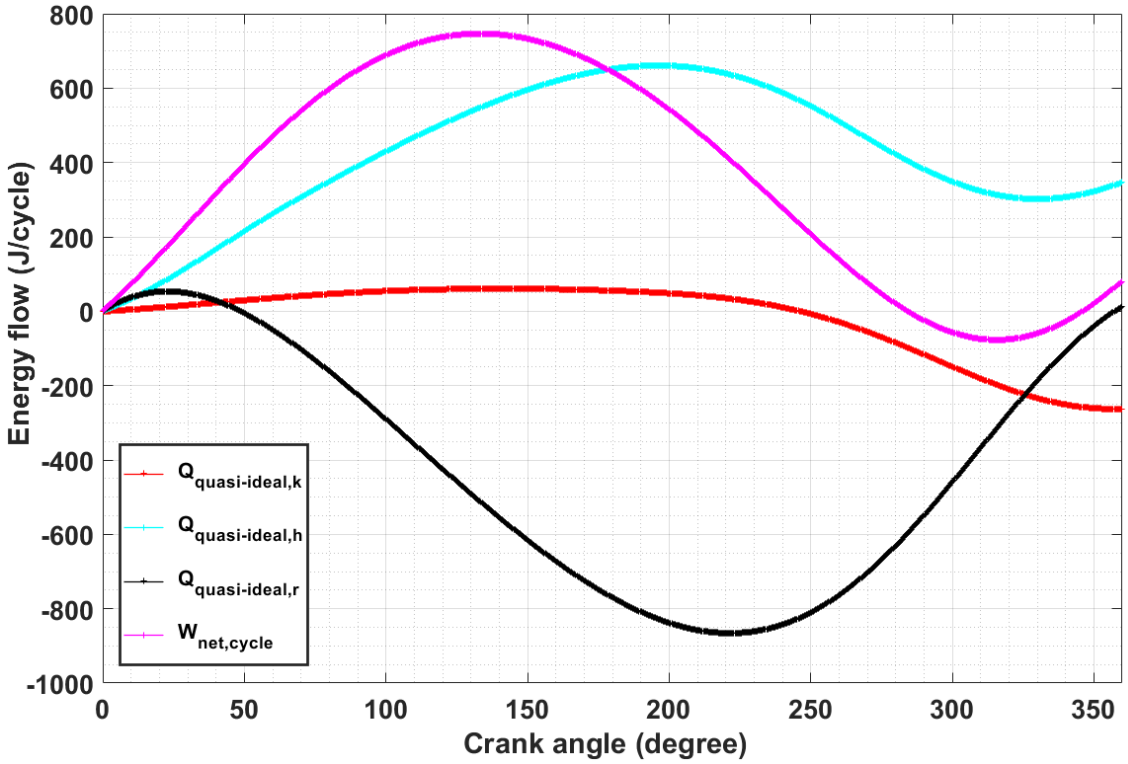

Fig. 5-9. Heat and work flow as a function of the crank angle in the engine.

5.3. Analysis of the engine work and heat transfer processes

The work diagram of the engine predicted by the developed model is presented in this section and the first law audit of the energy flow in the engine is performed and

presented in a Sankey diagram. Fig. 5-10 is the pressure-volume diagram predicted by the developed model for the hot and cold volumes of the engine. The region enclosed by the pressure-volume diagram, otherwise called the work diagram, represents the ideal cycle work done by the engine. However, in this study, the mass leakage into the cold space and the crankcase and shuttle heat loss have been coupled to the ideal adiabatic equations to obtain a non-ideal pressure variation in the engine as expressed in Chapter 4 and Eq. (4-12). As can be seen, the specific volume of the engine fluid in the cold space decreases between the crank angles of $\theta = 192\,°$ to $\theta = 360\,°$ in the compression process. On the other hand, it is seen that it decreases to the minimum volume in the hot space during the transfer process to the cold space, from $\theta = 96°$ to $\theta = 270°$. The maximum pressure in the cold space is recorded at $\theta = 24\,°$, just at the end of the compression process while it is observed at $\theta = 336\,°$ in the hot space, which is the early phase of the expansion process.

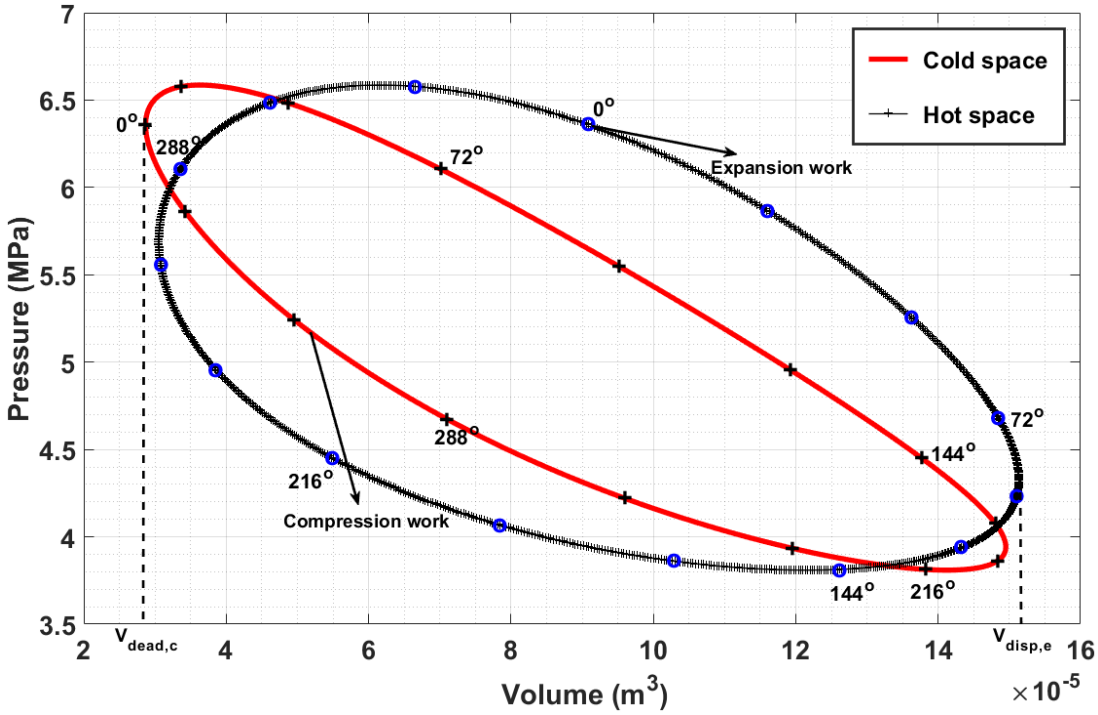

Fig. 5-10. Pressure-volume diagram of the working processes in the engine.

Thereafter, the pressure of the working fluid decreases while the volume increases in the hot space, indicating that the piston is doing some expansion work. It is seen that while the increase in the volume of the fluid started at $\theta = 0\,°$ or $360°$ in the cold space, it began at $\theta = 270\,°$ in the hot space, due to the $90°$ phase difference

between the displacer and the piston of the engine. Further, as expected, the expansion process encloses more volume compared with the compression process; thus, positive net cycle work is obtained from the engine. The hot CV where the expansion process takes place records higher pressure variation compared with the compression process in the cold CV. Therefore, the net cycle work in the engine can be enhanced by achieving higher pressures in the engine during the expansion process and lower pressures, in the compression process [184]. That way, the region enclosed by the hot CV will increase while the cold CV region will shrink and consequently, lower compression work and higher expansion work will be obtained.

Fig. 5-11 illustrates the energy flow audit in the Stirling engine. As it is evident, the second and third category losses in the engine have been accounted for in this energy audit. In Sections 4.2.2.1 and 4.2.2.2, the second and third category losses are accounted for in the enhanced model development, which are mainly the heat and work transfer losses, respectively, and these were presented and elaborately discussed.

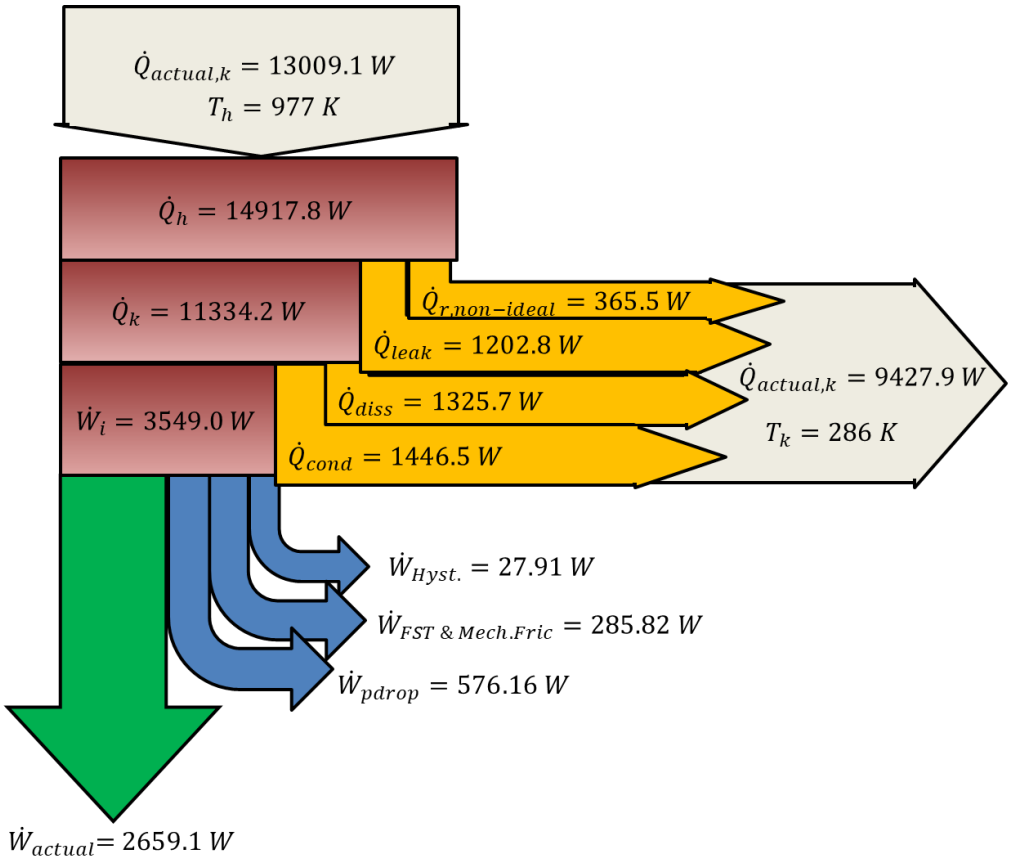

Fig. 5-11. Energy audit of the engine showing the second and third category losses.

As Fig. 5-11 shows, 13.0 kW of heat is supplied into the engine at a constant heater wall temperature of 977 K. This thermal energy heats up the working fluid and drives the operation of the engine. The brake power obtained from the engine is 2.65 kW and as expressed in Chapter 4 and Eq. 4-51, it is the difference between the net quasi-ideal cycle work and the work losses in the engine. It can be seen that the pressure drop in the heat exchangers contributes the highest work losses in the engine of 0.576 kW, while finite speed and mechanical frictional losses were the second highest work loss contributors in the engine. Conversely, 1.446 kW of heat is lost in the engine due to the conduction from the wall of the regenerator and this is the highest thermal energy loss recorded in the engine. Other major contributors of heat losses in the engine are dissipation losses and enthalpy leakage losses due to the leakage of the working fluid into the buffer space. However, hysteresis losses and losses due to the imperfection of the regenerator are the least sources of work and heat losses in the engine, respectively. Similar conclusions were reported in Ref. [68] for the hysteresis losses; nonetheless, they found leakage losses contributed the smallest amount of heat losses.

It can be observed from Fig. 5-11 that the net heat in the system is not equal to the net cycle work, and this is contrary to the expectation based on the law of conservation of energy. This is because the shuttle losses and mass leakage losses from the hot space to the cold space and into the crankcase have been coupled to the ideal equation of the engine. Therefore, the difference in the net heat added to the engine and the quasi-ideal work of 34.6 W could be as a result of the several stages of mass leakages in the engine. Finally, 9.427 kW of heat is sent to the sink from the cooler of the engine. This enormous amount of waste heat can be recovered to drive another heat engine, to improve the combined electrical efficiency or for other useful purposes.

5.4. Effect of varying key parameters on the engine performance

The effect of several geometrical and operating properties on the performance of the GPU-3 Stirling engine have been widely studied [157], [184], [243]. However, only a few studies have investigated the effect of the dimensionless gap number on the brake power and thermal efficiency of the engine [68]. Therefore, this section

presents the results of the effect of the dimensionless gap number (J/D_{d}) – the ratio of the clearance between the displacer and engine cylinder to the displacer diameter – on the brake power of the prototype Stirling engine. The engine operates with a heater wall temperature of 977 K, cooler wall temperature of 286 K, engine frequencies of 25 Hz, 33.33 Hz and 41.67 Hz and mean effective pressures (MEP) of 4.14 MPa, 2.76 MPa and 1.38 MPa, respectively. This study is intended to highlight the level of the influence the leakage of engine fluid into the cold space has on its performance at different engine operating conditions.

Fig. 5-12, Fig. 5-13, and Fig. 5-14 show the impact of the dimensionless gap number (J/D_{d}) on the brake power of the prototype Stirling engine for the aforementioned operating conditions, when the engine is operated with two engine gases (helium and hydrogen). In Fig. 5-12, it is evident that for both engine fluids and all the engine frequencies investigated, the brake power of the engine did not change substantially when the dimensionless gap number was below 1.5×10^{-4}. However, as the dimensionless gap number increases, the brake power declines dramatically. This is because, with the increase in the gap between the displacer and the wall of the cylinder, more of the engine fluid will leak from the hot CV into the cold CV.

Thus, there will be loss in the expansion work of the engine, leading to a corresponding gain in the compression work; hence, the net ideal work from the engine will decline. In addition, it is seen that the impact of the dimensionless gap number on the brake power is less intense at an engine frequency of 25 Hz, but becomes significant as the frequency increases from 33.3 Hz to 41.67 Hz. Consequently, the design point of the engine, $J/D_{\mathrm{d}} = 4.0 \times 10^{-4}$, drifted further from the optimum brake power with an increase in the operating frequency. Comparing the two working fluids, the impact of the dimensionless gap number on the brake power output of the engine is more severe for the engine utilising hydrogen gas at all the frequencies investigated. This is because hydrogen is lighter and this results in increased leakage into the compression space. Thus, the engine working with helium has its design point closer to the optimum power output than that operating on hydrogen gas.

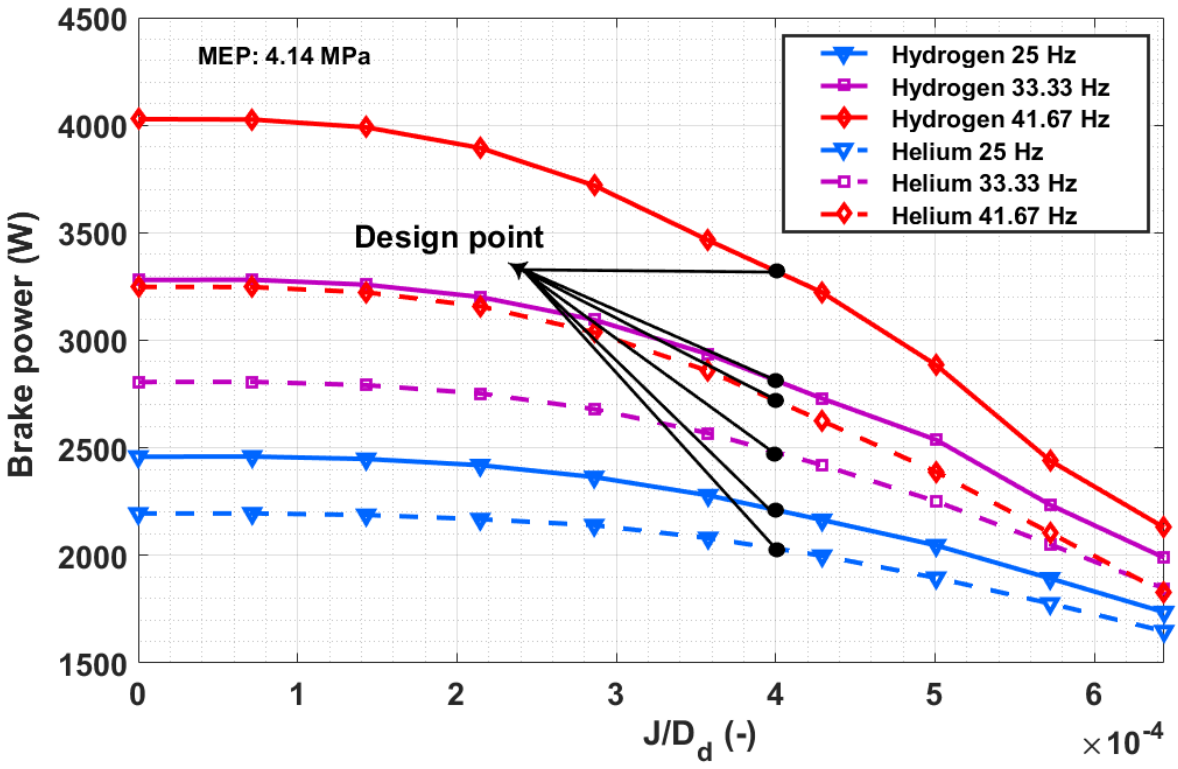

Fig. 5-12. The impact of the gap dimensionless number on the brake-power of the prototype Stirling engine, operating at different engine frequencies, T_{htr} = 977 K, T_k = 286 K, MEP of 4.14 MPa and utilizing helium or hydrogen as the working fluid.

Similarly, from Fig. 5-13, the change in the brake power of the engine became noticeable when the dimensionless gap number exceeds 2.0×10^{-4}, for MEP of 2.76 MPa. As in the case of the engine operating with MEP of 4.14 MPa, the brake power of the engine deteriorates significantly with the increase in the dimensionless gap number beyond this value. Nevertheless, the impact is less intense for helium gas than for hydrogen gas. Meanwhile, as the frequency of the engine increases the impact increases, while the design point of the engine is increasingly sub-optimal. However, compared with the engine operating at MEP of 4.14 MPa, the deterioration of the brake power with the increase in the dimensionless gap number is less severe at MEP of 2.76 MPa.

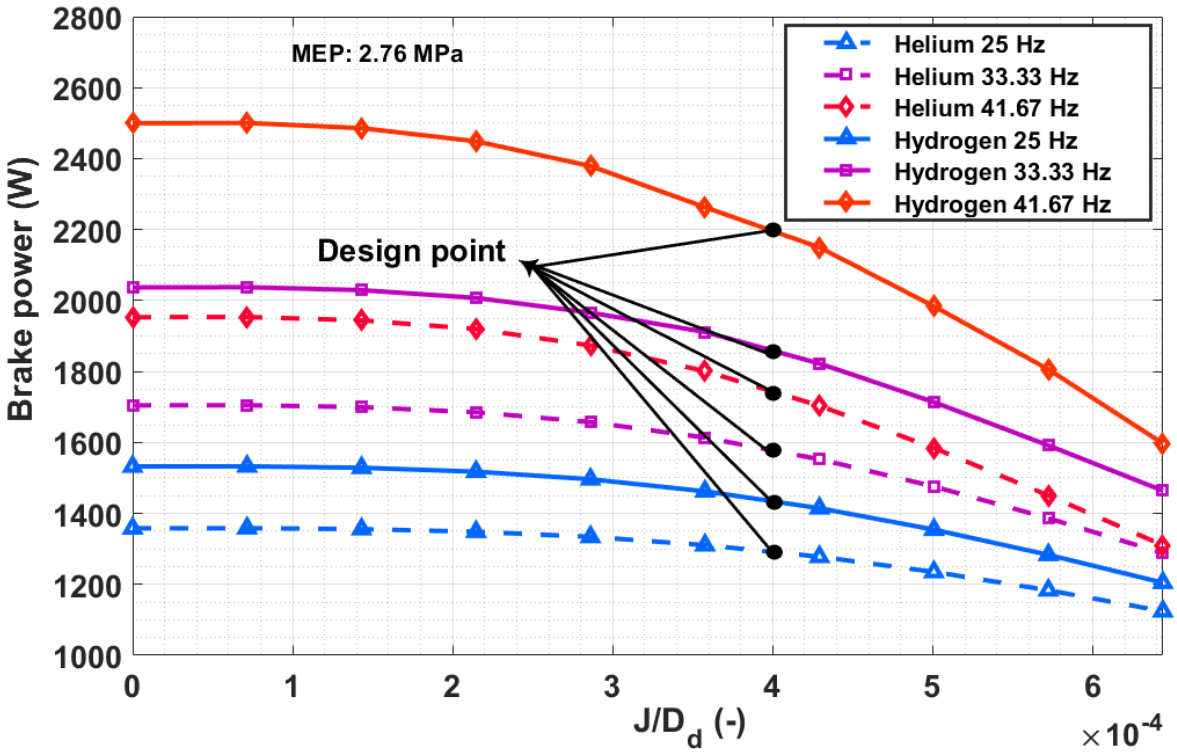

Fig. 5-13. The impact of the gap dimensionless number on the brake-power of the prototype Stirling engine operating at different engine frequencies, T_{htr} = 977 K, T_k = 286 K and MEP of 2.76 MPa and utilizing helium or hydrogen as the working fluid.

Likewise, based on Fig. 5-14, appreciable changes in the brake power output from the GPU-3 engine did not occur until a dimensionless gap number of 3.0×10^{-4} was obtained for the engine operating with a MEP of 1.38 MPa. Beyond this value, the brake power reduces significantly with the increase in the dimensionless gap number; however, the impact is not as pronounced as in the cases of MEPs of 2.76 MPa and 4.14 MPa. Meanwhile, comparing the two working fluids, the impact of the dimensionless gap number on the brake power is again more significant for hydrogen than for helium, while the change in the engine frequency has a similar impact as in the case of the engine operating with MEPs of 2.76 MPa or 4.14 MPa. However, the design point of the prototype engine is almost at the optimal brake power in this case than in the previous cases. Hence, the increase in the MEP of the engine contributes to the negative impact of the dimensionless gap number on the brake power of the GPU-3 engine. Similarly, an increase in the frequency of the engine leads to an increase in the deterioration of the power output as the dimensionless gap number increases with the effect being more pronounced in the

engine utilising hydrogen [182], [244]. Finally, at the design point of the GPU-3 Stirling engine, reducing the dimensionless gap number from 4.0×10^{-4} to 2.0×10^{-4} leads to a 16% increase in the brake power from the engine if helium gas is used as the working fluid and a 15% increase with hydrogen gas.

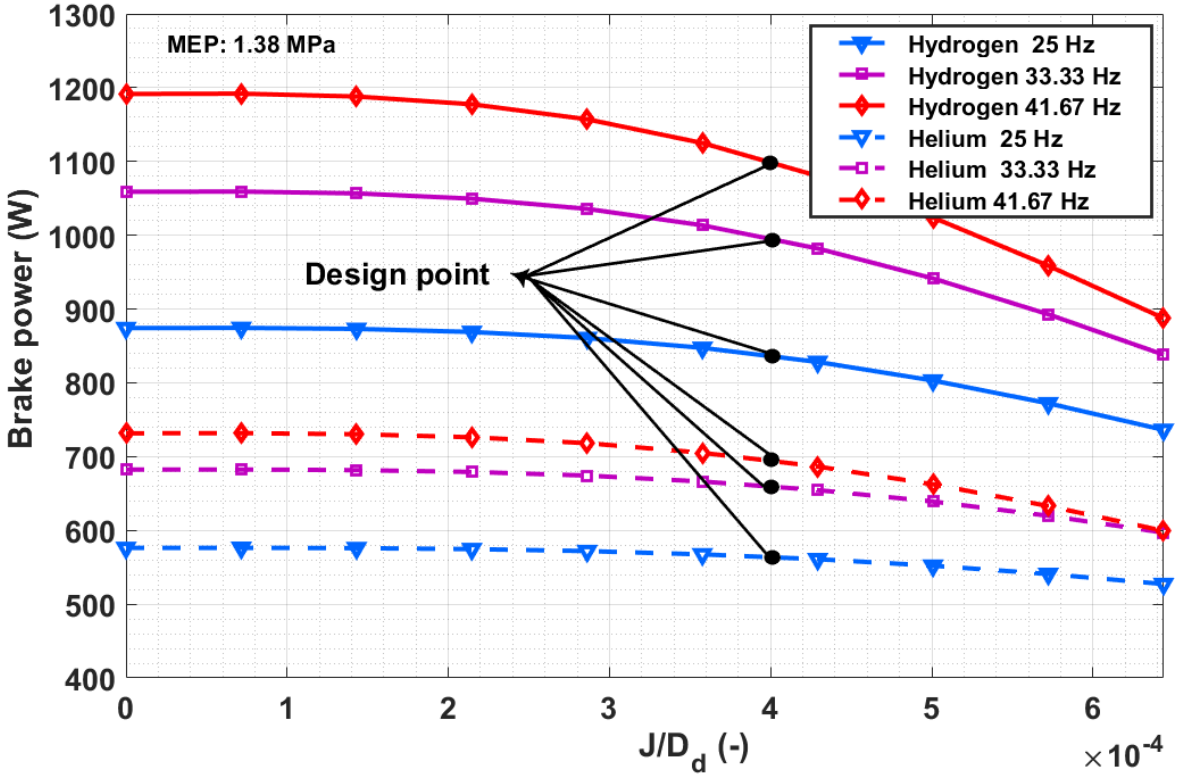

Fig. 5-14. The impact of the gap dimensionless number on the prototype Stirling engine, operating at different engine frequencies, T_{htr} = 977 K, T_k = 286 K and MEP of 1.38 MPa and utilizing helium or hydrogen as the working fluid.

Fig. 5-15, Fig. 5-16 and Fig. 5-17 represent the impact of the dimensionless gap number on the thermal efficiency of the GPU-3 for the operating conditions earlier mentioned. It is evident from Fig. 5-15 that for both engine gases, the thermal efficiency of the engine starts deteriorating significantly when the dimensionless gap number increases beyond 1.5×10^{-4}. As described in Chapter 4 and Eq. (4-2), with an increase in the displacer gap, the shuttle thermal loss decreases, thus resulting in a decrease in the thermal efficiency of the engine [68]. The decrease in the thermal efficiency is, however, more pronounced with hydrogen than with helium since the brake power deteriorated more in the former. Meanwhile, the thermal efficiencies were higher at higher frequencies for a smaller dimensionless gap number, but

decreases as this number increases. This is because the work losses in the engine deteriorated with the increase in the frequency of the engine and the dimensionless gap number. Again, the engine working with helium has the thermal efficiency at the design point closer to the optimum thermal efficiency compared with the hydrogen engine.

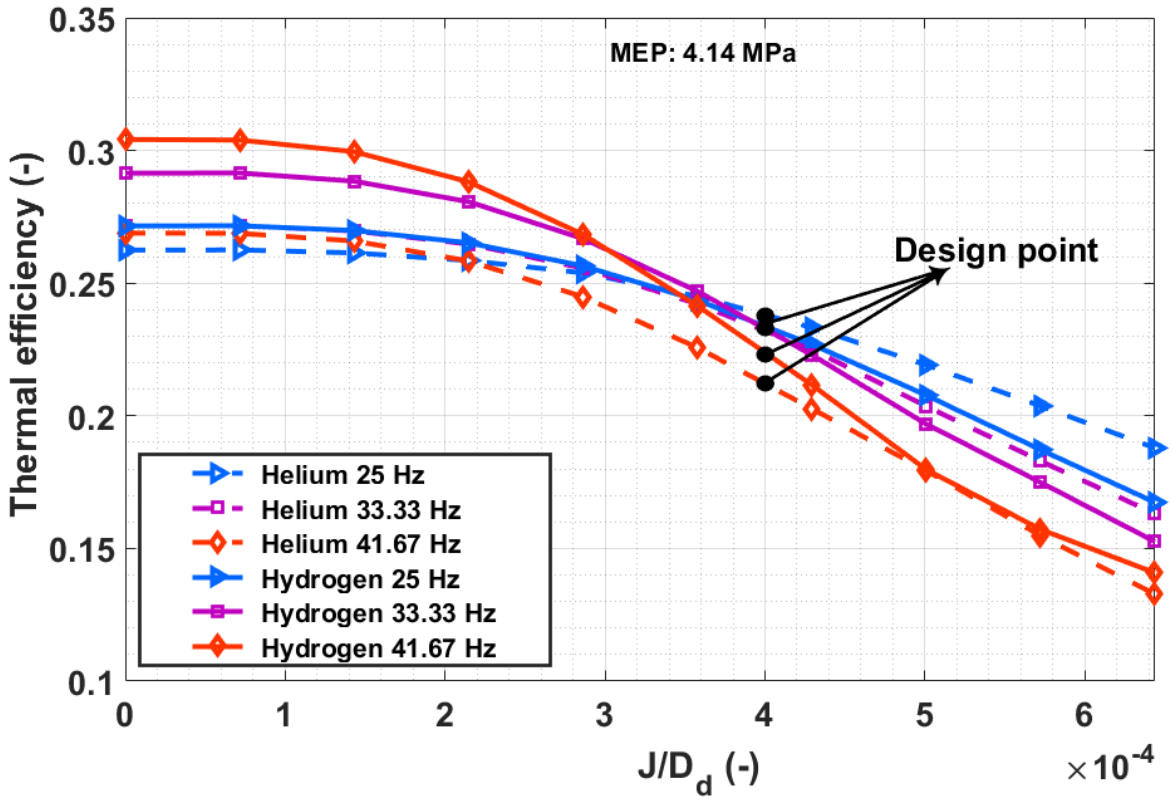

Fig. 5-15. The impact of the dimensionless gap number on the thermal efficiency of the prototype Stirling engine, for different engine frequencies, T_{htr} = 977 K, T_k = 286 K and MEP of 4.14 MPa and utilising helium gas or hydrogen as the working fluid.

As shown in Fig. 5-16, a similar trend as that observed when the engine is working with a MEP of 4.14 MPa is observed; except that there are appreciable changes in the thermal efficiency of the engine observed for the dimensionless gap number greater than 2.0×10^{-4}. This is as expected, since the brake power produced from the engine remained the same for a dimensionless gap number less than this value. However, the change in the thermal efficiency observed for a MEP of 2.76 MPa is less significant compared with the case of a MEP of 4.14 MPa. While the thermal efficiency

of the engine at the design point is much closer to the optimal engine efficiency, especially with the decrease in the frequency of the engine.

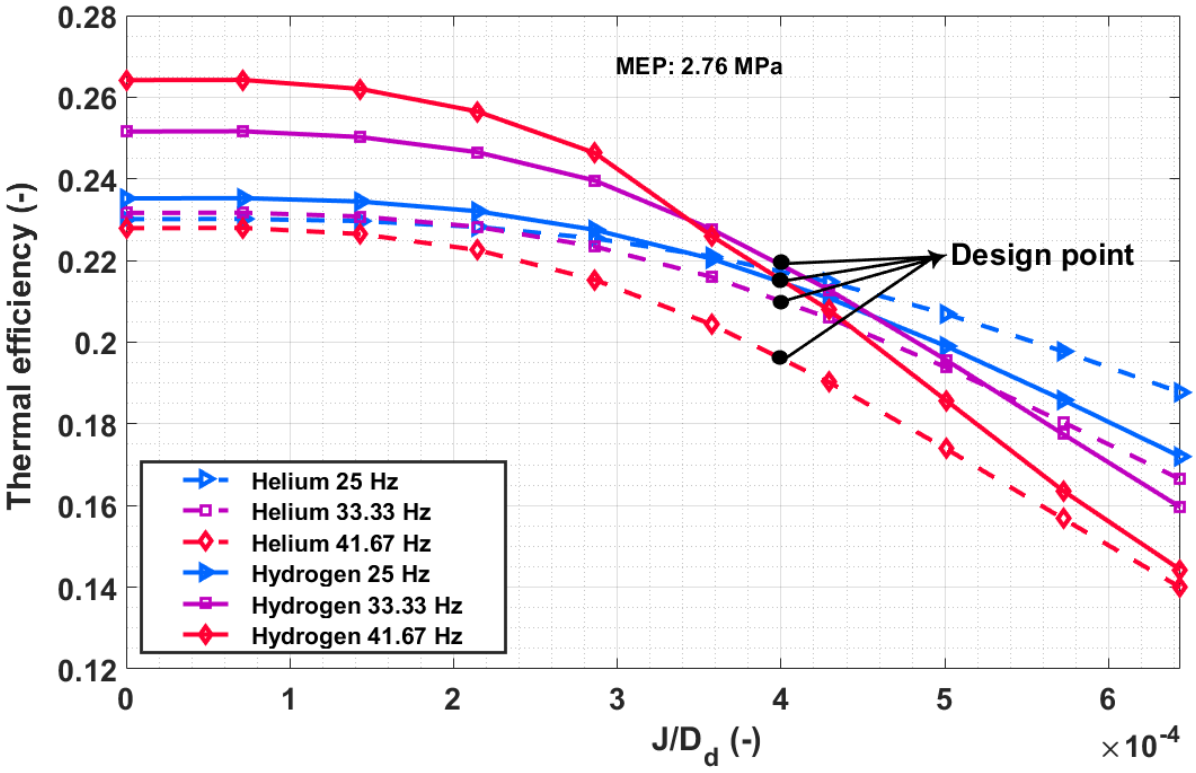

Fig. 5-16. The impact of the dimensionless gap number on the energetic efficiency of the prototype Stirling engine, for different engine frequencies, T_{htr} = 977 K, T_k = 286 K and MEP of 2.76 MPa and utilising helium gas or hydrogen as the working fluid.

The impact of the dimensionless gap number on the thermal efficiency of the GPU-3 engine is not so significant at MEP of 1.38 MPa, as seen in Fig. 5-17, especially for the engine using helium. It is seen that, at this low MEP, the frequency of the helium engine has more impact on the thermal efficiency than the dimensionless gap number. For the engine running on hydrogen, the dimensionless gap number still maintains a similar impact on the engine for MEP of 1.38 MPa as in the other cases, although the impact is less intense in this case. Finally, the thermal efficiency of the GPU-3 Stirling engine could improve by 22% for helium and 30% for hydrogen, if the dimensionless gap number is reduced from 4.0×10^{-4} to 2.0×10^{-4}.

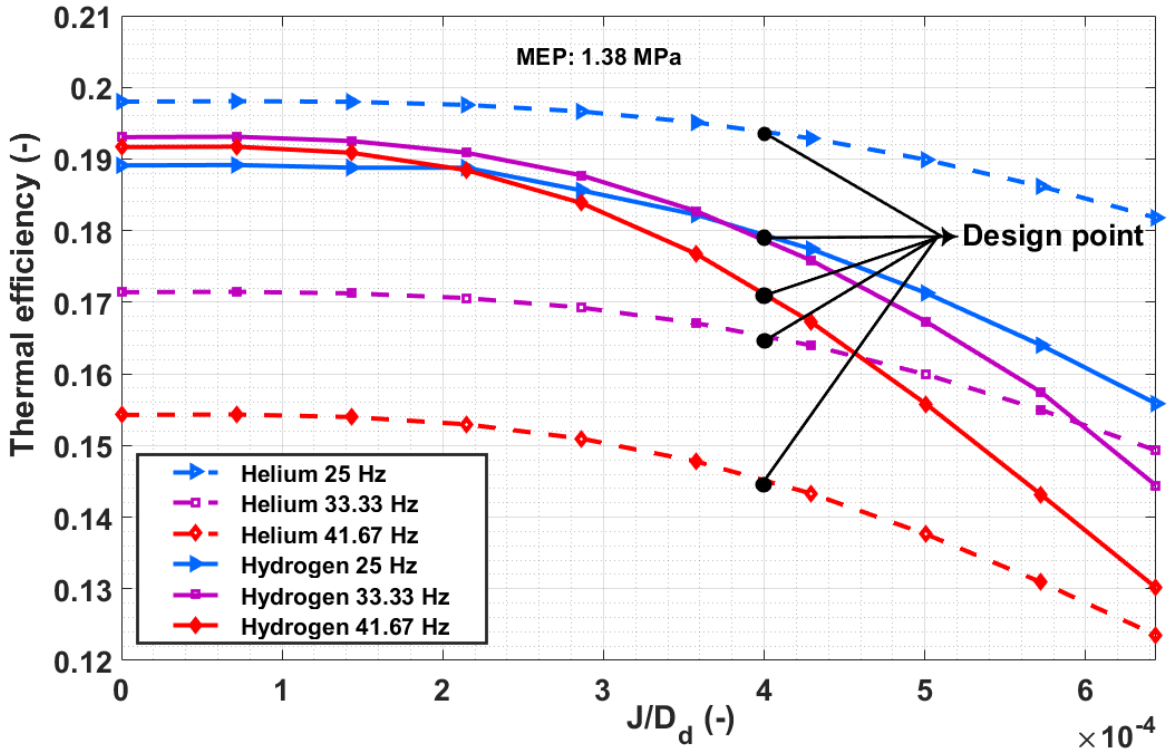

Fig. 5-17. The impact of the dimensionless gap number on the thermal efficiency of the prototype Stirling engine, for different engine frequencies, T_{htr} = 977 K, T_k = 286 K and MEP of 1.38 MPa and utilising helium gas or hydrogen as the working fluid.

5.5. Summary of the chapter

The new proposed thermal model of the GPU-3 Stirling engine has been tested with the engine geometrical and operating data. The results show the Present Model estimates the brake power of the experimental engine with greater accuracy compared with all the previous numerical and closed-form models at the engine frequencies investigated, apart from the newly developed PSML [68] model that predicts better results at higher engine frequencies. Whilst the predicted thermal efficiency was more consistent with the experimental data, at all the engine frequencies investigated, in contrast to other referenced models. Therefore, the new model developed in this chapter is more suitable for deployment in studies involving the dynamic operation of the Stirling engine, since it is consistent in predicting accurately the experimental data at all engine speeds.

Also, the model was deployed to study the dynamic variation of the mass and energy of the working fluid in the engine. The model predicts the variations in the mass and energy of the working fluid in the engine compartments that are consistent with the

cyclic processes in the engine. The energy audit reveals that the work and heat losses in the engine are predominantly driven by the pressure drops in the tubes of the heat exchangers and heat conduction from their walls, respectively. In addition, an enormous amount of heat is rejected from the heat engine and this could be recovered to drive another heat engine or for other useful purposes and will be investigated in the next chapter.

Finally, the impact of the dimensionless gap number on the brake power and thermal efficiency of the experimental engine at different mean effective pressures and engine operating frequencies was assessed and compared for hydrogen and helium working fluids. It was found that for a given mean effective pressure, a minimum dimensionless gap number exists below which the performance of the engine becomes insensitive to the displacer gap. Therefore, the engine performance could be improved significantly by optimising the design of the cylinder wall-displacer gap, especially if hydrogen serves as the working fluid of the engine.

Chapter 6 Simulation and Parametric Optimisation of a Multi-carrier Energy System

This chapter presents the modelling, integration, parametric analysis and optimisation of the new multi-carrier decentralised energy system configuration described in Chapter 3. Section 6.1 undertakes the development and validation of the models for the prediction of the performance of the subsystems of the multi-carrier energy system. In addition, it proposes an approach for the integration of the subsystems of the energy system and formulates metrics for evaluating its performance. Section 6.2 presents the parametric analyses of the simulated results of the system based on the formulated metrics over a range of operating conditions. Section 6.3 performs the formulation of the parametric optimisation problem and develops the optimisation method for finding the optimal solutions. This section also discusses the decision-making tools deployed to select the best solution from the set of optimal solution. Section 6.4 evaluates the results of the multi-objective optimisation and conducts a detailed analysis of the best solution. Finally, the summary of the chapter is presented to highlight the key findings from the work that has been undertaken. These findings and key results obtained have been published in the author's papers in a peer reviewed journal and in an international conference.

6.1. Multi-carrier decentralised energy system modelling

In Chapter 3, and Fig. 3-2 the schematic diagram and mode of operation of the multi-carrier decentralised energy system (MDES) configuration proposed in this chapter was presented. The proposed MDES comprises six main subsystems which are: biomass dryer (BMD), biomass combustor (BMC), Stirling engine (ST), organic Rankine cycle (ORC), single effect absorption refrigerator (VAR) and domestic water heater (DWH). This system is designed to simultaneously produce cooling, heating, power, and dry wood chips. The model for the prediction of the performance of the ST prime mover has been developed in Chapter 4 and the solution was implemented and validated in Chapter 5. This section presents the modelling and solution approaches implemented for the ORC, ARS, wood chips

drying, combustion and DWH systems as well as the performance metrics for its evaluation.

6.1.1. Modelling of the subsystems of the multi-carrier energy system

The modelling of the BMD, BMC, ORC, VAR, and DWH were undertaken in the Aspen plus® environment. Aspen plus® is a Fortran-based process modelling program that has extensive application in modelling various processes, such as energy systems and refineries. It has a large library of properties of several chemical compounds. In addition, there are custom blocks of commonly used process system components in Aspen plus® which can be easily connected, using materials, heat and work streams [245]. This robust software has been used in the past to model some of the subsystems of the proposed DES and the results obtained were comparable to that of other modelling tools, such as the engineering equation solver (EES). Hwang et al. [98] reported a relative error of 1.5% in the results obtained from their Aspen model of the lithium bromide/water ARS compared with that from the EES.

In Aspen plus® modelling, the thermo-physical properties of the working fluid are determined based on the equation of state; for a pure substance or activity coefficient methods; for non-ideal mixture of solvents [98]. Here, a combination of the Peng-Robinson and the steamNBS have been deployed as the equation of states to model the conventional components and pure water, respectively. On the other hand, the electrolyte non-random two liquid (ELECNRTL) – an activity coefficient method in Aspen plus® has been used to model the lithium-bromide/water solution. It is also required to define the stream class in Aspen plus® before specifying the streams. In this simulation, the MCINCPSD, which is compatible with mixed, conventional inert solid with particle size distribution (CIPSD) and non-conventional solids with particle size distribution (NCPSD) streams serve as the global stream class. The detailed description of the Aspen plus modelling for the various subsystems are undertaken in the following.

6.1.1.1. Aspen modelling of wood chips drying

The modelling of wood chips drying has been achieved with the aid of the dry reactor (DRY-REAC) and separator (DRY-FLSH) blocks (see, Fig. 3-2(a) for the Aspen

flowsheet). In the DRY-REAC, some of the volatile components in the wood chips (e.g., moisture) are vaporised with the aid of the high temperature flue gas. Then the feedstock is sent to the DRY-FLSH where the water vapour and the flue gas are separated from the dry wood chips. These processes require specifying the weight composition of all the components in the wood chips, defined on a dry basis from ultimate and proximate analyses (see, Table 6-1). A custom calculator block was deployed to control the moisture composition of the wood chips, at the end of the drying process. This block computes the fractional conversion of wood chips to water which is required to determine the mass flow rate of the wood chips after drying, by conducting a material balance [246]. The final moisture content of the biomass fuel is set by the user in the calculator block, while the other properties of the wet wood chips are retrieved from the wet wood chips stream.

Table 6-1. Proximate and Ultimate analyses of white wood chips [47,48].

Composition	Dry Weight (%)
Ultimate analysis	
Hydrogen	6.10
Carbon	51.80
Nitrogen	0.30
Oxygen	41.19
Chlorine	0.00
Sulfur	0.01
Ash	0.60
Moisture	10.00
Proximate analysis	
Moisture	30.00
Fixed Carbon	19.40
Volatile matter	80.00
Ash	0.60

6.1.1.2. Aspen modelling of wood chips combustion

In Aspen plus®, the combustion of solids is achieved in three steps [246]. First, the solid is broken down into its non-stoichiometric components in an Aspen block named RYield (DECOMP). Subsequently, the non-stoichiometric components and the heat of combustion are admitted into the RGibbs reactor (COMBUSTR). Here, based on the minimisation of the Gibbs free energy, these components will react

with air to produce the combustion products. Finally, the combustion products are sent into a solid splitter (SEPARATE) to remove the unburnt solid particles based on a predefined split fraction (see, Fig. 3-2(a)). To determine the actual composition of the components in the wood chips after the combustion process, a custom calculator block executed in a Fortran-based environment was deployed. The calculator block accessed the ultimate and proximate analyses of the woodchips in a vector form, based on the dry composition from the stream going to the drier. Using the moisture content in the proximate analysis, it converts the ultimate and proximate analyses to a wet basis [246].

6.1.1.3. Aspen modelling of the organic Rankine cycle

In this study, five custom Aspen plus® blocks have been used to achieve the ORC modelling, namely: heater (evaporator), expander, solution heat exchanger, pump, and another heat exchanger (condenser) (see, Fig. 3-2 (a) for the Aspen flowsheet). The use of a heater block to implement the evaporator in this design implies that the heat is assumed to be added at constant temperature (ST cooler temperature) to the refrigerant of the ORC. Note that the heat input to the heater is supplied from the cooler of the ST implemented in MATLAB by integrating Aspen plus® and MATLAB. The thermodynamic process in the expander is assumed to be polytropic. While a combination of the approach temperature, dryness fraction and discharge pressure have been used to determine the state of the stream at the outlet of the solution heat exchanger, condenser, and pump, respectively. Hence, the network output of the ORC and its efficiency is obtained from the following expressions:

$$\dot{W}_{ORC} = \dot{W}_{exp} - \dot{W}_{pump} \tag{6-1}$$

$$\eta_{ORC} = \frac{\dot{W}_{ORC}}{\dot{Q}_{\text{actual,k}}} \tag{6-2}$$

where $\dot{W}_{exp}$ (W) is the power produced by the ORC's turbine and $\dot{W}_{pump}$ (W) is the power consumed by the ORC's pump.

6.1.1.4. Aspen modelling of the absorption refrigeration system

Similar to [98], heater blocks were selected to implement the evaporator, absorber, and condenser of the ARS, on the assumption that heat is added to these

components at constant temperature. However, the waste heat from the absorber and condenser has been recovered in this study, to economise the water before it gets to the DWH. Two pressure reducing valve blocks have been selected to throttle down the refrigerant (water) and the strong LiBr/water solution to the evaporator pressure. While a pump block that requires only the discharge pressure to be supplied as an input lifts the weak solution from the absorber to the desorber. To improve the performance of the ARS, a solution heat exchanger (SHX) has been deployed between the desorber and absorber. The SHX extracts some of the heat from the hot strong solution leaving the desorber to heat up the cold weak solution returning to the desorber, thus helping to retain the internal energy of the working fluid. The SHX has been implemented in this design using two heater blocks, where heat is taken from the hot side to the cold side as seen in the flowsheet in Fig. 3-2 (b). Finally, owing to the complexity of the processes in the desorber, a combination of two heaters and a flash separator block were selected to implement this process.

Thus, the COP of the ARS can be obtained from the expression:

$$\xi_{ARS} = \frac{\dot{Q}_{evap}}{\dot{Q}_{\text{desorb}} + \dot{W}_{pump}} \tag{6-3}$$

where $\dot{Q}_{evap}\ (W)$ is the heat load of the evaporator of the refrigerator and $\dot{Q}_{desorb}\ (W)$ is the heat absorbed by the generator of the thermal chiller.

6.1.1.5. Aspen modelling of the water heater

In this DES system modelling, the heating of the domestic hot water was implemented in Aspen plus® using a heat-exchanger block (see, Fig. 3-2 (b) for the Aspen flowsheet). The approach temperature is the only input to the block required to determine the state of the hot water produced. Note that the cold stream input to this block is the water that has been economised in the absorber and condenser of the ARS, while waste heat exiting the desorber of the ARS serves as the hot stream inlet to the block.

6.1.2. Multi-carrier system performance index

For an energy system that integrates several sub-systems operating simultaneously in a close circuit, some performance indicators are required to assess the viability

of the system from thermodynamic, economic, and environmental perspectives. While several indices have been formulated to assess the performance of multi-carrier DES, only a few indicators have been reported to give deep insights into the system's performance. The commonly used performance indicators are those that compare the performance of the multi-carrier system which is modelled here as a micro-CCHP (μ-CCHP) to that of a conventional separate cooling, heating and power (SCHP) plant [249]. In this study, the energy utilisation factor, exergy efficiency, primary energy saving, artificial thermal efficiency and CO_2 emissions reduction have been used to assess the performance of the multi-carrier DES from technical, economic, and environmental perspectives.

a) Energy utilisation ratio:

The energy utilisation ratio (EUF) evaluates the performance of the DES from the first law perspective. However, because electric power is difficult to produce and highly priced compared with heating or cooling which can be produced with low grade energy and not commensurately priced, EUF is used instead of thermal efficiency. The EUF of a μ-CCHP is expressed as:

$$EUF = \frac{\dot{W}_{\mu-CCHP} + \dot{Q}_{cooling} + \dot{Q}_{heating}}{\dot{m}_{\text{woodchips}} HHV} \tag{6-4}$$

where $\dot{Q}_{cooling}\ (W)$ is the refrigerating effect of the ARS, $\dot{Q}_{heating}\ (W)$ is the heating load of the DWH, $\dot{m}_{\text{woodchips}}\ (\frac{kg}{s})$ is the mass flowrate of the wood chips fuel and $HHV(\frac{J}{kg})$ is the high heating value of the fuel. The net electrical power from the system, $\dot{W}_{\mu-CCHP} = \dot{W}_{actual,ST} + \dot{W}_{ORC}$.

b) Exergy efficiency:

Exergy efficiency (η_{II}) measures the quality of the energy conversion processes in the energy system. It is a thermodynamic performance indicator, derived from the second law of thermodynamics that maps the flow of energy supplied into a system, and reveals where thermodynamic imperfection in a system occurs the most. For a system operating at conditions above the dead state defined by temperature and pressure, $\mathrm{T_o} = 298.15\ \mathrm{K}$ and $\mathrm{P_o} = 101\ \mathrm{kPa}$, the exergy efficiency is expressed as:

$$\eta_{II} = \frac{\dot{W}_{\mu-CCHP} - \left(1 - \frac{T_0}{T_{cooling}}\right)\dot{Q}_{cooling} + \left(1 - \frac{T_0}{T_{heating}}\right)\dot{Q}_{heating}}{\left(1 - \frac{T_0}{T_{flue}}\right)\dot{Q}_{\mu-\mathrm{CCHP}}} \qquad (6\text{-}5)$$

where $T_{cooling}\ (K)$ is the evaporator temperature, $T_{heating}(K)$ is the temperature of the boiler and $T_{flue}\ (K)$ is the temperature of the flue gas.

c) Primary energy saving:

Another very insightful way of evaluating the performance of a multi-carrier DES is by comparing it to the performance of conventional SCHP plants. The primary energy savings (PES) estimates the amount of fuel that could be saved in running a plant as a CCHP instead of as a SCHP, and this could be deployed as an economic indicator. If the PES is positive, some of the input fuel energy has been saved, while a negative PES value suggests running the plant as a SCHP may be more beneficial. The PES of a CCHP can be obtained from the following expression [35], [101]:

$$PES = 1 - \frac{\dot{Q}_{\mu-\mathrm{CCHP}}}{\frac{\dot{W}_{CCHP}}{\eta_{elect,ref}} + \frac{\dot{Q}_{heating}}{\eta_{h,ref}} + \frac{\dot{Q}_{cooling}}{\eta_{h,ref}\xi_{ref}}} \qquad (6.6)$$

where $\eta_{elect,ref}\ (-)$ is the thermal efficiency of a conventional power plant, $\eta_{h,ref}\ (-)$ is the efficiency of a conventional boiler, and $\xi_{ref}\ (-)$ is the coefficient of performance (COP) of a conventional chiller.

d) Artificial thermal efficiency:

If the energy of the fuel used to produce the heating and cooling in a separate boiler with an efficiency, η_{h} and a separate thermal cooler with a COP, ξ_{ref} are deducted from the total fuel energy supplied to the CCHP, and the electrical power output of the plant is divided by the remaining fuel energy, then another performance criterion, called the artificial thermal efficiency (ATE), is the outcome. This performance indicator evaluates the efficiency of utilising the fuel to produce electric power in a CCHP system. Therefore, the ATE of the multi-carrier energy system is expressed as [88]:

$$ATE = \frac{\dot{W}_{\mathrm{CCHP}}}{\dot{Q}_{CCHP} - \frac{\dot{Q}_{heating}}{\eta_{h,ref}} - \frac{\dot{Q}_{cooling}}{\eta_{h,ref}\xi_{ref}}} \qquad (6\text{-}7)$$

e) CO_2 emissions reduction:

An established way of evaluating the performance of a MDES is by quantifying its impact on the environment [250]. This can be achieved by comparing the CO_2 emissions reduction (CO_2 ER) of the system to that of a conventional SCHP system. A positive CO_2 ER suggests that the energy system is emitting less emissions compared to the SCHP and vice versa. The CO_2 ER of the multi-carrier energy system can be evaluated from the following expression [87]:

$$CO_2ER = 1 - \frac{\chi_{CO_2^F} \cdot \dot{Q}_{\mathrm{CCHP}}}{\chi_{CO_2^W} \cdot \dot{W}_{\mathrm{CCHP}} + \frac{\chi_{CO_2^F} \cdot \dot{Q}_{heating}}{\eta_{h,ref}} + \frac{\chi_{CO_2^W} \cdot \dot{Q}_{cooling}}{\eta_{h,ref}\xi_{ref}}} \tag{6-8}$$

6.1.3. System integration and solution approach

Fig. 6-1 presents the algorithm for implementing the solutions of the MDES models in the MATLAB and Aspen plus® environment. A code has been developed in the MATLAB environment to interface the ST model with the models built in Aspen plus®. Hence, the control and operation of the system was achieved in the MATLAB environment.

As seen in the algorithm, the wood chips feed rate and required final moisture composition are exported to the respective Aspen plus blocks from MATLAB. The Aspen models of the BMD and BMC are run from MATLAB and the program paused. The temperature and specific heat capacity of the flue gas produced after the combustion of the wood chips is sent to the ST heater in MATLAB. Using a predefined pinch point temperature, the MATLAB model of the ST is run for a given speed of the engine. The algorithm for solving the governing equations of the ST has been presented in Chapter 4 and Fig. 4-4. If the ST model converges, the results of the energy consumed by the ST heater and that exhausted from the ST cooler are exported to the Aspen plus blocks to implement the Aspen plus models. The Aspen plus program is then run at this point and the steady state solutions of the ORC, ARS and DWH models are obtained. If the model converges, the results of the heat rates, work rates, exergy rates, etc. from these models are returned to MATLAB. Furthermore, these results and that generated for the ST are employed in the computation of the performance indicators of the multi-carrier system.

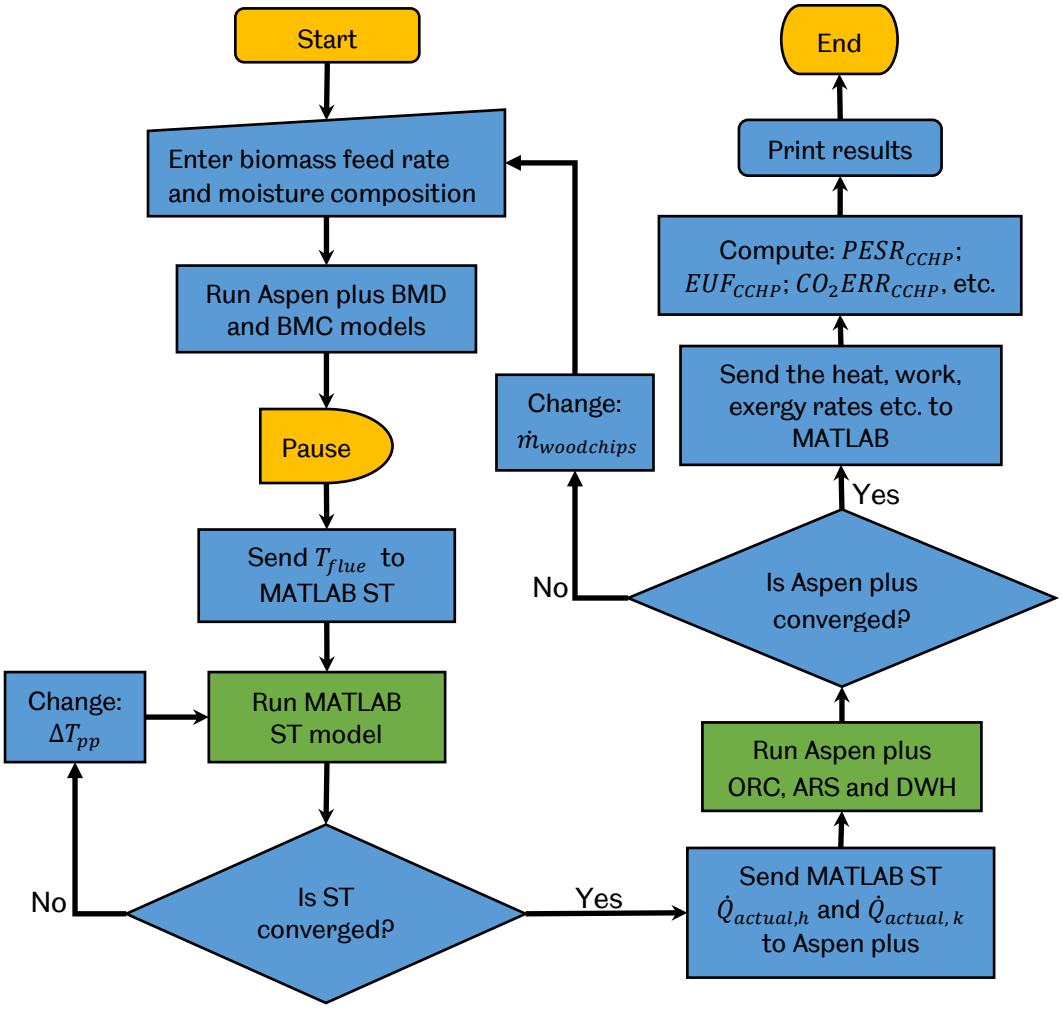

Fig. 6-1. Algorithm for the integration of the MATLAB and Aspen plus models of the subsystems of the multi-carrier DES.

The steps described so far are repeated iteratively for different mass flow rates of the refrigerant flowing through the ARS, to achieve different cooling ratios, $CR = \frac{\dot{Q}_{cooling}}{\dot{Q}_{cooling}+\dot{Q}_{heating}}$. Finally, the entire process is repeated for another speed of operation of the prime mover. Note that if the Aspen plus program does not converge, the woodchips feed rate, $\dot{m}_{woodchips}$ is changed. The Aspen model may not converge if the flue does not contain sufficient energy to drive some of the subsystems of the multi-carrier DES. On the other hand, if the MATLAB ST model does not converge, the pinch point, ΔT_{pp} between the flue gas and the ST heater temperature is adjusted. The MATLAB functions for implementing the parametric analysis of the multi-carrier system have been presented in Appendix B.

6.1.4. Validation of the subsystems of the micro-CCHP

This section presents the validation of the ST, ORC and ARS which are subsystems of the multi-carrier DES. The model results have been largely validated against other model results and experimental data derived from literature.

6.1.4.1. ORC validation

The model for the prediction of the performance of the ORC engine has been implemented in Aspen plus®. The predicted results from the ORC model have been validated against experimental data [20] from a laboratory scale micro-ORC utilising a scroll expander. Table 6-2 presents the comparison between the Aspen ORC model results and the experimental data, while Table 6-3 is the operating parameter of the experimental engine. As seen in Table 6-2, the model predicted results agree remarkably with the experimental data and the maximum relative error recorded in the deviation is 6.43% for the efficiency.

Table 6-2. Validation of the Aspen plus ORC model against experimental data.

Quantity	Model result	Experimental result	Relative error (%)
Net power (W)	1037	980	5.80
Heat added (W)	10441	10500	-0.56
Efficiency (%)	9.930	9.330	6.43
Refrigerant flow (kg/s)	0.045	0.045	0.00
Pressure ratio (-)	4.760	4.760	0.00

Table 6-3. Flow properties of the experimental ORC engine [20].

Stream	Fluid	State	T (℃)	$P\ (kPa)$	$\dot{m}\ (kg/s)$
12	R245fa	Vapour	89.54	1000.0	0.045
13	R245fa	Vapour	53	210.0	0.045
15	R245fa	Liquid	35	210.0	0.045
11	R245fa	Liquid	36	1000.0	0.045
CWI	Cold Water	Liquid	26	195.0	0.580
CWO	Cold Water	Liquid	32	195.0	0.580
c	Hot Water	Compressed	121	205.0	0.445
d	Hot Water	Compressed	113	158.4	0.445

6.1.4.2. Validation of the single-effect ARS

In this section, the validation of the ARS model developed in Aspen plus® is presented. In a previous study, Somer et al. [98] validated their ARS model built in Aspen plus® against results from the EES, due to the paucity of the experimental data. They remarked that the EES model results provide more information than would be obtained from the experimental data. The approach adopted in this study to validate the developed Aspen model of the ARS, compares the model results to the results obtained in Somer et al. [98]. To ensure consistency, similar operating data of the single-effect lithium bromide-water ARS has been used and is presented in Table 6-4. As seen in Table 6-5 that represents the results obtained from the model and Somer et al. [98], the discrepancy between both model results is less than 1%, indicating very good agreement between the models.

Table 6-4. Single-effect LiBr/water ARS operating parameters [98].

Stream	Fluid	$x\ (-)$	T (°C)	$P\ (kPa)$	$\dot{m}\ (kg/s)$	ξ_{LiBr} (%)
17	LiBr/H_2O	0	32.7	0.672	1	57.4
18	LiBr/H_2O	0	32.7	7.461	1	57.4
19	LiBr/H_2O	0	89.9	7.461	1	57.4
20	LiBr/H_2O	0	63.8	7.461	0.918	62.6
21	LiBr/H_2O	0	53.3	7.461	0.918	62.6
22	LiBr/H_2O	0.01	43.1	0.672	0.918	62.6
23	Water	1	78.4	7.461	0.083	0.0
24	Water	0	40.2	7.461	0.083	0.0
25	Water	0.07	1.3	0.672	0.083	0.0
26	water	1	1.3	0.672	0.083	0.0

Table 6-5. Results from the Aspen plus model of the ARS.

Quantity	Unit	Model result	Somer *et al.* [98]	Error (%)
$\dot{Q}_{evap}$	W	10764	10772	0.071
$\dot{Q}_{desorb}$	W	14665	14592	-0.500
$\dot{Q}_{abs}$	W	14000	13923	-0.552
$\dot{Q}_{cond}$	W	11429	11432	0.008
ξ_{ARS}	-	0.7330	0.738	0.670

6.2. Simulated results of multi-carrier system and discussion

Here, the impact of retrofitting the ST with an ORC on the power output and thermal efficiency is assessed and compared with a standalone ST for a range of speeds of operation of the ST prime mover. Thereafter, a detailed parametric analysis has been conducted on the effect of the cooling ratio and wood chips moisture composition on the dynamic performance of the proposed multi-carrier system that has been modelled as a micro-CCHP. Parametric analysis reveals the functional relationship between the operating parameters of a system and its performance. In general, it is very essential to highlight the domain of an optimisation problem and unveil the local and global optima and has been widely undertaken [69], [96] [125].

6.2.1. Results of the dynamic performance of the hybrid prime mover

In Chapter 3 and Fig. 3-3, the thermodynamic diagram of the combined power plant is presented. The ST is the topping cycle, while the ORC is the bottoming cycle that has been deployed to recover the exhaust waste heat and improve the combined performance of the heat engine. Therefore, in this section, the performance of the standalone ST is compared to that of a hybrid ST and ORC, over a range of operational speeds of the ST prime mover.

Fig. 6-2 indicates the power output of sole ST and ORC and ST+ORC as well as the thermal efficiency of the combined cycle over a range of speeds of the topping cycle. It is seen that the power output from the combined cycle nearly doubled for most of the speeds investigated compared with that of the standalone ST. The power output from the ST increases as the speed of the engine increases. However, a decrease in the power output with the increase in speed is observed at very high rotational speeds, which are characterised by an increase in the losses in the engine. Similarly, the power output from the ST+ORC combined power configuration increases appreciably with the increase in the speed of the ST, and slightly declines at the high speed of the prime mover. The noticeable reduction in the negative slope of the power output at high speeds for the ST+ORC system, compared with the ST only, can be attributed to the increase in the power output from the ORC, with the increase in the speed of the prime mover. Waste heat rejected by the cooler of the

ST increases as its speed increases, and therefore, more energy is available to fire the ORC; hence, the observed trend.

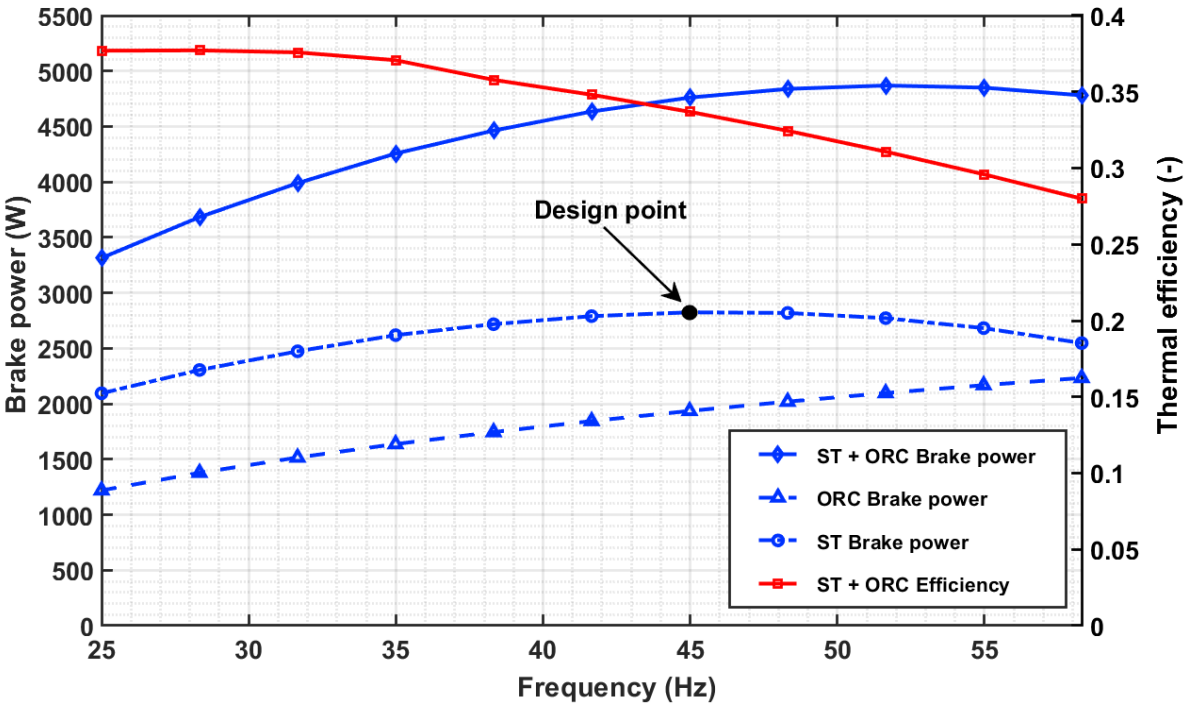

Fig. 6-2. Assessing the impact of retrofitting a ST with an ORC on the brake power and efficiency of a standalone ST.

Furthermore, the significance of operating a ST+ORC combined power configuration is evidenced by the stability in the combined efficiency. As seen in Fig. 6-2, the efficiency of the combined system remained above 27% even at high engine speeds when the losses in the engine were enormous and was largely above 30% for the rest of the speeds. This is a remarkable improvement compared to between 12.52 – 22.74% efficiency recorded for the range of speeds investigated in the standalone ST (Fig. 5-4). It is therefore worthy of note that retrofitting an ORC to a ST can significantly improve the performance of the standalone ST from a technical perspective.

6.2.2. Parametric analysis results of the ST+ORC driven micro-CCHP

This section presents the results for the parametric analyses conducted in this study, to evaluate the performance of the proposed system, from different viewpoints. To this end, three distinct moisture compositions of the wood chips fuel have been selected: 10%, 15% and 20% to represent the likely quality of dry wood

chips in the remote tropical locations as the climatic conditions change. This is intended to investigate the effect of the quality of the input fuel (in-situ drying of wood chips) on the plant's performance. Further, a parametric analysis has been conducted to evaluate the effect of the variation in the cooling and heating capacities of the ARS and DWH on the performance of the MDES. This will provide additional insights into the sizing of the proposed MDES, to obtain the mix of the energy vectors it should produce to guarantee optimal performance. The performance indicators deployed for the parametric analysis were formulated based on thermodynamic, economic, and environmental perspectives with the help of the expressions presented in Section 6.1.2. Table 6-6 presents the parameters of the reference conventional standalone plant used to evaluate these performance indicators.

Table 6-6. Input parameters for CCHP performance evaluation.

Parameter	Value	Unit
$\eta_{h,ref}$ [101]	85	-
$\eta_{elect,ref}$ [101]	0.23	-
$\chi_{CO_2^F}$ [87]	220	g (kWh)$^{-1}$
$\chi_{CO_2^W}$ [254]	836	g (kWh)$^{-1}$
ξ_{ref} [102]	3.0	-
*$HHV_{\ woodchips}$ [47,48]	19220	kJ/kg
$\eta_{m,pump}$	0.67	-
$\eta_{m,exp}$	0.95	-
$\eta_{poly,exp}$	0.87	-
$\eta_{t,pump}$	0.8	-

*The high heating value of woodchips ($\mathrm{HHV}_{\mathrm{woodchips}}$) is given on a dry basis.

6.2.2.1. Impact of cooling ratio on the multi-carrier EUF

Fig. 6-3 (a), (b) and (c) present the effect of the cooling ratio on the energy utilisation efficiency (EUF) of the proposed multi-carrier system in a 3-D plot, when fired with wood chips of different moisture compositions and for a range of rotational speeds of the prime mover. It is seen that the ratio of the cooling to heating loads has a strong impact on the EUF of the system. This impact is more

severe when the ST prime mover is operating at a low speed. The EUF declines remarkably as the CR increases, although the decline in EUF becomes less intense as the cooling ratio tends to unity [88]. This implies that the energy in the fuel is better utilised in producing some useful energy in the form of hot water, than in producing cooling. The high efficiency of the hot water boiler compared with the low COP of the single effect ARS may be responsible for the observed trend.

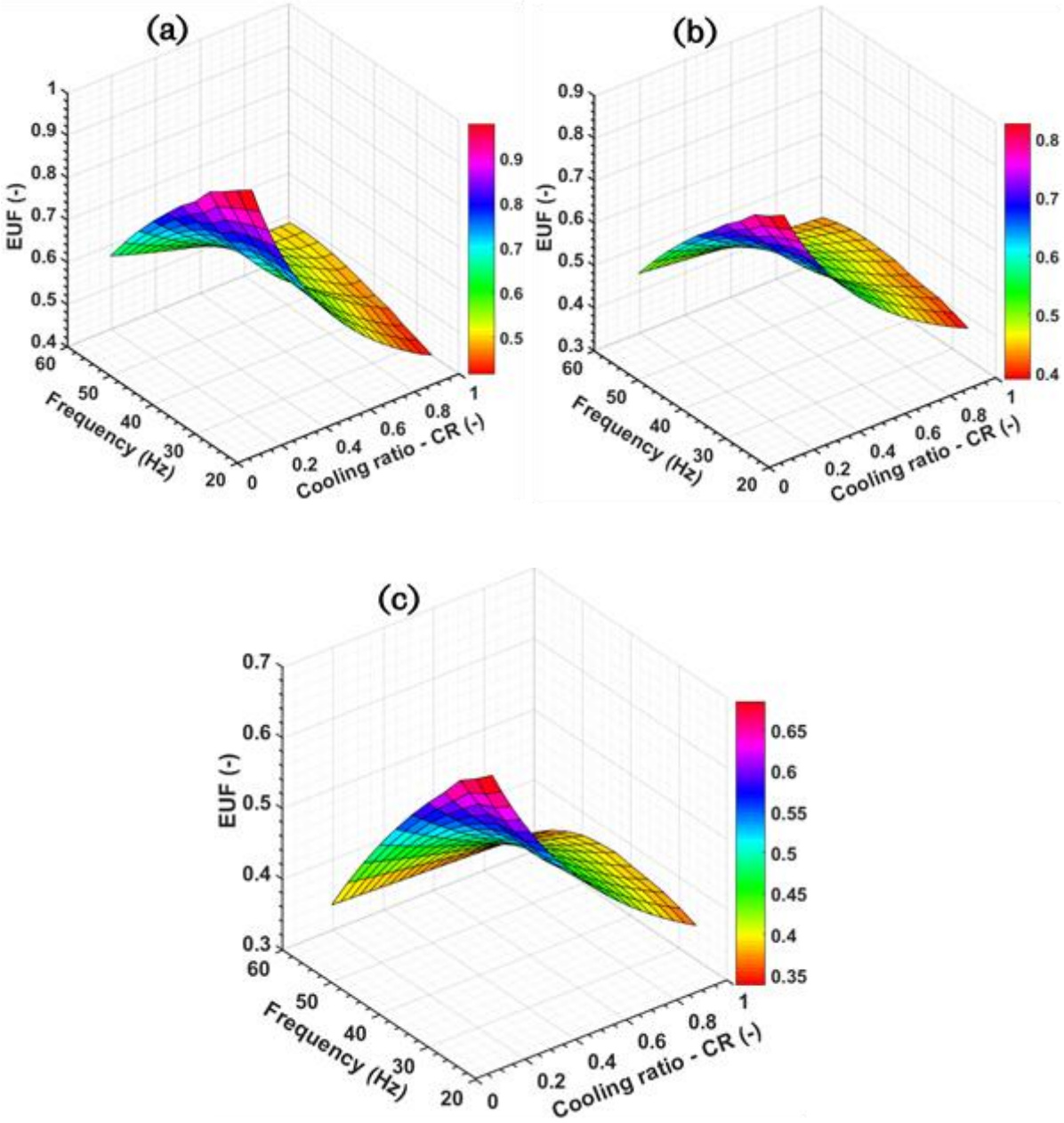

Fig. 6-3. Evaluating the impact of cooling ratio on the EUF of ST+ORC fired $MDES$ using wood chips of (a) 10%, (b) 15% and (c) 20% moisture compositions.

Meanwhile, when the system is producing more heating compared to cooling ($\mathrm{CR} < 0.5$), the EUF decreases with an increase in the speed of the prime mover. At low speed, the MDES utilises only a small proportion of the energy in the fuel to produce power, making the unused energy available for highly efficient hot water heating in the boiler. However, as the speed increases, the ST will start to consume more energy, because of the increase in the losses in the engine; hence, the observed decline in the EUF. In contrast, for $\mathrm{CR} > 0.5$, the EUF increases, then peaks at the mid-speed of about 41.67 Hz ($\mathrm{N} = 2500\ \mathrm{rpm}$) and starts to decrease. This behaviour of the EUF with an increase in the speed of the ST prime mover for $\mathrm{CR} > 0.5$ vary with the moisture content in the wood chips.

Thus, Fig. 6-3 (a) shows, for dry wood chips moisture composition of 10%, that the EUF slightly increases as the speed of the engine increases and plateaus at a high speed. This is because the sufficiently dry wood chips supply more energy to the combined power system, which enables it to generate significantly higher power than cooling. As a consequence, the EUF is influenced more by the combined power output, as seen in Eq. (6-4), resulting in a trend similar to the combined power output in Fig. 6-2. Therefore, a higher EUF is achieved as the quality of the wood chips fuel improves, with in-situ drying of the feedstock irrespective of the cooling ratio and speed of the prime mover.

6.2.2.2. Impact of the cooling ratio on the multi-carrier exergy efficiency

Fig. 6-4 (a), (b) and (c) show the impact of the cooling ratio and rotational speed of the prime mover on the exergy efficiency (η_{II}) of the proposed multi-carrier system on a surface plot when fired with wood chips of different moisture compositions. As seen in Fig. 6-4, η_{II} decreases with an increase in the cooling ratio, although this decrease is more evident when the woodchips is supplying more thermal energy, i.e., contains less moisture. While η_{II} increases with an increase in the speed of the ST but flattens out at high rotational speeds and for very low CRs when the energy system is producing more heating. This is the case since the energy conversion process in heating is very efficient; hence, yielding a higher η_{II}. Conversely, low grade energy is usually required to produce cooling in the ARS. Therefore, at low speeds,

when the combined power plant is generating less power, most of the unspent energy is destroyed in the stack, resulting in lower second law efficiencies (η_{II}).

Further, the high variation in η_{II} between the global optima ($\mathrm{CR} = 0.1$ and $\mathrm{Freq} = 41.67\ \mathrm{Hz}$) and the local optima ($\mathrm{CR} = 0.99$ and $\mathrm{Freq} = 25\ \mathrm{Hz}$) from 71% to 20% when using woodchips with 10% moisture content (Fig. 6-4 (a)) suggests that exergy destruction is more intense in this scenario because the plant is being run at higher temperatures. Hence, it is important to operate the MDES system within the optimum conditions of the cooling ratio and rotational speed, to fully utilise the available energy and enhance the efficiency.

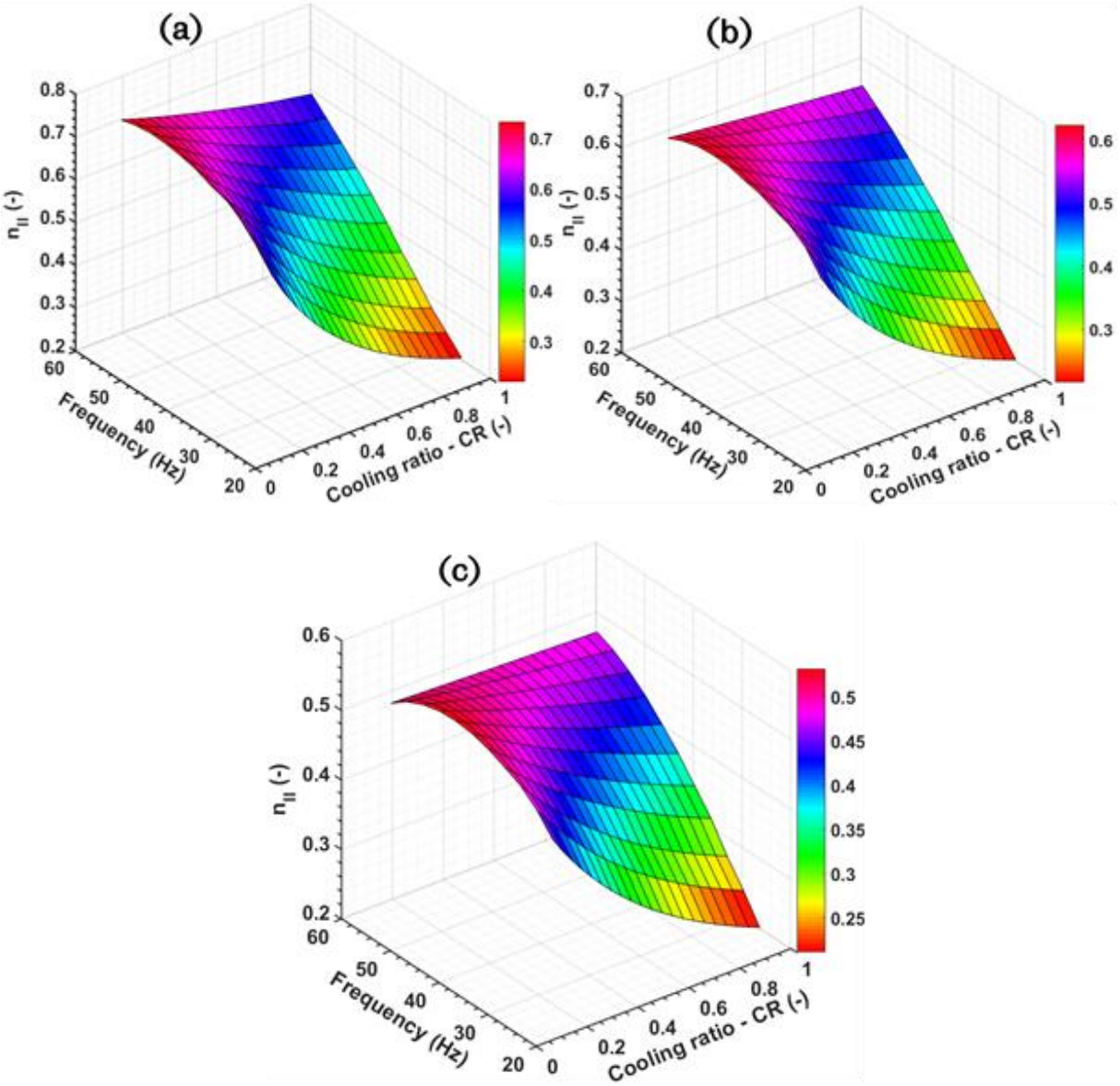

Fig. 6-4. Evaluating the impact of the cooling ratio on the MDES exergy efficiency using wood chips of (a) 10%, (b) 15% and (c) 20% moisture compositions.

6.2.2.3. Cooling ratio versus multi-carrier system PES

Fig. 6-5 (a), (b) and (c) are the surface plots depicting the combined influence of the cooling ratio and the rotational speed of the prime mover on the primary energy savings (PES) when wood chips of different moisture composition are deployed to fire the system. As defined in Section 6.1.2, the PES compares the energy consumption of the MDES to that of a SCHP.

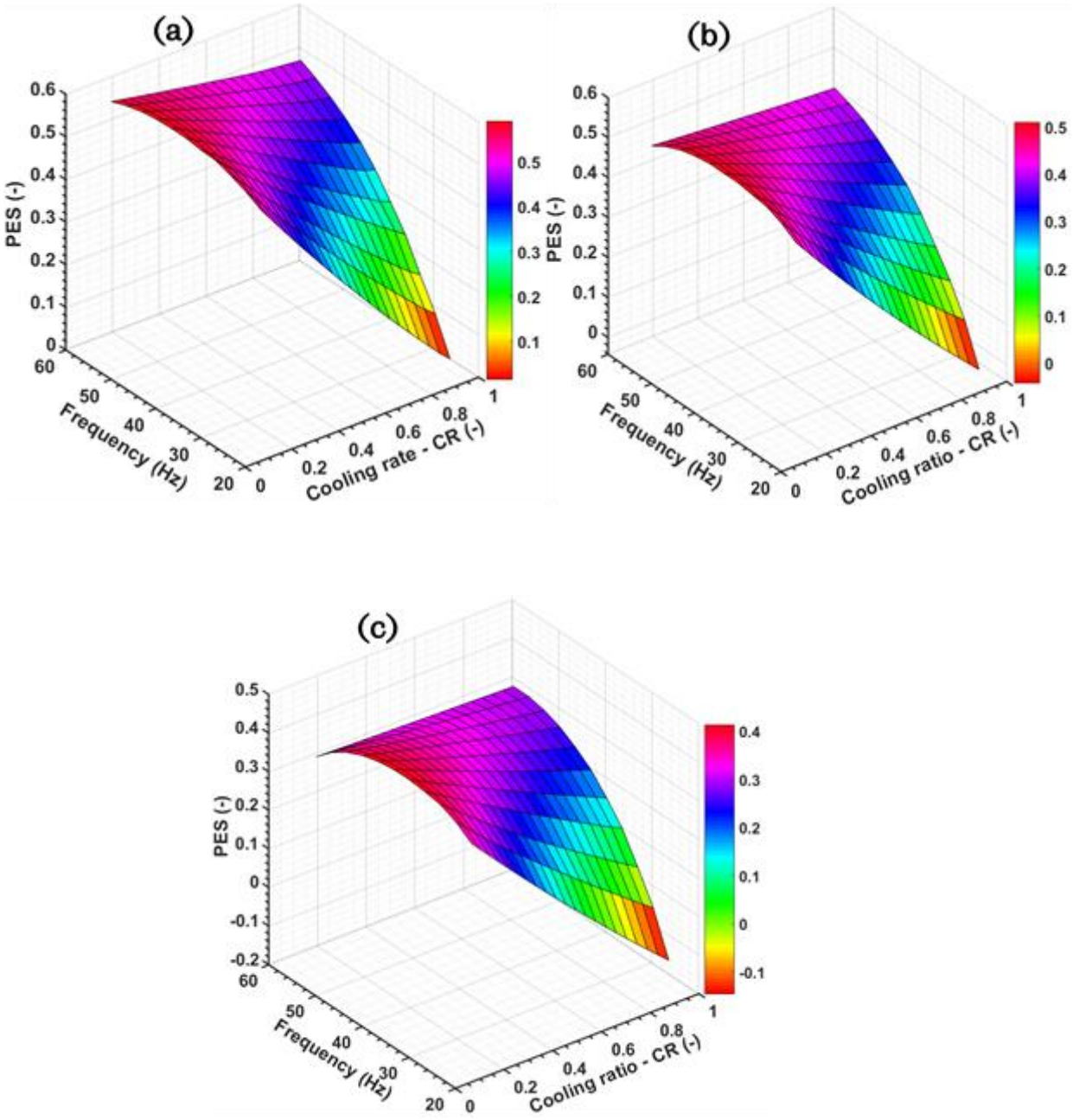

Fig. 6-5. Evaluating the impact of the cooling ratio on the PES of the ST+ORC fired MDES using wood chips of (a) 10% (b) 15% and (c) 20% moisture compositions.

It is seen that for $CR < 0.25$ (significantly more heating than cooling), the PES increases with the speed of the prime mover, peaks and decreases slightly [56], [133]. This behaviour is expected, given that the losses in the ST increases with an increase in speed, which makes less energy available for heating the water. However, as the CR tends to unity, the PES simply increases, peaks and plateaus as the speed increases. This is a consequence of the high ratio of the power to cooling being generated. In addition, it has been shown that retrofitting the ST with ORC helps to minimise the deterioration in the performance at high rotational speeds. Thus, the increasing losses in the ST at high rotational speeds has minimal impact on the PES; hence, the observed trend for $CR > 0.25$.

Meanwhile, very low and even negative PES is seen when the DES is producing more cooling than heating and the prime mover is operating at low speeds. In particular, for the ST operating between frequencies; $25 < Freq < 30\,Hz$ $(1500 < N < 1800\,rpmgfr)$ and $CR > 0.8$, negative PES is seen in Fig. 6-5 (b) and (c). Given that at low frequencies, and when producing a lot of cooling, the fuel energy supplied to the energy system is not efficiently utilised to produce power and cooling. Thus, negative PES is unavoidable in this range of operation of the engine. Therefore, it will be more beneficial to operate the energy system as a SCHP for these ranges of speeds and cooling ratios.

Further, over 40% PES is seen in Fig. 6-5 (a) for more than 60% of the surface. While in Fig. 6-5 (b) and (c), it is over 30% and 20% PES, respectively, for more than 60% of the surface. In this regard, the more the energy supplied into the system, the more likely it will be to save energy in a multi-carrier energy system arrangement where several forms of useful energy are co-produced. This underscores some of the advantages in operating multi-carrier system configuration compared to the conventional SCHP, such as thermal power plants, where only 30% of the input energy is actually utilised in running the plant. More importantly, from these results, some form of flexibility in the operation and management of the energy system is plausible, since significant primary energy savings is guaranteed over a range of speeds and cooling ratios regardless of the quality of the wood chips fuel.

6.2.2.4. Cooling ratio and frequency versus the multi-carrier DES ATE

Fig. 6-6 (a), (b) and (c) show the effect of the cooling ratio and the rotational speed of the prime mover on the artificial thermal efficiency (ATE) on a surface plot when wood chips of different moisture composition are deployed to fire the system. In Eq. (6-7), the ATE is expressed as the ratio of the power produced by the MDES and the energy consumed by the energy system with the exclusion of the energy that could have been utilised to produce cooling and heating, separately.

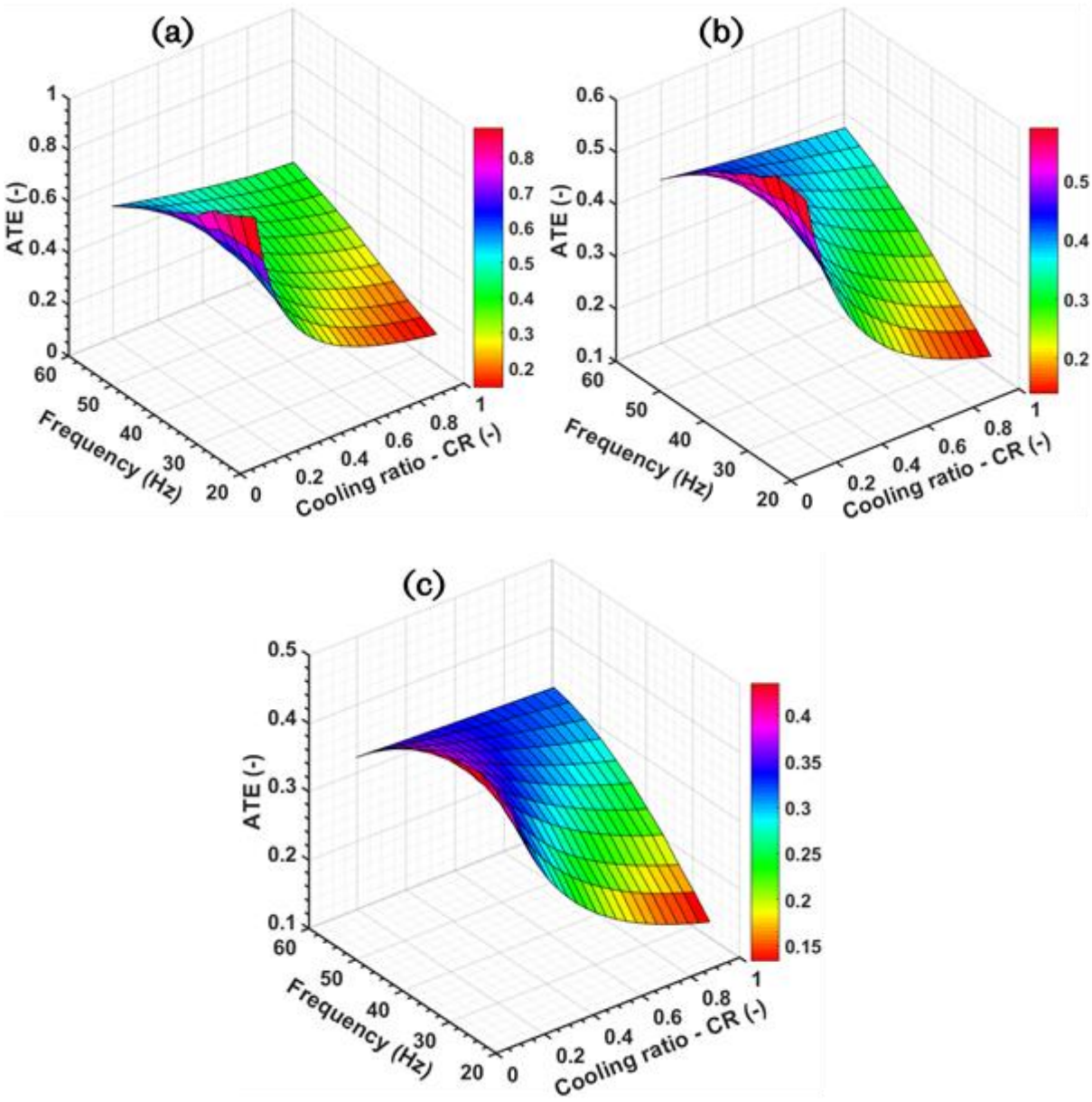

Fig. 6-6. Evaluating the impact of the cooling ratio on the ATE of the ST+ORC fired $MDES$ using woodchips fuel of (a) 10%, (b) 15% and (c) 20% moisture compositions.

As seen in Fig. 6-6, the ATE decreases with the increase in CR, especially at low speed of the prime mover. However, the rate of the decrease in ATE reduces as the CR tends to 1 [88]. The global optimum is seen in a region on the surface plots defined by $\mathrm{Freq} < 45\ \mathrm{Hz}$ and $\mathrm{CR} < 0.4$, although the region of the global optimum reduces and drifts towards the lower speed regions as the input fuel quality improves. At low rotational speed of the ST and low CR, when the system is producing more heating than cooling, only a small proportion of the energy supplied to the system is utilised to produce power. Correspondingly, high ATE is seen, as expected, from the denominator of Eq. (6-7), suggesting that the energy supplied has been efficiently utilised to produce power.

Further, as the speed of the prime mover increases (beyond $\mathrm{Freq} = 30\ \mathrm{Hz}$), the ATE starts to decrease for $\mathrm{CR} < 0.4$, due to the increase in the losses in the ST. On the other hand, for $\mathrm{CR} > 0.4$, the ATE increases as the speed of the ST prime mover increases. Comparing Fig. 6-6 (a), (b) and (c), the fuel is better utilised to produce power from the multi-carrier energy system, as opposed to producing other forms of useful energy products when the moisture content in the wood chips is low, i.e., higher input energy. This is seen from the $\mathrm{ATE} > 30\%$ recorded for over 70% of the surface area in Fig. 6-6 (a) compared with $\mathrm{ATE} > 25\%$ and $\mathrm{ATE} > 20\%$ for over 70% of the surface areas in Fig. 6-6 (b) and (c), respectively.

6.2.2.5. Cooling ratio and frequency versus the multi-carrier DES CO_2 ER

Fig. 6-7 (a), (b) and (c) compare the CO_2 emissions reduction (CO_2ER) of the proposed MDES to that of a SCHP for different cooling and heating capacities and rotational speed of the prime mover when wood chips of different moisture composition are deployed to fire the system. As seen in Fig. 6-7, the CO_2ER capability of the energy system declines as the quality of the input fuel declines. Given that with the increase in moisture content, the combustion process becomes more inefficient, this is expected and can be seen from Eq. (6-8). The CO_2 emissions reductions occur in over 80% (Fig. 6-7 (a)), 70% (Fig. 6-7 (b)), and 60% (Fig. 6-7 (c)) of the surface areas for moisture contents of 10%, 15%, and 20%, respectively.

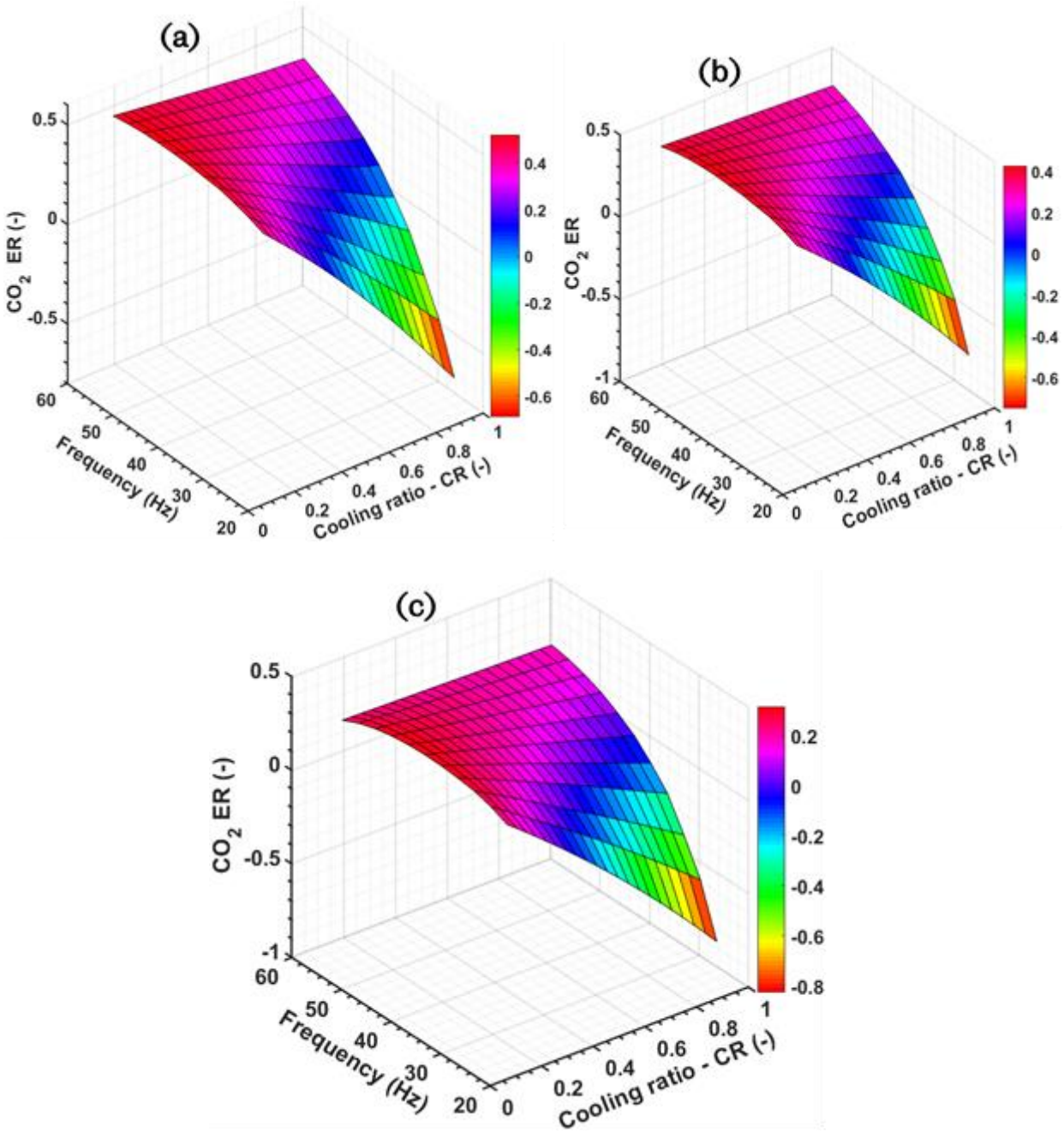

Fig. 6-7. Evaluating the impact of the cooling ratio on the CO_2 ER of the ST+ORC fired $MDES$ using wood chips fuel of (a) 10%, (b) 15% and (c) 20% moisture compositions.

Meanwhile, negative $\mathrm{CO_2ER}$ were localised in a region characterised by the low speed of the prime mover and high cooling ratios. Similar to what has been reported in the case of the PES, the low amount of power being generated by the ST prime mover at low speed is responsible for the observed trend. In addition, when producing a lot of cooling, only a fraction of the energy supplied to the energy system is utilised by the thermal chiller. The rest apparently will end in the environment as

exhaust gas. Thus, it is expected that a conventional SCHP would reduce the CO_2 emissions better, when operating in these regimes.

Generally, as more cooling is being produced relative to heating, $\mathrm{CO_2ER}$ declines because of the lower energy conversion efficiency in the cooling compared to heating. On the other hand, $\mathrm{CO_2ER}$ increases with the increase in the rotational speed of the prime mover and slightly declines at very high speed for the case of $\mathrm{CR} < 0.2$ and with high moisture in the fuel. Finally, up to 43%, 40%, and 31% reductions in CO_2 emissions can be achieved using wood chips of 10% (Fig. 6-7 (a)), 15% (Fig. 6-7 (b)) and 20% (Fig. 6-7 (c)) moisture contents, respectively.

6.2.3. Proposed multi-carrier system versus other system concepts

The performance results of the proposed ST+ORC biomass powered multi-carrier system have been compared to the results obtained from the literature for similar systems. In a broad sense, it is seen that deploying a hybrid of ST+ORC as prime movers in the proposed MDES concept minimises energy losses in the system and improves its performance indicators. In particular, compared to previous studies, the steep decline in the PES at high speed of the ST prime mover has been significantly reduced in this MDES configuration [55] [56], [133]. This is because the waste heat, which is rejected in other studies, has been utilised to produce additional power in the ORC.

A maximum of 55% savings in the primary energy is recorded when the system is fired by biomass fuel of 10% moisture content, producing more heating load, and operating at a rotational speed of 2500 rpm compared to a PES of 24.05%, 29.47% and 42% recorded in [55], [56] and [133], respectively. Similarly, higher $\mathrm{CO_2ER}$ are seen here compared with some previous studies. In this study, a maximum $\mathrm{CO_2ER}$ of 45% is recorded when biomass fuel with 10% moisture is deployed to produce a significant amount of heating and power at rotational speeds above 2000 rpm. This is more than the $\mathrm{CO_2ER}$ of 31.06%, and 36.22% obtained in the CCHP designs in [55] and [56], respectively, that utilised the ST only as the prime mover, but slightly lower than 46.6% seen in [133] where a hybrid of IC engine and ST was deployed. This underscores some of the gains in using hybrid prime movers in DES generating multiple energy vectors.

Further, the ratio of the cooling load to the heating load the system is designed to meet has a significant impact on its performance. This impact is seen to be very severe in the PES and CO_2ER where negative values were recorded, especially when the system was fired with fuel of high moisture content. It is seen that the MDES performed creditably when it serviced more of the heating load and power compared with the cooling load and power similar to the findings in [88]. There is an obvious need to size the system to determine how much cooling or heating it should service.

In addition, in-situ drying of the woodchips fuel is promising and has ensured that the quality of the input fuel is maintained in all seasons. The maximum values of PES, η_{II}, EUF, ATE and CO_2ER recorded for 10%, 15% and 20% moisture composition of wood chips fuel are: 55%, 71%, 94%, 85%, 43%; 50%, 61%, 81%, 60%, 40%; and 40%, 53%, 67%, 45%, 31%, respectively. The quality of the biomass fuel is seen to have impacted the system's performance metrics particularly, the EUF and ATE where a significant change is observed as the moisture content of the fuel increases.

6.3. Parametric optimisation of multi-carrier system

The parametric analysis conducted in the previous section highlights the need to undertake the parametric optimisation of the multi-carrier system. The goal of the parametric optimisation is to find the operating regime of the system that will guarantee its optimal performance. The formulation of the optimisation problem and the solution method have been presented in the following subsections.

6.3.1. Formulating optimisation problem

To conduct the parametric optimisation of the MDES, four performance metrics have been selected as the objective functions based on the observed results from the parametric study. The selected metrics for the multi-objective optimisation are: the energy utilisation factor (EUF), exergy efficiency (η_{II}), primary energy savings (PES) and artificial thermal efficiency (ATE). Based on the motivation to find the right mix of the energy vectors the system should produce to guarantee optimal technical and economic performance, the cooling ratio (CR) and frequency (Freq) of the prime mover have been selected as the decision variables for the optimisation. It is

seen that these objectives are conflicting as evidenced by the difference in the indicated global optima in Fig. 6-3 - Fig. 6-7.

Thus, based on the selected performance metrics, the optimisation problem is presented as:

$$maximise\ f(X) = f_1(X), f_2(X), f_3(X), f_4(X) \tag{6-9}$$

$$X\epsilon\{X_1, X_2\} \tag{6-10}$$

Subject to:

$$X_{min} \leq X \leq X_{max} \tag{6-11}$$

Eq. ((6-9)) expresses the objective functions where f_1 is the $\mathrm{EUF}(-)$, f_2 is the $\eta_{\mathrm{II}}\ (-)$, f_3 is the $\mathrm{PES}\ (-)$, and f_4 is the $\mathrm{ATE}\ (-)$ while the decision variables $X_1 \equiv \mathrm{Freq}$ (Hz) and $X_2 \equiv \mathrm{CR}\ (-)$ are expressed in Eq. (6-10). In Eq. (6-11), the constraints for the optimisation problem are presented showing the upper and lower bounds of the decision variables. The range of values used here are $\mathrm{Freq} = [25, 58.33]$ and $\mathrm{CR} = [0, 1]$.

6.3.2. Optimisation method

In Section 6.2.2, the results of the parametric analysis of the multi-carrier system were presented. It can be observed that the relationship between the performance metrics and the decision variables is non-linear and presents local and global optima. For optimisation problems that involve non-linear, complex and non-convex mathematical models, classical optimisation schemes get trapped in the local optimum and return suboptimal final results [255]. Thus, multi-objective evolutionary algorithms (MOEA) that are capable of avoiding getting trapped in the local optima have been extensively deployed to conduct parametric optimisation of complex and non-linear energy systems [69], [126], [152], [154], [196].

In this study, the non-dominated sorting genetic algorithm II (NSGA-II) was deployed to obtain the optimum solution in the form of a Pareto frontier. The elitist NSGA-II utilises three operators that mimic the natural selection and genetic principles in its operation, namely: selection, crossover and mutation, to generate the next offspring. It works with a population of points called individuals that consists of the values

(binary or integer) of the decision variables and are potential solutions to the optimisation problem. These points are chosen randomly, tested for fitness, mated (cross-over) and mutated to produce a new set of individuals for the subsequent generation, until the stopping criteria is attained. The evolutionary based optimisation methods generate a set of non-dominated optimal solutions called the Pareto frontier [256]. More details on the principles of evolutionary based optimisation algorithms can be found in [257], [258].

In this study, a MATLAB function that calls in the multi-objective genetic algorithm (GA) operator from the Math-works toolbox has been deployed to solve the optimisation problem and can be found in Appendix B.3. The details of the GA operator are presented in Table 6-7. An integration between MATLAB and Aspen plus® has been created to determine the objective functions by establishing a link that exchanges the necessary variables between the two software.

Table 6-7. Specifications of the GA operator.

Parameter	Value
Population size	50
Population type	Double vector
Pareto fraction	0.5
Maximum generation	100
Cross-over operator	Intermediate
Cross-over fraction	0.8

6.3.3. Decision making procedure

As has been noted in the literature review conducted on optimisation of DES in Chapter 2, the evolutionary based optimisation techniques produce a set of Pareto optimal solutions for the multi-objective optimisation problem. Any solution in the Pareto frontier can be considered as an optimal operating regime of the multi-carrier system. Therefore, it is at the discretion of the designer to select the best solution from the Pareto set [218]. One popular way of doing this is by deploying a decision making tool [218]. Several decision making tools have been formulated in the literature for selecting the optimal solution from the Pareto optimal set [218][219][220]. Here, the technique for order preference by similarity to the ideal

solution (TOPSIS) has been deployed to select the best solution from the set of optimal operating regimes obtained from the multi-objective optimisation of the MDES.

The following are the steps in the TOPSIS decision making process [259]:

(a) Compute the weighted normalised optimised results. The weighted normalised data u_{ij} is given as:

$$u_{ij} = w_j . \frac{x_{ij}}{\sqrt{\sum_{i=1}^{n} x_{ij}^2}} \; i = 1,2..n; j = 1,2..m \tag{6-12}$$

where w_j is the weight obtained from the decision matrix and x_{ij} are the optimised results.

(b) Calculate the separation of each of the weighted normalised results from the positive and negative ideal solutions, PIS and NIS, respectively. The Euclidean distance between an alternative and the PIS is given as:

$$D_i^+ = \sqrt{\sum_{j=1}^{n} \left(u_{ij} - u_j^+\right)^2} \; i = 1,2, \ldots n \tag{6-13}$$

In a similar manner, the distance between an alternative and the NIS is given as:

$$D_i^- = \sqrt{\sum_{j=1}^{n} \left(u_{ij} - u_j^-\right)^2} \; i = 1,2, \ldots n \tag{6-14}$$

where the positive ideal solution is the maximum solution (minimum solution in a minimisation problem) in a maximisation problem, given as: $u_j^+ = \max_{\forall i} u_{ij}$ and the negative ideal solution is the minimum solution (maximum solution in a minimisation problem) in a maximisation problem, given as: $u_j^- = \min_{\forall i} u_{ij}$ [259].

(c) Calculate the ranking index and arrange the ranking indices in a descending order. The ranking index is given as:

$$RI_i = \frac{D_i^-}{D_i^- + D_i^+} \; i = 1,2 \ldots . . n \tag{6-15}$$

The alternative with the highest RI_i is selected based on this approach.

Based on the scoring criteria listed in Table 6-8 the decision matrix has been obtained with the input of some experts and is shown in Table 6-9. The decision matrix is solved to determine the maximum eigenvalue ($\max|\det(A-\lambda I)=0|$) and the corresponding eigenvector ($(A-\lambda I)=0$), which is then normalised to obtain the desired weight of the objective function, w_j in Eq.6-12 for each of the alternatives.

Table 6-8. Judgement criteria for the decision matrix [260].

Intensity of importance	Definition
1	Equal importance
3	Weak importance
5	Essential or strong importance
7	Demonstrated importance
9	Absolute importance
2,4,6	Intermediate values

Table 6-9. Decision matrix from experts for TOPSIS analysis

	EUF	η_{II}	PES	ATE
EUF	1	$1/4$	$1/3$	2
η_{II}	4	1	$1/2$	5
PES	3	2	1	3
ATE	$1/2$	$1/5$	$1/3$	1

6.4. Multi-carrier system parametric optimisation results

This section presents the Pareto optimal solutions obtained from the multi-objective optimisation problem, from qualitative and quantitative perspectives. Fig. 6-8 shows quantitatively the Pareto frontier of the optimal solutions in a 3-D plot when wood

chips fuel containing 10% moisture after drying is combusted to power the MDES. The conflict in the objective functions is evidenced by the spread in the optimised data. As seen in Fig. 6-8, the optimal data present both dominated and non-dominated solutions. It is also evident that there is no single solution that maximises all the objectives; every single solution on the Pareto frontier is a plausible optimal operating regime of the energy system. Hence, the need to apply the TOPSIS decision making tool to select the best alternative.

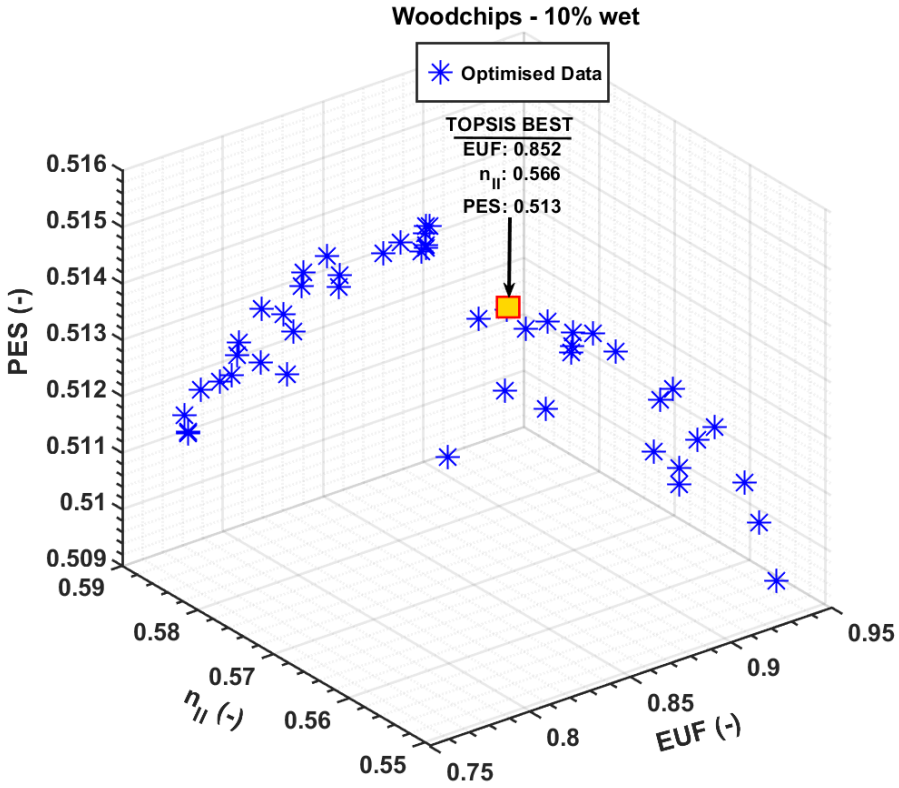

Fig. 6-8. Pareto frontier of the optimised results and the TOPSIS best solution.

The weight assigned to each of the objective functions has been obtained as described in Section 6.3.3 and are 12.68%, 36.07%, 42.57%, and 8.67%, for the EUF, η_{II}, PES and ATE, respectively. Using these weights and the TOPSIS steps described in Section 6.3.3, the TOPSIS scheme was deployed and the best solution was selected. The TOPSIS best gives $\mathrm{EUF} = 0.85$, $\eta_{\mathrm{II}} = 0.57$, $\mathrm{PES} = 0.51$ and $\mathrm{ATE} = 0.62$. These values were obtained for the decision variables; $\mathrm{Freq} = 29.11$ (Hz) and $\mathrm{CR} = 0.238\ (-)$. Thus, when operating optimally, the proposed multi-carrier DES will operate at low to medium speed and produce at least 3 times more heating than cooling.

Fig. 6-9 - Fig. 6-10 show the qualitative presentation of the Pareto optimal results obtained for each of the objective functions plotted against the decision variables, on the simulated solution domain. The TOPSIS best selected for each of the objective functions is also indicated in these figures.

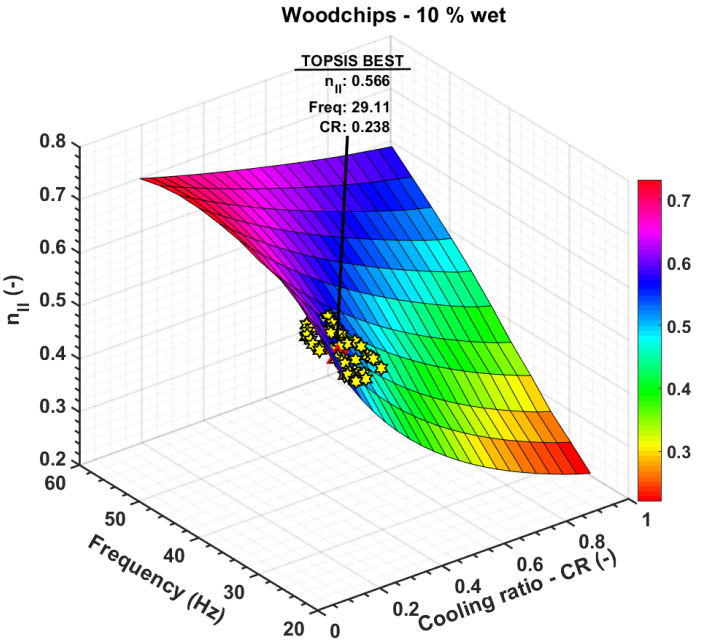

Fig. 6-9. Optimised exergy efficiency plotted against the decision variables and showing the TOPSIS best for dry wood chips fuel.

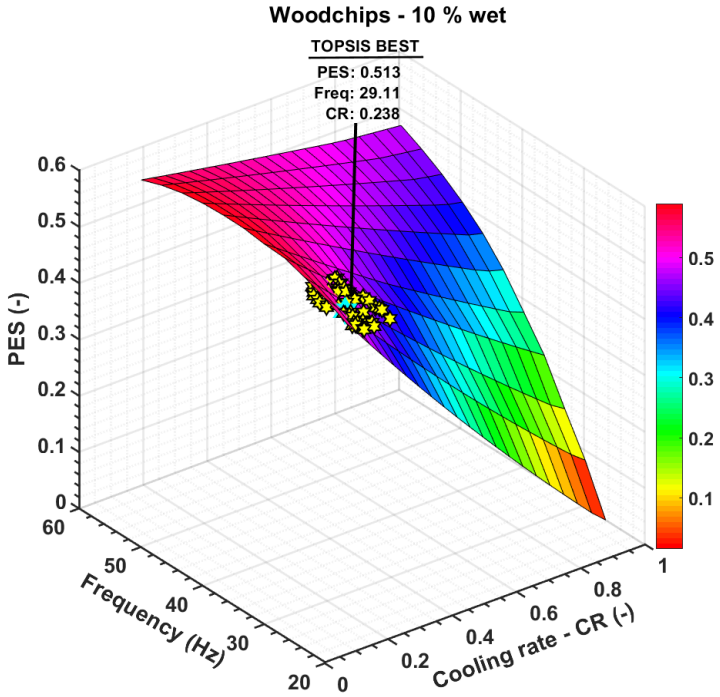

Fig. 6-10. Optimised results of primary energy savings plotted against the decision variables and showing the TOPSIS best.

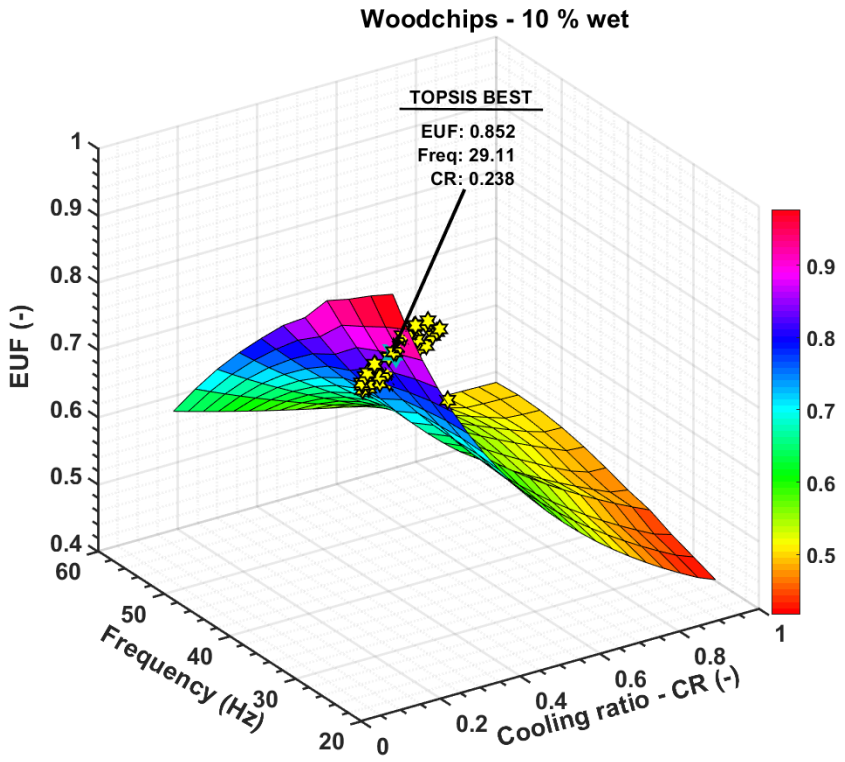

Fig. 6-11. Optimised results of energy utilisation efficiency plotted against the decision variables and showing the TOPSIS best for dry wood chips fuel.

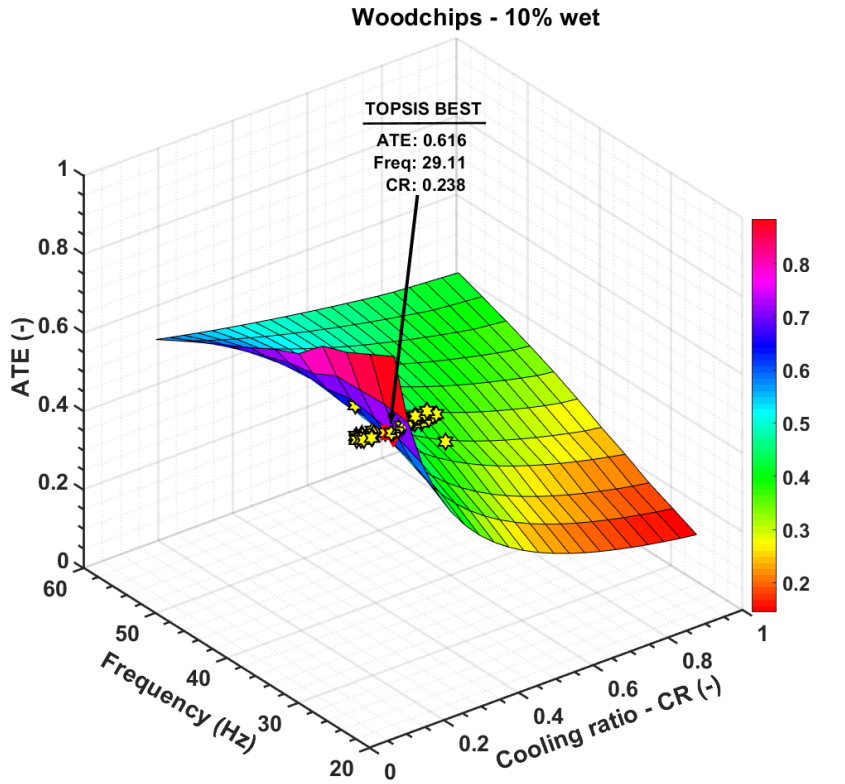

Fig. 6-12. Optimal results of artificial thermal efficiency plotted against the decision variables and showing the TOPSIS best for dry wood chips fuel.

It can be observed that there is a low scatter in the optimal results obtained for the exergy efficiency and primary energy savings in Fig. 6-9 and Fig. 6-10, respectively. Three optima regions are noticeable for the η_{II} and PES, indicated at the low speed and low cooling ratio, high speed and high cooling ratio and medium/high speed and low cooling ratio regions. Although the global optima for the η_{II} and PES are indicated at the medium/high ST frequency ($\mathrm{Freq} > 50$ (Hz)) and low cooling ratio ($\mathrm{CR} < 0.30\ (-)$), the optimised results were largely found in one of the local optima domains characterised by low frequency and cooling ratio ($\mathrm{Freq} < 30$ (Hz)).

On the other hand, high-level scatter in the optimal results is seen in the EUF and ATE presented in Fig. 6-11 and Fig. 6-12, respectively. By contrast to the η_{II} and PES, the Pareto optimal results for the EUF and ATE are populated in the indicated global optima, which is characterised by low speed of the ST prime mover and low cooling ratio. Unlike the former (η_{II} and PES), the EUF and ATE deteriorates sharply with the increase in the speed of the prime mover at low cooling ratio, i.e., when the MDES is generating high heating load compared to cooling and electric power. Consequently, no local optima exists in Fig. 6-11 and Fig. 6-12 in the high frequency and low cooling ratio regions. The search for the optimal solution is therefore constrained in the low cooling ratio and frequency region. This further highlights the conflicting nature of the multi-objective problem.

Finally, the TOPSIS selected optimal operating regime lies in the low cooling ratio and low-mid speed region. In this region of operation, the multi-carrier system generates low cooling and electric power and high heating load. Thus, because boilers have higher efficiencies and the losses in the prime mover are minimal at lower engine speeds, the available energy is better utilised; hence, the consequent high EUF and ATE. However, the PES, is slightly suboptimal because the ST prime mover is being operated at low speed, i.e., close to the inefficient idling conditions. Similarly, the MDES will have reduced exergy efficiency when operating in the optimal regime. Therefore, there is potential for performance enhancement of the proposed MDES by undertaking advanced waste heat recovery without altering the optimal operating regime of the system.

6.5. Summary of the chapter

The modelling, parametric analysis and optimisation of a novel multi-carrier decentralised energy system driven by a dual ST+ORC prime mover to co-produce cooling, heating, power, and dry wood chips has been performed. The models for predicting the performance of the subsystems of the multi-carrier system were developed in ASPEN plus except for the ST that has been previously developed in MATLAB. A link was established between the two software to enable the easy exchange of data, while MATLAB served as the interface for the control of the operation of the multi-carrier system which was modelled as a micro-CCHP. The preliminary results suggest that the deployment of ORC bottoming cycle improved the brake power and thermal efficiency of the standalone ST by 55% and 62%, respectively, and minimised the performance deterioration of the prime mover at high rotational speeds. Results of parametric analysis reveal the cooling ratio and speed of the prime mover have significant impact on the evaluated performance metrics, while the moisture content in the wood chips has marginal impact on the system performance.

Increasing the cooling ratio results in a decrease in the system performance especially at low speed of operation of the prime mover, while an increase in the speed of the prime mover has conflicting impacts on the performance indicators. In general, the proposed multi-carrier system performed significantly better than the systems separately producing cooling, heating, or electric power. The obtained results from the parametric studies highlight the need to undertake a parametric optimisation of the system to find the optimal operating regime. Thus, four objectives optimisation of the system have been conducted considering the exergy efficiency, energy utilisation factor, artificial thermal efficiency and primary energy savings, while frequency and cooling ratio served as the decision variables. The results demonstrate the conflicting nature of the optimisation problem. Finally, the multi-carrier system can reduce the primary energy consumption and CO_2 emissions of a separate cooling, heating or power system by 51% and 40%, respectively.

Chapter 7 Optimal Sizing and Simulation of New Hybrid Renewable Energy System Configuration

This chapter presents the optimal sizing and hourly simulation of the performance of the new hybrid renewable energy system (HRES) configuration proposed in this study. Section 7.1 describes the mathematical models of the components of the HRES deployed to simulate the system performance. Section 7.2 discusses the rule-based strategy proposed to coordinate the flow of energy from the system units. Section 7.3 outlines the system sizing optimisation problem designed to find the optimal number of components in the HRES configuration. Section 7.4 presents the solution approach for the system performance simulation and optimisation. Section 7.5 analyses the optimisation results and compares it to the base case. It discusses the results of the dynamic behaviour of the system in the test location. Also, this section presents the results of the sensitivity analysis that was undertaken to study the impact of the variation in the decision variables on the optimal system performance. Finally, a summary of the findings of the chapter is presented. The key findings of this results chapter have been published in a scientific Journal.

7.1. Mathematical modelling of the components of the HRES

In Chapter 3 and Fig. 3-1, the schematic diagram and the mode of operation of the new HRES configuration proposed in this study have been presented. The proposed HRES configuration is compried of wind turbines (WT), solar photovoltaic panels (PV), battery energy storage system (BSS) and Stirling engines (ST) and organic Rankine cycle (ORC) back-up. The system has an interesting unique feature of deploying a combined power cycle of ST+ORC as the back-up to augment its reliability. The deployment of split ST to minimise the excessive dumping of power, energy cost and emissions when the back-up is operational is another innovative idea implemented in this HRES concept. This section presents the mathematical models for predicting the performance of the components of the proposed HRES.

7.1.1. Modelling the performance of the photovoltaic modules

The models for predicting the performance of a photovoltaic module have been presented in [38]. A PV module has several cells connected in series to achieve the

required battery voltage. For a single diode with N_s, number of cells connected in series and N_p, number of modules arranged in parallel, the array current is related to the voltage by the following expression [38]:

$$I = N_p \left[I_{ph} - I_0 \left[exp\left(\frac{q(V + IR_s)}{nKTN_s} \right) - 1 \right] - I_{sh} \right] \quad (7\text{-}1)$$

where q (C) is the electron charge, K $(-)$ is the Boltzmann's constant, n $(-)$ is the diode ideality factor, and T (°C) is the cell temperature. The inverse saturation current, I_0 (A) is given by

$$I_0 = I_{rs} \left(\frac{T_c}{T_{ref}} \right)^3 exp\left[\frac{qnE_{GO}}{K} \left(\frac{1}{T_{ref}} - \frac{1}{T} \right) \right] \quad (7\text{-}2)$$

where E_{GO} (J) is the band gap energy of the semiconductor used in the cell and T_{ref} (°C) is the reference temperature. The phase current, I_{ph} (A), shunt current, I_{sh} (A) and reverse saturation current, I_{rs} (A) are however given in the following expressions:

$$I_{ph} = \left[\left(I_{sc} + k_i (T_c - T_{ref}) \right) \right] \frac{G_t}{1000}, \; I_{sh} = \frac{V + IR_s}{R_{sh}} \quad (7\text{-}3)$$

and,

$$I_{rs} = \frac{I_{sc}}{\left(exp\left[\frac{(qV_{oc})}{(nN_s kT)} \right] \right)} \quad (7\text{-}4)$$

I_{sc} (A) is the cell short circuit current at the reference temperature and solar irradiance, k_{i} is the short circuit current temperature coefficient, V_{oc} (V) is the open voltage, R_{sh} (ohm) is the shunt resistance, R_{s} (ohm) is the series resistance, V (V) is the cell voltage and G_{t} $\left(\frac{\mathrm{W}}{\mathrm{m}^2}\right)$ is the solar irradiance.

These models have been deployed to build a PV block in Simulink, to study the voltage-current and power-voltage characteristics of the PV module. However, for the determination of the optimal number of the PV modules required to fulfil the load, the following models were deployed to simulate the hourly power generation from the photovoltaic modules [14]:

$$P_{pv}(t) = \eta_{PV} A_{PV} G_h(t) = P_{STC}\left[\frac{G_h(t)}{G_{STC}}\left(1 + \frac{\alpha}{100}\left(T_c(t) - T_a(t)\right)\right)\right] F_{diss} \quad (7\text{-}5)$$

where P_{STC} (W) is the module maximum power at standard test conditions, A_{PV} (m^2), is the area of the module, G_{h} $(\frac{W}{m^2})$ is the hourly global solar irradiance, G_{STC} $(\frac{W}{m^2})$ is the irradiance at the test conditions, α (%/°C) is the temperature coefficient, T_{a} (°C) is the ambient temperature and F_{diss} $(-)$ is a factor that accounts for power dissipation due to dirt, wires, modules mismatch, and other losses. The efficiency of a PV panel is expressed as a function of the cell temperature, and it is given as [14]:

$$\eta_{PV}(t) = \eta_{r-PV}\eta_{pc}\left[1 - \beta\left(T_c(t) - T_{c,ref}\right)\right] \quad (7\text{-}6)$$

where $\beta = (0.004 - 0.006)/°\mathrm{C}$ is the temperature coefficient, η_{pc} is the modular power conditioning efficiency, η_{r-PV} is the reference cell efficiency and $T_{c,ref}$ (°C) is the reference cell temperature.

The cell temperature T_{c} (°C) is obtained from the following expression:

$$T_c(t) = T_a(t) + \left(\frac{NOCT - 20}{0.8}\right)\frac{G_h(t)}{G_{STC}} \quad (7\text{-}7)$$

where $NOCT$ (°C) is the nominal operating cell temperature.

Consequently, the power produced from the PV array at any time step, t, can be obtained as a function of the cell current and voltage and is given as follows:

$$P_{array}(t) = IV = P_{pv}(t) N_s N_p \quad (7\text{-}8)$$

The number of PV modules arranged in series, N_{s} is given as a function of the bus voltage, V_{bus} and the rated voltage of the PV panel given by the manufacturer, V_{PV} :

$$N_s = \frac{V_{bus}}{V_{PV}} \quad (7\text{-}9)$$

7.1.2. Modelling the performance of wind turbines

The modelling of the power generation from the wind turbine is presented in this section. The actual power output from the wind turbine can be estimated from the power curve in Fig. 7-1, which is usually furnished by the manufacturer.

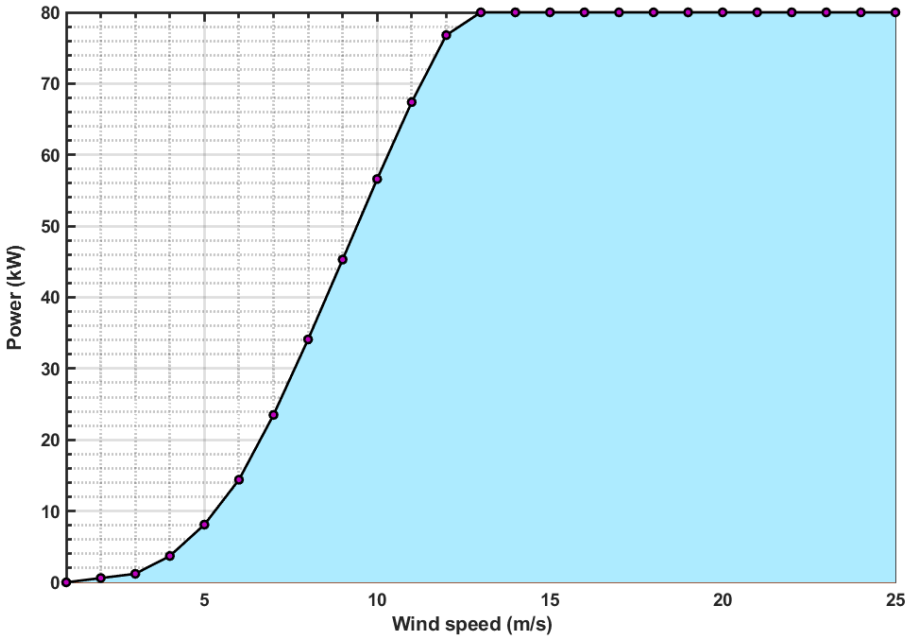

Fig. 7-1. Power curve of the Enercon E-18 wind turbine [261].

Based on the power curve provided by the manufacturer, the power that can be extracted from a moving stream of air at any time step, t, can be expressed as a function of the wind speed and hub height of the wind turbine as given in the following [38], [207], [262]:

$$P_{WT}(t) = \begin{cases} \frac{v^3 - v_c^3}{v_R^3 - v_c^3} . P_R & v_C \leq v \leq v_R \\ P_R & v_R \leq v \leq v_F \\ 0 & v \leq v_C \; and \; v \geq v_F \end{cases} \quad (7\text{-}10)$$

where v (m/s) is the wind speed in the test location, v_{C} $(\mathrm{m/s})$ is the cut-in wind speed, v_{R} (m/s) is the rated wind speed, v_{F} (m/s) is the cut-out wind speed and P_{R} (W) is the rated power of the turbine. The wind speed data at the location has been obtained from PVGIS [241] for a period of one year and was measured at 10m hub height.

To obtain the wind speed at the hub height of the selected turbines, the following logarithmic law is employed [38], [207]:

$$v_{hub} = v_r . \frac{\ln \frac{Z_{hub}}{Z_0}}{\ln \frac{Z_r}{Z_0}} \quad (7\text{-}11)$$

where v_{hub} (m/s) is the wind speed at the hub height, Z_{hub} (m) is the desired hub height, $Z_{\mathrm{r}}(\mathrm{m})$ is the reference height, v_{r} (m/s) is the wind velocity at the hub height, Z_0 (m) is the surface roughness height.

7.1.3. Combined ST+ORC back-up modelling

As previously stated, this study proposes deploying a combined ST and ORC as the back-up to the HRES system to augment the electricity generation from the renewable generators. However, sole Stirling back-up is also proposed to compare results and assess the performance improvements. The power supplied by the combined ST+ORC back-up at any time step is determined by the availability of the renewable generators, the dispatch strategy and the state of charge (SOC) of the battery. In this study, the biomass fuel consumption of the ST+ORC (or Stirling only), $FC_{\mathrm{ST\ or\ ST+ORC,}}$ (kg) will be determined from the energy balance of the heat engine and is expressed as:

$$FC_j(t) = \frac{3600 P_{gen,j}(t)}{\eta_{combustor} HV_{woodchips} \eta_j}, j = ST\ or\ ST + ORC \qquad (7\text{-}12)$$

where P_{j} (Wh) is the power delivered by the back-up at a given time step, $\eta_{\mathrm{combustor}}$ $(-)$ is the efficiency of the biomass combustor, $HV_{\mathrm{woodchips}}$ (J/kg) is the calorific value of wood chips and η_j $(-)$ is the electrical efficiency of the back-up. The sole efficiency of the ST and combined efficiency of the ST+ORC at the engine design point have been presented in Chapter 5 and Chapter 6, respectively, while the combustor efficiency has been cited in Chapter 6.

7.1.4. Modelling the diesel generator

The deployment of the ST in combined cycle power mode with an ORC has been proposed as the back-up in this HRES configuration. Nonetheless, the DG that has been popularly utilised as the back-up to HRES systems will be modelled here and it will serve as the base case to compare results. The power supplied by the DG at any time step is determined by the power generation capacity of the PV and WT, the load, the control strategy and the SOC of the battery. It is modelled based on the hourly fuel consumption, FC_{DG} $(\frac{\mathrm{l}}{\mathrm{Wh}})$ and can be expressed as [207]:

$$FC_{DG}(t) = AP_{gen,DG}(t) + BP_{rated,DG} \quad (7\text{-}13)$$

where $P_{\text{gen,DG}}$ $(\frac{\text{W}}{\text{h}})$ is the power delivered by the DG at a given time step, $P_{\text{rated,DG}}$ (W) is the rated capacity of the DG. The experimental constants, A $(\frac{\text{l}}{\text{Wh}})$ and B $(\frac{\text{l}}{\text{Wh}})$ in the above equation have been obtained as 0.246 and 0.08415, respectively [14].

In addition, the greenhouse gas (GHG) emissions produced by the traditional DG back-up has been compared to that of the proposed biomass fired ST+ORC (and ST only) back-up. The GHG emitted by the DG or ST is determined according to the guidelines of the international panel on climate change (IPCC) and is given as [263]:

$$y_{GHG}^{F} = HV_F\ \chi_{GHG}^{F} FC_j, \qquad j = DG\ or\ ST \quad (7\text{-}14)$$

where HV_{F} $\left(\frac{\text{J}}{\text{kg}}\right)$ is the heating value of the fuel, $\chi_{\text{GHG}}^{\text{F}}(\frac{\text{g GHG}}{\text{J fuel}})$ is the emission factor. The value of these constants has been extracted from [263], [264] and presented in Table 7-1.

Table 7-1. Constants for the evaluation of the GHG emissions [263], [264].

Parameter	Value
Diesel	
Heating value (MJ/kg)	45
CO_2 emissions factor (kg CO_2/ MJ)	0.074
N_2O emissions factor (kg N_2O / MJ)	0.6×10^{-7}
Woodchips	
Heating value (MJ/kg)	19.2
CO_2 emissions factor (kg CO_2/ MJ)	0.112
N_2O emissions factor (kg N_2O / MJ)	4×10^{-6}

7.1.5. Battery storage system modelling

The battery is one of the dispatchable units deployed to augment the power deficit in the proposed HRES configuration. In this study, the amount of energy the battery supplies or retains is determined by the control strategy deployed as well as the

state of charge (SOC) of the battery. At any time, t, the energy stored or released by the battery banks can be obtained from the following expressions:

$Charging$:

$$SOC\ (t+\Delta t) = \begin{cases} SOC\ (t) + \eta_{ch}\left(\frac{\left(P_{PV}(t)+P_{WT}(t)-P_L(t)\right)}{V_{Bat}}\right)\Delta t/C_{Bat}, & \text{LF} \\ SOC\ (t) + \eta_{ch}\left(\frac{\left(P_{PV}(t)+P_{WT}(t)+P_{ST+ORC}(t)-P_L(t)\right)}{V_{Bat}}\right)\Delta t/C_{Bat}, & \text{CC} \end{cases} \quad (7\text{-}15)$$

$discharging$:

$$SOC\ (t+\Delta t) = SOC\ (t) - \left(\frac{\left(P_L(t)-P_{PV}(t)-P_{WT}(t)-P_{ST+ORC}(t)\right)}{\eta_{disch}.V_{Bat}}\right).\Delta t/C_{Bat} \quad (7\text{-}16)$$

where $\eta_{\mathrm{ch}}\ (-)$, $\eta_{\mathrm{disch}}\ (-)$, V_{Bat} (V), C_{Bat} (Ah) are the charging efficiency, discharge efficiency, voltage and nominal capacity of the battery, respectively, P_{PV} (W), P_{WT} (W), and $P_{\mathrm{ST+ORC}}$ (W) are the electric power produced by the PV, WT and ST+ORC, respectively, P_{L} (W) is the electric load, $\Delta\mathrm{t}\ (\mathrm{s})$ is the time interval. The time interval used in this study is 1 hour. The specification of the components of the system are given in Table 7-2.

7.2. Rule-based control of system components

The renewable generators in the proposed system rely strongly on the local weather data to generate power. Consequently, it is unable to satisfactorily match the hourly electric load demand at the test location. It has been mentioned that battery storage systems and ST+ORC back-up will be deployed to augment the power supply. Further, the battery storage system is designed to serve as the first priority to match the positive net load in the system, and when it fails, the ST+ORC back-up will be deployed. Additionally, four small STs have been proposed to minimise the hourly commitment of the ST when it is deployed to supply the deficit power. The number of the small ST that is switched ON in parallel to augment the load will be determined. This is by the net load and the state of charge (SOC) of the battery.

Table 7-2. Specifications of the components of the HRES.

Component	Type	Specification	Value
Batteries (3 types) [265]	Hoppecke Sun AGM	Voltage, (V)	2
		Capacity, (Ah)	1120
	Hoppecke Sun AGM	Voltage, (V)	2
		Capacity, (Ah)	890
	Hoppecke Sun AGM	Voltage, (V)	2
		Capacity, (Ah)	620
Wind turbines (2 types) [261]	EWT DW 52-250 HH40	Cut-in speed, (m/s)	2.5
		Cut-out speed, (m/s)	25
		Rated speed, (m/s)	8
		Rated power, (kW)	250
	Enercon E-18	Cut-in speed, (m/s)	2.5
		Cut-out speed, (m/s)	25
		Rated speed, (m/s)	12
		Rated power, (kW)	80
PV modules (1 type) [266]	Canadian solar Hiku 7	Rated power, (W)	665
		Module efficiency, (%)	21.1
		Operating current, (A)	17.28
		Operating voltage, (V)	38.5
		Open circuit voltage, (V)	45.6
		Short circuit current, (A)	18.51
		NOCT, (℃)	42 ± 3
		Temperature coefficient,	-0.26
		Lifetime, (years)	20
MLPE inverter	AC rated	Capacity, (kVA)	48

Correspondingly, some set of rules are required to manage efficiently the flow of electric power in the proposed HRES. Therefore, the circuit charging with split ST option and the load following rule-based energy management strategies have been proposed in this study. In these strategies, four rules based on if-then constructs are deployed to control the charging and discharging of the battery system, the dispatch of power from the back-up and the dumping of excess power from the HRES. These rules are formulated based on the state of charge of the battery at a given time step, $\mathrm{SOC}\ (t)$ and the net load, $P_{\mathrm{net}}\ (t)$, where, $P_{\mathrm{net}}(t) = P_{\mathrm{L}}(t) - P_{\mathrm{PV}}(t) - P_{\mathrm{WT}}(t)$ [72]. Fig. 7-2 and Fig. 7-3 show the algorithm for managing the energy flow in the energy system based on the following rules:

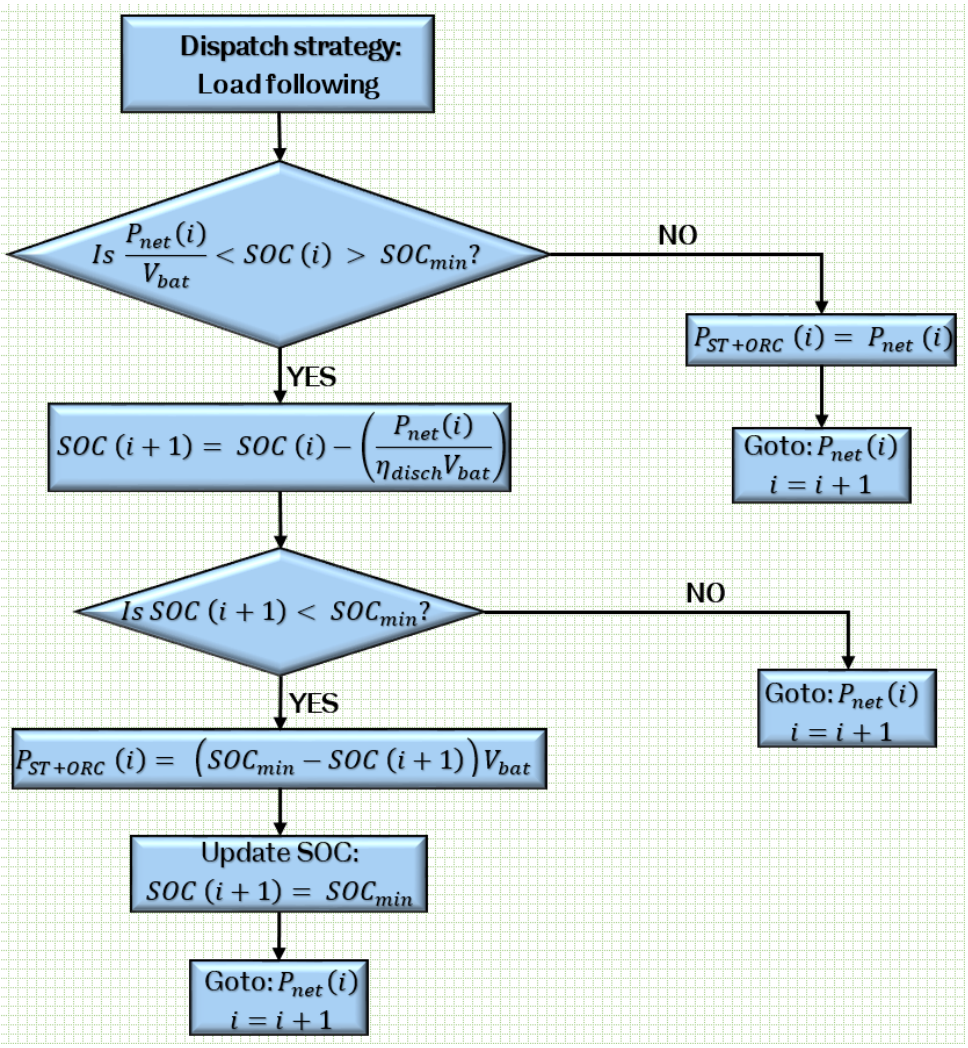

Fig. 7-2. Algorithm for load following control strategy.

Battery charging mode: In this energy management strategy, two conditions control the charging of the battery.

- $Condition\ 1$: $[P_{\mathrm{L}}(t) - P_{\mathrm{PV}}(t) - P_{\mathrm{WT}}(t) < 0\ ][SOC(t) < SOC_{\max}]$

When $P_{\mathrm{net}}(t) < 0$, i.e., the total power generation from the WT and PV exceeds the load and the charge in the battery is below its maximum capacity, the excess power is stored in the battery until it is fully charged. To achieve the charging of the battery by the excess power from the green generators, switches S4 and S5 in Fig. 3-1 are closed allowing excess power to flow to the batteries.

- $Condition\ 2$: $[P_{\mathrm{net}}(t) > 0\ ][P_{\mathrm{net}}(t) < P_{\mathrm{ST+ORC}}(t)\ ][SOC(t) < SOC_{\max}\ ]$

In this case, the net load in the system is positive and the ST+ORC back-up is deployed to simultaneously augment the power and charge the battery. Switches S4, S5 and S7 in Fig. 3-1 are switched on to accomplish this task in practice. Note that

in the load following strategy, only the excess power from the renewable generators is deployed to charge the batteries; hence, this condition is not applicable in LF.

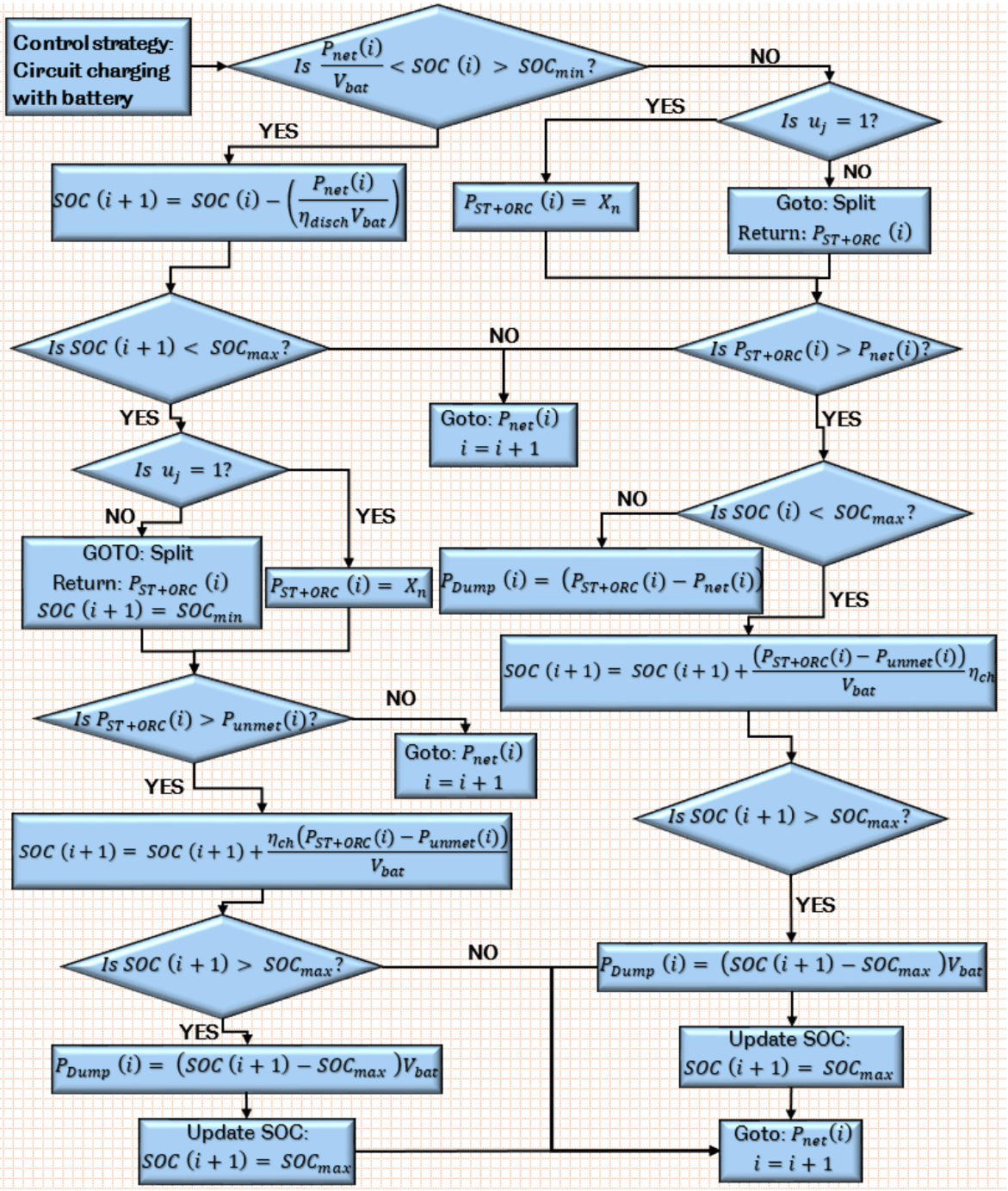

Fig. 7-3. Algorithm for circuit charging rule-based dispatch strategy with split Stirling engine option.

Power dumping mode: Similarly, additional two conditions, which are mirrored from the charging mode are deployed here to dump the excess power produced in the system.

- $Condition1$: $[P_{\mathrm{L}}(t) - P_{\mathrm{PV}}(t) - P_{\mathrm{WT}}(t) \ < 0 \ ][SOC(t) = SOC_{\max}]$

This rule controls the dumping of excess power produced from renewable energy generators. Therefore, if there is negative net load in the system and the battery is fully charged, the excess power is dumped via resistive loads.

- $Condition\ 2$: $[P_{\mathrm{net}}(t) \ < 0 \ ][P_{\mathrm{net}}(t) \ < P_{\mathrm{ST+ORC}}(t) \ ][SOC(t) = SOC_{\max} \ ]$

Conversely, this rule controls the dumping of excess power produced from the ST+ORC back-up after fulfilling its commitments to augment the power supply in the system and charge the batteries. Any excess power produced at this point is dumped via resistive loads. Note that in the load following strategy, the back-up follows the load strictly. Thus, this condition does not apply in this dispatch approach.

Battery discharging mode: $Condition$: $[P_{\mathrm{net}}(t) \ > 0 \ ][SOC(t) \ > SOC_{\min} \ ]$

When the total generation from the WT and PV is insufficient to match the load, i.e., there is positive net load in the system and the battery is above its minimum SOC, it is switched on to supply the load. Therefore, switch S3 is closed and this will allow the battery discharge its power through the inverter to the load bus. However, the battery's SOC must not fall below its minimum SOC, $SOC_{\min}$.

Back-up dispatching mode: The dispatch of power from the back-up is determined by the net positive load in the system. Additionally, this study proposes four-split Stirling engines back-up. To compare performance improvements between split STs and one big ST, a control vector, u_{j} has been deployed to switch from one ST to split STs as seen in Fig. 7-3 and Fig. 7-4. So, if $u_{\mathrm{j}} = 1$, one ST is deployed in the simulation of the dispatch strategy, otherwise, split STs are deployed. Note that X_{n} in these figures is the total capacity of the back-up system. Also, the split STs cases does not apply in the load following strategy, where the back-up is expected to follow the load (see, Fig. 7-2). Based on these two factors, the power dispatch by the back-up is controlled by the following conditions.

- $Condition\ 1$: $[P_{\mathrm{net}}(t) \ > 0 \ ][u_{\mathrm{j}} = 1 \ ]$

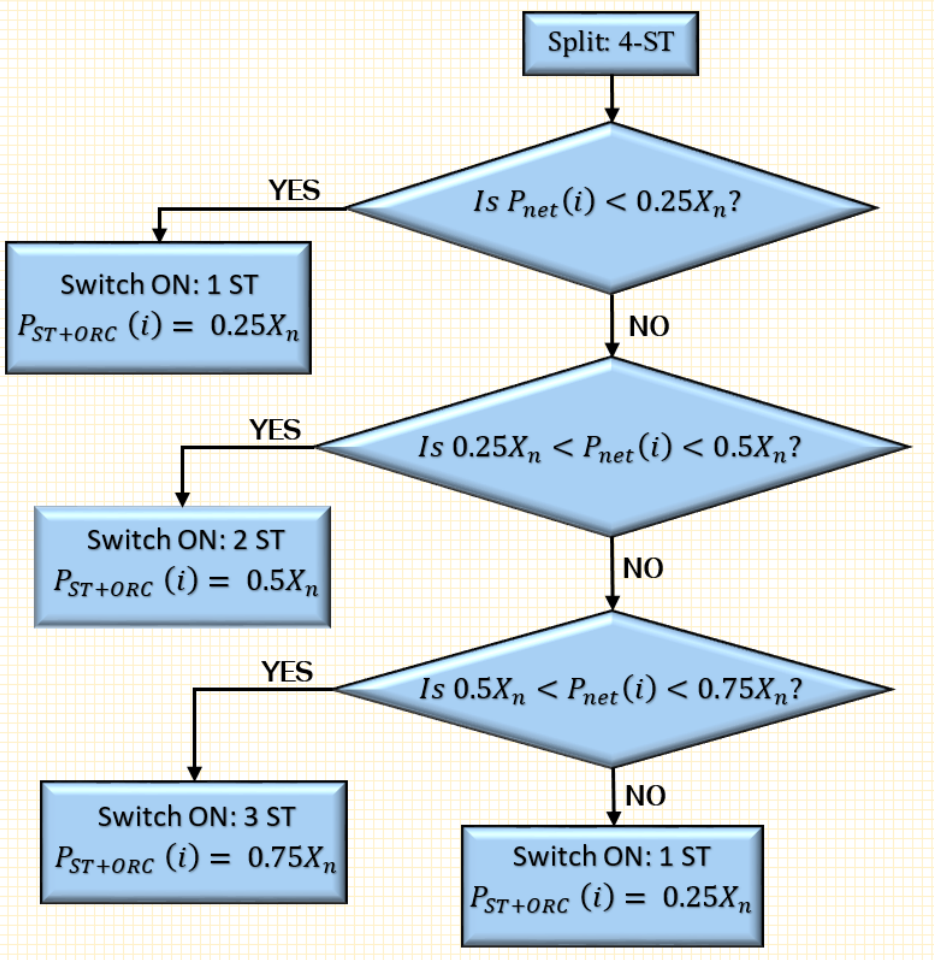

Fig. 7-4. Algorithm for implementing the power dispatch from four small Stirling engines.

In this case, the ST+ORC back-up is deployed to match the unmet load while operating at its rated capacity. This is achieved by closing all the Switches, S8 to S11 controlling the small STs. In the load following strategy, the ST+ORC back-up will operate mostly below its rated capacity to follow the load.

- $Condition\ 2: [P_{\mathrm{net}}(t)\ > 0\ ][P_{\mathrm{net}}(t) \leq P_{1-\mathrm{ST}}\ ][u_{\mathrm{j}} = 2\ ]$

Here, one small ST is deployed if the net load in the system is positive but below the capacity of one small ST. Therefore, one of the STs in the 4-split ST back-up is switched ON by closing any of the switches S8 to S11.

- $Condition\ 3: [P_{\mathrm{net}}(t)\ > 0\ ][P_{1-\mathrm{ST}} < P_{\mathrm{net}}(t) \leq P_{2-\mathrm{ST}}\ ][u_{\mathrm{j}} = 2\ ]$

Contrary to condition two, two of the STs are powered ON here to meet the deficit power, because it is above the capacity only one ST in the split can handle. Thus, any two switches from switches S8 to S11 are closed to power ON two STs to operate in parallel and supply the unmet load.

- $Condition\ 4: [P_{\text{net}}(t)\ > 0\ ][P_{2-\text{ST}} < P_{\text{net}}(t) \leq P_{3-\text{ST}}\ ][u_{\text{j}} = 2\ ]$

Here, three-split STs are simultaneously deployed to match the positive net load in the system by switching ON any of the three switches controlling the split STs (S8 – S11). Obviously, two-split STs are unable to handle the deficit power here.

- $Condition\ 5: [P_{\text{net}}(t)\ > 0\ ][P_{\text{net}}(t) \geq P_{3-\text{ST}}\ ][u_{\text{j}} = 2\ ]$

If the deficit power in the system is higher than that can be handled by 3-split STs back-up, all the switches controlling the split STs are closed and the engines will be powered ON simultaneously. Condition 5 is similar to the first condition. These rules have been deployed to manage the flow of energy in the system in the inner loop of the sizing optimisation procedure and fulfill the hourly commitments of its components.

7.3. Problem formulation

The formulation of the optimisation problem is performed in this section. First, the metrics for evaluating the design of the HRES are presented and then the optimisation problem is presented.

7.3.1. Evaluation metrics

Based on the reviewed literature and the objectives of this study, the loss of power supply probability (LPSP), levelised cost of energy (LCOE) and dumped power have been selected as the metrics for undertaking the sizing optimisation of the HRES.

(i) Levelised Cost of Energy

The levelised cost of energy (LCOE) is an economic indicator that quantifies the cost of the energy produced from the system over its life cycle. It is the ratio of the net present cost (NPC) for generating power from the system to the total electricity demand [267]. The NPC is composed of the installation and acquisition cost of the components, the operating and maintenance (O&M) cost, the replacement cost of components, and the cost of fuel for the entire life of the system converted back to the initial time of purchase of the components (year 1). Considering the interest and inflation rates, the NPC can be expressed as [207], [262]:

$$NPC = \sum_{j} \left(Annc_{I\&A,j} + Annc_{O\&M,j} + Annc_{rep,j} + Annc_{fuel,j} \right), \quad j \equiv PV, WT, Bat, ORC, ST, Inv \tag{7-17}$$

where the annualised acquisition and installation cost, $Annc_{\mathrm{I\&A}}$, annual operating and maintenance cost, $\mathrm{Annc}_{\mathrm{O\&M,j}}$, annual replacement cost, $Annc_{\mathrm{rep,j}}$ and annual fuel cost, $\mathrm{Annc}_{\mathrm{fuel,j}}$, respectively of a component, j are given by:

$$Annc_{I\&A} = \sum_{j} C_{I\&A,j} \times N_j \tag{7-18}$$

$$Annc_{O\&M} = \sum_{i=1}^{n_{system}} C_{O\&M,j} \left(\frac{\left(1 + r_{inf}\right)^{n_{system}}}{(1 + r_{int})^{n_{system}}} \right) \tag{7-19}$$

$$Annc_{rep} = \sum_{m=1}^{N_{rep,j}} C_{I\&A,j} \left(\frac{\left(1 + r_{inf}\right)^{m.n_j}}{(1 + r_{int})^{m.n_j}} \right) - C_j \left(\frac{n_j - \left(n_{system} - N_{rep,j} n_j\right)}{n_j} \right) \left(\frac{\left(1 + r_{inf}\right)^{n_{system}}}{(1 + r_{int})^{n_{system}}} \right) \tag{7-20}$$

$$Annc_{fuel,j} = \sum_{i=1}^{n_{system}} C_{fuel,j} \left(\frac{\left(1 + r_{inf}\right)^{n_{system}}}{(1 + r_{int})^{n_{system}}} \right) \tag{7-21}$$

where $N_{\mathrm{j}}\ (-)$ is the number of components, j, $C_{\mathrm{I\&A,j}}\ (\$)$ is the installation and acquisition cost, $C_{\mathrm{O\&M,j}}\ (\$)$ is the operating and maintenance cost, $N_{\mathrm{rep,j}}\ (-)$ is the number of replacements of component, j, $\mathrm{C}_{\mathrm{fuel,j}}\ (\$)$ is the cost of fuel, $n\ (-)$ is the life of the component or system, $r_{inf}\ (\%)$ is the inflation rate and $r_{int}\ (\%)$ is the interest rate.

The cost of fuel, $C_{fuel,j}$ is given as:

$$C_{fuel,j} = \left\{ c_{fuel,j} \sum_{t=0}^{8760} FC_{i=DG,ST+ORC}(t)\ , j = diesel\ or\ woodchips \right. \tag{7-22}$$

where c_{fuel} ($/kg or $/l) is the unit cost of the fuel. The levelised cost of energy is therefore given as [225]:

$$LCOE = \frac{NPC}{\sum_{t=1}^{t=8760} P_L(t)} \tag{7-23}$$

The cost data of the components and other financial assumptions used to evaluate the economic objective in this study are provided in Table 7-3.

(ii) Loss of Power Supply Probability

The loss of power supply probability (LPSP) is a statistical parameter that assesses the reliability of the renewable energy resources in meeting the electricity demand of the design location. A low LPSP indicates that the renewable energy resources are sufficiently matching the load requirements. On the contrary, high LPSP implies that the renewable energy resources are unable to meet the energy demand of the location and as a result, the system may rely more on the back-up power sources to match the demand. While it is desirable to have low LPSP, i.e., high penetration of renewable energy resources, it is important to ensure that the system is not oversized to avoid excessive dumping of power. The LPSP has been expressed as follows [225], [267]:

$$LPSP = \frac{\sum_{t=1}^{t=8760}\left(P_L(t) - (P_{PV}(t) + P_{WT}(t)) + P_{ST+ORC}(t) + P_{Bat,SOC^{min}}\right)}{\sum_{t=1}^{t=8760} P_L(t)} \tag{7-24}$$

(iii) Dumped Power

The dumped power quantifies the amount of excess electricity being generated by the HRES that is dumped via resistive loads. The generation of excess power is inevitable in a HRES because PV and WT power generation is at variance with the electricity load consumption. Hence, excess power is generated from the HRES, which also indicates that the system is over-sized, and this results in high energy cost. On the other hand, power curtailment with the intention of reducing dumped power, results in high energy cost and increased emissions because of the increased reliance on the back-up to fulfill the net load. It is, therefore, important to minimise

the dumped power from the renewable generators in a HRES while simultaneously minimising the deployment of the back-up.

Table 7-3. Market price of the system components.

Component	Description	Value
	Acquisition and installation cost	
Wind turbine	Enercon E-18 per kW (US $)	700 [268]
	EWT DW 52-250 per kW (US $)	700 [268]
Solar PV	Hiku 7 cost per panel (US $)	987 [266]
Battery	Hoppecke 620 Ah (US $)	350 [265]
	Hoppecke 890 Ah (US $)	405 [265]
	Hoppecke 1120 Ah (US $)	530 [265]
Stirling engine	Acquisition cost per kW (US $)	500 [58]*
ORC engine	Acquisition cost per kW (US $)	1700 [269]*
DG	Acquisition cost per kW (US $)	1000 [221]
MLPE inverter	Cost per kW (US $)	120 [268]
	Operating and maintenance cost	
Fuel cost	Nigerian wood chips (US $/tonne)	85
Fuel cost	Diesel fuel (US $/litre)	0.689
Wind turbine	Maintenance cost per kW (US $)	0.02 [119]
PV	Maintenance cost per kW (US $)	0.005 [119]
Stirling engine	Maintenance cost per kW (US $)	0.0095 [58]*
ORC engine	Maintenance cost per kW (US $)	0.008 [269]*
DG	Maintenance cost per kW (US $)	0.064 [221]
	Financial assumptions	
Interest rate	Bank interest rate on capital	12.5
Inflation rate	Inflation rate on capital	15
DG life	Lifespan of DG (years)	5
ST life	Lifespan of ST (years)	10
ORC life	Lifespan of ORC (years)	10
Plant life	Lifespan of the system (years)	20

*Please note that the acquisition and maintenance costs of the ST and ORC obtained from the referenced sources may be underestimated and below the market value.

The dumped power from the HRES can be obtained as follows:

$$P_{Dumped} = \begin{cases} \sum_{t=1}^{t=8760} \big((P_{PV}(t) + P_{WT}(t)) - P_L(t)\big), & (P_{PV}(t) + P_{WT}(t) > P_L(t) \\ \big(P_{ST+ORC}(t) - P_L(t)\big), & P_{ST+ORC}(t) > P_L(t) \end{cases} \quad (7\text{-}25)$$

7.3.2. Optimisation problem

The mathematical formulation of the evaluation metrics has been undertaken and the expressions presented in Eqn. (7-17) – (7-25). For a predefined load profile of the consumer, the optimisation problem aims to determine the optimal number of system components and type of the components that will minimise the levelised cost of energy (LCOE), loss of power supply (LPSP), dumped power (P_{Dumped}) and greenhouse gas (GHG) emissions ($y_{\mathrm{GHG}}^{\mathrm{F}}$) over the plant life of 20 years. This section presents the formulation of the objective functions and the constraints that must be satisfied to select an optimum system configuration.

7.3.2.1. Optimisation functions

The formulated evaluation metrics are the mathematical expressions of the objective functions. The optimisation problem is formulated as a multi-objective problem aimed at simultaneously minimising the three objective functions and is presented as follows:

$$minimise\ f(X) = f_i(X), f_j(X), f_k(X) \qquad i \neq j \neq k \quad (7\text{-}26)$$

$$\forall: g_i(X) = 0\ and\ h_i(X) \leq 0 \quad (7\text{-}27)$$

$$X\epsilon\{X_i, i = 1,2, \dots \dots n-1, n\} \quad (7\text{-}28)$$

where $i, j, k\ \epsilon\ \{1,2,3\}$, the objective functions, $f\ \epsilon\ \{\mathrm{LCOE}, \mathrm{LPSP}, P_{\mathrm{dumped}}\}$, g_{i} are the equality constraints, h_{i} are the inequality constraints and X are the decision variables. $X_1 =$ number of PV modules in parallel, $X_2 =$ number of wind turbines, $X_3 =$ types of wind turbine, $X_4 =$ the capacity of the back-up power block and $X_5 =$ number of batteries in parallel and $X_6 =$ types of battery. Here, two wind turbine types of different specifications and from different manufacturers (see, Table 7-2)

have been selected while three battery types of different capacities were selected (see, Table 7-2).

7.3.2.2. Defining constraints

The optimal solution must satisfy the following conditions:

a) Energy generation and consumption matching: for the worst days, i.e. days characterised by bad weather and poor energy generation from the renewable energy sources:

$$\sum_{t=1}^{t=24}(P_{PV}(t)+P_{WT}(t)) \geq \sum_{t=1}^{t=24}\left(P_L(t)\right) \tag{7-29}$$

Note that a "worse day" as used here implies a day the PV or WT generator may be unable to generate any power at all, because of heavy thunderstorms. It is not plausible that the total generation on a worse day will exceed the demand for obvious reasons. Besides, PV or WT are only available to generate power for some hours even on a bright day. Hence, back-ups cannot be dispensed in these systems.

b) Back-up power and demand matching: total capacity of the ST+ORC or ST only should not go below a threshold,

$$\sum_{i=1}^{n} P_{ST\ or\ ST+ORC}(t) \geq x_f P_L \tag{7-30}$$

where $\mathrm{x_f}\ (-)$ is the minimum power threshold of the back-up.

c) Battery storage and discharge limit: the maximum depth of discharge (DOD) of the battery has been furnished by the manufacturer. In this study, the battery is only expected to discharge power when its SOC is above the $\mathrm{SOC_{min}}$. By contrast, in the charging mode, the power stored in the battery is not expected to exceed $\mathrm{SOC_{max}}$.

$$(1-DOD)\left(\frac{N_{Bat}}{N_{Bat,S}}\right)C_{Bat,max} \leq C_{Bat}(t) \leq \left(\frac{N_{Bat}}{N_{Bat,S}}\right)C_{Bat,max} \tag{7-31}$$

where $N_{\mathrm{Bat}}\ (-)$ is the total number of batteries, $N_{\mathrm{Bat,S}} = \frac{\mathrm{V_{Bus}}}{\mathrm{V_{Bat}}}$ is the number of batteries in series, $V_{\mathrm{Bus}}\ (\mathrm{V})$ is the bus voltage, $C_{\mathrm{Bat,max}}\ (\mathrm{Ah})$ is the maximum capacity

of the battery. Furthermore, the power stored in the battery or discharged from the battery must not exceed the capacity of the battery

$$\text{Battery discharge mode: } P_{disch,Bat}(t) \leq \left(\frac{N_{Bat}}{N_{Bat,S}}\right) C_{Bat,max} V_{Bat} \tag{7-32}$$

$$\text{Battery charge mode: } P_{ch,Bat}(t) \leq \left(\frac{N_{Bat}}{N_{Bat,S}}\right) C_{Bat,max} V_{Bat} \tag{7-33}$$

d) Battery capacity limit: In this study, the battery storage has been designed to handle mainly the constant base load demand in the morning. Hence, a constraint to ensure the battery capacity is sufficient to match the base load when it is in the power discharge mode has been introduced into the system sizing optimisation:

$$\text{Battery capacity: } N_{Bat}.\, C_{Bat,max} \geq x_f P_L \tag{7-34}$$

where x_f $(-)$ is the minimum threshold of the capacity of the battery.

e) Limits on components: upper and lower limits have been set on the number of components and types of components. In the case of the type of components, the absolute value of the random number generated within the given range represents the type of the component, j selected and this will prompt the release of the corresponding component data.

$$X_{j,min} \leq X_j \leq X_{j,max} \tag{7-35}$$

where $X_{\mathrm{j,min}}$ $(-)$ is the lower bound, $X_{\mathrm{j,max}}$ $(-)$ is the upper bound and X_{j} $(-)$ is the number or type of component, j. The range of values of the decision variables are given in Table 7-4. These range of values are selected considering the constraint on land availability and other economic and environmental considerations.

Table 7-4. The upper and lower bounds of the decision variables.

Parameter	Lower bound	Upper bound
Number of PV in parallel	1	1200
Number of type 1 wind turbine	0	5
Number of type 2 wind	0	8
Wind turbine type	1	2
ST+ORC capacity (kW)	140	220
Control strategy	1	4
Number of batteries in parallel	1	30
Battery type	1	3
Number of split	1	2

7.4. HRES solution approach

The solution approach to the optimisation problem that was earlier formulated is presented in this section. As can be seen from the models developed in Section 7.1 the power generation from the HRES components is strongly dependent on the unpredictable weather and electricity demand data, which introduces some complexity in the optimisation problem. Consequently, different heuristic tools have been deployed to solve optimisation problems that involve HRES sizing including, genetic algorithm (GA) [14], [113], [119], [215], particle swarm optimisation (PSO) [76], [121], [124], fruit fly optimisation [71], grasshopper optimisation [217], [221] and multi-objective self-adaptive differential evolution (MOSaDE) [225]. GA has been widely deployed in sizing HRES among all the heuristic tools. It is a robust evolution algorithm with the advantage of avoiding getting trapped in the local optima; however, it does not converge at the global optimal [14], [216]. This problem is overcome by hybridising GA with other local search optimisation tools. Therefore, the Pareto front multi-objective evolution algorithm (MOEA) hybridised with a classical optimisation tool was deployed in solving the multi-objective optimisation problem. The details of the GA operators are presented in Table 7-5.

Table 7-5. Specifications of the GA operator.

Parameter	Value
Population size	250
Population type	Double vector
Pareto fraction	0.5
Maximum generation	200
Cross-over operator	Intermediate
Cross-over fraction	0.8
Hybrid function	fgoalattain

The algorithm for the implementation of the solution to the optimisation problem is presented in Fig. 7-5. Matlab Simulink blocks of the PV and WT generators were built with the models presented in Section 7.1, for the hourly simulation of the renewable generators. These Simulink blocks rely on the local weather data (solar irradiance, wind speed and temperature) and the manufacturers' data of the components (see, Table 7-2) to simulate the power generation of the renewable generators. Therefore, as seen in Fig. 7-5, the load and weather data (solar irradiance, wind speed and temperature) for a period of one year are fed into the Simulink blocks from an Excel database. These weather and load data and system configuration data (number and types of component) encoded in the initial random population of individuals generated by the GA, have been used to compute the hourly power generation from the PV and WT generators. The initial population of individuals, Pop_i in the first generation, G_i comprises n different configurations of the HRES that needs to be evaluated to obtain the configuration that best satisfies the objectives and meets all the constraints. It is represented in a vector form as:

$$Pop_i = \begin{bmatrix} X_1^1 & X_2^1 & X_3^1 & X_4^1 & X_5^1 & X_6^1 \\ X_1^2 & X_2^2 & X_3^2 & X_4^2 & X_5^2 & X_6^2 \\ X_1^3 & X_2^3 & X_3^3 & X_4^3 & X_5^3 & X_6^3 \\ \cdot & \cdot & \cdot & \cdot & \cdot & \cdot \\ \cdot & \cdot & \cdot & \cdot & \cdot & \cdot \\ \cdot & \cdot & \cdot & \cdot & \cdot & \cdot \\ \cdot & \cdot & \cdot & \cdot & \cdot & \cdot \\ X_1^n & X_2^n & X_3^n & X_4^n & X_5^n & X_6^n \end{bmatrix} = \begin{bmatrix} X_1 \\ X_2 \\ X_3 \\ \cdot \\ \cdot \\ \cdot \\ \cdot \\ X_n \end{bmatrix} \quad (7\text{-}36)$$

where X is a vector representing the genotype of each individual in the population.

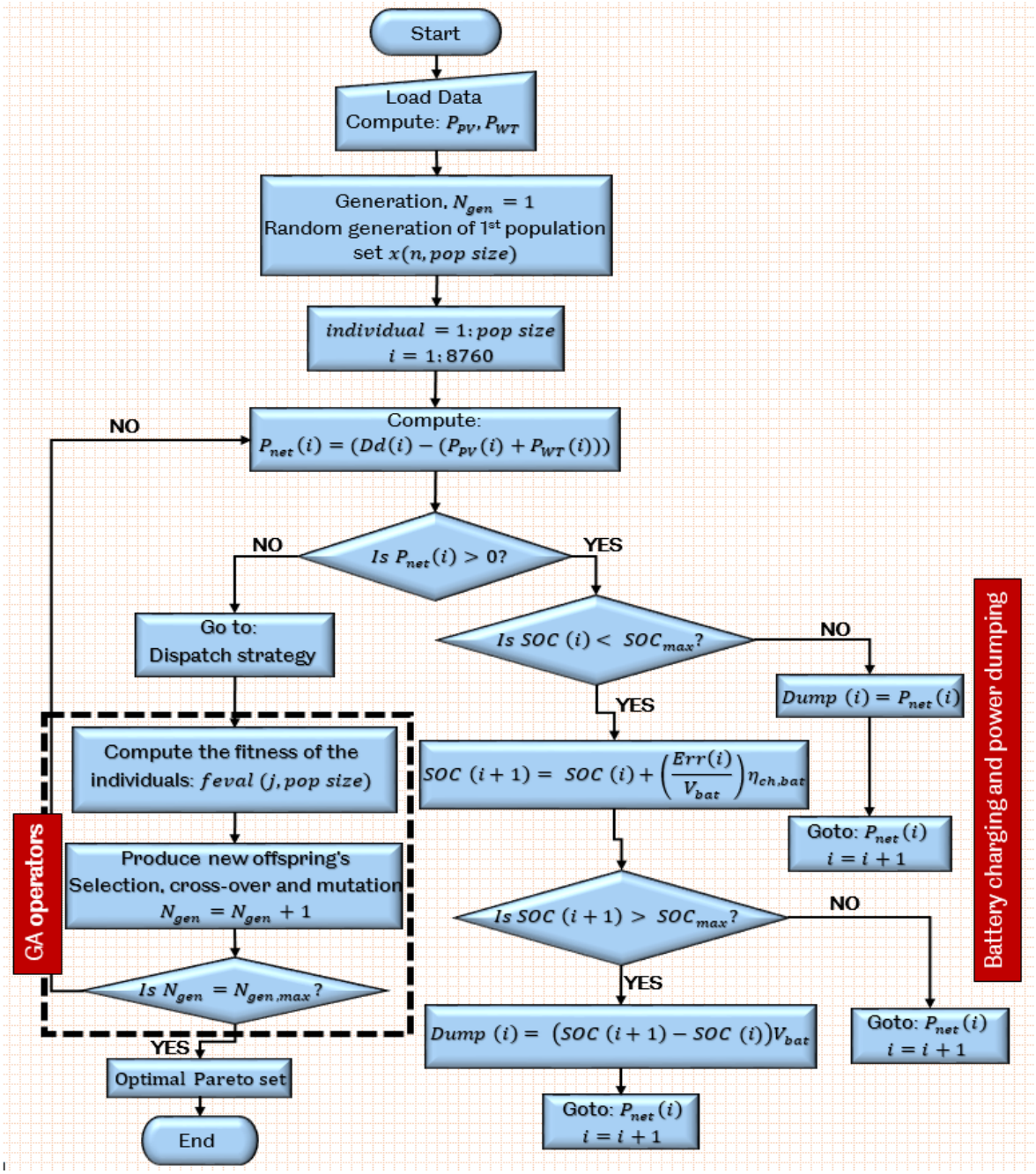

Fig. 7-5. Algorithm for the HRES system sizing optimisation.

The difference between power generation and demand is determined and depending on the net load in the system, the optimisation will proceed to implement the rule-based dispatch strategies described in Section 7.2 and obtain $P_{\text{disch,Bat}}\ (t)$, $P_{\text{ch,Bat}}$, $P_{\text{ST+ORC}}(t)$, $P_{\text{Dumped}}\ (t)$ and $SOC\ (t)$ for every hour in one year (t = 8760). Thereafter, the objective functions, i.e., fitness of the individuals are computed. Subsequently, the GA operators (selection, crossover and mutation) are deployed to generate the next generation of individuals and the entire process is repeated

until the stopping criteria is met. The MATLAB function developed for this purpose has been described in Appendix C.

In the case of the simultaneous optimisation of two or three objective functions that are usually conflicting, the MOEA presents the optimal solutions of the system configuration in the form of a Pareto front that contains non-dominated optimal solutions. In this case, it is necessary to deploy a multi-criteria decision making (MCDM) tool to select the best optimal system configuration from the Pareto set. This study deploys the TOPSIS approach which has been described in Section 6.3.3, to select the best solution from the Pareto set. As already described in Chapter 6, a decision matrix is developed based on a scoring criteria and then solved to determine the maximum eigenvalue $(max|det(A-\lambda I)=0|)$ and corresponding eigenvector $((A-\lambda I)=0)$, in order to obtain the weight assigned to each of the objectives. The scoring criteria and the resulting decision matrix are presented in the Appendix D. The TOPSIS MCDM selects the best system configuration, $X^{best} = \left[X_1^{best}\ X_2^{best}\ X_3^{best}\ X_4^{best}\ X_5^{best}\ X_6^{best}\right]$ from the Pareto set of optimal solutions.

7.5. Results and discussion

This section presents the optimal system configuration obtained from the HRES sizing optimisation as well as the corresponding system performance. Further results are presented for the dynamic simulation of the system, while the results of the sensitivity analysis performed to study the response of the optimal system to changes in the price and size of the key system components have also been presented.

7.5.1. Results of optimal hybrid system configurations

In this study, several HRES cases based on the two main dispatch strategies examined have been formulated to compare the results to the base case: HRES with DG back-up. The Pareto optimal set, which are a combination of the sizes and types of the components of the proposed HRES and the formulated cases that simultaneously minimises the LPSP, LCOE and dumped power have been found after 150 generations of the GA optimisation procedure.

Fig. 7-6 presents the Pareto optimal solutions obtained from the multi-objective optimisation of the HRES for the load following strategy with ST+ORC back-up. The conflicting nature of the multi-objective problem is evidenced by the degree of scatter in the Pareto front. This is even more obvious from the trend of the graph in Fig. 7-6 indicating the relationship between the objective functions.

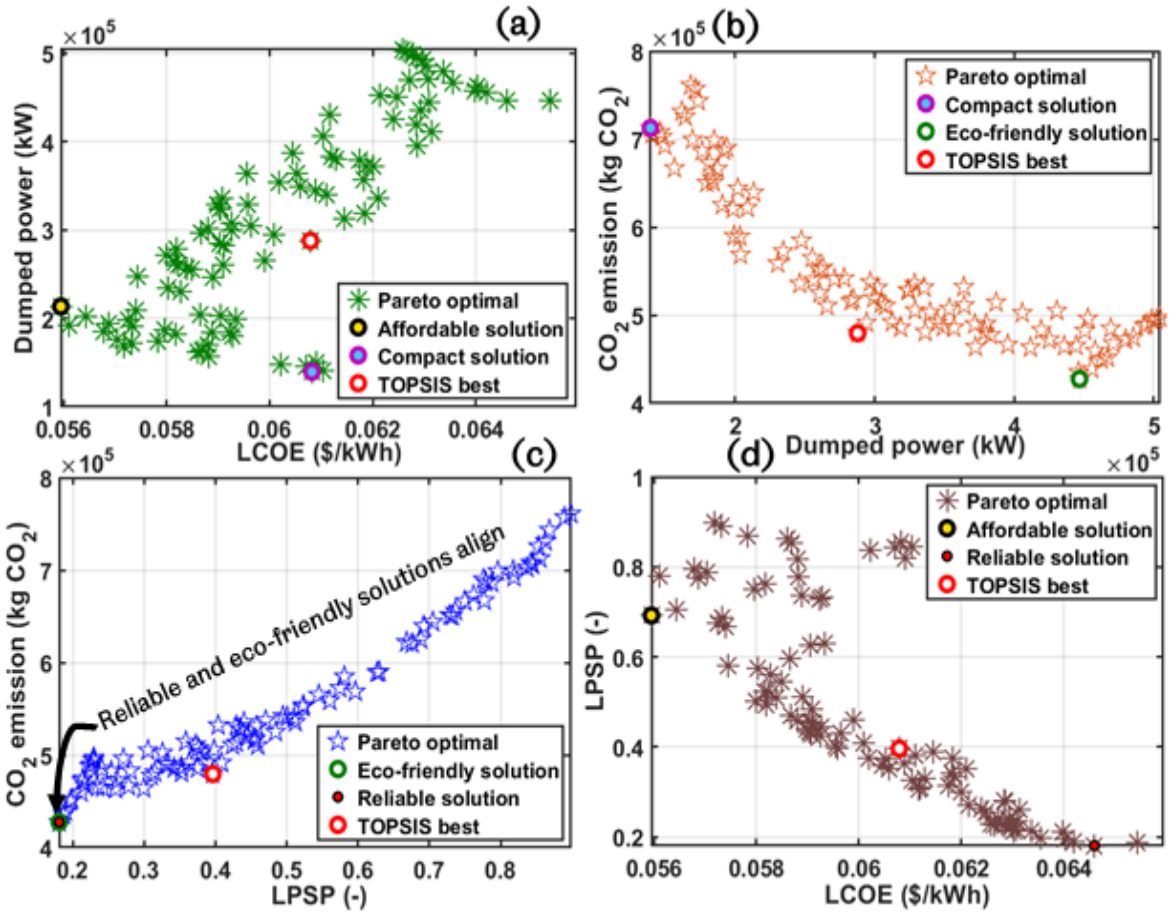

Fig. 7-6. Pareto front of the optimal system configuration found from the multi-objective optimisation, for the load following with ST+ORC back-up case.

As Fig. 7-6 (a) demonstrates, the LCOE and dumped power noticeably exhibit a positive relationship since an increase in the size of the system will raise the energy cost and increase the excess power produced. On the other hand, the dumped power and the CO_2 emitted from the energy system are contradictory as observed in Fig. 7-6 (b), because high penetration of green energy generators that are periodic and anti-correlated with load demand, reduces the carbon emissions but increases the dumped power. For similar reasons, the LPSP is consistent with the CO_2 emissions as can be observed in Fig. 7-6 (c). While the LCOE exhibits an indirect

relationship with the LPSP, i.e., it will cost more to achieve an energy system that is reliable (Fig. 7-6 (d)).

Further, the ideal solutions from the perspective of reliability, eco-friendliness, compactness, and affordability have been marked in Fig. 7-6 and it is evident that no solution simultaneously meets the ideal conditions from these standpoints. Hence, TOPSIS decision-making tool has been employed to obtain the best system configuration from the Pareto set in each case as highlighted in Fig. 7-6. The TOPSIS best indicates the cheapest solution in Fig. 7-6 (a) but dumps more power than the indicated ideal solution from the perspective of compactness of the system. Similarly, in Fig. 7-6 (b), the TOPSIS best prioritises reducing carbon emissions over dumped power and indicates a solution that best minimises carbon emissions. Regarding LPSP and CO_2 emissions, as it is evident in Fig. 7-6 (c), the TOPSIS best ensures equal trade-off in these two objectives, while the LCOE is slightly prioritised more than the reliability (LPSP) in Fig. 7-6 (d). The priorities demonstrated in selecting the TOPSIS best reflects the weight assigned to each of these objectives in the selection process. Apparently, the reduction in the energy cost has been given the top priority, while reliability and sustainability are rated second and over the size.

Similar steps have been replicated to obtain the best system configuration in each of the examined system cases. This section presents the comparison of the optimal system configurations obtained from the different cases to the base case (DG back-up HRES) from technical, economic and environmental perspectives.

7.5.1.1. Optimal system configurations in load following

Two hybrid system configuration cases that utilise the load following (LF) dispatch strategy have been proposed in this study. Table 7-6 presents the optimal system configuration obtained for these cases and for the base case, while Fig. 7-7 presents the comparative results of the optimal system performance.

(i) Case 1: Hybrid WT-PV-BSS with ST back-up

This hybrid system case deploys a sole Stirling engine to follow the positive net load in the system, when the renewable generators are unable to meet the consumers load demand. Unlike in the base case where the DG is deployed for a similar purpose,

the obtained optimal configuration in case 1 utilises slightly more PV generators (983 PV panels in parallel) as seen in Table 7-6. Therefore, the total power generated from the renewable generators increased marginally by 0.42% compared to the base case; hence, the slight increase in the dumped power by 2 MWh in case 1, since the both cases deployed equal amounts of BSS to store the excess power. Correspondingly, the LPSP in case 1 (LPSP of 0.3501) is better than in the base case (LPSP of 0.3962), because the former utilised more PV generators (see, Fig. 7-7). Thus, the optimum configuration in case 1 is more reliable compared to the base case. On the other hand, LCOE of 7.72 cents/kWh is obtained in case 1, which represents a decrease of 50.45% compared to the base case (LCOE of 15.58 cents/kWh). This decrease is attributable to the lower unit cost of fuel, cost of maintenance, capital cost, and even replacement cost associated with the deployment of the biomass fired ST back-up compared with the DG back-up. However, slight increase in the GHG emissions of 2.12% is notable in case 1 compared with the base case, due to the marginal increase in the utilisation of the ST back-up in the former compared to the latter as can be seen in Table 7-6.

Table 7-6. Optimal system configuration in load following for all the examined cases.

Objective function	Case 1	Case 2	Base case
LCOE (cent/kWh)	7.72	6.08	15.58
LPSP (-)	0.3507	0.3962	0.3527
Dumped power (MWh)	309.7	287.8	305.9
CO_2 emissions (kg CO_2)	8.342×10^5	4.795×10^5	7.232×10^5
Number of PV	4×983	4×935	4×977
Wind Turbine type	Type 1	Type 1	Type 1
Number of WT	5	5	5
Battery Type	Type 3	Type 2	Type 3
Number of batteries	4×30	4×26	4×30
Capacity of back-up engine (kW)	190	193	182.12
Annual PV Power (MWh)	724.25	688.16	719.84
Annual WT power (MWh)	330.26	330.26	330.26
Annual back-up power (MWh)	347.59	361.71	345.30

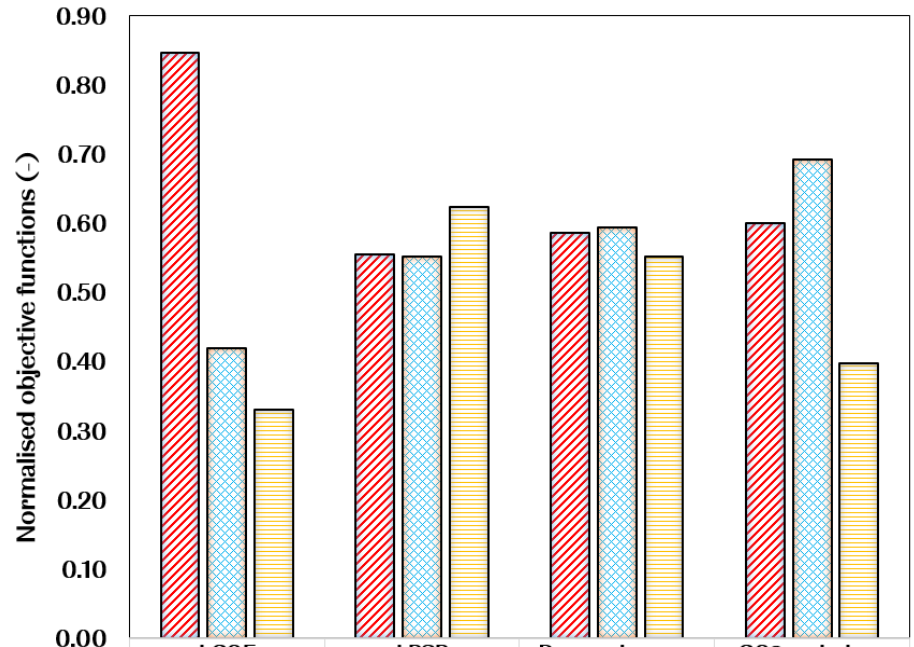

	LCOE	LPSP	Dumped power	CO2 emissions
Base case	0.85	0.55	0.59	0.60
Case 1	0.42	0.55	0.59	0.69
Case 2	0.33	0.62	0.55	0.40

Fig. 7-7. Comparison of the results obtained from the optimal system configuration of the various system cases in load following for the normalised objective functions.

(ii) Case 2: Hybrid WT-PV-BSS with ST+ORC back-up

This case proposes the deployment of combined ST+ORC to serve as the back-up to the hybrid energy system and augment its reliability. As it is evident in Table 7-6, the optimal system in case 2 employs fewer number of PV modules (935 PV panels in parallel) and BSS (26 type 2 BSS in parallel) with slightly higher capacity of ST+ORC back-up, to match the load. Consequently, the renewable generators produce 3.01% and 3.42% less power compared with the base case and case 1, respectively, and this results in a reduction in the dumped power by 18.1 MWh and 21.9 MWh in case 2 compared to the base case and case 1, respectively. As a result of the reduction in the deployment of renewable generators in the optimal configuration in this case, the system is more reliant on the ST+ORC back-up and this is evidenced by the slightly higher LPSP of 0.3962 compared to the base case (LPSP of 0.3527) and case 1 (LPSP of 0.3507) observed in Fig. 7-7.

Interestingly, the higher LPSP evident in case 2, which also implies higher deployment of the ST+ORC back-up, did not result in the increase in energy cost or emissions. This is because, the ORC utilises the recovered waste heat from the ST

cooler to produce additional power; consequently, less fuel is consumed to produce power to fulfil the net load by the back-up. Moreover, unlike in case 1, the ST+ORC back-up operates at a higher efficiency, which implies that more useful work is produced with less fuel. Therefore, an energy cost of 6.08 cents/kWh is obtained which is 60.79% lower than the base case and represents 21.14% reductions in LCOE compared with the sole ST back-up case. Similarly, the optimal configuration that deploys ST+ORC back-up reduces emissions by 33.70% (4.795×10^5 kg of CO_2) compared to the base case (7.232×10^5 kg of CO_2) and 42.52% compared to case 1 (8.342×10^5 kg of CO_2), because of the reduced consumption of wood chips and higher engine efficiency compared to the sole ST case.

Finally, from these results, it is evident that the optimal system configuration in case 2 that deploys combined ST+ORC back-up to follow the unmet load, offers reduced emissions, and cheaper energy due to the reduced fuel consumption, and a compact system size indicated by the low dumped power. However, it relies more on the ST+ORC back-up because of the high system efficiency of the combined power configuration.

7.5.1.2. Optimal system configurations in circuit charging

For the circuit charging dispatch strategy, five different system configuration cases have been formulated. The optimal system configurations obtained in these cases have been presented in Table 7-7, while Fig. 7-8 presents the comparison of the results of the optimal system performance.

(i) Case 1: Hybrid WT-PV-BSS with 4-split DG back-up

Here, four-split DG have been deployed to fulfill the load when the renewable generators are unable to match the energy demand. The split DG will also charge the BSS while supplying the deficit power. As seen in Table 7-7, the optimal system configuration obtained in this case has similar number of components as in the base case, although it deployed six additional PV panels in parallel to fulfill the energy demand compared to the base case. On the other hand, case 1 generates far less power from the DG back-up and this reduces the dumped power by 5% compared with the base case as it is evident in Fig. 7-8. Similarly, the optimal system in this case has higher renewable fraction as indicated by the considerably lower LPSP of 0.3513

compared to the LPSP of 0.3796 obtained for the base case (see, Fig. 7-8). With the deployment of split DG, the commitment of the back-up to fulfilling the positive net load in the system is minimised; hence, the observed reductions in the dumped power and LPSP. Notwithstanding the remarkable reductions in the power dispatched from the DG back-up in this HRES case, the LCOE of the optimal system did not change significantly compared to the base case, because of the higher number of PV generators deployed (see, Fig. 7-8). Finally, the deployment of 4-split DG minimises the carbon emissions from the one big DG case marginally by 1.41% as can be seen in Fig. 7-8.

(ii) Case 2: Hybrid WT-PV-BSS with one big ST back-up

This hybrid system configuration proposes the utilisation of one big ST back-up to augment the system reliability and charge the batteries. As Table 7-7 shows, the optimal configuration in case 2 has similar configuration as in the base case; however it deploys more PV generators and produces 10.32 MWh more power from the renewable generators than the latter. On the contrary, it generates slightly less power from the ST back-up and correspondingly, yields lower LPSP of 0.3611 (see, Fig. 7-8) but with higher dumped power of 351.50 MWh compared to the base case (LPSP of 0.3796 and dumped power of 343.60 MWh).

Table 7-7. Optimal system configuration in circuit charging for all the back-up cases.

Objective function	Case 1	Case 2	Case 3	Base case
LCOE (cent/kWh)	15.89	8.13	7.88	15.91
LPSP (-)	0.3513	0.3677	0.3447	0.3796
Dumped power (MWh)	326.3	351.5	333.6	343.6
CO_2 emissions (kg CO_2)	7.53×10^5	7.42×10^5	9.21×10^5	7.53×10^5
Number of PV	4×999	4×1007	4×1009	4×993
Wind Turbine type	Type 1	Type 1	Type 1	Type 1
Number of WT	5	5	5	5
Battery Type	Type 3	Type 3	Type 3	Type 3
Number of batteries	4×30	4×30	4×29	4×30
Capacity of back-up (kW)	185	182	187	180
Annual PV Power (MWh)	736.05	741.94	743.09	731.62
Annual WT power (MWh)	330.25	330.25	330.25	330.25
Annual back-up power (MWh)	360.00	383.77	360.14	386.40

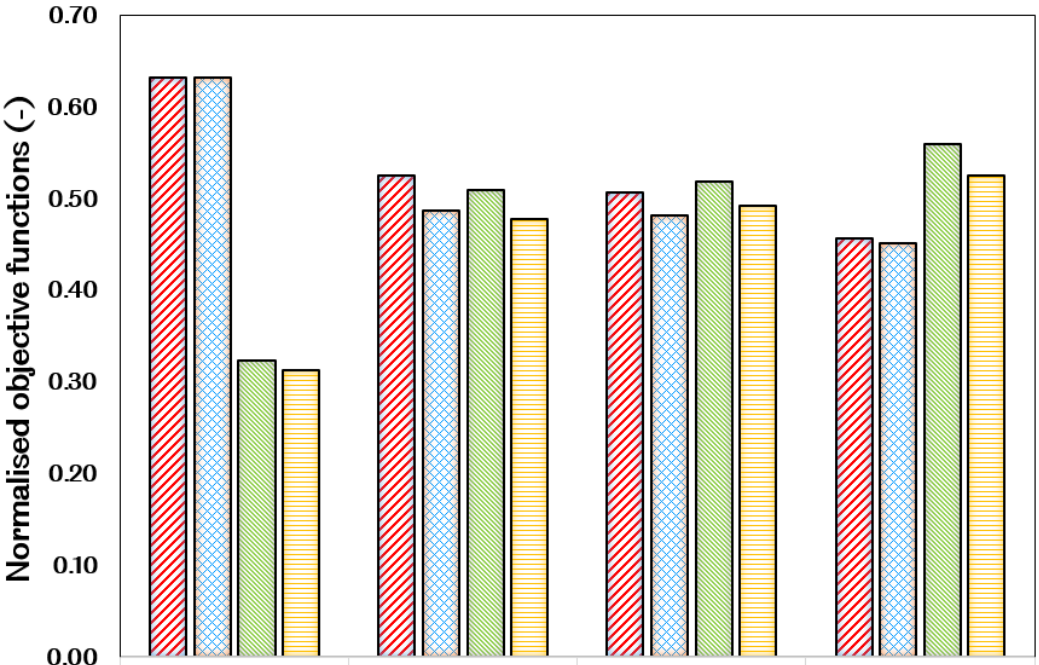

	LCOE	LPSP	Dumped power	CO2 emissions
Base case	0.63	0.53	0.51	0.46
Case 1	0.63	0.49	0.48	0.45
Case 2	0.32	0.51	0.52	0.56
Case 3	0.31	0.48	0.49	0.52

Fig. 7-8. Comparison of the results obtained from the optimal system configuration of the various HRES cases in circuit charging for the normalised objective functions.

Further, the deployment of ST back-up to augment the reliability of the hybrid system minimises the energy cost by 48.9% (LCOE of 8.13 cent/kWh) as seen in Fig. 7-8 compared with the base case (LCOE of 15.91 cent/kWh), due to the higher cost of maintenance, replacement cost of DG and fuel cost. Unfortunately, the carbon emissions increase by 22.38% with this HRES configuration compared to the base case, because of the low electrical efficiency of the heat engine ($\eta_{ST} = 0.21$). Finally, compared to case 1, this case only offers an advantage in the form of reduced energy cost but dumps more power and has lower reliability and higher emissions than the former.

(iii) Case 3: Hybrid WT-PV-BSS with 4-split ST back-up

In this HRES configuration, four-split STs are deployed to supply the positive net load while simultaneously charging the batteries. It is seen in Table 7-7 that the optimal configuration deploys more PV generators and slightly higher BSS compared to the base case and generates 11.47 MWh more power from the renewable generators.

Consequently, it is 9.19% more reliant on renewable generators as represented by the lower LPSP of 0.3447 compared to 0.3796 for the base case (see, Fig. 7-8). Fig. 7-9 compares the power dispatch from the 4-split STs to one big ST in circuit charging. The gradual deployment of the 4-small STs to fulfil the hourly net electric load is noticeable. Apparently, the commitment of the back-up to this goal is minimised by the deployment of split STs. Consequently, some remarkable savings in the power dispatched by the split ST back-ups is seen in Fig. 7-9 in contrast to deploying one big ST to fulfill the load.

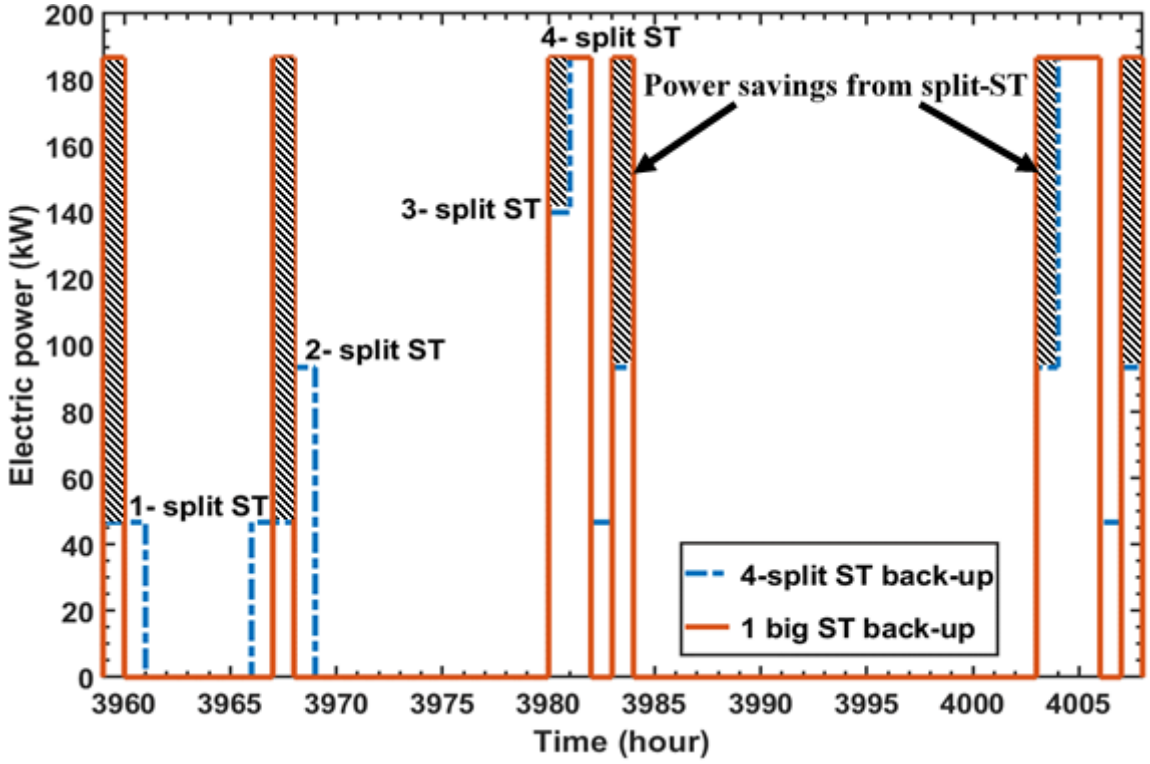

Fig. 7-9. Comparing hourly power dispatch from one big ST and 4-split ST.

Therefore, the notable power reductions in the deployment of 4-split ST back-ups compared to one big ST (or DG) seen in Fig. 7-9 is another evidence of the high system reliability of this HRES case. Hence, the dumped power is lower (10 MWh less) in this case compared to the base case. In addition, the reduction in the commitment of the ST back-up to fulfilling the load with the utilisation of 4-split STs, the lower maintenance cost and fuel cost culminate in 50.5% decline in the LCOE in this case (LCOE of 7.88 cent/kWh) compared to the base case (LCOE of 15.91 cent/kWh). Nonetheless, the optimal configuration in case 3 emits 14.5% more CO_2 than in the base case (see, Fig. 7-8), due to the low electrical efficiency of the ST

although not as much as was emitted in case 2, because of the reduction in the wood chips consumption with the utilisation of split STs. Finally, case 3 offers lower LCOE and LPSP but higher emissions and dumped power compared to case 1, while it performs better than the one big ST case from all indications.

7.5.1.3. Impact of deploying ST+ORC on optimal system in circuit charging

Two additional hybrid system configurations have been proposed to evaluate the optimal system performance when ST+ORC is deployed in circuit charging dispatch mode. The optimal configurations from these cases are presented in Table 7-8, while the performance indicators are presented in Fig. 7-10 and have been compared to the previous cases.

(i) Case 4: Hybrid WT-PV-BSS with ST+ORC back-up

This configuration utilises ST+ORC as the back-up to the HRES while operating at the rated capacity of the topping cycle and also charging the BSS with the excess power generated. It is seen in Table 7-8 that the optimal system configuration obtained in this case utilises fewer PV generators but generates more power from the combined power back-up compared to cases 2 and 3. Consequently, the HRES in this case relies more on the back-up to fulfil the load demand and that is evidenced by the higher LPSP of 0.3801 compared to 0.3677 and 0.3447 for cases 2 and 3, respectively (see, Fig. 7-10).

In addition, the dumped power in this optimal configuration is less than in case 2 but higher than in case 3 that deploys 4-split STs. In spite of some of the observed unfavourable performance data in this HRES case, the utilisation of combined ST+ORC back-up here reduces the LCOE and CO_2 emissions by 22.26% and 44.25% and 19.79% and 40.53%, respectively compared with cases 2 and 3, respectively. This is due to the higher efficiency of the ST+ORC back-up and the reduction in the fuel consumption compared to ST only case. In contrast to the base case (one big DG back-up), the optimal system in this case offers 60.27% and 31.7% (slightly higher for case 3) lower LCOE and CO_2 emissions, respectively.

Table 7-8. Optimal system configuration in circuit charging for all the back-up cases.

Objective function	Case 2	Case 3	Case 4	Case 5
LCOE (cent/kWh)	8.13	7.88	6.32	6.14
LPSP (-)	0.3677	0.3747	0.3801	0.3929
Dumped power (MWh)	351.5	333.6	337.3	320.0
CO_2 emissions (kg CO_2)	9.21×10^5	8.64×10^5	5.14×10^5	5.04×10^5
Number of PV	4×1007	4×1009	4×995	4×965
Wind Turbine type	Type 1	Type 1	Type 1	Type 1
Number of WT	5	5	5	5
Battery Type	Type 3	Type 3	Type 3	Type 2
Number of batteries	4×30	4×29	4×30	4×29
Capacity of back-up (kW)	182	187	180	190
Annual PV power (MWh)	741.94	743.09	733.10	711.00
Annual WT power (MWh)	330.25	330.25	330.25	330.25
Annual back-up power (MWh)	383.77	360.14	387.50	361.52

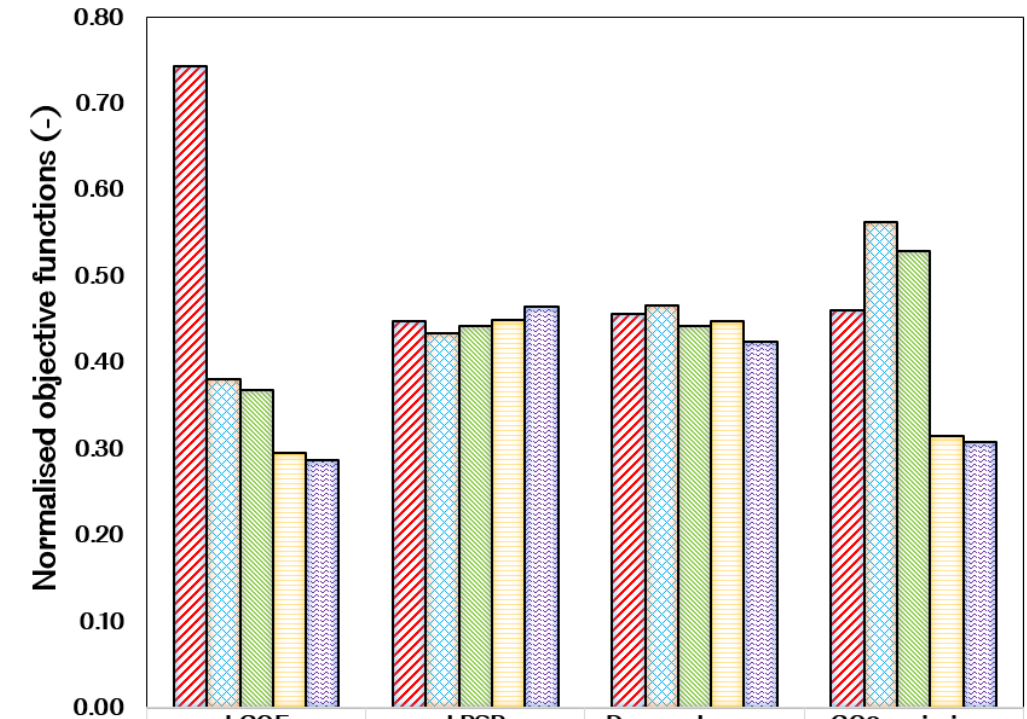

	LCOE	LPSP	Dumped power	CO2 emissions
Base case	0.74	0.45	0.46	0.46
Case 2	0.38	0.43	0.47	0.56
Case 3	0.37	0.44	0.44	0.53
Case 4	0.30	0.45	0.45	0.31
Case 5	0.29	0.46	0.42	0.31

Fig. 7-10. Comparison of the results obtained from the optimal system configuration using biomass fuelled back-up in circuit charging to the base case for the normalised objective functions.

(ii) Case 5: Hybrid WT-PV-BSS with 4-split ST+ORC back-up

Case 5 deploys 4 small capacity STs operating at their design points as the back-up to the HRES with ORC bottoming cycle and will charge the batteries if generating excess power. As Table 7-8 reveals, the optimal configuration in this case is characterised by fewer PV generators (965 PV panels in parallel), reduced battery capacity (29 type 2 batteries in parallel) and lower or comparable back-up power compared to the other cases. Consequently, it has high LPSP (LPSP of 0.3929), i.e., increased reliance on biomass powered back-up generators but reduced dumped power compared to the other cases. In terms of energy cost and emissions, this HRES case reduces energy cost by 22.08%, 24.47% and 61.4% and emits less carbon (5.0429×10^5 kg of CO_2), which is evidenced by the reductions in emission of 41.65%, 45.25% and 33% than that of case 3, case 2 and the base case, respectively, but marginally lower than case 4 (see, Fig. 7-8). This can be attributed to the reduction in the commitment of the back-up to fulfilling the load demand, with the deployment of 4-split STs. In addition, the utilisation of combined power configuration that minimises the fuel consumption of the ST+ORC back-up, by recovering the waste heat from the topping cycle, also contributed to the observed trend.

It is clear from the presented results that the deployment of 4-split STs improves the system performance compared to the base case [83]. Further improvements in system performance indicators are notable with the deployment of ST+ORC back-up and split STs in CC. Nevertheless, the deployment of ST+ORC back-up in LF offers the best performance indicators. This HRES configuration is, therefore, adopted for the simulation and sensitivity analysis undertaken in the subsequent sections.

7.5.2. Simulated results of optimal HRES configuration

This section presents the results of the dynamic simulation of the best optimal configuration that gave the least LCOE, LPSP, dumped power, and CO_2 emissions for the test location. As has been mentioned in Section 7.5, case 2 that deploys combined ST+ORC back-up to augment the reliability of the HRES in the LF mode offers the best performance indicators. Consequently, the hourly electric generation from the system units to fulfil the electric load of the customers in the

two main seasonal conditions experienced annually in the test location; the dry and wet seasons [221] has been evaluated.

Fig. 7-11 shows the hourly power generation from the renewable generators in the test location for the best optimal system configuration. As it is evident in Fig. 7-11 (a), the power generation from the PV generator is periodic and varies between 450 kW at the beginning of the year (dry season) to 200 kW at the mid-year period (wet season). On the contrary, the power generation from the WT generator, Fig. 7-11 (b) is stochastic and a few high spikes of nearly 600 kW in the mid-year period (wet season) can be seen. It is also noticeable in Fig. 7-11 (c) that the combined generation from the renewable generators increases remarkably with the hybridisation of the WT and PV and minimises the power dips in the wet season from the PV generator as well as the high power spikes from the WT generator. This observed trend highlights the complementarity of wind and PV and supports their hybridisation.

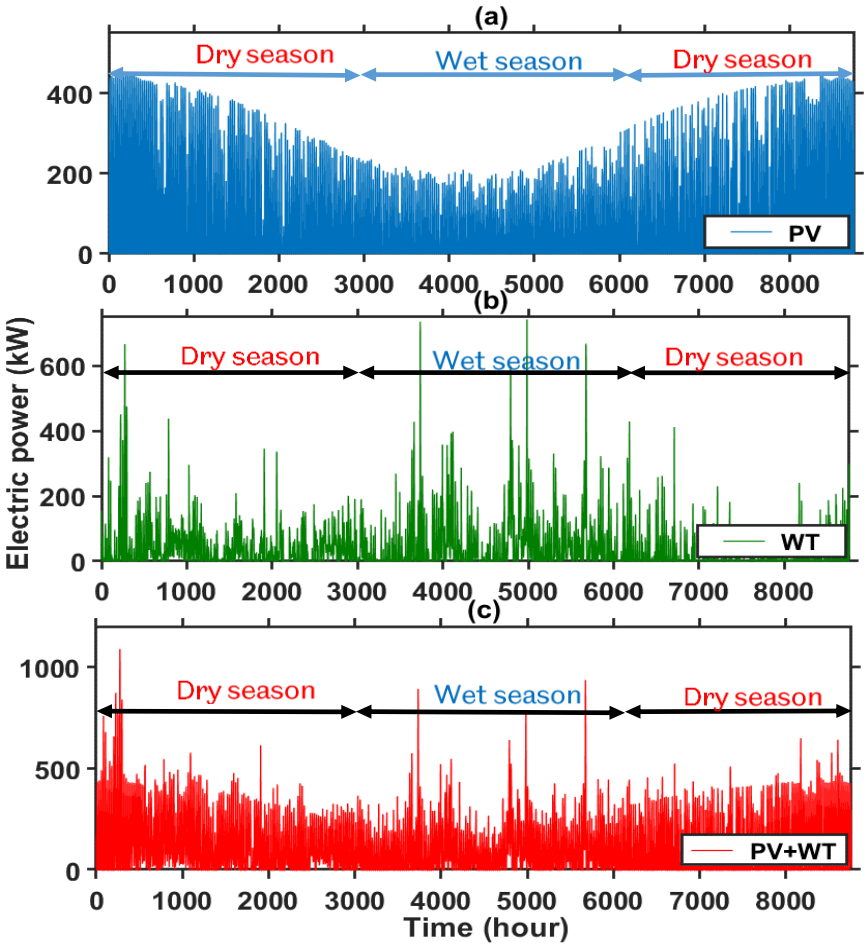

Fig. 7-11. Hourly generated power from the renewable generators in the optimal energy system configuration.

Fig. 7-12 presents the hourly electric load and power dispatch from the battery and ST+ORC for one whole year of operation of the optimal HRES. Also, Fig. 7-12 (b) shows the hourly dispatch of the battery storage to augment the system reliability. The BSS appears to have discharged more power in the dry season than in the wet season, since the renewable generators generated sufficient excess energy to charge the batteries (see, Fig. 7-11 (c)). On the other hand, it is evident from Fig. 7-12 (c) that the ST+ORC back-up is more active when the battery is less utilised. Note that the programmable back-up is expected to follow the load in this optimal HRES configuration, only when the battery is fully discharged, and the renewable generators are not generating enough power.

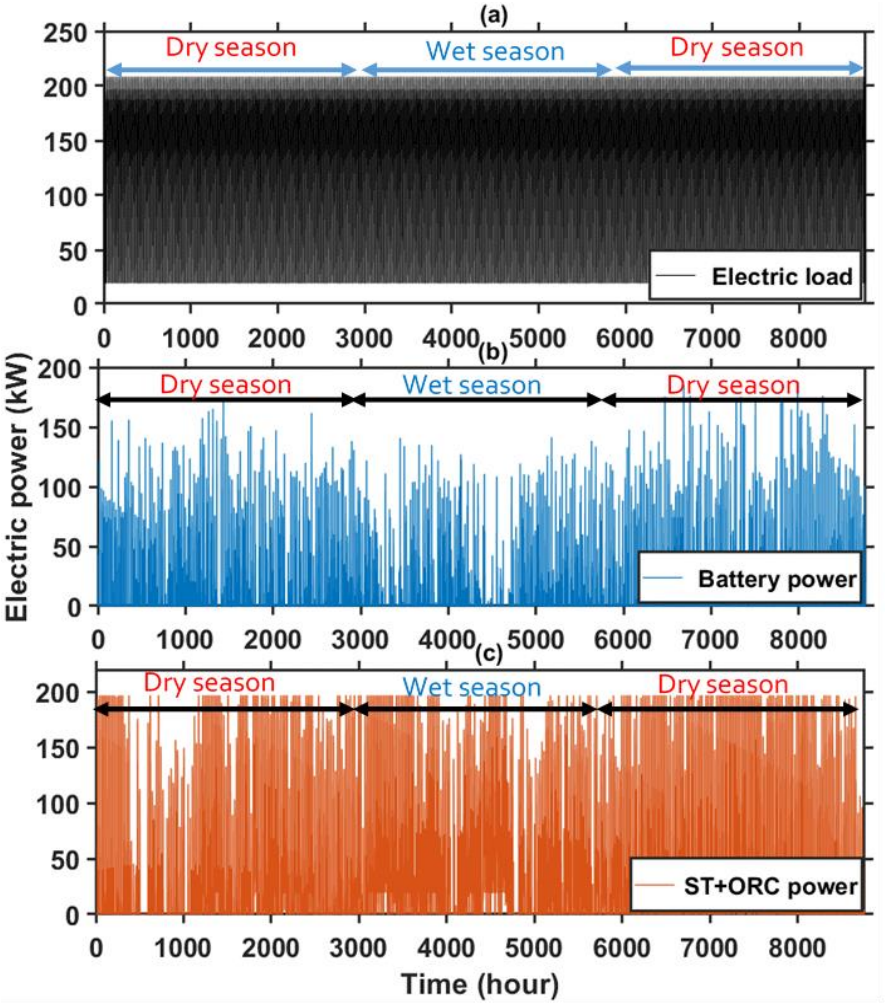

Fig. 7-12. Hourly electric load and power dispatch from the programmable generators.

Further results of the dynamic performance of the best optimum HRES configuration, for two consecutive days in the (a) dry season and (b) wet season

have been presented to highlight the impact of the seasonal variation on the optimal system performance. In Fig. 7-13, the dynamic simulation of the optimal system configuration in the test location has been presented for two-consecutive days in the dry season (Fig. 7-13 (a)) and wet season (Fig. 7-13 (b)). Here, the energy stored in the BSS is assumed to be negative, because it is extracted from the excess power produced by the green generators.

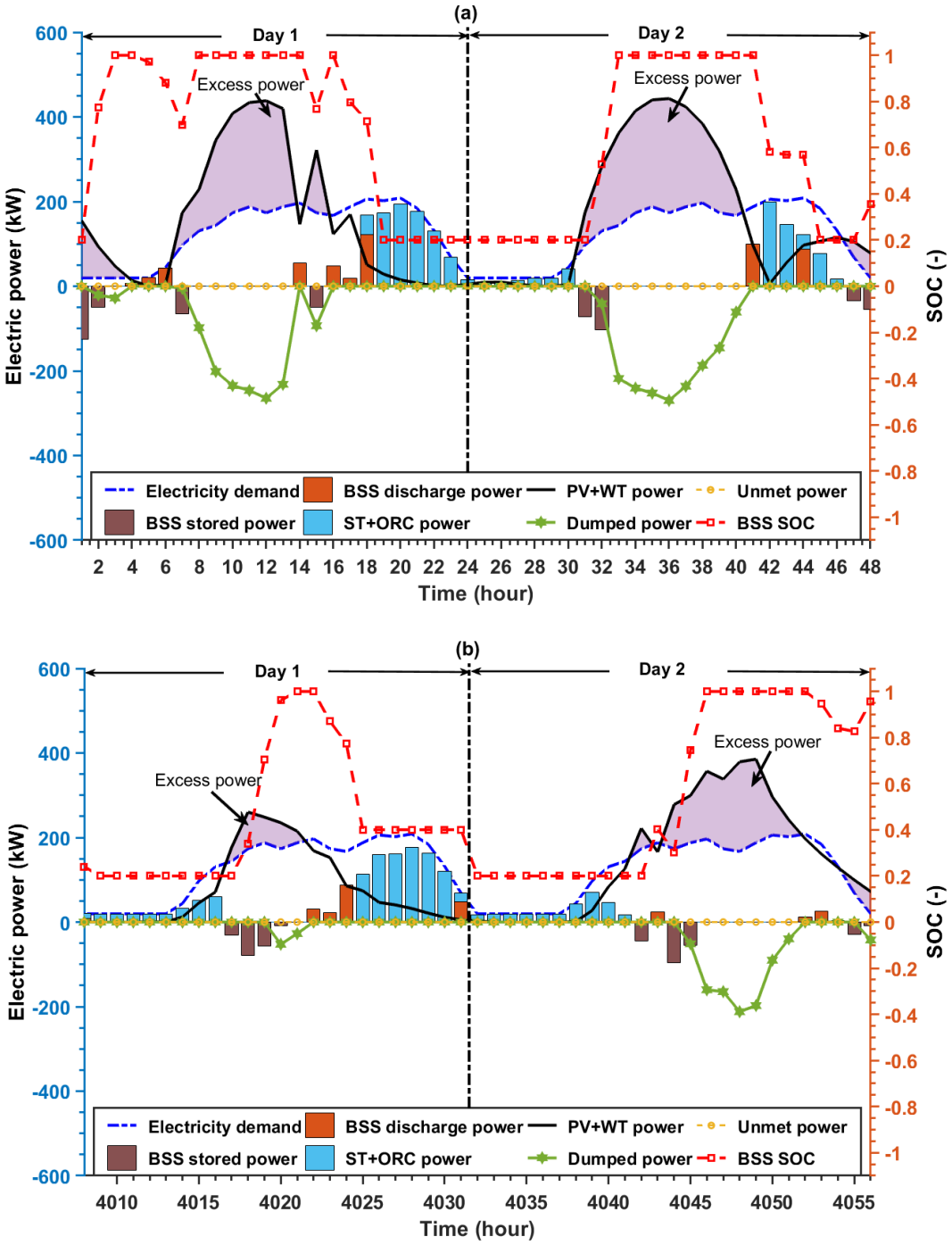

Fig. 7-13. Dynamic simulation of the optimal system configuration for two consecutive days in the design location in (a) dry season and (b) wet season.

As it is evident in Fig. 7-13 (a), due to the clear weather which characterises the dry season, more power is generated by the solar PV and WT. Hence, the high excess power in the dry season compared to the wet season. Correspondingly, the battery is deployed more in the dry season to supply the unmet load as evidenced by the several cycles of charging and discharging of the battery in Fig. 7-14. On the other hand, the ST+ORC back-up follows the load only a few times in the dry season, which helps to minimise its contribution to fulfilling the load. Unlike in the dry season, the wet season is marked with high deployment of the ST+ORC back-up to augment the reliability of the HRES, due to the low power generation from the green generators. Consequently, there is insufficient excess power to charge the batteries, which is responsible for the few cycles of charging and discharging of the battery noticeable in Fig. 7-14, in the wet season. So, the battery remains in its minimum SOC most of the time in this season, and this regrettably may affect the battery life [207].

Therefore, because batteries are utilised more in the dry season compared with the ST+ORC back-up, the energy cost is lower in the dry season than in the wet season. Nonetheless, high dumped power is evident in the dry season as can be seen in Fig. 7-15 compared to the wet season, because of the higher power generation from the non-programmable generators. Further, there may be challenges with the availability of the biomass fuel in the wet season, considering that the system is designed for use in a remote location, where the common practice is to deploy the traditional open solar drying to regulate the moisture content of the woodchips. To solve this problem, in-situ drying of the woodchips fuel has been proposed in the system model undertaken in Chapter 6, whereby the waste flue gas will be deployed to dry the wood chips fuel in the wet season. Thus, the quality of the wood chips fuel is regulated, and its availability is guaranteed all year round.

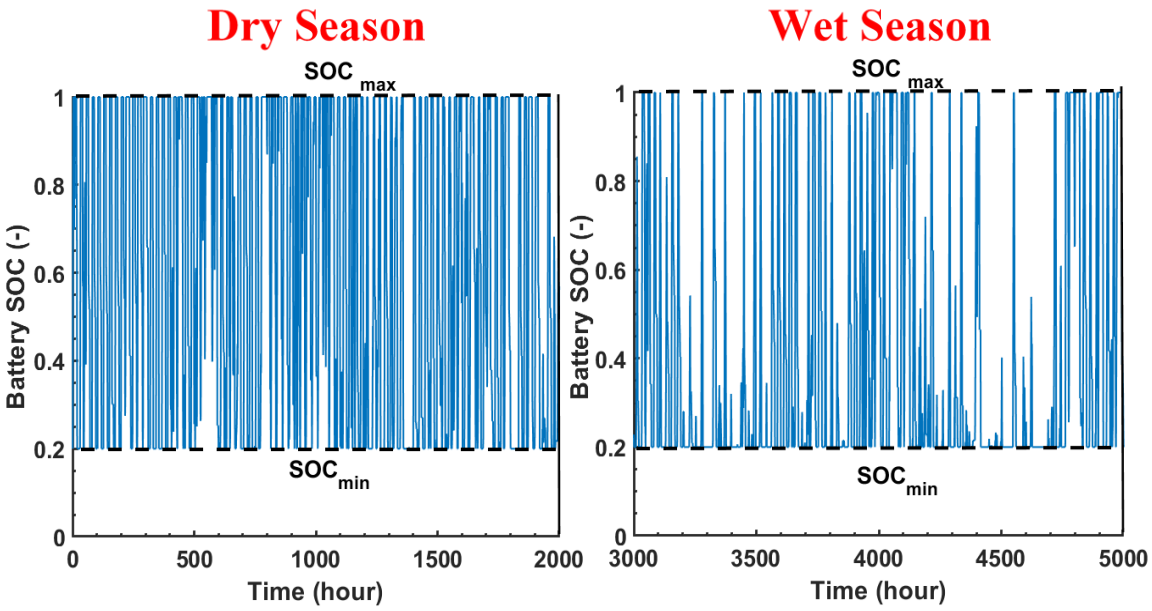

Fig. 7-14. Battery state of charge in the dry and wet seasons when deployed to argument system reliability in the test location.

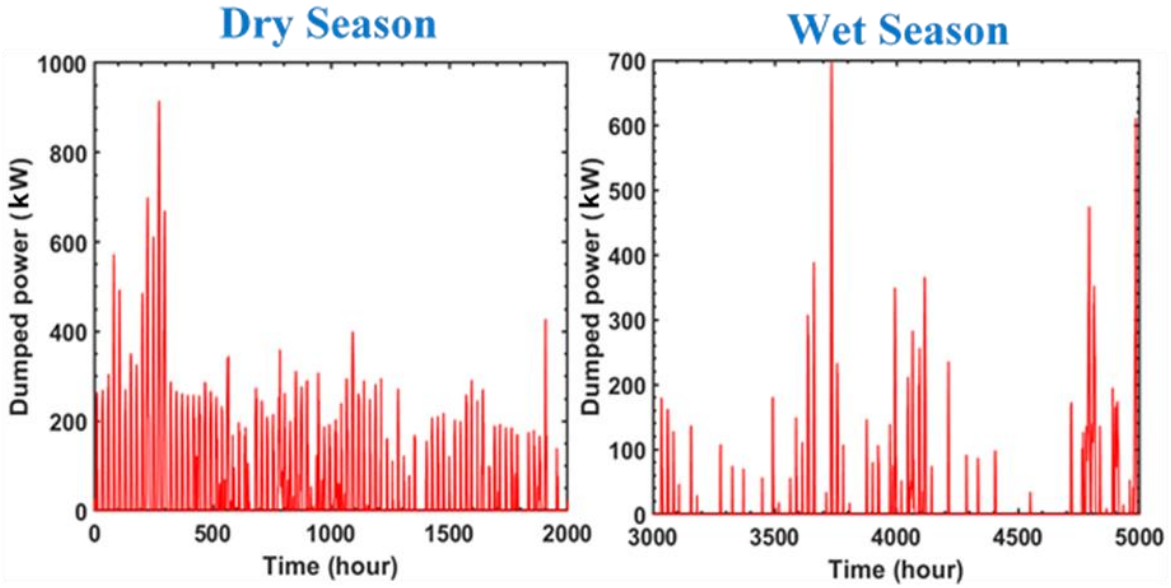

Fig. 7-15. Dumped power from the energy system when deployed to meet the electric load in the test load in the dry and wet seasons.

7.5.3. Results of sensitivity analysis

To investigate the response of the optimal HRES system to the variations in the market price and size of key system components, sensitivity analysis was undertaken. In the first instance, the unit price of the PV panel, wind turbine, wood chips fuel and battery were varied between -50% to +50% with a step increase of

10%, while keeping the others constant. Then, the GA optimiser and TOPSIS are deployed for each step size, to find the optimum system configuration as well as obtain the corresponding LPSP, LCOE, dumped power and CO_2 emissions. On the other hand, the quantity (size) of one of the key system components (PV panel, WT, batteries and ST+ORC) in the optimal system configuration obtained for the proposed dispatch strategies were altered by -50% to +50% with a step increase of 5%, while the others are kept constant. Then, the optimum configuration is simulated and consequently, the LPSP, LCOE, dumped power and CO_2 emissions for each step increase is obtained.

Fig. 7-16 presents the results of the component price sensitivity analysis carried out on the optimal system configuration on a radar chart. As Fig. 7-16 (a) demonstrates, the increase in the cost of the PV generators results in a decrease in the dumped power by as high as 28% for 50% increase in price, because fewer components are deployed. Consequently, the system emits more carbon pollutants (see, Fig. 7-16 (b)) and also becomes less reliable as evidenced by the high LPSP (more than 50% change) in Fig. 7-16 (c). This also confirms the indicated positive relationship between reliability and eco-friendliness in the Pareto front in Fig. 7-6. Meanwhile, the LCOE of the system increases marginally as the PV price increases and about 8.33% rise in LCOE is observed for a 50% hike in the component's price in Fig. 7-16 (d). An opposite effect is noticeable with the decrease in the cost of the component although it is less evident, for all other objective functions with the exception of the dumped power.

Contrarily, an increase in the price of the WT produces a dramatic effect on the objective functions. The CO_2 emissions and LPSP increase slightly before decreasing marginally (about 13% decline in the LPSP for 50% price change) as noticeable Fig. 7-16 (b) and Fig. 7-16 (c), respectively. This dramatic trend is driven by the fact that with further increase in the cost of the WT, the system opts for cheaper PV generators to replace the former resulting in the observed decline. Consequently, the dumped power initially decreases with the increase in the price of the green generator but increases substantially as more PV generators are deployed with the increase in price and contributed about 25% increase with 50% rise in component's

price as seen in Fig. 7-16 (a). On the other hand, as the price of the WT increases, the LCOE increases substantially by the same magnitude as in the PV (see, Fig. 7-16 (d)). However, the decrease in the price of this non-programmable generator produces a similar and comparable effect as the decrease in the price of the PV generator.

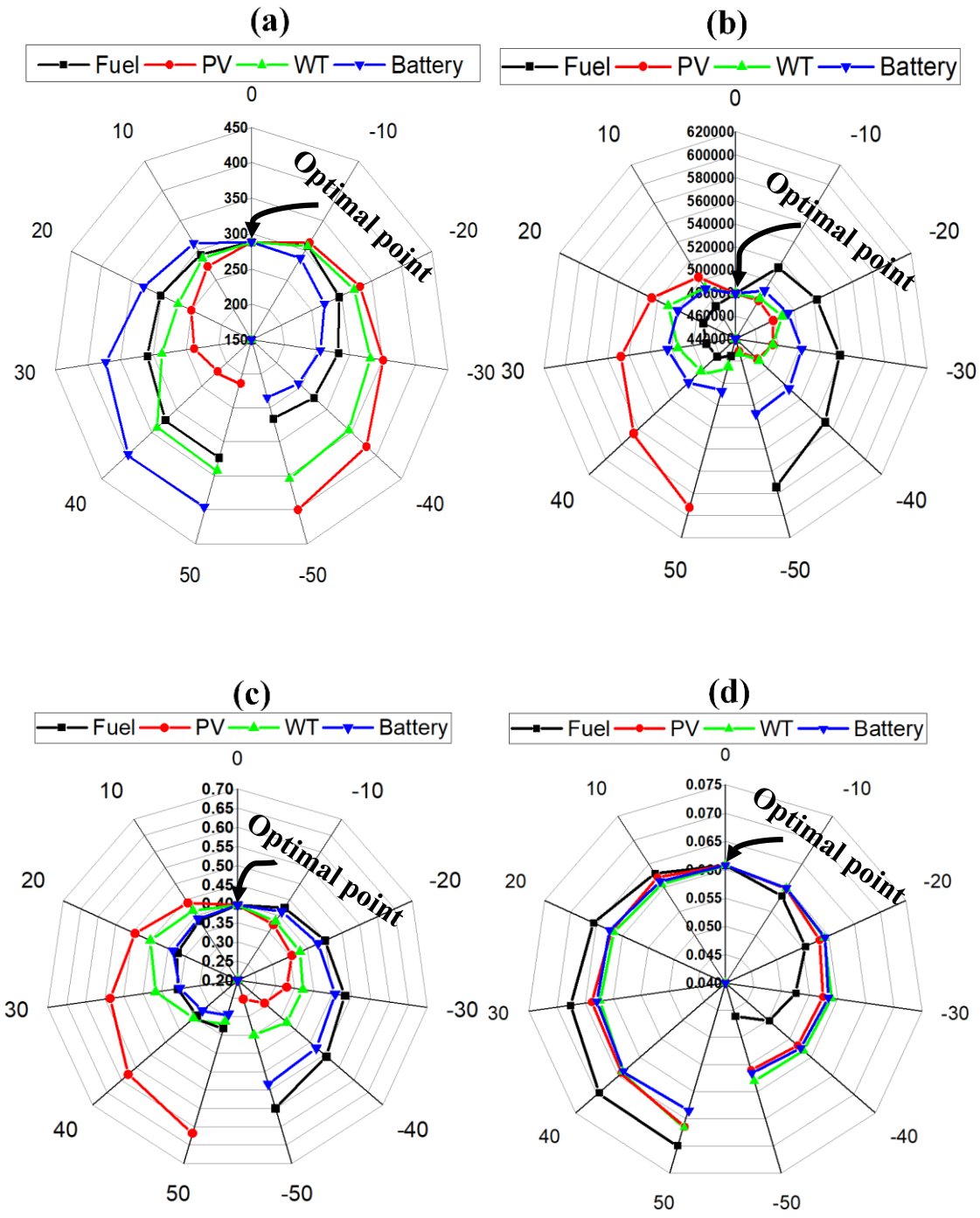

Fig. 7-16. Impact of changes in component and fuel price on the (a) dumped power (MWh), (b) carbon emissions (kg CO_2), (c) LPSP (-) and (d) LCOE (cent/kWh) of the best optimal configuration.

A decrease in the price of the WT decreases all other objective functions except the dumped power that notably increases because more clean generators are deployed.

The increase in the price of the batteries significantly increases the dumped power as expected by about 30% for a 50% change in component's price (see, Fig. 7-16 (a)), due to the corresponding reduction in the storage capacity. Hence, more green generators are included in the optimal system to augment the apparent shortfall in the storage capacity of the batteries. Correspondingly, the carbon emissions and LPSP that are complementary (see, Fig. 7-6) evidently reduce albeit marginally, with the increase in price of the batteries (see, Fig. 7-16 (b) and (c)). However, as can be observed, the LCOE increases significantly with the increase in the price of this component (Fig. 7-16 (d)). The opposite trend is evident as the price of the batteries fall and the most significant change can be observed in the LPSP.

Similarly, as the price of the wood chips fuel increases, the dumped power increases by about 11% for 50% change in price (Fig. 7-16 (a)), while the energy cost rose by almost 15% for a similar price change (Fig. 7-16 (d)). This is expected because more green generators are deployed to reduce the impact of the high cost of the fuel. Hence, the CO_2 emissions and LPSP decrease with the increase in the cost of the fuel as it is evident in Fig. 7-16 (b) and (c). The opposite effect is noticeable with the reduction in the price of the wood chips fuel. Overall, the change in the price of the PV has the most impact on the optimal system's LPSP and CO_2 emissions, while the change in the price of the battery and wood chips fuel have profound effect on the dumped power and LCOE, respectively.

Fig. 7-17 and Fig. 7-18 represent the impact of the changes in the number of PV, WT, BSS and capacity of ST+ORC back-up on the dumped power, CO_2 emissions, LPSP and LCOE of the best optimal HRES configuration in the load following (Case 2) and circuit charging (case 5) dispatch modes, respectively. It is evident in Fig. 7-17 (a) and Fig. 7-18 (a) that, increasing the size of the renewable generators leads to an increase in the dumped power, while the dumped power decreases with a decrease in the number of these components. The renewable generators are non-programmable and periodic (or stochastic) in power generation; hence, their hourly power generation anti-correlates with the load demand [42]. Correspondingly, the carbon

emissions (Fig. 7-17 (b) and Fig. 7-18 (b)) and LPSP (Fig. 7-17 (c) and Fig. 7-18 (c)) decrease while the LCOE increases (Fig. 7-17 (d) and Fig. 7-18 (d)) with the increase in the number of PV and WT. The opposite trend is indicated with the decrease in the number of these renewable generators.

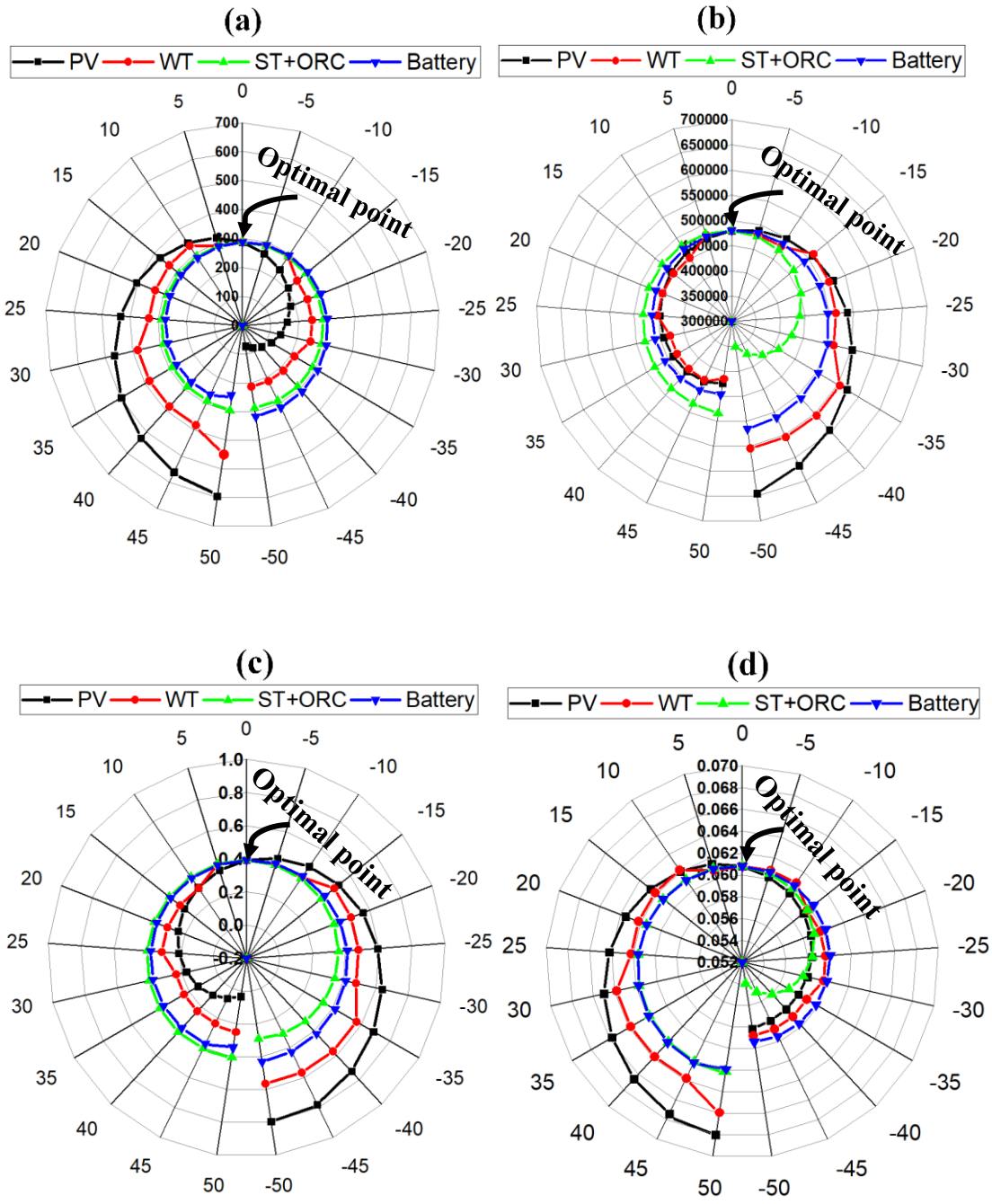

Fig. 7-17. Impact of changes in component size on the (a) dumped power (MWh), (b) carbon emissions (kg CO_2), (c) LPSP (-), and (d) LCOE (cent/kWh) of the best optimal configuration in load following.

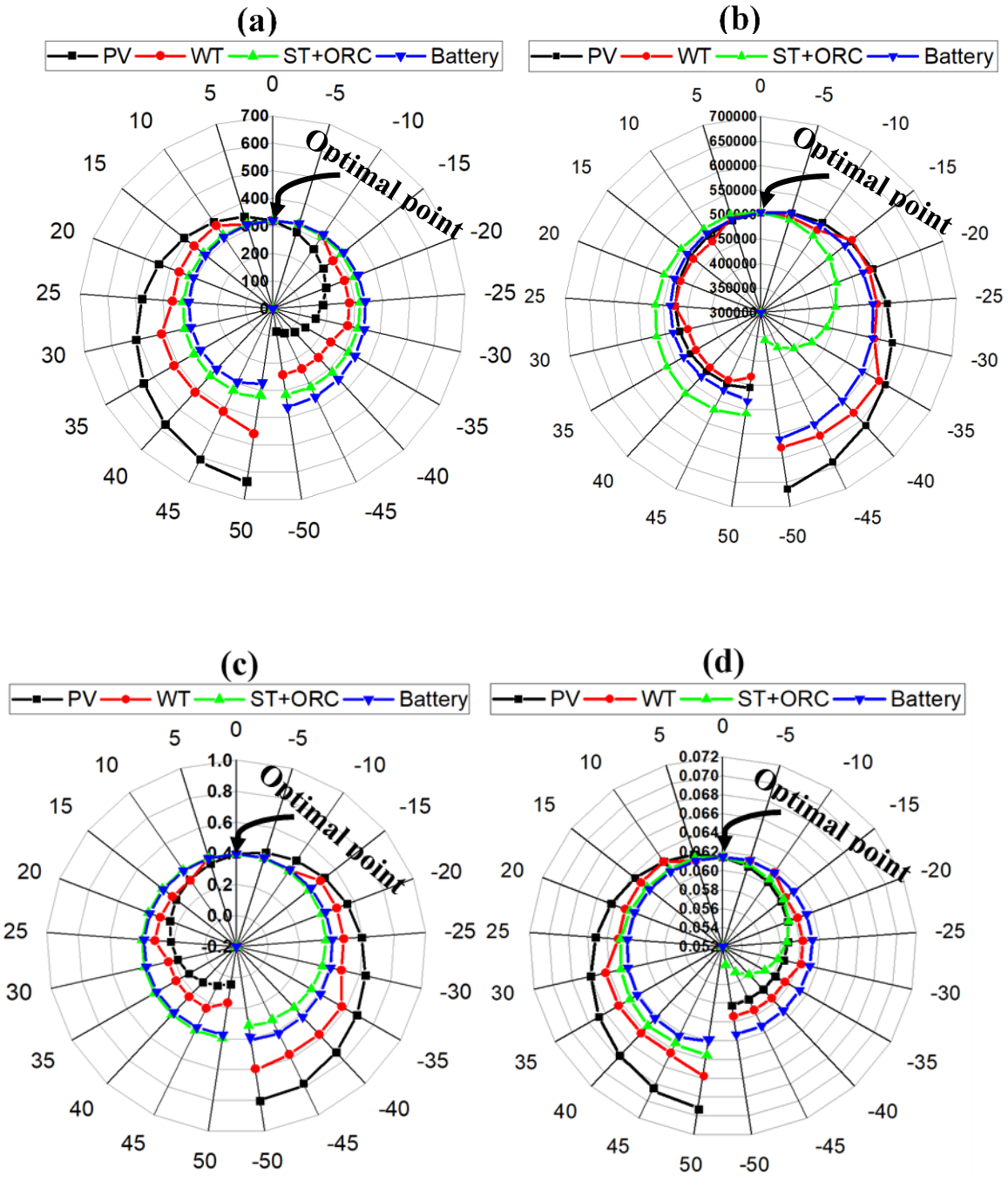

Fig. 7-18. Impact of changes in component size on the (a) dumped power (MWh), (b) carbon emissions (kg CO_2), (c) LPSP (-), and (d) LCOE (cent/kWh) of the best optimal configuration in circuit charging.

On the contrary, as the number of batteries in the optimum system configuration increases, the dumped power reduces as evident in Fig. 7-17 (a) and Fig. 7-18 (a), because more excess power is stored in the BSS, while the opposite effect is observed with a reduction in the number of this component in the optimum

configuration. As a consequence, the carbon emissions reduces as seen in Fig. 7-17 (b) and Fig. 7-18 (b), while the LPSP changes only marginally (Fig. 7-17 (c) and Fig. 7-18 (c)) whereas the LCOE increases substantially with the increase in the number of the BSS (Fig. 7-17 (d) and Fig. 7-18 (d)). The opposite trend is indicated with the reduction in the number of the BSS.

Meanwhile, the variation in the capacity of the ST+ORC back-up did not impact the dumped power in the load following mode (Fig. 7-17 (a)) as could be imagined, because the back-up merely follows the load but leads to a slight change in the dumped power in the circuit charging dispatch mode (Fig. 7-18 (a)). However, the system emits more CO_2 and becomes less reliable as evidenced by the slight increase in the LPSP with the increase in the capacity of the ST+ORC back-up (see, Fig. 7-17 and Fig. 7-18: b and c). Similarly, the LCOE increases remarkably with the increase in the capacity of the engine. The LCOE and CO_2 emissions decrease significantly as the capacity of the back-up decreases, while a marginal increase in the LPSP is observed. The dumped power did not change except for the slight change seen in CC mode (Fig. 7-18 (a)).

Therefore, the variation in the number of PV generators in the optimum system configuration altered the dumped power, LPSP and LCOE [225] more than any other component, while higher variation in dumped power is notable in the circuit charging dispatch mode. The most significant changes in the carbon emissions is observed with the variation in the number of PV and capacity of ST+ORC back-up in the optimum system configuration, for both dispatch modes. While the change in the number of WT generators and ST+ORC back-up capacity has a comparable impact on the system's energy cost. The variation in the number of BSS in the optimal system configuration affects the LCOE only marginally. Finally, the change in the number of PV generators that generates about 50% of the total power supplied to the electric load by the HRES, expectedly has the most impact on the system's performance in all the examined dispatch modes and this further highlights the significance of the PV generator in the optimal HRES configuration for this test location.

7.6. Chapter summary

The modelling, optimisation and simulation of different hybrid renewable energy system (HRES) configurations hybridising wind, solar and battery storage systems have been undertaken. The impact of the deployment of wood chips fuel powered combined ST+ORC and split ST back-ups to augment the reliability of a hybrid WT-PV-BSS when the system is in the load following (LF) and circuit charging (CC) dispatch modes on the performance of the HRES has been investigated. The optimal number and types of the system components that simultaneously minimised the levelised cost of energy (LCOE), loss of power supply probability (LPSP) and dumped power in each of the proposed HRES configurations have been found by the deployment of multi-objective genetic algorithm and the TOPSIS decision making tool. Thereafter, the optimal HRES performance was compared to the base case; DG back-up system in both dispatch modes and other test cases formulated. Further, the hourly performance of the best system configuration was simulated for the two seasons that characterise the test location. In the final section of this study, the impact of the changes in the market price and size of the system components and fuel on the performance of the optimum system configuration were investigated by means of a sensitivity analysis.

The observed results show the proposed back-ups that deployed 4-split STs and ST+ORC performed better than the base case from economic, reliability and environmental perspectives. Additional results indicate seasonal changes in the test location significantly affect the LCOE, LPSP, dumped power, and carbon emissions of the optimal system. While it is found that the optimal system responds substantially to the changes in the price and size of the components, and that the change in the price and size of the PV generator has the most impact on the system performance. Therefore, bi-level-optimisation of the system will be conducted in the next chapter, to simultaneously optimise the configuration and the control strategy as well as obtain the optimal number of split back-ups. In addition, the impact of the dispatch strategies on the generation of other energy vectors will be investigated extensively in the next chapter.

Chapter 8 Bi-level Optimisation and Dynamic Simulation of an Integrated Energy System.

This chapter presents the bi-level optimisation involving the component sizing and energy management of the HRES integrated multi-carrier energy system proposed in this thesis and described in Chapter 3. Section 8.1 describes the formulation of the energy management strategies proposed in this study. Section 8.2 contains the mathematical expressions of the objective functions and constraints considered in the sizing optimisation. Section 8.3 discusses the solution approach deployed for the bi-level sizing optimisation and dynamic simulation of the energy system. Section 8.4 analyses the results obtained from the optimisation and discusses the results of the dynamic simulation of the system performance. Finally, the key findings in this work are highlighted in the concluding section. The results obtained from the work performed here have been published in a peer reviewed journal.

8.1. Formulation of the proposed control strategies

The energy management of an integrated multi-carrier energy system is a critical aspect of the design and operation of the system [79]. That is to say, the optimal system configuration is influenced by the energy management strategy (EMS) deployed to coordinate the flow of the energy in the system. Therefore, it is important to consider the EMS at the point of the design of the energy system and study its impact on the dynamic operation of the system. This work is focused on undertaking a bi-level sizing optimisation of the HRES subsystem of the proposed HRES integrated MDES configuration. A memetic algorithm is employed in the outer-loop to obtain the optimal size of the components of the HRES, while the optimisation of the energy management is undertaken in the inner-loop, by optimising the control parameters of the system. Thereafter, the hourly simulation of the performance of the integrated system is performed with the optimal system configuration found, to draw insight into the impact of the management strategies on the energy generation, storage, and dispatch from the components of the system.

In Section 3.1.3, the working diagram of the proposed integrated DES has been presented, while in Chapter 4 - Chapter 7, the mathematical models of the

components and subsystems of the components of the energy system were formulated and validated. The proposed integrated system is a hybrid of the MDES studied in Chapter 6 and the HRES studied in Chapter 7 that deploys the combined ST and ORC to drive the former while it serves as the back-up in the latter. This section focuses on the formulation of the control strategies proposed for the management of the flow of energy in the MDES.

Four main control strategies based on the modification of the traditional rule-based control strategies have been formulated herein. They are, the load following (LF) without battery, load following with battery, circuit charging (CC) without battery and circuit charging with battery. The net load, $P_{\mathrm{net}}(\mathrm{t}) = \left(P_{\mathrm{L}}(\mathrm{t}) - P_{\mathrm{PV}}(\mathrm{t}) - P_{\mathrm{WT}}(\mathrm{t})\right)$ i.e., the difference between the electric load and the power generated from the PV and WT systems, the state of charge of the battery (SOC) and the split of the ST are the parameters that control the ON/OFF operation of the ST and the discharging and charging of the batteries. To achieve the efficient management of the system, the central controller is expected to check the SOC of the battery and P_{net} at each time step (every 1 hour). The other conditions required for the efficient control of the energy system are:

a) Uninterrupted energy flow from the different generators, PV, WT and buffer storage at every time step must be maintained.
b) All power generators may operate simultaneously when necessary.
c) Excess power generated from the generating units should be dumped via resistive loads when the battery is fully charged to protect the load from over-voltage.
d) Battery charging and discharging limits must be maintained to prevent excessive charging and total discharge of the battery.
e) When the ST is powered ON, the low grade flue gas should be deployed to produce some cooling and heating.
f) To avoid wet expansion in the turbine of the ORC due to low grade waste heat from the ST, the ORC should only be operated when the ST is operating above a minimum threshold.

In the next subsections, the rule-based formulation and operational conditions for the storage, generation and dispatch of energy for each of the proposed control strategies are presented.

8.1.1. Load following strategy without battery

In this control strategy, the ST+ORC is powered ON to follow the load whenever there is a positive net load in the system. This strategy does not include batteries; hence, the back-up ST will supply all of the deficit power. The operating conditions for the control of the powering ON of the ST+ORC are described in the following subsections, while the algorithm is shown in Fig. 8-1. u_j *and* u_k are state variables that define the number of splits of the Stirling engine and the control strategy, respectively.

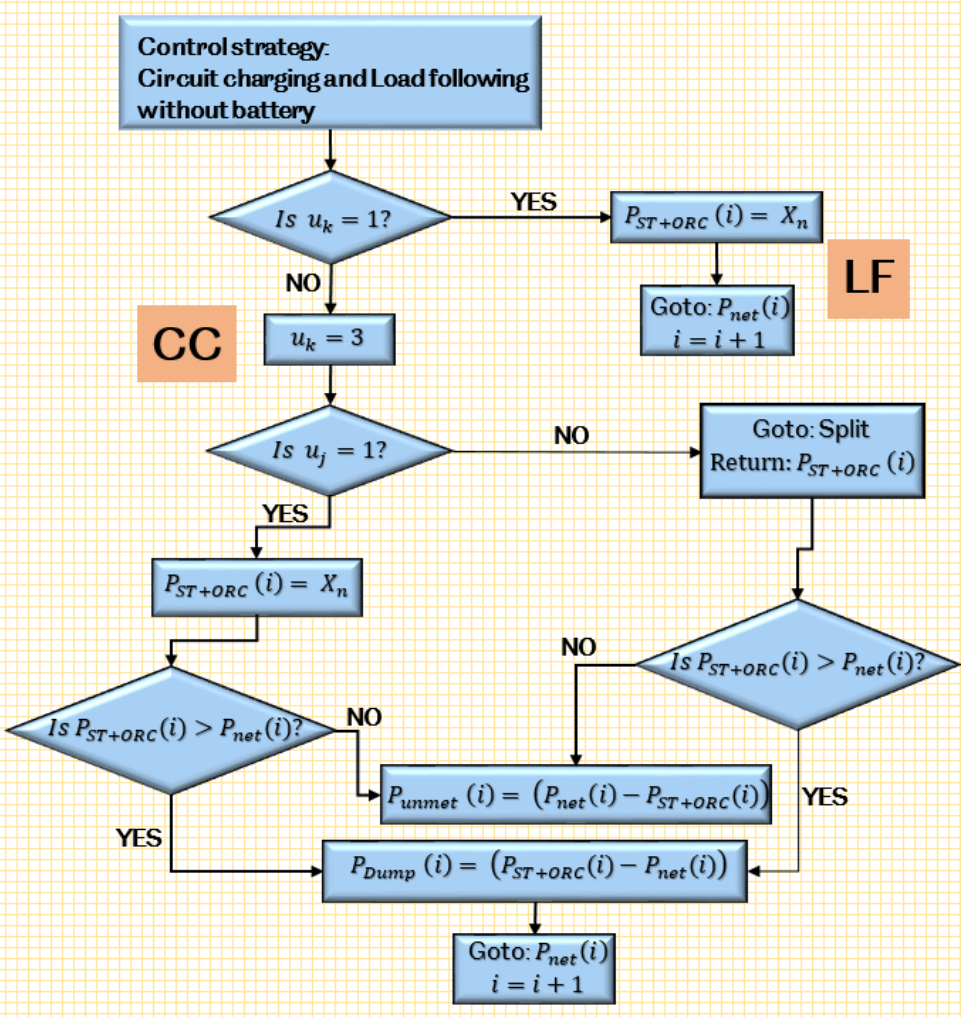

Fig. 8-1. Algorithm for the load following and circuit charging control strategy without a battery.

- $Condition\ 1$: $[P_{\mathrm{L}}(t) - P_{\mathrm{PV}}(t) - P_{\mathrm{WT}}(t) > 0]$

When the total energy generation from the renewable resources (PV and WT) is unable to match the load, i.e., positive net load in the system, the ST+ORC back-up is powered ON to supply the deficit electric power. To achieve the start-up in practice, switch S6 is closed in Fig. 3-4, enabling the flow of electric power to the load bus. Here, it is assumed that only one ST is deployed to follow the load.

8.1.2. Load following strategy with battery storage

Unlike in the load following without battery dispatch strategy, the ST+ORC back-up is switched ON to follow the load in this EMS mode only when there is positive net load and the battery storage is at its minimum SOC. Thus, the battery storage is the first priority to supply the deficit power and it is only charged by the excess power generation from the renewable generators (PV and WT), while the ST+ORC follows the unmet load as the second priority. The operating conditions for the control of the start-ups of the ST+ORC, the charging and discharging of the battery have been presented and described in Section 7.2 and the algorithm has been shown in Fig. 7-2.

8.1.3. Circuit charging without battery

In contrast to the traditional circuit charging where batteries are charged simultaneously while the back-up is supplying the unmet power, this strategy assumes there are no BSS in the system configuration. It however shares one of the characteristics of circuit charging, which is the operation of the ST+ORC back-up at its rated capacity while operational. This EMS strategy is proposed to study the effect deploying split STs of equal capacity in CC will have on the system performance in the absence of battery storage. Consequently, three different concepts of CC without BSS were formulated to reflect the deployment of split STs as the back-up. The algorithm for the control of the start-ups of the split STs is presented in Fig. 8-2. These cases and the complementary conditions for dispatching the power are given in the following subsections.

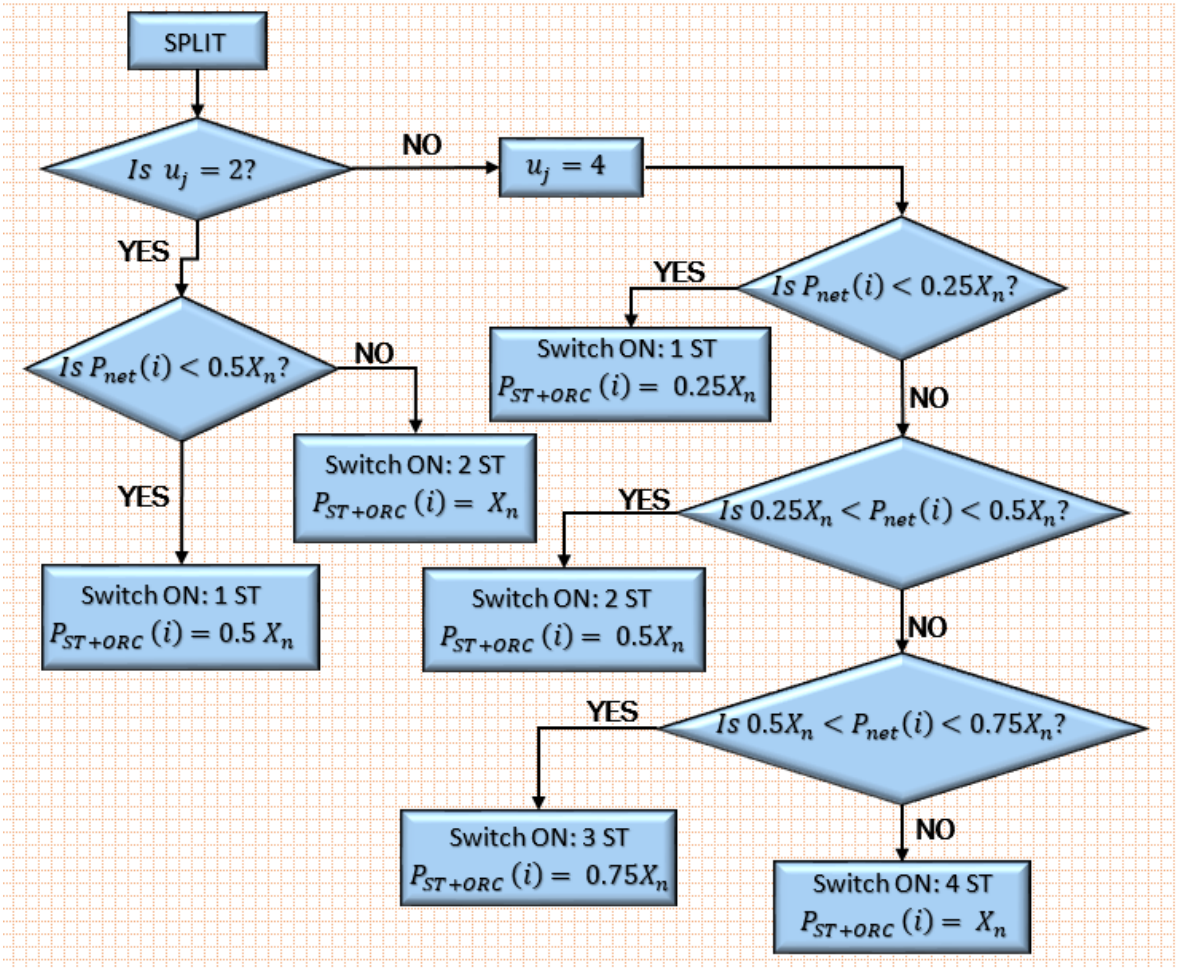

Fig. 8-2. Algorithm for implementing the control of the small split Stirling engines.

8.1.3.1. Case 1: One ST+ORC back-up

The concept here is to deploy one ST in combined generation with an ORC as the back-up to supply the unmet load. The operational condition for the start-up of the ST+ORC back-up is given below.

- $Condition\ 1: [P_{\mathrm{L}}(t) - P_{\mathrm{PV}}(t) - P_{\mathrm{WT}}(t)\ > 0\ ]$

When the total generation from the renewable generators is insufficient to fulfill the load demand, the ST+ORC back-up is powered ON to supply the load. However, the back-up is expected to operate at its rated capacity while in operation. Therefore, the central controller closes switch S6 having received the signal from the comparator.

8.1.3.2. Case 2: 2-split ST+ORC back-up

In this EMS scenario, two STs of equal capacity in combined generation mode with an ORC serve as the back-up to match the deficit power not met by the non-

programmable generators. Hence, the number of STs that are powered ON at any time will be determined by the net load to be met as described by the following conditions.

- $Condition\ 1: [P_{\mathrm{L}}(t) - P_{\mathrm{PV}}(t) - P_{\mathrm{WT}}(t)\ > 0\ ][P_{\mathrm{net}}(t) \leq P_{1-\mathrm{ST}}\ ]$

When there is a positive net load in the system and it is within the capacity of one ST, then one of the STs is powered ON to supply the load while operating at its rated capacity. The central controller receives a signal from the comparator to determine if the deficit power can be handled by one of the STs and then, it closes switch S6 and any of switches S8 to Sn (where $n = 9$).

- $Condition\ 2: [P_{\mathrm{L}}(t) - P_{\mathrm{PV}}(t) - P_{\mathrm{WT}}(t)\ > 0\ ][P_{\mathrm{net}}(t) > P_{1-\mathrm{ST}}\ ]$

If in the previous condition the central controller determines that the deficit power cannot be met by one ST, it will close switches S8 and S9 and this will automatically power ON the two-split ST back-ups to match the load. Both STs in this case are expected to operate at their rated capacities while in operation.

8.1.3.3. Case 3: 4-split ST+ORC back-up

In this case, four small Stirling engines of equal capacity in combined generation with an ORC will serve as the back-up to meet the positive net load in the system. Consequently, n-STs will be operating in parallel at every time step and the number of STs powered ON will be determined by the positive net load in the system as described by the following conditions.

- $Condition\ 1: [P_{\mathrm{L}}(t) - P_{\mathrm{PV}}(t) - P_{\mathrm{WT}}(t)\ > 0\ ][P_{\mathrm{net}}(t) \leq P_{1-\mathrm{ST}}\ ]$

When $P_{\mathrm{net}}(t)$ is positive and within the capacity of one ST, then one of the split ST back-ups is switched on to supply the load while operating at its rated capacity. The central controller receives a signal from the comparator to determine if the deficit power can be handled by one of the STs and then, it will close switch S6 and either of switches S8 to Sn (where $n = 11$).

- $Condition\ 2: [P_{\mathrm{L}}(t) - P_{\mathrm{PV}}(t) - P_{\mathrm{WT}}(t)\ > 0\ ][P_{1-\mathrm{ST}} < P_{\mathrm{net}}(t) \leq P_{2-\mathrm{ST}}\ ]$

If the unmet power exceeds the capacity one ST can handle, the central controller will close any two of the switches S8 to S11, which will automatically power ON two small ST back-ups to supply the net power. Both engines in this case are expected to operate at their rated capacities while in operation.

- $Condition\ 3: [P_{\mathrm{L}}(t) - P_{\mathrm{PV}}(t) - P_{\mathrm{WT}}(t) > 0\ ][P_{2-\mathrm{ST}} < P_{\mathrm{net}}(t) \leq P_{3-\mathrm{ST}}\ ]$

This condition switches ON three-split ST+ORC back-ups to meet the unmet power when the generation by the non-dispatchable generators does not match the load. The central controller in this case closes any of the three switches to power ON three-split ST back-ups to supply the deficit power while operating at their rated capacities.

- $Condition\ 4: [P_{\mathrm{L}}(t) - P_{\mathrm{PV}}(t) - P_{\mathrm{WT}}(t) > 0\ ][P_{\mathrm{net}}(t) \geq P_{3-\mathrm{ST}}\ ]$

When the central controller confirms that all the four STs will be required to match the electric load, due to the low generation from the PV and WT, it will close switches S8 to S11. Thus, all the four STs and the ORC are deployed while operating at their rated capacities.

8.1.4. Circuit charging with battery

Similar to the traditional circuit charging, the ST+ORC back-up is expected to operate at its rated capacity and charge the BSS with any excess power being generated. In addition, due to the high operational cost of deploying the ST, this study proposes to place a constraint on the maximum capacity of the back-up. That way, when the ST+ORC back-up is insufficient to match the deficit load, the battery can be deployed to meet the transient load at that time step. Consequently, this dispatch strategy is in principle, a combination of circuit charging and peak shaving. The conditions for charging the BSS at any time step is given in what follows. Note that the ST+ORC is powered OFF if the battery is fully charged or the PV and WT are generating enough power to fulfill the electric load. The algorithm for the implementation of CC with battery storage has been illustrated in Fig. 7-3 and Chapter 7.

- $Condition\ 1: [P_{\mathrm{net}}(t) < 0\ ][P_{\mathrm{net}}(t) < P_{\mathrm{ST+ORC}}(t)\ ][SOC(t) < SOC_{\max}\ ]$

When there is negative net load in the system and the battery is not fully charged, the excess power is stored in the BSS until the battery attains its maximum capacity. The excess power produced afterwards is dumped in a resistive load. To achieve the charging of the battery by the excess power from green energy generators or the ST+ORC back-up, the central controller closes switches S4, S5 and S7 in Fig. 3-4 based on the signal passed to it from the comparator and the charge controller.

d) $Condition\ 2: [P_{\text{net}}(t)\ > 0\ ][SOC(t)\ > SOC_{\min}\ ][P_{\text{net}}(t)\ \leq C_{\text{Bat}}(t)\ ]$

In any case, if the generation from the renewable generators is insufficient to match the load and within the capacity of the battery at a time step, the battery is dispatched to supply the load. Therefore, the central controller closes switch S3, which will allow the battery discharge its power through the inverter to the load bus. Thus, this condition controls the discharge of power from the battery if the net load consumption is positive.

Three different concepts of circuit charging with battery were formulated to investigate the deployment of split ST back-ups and battery in circuit charging. These cases and the complementary conditions for dispatching the power from the ST back-ups and the batteries are given in the following subsections.

8.1.4.1. Case 1: one big ST+ORC back-up with battery storage

In this case, one ST and ORC with battery storage are deployed to match the unmet power. The battery is the first priority to supply the net load when it is within its capacity, then the ST+ORC will fulfill the unmet power in the system. Where the net load exceeds the capacity the battery can handled, the ST+ORC is first dispatched to fulfill the load and any unmet load due to the size constraint placed on the back-up, will be met by the battery. Note that the central controller is expected to assess the SOC of the battery at every time step, to ensure any excess power generated by the back-up is utilised to charge the BSS. The operational conditions for switching on the ST+ORC back-up and discharging the BSS are given below.

- $Condition\ 1: [P_{\text{net}}(t)\ > 0\ ][SOC(t)\ > SOC_{\min}\ ][P_{\text{net}}(t)\ > C_{\text{Bat}}(t)\ ]$

In this dispatch scenario, the ST+ORC back-up is deployed to match the unmet load while operating at its maximum capacity. If there are still some unmet loads in the system at this point, the BSS will be discharged provided it is above its minimum SOC. For the first scenario, switch S6 is closed while switch S3 is closed in the second scenario.

8.1.4.2. Case 2: 2-split ST+ORC back-up with battery

In contrast to case 1, 2-split STs of equal capacity in combined power mode with an ORC are deployed here with battery storage, to serve as the back-up to match the

unmet power. Hence, the number of STs that can be powered ON at any time step, is determined by the net load in the system as described by the following conditions. Note that the battery is the first priority to supply the net load.

- $Condition\ 1: [P_{\text{net}}(t)\ > 0\ ][P_{\text{net}}(t) < P_{1-\text{ST}}\ ]$

Once the central controller confirms that the battery cannot meet the unmet load, it switches ON any of the two-split STs in the combined power block to fulfill the electric load. To achieve this, it will close one of switches S8 and S9, and this will automatically power ON one of the two-split STs to supply the net load while operating at its rated capacity.

- $Condition\ 2: [P_{\text{net}}(t)\ > 0][P_{\text{net}}(t) > P_{1-\text{ST}}\ ][SOC(t)\ > SOC_{\text{min}}]$

In this scenario, all the two-split STs are deployed to meet the load while the battery supplies any transient load provided the SOC of the battery is above its minimum. All the two switches (S8 and S9) controlling the STs are closed by the central controller and switch S3 closes only when the battery is in discharging mode.

8.1.4.3. Case 3: 4-split ST+ORC back-up power with battery

Case 3 deploys four-split STs of equal capacity in combined generation with an ORC as the back-up to meet the deficit power in the system, while the BSS will supply the transient load not met by the back-up. In addition, the battery is the first priority to dispatch power to supply the unmet power. Consequently, any number of STs can be powered ON to run in parallel based on the amount of deficit power to be met. The conditions for starting-up the ST+ORC back-up has been described in Chapter 7 and Section 7.2.

8.2. System optimisation problem

The bi-level optimisation of the energy system has been formulated as a multi-objective problem in the outer loop that deals with the sizing of the system components. Thus, the optimal system configuration is found by the simultaneous minimisation of the loss of power supply probability (LPSP), levelised cost of energy (LCOE) and dumped power. These performance evaluation metrics of the HRES were aprior developed in Chapter 7 and Section 7.3.1 and are adopted as the objective functions in the system optimisation. However, the start-up costs of the

ST+ORC back-up has been modelled and coupled to the total system cost. The start-up cost of the back-up is given as [212]:

$$C_{start-up,j} = \sigma_j + \delta_j \left[1 - exp\left(\frac{-T_{off,j}}{\tau_j}\right)\right], j = ST\ or\ ORC \quad (8\text{-}1)$$

where σ_j is the hot start-up cost of the engine, cold start-up cost of the engine, T_{off} is the period of engine shut down and τ_j is the constant for engine cooling time.

Thus, the multi-objective sizing optimisation of the HRES subsystem of the integrated multi-carrier DES is presented as:

$$minimise\ f(X) = f_i(X), f_j(X), f_k(X) \qquad i \neq j \neq k \quad (8\text{-}2)$$

$$\forall: g_i(X) = 0\ and\ h_i(X) \leq 0 \quad (8\text{-}3)$$

$$X\epsilon\{X_i, i = 1,2, \ldots \ldots n-1, n\} \quad (8\text{-}4)$$

where $i, j, k\ \epsilon\ \{1,2,3\}$, the objective functions, $f\ \epsilon\ \{\mathrm{LCOE}, \mathrm{LPSP}, P_{\mathrm{dumped}}\}$, g_i are the equality constraints, h_i are the inequality constraints and X are the decision variables. X_1 = number of PV modules in parallel, X_2 = number of wind turbines, X_3 = types of wind turbine, X_4 = the capacity of the ST+ORC back-up, X_5 = number of batteries in parallel, X_6 = types of battery, X_7 = number of split and X_8 = control strategy. Two wind turbine types of different specifications and from different manufacturers (see, Chapter 7 and Table 7-2) have been selected while three battery types of different capacities were selected (see, Chapter 7 and Table 7-2). All the equality and inequality constraints on load demand matching, capacity of ST+ORC back-up, battery storage capacity and charging and discharging limits, and number and types of system components presented in Chapter 7 and Section 7.3.2.2 have been adopted for the system sizing in the outer loop.

8.3. Bi-level optimisation solution method

The solution approach for the bi-level optimisation performed in this study to determine the optimal size of the components of the HRES system, by integrating the system sizing optimisation and the control strategy is presented in this section. The modified non-dominated sorting genetic algorithm (NSGA-II) has been

deployed to solve the formulated optimisation problem. As seen in Chapter 7 and Fig. 7-5, it starts by generating the initial cluster of possible solutions to the optimisation problem, which is a set of combinations of the component types, number and capacity including the control strategy and number of splits of the Stirling engine. The initial population of individuals, Pop_{i} in the first generation, G_{i} comprises n different configurations of the HRES that will be evaluated to determine the configuration that best minimises the LPSP, LCOE and dumped power, after several generations. The initial population, Pop_{i} is represented in a vector form as:

$$Pop_i = \begin{bmatrix} X_1^1 & X_2^1 & X_3^1 & X_4^1 & X_5^1 & X_6^1 & X_7^1 & X_8^1 \\ X_1^2 & X_2^2 & X_3^2 & X_4^2 & X_5^2 & X_6^2 & X_7^2 & X_8^2 \\ X_1^3 & X_2^3 & X_3^3 & X_4^3 & X_5^3 & X_6^3 & X_7^3 & X_8^3 \\ \cdot & \cdot & \cdot & \cdot & \cdot & \cdot & \cdot & \cdot \\ \cdot & \cdot & \cdot & \cdot & \cdot & \cdot & \cdot & \cdot \\ \cdot & \cdot & \cdot & \cdot & \cdot & \cdot & \cdot & \cdot \\ \cdot & \cdot & \cdot & \cdot & \cdot & \cdot & \cdot & \cdot \\ X_1^n & X_2^n & X_3^n & X_4^n & X_5^n & X_6^n & X_7^n & X_8^n \end{bmatrix} = \begin{bmatrix} X_1 \\ X_2 \\ X_3 \\ \cdot \\ \cdot \\ \cdot \\ \cdot \\ X_n \end{bmatrix} \quad (8\text{-}5)$$

where X is a vector representing the genotype of each individual in the population.

Fig. 8-3 illustrates the interconnection between the HRES sizing optimisation and the implementation of the control strategy. As Fig. 8-3 shows, the control parameters, $x_{\mathrm{k}} \ni \left(P_{\mathrm{net}}(t), SOC(t), u_{\mathrm{j}}, u_{\mathrm{k}}\right)$ are sent to the inner loop to simulate the hourly energy dispatch for a given control strategy, $u_{\mathrm{j}} \in (1{,}4)$ as described in Section 8.1. Then, the computed output signals including the power supplied by the ST+ORC and battery as well as the SOC of the battery are relayed to the outer loop at the end of the time steps, $t = 8760$, representative of one year, to compute the objective functions. These steps are repeated for all the individuals in a population, and then the optimisation operators are deployed to generate the next generation of individuals. This iterative process is performed hourly until the stopping criteria is met. The optimal system configuration is selected from the Pareto set of non-dominated solutions by deploying the TOPSIS decision making tool and it is given as:

$$X^{best} = \left[X_1^{best} \;\; X_2^{best} \;\; X_3^{best} \;\; X_4^{best} \;\; X_5^{best} \;\; X_6^{best} \;\; X_7^{best} \;\; X_8^{best}\right] \quad (8\text{-}6)$$

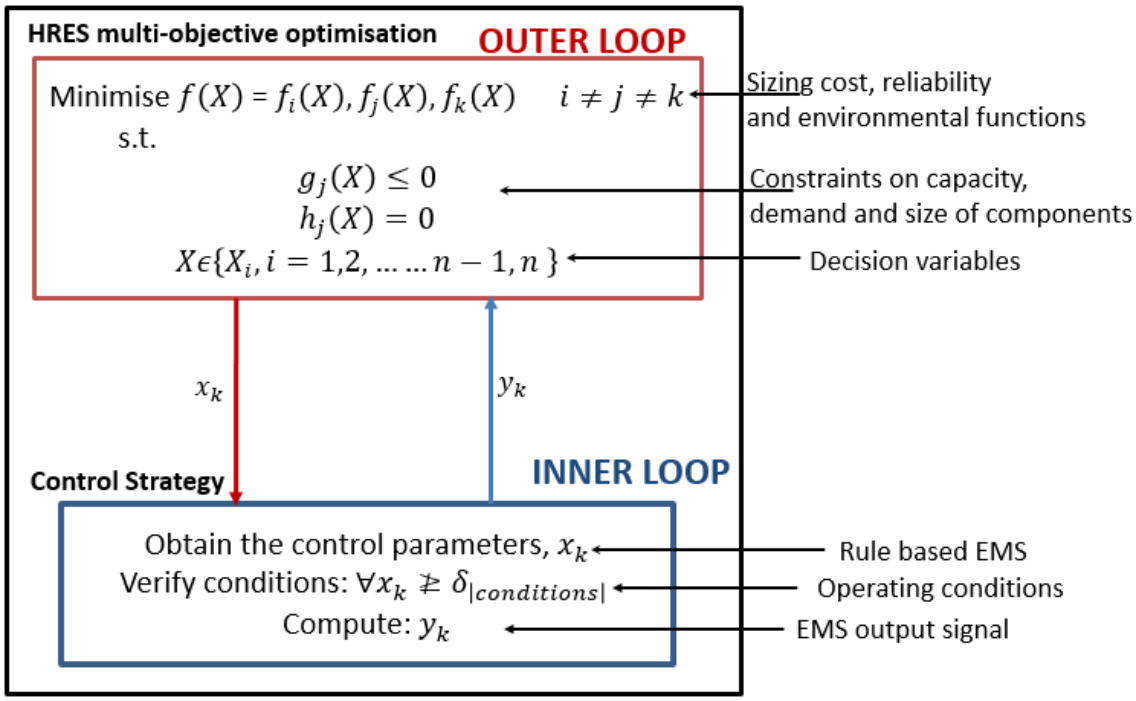

Fig. 8-3. Algorithm for the bi-level optimisation of the HRES and EMS.

Finally, the hourly performance of the optimal HRES configuration for each control strategy is simulated by deploying the algorithms already described. The implementation of the optimisation and dynamic simulation have been performed in MATLAB. A connection has been established between MATLAB and Aspen plus environment as described in Chapter 6, to control the operation of the Aspen models of the thermal chiller, ORC, boiler and the drying and combustion of the wood chips fuel. However, the models for the simulation of the generation from the PV and WT have been built in Simulink and the input weather and load data of the test location presented in Chapter 3 and Section 3.2.1 have been linked to the ports of the Simulink block from Excel spreadsheet. The MATLAB functions developed in this study to implement the control strategies in the inner loop of the optimisation procedure and undertake the sizing optimisation in the outer loop have been presented in Appendix C.

8.4. Results and discussion

The results of the optimal configuration of the HRES obtained from the bi-level sizing optimisation has been presented in this section. Also, the results of the dynamic simulation of the multi-carrier system based on the formulated control strategies

have been presented for a test location. Several fuzzy-logic based EMS have been proposed in this thesis to manage the generation, storage, and dispatch of energy from the units of the system. The simulated results obtained with the respective optimal system configuration of each of the control strategies have been robustly analysed and compared for two consecutive days in the test location with slightly different weather conditions. These simulations are intended to reveal the behaviour of the system on an hourly time resolution when deployed to fulfill the energy demand of the location. Further, it will provide new insights on the impact of the dispatch strategies on the generation of the energy vectors and how it affects the utilisation of the constituent units of the energy system.

8.4.1. Results of optimal system configuration

The bi-level system sizing and control strategy optimisation have been implemented in MATLAB with the weather and load data obtained from a test location in Southern Nigeria. The resource assessment of the test location has been performed in Chapter 3 and based on the presented data, the total daily electricity consumption in this location is 2.952 MWh/day. The optimal system configuration and control strategy that minimise the LPSP, LCOE and dumped power have been obtained after 150 generations of the GA and is presented in Fig. 8-4.

Fig. 8-4 represents the Pareto optimal solutions obtained from the bi-level multi-objective optimisation of the HRES sub-system of the integrated MDES. The conflicting nature of the multi-objective problem is evidenced by the high degree of scatter in the Pareto front. The degree of conflict in the objectives is further demonstrated by the trend in the Pareto optimal solutions presented in Fig. 8-4, which is expected particularly for a bi-level multi-objective optimisation problem integrating component sizing with the energy management. It is observed that the LPSP exhibits a direct relationship with the CO_2 emitted from the system, i.e., high renewable energy penetration yields reduced emissions. While the latter is inversely correlated to the dumped power, because of the periodic nature of the renewable generators. On the other hand, low LCOE coincides with high LPSP and vice versa, whereas the former enjoys a positive relationship with the dumped power.

In addition, the ideal solutions from the perspective of reliability, eco-friendliness, compact size and affordability have been featured in Fig. 8-4. It is clear from these results that no single solution satisfies all the four objectives equally. Hence, TOPSIS decision making tool has been deployed to obtain the best configuration in each case as highlighted in Fig. 8-4 and the detailed specifications of the TOPSIS best optimal system for each control strategy have been specified in Table 8-1. The TOPSIS best evidently ensures a reasonable trade-off in the objectives.

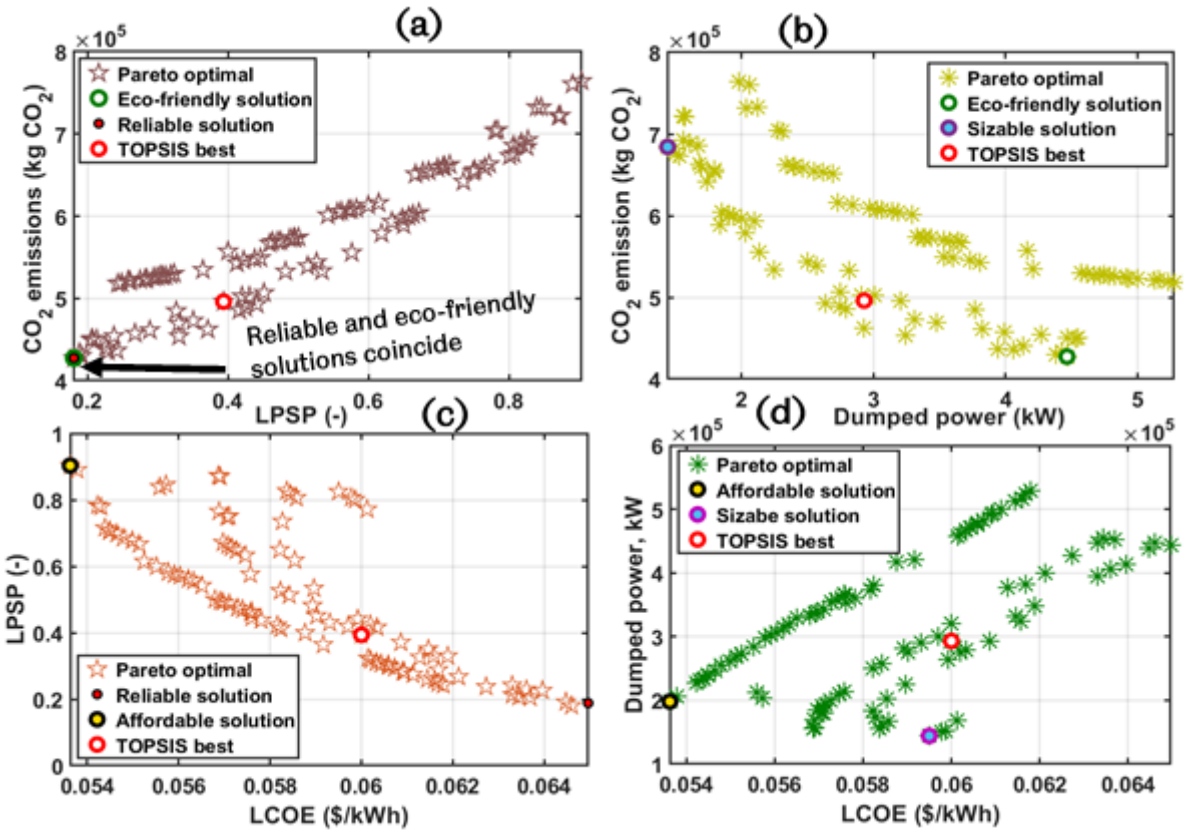

Fig. 8-4. Pareto optimal solutions obtained from the bi-level multi-objective optimisation of the energy system.

Table 8-1 contains the specification of the optimal system configurations and their respective performance indicators obtained from the bi-level optimisation. As has been previously mentioned, in this thesis, control strategy 1 is load following without batteries, control strategy 2 is load following with battery, control strategy 3 is circuit charging without battery and control strategy 4 is circuit charging with battery.

Table 8-1. Results of optimal system configuration of HRES components for different control strategies.

Control strategy	1	2	3	4
LCOE (cent/kWh)	5.835	6.08	9.09	6.32
LPSP (-)	0.4074	0.3962	0.8924	0.3801
Dumped power (MWh)	385.10	287.8	987.4	337.3
Number of PV	4×982	4×934	4×1032	4×982
Wind Turbine type	Type 2	Type 2	Type 2	Type 2
Number of WT	4	5	5	5
Battery Type	–	Type 2	–	Type 3
Number of batteries	–	4×26	–	4×30
Capacity of ST+ORC (kW)	180	193	180	180
Annual PV power (MWh)	723.53	688.16	760.37	723.53
Annual WT power (MWh)	264.21	330.26	330.26	330.26
Annual ST+ORC power (MWh)	408.81	361.71	937.50	387.50
CO2 emissions (kg CO_2)	0.54×10^6	0.48×10^6	1.29×10^6	0.51×10^6

It is evident in Table 8-1 that the optimal configuration obtained for control strategy 2 deploys the least number of renewable generators (PV and WT) to fulfill the load and generates 688.16 MWh and 330.26 MWh of solar and wind power, respectively. On the contrary, the optimal system configuration in CC without battery storage (control strategy 3) utilises the most number of PV generators and generates 760.37 MWh and 330.26 MWh of PV and wind power, respectively. Regarding the deployment of battery storage, if the optimal system configuration in control strategy 1 is compared to that in control strategy 2, it is notable that the total power generated by the renewable generator in the latter exceeds the former by 30.68 MWh. However, the former deploys the ST+ORC back-up more and consumes 47.1 MWh more power from the back-up compared to the LF with BSS. The higher power generation from the renewable generators in control strategy 2 compared with control strategy 1 is driven by the need to store excess power in the batteries and minimise the utilisation of the ST+ORC back-up. Consequently, the LPSP, LCOE, dumped power, CO_2 emissions obtained in control strategy 2 is lower compared with control strategy 1. The dumped power, CO_2 emissions and LPSP reduce by 25.3%, 11.62%, 2.75%, respectively, while the LCOE increases by 4.18%, with the deployment of battery storage in load following.

Conversely, it is evident from the optimal system configuration obtained in CC mode that the inclusion of batteries to store excess power generated from the dispatchable and non-dispatchable units (control strategy 4), reduces the capacity of the green generators compared to the case of CC without battery (control strategy 3). A huge difference in the dumped power by the ST+ORC back-up of 650 MWh (65.8% higher) in control strategy 3 compared with control strategy 4 is remarkable. This is because the ST+ORC back-up operates at its rated capacity in CC mode and the absence of BSS in control strategy 3 suggests that the excess power generated in its operation will all be dumped. Additionally, the absence of BSS results in more frequent deployment of the ST+ORC back-up in this EMS strategy. Consequently, the LCOE, LPSP, and CO_2 emissions of the optimal system in control strategy 3 drastically reduce by 30.47%, 57.41%, and 60.18% with the deployment of BSS in control strategy 4.

It is observed that with the inclusion of battery storage in the optimal system, the renewable generators compared to the system without BSS, particularly in the LF mode, generate more power. Unlike in CC where the back-up charges the batteries and fulfils the load in parallel, only the excess power generated by the renewable generators are deployed to charge the batteries in LF; hence, the increased capacity of the green generators. Finally, the optimal configuration in control strategy 2 (load following with battery) offered the lowest LCOE, LPSP, dumped power and CO_2 emissions.

In Table 8-2 and Table 8-3 the optimal system configurations obtained with the deployment of two and four-split STs cases in control strategies 3 and 4, respectively have been presented. Here, deploying two-split STs and four-split STs in control strategy 3 have been represented by (Ctr 3a) and (Ctr 3b), respectively, while deploying two-split STs and four-split STs in control strategy 4 are represented as (Ctr 4a) and (Ctr 4b), respectively. As can be seen in Table 8-2, the capacities of the renewable generators, BSS and the ST+ORC back-up reduce with the increase in the number of splits deployed in CC without battery (control strategy 3) [83]. Consequently, the LCOE, LPSP, dumped power and CO_2 emissions decline with the increase in the number of splits. Remarkable reductions are seen in the dumped

power that records 30.75% and 35.9% decrease and CO_2 emissions with observed decreases of 46.32% and 52.22%, with the deployment of 2-split STs and 4-split STs, respectively. Therefore, the deployment of split ST reduces the capacity of the system and significantly improves its global performance in circuit charging without battery.

Table 8-2. Results of optimal system configuration of HRES with the deployment of split ST in control strategy 3.

Number of split	1 (Ctr 3)	2 (Ctr 3a)	4 (Ctr 3b)
LCOE (cent/kWh)	9.09	7.26	6.39
LPSP (-)	0.8924	0.6682	0.5378
Dumped power (MWh)	987.4	632.9	471.8
Number of PV	4×1032	4×964	4×944
Wind Turbine type	EWT 52-250	EWT 52-250	EWT 52-250
Number of WT	5	5	5
Battery Type	–	–	–
Number of batteries	–	–	–
Capacity of ST+ORC (kW)	180	180	180
Annual PV power (MWh)	760.37	710.26	695.52
Annual WT power (MWh)	330.26	330.26	330.26
Annual ST+ORC power (MWh)	937.50	673.04	522.70
CO2 emissions (kg CO_2)	1.291×10^6	0.894×10^6	0.693×10^6

Similarly, when batteries are deployed to store the excess power generated by the renewable generators in control strategy 4 as seen in Table 8-3, the deployment of split ST reduces the dumped power with the increase in the number of splits. Further, the deployment of 2-split STs in Ctr 4a reduces the LCOE slightly, but contrary to the claim in the literature [83] and the findings in CC without battery storage, further reductions in the LCOE is not seen with the deployment of 4-split STs. As it is noticeable in Fig. 8-5 that depicts the annual start-ups of the back-up and the associated costs, the number of start-ups in CC with BSS increases with the increase in the number of splits.

Table 8-3. Results of optimal system configuration of HRES with the deployment of split ST in control strategy 4.

Number of split	1 (Ctr 4)	2 (Ctr 4a)	4 (Ctr 4b)
LCOE (cent/kWh)	6.32	6.131	6.144
LPSP (-)	0.3801	0.3978	0.3929
Dumped power (MWh)	337.3	323.5	320.0
Number of PV	4×982	4×959	4×965
Wind Turbine type	EWT 52-250	EWT 52-250	EWT 52-250
Number of WT	5	5	5
Battery Type	Type 3	Type 2	Type 2
Number of batteries	4×30	4×29	4×29
Capacity of ST+ORC (kW)	180	186	190
Annual PV power (MWh)	723.53	703.70	711.00
Annual WT power (MWh)	330.26	330.26	330.26
Annual ST+ORC power (MWh)	387.50	393.99	361.52
CO2 emissions (kg CO_2)	0.514×10^6	0.523×10^6	0.504×10^6

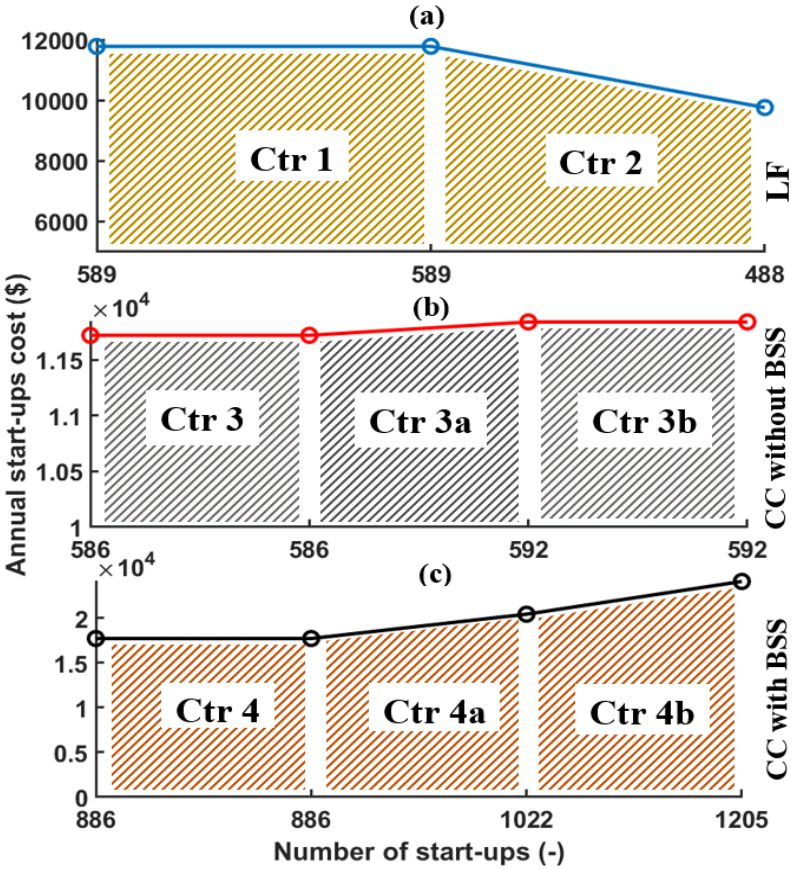

Fig. 8-5. Start-up frequency and costs from the back-up in the control strategies.

There were 1205 start-ups when 4-split STs were deployed, which is 183 and 319 start-ups more than when 2-split STs and 1-big ST were deployed, respectively. By comparison, the number of start-ups in CC without BSS (control strategy 3) increased slightly from 586 to 592 with the deployment of 2-split ST but did not change with further increase in the number of splits. On the other hand, in the LF, the inclusion of BSS reduces the number of start-ups, because the battery will be deployed a few times, minimising the dependence on the ST back-up.

On the contrary, the inclusion of batteries produces an opposite effect in CC with BSS, because of the dual role of the ST+ORC back-up in this case. Therefore, as the commitment of the back-up in fulfilling the net load reduces with the increase in the number of splits in Control strategy 4, its capacity to charge the batteries declines. Consequently, there will be more start-ups and corresponding increase in the running cost of the system, which is responsible for the slight increase in the LCOE. Nevertheless, the LCOE in Ctr 4b is still lower than Ctr 4 that utilises one big ST, because of the fewer components deployed in the former and significantly reduced deployment of ST+ORC back-up (15.9 MWh less). Further, the CO_2 emissions and LPSP decline with the deployment of 4-split STs in Ctr 4b but increase slightly when 2-split STs is deployed compared to 1-big ST case. Thus, the deployment of 4-split STs improves the system performance slightly in this case but introduces some augmented start-up costs.

8.4.1.1. Comparison of electricity generation and dispatch from the control strategies.

This section presents the results of the simulations of the hourly electricity generation and storage of the optimal MDES configurations in the proposed control strategies, for two consecutive days with slightly different weather conditions. The hourly commitment of the programmable and non-programmable units of the energy system towards the fulfilment of the electric load of the energy consumers in the test location are presented in Fig. 8-6 and Fig. 8-7 for the LF and CC control strategies, respectively. The optimal system configuration found from the bi-level optimisation varies for all the control strategies as observed in Table 8-1.

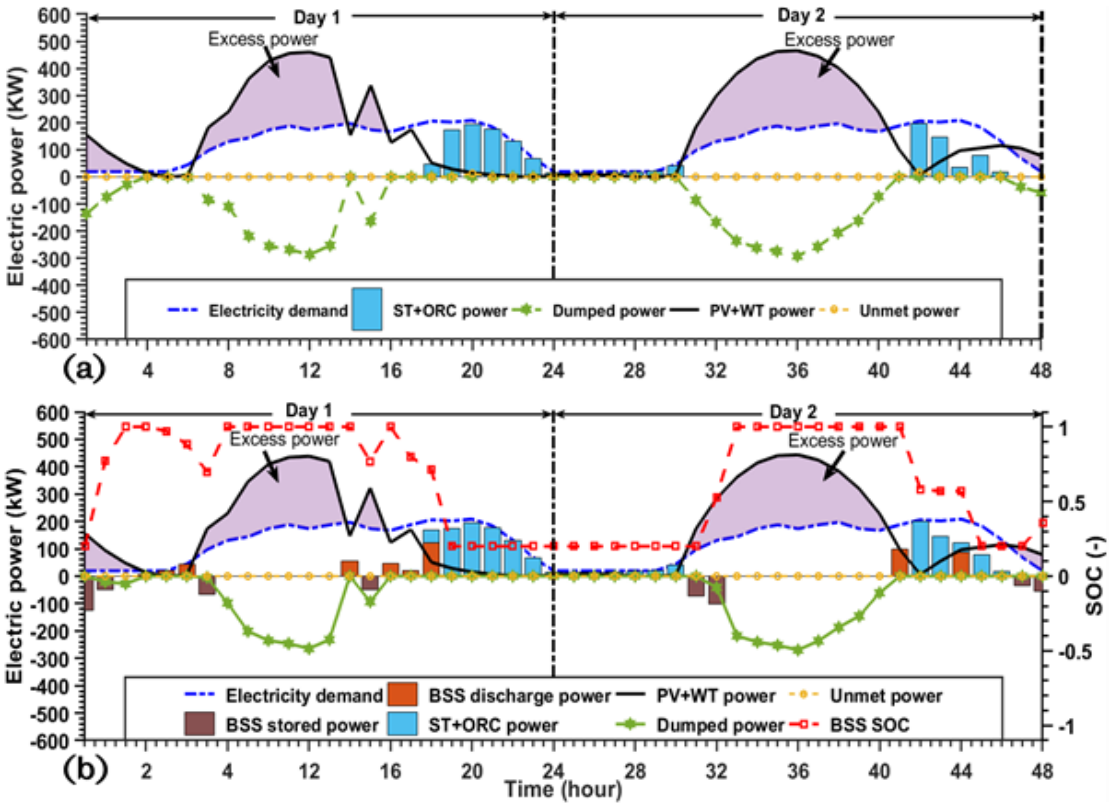

Fig. 8-6. Hourly commitments of system units in fulfilling customer electricity demand by the load following mode (a) without battery and (b) with battery.

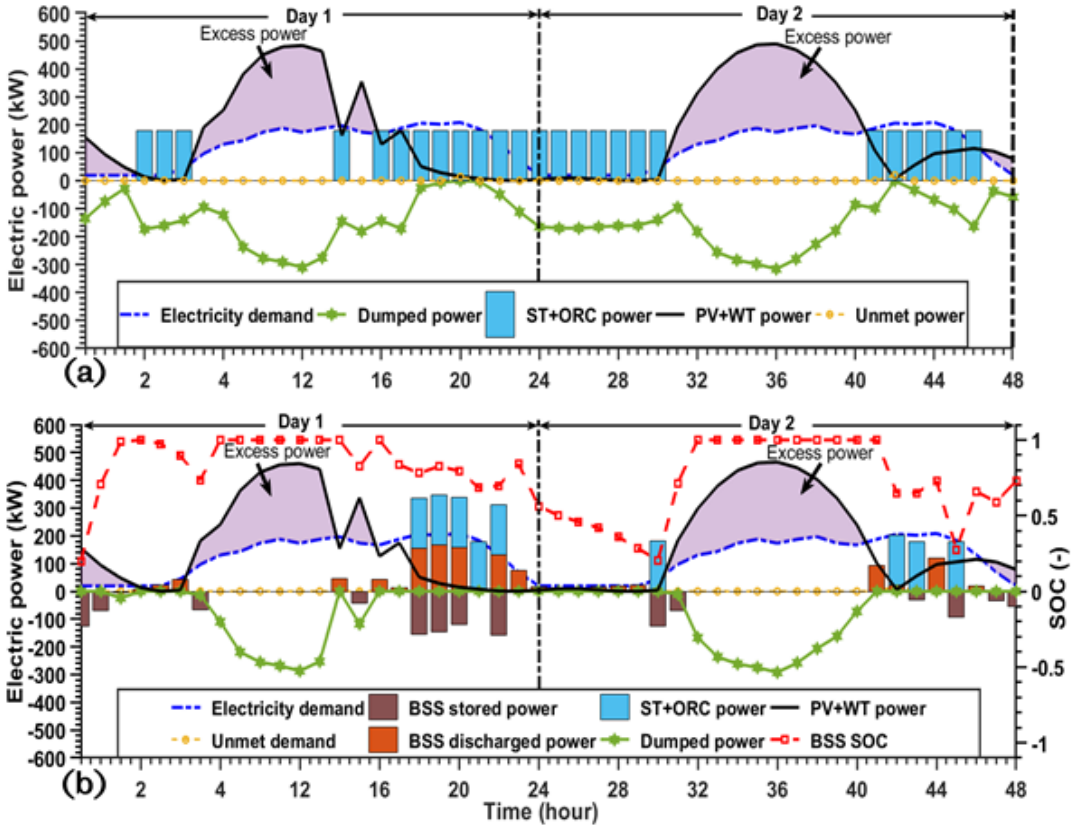

Fig. 8-7. Hourly commitments of system units in fulfilling customer electricity demand by the circuit charging mode (a) without battery and (b) with battery.

Simulations are presented on a 48-h timescale and it is noticeable that Day 1 is characterised by an extended period of power generation from the renewable generators (20 h of generation). On the other hand, Day 2 did not show much prospects for generation from the WT in the morning (0 h - 6 h) and could be representative of a day with a low wind speed. Based on the frequency of start-ups of the back-up, battery storage limits and the dumped power, the following striking points are noted:

e) The LF approach limits the frequency of start-ups of the ST+ORC back-up, contrary to the findings in Ref. [73]. The CC mode (Fig. 8-7) requires four start-ups of the back-up to fulfil the load, which is double the number in the LF mode (Fig. 8-6) and this will result in high system operational cost in this EMS mode. It is seen that the green generators stopped generating power from the 22 h in the first day to the 6 h in the next day. This long period of inactivity of the green generators forced the system to rely on the BSS and back-up. However, unlike in CC that the back-up goes through a cycle of start-up and shut-down with the BSS, in LF, once the BSS is discharged, the ST+ORC back-up simply follows the load minimising the number of start-ups.

f) The utilisation of BSS to store the excess power from the non-programmable generators reduces the dumping of power in the LF and CC EMS modes, as it can be observed in Fig. 8-6 and Fig. 8-7, respectively. The worst case of power dumping occurs in the CC without battery, where the ST+ORC back-up operates at its rated capacity when in operation. Consequently, the programmable power block contributed to the dumping of power while fulfilling the load, unlike in the LF without battery where it simply follows the load.

g) It is seen in Fig. 8-6 (b) (LF with battery) that the BSS remains in its minimum state of charge ($\mathrm{SOC}_{\min} = 20\%$) after discharging its power from the 19 h in the first day until the 9 h in the next day, when the PV starts to generate some excess power. This is undesirable because prolonged stay of the battery in its minimum SOC could shorten the life of this storage system [156]. On the contrary, due to the simultaneous charging of the batteries while supplying the unmet load by the ST+ORC back-up in CC with battery storage mode (Fig. 8-7 (b)), high SOC of battery is maintained. Consequently, the BSS fulfils the energy demand from the

24 h to the 6 h on the second day (1 hour before the PV generator starts producing) minimising the dispatch of power from the back-up.

- The cumulative power handled by the BSS, i.e., stored and discharged power and the energy flux have been presented in Fig. 8-8 for control strategies 2 and 4, where batteries are included in the optimal system configuration. It can be observed that the BSS is more active in the CC dispatch mode as evidenced by the high cumulative power of 1.4 MWh handled by the battery, which is 0.35 MWh more than in the LF mode. However, the BSS experiences many cycles of charging and discharging in CC mode, particularly on the second day marked by low generation from the WT and PV. These many cycles of charging and discharging may result in high wear of the batteries [73], [156]. Nevertheless, similar storage and discharge limits are indicated by the BSS for both dispatch strategies.
- Regarding the use of the ORC to supply the unmet power when the ST back-up is operational, the trend of the commitment of ST and ORC is presented in Fig. 8-9 - Fig. 8-12. The ORC is deployed only six times in control strategy 2 (Fig. 8-9 (b)), because the ST back-up is forced to follow the load. Consequently, the quality of the waste heat is inadequate most times to power the bottoming cycle, which helps to reduce the operating cost of the system. On the contrary, with the increase in the quality of the waste heat produced by the topping cycle in CC without battery (Fig. 8-12 (a)), the ORC is operated 25 times in the two days: the highest number of times for all the control strategies.

Overall, the deployment of battery storage minimises the commitment of the back-up to fulfilling the load and plays a crucial role in the reduction of the carbon emissions as well as the dumped power. Unfortunately, the inclusion of battery storage in the optimal system contributes to the increase in the frequency of start-ups of the ST back-up in the CC mode, because of the need to charge the batteries. Finally, BSS is more actively deployed in CC mode to fulfil the unmet load in the system in this test location compared to the LF mode.

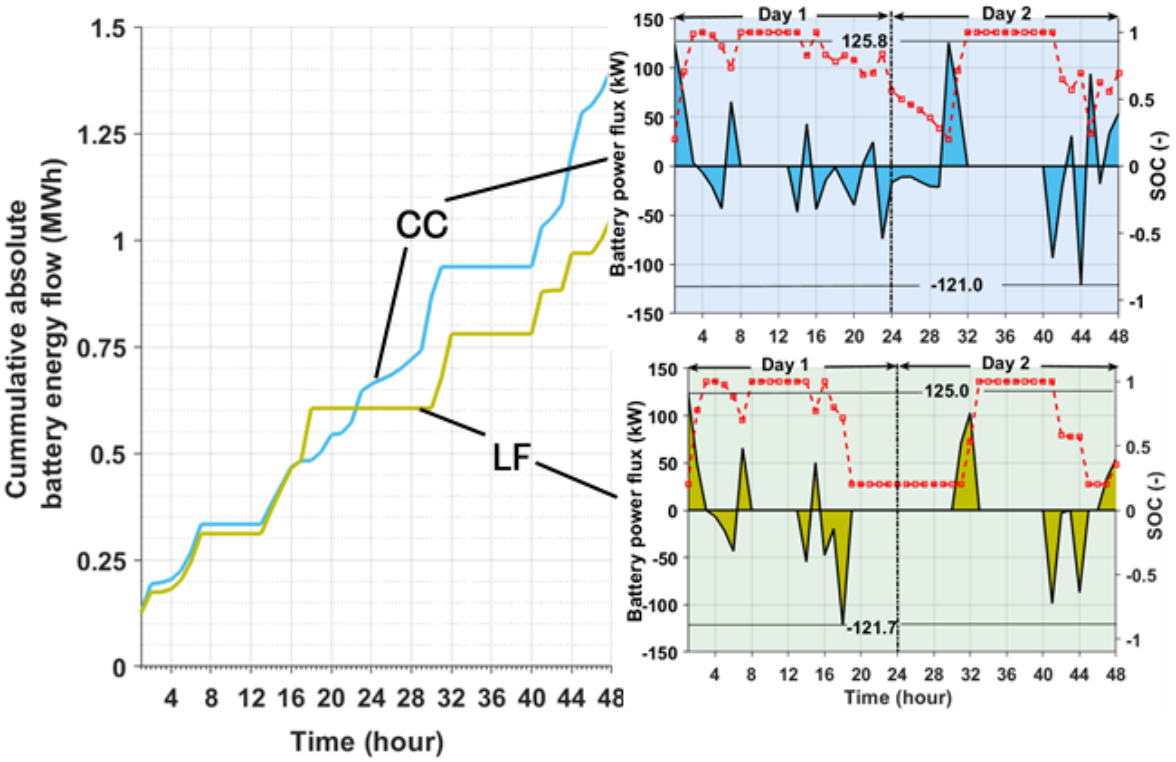

Fig. 8-8. Hourly energy flow through the batteries for different control strategies.

8.4.1.2. Impact of dispatch strategies on the cooling generation

The investigation of the impact of the proposed control strategies on the cooling generation of the multi-carrier energy system is another notable contribution in this study. A single effect lithium bromide-water thermal chiller that has a fixed capacity of 96.6 kW has been deployed to produce the cooling and would be fired by the waste heat from the flue gas produced from wood chips combustion. Due to the unavailability of the cooling demand for the test location, this study has been focused on the variation in the cooling generation from the proposed EMS.

Fig. 8-9 and Fig. 8-10 present the hourly generation of refrigerating effect by the thermal chiller when the biomass fired ST+ORC back-up is operational in the LF and CC control strategies, respectively. It is evident that the control strategies that deploy the programmable back-up more frequently produce more cooling (Fig. 8-9 (a) and Fig. 8-10 (a)). Hence, the LF and CC without battery produce more cooling (Fig. 8-9 (a) and Fig. 8-10 (a)) compared to the LF and CC with battery that deploy the ST+ORC back-up fewer times to supply the deficit power as can be observed in

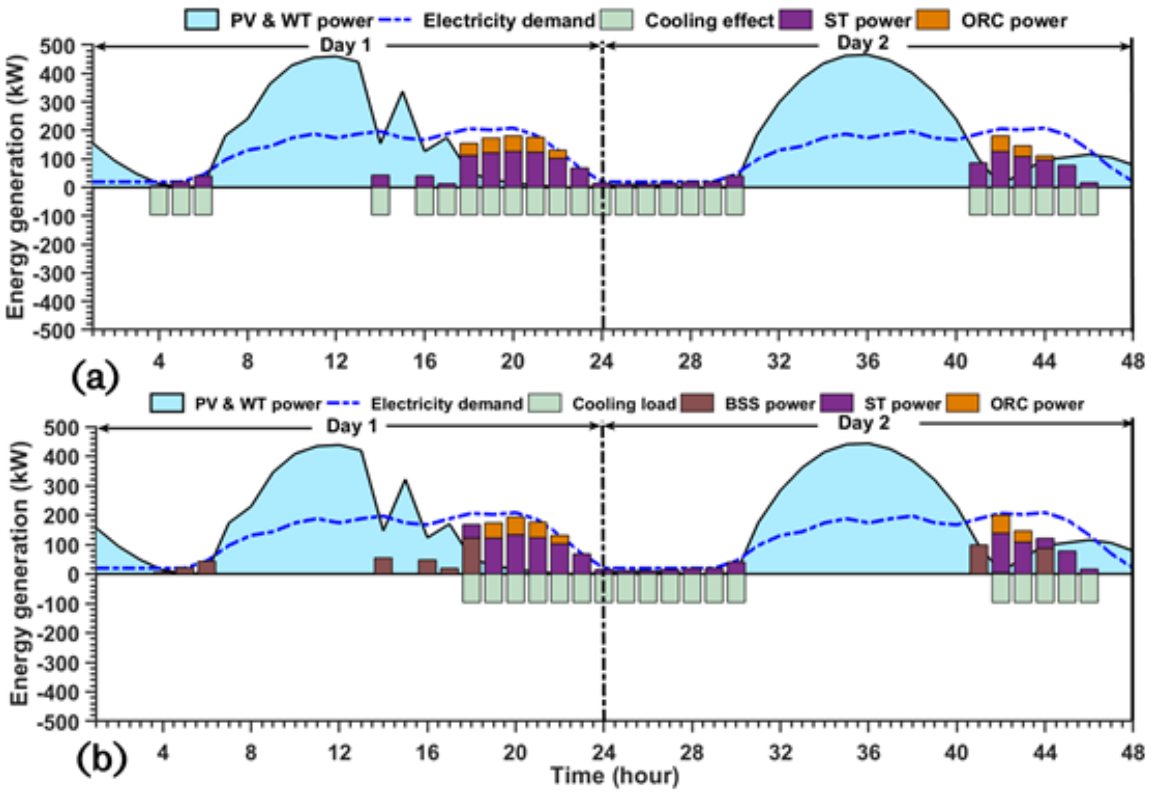

Fig. 8-9. Hourly generation of cooling and commitments of the dispatchable generators in load following (a) without battery and (b) with battery.

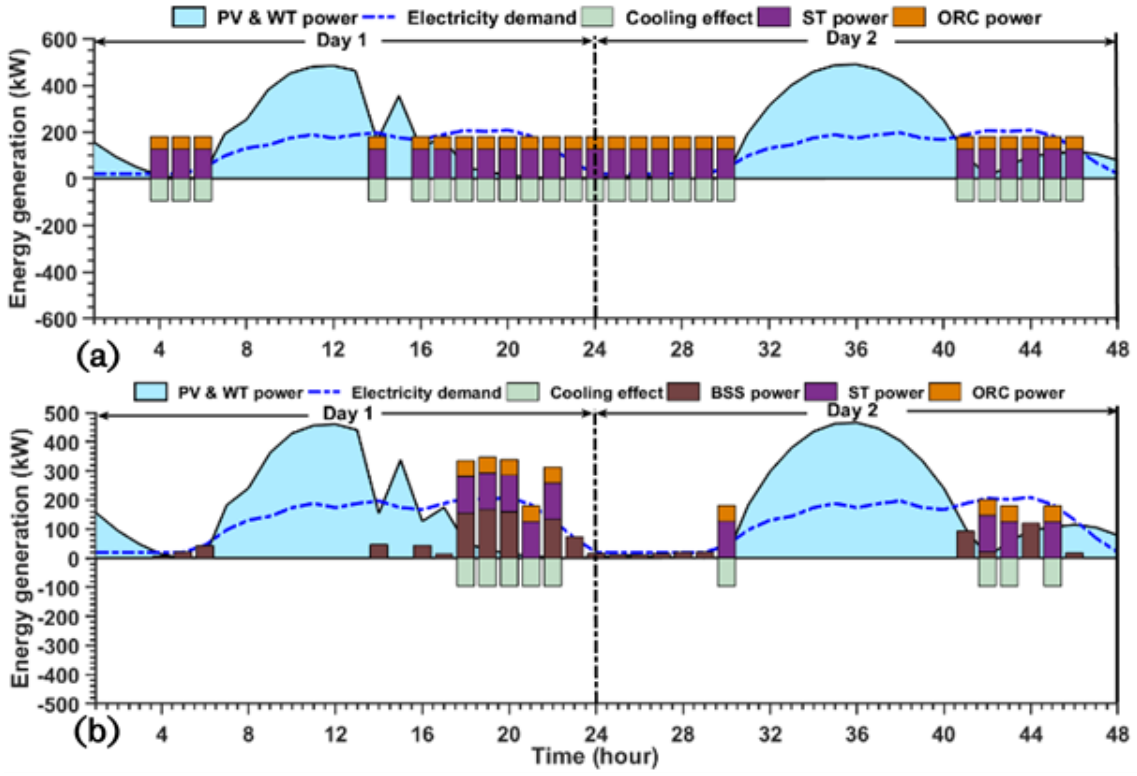

Fig. 8-10. Hourly generation of cooling and commitments of the dispatchable generators in circuit charging (a) without battery and (b) with battery.

Fig. 8-9 (b) and Fig. 8-10 (b), respectively. Finally, the absorption chiller is only deployed to produce cooling nine times (in two days) in control strategy 4 (Fig. 8-10 (b)), because batteries supply most of the unmet power in this strategy compared with any other control strategy and that highlights the unfavourable impact of deploying battery storage on cooling generation.

8.4.1.3. Impact of dispatch strategies on the heating generation

This section presents the simulated results of the impact of the proposed rule-based dispatch strategies on the heating generation of the MDES. Unlike in the case of the cooling generation, the capacity of the boiler in this case is determined by the available energy in the flue gas. In principle, the heating load and buffer storage will determine the amount of heating that is generated on an hourly basis [73]. Unfortunately, because the proposed system is designed for a remote test location, the daily hourly heating load is not defined. Hence, this simulation has been focused mainly on the generation potential of the energy vector.

Fig. 8-11 and Fig. 8-12 represent the hourly heating generation from the water boiler for the LF and CC control strategies proposed in this study, respectively. It is apparent in Fig. 8-11 and Fig. 8-12 that the heating generation varies for all the control strategies. In particular, as the commitment of the ST+ORC back-up in fulfilling the electric load increases, the generation of heating reduces, because less thermal energy is available to produce additional goods in the form of heating or hot water. The heating load generation is generally high in the LF mode (Fig. 8-11) compared with the CC (Fig. 8-12), because in the former, the ST+ORC back-up is forced to follow the load. Hence, at most times in its operation, the ST main driver consumes a small fraction of the energy in the flue gas, and this makes more energy available to produce heating. In addition, since in the LF with battery storage (Fig. 8-11 (b)) the ST+ORC back-up does not charge the BSS, the system becomes more reliant on the dispatchable unit to fulfil the load in the absence of the green generators.

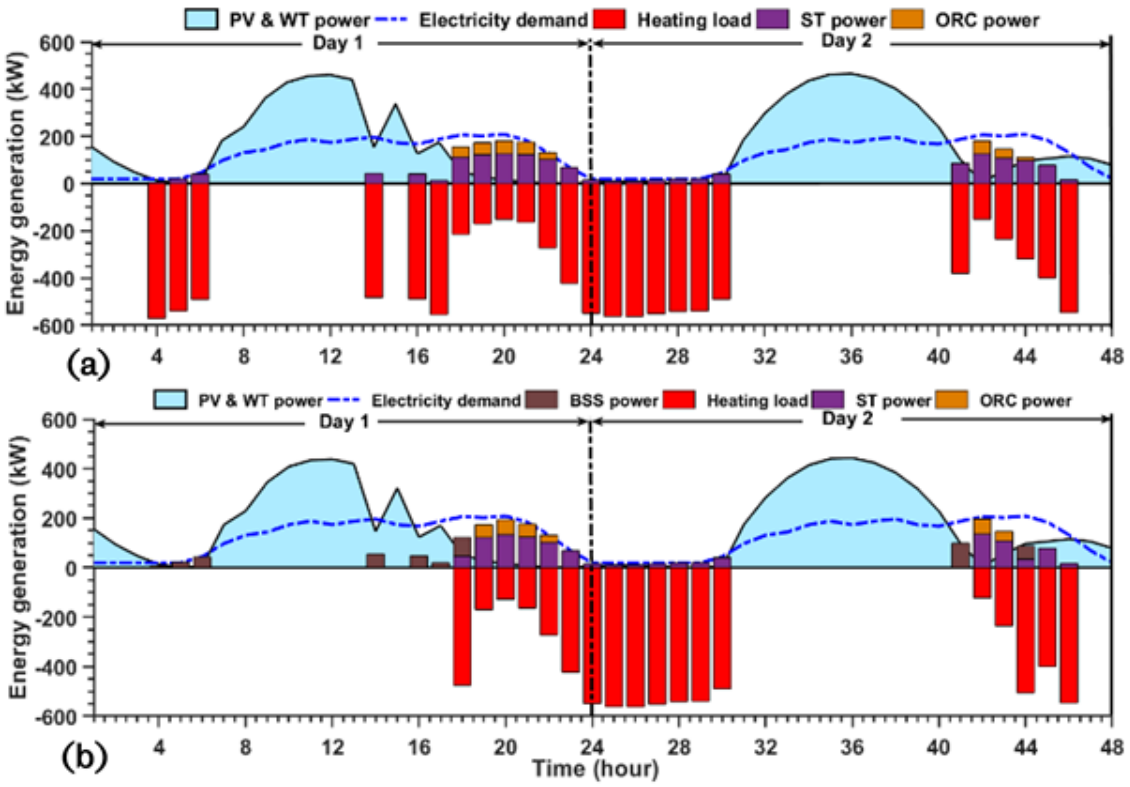

Fig. 8-11. Hourly generation of heating and commitments of the dispatchable generators in load following (a) without battery and (b) with battery.

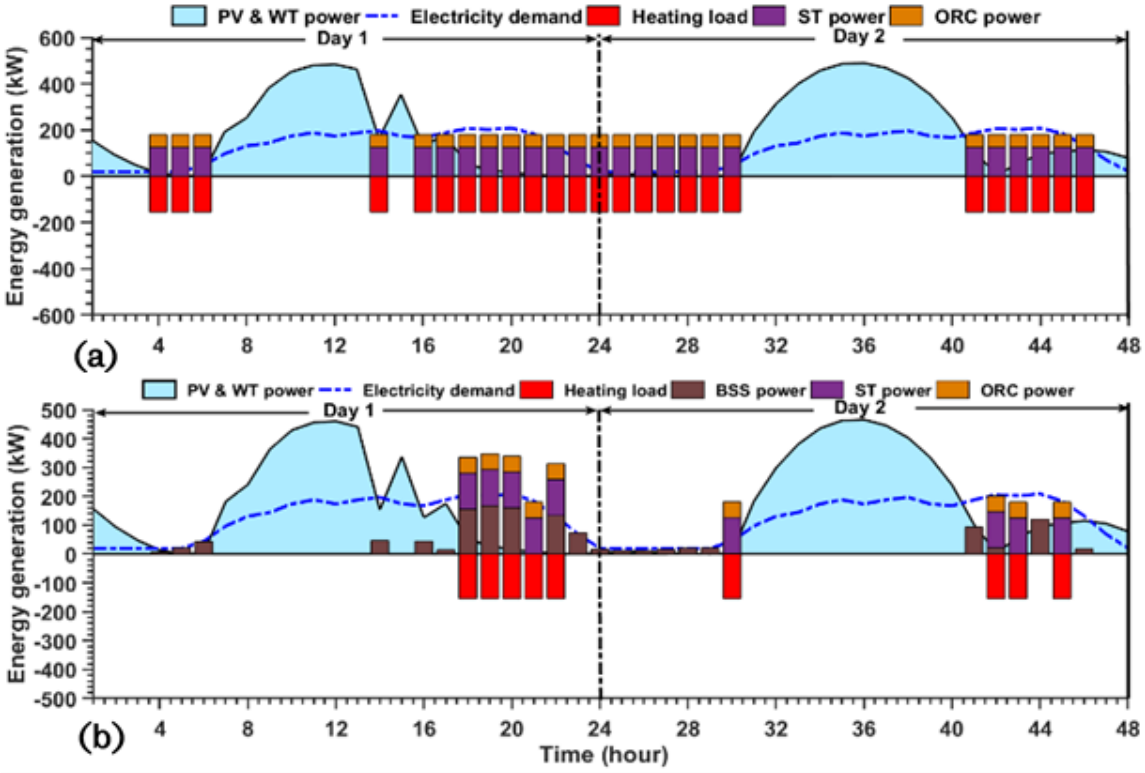

Fig. 8-12. Hourly generation of heating and commitments of the dispatchable generators in circuit charging (a) without battery and (b) with battery.

On the other hand, the CC with battery storage produces the least amount of heating, due to the increased deployment of batteries to supply the unmet power (Fig. 8-12 (b)). Finally, the inclusion of battery storage in the HRES design and the availability of the WT and PV generators affect the heating generation. Where batteries are not deployed to store the excess power produced by the renewable generators, more heating will be generated on days with poor weather, because of the inexorable increase in the dispatch of the ST+ORC back-up to fulfill the electricity demand. This is noticeable on the second day with poor weather conditions, in Fig. 8-11 and Fig. 8-12.

8.4.2. Impact of split back-ups on optimal multi-carrier system

The impact of deploying split ST to match the electric load of the test location has been evaluated for two-split (2-split) and four-split (4-split) STs cases. Split ST has been deployed only in the CC strategy where it is applicable. As has been remarked in Section 8.4.1, the optimal system configuration in each case varies as the number of split back-ups deployed varies. Therefore, based on the optimal system configurations presented in Table 8-2 and Table 8-3, the effect of deploying split ST on the hourly generation and storage of heating, cooling and electricity by the MDES has been examined and the results are presented in this section.

8.4.2.1. Effect of split Stirling back-up on electricity production

Fig. 8-13 and Fig. 8-14 show the hourly commitments of the ST+ORC back-up and battery storage when split ST is deployed in CC to fulfill the electricity demand. It is evident that the number of start-ups of the ST+ORC back-up is invariant when 2-split STs and 4-split STs were deployed to augment the positive net electric load with the exclusion of battery storage in the system configuration (Fig. 8-13 (a) and (b)). However, the dumped power unarguably reduces, because of the reduction in the commitment of the back-up to fulfilling the load. The undeniable significant reduction in the commitment of the back-up will reduce the fuel consumption and emissions as evidenced by the results presented in Table 8-2. Conversely, in Fig. 8-14 (a) and (b) where 2-split and 4-split STs were deployed, respectively with the inclusion of battery storage, the frequency of power dispatch from the back-up incr-

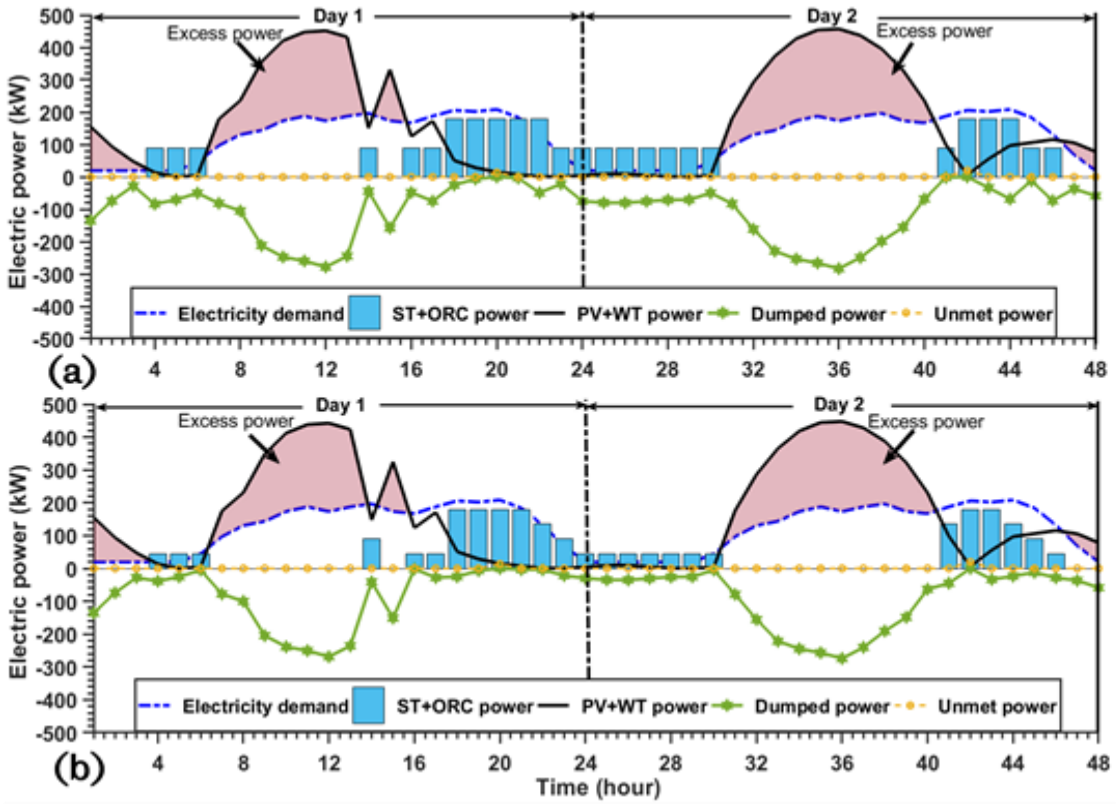

Fig. 8-13. Hourly commitments of the system units to fulfill the electric load in circuit charging mode without battery for (a) 2-split ST and (b) 4-split ST cases.

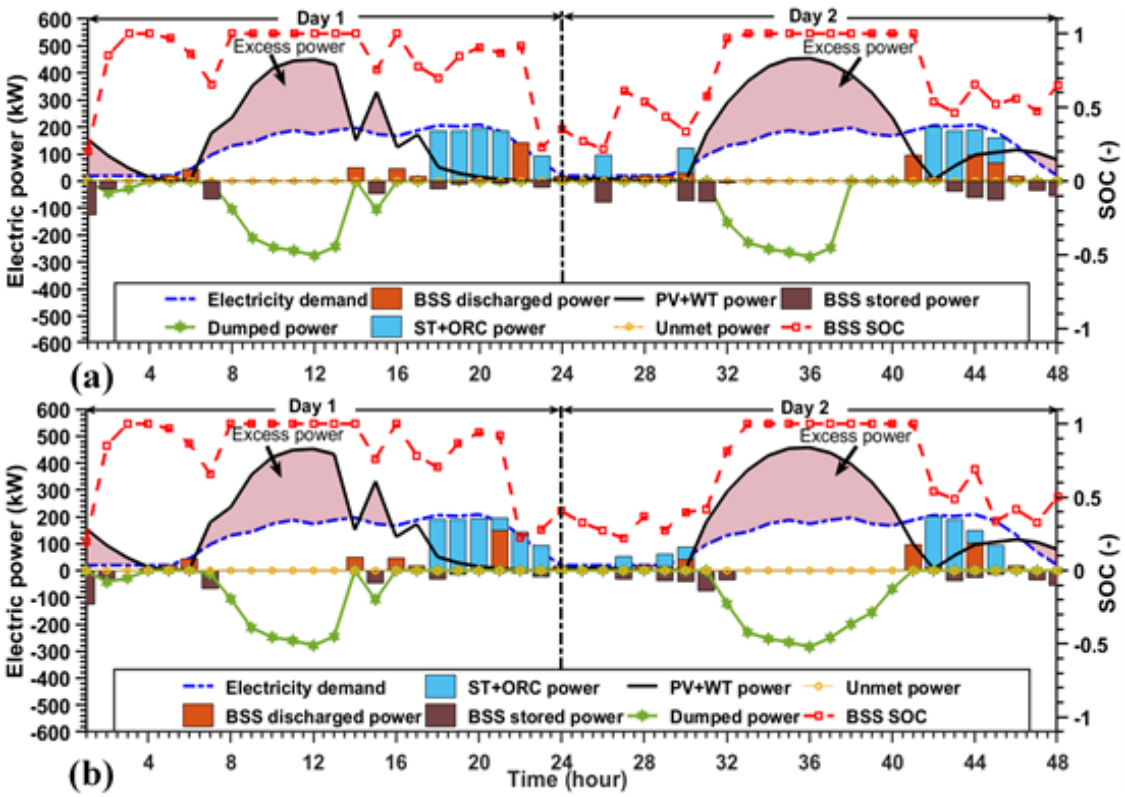

Fig. 8-14. Hourly commitments of the system units to fulfill the electric load in circuit charging mode with battery for (a) 2-split STs and (b) 4-split ST cases.

-eases as the number of split increases. In the case of 2-split STs, the back-up was operational for eleven hours in the two days to fulfil the load, but this increased to 13 hours with the deployment of 4-split STs. When compared with the one big ST case (Fig. 8-7 (b)), it is seen that the ST back-up was operational for a total duration of nine hours in the two days. The increase in the frequency of operation of the back-up with the increase in the number of splits is as a result of the increasing reduction in the excess power generated. As the number of splits increases, the capacity of each of the STs in the split reduces, which contributes to a decrease in the excess power generated from the back-up. Consequently, it becomes difficult to charge the batteries once the non-programmable renewable generators are unavailable to generate excess power and this forces the ST+ORC back-up to operate more frequently.

Also, the introduction of the split ST concept impacts the battery negatively. Fig. 8-15 represents the cumulative energy flux through the batteries when 2-split and 4-split STs are deployed to match the unmet load in the system in CC mode. It is self-evident that the cumulative power handled by the BSS reduces with the increase in the number of small ST back-ups. Further, the BSS noticeably undergoes deep discharge of power with the deployment of split back-up. When 4-split STs are deployed, the maximum discharged power is 144.5 kW compared to 121 kW recorded with 1-big ST. Further, the number of cycles of charging and discharging of the batteries increase with the deployment of split ST; however, a comparable number of duty cycles are indicated for 2-split and 4-split cases. Apparently, the reduction in the ST back-up capacity with the increase in the number of splits suggests that the battery will be insufficiently charged; hence, the undesirable increase in the number of deep cycles that is inimical to the life of the battery [207] .

On a positive note, the introduction of split ST minimises the dumping of excess power from the back-up, which also translates to the reduction in the fuel consumption. Additionally, with the increasing number of split ST, the number of start-ups and operational hours of the ORC bottoming cycle reduce, as is evident in Fig. 8-16 - Fig. 8-19. This is because of the drop in the quality of the waste heat from

the ST. For this reason, the operational cost of the system will reduce, i.e., the cost of maintenance and start-ups of the ORC and the reduction will be remarkable on the second day, where the ORC has been deployed for an average of 2.5 h in all the examined dispatch cases. Finally, it is evident that as the number of splits of the back-up increases, the behaviour of the energy system in CC mode approximates that of the LF mode. Consequently, the dumped power is minimised. Sadly, this introduces new cost elements, mainly derived from the additional commitments to the battery storage, but it has the advantage of making the back-up to operate efficiently at its rated conditions, and minimise fuel consumption and emissions, unlike in the LF mode.

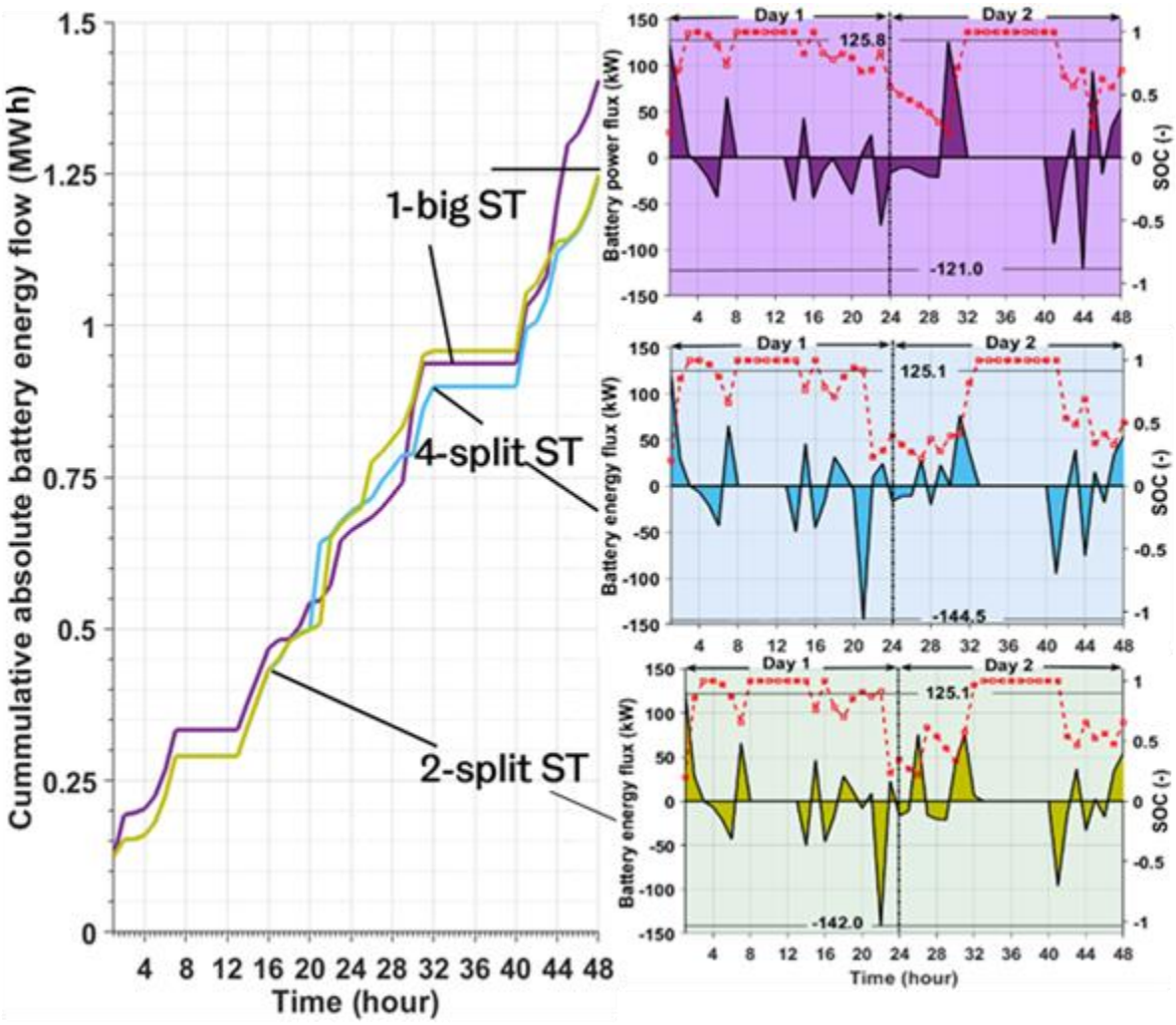

Fig. 8-15. Hourly energy flow through the battery storage in circuit charging mode.

8.4.2.2. Effect of split Stirling back-up on cooling generation

Fig. 8-16 and Fig. 8-17 present the hourly generation of cooling by the thermal chiller when many small split STs are deployed in the circuit charging strategy to follow the electric load in the test location, without the exclusion of battery storage and otherwise, respectively. It is seen from Fig. 8-16 (a) and (b) that the amount of cooling generation did not change with the deployment of 2-split and 4-split STs. This is because the operational hours and number of start-ups of the ST back-up were invariant with the increase in the number of splits. Consequently, the thermal chiller operates for equal number of hours regardless of the number of split back-ups deployed. Also, if it is noted that this cooling system can be operated satisfactorily with low grade heat of temperature less than 100 ℃ [99], [270], [271], the increase in the capacity of the ST which will reduce the quality of the flue gas, will not significantly affect its performance.

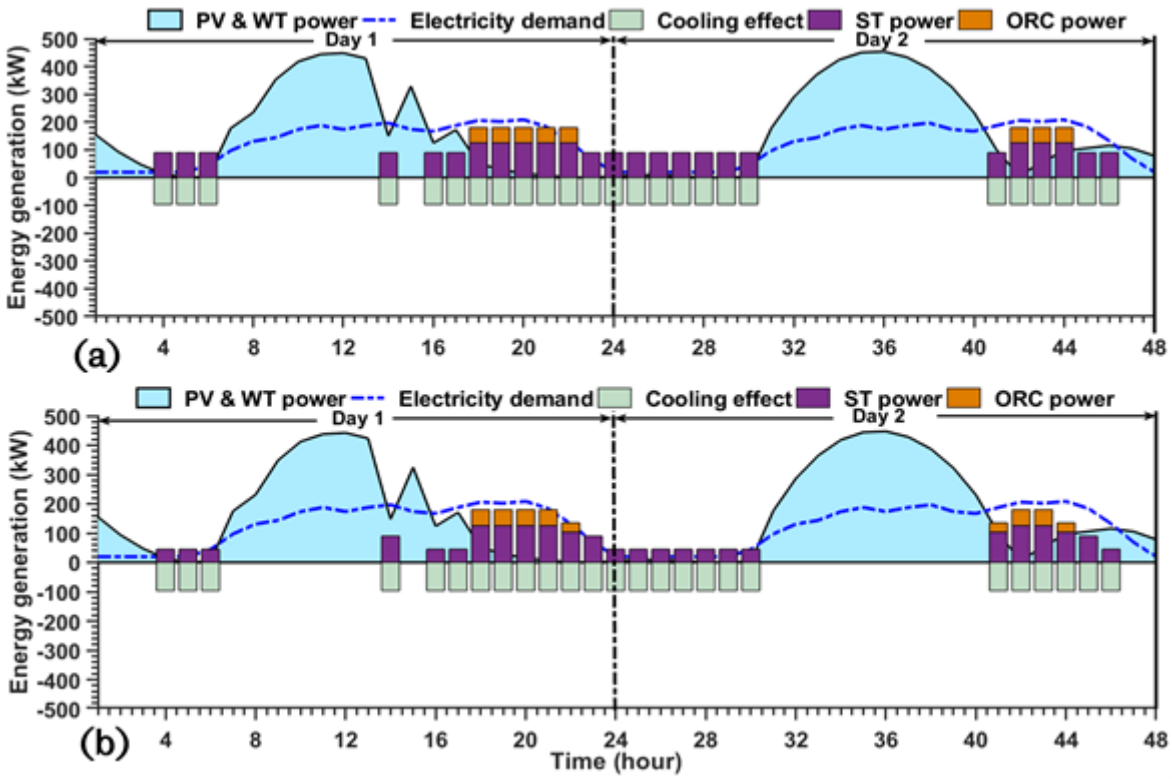

Fig. 8-16. Hourly generation of cooling and commitments of the dispatchable generators in circuit charging without battery mode using (a) 2-split ST and (b) 4-split ST back-ups.

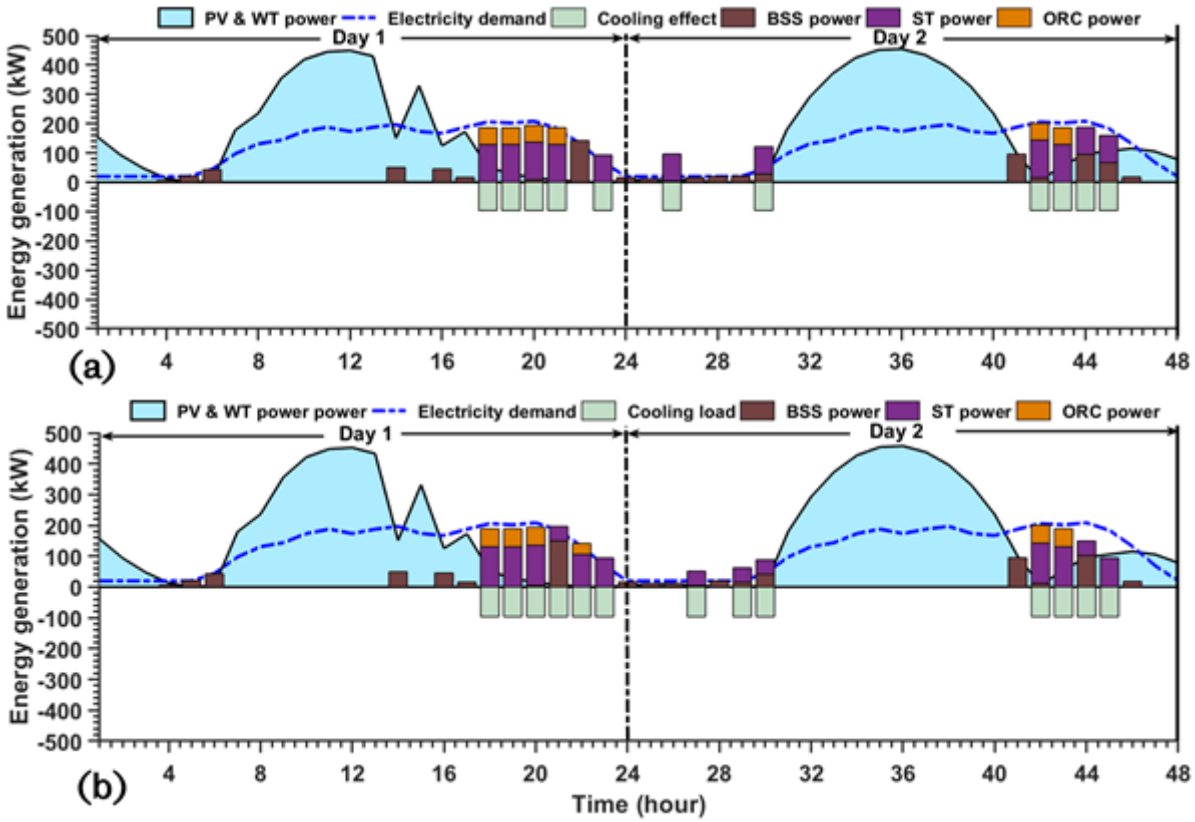

Fig. 8-17. Hourly generation of cooling and commitments of the dispatchable generators in circuit charging with battery mode using (a) 2-split ST and (b) 4-split ST back-ups.

Contrarily, the generation of cooling increases with the increase in the number of splits as seen in Fig. 8-17 (a) and (b), due to the increase in the hours of operation of the ST back-up. Therefore, on cloudy days with less generation from the PV and WT, it is expected that there will be an increase in the generation of cooling. Conclusively, while the inclusion of battery storage in the optimal system has a negative impact on the cooling generation, the combined deployment of battery storage and split ST favours the generation of cooling from the thermal chiller, because of the increased deployment of the back-up.

8.4.2.3. Effect of split Stirling back-up on heating generation

The impact of deploying split Stirling engines on heating generation when the energy generation, storage and dispatch of the system is coordinated by the CC mode has been evaluated. Fig. 8-18 and Fig. 8-19 show the hourly generation of heating when 2-split STs and 4-split STs are deployed in CC without battery storage and with battery storage, respectively. It is seen in Fig. 8-18 (a) and (b) that the heating generation

potential of the system more than doubled as the number of splits of the ST increases. As the number of split increases, the quality of the flue gas that is sent to the boiler increases, because of the reduction in the capacity of the ST. This reduction in the capacity of the ST suggests that less energy will be required to fire the heat engine. Further, in Fig. 8-19 (a) and (b) where batteries were deployed, it has been remarked that the deployment of split ST in these cases, reduces the capacity of the back-up to charge the BSS.

Consequently, the number of times the ST is deployed increases; hence, the observed increase in the generation of heating with the increase in the number of splits. Day 2 that is marked with a reduced period of generation from the renewables generates more heating than Day 1. Again, the combination of battery storage and split back-up in the optimal system configuration favours the generation of heating.

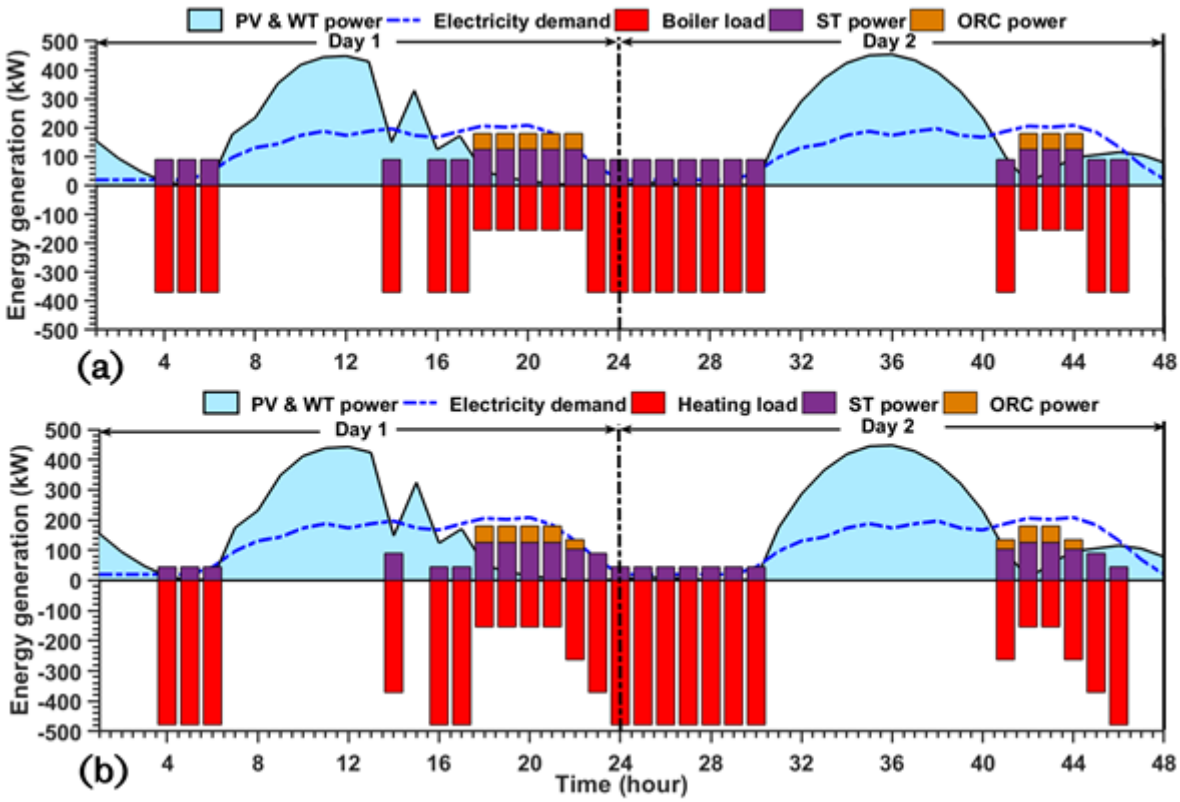

Fig. 8-18. Hourly generation of heating and commitments of the dispatchable generators in circuit charging mode without battery storage using (a) 2-split and (b) 4-split ST back-up.

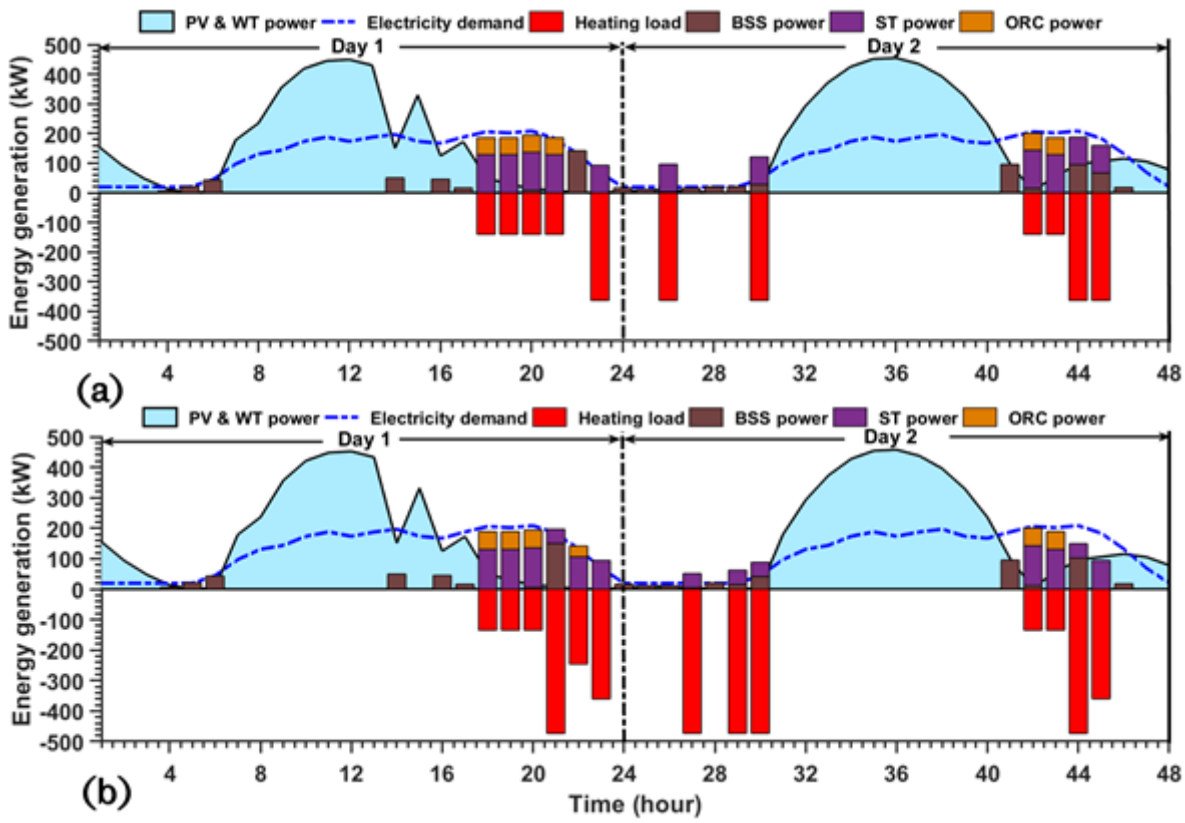

Fig. 8-19. Hourly generation of heating and commitments of the dispatchable generators in circuit charging mode with battery storage using (a) 2-split and (b) 4-split ST back-up.

8.5. Chapter summary

This chapter proposed the deployment of modified rule-based energy management strategies (EMS) to coordinate the continuous generation, storage and dispatch of several energy vectors and other goods from a hybrid solar PV-wind and battery storage integrated multi-carrier system deploying Stirling (ST) and ORC as back-up and prime mover. First, bi-level sizing optimisation has been conducted to obtain the optimal number of system components that minimises the system operational cost (and offers cheap energy (LCOE)), loss of power supply probability (LPSP), CO_2 emissions and dumped power in the outer loop. Then, the EMS has been implemented in the inner loop with the optimal system components including the control parameters generated in the outer loop. In addition, the hourly simulation of the optimal system configuration obtained in this study has been undertaken to understand its dynamic behaviour in fulfilling the energy demand. It is evident that the choice of control strategy formulated to manage the multi-carrier system plays

a key role in determining the size of the components of the optimal system configuration.

Finally, the proposed modified traditional rule-based energy management system, which deploys split ST back-up reduces the dumping of power and emissions from the optimal system. This is achieved by reducing the hourly commitments of the back-up in fulfilling the load and enhances the cooling and heating generation potentials of the multi-carrier energy system, by improving the quality of the combustion flue sent to these units. Unfortunately, it produces many cycles of charging and discharging of the battery storage when compared to the traditional LF and CC, and augments the operational cost by increasing the number of start-ups of the split back-up. This challenge can be overcome by simultaneously prioritising the charging of the batteries and fulfilment of the load in the dispatch of the split back up and is therefore, an interesting topic for future work.

Chapter 9 Conclusions and Plans for Future Work

Massive deployment of clean energy based solutions is a promising pathway to resolve the quadrilemma in energy production and consumption. Therefore, new clean energy configurations are required and this has become a hot topic in the scientific community. In Chapter 3, three new configurations of clean energy based decentralised energy systems were proposed. The research work undertaken in this thesis generally focused on the modelling, optimisation, simulation and control of the proposed energy systems.

This chapter outlines the findings, original contributions to existing knowledge and some recommendations for future work. Section 9.1 highlights the key findings obtained from fulfilling the objectives that were outlined in Chapter 1 of this thesis. Section 9.2 discusses the contributions to knowledge from this study and its originality and application. Finally, Section 9.3 provides some roadmaps for future work to enrich the existing knowledge.

9.1. Summary of research findings

The overall aim of this research undertaking is the modelling, optimisation, simulation and management of the operation of different configurations of clean energy based decentralised energy systems (DES), with the potential to produce cooling, heating, electricity and dry wood chips either independently or simultaneously. The following concluding remarks are very important from this study, regarding the proposed decentralised energy system concepts:

System Concept I: Stirling and ORC driven multi-carrier decentralised system

The modelling, parametric analyses and optimisation of this DES configuration have been achieved in three phases. Firstly, a comprehensive thermal model of the Stirling engine main prime mover was developed in Chapter 4, to predict accurate performance results at the various operational speeds of the experimental engine. The enhanced model was developed by coupling the mass leakages of the engine gas into the engine working spaces and the crankcase and the displacer shuttle heat loss to the traditional model developed in [64], thus invalidating the assumed adiabatic conditions and several other assumptions made in the simplified model. Similar to

other modelling efforts, several work and heat transfer losses were accounted for at the end of a cycle of operation of the engine. Subsequently, the differential equations governing the operation of the engine were implemented in MATLAB with the geometric data of an experimental engine (General Motors GPU 3 engine) by deploying the fourth-order Runge-kutta iterative scheme. The model predicted results were validated robustly against the experimental data obtained from literature and compared to other theoretical model results as reported in Chapter 5. The developed model predicts the brake power and thermal efficiency of the experimental engine with relative errors of +0.3% and -4.02%, respectively and more accurately than all the previous numerical and closed-form models at all the engine frequencies investigated, apart from the PSML [67] model that predicted better results at higher engine frequencies. Other highlights from the model predicted results are as follows:

- Increasing the pressure of the engine in the expansion process and lowering it during the compression process will increase the net cycle work.
- Pressure drops in the heat exchangers contribute most of the work losses in the engine while hysteresis loss records the least work loss confirming the results in [186].
- Conduction losses from the regenerator walls are the main contributors of heat losses in the engine and this agrees with the findings in Ref. [67].
- Increase in engine frequency leads to a decline in the power output as the dimensionless number increases, due to the increase in the mass leakage and this is more evident with a lighter engine fluid like hydrogen [184], [247].
- 9.427 kW of heat is lost to the heat sink and this can be recovered to power another heat engine or for other useful purposes.

In the second phase of this work reported in Chapter 6, the enhanced Stirling model was deployed for the parametric analysis of a multi-carrier DES driven by the Stirling engine. The models of the other system components were developed in Aspen plus and validated against experimental data. A link was established between Aspen and MATLAB to control the operation of the Aspen models from MATLAB and exchange data between the models as well as to enable the simulation of the system performance. Parametric analysis was conducted to examine the effect of the

quality of the biomass fuel, cooling ratio and speed of the Stirling main driver on some system performance indicators and the following are the main conclusions from this study:

- Energy utilisation efficiency (EUF) declines remarkably as cooling ratio increases but the intensity reduces as cooling ratio tends to one and this is more evident with the reduction in the quality of the wood chips fuel.
- EUF decreases with an increase in the speed of the main prime mover when the energy system operates as a combined heating and power (CHP) system, i.e., $CR << 0.1$ but increases with speed when it operates as a combined cooling and power (CCP) system, i.e. $CR >> 0.1$.
- Exergy efficiency decreases with increase in CR and it is more evident with the reduction in the moisture content of fuel, because the engine is operating at higher temperatures. It generally increases with the increase in speed.
- Primary energy savings (PES) generally improves with the increase in the speed of the prime mover but reduces with the reduction of the cooling ratio. It, however, increases with the increase in the quality of the fuel.
- On the other hand, artificial thermal efficiency (ATE) decreases with increase in CR particularly at lower engine speed but slows down as CR tends to 1.
- Also, as the engine frequency increases, ATE decreases at low CR when the multi-carrier system is working as a CHP but increases with increase in speed at high CR.
- Finally, while EUF and ATE indicate global optima at the low speed and CR region, PES and exergy efficiency record global optima at the high speed and low CR region, and this highlights the need for parametric optimisation of the system to obtain the optimal operating regime.

Consequently, in the final phase of this work reported in Chapter 6, parametric optimisation of the system was performed from a multi-objective perspective, by simultaneously minimising these system performance indicators while the cooling ratio and engine frequency were selected as the decision variables. The multi-objective parametric optimisation was implemented in MATLAB with a multi-objective evolutionary algorithm (MOEA). The optimal operating regime was found from the Pareto set by deploying TOPSIS decision making tool and it gives $EUF =$

0.85, $\eta_{\mathrm{II}} = 0.57$, $\mathrm{PES} = 0.51$ and $\mathrm{ATE} = 0.62$ and optimum $\mathrm{Freq} = 29.11$ (Hz) and $\mathrm{CR} = 0.238\ (-)$. Additional concluding remarks from this study include:

- When operating optimally, the Stirling prime mover will operate at low-medium speed and will prioritise generating heating to cooling.
- Optimised results were populated in one of the indicated local optima in the case of the maximisation of PES and exergy efficiency.
- Conversely, optimised results are found in the global optimum domain for the EUF and ATE, which did not indicate local optima in the high speed and low cooling ratio regime.
- Finally, the conflict in the objective functions constrained the optimisation search tool to search for the optimum result at the low to mid-speed and low cooling ratio region.

System Concept II: Hybrid renewable energy system with biomass back-ups

The modelling, sizing optimisation, dynamic simulation and sensitivity analysis of this energy system configuration have been performed in Chapter 7. The mathematical models for simulating the hourly generation and storage of the system components were developed. The set of rules that coordinate the generation, storage and dispatch of power from the programmable and non-programmable system units were formulated. Subsequently, the objective functions from the standpoints of reliability, cost, emissions and size of the system were developed for the multi-objective system sizing optimisation and implemented in MATLAB with the non-dominated sorting genetic algorithm (NSGA II) optimisation method. It was implemented with the weather and load data of a test location in Southern Nigeria and a set of optimal configurations were found. High scatter is evident in the Pareto optimal set which is representative of the degree of conflict between the objective functions. This is further highlighted by the relationship between the objectives, and regarding this, the following conclusions can be drawn:

- Levelised cost of energy (LCOE) and dumped power demonstrate a positive trend while dumped power and CO_2 emissions are contradictory.
- Loss of power supply probability (LPSP) and CO_2 emissions are complementary but LCOE and LPSP are conflicting.

- The optimum configuration of the HRES from the perspectives of affordability, reliability, sustainability and compactness have been indicated in the Pareto front as well as the TOPSIS best. The following conclusions are notable:
    - Optimal configuration obtained by the TOPSIS method corresponds to the ideal solution from the standpoint of affordability, while the TOPSIS best generates more dumped power than the indicated ideal solution from the perspective of compactness.
    - The TOPSIS best shares close proximity to the ideal solution from the stand-points of reliability and sustainability.
    - These results reflect the priority set on the objective functions in the multi-criteria decision making process, where affordability of the energy is on top of the scale, followed by reliability and sustainability while compactness has the least priority.

The TOPSIS best system configuration for each dispatch case was compared to the corresponding base case, i.e., DG back-up system and these are the findings:

- Woodchips powered ST back-up in load following (LF) minimises optimal system LCOE by 50.45% compared to the base case but increases the CO_2 emissions marginally.
- Combined ST+ORC back-up in LF minimises LCOE and CO_2 emissions by 60.8% and 33.7%, respectively and reduces dumped power by 18.1 MWh but slightly increases the LPSP.
- Deploying 4-split DG in circuit charging (CC) reduces the LPSP and dumped power significantly compared to the base case while it reduces the CO_2 emissions and LCOE only marginally.
- Deploying one-big ST in CC reduces the LCOE by about 48% and improves the system reliability but increases the dumped power and emissions significantly.
- Utilising 4-split ST back-ups in CC lowers the dumped power by 10 MWh, and improves the system reliability and the energy cost by as much as 9% and 50%, respectively. However, it produces higher carbon emissions compared to the base case but less than one big-ST case.

- LCOE and CO_2 emissions reduce by 60.27% and 31.7% with the deployment of combined ST+ORC compared to the base case in CC while the LPSP increases slightly.
- LCOE and CO_2 emissions reduce by 61.4% and 33% with the deployment of 4-split ST+ORC in CC compared to the base case while the LPSP increases significantly but dumped power declines remarkably.
- Conclusively, deploying ST+ORC back-up in LF offers the least energy cost, carbon emissions and dumped power and the best system reliability for this test location based on the available data.

Based on the optimal system configuration found, dynamic simulation was performed to examine the effect of seasonal changes on the performance of the system. It is evident that the change in the climatic conditions in the test location significantly affects the system performance. Additional conclusions that can be drawn from this investigation include:

- The hybridisation of wind and solar power evidently increases the power generation from these green technologies and minimises the impact of seasonal variations on their availability.
- Frequent deployment of batteries to fulfill the load is observed in the dry season while the dispatch of the biomass fired back-up is minimised.
- Low generation of power from the green generators in the wet season increases the deployment of the back-up and leaves the battery inactive most times.
- System LCOE, LPSP, and carbon emissions are low in the dry season but increases in the wet season. However, the dry season notably increases dumped power in the system while dumped power is low in the wet season.

Finally, a sensitivity analysis was performed to investigate the impact of change in price and size of the green generators, wood chips fuel, battery, and back-up on the optimal system performance. Observed results show changes in component and fuel market price and size affect system performance and the degree of impact varies for the components. These are the conclusions drawn from this study:

- An increase in the cost of fuel increases dumped power and LCOE significantly due to the increased deployment of green generators, but substantially reduces the carbon emissions and LPSP.

- As the cost of solar PV increases, dumped power substantially reduces, but carbon emissions, LCOE and LPSP increase significantly.
- An increase in the battery cost increases LCOE and dumped power significantly but substantially reduces CO_2 emissions and LPSP.
- By increasing the WT cost, dumped power slightly decreases before increasing steeply while LCOE increases significantly, but carbon emissions and LPSP marginally increase before decreasing substantially.
- Inclusion of more renewable generators in the optimal system configuration increases dumped power and LCOE but reduces the carbon emissions and improves the system reliability.
- An increase in the number of batteries decreases the dumped power, carbon emissions and LPSP marginally but increases the LCOE substantially.
- Finally, an increase in the capacity of the back-up has no impact on the dumped power in LF but marginally increases the dumped power in CC. While it increases carbon emissions and energy cost significantly but increases LPSP only marginally.

System Concept III: Hybrid renewable energy integrated multi-carrier system

The bi-level sizing optimisation, energy management and dynamic simulation of this clean energy based decentralised system configuration have been performed in Chapter 8. The mathematical models of the system components previously developed in this research work have been deployed for this study. Additionally, some rule-based energy management strategies that modified the traditional LF and CC have been proposed to manage the operation of the integrated multi-carrier energy system. The bi-level sizing optimisation was implemented with MOEA and the optimal system configurations have been obtained. High scatter is observed in the Pareto front and this demonstrates the level of conflict in the objectives in this bi-level optimisation problem. The obtained system configurations have been deployed to investigate the impact of the proposed energy management strategies on the battery storage utilisation, start-ups of the back-up, dumped power and the generation of heating and cooling from the multi-carrier system. It is observed that the proposed EMS substantially impacts the use of the batteries, frequency of start-

ups and dispatch of the ST back-up, dumped power and generation of cooling and heating. Other remarkable conclusions drawn from this study are as follows:

- Including battery storage in the optimal system in LF reduces the system's capacity and results in 25.3%, 11.62%, 2.75%, reductions in the dumped power, CO_2 emissions and LPSP, respectively, but increases the LCOE by 4.18% compared to the system without battery.
- Similarly, when batteries are included in the optimal system in CC, the LCOE, LPSP, CO_2 emissions and dumped power reduce drastically by 30.47%, 57.41%, 60.18% and 65.8%, respectively compared to CC without battery.
- With the deployment of split ST back-up in CC, the performance of the system improves significantly as the number of splits increases for the optimal hybrid system without battery storage.
- For the optimal system inclusive of batteries, the increase in the number of splits of the back-up in CC results in a substantial decrease in the dumped power, carbon emissions and LPSP. However, the LCOE fell slightly when 2-split STs back-up was deployed but increased marginally with the deployment of 4-split STs back-up contrary to ref [83].
- Regarding the number of start-ups of the back-up, there are more start-ups of the back-up in CC than in LF which contradicts Ref. [73] . While the number of start-ups of the back-up increases with the increase in the number of splits in CC with battery storage but remains invariant when batteries are excluded.
- High dumped power is notable for the optimal systems without battery storage in CC and LF. It reduces with the increase in the number of split ST back-ups and this is more evident when batteries are excluded in the optimal system.
- Prolonged stay of the batteries in the minimum state of charge is observed in the LF mode but better utilisation is notable in the CC mode as evidenced by the high SOC of the battery most times in this mode.
- Deployment of split ST affects the battery utilisation negatively. The net power flux through the batteries declines with the increase in the number of splits and the BSS undergoes deep discharge in this mode.
- Low quality of the waste heat results in reduced dispatch of the auxiliary ORC back-up in LF compared to CC, while increased dispatch of the ORC is

witnessed when batteries are not included in CC but it reduces with the increase in the number of splits and more evidently when the optimal system includes batteries.

- Cooling generation potentials of the multi-carrier system increases with the increase in the frequency of dispatch of the back-up in both LF and CC when the optimal system excludes batteries. While the addition of battery storage to the optimal system reduces the cooling generation capacity.
- An increase in the number of split ST in CC does not affect the cooling generation capacity of the system when battery storage system is excluded but with the inclusion of battery storage, cooling generation increases with the increase in the number of splits.
- With the inclusion of batteries in the optimal system, the heating generation capacity reduces as the frequency of dispatch of the back-up reduces in both LF and CC modes.
- Heating generation increases by more than 100% with the increase in the quality of the flue gas sent to the boiler as the number of split back-ups increases in CC with or without the inclusion of battery storage systems.

9.2. Original contributions to scientific knowledge

The findings from this study contributes to the existing knowledge in the modelling, optimisation and energy management of clean energy based decentralised energy systems. Although the study explored the development of new energy system configurations for a location in Nigeria, the methods deployed are well tested and have been popularly deployed in the literature.

In the literature, several degrees of modelling efforts have been made to understand the behaviour of the Stirling engine. However, there is a consensus that the second-order thermal model of the engine offers accurate results with limited computational cost. Consequently, numerous studies targeted the improvement of the prediction accuracy of the second-order adiabatic models by considering the losses in the engine. However, most of these efforts decoupled the losses in the engine from its governing equations. Unfortunately, the losses in the engine interact with the conditions of the fluid, necessitating their direct coupling to the basic

equations of the engine. Therefore, in this study, a new approach that couples the mass and heat leakages in the engine to the governing differential equations and considers additional loss effects has been undertaken, to develop a comprehensive model of the engine with improved prediction accuracy. The developed model has been robustly validated against experimental data and compared to other theoretical model results. It predicts more accurate results of the engine's performance compared to the models developed in [64], [66], [178], [183], [245] with the exception of the model developed in [67] that predicts better results at high engine rotational speeds. The new enhanced thermal model is suitable for the dynamic simulation of the performance of the engine. This modelling effort has been documented and published in the author's paper titled, "A new non-ideal second-order thermal model with additional loss effects for simulating beta-Stirling engines".

Whilst several previous works have considered deploying a dual prime mover to improve the electrical efficiency and overall performance of a multi-carrier energy system, there are no evidence of studies that considered deploying combined Stirling engine and ORC as the prime movers of a multi-carrier system. Moreover, there are no records of similar systems that considered in-situ drying of the wood chips fuel, to regulate the quality of the fuel. Therefore, this study proposed for the first time the detailed dynamic performance of a Stirling engine driven CCHP with an ORC as the bottoming cycle, and utilising the exhaust waste heat to dry the biomass feedstock, produce cooling in an ARS and hot water in a domestic boiler. Also, the impact of cooling ratio, speed of the prime mover and quality of the biomass fuel on the system performance has been investigated by conducting parametric analysis and results were compared to the conventional separate cooling, heating and power systems. The observed results support the existing knowledge that co-generation of cooling, heating, and power results in improved performance. The steep decline in PES observed in [55] [56], [133] at high speed of the ST prime mover has been significantly reduced by deploying an ORC to recover the waste heat in this concept. Also, maximum PES and CO_2ER of 55% and 45% were obtained compared to 24.05%, 29.47% and 42% and 31.06%, 36.22%, and 46.6% recorded in Ref. [55], [56] and [133], respectively. These results have been published by the author in a paper

titled “Conceptual design and dynamic performance evaluation of a biomass fuelled micro-CCHP driven by a hybrid Stirling and ORC engine: a techno-enviro-economic assessment”.

Parametric optimisation is popular for determining the optimal operating regime of energy systems. This approach has been extensively reported in the literature for the optimisation of different energy systems. Unfortunately, there is no known record of parametric optimisation that has been performed on the multi-carrier system proposed in this study to determine its optimal operating regime. Therefore, multi-objective optimisation of the energy system was performed by simultaneously maximising the EUF, PES, exergy efficiency and ATE for the range of cooling ratios and engine frequencies simulated in the parametric analyses. The optimal operating regime of the multi-carrier system has been obtained and it provides the engine speed and mix of energy vector production that will guarantee its optimal performance. A conference paper produced by the author and titled, “Multi-objective optimal sizing of a biomass fuelled hybrid Stirling engine coupled with an ORC decentralised micro-CCHP system” summarises the findings of this work.

Previous studies have proposed three-split DG back-ups to minimise the commitment of the DG in fulfilling the load of HRES, and consequently reduce the cost and emissions. However, no previous research has considered deploying split ST powered by biomass to augment the reliability of HRES. Moreover, the inefficient operation of the back-up when fulfilling the demand in load following mode can be overcome by utilising the combined cycle configuration. While deploying combined cycle configuration is popular in improving the electrical efficiency of the prime mover in multi-carrier systems, there is no evidence of its deployment to augment the reliability of HRES. Therefore, this study proposed the deployment of split ST back-up or combined ST+ORC back-up in CC or LF to fulfill the load of a hybrid solar and wind power with battery storage system. It provides new data on the system sizing optimisation from techno-enviro-economic perspectives and establishes the existing knowledge on the relationship between the objectives. Additionally, several cases of optimal system configurations were investigated and compared to the traditional DG base case. The findings in this study support previous findings on the

deployment of split back-up but provides new insights into the potentials of replacing diesel generators with a biomass fired ST+ORC to fulfill the load of a hybrid system. These findings have been published in a journal paper by the author.

Finally, rule-based energy management strategies (EMS) are popular for managing HRES; however, they have limited application in managing integrated multi-carrier systems. Consequently, rule-based EMS that modifies the traditional approach by deploying combined cycle and split back-up to ensure the uninterrupted operation of a multi-carrier system have been proposed. The deployment of split back-ups has been established to minimise the dumped power in a HRES and improve the system's reliability. However, it is not clear how its deployment will impact the performance of the battery storage. Further, as the number of splits of the back-up increases, the frequency of start-ups of the back-up may increase and this could increase the operational cost of the system. Unfortunately, there is limited knowledge of the global impact this will have on the cost of energy of the system with or without the inclusion of batteries. Finally, it will be insightful to investigate the impact of the inclusion of BSS and split back-up on the generation of other energy vectors in the multi-carrier system. Therefore, a study was commissioned to fill these gaps and provide new insights into the impact of the deployment of split ST in the proposed rule-based EMS on the cost, reliability, emissions, dumped power, battery use optimisation and start-up costs of the system. These results have been published in a scientific journal.

9.3. Recommendations for future work

In conducting this research, several assumptions were made to simplify most of the complex processes and this may limit the accuracy of the results presented. Therefore, it is instructive to state that the results and conclusions drawn from this study are only accurate and valid within the scope clearly stated in the assumptions made in the respective pieces of work done in this thesis. To draw further insights into the modelling, optimisation and simulation of the decentralised energy systems undertaken herein, the following future works are recommended:

- The Stirling model developed in this thesis predicted accurate results at the design conditions of the experimental engine. However, it notably recorded low

prediction accuracy at off-design conditions of the engine. To improve on the prediction accuracy of the model at off-design conditions of the engine, further experimental campaigns are needed to provide new data to enable advanced modelling efforts on the off-design behaviour of the Stirling engine.

- Experimental studies are required to calibrate the performance of the multi-carrier system developed in this thesis against field data, while further studies may consider expanding the scope of work done in the parametric analysis and optimisation of the energy system by evaluating the effect of other key variables on its performance. This work may include the design optimisation of the multi-carrier system to improve its global performance.
- The work done on the energy management of the HRES integrated multi-carrier system in this thesis has been limited to only the generation potentials of the energy vectors, due to the paucity of measured data for the cooling and heating demands at the test location. Future studies should expand the scope of this work by evaluating the performance of the proposed rule-based EMS in matching the generation of several energy vectors with the hourly demand of the test location.
- Throughout this thesis, the parametric and design optimisation that have been conducted were implemented by deploying the multi-objective evolutionary genetic algorithm. Some memetic optimisation methods such as the grasshopper and ant colony optimisation methods, which could yield faster convergence rate have been proposed in the literature and may be explored for the design optimisation undertaken here to compare results.
- A modified TOPSIS has been implemented to select the best solution from the Pareto set of optimal solutions. Other decision making tools such as Fuzzy-logic and linear programming techniques for multi-dimensional analysis of preference could be explored to compare results.
- Two new rule-based energy management systems were proposed to manage the operation of the hybrid renewable energy integrated multi-carrier system and their performance were compared to the traditional EMS. Future studies may explore comparing the performance of the proposed EMS to the MILP approach to gain further insights into the strengths of the proposed EMS.

References

[1] P. Ahmadi, "Modeling, Analysis and Optimization of Integrated Energy Systems for Multigeneration Purposes," *ProQuest Diss. Theses*, no. August, p. 229, 2013 [Online]. Available: http://160.75.22.2/docview/1460765492?accountid=11638%5Cnhttp://re5tm7xf6s.search.serialssolutions.com/?ctx_ver=Z39.88-2004&ctx_enc=info:ofi/enc:UTF-8&rfr_id=info:sid/ProQuest+Dissertations+&+Theses+Global&rft_val_fmt=info:ofi/fmt:kev:mtx:dissertation&rft

[2] United Nations, "United Nations Population Fund," 2021. [Online]. Available: https://www.unfpa.org/data/world-population-dashboard. [Accessed: 20-Sep-2021]

[3] J. Skea and S. Nishioka, "Policies and practices for a low-carbon society," *Climate Policy*, vol. 8, no. 2008, pp. S5–S16, 2008.

[4] H. Meng, M. Wang, M. Aneke, X. Luo, and O. Olumayegun, "Technical performance analysis and economic evaluation of a compressed air energy storage system integrated with an organic Rankine cycle," *Fuel*, vol. 211, no. July 2017, pp. 318–330, 2018 [Online]. Available: http://dx.doi.org/10.1016/j.fuel.2017.09.042

[5] X. Luo, J. Wang, M. Dooner, and J. Clarke, "Overview of current development in electrical energy storage technologies and the application potential in power system operation q," *Appl. Energy*, vol. 137, pp. 511–536, 2015 [Online]. Available: http://dx.doi.org/10.1016/j.apenergy.2014.09.081

[6] Y. Li, "Cryogen Based Energy Storage : Process Modelling and Optimisation," no. September, 2011 [Online]. Available: http://etheses.whiterose.ac.uk/2022/1/PhD_thesis_Y._Li_200368536.pdf%5Cnhttp://etheses.whiterose.ac.uk/2022/

[7] Y. S. Mohammed, M. W. Mustafa, and N. Bashir, "Hybrid renewable energy systems for off-grid electric power: Review of substantial issues," *Renew. Sustain. Energy Rev.*, vol. 35, pp. 527–539, 2014 [Online]. Available:

http://dx.doi.org/10.1016/j.rser.2014.04.022

[8] J. Osorio, “MODELING AND OPTIMIZATION OF A CONCENTRATED SOLAR SUPERCRITICAL CO 2 POWER PLANT,” Florida State University, 2016.

[9] BP, “Statistical Review of World Energy 2021,” 2021 [Online]. Available: https://www.bp.com/content/dam/bp/business-sites/en/global/corporate/pdfs/energy-economics/statistical-review/bp-stats-review-2021-full-report.pdf

[10] I. R. E. A. IRENA, “Renewable energy statistics,” 2021. [Online]. Available: https://public.tableau.com/views/IRENARETimeSeries/Charts?:embed=y&:showVizHome=no&publish=yes&:toolbar=no

[11] S. Anuphappharadorn, S. Sukchai, C. Sirisamphanwong, and N. Ketjoy, “Comparison the economic analysis of the battery between lithium-ion and lead-acid in PV stand-alone application,” *Energy Procedia*, vol. 56, no. C, pp. 352–358, 2014 [Online]. Available: http://dx.doi.org/10.1016/j.egypro.2014.07.167

[12] D. Mikielewicz and J. Mikielewicz, “A thermodynamic criterion for selection of working fluid for subcritical and supercritical domestic micro CHP,” *Appl. Therm. Eng.*, vol. 30, no. 16, pp. 2357–2362, 2010.

[13] N. Phuangpornpitak and S. Kumar, “PV hybrid systems for rural electrification in Thailand,” *Renew. Sustain. Energy Rev.*, vol. 11, no. 7, pp. 1530–1543, 2007.

[14] I. R. Cristóbal-Monreal and R. Dufo-López, “Optimisation of photovoltaic-diesel-battery stand-alone systems minimising system weight,” *Energy Convers. Manag.*, vol. 119, pp. 279–288, 2016.

[15] S. Diaf, M. Belhamel, M. Haddadi, and A. Louche, “Technical and economic assessment of hybrid photovoltaic/wind system with battery storage in Corsica island,” *Energy Policy*, vol. 36, no. 2, pp. 743–754, 2008.

[16] P. Bajpai and V. Dash, “Hybrid renewable energy systems for power generation in stand-alone applications: A review,” *Renew. Sustain. Energy Rev.*, vol. 16, no. 5, pp. 2926–2939, 2012 [Online]. Available: http://dx.doi.org/10.1016/j.rser.2012.02.009

[17] H. Birch, “A Study Into The Feasibility of Local Renewable Energy Systems With Storage, Using Security and Sustainability Metrics for Optimisation and Evaluation,” University of Sheffield, 2015.

[18] R. Lizarte, M. E. Palacios-Lorenzo, and J. D. Marcos, “Parametric study of a novel organic Rankine cycle combined with a cascade refrigeration cycle (ORC-CRS) using natural refrigerants,” *Appl. Therm. Eng.*, vol. 127, pp. 378–389, 2017 [Online]. Available: https://doi.org/10.1016/j.applthermaleng.2017.08.063

[19] S. Singh, M. Singh, and S. C. Kaushik, “A review on optimization techniques for sizing of solar-wind hybrid energy systems,” *Int. J. Green Energy*, vol. 13, no. 15, pp. 1564–1578, 2016 [Online]. Available: http://dx.doi.org/10.1080/15435075.2016.1207079

[20] S. Baral, D. Kim, E. Yun, and K. C. Kim, “Energy, exergy and performance analysis of small-scale organic rankine cycle systems for electrical power generation applicable in rural areas of developing countries,” *Energies*, vol. 8, no. 2, pp. 684–713, 2015.

[21] A. Zahnd and H. M. Kimber, “Benefits from a renewable energy village electrification system,” *Renew. Energy*, vol. 34, no. 2, pp. 362–368, 2009 [Online]. Available: http://dx.doi.org/10.1016/j.renene.2008.05.011

[22] UNCTAD, “The Least Developed Countries Report 2017: Transformational energy access,” 2017.

[23] Nigerian Rural Electrification Agency, “Nigeria minigrid investment brief,” no. December, p. 25, 2017.

[24] S. Mandelli, J. Barbieri, R. Mereu, and E. Colombo, “Off-grid systems for rural electrification in developing countries: Definitions, classification and a comprehensive literature review,” *Renew. Sustain. Energy Rev.*, vol. 58, pp. 1621–1646, 2016.

[25] I. E. A. IEA, “CO2 Emissions from Fuel Combustion 2017 - Highlights,” *Int. Energy Agency*, vol. 1, pp. 1–162, 2017 [Online]. Available: https://www.iea.org/publications/freepublications/publication/CO2Emission

sfromFuelCombustionHighlights2017.pdf

[26] BP Energy Economics, "2018 BP Energy Outlook 2018 BP Energy Outlook," p. 125, 2018 [Online]. Available: https://www.bp.com/content/dam/bp/en/corporate/pdf/energy-economics/energy-outlook/bp-energy-outlook-2018.pdf

[27] E. O. Diemuodeke, A. Addo, I. Dabipi-Kalio, C. O. C. Oko, and Y. Mulugetta, "Domestic energy demand assessment of coastline rural communities with solar electrification," *Energy Policy Res.*, vol. 4, no. 1, pp. 1–9, 2017 [Online]. Available: https://doi.org/10.1080/23815639.2017.1280431

[28] G. Qiu, H. Liu, and S. Riffat, "Expanders for micro-CHP systems with organic Rankine cycle," *Appl. Therm. Eng.*, vol. 31, no. 16, pp. 3301–3307, 2011 [Online]. Available: http://dx.doi.org/10.1016/j.applthermaleng.2011.06.008

[29] R. Lunn, "Independent Experts Needed to Help Solve 'Energy Quadrilemma,'" *The Herald*, 2020. [Online]. Available: https://www.heraldscotland.com/news/17809085.professor-rebecca-lunn-independent-experts-needed-help-solve-energy-quadrilemma/

[30] N. E. R. C. NERC, "Power generation in Nigeria." [Online]. Available: https://nerc.gov.ng/index.php/home/nesi/403-generation. [Accessed: 21-Sep-2021]

[31] V. A. Ani, "Design of a stand-alone Photovoltaic Model for home lightings and clean environment," vol. 3, no. January, pp. 1–12, 2016.

[32] S. Sinha and S. S. Chandel, "Improving the reliability of photovoltaic-based hybrid power system with battery storage in low wind locations," *Sustain. Energy Technol. Assessments*, vol. 19, pp. 146–159, 2017 [Online]. Available: http://dx.doi.org/10.1016/j.seta.2017.01.008

[33] L. Olatomiwa, S. Mekhilef, A. S. N. Huda, and O. S. Ohunakin, "Economic evaluation of hybrid energy systems for rural electrification in six geo-political zones of Nigeria," *Renew. Energy*, vol. 83, pp. 435–446, 2015 [Online]. Available: http://dx.doi.org/10.1016/j.renene.2015.04.057

[34] L. Olatomiwa, S. Mekhilef, and O. S. Ohunakin, "Hybrid renewable power supply

for rural health clinics (RHC) in six geo-political zones of Nigeria," *Sustain. Energy Technol. Assessments*, vol. 13, pp. 1–12, 2016.

[35] A. Piacentino, C. Barbaro, F. Cardona, R. Gallea, and E. Cardona, "A comprehensive tool for efficient design and operation of polygeneration-based energy μgrids serving a cluster of buildings. Part I: Description of the method," *Appl. Energy*, vol. 111, pp. 1204–1221, 2013 [Online]. Available: http://dx.doi.org/10.1016/j.apenergy.2012.11.078

[36] M. Renzi and C. Brandoni, "Study and application of a regenerative Stirling cogeneration device based on biomass combustion," *Appl. Therm. Eng.*, vol. 67, no. 1–2, pp. 341–351, 2014 [Online]. Available: http://dx.doi.org/10.1016/j.applthermaleng.2014.03.045

[37] A. Kaabeche and R. Ibtiouen, "Techno-economic optimization of hybrid photovoltaic/wind/diesel/battery generation in a stand-alone power system," *Sol. Energy*, vol. 103, pp. 171–182, 2014 [Online]. Available: http://dx.doi.org/10.1016/j.solener.2014.02.017

[38] B. Bhandari, S. R. Poudel, K.-T. Lee, and S.-H. Ahn, "Mathematical modeling of hybrid renewable energy system: A review on small hydro-solar-wind power generation," *Int. J. Precis. Eng. Manuf. Technol.*, vol. 1, no. 2, pp. 157–173, 2014 [Online]. Available: http://link.springer.com/10.1007/s40684-014-0021-4

[39] M. S. Ismail, M. Moghavvemi, and T. M. I. Mahlia, "Design of an optimized photovoltaic and microturbine hybrid power system for a remote small community: Case study of Palestine," *Energy Convers. Manag.*, vol. 75, pp. 271–281, 2013 [Online]. Available: http://dx.doi.org/10.1016/j.enconman.2013.06.019

[40] E. D. Giannoulis and D. A. Haralambopoulos, "Distributed Generation in an isolated grid: Methodology of case study for Lesvos - Greece," *Appl. Energy*, vol. 88, no. 7, pp. 2530–2540, 2011 [Online]. Available: http://dx.doi.org/10.1016/j.apenergy.2011.01.046

[41] Y. Du, "Cold Energy Storage : Fundamentals and Applications," no. October, 2014.

[42] H. Park and R. Baldick, "Integration of compressed air energy storage systems

co-located with wind resources in the ERCOT transmission system," *Int. J. Electr. Power Energy Syst.*, vol. 90, pp. 181–189, 2017 [Online]. Available: http://dx.doi.org/10.1016/j.ijepes.2017.01.021

[43] R. Kumar, R. A. Gupta, and A. K. Bansal, "Economic analysis and power management of a stand-alone wind/photovoltaic hybrid energy system using biogeography based optimization algorithm," *Swarm Evol. Comput.*, vol. 8, pp. 33–43, 2013 [Online]. Available: http://dx.doi.org/10.1016/j.swevo.2012.08.002

[44] S. M. Elhadidy, M A.,Shaahid and S. M. Shaahid, "Optimal sizing of battery storage for hybrid (wind+ diesel) power systems," *Renew. Energy*, pp. 66–75, 1999 [Online]. Available: http://www.sciencedirect.com/science/article/pii/S0960148198007964

[45] M. A. Elhadidy and S. M. Shaahid, "Promoting applications of hybrid (wind+photovoltaic+diesel+battery) power systems in hot regions," *Renew. Energy*, vol. 29, no. 4, pp. 517–528, 2004.

[46] R. Belfkira, L. Zhang, and G. Barakat, "Optimal sizing study of hybrid wind/PV/diesel power generation unit," *Sol. Energy*, vol. 85, no. 1, pp. 100–110, 2011 [Online]. Available: http://dx.doi.org/10.1016/j.solener.2010.10.018

[47] C. Jian, C. Yanbo, and Z. Lihua, "Design and research of off-grid wind-solar hybrid power generation systems," *4th Int. Conf. Power Electron. Syst. Appl.*, pp. 1–5, 2011.

[48] A. Gonzalez, J.-R. Riba, B. Esteban, and A. Rius, "Environmental and cost optimal design of a biomass–Wind–PV electricity generation system," *Renew. Energy*, vol. 126, pp. 420–430, 2018 [Online]. Available: https://www.sciencedirect.com/science/article/pii/S0960148118303732

[49] Y. Sawle, S. C. Gupta, and A. K. Bohre, "Optimal sizing of standalone PV/Wind/Biomass hybrid energy system using GA and PSO optimization technique," *Energy Procedia*, vol. 117, pp. 690–698, 2017 [Online]. Available: http://dx.doi.org/10.1016/j.egypro.2017.05.183

[50] C. Duan, X. Wang, S. Shu, C. Jing, and H. Chang, "Thermodynamic design of Stirling engine using multi-objective particle swarm optimization algorithm,"

Energy Convers. Manag., vol. 84, pp. 88–96, 2014 [Online]. Available: http://dx.doi.org/10.1016/j.enconman.2014.04.003

[51] M. H. Ahmadi, H. Hosseinzade, H. Sayyaadi, A. H. Mohammadi, and F. Kimiaghalam, "Application of the multi-objective optimization method for designing a powered Stirling heat engine: Design with maximized power, thermal efficiency and minimized pressure loss," *Renew. Energy*, vol. 60, pp. 313–322, 2013 [Online]. Available: http://dx.doi.org/10.1016/j.renene.2013.05.005

[52] S. Toghyani, A. Kasaeian, and M. H. Ahmadi, "Multi-objective optimization of Stirling engine using non-ideal adiabatic method," *Energy Convers. Manag.*, vol. 80, pp. 54–62, 2014 [Online]. Available: http://dx.doi.org/10.1016/j.enconman.2014.01.022

[53] A. Parente, C. Galletti, J. Riccardi, M. Schiavetti, and L. Tognotti, "Experimental and numerical investigation of a micro-CHP flameless unit," *Appl. Energy*, vol. 89, no. 1, pp. 203–214, 2012 [Online]. Available: http://dx.doi.org/10.1016/j.apenergy.2011.06.055

[54] S. Thiers, B. Aoun, and B. Peuportier, "Experimental characterization, modeling and simulation of a wood pellet micro-combined heat and power unit used as a heat source for a residential building," *Energy Build.*, vol. 42, no. 6, pp. 896–903, 2010.

[55] M. Chahartaghi and M. Sheykhi, "Energy, environmental and economic evaluations of a CCHP system driven by Stirling engine with helium and hydrogen as working gases," *Energy*, vol. 174, pp. 1251–1266, 2019 [Online]. Available: https://doi.org/10.1016/j.energy.2019.03.012

[56] M. Sheykhi, M. Chahartaghi, M. M. Balakheli, B. A. Kharkeshi, and S. M. Miri, "Energy, exergy, environmental, and economic modeling of combined cooling, heating and power system with Stirling engine and absorption chiller," *Energy Convers. Manag.*, 2019.

[57] M. Korlu, J. Pirkandi, and A. Maroufi, "Thermodynamic analysis of a gas turbine cycle equipped with a non-ideal adiabatic model for a double acting Stirling

engine," *Energy Convers. Manag.*, vol. 147, pp. 120–134, 2017 [Online]. Available: http://dx.doi.org/10.1016/j.enconman.2017.04.049

[58] A. Entezari, A. Manizadeh, and R. Ahmadi, "Energetical, exergetical and economical optimization analysis of combined power generation system of gas turbine and Stirling engine," *Energy Convers. Manag.*, vol. 159, pp. 189–203, 2018.

[59] J. Hosseinpour, M. Sadeghi, A. Chitsaz, F. Ranjbar, and M. A. Rosen, "Exergy assessment and optimization of a cogeneration system based on a solid oxide fuel cell integrated with a Stirling engine," *Energy Convers. Manag.*, vol. 143, pp. 448–458, 2017 [Online]. Available: http://dx.doi.org/10.1016/j.enconman.2017.04.021

[60] M. Bahrami, A. A. Hamidi, and S. Porkhial, "Investigation of the effect of organic working fluids on thermodynamic performance of combined cycle Stirling-ORC," *Int. J. Energy Environ. Eng.*, vol. 4, no. 12, pp. 1–9, 2013.

[61] R. Z. Mathkor, B. Agnew, M. A. Al-Weshahi, and F. Latrsh, "Exergetic analysis of an integrated tri-generation organic rankine cycle," *Energies*, vol. 8, no. 8, pp. 8835–8856, 2015.

[62] N. L. Mustelier, M. F. Almeida, J. Cavalheiro, and F. Castro, "Evaluation of pellets produced with undergrowth to be used as biofuel," *Waste and Biomass Valorization*, vol. 3, no. 3, pp. 285–294, 2012.

[63] S. A. El-Ghafour, M. El-Ghandour, and N. N. Mikhael, "Three-dimensional computational fluid dynamics simulation of stirling engine," *Energy Convers. Manag.*, vol. 180, no. November 2018, pp. 533–549, 2019 [Online]. Available: https://doi.org/10.1016/j.enconman.2018.10.103

[64] I. Urieli and D. . Berchowitz, "Stirling cyle engine analysis," *Adam Hilger LTD*, 1984.

[65] T. Finkelstein, "Thermodynamic analysis of Stirling engines," *J. Spacecr. Rocket.*, vol. 4, no. 1184, pp. 1–9, 1967.

[66] M. Babaelahi and H. Sayyaadi, "A new thermal model based on polytropic numerical simulation of Stirling engines," *Appl. Energy*, vol. 141, pp. 143–159,

2015 [Online]. Available: http://dx.doi.org/10.1016/j.apenergy.2014.12.033

[67] R. Li, L. Grosu, and W. Li, "New polytropic model to predict the performance of beta and gamma type Stirling engine," *Energy*, vol. 128, pp. 62–76, 2017 [Online]. Available: http://dx.doi.org/10.1016/j.energy.2017.04.001

[68] Z. Shengjun, W. Huaixin, and G. Tao, "Performance comparison and parametric optimization of subcritical Organic Rankine Cycle (ORC) and transcritical power cycle system for low-temperature geothermal power generation," *Appl. Energy*, vol. 88, no. 8, pp. 2740–2754, 2011 [Online]. Available: http://dx.doi.org/10.1016/j.apenergy.2011.02.034

[69] F. A. Boyaghchi and H. Safari, "Parametric study and multi-criteria optimization of total exergetic and cost rates improvement potentials of a new geothermal based quadruple energy system," *Energy Convers. Manag.*, vol. 137, pp. 130–141, 2017 [Online]. Available: http://dx.doi.org/10.1016/j.enconman.2017.01.047

[70] J. Wu, Z. Tan, K. Wang, Y. Liang, and J. Zhou, "Research on multi-objective optimization model for hybrid energy system considering combination of wind power and energy storage," *Sustain.*, vol. 13, no. 6, 2021.

[71] J. Zhao and X. Yuan, "Multi-objective optimization of stand-alone hybrid PV-wind-diesel-battery system using improved fruit fly optimization algorithm," *Soft Comput.*, vol. 20, no. 7, pp. 2841–2853, 2016 [Online]. Available: http://dx.doi.org/10.1007/s00500-015-1685-6

[72] L. Olatomiwa, S. Mekhilef, M. S. Ismail, and M. Moghavvemi, "Energy management strategies in hybrid renewable energy systems: A review," *Renew. Sustain. Energy Rev.*, vol. 62, pp. 821–835, 2016 [Online]. Available: http://dx.doi.org/10.1016/j.rser.2016.05.040

[73] S. Mazzola, M. Astolfi, and E. Macchi, "A detailed model for the optimal management of a multigood microgrid," *Appl. Energy*, vol. 154, pp. 862–873, 2015 [Online]. Available: http://dx.doi.org/10.1016/j.apenergy.2015.05.078

[74] C. Ammari, D. Belatrache, B. Touhami, and S. Makhloufi, "Sizing, optimization, control and energy management of hybrid renewable energy system- a review," *Energy Built Environ.*, 2021 [Online]. Available:

https://doi.org/10.1016/j.enbenv.2021.04.002

[75] H. R. Baghaee, M. Mirsalim, and G. B. Gharehpetian, "Multi-objective optimal power management and sizing of a reliable wind/PV microgrid with hydrogen energy storage using MOPSO," *J. Intell. Fuzzy Syst.*, vol. 32, no. 3, pp. 1753–1773, 2017.

[76] M. Azaza and F. Wallin, "Multi objective particle swarm optimization of hybrid micro-grid system: A case study in Sweden," *Energy*, vol. 123, pp. 108–118, 2017 [Online]. Available: http://dx.doi.org/10.1016/j.energy.2017.01.149

[77] H. M. K. Al-Masri and A. A. Al-Sharqi, "Technical design and optimal energy management of a hybrid photovoltaic biogas energy system using multi-objective grey Wolf optimisation," *IET Renew. Power Gener.*, vol. 14, no. 14, pp. 2765–2778, 2020.

[78] A. B. Forough and R. Roshandel, "Lifetime optimization framework for a hybrid renewable energy system based on receding horizon optimization," *Energy*, vol. 150, pp. 617–630, 2018 [Online]. Available: https://doi.org/10.1016/j.energy.2018.02.158

[79] P. Rullo, L. Braccia, P. Luppi, D. Zumoffen, and D. Feroldi, "Integration of sizing and energy management based on economic predictive control for standalone hybrid renewable energy systems," *Renew. Energy*, vol. 140, pp. 436–451, 2019 [Online]. Available: https://doi.org/10.1016/j.renene.2019.03.074

[80] R. Dufo-López, J. M. Lujano-Rojas, and J. L. Bernal-Agustín, "Comparison of different lead-acid battery lifetime prediction models for use in simulation of stand-alone photovoltaic systems," *Appl. Energy*, vol. 115, pp. 242–253, 2014.

[81] A. Gupta, R. P. Saini, and M. P. Sharma, "Modelling of hybrid energy system-Part II: Combined dispatch strategies and solution algorithm," *Renew. Energy*, vol. 36, no. 2, pp. 466–473, 2011 [Online]. Available: http://dx.doi.org/10.1016/j.renene.2009.04.035

[82] B. K. Das and F. Zaman, "Performance analysis of a PV/Diesel hybrid system for a remote area in Bangladesh: Effects of dispatch strategies, batteries, and generator selection," *Energy*, vol. 169, pp. 263–276, 2019 [Online]. Available:

https://doi.org/10.1016/j.energy.2018.12.014

[83] A. S. O. Ogunjuyigbe, T. R. Ayodele, and O. A. Akinola, "Optimal allocation and sizing of PV/Wind/Split-diesel/Battery hybrid energy system for minimizing life cycle cost, carbon emission and dump energy of remote residential building," *Appl. Energy*, vol. 171, pp. 153–171, 2016 [Online]. Available: http://dx.doi.org/10.1016/j.apenergy.2016.03.051

[84] X. Lu, K. Zhou, and S. Yang, "Multi-objective optimal dispatch of microgrid containing electric vehicles," *J. Clean. Prod.*, vol. 165, pp. 1572–1581, 2017 [Online]. Available: http://dx.doi.org/10.1016/j.jclepro.2017.07.221

[85] H. Yousefi, M. H. Ghodusinejad, and A. Kasaeian, "Multi-objective optimal component sizing of a hybrid ICE + PV/T driven CCHP microgrid," *Appl. Therm. Eng.*, vol. 122, pp. 126–138, 2017 [Online]. Available: http://dx.doi.org/10.1016/j.applthermaleng.2017.05.017

[86] M. Ebrahimi and A. Keshavarz, "Sizing the prime mover of a residential micro-combined cooling heating and power (CCHP) system by multi-criteria sizing method for different climates," *Energy*, vol. 54, pp. 291–301, 2013 [Online]. Available: http://dx.doi.org/10.1016/j.energy.2013.01.061

[87] G. Chicco and P. Mancarella, "Assessment of the greenhouse gas emissions from cogeneration and trigeneration systems. Part I: Models and indicators," *Energy*, vol. 33, no. 3, pp. 410–417, 2008.

[88] D. Maraver, A. Sin, J. Royo, and F. Sebastián, "Assessment of CCHP systems based on biomass combustion for small-scale applications through a review of the technology and analysis of energy efficiency parameters," *Appl. Energy*, vol. 102, pp. 1303–1313, 2013 [Online]. Available: http://dx.doi.org/10.1016/j.apenergy.2012.07.012

[89] E. Bocci, M. Sisinni, M. Moneti, L. Vecchione, A. Di Carlo, and M. Villarini, "State of art of small scale biomass gasification power systems: A review of the different typologies," *Energy Procedia*, vol. 45, pp. 247–256, 2014 [Online]. Available: http://dx.doi.org/10.1016/j.egypro.2014.01.027

[90] I. González-Pino, A. Campos-Celador, E. Pérez-Iribarren, J. Terés-Zubiaga, and

J. M. Sala, “Parametric study of the operational and economic feasibility of Stirling micro-cogeneration devices in Spain,” *Appl. Therm. Eng.*, vol. 71, no. 2, pp. 821–829, 2014 [Online]. Available: http://dx.doi.org/10.1016/j.applthermaleng.2013.12.020

[91] A. González, J. R. Riba, R. Puig, and P. Navarro, “Review of micro- and small-scale technologies to produce electricity and heat from Mediterranean forests’ wood chips,” *Renew. Sustain. Energy Rev.*, vol. 43, pp. 143–155, 2015 [Online]. Available: http://dx.doi.org/10.1016/j.rser.2014.11.013

[92] D. Maraver, A. Sin, J. Royo, and F. Sebastián, “Assessment of CCHP systems based on biomass combustion for small-scale applications through a review of the technology and analysis of energy efficiency parameters,” *Appl. Energy*, vol. 102, pp. 1303–1313, 2013 [Online]. Available: http://dx.doi.org/10.1016/j.apenergy.2012.07.012

[93] M. Kimming *et al.*, “Biomass from agriculture in small-scale combined heat and power plants - A comparative life cycle assessment,” *Biomass and Bioenergy*, vol. 35, no. 4, pp. 1572–1581, 2011.

[94] E. Wang, Z. Yu, H. Zhang, and F. Yang, “A regenerative supercritical-subcritical dual-loop organic Rankine cycle system for energy recovery from the waste heat of internal combustion engines,” *Appl. Energy*, vol. 190, pp. 574–590, 2017 [Online]. Available: http://dx.doi.org/10.1016/j.apenergy.2016.12.122

[95] X. Wang, G. Shu, H. Tian, P. Liu, X. Li, and D. Jing, “Engine working condition effects on the dynamic response of organic Rankine cycle as exhaust waste heat recovery system,” *Appl. Therm. Eng.*, vol. 123, pp. 670–681, 2017 [Online]. Available: http://dx.doi.org/10.1016/j.applthermaleng.2017.05.088

[96] G. Shu *et al.*, “Experimental investigation on thermal OS/ORC (Oil Storage/Organic Rankine Cycle) system for waste heat recovery from diesel engine,” *Energy*, vol. 107, pp. 693–706, 2016 [Online]. Available: http://dx.doi.org/10.1016/j.energy.2016.04.062

[97] C. Zhao, S. Zheng, J. Zhang, and Y. Zhang, “Exergy and economic analysis of organic Rankine cycle hybrid system utilizing biogas and solar energy in rural

area of China," *Int. J. Green Energy*, vol. 14, no. 14, pp. 1221–1229, 2017 [Online]. Available: https://doi.org/10.1080/15435075.2017.1382362

[98] P. Liu, G. Shu, H. Tian, and X. Wang, "Engine Load Effects on the Energy and Exergy Performance of a Medium Cycle / Organic Rankine," 2018.

[99] C. Somers, A. Mortazavi, Y. Hwang, R. Radermacher, P. Rodgers, and S. Al-Hashimi, "Modeling water/lithium bromide absorption chillers in ASPEN Plus," *Appl. Energy*, vol. 88, no. 11, pp. 4197–4205, 2011 [Online]. Available: http://dx.doi.org/10.1016/j.apenergy.2011.05.018

[100] B. Kölsch and J. Radulovic, "Utilisation of diesel engine waste heat by Organic Rankine Cycle," *Appl. Therm. Eng.*, vol. 78, pp. 437–448, 2015.

[101] F. Yang *et al.*, "Parametric optimization and heat transfer analysis of a dual loop ORC (organic Rankine cycle) system for CNG engine waste heat recovery," *Energy*, vol. 118, pp. 753–775, 2017 [Online]. Available: http://dx.doi.org/10.1016/j.energy.2016.10.119

[102] N. Badea, *Design for Micro-Combined Cooling, Heating and Power Systems*. Springer Berlin Heidelberg, 2015 [Online]. Available: http://link.springer.com/10.1007/978-1-4471-6254-4

[103] A. Kaabeche, M. Belhamel, and R. Ibtiouen, "Sizing optimization of grid-independent hybrid photovoltaic/wind power generation system," *Energy*, vol. 36, no. 2, pp. 1214–1222, 2011 [Online]. Available: http://dx.doi.org/10.1016/j.energy.2010.11.024

[104] S. Bracco, F. Delfino, F. Pampararo, M. Robba, and M. Rossi, "A dynamic optimization-based architecture for polygeneration microgrids with tri-generation, renewables, storage systems and electrical vehicles," *Energy Convers. Manag.*, vol. 96, pp. 511–520, 2015 [Online]. Available: http://dx.doi.org/10.1016/j.enconman.2015.03.013

[105] A. Parisio, E. Rikos, L. Glielmo, and S. Member, "A Model Predictive Control Approach to Microgrid Operation Optimization," vol. 22, no. 5, pp. 1813–1827, 2014.

[106] R. AlBadwawi, M. Abusara, and T. Mallick, "A Review of Hybrid Solar PV and

Wind Energy System," *Smart Sci.*, vol. 3, no. 3, pp. 127–138, 2015.

[107] W. N. Macedo *et al.*, "Biomass based microturbine system for electricity generation for isolated communities in amazon region," *Renew. Energy*, vol. 91, pp. 323–333, 2016.

[108] E. Podesser, "Electricity production in rural villages with a biomass Stirling engine," *Renew. Energy*, vol. 16, no. 1–4, pp. 1049–1052, 1999 [Online]. Available: http://linkinghub.elsevier.com/retrieve/pii/S0960148198003693

[109] P. Arranz-Piera, F. Kemausuor, L. Darkwah, I. Edjekumhene, J. Cortés, and E. Velo, "Mini-grid electricity service based on local agricultural residues: Feasibility study in rural Ghana," *Energy*, vol. 153, pp. 443–454, 2018 [Online]. Available: https://www.sciencedirect.com/science/article/pii/S0360544218306650

[110] R. Dufo-López *et al.*, "Multi-objective optimization minimizing cost and life cycle emissions of stand-alone PV-wind-diesel systems with batteries storage," *Appl. Energy*, vol. 88, no. 11, pp. 4033–4041, 2011.

[111] A. G. Kraj, E. L. Bibeau, and E. Feitosa, "Simulation and Optimization of a Multi-Renewable Energy System for Remote Power Generation at Fernando de Noronha , Brazil," *Brazil Wind. 2013 Conf. Exhib.*, pp. 1–8, 2013.

[112] S. K. Bhargava, S. S. Das, and P. Paliwal, "Multi-Objective Optimization for Sizing of Solar-Wind Based Hybrid Power System : A Review," vol. 3, no. 3, pp. 195–201, 2014.

[113] D. P. Clarke, Y. M. Al-Abdeli, and G. Kothapalli, "Multi-objective optimisation of renewable hybrid energy systems with desalination," *Energy*, vol. 88, pp. 457–468, 2015.

[114] A. S. Al Busaidi, H. A. Kazem, A. H. Al-Badi, and M. Farooq Khan, "A review of optimum sizing of hybrid PV-Wind renewable energy systems in oman," *Renewable and Sustainable Energy Reviews*, vol. 53. pp. 185–193, 2016.

[115] M. I. Efunbote and M. B. Adeleke, "Design of Hybrid Solar-Wind Power System for a Coaster Area in Lagos State , South Western," vol. 2, no. 3, pp. 135–152, 2015.

[116] S. Bhakta, V. Mukherjee, and B. Shaw, "Techno-economic analysis of standalone photovoltaic/wind hybrid system for application in isolated hamlets of North-East India," *J. Renew. Sustain. Energy*, vol. 7, no. 2, 2015.

[117] S. Bhakta and V. Mukherjee, *Techno-economic viability analysis of fixed-tilt and two axis tracking stand-alone photovoltaic power system for Indian bio-climatic classification zones*, vol. 9, no. 1. 2017.

[118] M. S. Adaramola, M. Agelin-Chaab, and S. S. Paul, "Analysis of hybrid energy systems for application in southern Ghana," *Energy Convers. Manag.*, vol. 88, no. 2014, pp. 284–295, 2014 [Online]. Available: http://dx.doi.org/10.1016/j.enconman.2014.08.029

[119] I. Tégani, A. Aboubou, M. Y. Ayad, M. Becherif, R. Saadi, and O. Kraa, "Optimal sizing design and energy management of stand-alone photovoltaic/wind generator systems," *Energy Procedia*, vol. 50, no. 0, pp. 163–170, 2014 [Online]. Available: http://dx.doi.org/10.1016/j.egypro.2014.06.020

[120] A. Maleki, M. A. Rosen, and F. Pourfayaz, "Optimal Operation of a Grid-Connected Hybrid Renewable Energy System for Residential Applications," 2017.

[121] X. Xu, W. Hu, D. Cao, Q. Huang, C. Chen, and Z. Chen, "Optimized sizing of a standalone PV-wind-hydropower station with pumped-storage installation hybrid energy system," *Renew. Energy*, vol. 147, pp. 1418–1431, 2020.

[122] K. Y. Lau, M. F. M. Yousof, S. N. M. Arshad, M. Anwari, and A. H. M. Yatim, "Performance analysis of hybrid photovoltaic/diesel energy system under Malaysian conditions," *Energy*, vol. 35, no. 8, pp. 3245–3255, 2010 [Online]. Available: http://dx.doi.org/10.1016/j.energy.2010.04.008

[123] E. M. Nfah and J. M. Ngundam, "Modelling of wind/Diesel/battery hybrid power systems for far North Cameroon," *Energy Convers. Manag.*, vol. 49, no. 6, pp. 1295–1301, 2008.

[124] A. M. Patel and S. K. Singal, "Economic analysis of integrated renewable energy system for electrification of remote rural area having scattered population," *Int. J. Renew. Energy Res.*, vol. 8, no. 1, pp. 523–539, 2018.

[125] S. G. Sigarchian, R. Paleta, A. Malmquist, and A. Pina, “Feasibility study of using a biogas engine as backup in a decentralized hybrid (PV/wind/battery) power generation system - Case study Kenya,” *Energy*, vol. 90, pp. 1830–1841, 2015.

[126] H. Ghaebi, T. Parikhani, H. Rostamzadeh, and B. Farhang, “Thermodynamic and thermoeconomic analysis and optimization of a novel combined cooling and power (CCP) cycle by integrating of ejector refrigeration and Kalina cycles,” *Energy*, vol. 139, pp. 262–276, 2017 [Online]. Available: https://doi.org/10.1016/j.energy.2017.07.154

[127] I. González-Pino, A. Campos-Celador, E. Pérez-Iribarren, J. Terés-Zubiaga, and J. M. Sala, “Parametric study of the operational and economic feasibility of Stirling micro-cogeneration devices in Spain,” *Appl. Therm. Eng.*, vol. 71, no. 2, pp. 821–829, 2014 [Online]. Available: http://dx.doi.org/10.1016/j.applthermaleng.2013.12.020

[128] S. R. Asaee, V. I. Ugursal, and I. Beausoleil-Morrison, “Techno-economic evaluation of internal combustion engine based cogeneration system retrofits in Canadian houses - A preliminary study,” *Appl. Energy*, vol. 140, pp. 171–183, 2015 [Online]. Available: http://dx.doi.org/10.1016/j.apenergy.2014.11.068

[129] P. Arbabi, A. Abbassi, Z. Mansoori, and M. Seyfi, “Joint numerical-technical analysis and economical evaluation of applying small internal combustion engines in combined heat and power (CHP),” *Appl. Therm. Eng.*, vol. 113, pp. 694–704, 2017 [Online]. Available: http://dx.doi.org/10.1016/j.applthermaleng.2016.11.064

[130] A. C. Ferreira, M. L. Nunes, J. C. F. Teixeira, L. A. S. B. Martins, and S. F. C. F. Teixeira, “Thermodynamic and economic optimization of a solar-powered Stirling engine for micro-cogeneration purposes,” *Energy*, vol. 111, no. 2016, pp. 1–17, 2016.

[131] E. Cardozo and A. Malmquist, “Performance comparison between the use of wood and sugarcane bagasse pellets in a Stirling engine micro-CHP system,” *Appl. Therm. Eng.*, vol. 159, no. May, p. 113945, 2019 [Online]. Available: https://doi.org/10.1016/j.applthermaleng.2019.113945

[132] H. Damirchi *et al.*, "Micro Combined Heat and Power to provide heat and electrical power using biomass and Gamma-type Stirling engine," *Appl. Therm. Eng.*, vol. 103, pp. 1460–1469, 2016 [Online]. Available: http://dx.doi.org/10.1016/j.applthermaleng.2016.04.118

[133] M. Sheykhi, M. Chahartaghi, M. M. Balakheli, S. M. Hashemian, S. M. Miri, and N. Rafiee, "Performance investigation of a combined heat and power system with internal and external combustion engines," *Energy Convers. Manag.*, vol. 185, no. November 2018, pp. 291–303, 2019.

[134] M. Rokni, "Thermodynamic analysis of SOFC (solid oxide fuel cell)-Stirling hybrid plants using alternative fuels," *Energy*, vol. 61, pp. 87–97, 2013 [Online]. Available: http://dx.doi.org/10.1016/j.energy.2013.06.001

[135] M. Rokni, "Thermodynamic analyses of municipal solid waste gasification plant integrated with solid oxide fuel cell and Stirling hybrid system," *Int. J. Hydrogen Energy*, vol. 40, no. 24, pp. 7855–7869, 2015 [Online]. Available: http://dx.doi.org/10.1016/j.ijhydene.2014.11.046

[136] M. Mehrpooya and M. M. M. Sharifzadeh, "Conceptual and basic design of a novel integrated cogeneration power plant energy system," *Energy*, vol. 127, pp. 516–533, 2017 [Online]. Available: http://dx.doi.org/10.1016/j.energy.2017.03.127

[137] L. Khani, S. M. S. Mahmoudi, A. Chitsaz, and M. A. Rosen, "Energy and exergoeconomic evaluation of a new power/cooling cogeneration system based on a solid oxide fuel cell," *Energy*, vol. 94, pp. 64–77, 2016 [Online]. Available: http://dx.doi.org/10.1016/j.energy.2015.11.001

[138] O. J. Ogorure, C. O. C. Oko, E. O. Diemuodeke, and K. Owebor, "Energy, exergy, environmental and economic analysis of an agricultural waste-to-energy integrated multigeneration thermal power plant," *Energy Convers. Manag.*, vol. 171, no. March, pp. 222–240, 2018.

[139] S. Sanaye and A. Katebi, "4E analysis and multi objective optimization of a micro gas turbine and solid oxide fuel cell hybrid combined heat and power system," *J. Power Sources*, vol. 247, pp. 294–306, 2014 [Online]. Available:

http://dx.doi.org/10.1016/j.jpowsour.2013.08.065

[140] S. Javan, V. Mohamadi, P. Ahmadi, and P. Hanafizadeh, "Fluid selection optimization of a combined cooling, heating and power (CCHP) system for residential applications," *Appl. Therm. Eng.*, vol. 96, pp. 26–38, 2016 [Online]. Available: http://dx.doi.org/10.1016/j.applthermaleng.2015.11.060

[141] M. Rokni, "Design and analysis of a waste gasification energy system with solid oxide fuel cells and absorption chillers," *Int. J. Hydrogen Energy*, vol. 43, no. 11, pp. 5922–5938, 2018 [Online]. Available: https://doi.org/10.1016/j.ijhydene.2017.10.123

[142] S. Karellas and K. Braimakis, "Energy-exergy analysis and economic investigation of a cogeneration and trigeneration ORC-VCC hybrid system utilizing biomass fuel and solar power," *Energy Convers. Manag.*, vol. 107, pp. 103–113, 2016 [Online]. Available: http://dx.doi.org/10.1016/j.enconman.2015.06.080

[143] R. Karami and H. Sayyaadi, "Optimal sizing of Stirling-CCHP systems for residential buildings at diverse climatic conditions," *Appl. Therm. Eng.*, vol. 89, pp. 377–393, 2015 [Online]. Available: http://dx.doi.org/10.1016/j.applthermaleng.2015.06.022

[144] M. Ebrahimi and E. Derakhshan, "Design and evaluation of a micro combined cooling, heating, and power system based on polymer exchange membrane fuel cell and thermoelectric cooler," *Energy Convers. Manag.*, vol. 171, no. June, pp. 507–517, 2018 [Online]. Available: https://doi.org/10.1016/j.enconman.2018.06.007

[145] M. Chahartaghi and B. A. Kharkeshi, "Performance analysis of a combined cooling, heating and power system with PEM fuel cell as a prime mover," *Appl. Therm. Eng.*, vol. 128, pp. 805–817, 2018 [Online]. Available: https://doi.org/10.1016/j.applthermaleng.2017.09.072

[146] B. J. Kaldehi, A. Keshavarz, A. A. Safaei Pirooz, A. Batooei, and M. Ebrahimi, "Designing a micro Stirling engine for cleaner production of combined cooling heating and power in residential sector of different climates," *J. Clean. Prod.*,

vol. 154, pp. 502–516, 2017 [Online]. Available: http://dx.doi.org/10.1016/j.jclepro.2017.04.006

[147] J. Harrod and P. J. Mago, "Performance analysis of a combined cooling, heating, and power system driven by a waste biomass fired Stirling engine," *Proc. Inst. Mech. Eng. Part C J. Mech. Eng. Sci.*, vol. 225, no. 2, pp. 420–428, 2011.

[148] M. Ebrahimi, "The environ-thermo-economical potentials of operating gas turbines in industry for combined cooling, heating, power and process (CCHPP)," *J. Clean. Prod.*, vol. 142, pp. 4258–4269, 2017 [Online]. Available: http://dx.doi.org/10.1016/j.jclepro.2016.12.001

[149] H. Ansarinasab and M. Mehrpooya, "Investigation of a combined molten carbonate fuel cell, gas turbine and Stirling engine combined cooling heating and power (CCHP) process by exergy cost sensitivity analysis," *Energy Convers. Manag.*, vol. 165, no. March, pp. 291–303, 2018 [Online]. Available: https://doi.org/10.1016/j.enconman.2018.03.067

[150] F. A. Al-Sulaiman, I. Dincer, and F. Hamdullahpur, "Energy analysis of a trigeneration plant based on solid oxide fuel cell and organic Rankine cycle," *Int. J. Hydrogen Energy*, vol. 35, no. 10, pp. 5104–5113, 2010 [Online]. Available: http://dx.doi.org/10.1016/j.ijhydene.2009.09.047

[151] M. Mehrpooya, S. Sayyad, and M. J. Zonouz, "Energy, exergy and sensitivity analyses of a hybrid combined cooling, heating and power (CCHP) plant with molten carbonate fuel cell (MCFC) and Stirling engine," *J. Clean. Prod.*, vol. 148, pp. 283–294, 2017 [Online]. Available: http://dx.doi.org/10.1016/j.jclepro.2017.01.157

[152] P. Ahmadi, I. Dincer, and M. A. Rosen, "Multi-objective optimization of a novel solar-based multigeneration energy system," *Sol. Energy*, vol. 108, pp. 576–591, 2014 [Online]. Available: http://dx.doi.org/10.1016/j.solener.2014.07.022

[153] A. Mohammadi and M. Mehrpooya, "Energy and exergy analyses of a combined desalination and CCHP system driven by geothermal energy," *Appl. Therm. Eng.*, vol. 116, pp. 685–694, 2017 [Online]. Available: http://dx.doi.org/10.1016/j.applthermaleng.2017.01.114

[154] P. Ahmadi, I. Dincer, and M. A. Rosen, "Thermodynamic modeling and multi-objective evolutionary-based optimization of a new multigeneration energy system," *Energy Convers. Manag.*, vol. 76, pp. 282–300, 2013 [Online]. Available: http://dx.doi.org/10.1016/j.enconman.2013.07.049

[155] S. Bracco, F. Delfino, F. Pampararo, M. Robba, and M. Rossi, "A mathematical model for the optimal operation of the University of Genoa Smart Polygeneration Microgrid: Evaluation of technical, economic and environmental performance indicators," *Energy*, vol. 64, pp. 912–922, 2014.

[156] J. M. Lujano-Rojas, R. Dufo-López, J. L. Atencio-Guerra, E. M. G. Rodrigues, J. L. Bernal-Agustín, and J. P. S. Catalão, "Operating conditions of lead-acid batteries in the optimization of hybrid energy systems and microgrids," *Appl. Energy*, vol. 179, pp. 590–600, 2016 [Online]. Available: http://dx.doi.org/10.1016/j.apenergy.2016.07.018

[157] J. Bert, D. Chrenko, T. Sophy, L. Le Moyne, and F. Sirot, "Simulation, experimental validation and kinematic optimization of a Stirling engine using air and helium," *Energy*, vol. 78, pp. 701–712, 2014.

[158] J. Podešva and Z. Poruba, "The Stirling engine mechanism optimization," *Perspect. Sci.*, vol. 7, pp. 341–346, 2016 [Online]. Available: http://linkinghub.elsevier.com/retrieve/pii/S2213020915001020

[159] J. A. Araoz, E. Cardozo, M. Salomon, L. Alejo, and T. H. Fransson, "Development and validation of a thermodynamic model for the performance analysis of a gamma Stirling engine prototype," *Appl. Therm. Eng.*, vol. 83, pp. 16–30, 2015 [Online]. Available: http://dx.doi.org/10.1016/j.applthermaleng.2015.03.006

[160] K. Wang, S. R. Sanders, S. Dubey, F. H. Choo, and F. Duan, "Stirling cycle engines for recovering low and moderate temperature heat: A review," *Renew. Sustain. Energy Rev.*, vol. 62, pp. 89–108, 2016 [Online]. Available: http://dx.doi.org/10.1016/j.rser.2016.04.031

[161] J. A. Araoz, M. Salomon, L. Alejo, and T. H. Fransson, "Numerical simulation for the design analysis of kinematic Stirling engines," *Appl. Energy*, vol. 159, 2015.

[162] M. H. Ahmadi, M. A. Ahmadi, and F. Pourfayaz, "Thermal models for analysis of

performance of Stirling engine: A review," *Renew. Sustain. Energy Rev.*, vol. 68, no. July 2015, pp. 168–184, 2017 [Online]. Available: http://dx.doi.org/10.1016/j.rser.2016.09.033

[163] H. Hachem, R. Gheith, F. Aloui, and S. Ben Nasrallah, "Technological challenges and optimization efforts of the Stirling machine: A review," *Energy Convers. Manag.*, vol. 171, no. March, pp. 1365–1387, 2018.

[164] N. Izadiamoli and H. Sayyaadi, "Conceptual design, optimization, and assessment of a hybrid Otto-Stirling engine/cooler for recovering the thermal energy of the exhaust gasses for automotive applications," *Energy Convers. Manag.*, vol. 171, no. April, pp. 1063–1082, 2018 [Online]. Available: https://doi.org/10.1016/j.enconman.2018.06.056

[165] J. Egas, "Stirling Engine Configuration Selection," *Energies*, pp. 1–22, 2018.

[166] B. Kongtragool and S. Wongwises, "Investigation on power output of the gamma-configuration low temperature differential Stirling engines," *Renew. Energy*, vol. 30, no. 3, pp. 465–476, 2005.

[167] W. T. Beale, J. G. Wood, and B. F. Chagnot, "Stirling engine for developing countries," *Am Inst Aeronaut Astronaut*, no. 1971–5, 1980.

[168] D. Gedeon and J. G. Wood, "Oscillating flow regenerator test rig: hardware and theory with derived correlations for screens and felts," 1996.

[169] G. Walker, "Elementary design guidelines for Stirling engines," in *Proceedings of the 14th Intersociety Energy Conversion Engineering Conference*, 1979.

[170] G. Schmidt, "Theorie der Lehmannschen calorischen maschine," *Zeitschrift des Vereines Dtsch. Ingenieure*, vol. 15, no. 1–12, pp. 97–112, 1871.

[171] W. Martini, "Stirling Engine Design Manual Conservation and Renewable Energy," *Methods*, p. 412, 1983.

[172] C. H. Cheng and H. S. Yang, "Optimization of geometrical parameters for Stirling engines based on theoretical analysis," *Appl. Energy*, vol. 92, pp. 395–405, 2012 [Online]. Available: http://dx.doi.org/10.1016/j.apenergy.2011.11.046

[173] D. Dai, Z. Liu, F. Yuan, R. Long, and W. Liu, "Finite time thermodynamic analysis

of a solar duplex Stirling refrigerator," *Appl. Therm. Eng.*, vol. 156, no. August 2018, pp. 597–605, 2019 [Online]. Available: https://doi.org/10.1016/j.applthermaleng.2019.04.098

[174] M. H. Ahmadi, M. A. Ahmadi, F. Pourfayaz, M. Bidi, H. Hosseinzade, and M. Feidt, "Optimization of powered Stirling heat engine with finite speed thermodynamics," *Energy Convers. Manag.*, vol. 108, pp. 96–105, 2016 [Online]. Available: http://dx.doi.org/10.1016/j.enconman.2015.11.005

[175] M. Costea, S. Petrescu, and C. Harman, "Effect of irreversibilities on solar Stirling engine cycle performance," *Energy Convers. Manag.*, vol. 40, no. 15, pp. 1723–1731, 1999.

[176] S. Petrescu, M. Costea, C. Harman, and T. Florea, "Application of the direct method to irreversibile Stirling cycles with finite speed," *Int. J. Energy Res*, vol. 26, pp. 589–609, 2002.

[177] S. Petrescu and M. Costea, "Development of thermodynamics with finite speed and direct method.," *Ed. AGIR*, 2011.

[178] H. Hosseinzade, H. Sayyaadi, and M. Babaelahi, "A new closed-form analytical thermal model for simulating Stirling engines based on polytropic-finite speed thermodynamics," *Energy Convers. Manag.*, vol. 90, pp. 395–408, 2015 [Online]. Available: http://dx.doi.org/10.1016/j.enconman.2014.11.043

[179] M. Chahartaghi and M. Sheykhi, "Thermal modeling of a trigeneration system based on beta-type Stirling engine for reductions of fuel consumption and pollutant emission," *J. Clean. Prod.*, vol. 205, pp. 145–162, 2018 [Online]. Available: https://doi.org/10.1016/j.jclepro.2018.09.008

[180] Y. T. Ã, I. Tlili, and S. Ben Nasrallah, "Design and performance optimization of GPU-3 Stirling engines," *Energy*, vol. 33, pp. 1100–1114, 2008.

[181] C. H. Cheng, H. S. Yang, and L. Keong, "Theoretical and experimental study of a 300-W beta-type Stirling engine," *Energy*, vol. 59, pp. 590–599, 2013 [Online]. Available: http://dx.doi.org/10.1016/j.energy.2013.06.060

[182] S. Alfarawi, R. Al-Dadah, and S. Mahmoud, "Enhanced thermodynamic modelling of a gamma-type Stirling engine," *Appl. Therm. Eng.*, vol. 106, pp.

1380–1390, 2016 [Online]. Available: http://dx.doi.org/10.1016/j.applthermaleng.2016.06.145

[183] M. Babaelahi and H. Sayyaadi, "Simple-II: A new numerical thermal model for predicting thermal performance of Stirling engines," *Energy*, vol. 69, pp. 873–890, 2014 [Online]. Available: http://dx.doi.org/10.1016/j.energy.2014.03.084

[184] M. Babaelahi and H. Sayyaadi, "Modified PSVL: A second order model for thermal simulation of Stirling engines based on convective-polytropic heat transfer of working spaces," *Appl. Therm. Eng.*, vol. 85, pp. 340–355, 2015 [Online]. Available: http://dx.doi.org/10.1016/j.applthermaleng.2015.03.018

[185] H. Sayyaadi and H. Ghasemi, "A novel second-order thermal model of Stirling engines with consideration of losses due to the speed of the crack system," *Energy Convers. Manag.*, 2018.

[186] J. A. Araoz, M. Salomon, L. Alejo, and T. H. Fransson, "Non-ideal Stirling engine thermodynamic model suitable for the integration into overall energy systems," *Appl. Therm. Eng.*, vol. 73, no. 1, pp. 203–219, 2014 [Online]. Available: http://dx.doi.org/10.1016/j.applthermaleng.2014.07.050

[187] S. Toghyani, A. Kasaeian, S. H. Hashemabadi, and M. Salimi, "Multi-objective optimization of GPU3 Stirling engine using third order analysis," *Energy Convers. Manag.*, vol. 87, pp. 521–529, 2014 [Online]. Available: http://dx.doi.org/10.1016/j.enconman.2014.06.066

[188] W. Jan and P. Marek, "Mathematical Modeling of the Stirling Engine," *Procedia Eng.*, vol. 157, pp. 349–356, 2016 [Online]. Available: http://dx.doi.org/10.1016/j.proeng.2016.08.376

[189] M. A. Mohammadi and A. Jafarian, "CFD simulation to investigate hydrodynamics of oscillating flow in a beta-type Stirling engine," *Energy*, vol. 153, pp. 287–300, 2018 [Online]. Available: https://doi.org/10.1016/j.energy.2018.04.017

[190] A. Abuelyamen, R. Ben-Mansour, H. Abualhamayel, and E. M. A. Mokheimer, "Parametric study on beta-type Stirling engine," *Energy Convers. Manag.*, vol. 145, pp. 53–63, 2017 [Online]. Available:

http://dx.doi.org/10.1016/j.enconman.2017.04.098

[191] A. Abuelyamen and R. Ben-Mansour, "Energy efficiency comparison of Stirling engine types (α, β, and γ) using detailed CFD modeling," *Int. J. Therm. Sci.*, vol. 132, no. May, pp. 411–423, 2018 [Online]. Available: https://doi.org/10.1016/j.ijthermalsci.2018.06.026

[192] A. K. Almajri, S. Mahmoud, and R. Al-Dadah, "Modelling and parametric study of an efficient Alpha type Stirling engine performance based on 3D CFD analysis," *Energy Convers. Manag.*, vol. 145, pp. 93–106, 2017 [Online]. Available: http://dx.doi.org/10.1016/j.enconman.2017.04.073

[193] G. Xiao *et al.*, "Design optimization with computational fluid dynamic analysis of β-type Stirling engine," *Appl. Therm. Eng.*, vol. 113, pp. 87–102, 2017 [Online]. Available: http://dx.doi.org/10.1016/j.applthermaleng.2016.10.063

[194] S. Alfarawi, R. AL-Dadah, and S. Mahmoud, "Influence of phase angle and dead volume on gamma-type Stirling engine power using CFD simulation," *Energy Convers. Manag.*, vol. 124, pp. 130–140, 2016 [Online]. Available: http://dx.doi.org/10.1016/j.enconman.2016.07.016

[195] G. Shu, M. Zhao, H. Tian, Y. Huo, and W. Zhu, "Experimental comparison of R123 and R245fa as working fluids for waste heat recovery from heavy-duty diesel engine," *Energy*, vol. 115, pp. 756–769, 2016 [Online]. Available: http://dx.doi.org/10.1016/j.energy.2016.09.082

[196] F. Yang, H. Zhang, S. Song, C. Bei, H. Wang, and E. Wang, "Thermoeconomic multi-objective optimization of an organic Rankine cycle for exhaust waste heat recovery of a diesel engine," *Energy*, vol. 93, pp. 2208–2228, 2015 [Online]. Available: http://dx.doi.org/10.1016/j.energy.2015.10.117

[197] C. W. Chan, J. Ling-Chin, and A. P. Roskilly, "A review of chemical heat pumps, thermodynamic cycles and thermal energy storage technologies for low grade heat utilisation," *Appl. Therm. Eng.*, vol. 50, no. 1, pp. 1257–1273, 2013 [Online]. Available: http://dx.doi.org/10.1016/j.applthermaleng.2012.06.041

[198] E. H. Wang, H. G. Zhang, Y. Zhao, B. Y. Fan, Y. T. Wu, and Q. H. Mu, "Performance analysis of a novel system combining a dual loop organic Rankine cycle (ORC)

with a gasoline engine," *Energy*, vol. 43, no. 1, pp. 385–395, 2012.

[199] S. H. Kang, "Design and experimental study of ORC (organic Rankine cycle) and radial turbine using R245fa working fluid," *Energy*, vol. 41, no. 1, pp. 514–524, 2012 [Online]. Available: http://dx.doi.org/10.1016/j.energy.2012.02.035

[200] J. Ni *et al.*, "Dynamic simulation and analysis of Organic Rankine Cycle system for waste recovery from diesel engine," *Energy Procedia*, vol. 142, pp. 1274–1281, 2017 [Online]. Available: https://doi.org/10.1016/j.egypro.2017.12.485

[201] U. Muhammad, M. Imran, D. H. Lee, and B. S. Park, "Design and experimental investigation of a 1 kW organic Rankine cycle system using R245fa as working fluid for low-grade waste heat recovery from steam," *Energy Convers. Manag.*, vol. 103, pp. 1089–1100, 2015 [Online]. Available: http://dx.doi.org/10.1016/j.enconman.2015.07.045

[202] J. Wang, Z. Yan, P. Zhao, and Y. Dai, "Off-design performance analysis of a solar-powered organic Rankine cycle," *Energy Convers. Manag.*, vol. 80, pp. 150–157, 2014 [Online]. Available: http://dx.doi.org/10.1016/j.enconman.2014.01.032

[203] B. F. Tchanche, G. Lambrinos, A. Frangoudakis, and G. Papadakis, "Exergy analysis of micro-organic Rankine power cycles for a small scale solar driven reverse osmosis desalination system," *Appl. Energy*, vol. 87, no. 4, pp. 1295–1306, 2010 [Online]. Available: http://dx.doi.org/10.1016/j.apenergy.2009.07.011

[204] E. Bou Lawz Ksayer, "Design of an ORC system operating with solar heat and producing sanitary hot water," *Energy Procedia*, vol. 6, pp. 389–395, 2011 [Online]. Available: http://dx.doi.org/10.1016/j.egypro.2011.05.045

[205] J. C. Rojas-Zerpa and J. M. Yusta, "Application of multicriteria decision methods for electric supply planning in rural and remote areas," *Renew. Sustain. Energy Rev.*, vol. 52, pp. 557–571, 2015.

[206] L. Ã. Bernal-agustı, R. Dufo-lo, and D. M. Rivas-ascaso, "Design of isolated hybrid systems minimizing costs and pollutant emissions," vol. 31, pp. 2227–2244, 2006.

[207] R. Dufo-López, I. R. Cristóbal-Monreal, and J. M. Yusta, "Optimisation of PV-wind-diesel-battery stand-alone systems to minimise cost and maximise

human development index and job creation," *Renew. Energy*, vol. 94, pp. 280–293, 2016.

[208] S. Sinha and S. S. Chandel, "Review of software tools for hybrid renewable energy systems," *Renew. Sustain. Energy Rev.*, vol. 32, pp. 192–205, 2014 [Online]. Available: http://dx.doi.org/10.1016/j.rser.2014.01.035

[209] J. L. Bernal-agustín, R. Dufo-lópez, and D. M. Rivas-ascaso, "Design of Isolated Hybrid Systems Minimizing Costs and Pollutant Emissions," vol. 31, pp. 2227–2244, 2005.

[210] H. R. Baghaee, M. Mirsalim, G. B. Gharehpetian, and H. A. Talebi, "Reliability/cost-based multi-objective Pareto optimal design of stand-alone wind/PV/FC generation microgrid system," *Energy*, vol. 115, pp. 1022–1041, 2016 [Online]. Available: http://dx.doi.org/10.1016/j.energy.2016.09.007

[211] A. Saif, K. G. Elrab, H. H. Zeineldin, S. Kennedy, and J. L. Kirtley, "Multi-objective capacity planning of a PV-wind-diesel-battery hybrid power system," in *2010 IEEE International Energy Conference and Exhibition, EnergyCon 2010*, 2010, pp. 217–222.

[212] H. Moradi, M. Esfahanian, A. Abtahi, and A. Zilouchian, "Optimization and energy management of a standalone hybrid microgrid in the presence of battery storage system," *Energy*, vol. 147, pp. 226–238, 2018 [Online]. Available: https://doi.org/10.1016/j.energy.2018.01.016

[213] O. B. B, N. D, S. V, A. N. P, and N. M, "Multi-objective optimization of hybrid PV/wind/diesel/battery systems for decentralized application by minimizing the levelized cost of energy and the CO2 emissions," *Int. J. Phys. Sci.*, vol. 10, no. 5, pp. 192–203, 2015 [Online]. Available: http://academicjournals.org/journal/IJPS/article-abstract/AFFFBE050836

[214] T. Leejarkpai, T. Mungcharoen, and U. Suwanmanee, "Comparative assessment of global warming impact and eco-efficiency of PS (polystyrene), PET (polyethylene terephthalate) and PLA (polylactic acid) boxes," *J. Clean. Prod.*, vol. 125, pp. 95–107, 2016 [Online]. Available: http://dx.doi.org/10.1016/j.jclepro.2016.03.029

[215] H. Shayeghi and Y. Hashemi, “Application of fuzzy decision-making based on INSGA-II to designing PV-wind hybrid system,” *Eng. Appl. Artif. Intell.*, vol. 45, pp. 1–17, 2015.

[216] P. Nagapurkar and J. D. Smith, “Techno-economic optimization and environmental Life Cycle Assessment (LCA) of microgrids located in the US using genetic algorithm,” *Energy Convers. Manag.*, vol. 181, no. November 2018, pp. 272–291, 2019 [Online]. Available: https://doi.org/10.1016/j.enconman.2018.11.072

[217] A. L. Bukar, C. W. Tan, and K. Y. Lau, “Optimal sizing of an autonomous photovoltaic/wind/battery/diesel generator microgrid using grasshopper optimization algorithm,” *Sol. Energy*, vol. 188, no. March, pp. 685–696, 2019 [Online]. Available: https://doi.org/10.1016/j.solener.2019.06.050

[218] A. T. D. Perera, R. A. Attalage, K. K. C. K. Perera, and V. P. C. Dassanayake, “A hybrid tool to combine multi-objective optimization and multi-criterion decision making in designing standalone hybrid energy systems,” *Appl. Energy*, vol. 107, pp. 412–425, 2013 [Online]. Available: http://dx.doi.org/10.1016/j.apenergy.2013.02.049

[219] S. Sanaye, M. M. Ghafurian, and F. T. Dastjerd, “Applying Relative Net Present or Relative Net Future Worth Benefit and exergy efficiency for optimum selection of a natural gas engine based CCHP system for a hotel building,” *J. Nat. Gas Sci. Eng.*, vol. 34, pp. 305–317, 2016 [Online]. Available: http://dx.doi.org/10.1016/j.jngse.2016.06.038

[220] H. Shayeghi and Y. Hashemi, “Engineering Applications of Arti fi cial Intelligence Application of fuzzy decision-making based on INSGA-II to designing PV – wind hybrid system,” *Eng. Appl. Artif. Intell.*, vol. 45, pp. 1–17, 2015 [Online]. Available: http://dx.doi.org/10.1016/j.engappai.2015.04.013

[221] A. L. Bukar, C. W. Tan, L. K. Yiew, R. Ayop, and W. S. Tan, “A rule-based energy management scheme for long-term optimal capacity planning of grid-independent microgrid optimized by multi-objective grasshopper optimization algorithm,” *Energy Convers. Manag.*, vol. 221, no. June, 2020.

[222] M. Belouda, M. Hajjaji, H. Sliti, and A. Mami, “Bi-objective optimization of a standalone hybrid PV–Wind–battery system generation in a remote area in Tunisia,” *Sustain. Energy, Grids Networks*, vol. 16, pp. 315–326, 2018 [Online]. Available: https://doi.org/10.1016/j.segan.2018.09.005

[223] D. Sadeghi, A. Hesami Naghshbandy, and S. Bahramara, “Optimal sizing of hybrid renewable energy systems in presence of electric vehicles using multi-objective particle swarm optimization,” *Energy*, vol. 209, p. 118471, 2020 [Online]. Available: https://doi.org/10.1016/j.energy.2020.118471

[224] S. Barakat, H. Ibrahim, and A. A. Elbaset, “Multi-objective optimization of grid-connected PV-wind hybrid system considering reliability, cost, and environmental aspects,” *Sustain. Cities Soc.*, vol. 60, no. April, p. 102178, 2020 [Online]. Available: https://doi.org/10.1016/j.scs.2020.102178

[225] M. A. M. Ramli, H. R. E. H. Bouchekara, and A. S. Alghamdi, “Optimal sizing of PV/wind/diesel hybrid microgrid system using multi-objective self-adaptive differential evolution algorithm,” *Renew. Energy*, vol. 121, pp. 400–411, 2018 [Online]. Available: https://doi.org/10.1016/j.renene.2018.01.058

[226] B. Sun, “A multi-objective optimization model for fast electric vehicle charging stations with wind, PV power and energy storage,” *J. Clean. Prod.*, vol. 288, p. 125564, 2021 [Online]. Available: https://doi.org/10.1016/j.jclepro.2020.125564

[227] R. J. Rathish, K. Mahadevan, S. K. Selvaraj, and J. Booma, “Multi-objective evolutionary optimization with genetic algorithm for the design of off-grid PV-wind-battery-diesel system,” *Soft Comput.*, vol. 25, no. 4, pp. 3175–3194, 2021 [Online]. Available: https://doi.org/10.1007/s00500-020-05372-y

[228] M. Hooshang, R. Askari Moghadam, S. Alizadeh Nia, and M. T. Masouleh, “Optimization of Stirling engine design parameters using neural networks,” *Renew. Energy*, vol. 74, pp. 855–866, 2015 [Online]. Available: http://dx.doi.org/10.1016/j.renene.2014.09.012

[229] V. Patel, V. Savsani, and A. Mudgal, “Many-objective thermodynamic optimization of Stirling heat engine,” *Energy*, vol. 125, pp. 629–642, 2017 [Online]. Available: http://dx.doi.org/10.1016/j.energy.2017.02.151

[230] F. Ahmed, H. Hulin, and A. M. Khan, “Numerical modeling and optimization of beta-type Stirling engine,” *Appl. Therm. Eng.*, vol. 149, no. December 2018, pp. 385–400, 2019 [Online]. Available: https://doi.org/10.1016/j.applthermaleng.2018.12.003

[231] A. M. Delgado-Torres and L. García-Rodríguez, “Analysis and optimization of the low-temperature solar organic Rankine cycle (ORC),” *Energy Convers. Manag.*, vol. 51, no. 12, pp. 2846–2856, 2010.

[232] J. Silvente and L. G. Papageorgiou, “An MILP formulation for the optimal management of microgrids with task interruptions,” *Appl. Energy*, vol. 206, no. March, pp. 1131–1146, 2017 [Online]. Available: https://doi.org/10.1016/j.apenergy.2017.08.147

[233] B. Li, R. Roche, and A. Miraoui, “Microgrid sizing with combined evolutionary algorithm and MILP unit commitment,” *Appl. Energy*, vol. 188, pp. 547–562, 2017 [Online]. Available: http://dx.doi.org/10.1016/j.apenergy.2016.12.038

[234] R. Dufo-López *et al.*, “Multi-objective optimization minimizing cost and life cycle emissions of stand-alone PV-wind-diesel systems with batteries storage,” *Appl. Energy*, vol. 88, no. 11, pp. 4033–4041, 2011.

[235] M. Rouholamini and M. Mohammadian, “Heuristic-based power management of a grid-connected hybrid energy system combined with hydrogen storage,” *Renew. Energy*, vol. 96, pp. 354–365, 2016 [Online]. Available: http://dx.doi.org/10.1016/j.renene.2016.04.085

[236] G. Boukettaya and L. Krichen, “A dynamic power management strategy of a grid connected hybrid generation system using wind, photovoltaic and Flywheel Energy Storage System in residential applications,” *Energy*, vol. 71, pp. 148–159, 2014.

[237] A. R. Bhatti and Z. Salam, “A rule-based energy management scheme for uninterrupted electric vehicles charging at constant price using photovoltaic-grid system,” *Renew. Energy*, vol. 125, pp. 384–400, 2018 [Online]. Available: https://doi.org/10.1016/j.renene.2018.02.126

[238] M. P. Bonkile and V. Ramadesigan, “Power management control strategy using

physics-based battery models in standalone PV-battery hybrid systems," *J. Energy Storage*, vol. 23, no. March, pp. 258–268, 2019 [Online]. Available: https://doi.org/10.1016/j.est.2019.03.016

[239] S. Nasri, B. S. Sami, and A. Cherif, "Power management strategy for hybrid autonomous power system using hydrogen storage," *Int. J. Hydrogen Energy*, vol. 41, no. 2, pp. 857–865, 2016 [Online]. Available: http://dx.doi.org/10.1016/j.ijhydene.2015.11.085

[240] Solargis, "Solar Map." [Online]. Available: https://solargis.com/maps-and-gis-data/download/nigeria. [Accessed: 05-Mar-2021]

[241] PV GIS, "Satellite data." [Online]. Available: https://ec.europa.eu/jrc/en/PVGIS/releases/pvgis51. [Accessed: 08-Jan-2021]

[242] F. S. Akinrinola, "Torrefaction and Combustion Properties of some Nigerian Biomass," University of Leeds, 2014.

[243] V. M. Homutescu, G. Dumitrascu, and B. Horbaniuc, "Evaluation of the work lost due to leaks through cylinder-displacer gap," 2008.

[244] W. M. Kays and A. L. London, *Compact Heat Exchangers*. Krieger Pub Co., 1998.

[245] H. Hosseinzade and H. Sayyaadi, "CAFS: The Combined Adiabatic-Finite Speed thermal model for simulation and optimization of Stirling engines," *Energy Convers. Manag.*, vol. 91, pp. 32–53, 2015 [Online]. Available: http://dx.doi.org/10.1016/j.enconman.2014.11.049

[246] Z. Buliński *et al.*, "A Computational Fluid Dynamics analysis of the influence of the regenerator on the performance of the cold Stirling engine at different working conditions," *Energy Convers. Manag.*, vol. 195, no. May, pp. 125–138, 2019.

[247] M. T. Mabrouk, A. Kheiri, and M. Feidt, "Effect of leakage losses on the performance of a β type Stirling engine," *Energy*, vol. 88, pp. 111–117, 2015.

[248] G. Ye, D. Xie, W. Qiao, J. R. Grace, and C. J. Lim, "Modeling of fluidized bed membrane reactors for hydrogen production from steam methane reforming with Aspen Plus," *Int. J. Hydrogen Energy*, vol. 34, no. 11, pp. 4755–4762, 2009

[Online]. Available: http://dx.doi.org/10.1016/j.ijhydene.2009.03.047

[249] Aspen Plus, "Getting Started Modeling Processes with Solids Aspen Plus," *Toll Free*, 2012 [Online]. Available: http://profsite.um.ac.ir/~fanaei/_private/Solids 8_4.pdf

[250] I. Dimitriou, H. Goldingay, and A. V. Bridgwater, "Techno-economic and uncertainty analysis of Biomass to Liquid (BTL) systems for transport fuel production," *Renew. Sustain. Energy Rev.*, vol. 88, no. March, pp. 160–175, 2018 [Online]. Available: https://doi.org/10.1016/j.rser.2018.02.023

[251] S. Michailos, O. Emenike, D. Ingham, K. J. Hughes, and M. Pourkashanian, "Methane production via syngas fermentation within the bio-CCS concept: A techno-economic assessment," *Biochem. Eng. J.*, vol. 150, no. February, p. 107290, 2019 [Online]. Available: https://doi.org/10.1016/j.bej.2019.107290

[252] E. Cardona and A. Piacentino, "A methodology for sizing a trigeneration plant in mediterranean areas," *Appl. Therm. Eng.*, vol. 23, no. 13, pp. 1665–1680, 2003.

[253] M. Foumani and K. Smith-Miles, "The impact of various carbon reduction policies on green flowshop scheduling," *Appl. Energy*, vol. 249, no. March, pp. 300–315, 2019 [Online]. Available: https://doi.org/10.1016/j.apenergy.2019.04.155

[254] G. Chicco and P. Mancarella, *Assessment of the greenhouse gas emissions from cogeneration and trigeneration systems. Part I: Models and indicators*, vol. 33, no. 3. p. 410–417.

[255] S. Sinha and S. S. Chandel, "Review of software tools for hybrid renewable energy systems," *Renewable and Sustainable Energy Reviews*, vol. 32. Elsevier, pp. 192–205, 2014.

[256] K. Kraitong, "Numerical Modelling and Design Optimisation of Stirling Engines for Power Production," Northumbria University, 2012 [Online]. Available: http://nrl.northumbria.ac.uk/8100/

[257] T. Ba¨ck, D. Fogel, and Z. Michalewicz, *Evolutionary computation 1: basic algorithms and operators*. Bristol and Philadephia: Institute of Physics Publishing, 2000.

[258] K. Deb, *Multi-objective optimization using evolutionary algorithms*. New York: Wiley, 2001.

[259] T. Kuo, "A modified TOPSIS with a different ranking index," *Eur. J. Oper. Res.*, vol. 260, no. 1, pp. 152–160, 2017 [Online]. Available: http://dx.doi.org/10.1016/j.ejor.2016.11.052

[260] T. L. Saaty, "A scaling method for priorities in hierarchical structures," *J. Math. Psychol.*, vol. 15, no. 3, pp. 234–281, 1977.

[261] W. T. Models, "Wind Turbines." [Online]. Available: www.en.wind-turbine-models.com. [Accessed: 01-Jun-2021]

[262] J. M. Lujano-Rojas, R. Dufo-López, and J. L. Bernal-Agustín, "Optimal sizing of small wind/battery systems considering the DC bus voltage stability effect on energy capture, wind speed variability, and load uncertainty," *Appl. Energy*, vol. 93, pp. 404–412, 2012 [Online]. Available: http://dx.doi.org/10.1016/j.apenergy.2011.12.035

[263] R. Cozzolino, L. Tribioli, and G. Bella, "Power management of a hybrid renewable system for artificial islands: A case study," *Energy*, vol. 106, pp. 774–789, 2016 [Online]. Available: http://dx.doi.org/10.1016/j.energy.2015.12.118

[264] ICPC, "ICPC report on emissions." [Online]. Available: http://www.ipcc-nggip.iges.or.jp/public/2006gl/pdf/2_Volume2/V2_2_Ch2_Stationary_Combustion.pdf

[265] "HOPPECKE Sun Power." [Online]. Available: https://voltaconsolar.com/batteries/agm-lead-acid/hoppecke-sun-power.html. [Accessed: 05-Feb-2021]

[266] Solaris, "Candian Solar Panel." [Online]. Available: https://www.solaris-shop.com/canadian-solar-kumax-cs3u-340p-340w-poly-solar-panel/. [Accessed: 06-Mar-2021]

[267] J. Lu, W. Wang, Y. Zhang, and S. Cheng, "Multi-Objective Optimal Design of Stand-Alone Hybrid Energy System Using Entropy Weight Method Based on HOMER," *Energies*, vol. 10, no. 10, p. 1664, 2017 [Online]. Available: http://www.mdpi.com/1996-1073/10/10/1664

[268] National Renewable Energy Laboratory, “U.S. Solar Photovoltaic System and Energy Storage Cost Benchmark: Q1 2020,” 2021.

[269] S. Quoilin, M. Van Den Broek, S. Declaye, P. Dewallef, and V. Lemort, “Techno-economic survey of organic rankine cycle (ORC) systems,” *Renew. Sustain. Energy Rev.*, vol. 22, pp. 168–186, 2013.

[270] K. Wang, O. Abdelaziz, P. Kisari, and E. A. Vineyard, “State-of-the-art review on crystallization control technologies for water/LiBr absorption heat pumps,” *Int. J. Refrig.*, vol. 34, no. 6, pp. 1325–1337, 2011 [Online]. Available: http://dx.doi.org/10.1016/j.ijrefrig.2011.04.006

[271] P. Srikhirin, S. Aphornratana, and S. Chungpaibulpatana, “A review of absorption refrigeration technologies,” *Renew. Energy Rev.*, vol. 5, no. 6471, pp. 343–372, 2001.

Appendix A MATLAB codes for Stirling engine simulation

A.1. Function for Stirling numerical integration

```
function yy = Stirling_model(u)
% Second-order model of the kinematic Stirling engine derived from the
% Adiabatic model originally developed by Uriel and Timoumi
freq=u;
Stirling_parameter
global_file_betaStirling
t=0;
Pin=5;
y(Pin)=Pfinal; Pmean = P0; xDsp=1;
Twhtr=977;
y(xDsp)=CVcomp; xDsd=2;
y(xDsd)=CVexp;
degree=theta*pi/180;
theta=2*pi*freq*t;
y(xDsp)=Zc/2*((1-cos(theta+alfa))); %displacer displacement
y(xDsd)=Zc/2 *(1+cos(theta));
Vcomp=3;
y(Vcomp)= Vl/2*(1+sin(theta-alfa))+Deadspacec;% udeh's best model recent
Vexp=4;
y(Vexp)=Vl/2*(1+sin(theta))+Deadspace;%Udeh's best model22 recent
Tcomp=16; y(Tcomp)= yTcomp; Mcomp=11; Mk=13; Mreg=15; Mhtr=14; Mexp=12;
Texp=17;
y(Texp)=yTexp;Tk=8;y(Tk)=yTk;Treg=10;y(Treg)=yTreg;Thtr=9;y(Thtr)=yThtr;
y(Mcomp)=(y(Pin).*y(Vcomp))./(R*y(Tcomp));
y(Mk)= (y(Pin).*Vk)./(R*y(Tk)); y(Mreg)=(y(Pin).*Vreg)./(R*y(Treg));
y(Mhtr)=(y(Pin).*Vhtr)./(R*y(Thtr)); y(Mexp)=(y(Pin).*y(Vexp))./(R*y(Texp));
Mcompexp=23;Mcompk=24;Mkreg=25;Mhtrexp=26;Mreghtr=27;
y(Mcompexp)=0.000001;y(Mcompk)=0.00001;y(Mkreg)=0.00001;
y(Mhtrexp)=0.00001;y(Mreghtr)=0.00001;
Tcompk=28;Thtrexp=30;Tkreg=31;Treghtr=32;Tcompexp=29; y(Tcompk)=yTk;
y(Thtrexp)=yThtr; y(Tcompexp)=yThtr; y(Tkreg)=yTkreg; y(Treghtr)=yTreghtr;
Wexp=19; y(Wexp)=0; Wcomp=18; y(Wcomp)=0; dyWexp=19; dy(dyWexp)=0;
dyWcomp=18; dy(dyWcomp)=0; dyMexp=12; dy(dyMexp)=0; dyMcomp=11;
dy(dyMcomp)=0; dyMk=13; dy(dyMk)=0; dyMreg=15; dy(dyMreg)=0; dyMhtr=14;
dy(dyMhtr)=0; Wloss=36; y(Wloss)=0; Wlossfs=37; y(Wlossfs)=0;
Qk=33; y(Qk)=0;  %heat transfered to the expanded working fluid in the hot space
Qreg=34; y(Qreg)= 0;  %heat transfer in the regenerator
Qhtr=35; y(Qhtr)=0; dyQk=33; dy(dyQk)=0;  %heat transfered to the expanded
working fluid in the hot space
dyQreg=34; dy(dyQreg)= 0;  %heat transfer in the regenerator
dyQhtr=35; dy(dyQhtr)=0; Qdiss_k=0; Qdiss_reg=0; Qdiss_htr=0; Qleak=45;
y(Qleak)=0;
    %cycle convergence criteria
cov(1)=5; cov(2)=5; cov(3)=100000; cov(4)=20; cov(5)=10; cov(6)=1000000;
```

```
Pdrop_total=0; P0new=P0; Dspmax=y(xDsp); Dsdmax=y(xDsd);
iteration = 1;
Eff_reg=46;
y(Eff_reg)=Eff_reg2;
t=0;
while(abs(cov(1))>=0.1||abs(cov(2))>=0.1||abs(cov(3))>=5000||abs(cov(4))>=0.01||
abs(cov(5))>=0.01)&&iteration<=94
   fprintf('iteration = %6.3f\n',iteration)
   cycle_number=1;
   for j=1:1:cycle
      Texp0=y(Texp);Tcomp0=y(Tcomp);Dsp0max=Dspmax;Dsd0max=Dsdmax;
Pmean0=Pmean;
      y(Qk)=0;y(Qreg)=0;y(Qhtr)=0;y(Wcomp)=0;y(Wexp)=0;dy(dyQhtr)=0;
dy(dyQk)=0;dy(dyQreg)=0;dy(dyWexp)=0;dy(dyWcomp)=0;y(Wloss)=0;y(Wlossfs)
=0;
      time=zeros(1,numberoftimestep); Dsp=zeros(1,numberoftimestep);
      Dsd=zeros(1,numberoftimestep);  DVexp=zeros(1,numberoftimestep);
      DVcomp=zeros(1,numberoftimestep); DdVexp=zeros(1,numberoftimestep);
      DdVcomp=zeros(1,numberoftimestep); DTexp=zeros(1,numberoftimestep);
      DTcomp=zeros(1,numberoftimestep); DTk=zeros(1,numberoftimestep);
      DTreg=zeros(1,numberoftimestep);  DThtr=zeros(1,numberoftimestep);
      DPin=zeros(1,numberoftimestep);  DdPin=zeros(1,numberoftimestep);
      Ddegree=zeros(1,numberoftimestep); DdWexp=zeros(1,numberoftimestep);
      DdWcomp=zeros(1,numberoftimestep); DdWloss=zeros(1,numberoftimestep);
      DdWlossfs=zeros(1,numberoftimestep); DWnet=zeros(1,numberoftimestep);
      DQk=zeros(1,numberoftimestep); DQreg=zeros(1,numberoftimestep);
      DQhtr=zeros(1,numberoftimestep); DMcomp=zeros(1,numberoftimestep);
      DMexp=zeros(1,numberoftimestep); DMk=zeros(1,numberoftimestep);
      DMhtr=zeros(1,numberoftimestep);  DMreg=zeros(1,numberoftimestep);
      Dxflowk=zeros(1,numberoftimestep); Dxflowreg=zeros(1,numberoftimestep);
      Dxflowhtr=zeros(1,numberoftimestep); DRek=zeros(1,numberoftimestep);
      DRereg=zeros(1,numberoftimestep); DRehtr=zeros(1,numberoftimestep);
      DPdropk=zeros(1,numberoftimestep);DPdropreg=zeros(1,numberoftimestep);
      DPdrophtr=zeros(1,numberoftimestep);
      DMcompk=zeros(1,numberoftimestep);
      DMkreg=zeros(1,numberoftimestep);
      DMreghtr=zeros(1,numberoftimestep);
      DMhtrexp=zeros(1,numberoftimestep);
      DTcompk=zeros(1,numberoftimestep);
      DTkreg=zeros(1,numberoftimestep);
      DTreghtr=zeros(1,numberoftimestep);
      DThtrexp=zeros(1,numberoftimestep);
      DQdissk=zeros(1,numberoftimestep);
      DQdissreg=zeros(1,numberoftimestep);
      DQdisshtr=zeros(1,numberoftimestep);
      DQdiss_total=zeros(1,numberoftimestep);
      DQleak=zeros(1,numberoftimestep);
      for i=1:1:numberoftimestep
```

```
        [t,y,dy]=rk4_Stirling('Deriv_Stirling',t,dt,freq);
        fprintf('numberoftimestep = %8.3f  t= %8.3f  Pin=  %8.3f %Texp=  %8.3f
        Dsp=  %8.3f  Mk=   %8.3f\n\n',i,t,y(Pin),y(Texp),y(Tcomp),y(xDsp),y(Mk));
        theta=2*pi*freq*t; degreed=theta.*180/pi; time(i)=t; Dsp(i)=y(xDsp);
        Dsd(i)=y(xDsd);  DVexp(i)=y(Vexp);   DVcomp(i)=y(Vcomp);
        DdVexp(i)=dy(dyVexp);  DdVcomp(i)=dy(dyVcomp);  DTexp(i)=y(Texp);
        DTcomp(i)=y(Tcomp);  DTk(i)=y(Tk); DTreg(i)=y(Treg);
        DThtr(i)=y(nThtr);  DPin(i)=y(Pin); DdPin(i)=dy(dyPin);
        Ddegree(i)=degreed;   DdWexp(i)=y(Wexp);  DdWcomp(i)=y(Wcomp);
        DdWloss(i)=y(Wloss); DdWlossfs(i)=y(Wlossfs);
        DWnet(i)=y(Wexp)+y(Wcomp); DQk(i)=y(Qk);  DQreg(i)=y(Qreg);
        DQhtr(i)=y(Qhtr); DMcomp(i)=y(Mcomp); DMexp(i)=y(Mexp);
        DMk(i)=y(Mk); DMhtr(i)=y(Mhtr); DMreg(i)=y(Mreg);
        Dxflowk(i)=xflowk; Dxflowreg(i)=jhtr; Dxflowhtr(i)=jk;
        DRek(i)=Vfluid(1);  DRereg(i)=Vfluid(2);  DRehtr(i)=Vfluid(3);
        DPdropk(i)=Pdropk; DPdropreg(i)=Pdropreg; DPdrophtr(i)=Pdrophtr;
        DMcompk(i)=y(Mcompk);  DMkreg(i)=y(Mkreg); DMreghtr(i)=y(Mreghtr);
        DMhtrexp(i)=y(Mhtrexp); DTcompk(i)=y(Tcompk);  DTkreg(i)=y(Tkreg);
        DTreghtr(i)=y(Treghtr);  DThtrexp(i)=y(Thtrexp); DQdissk(i)=Qdiss_k;
        DQdissreg(i)=Qdiss_reg;  DQdisshtr(i)=Qdiss_htr;
        DQdiss_total(i)=Qdiss_total; DQleak(i)=y(Qleak);
    end
    DPin1=DPin./1e6;  Pmean=(sum(DPin)*timestep)/Tt; Pinmax=max(DPin);
    DVtotal=DVcomp+DVexp;  Vtotal_ave=(sum(DVtotal)*timestep)/Tt;
    Wexpa=y(Wexp); Wcompa=y(Wcomp);  Wnet= Wexpa+Wcompa;
    Wrate_ideal= Wnet*freq; %Ideal work done in the engine
    %loss due to pressure drop in the heatexchangers of the engine
    Wloss_rate_pdrop=y(Wloss)*freq;
    Const_ccomp = (3*R*y(Tcomp))^0.5;
    Const_cexp = (3*R*y(Texp))^0.5;
    Const_pfl=((((0.4 + 0.0045*Zc*freq)*10^5)/(3*Compratioconst))*(1-
(1/Compressionratio)));
    Wloss_mechfric = 2*(Pmean*(((((const_a*Velp)/Const_ccomp)+
(Const_pfl/Pmean))*Vp)+((((const_a*Velp)/Const_cexp)-
(Const_pfl/Pmean))*Vl)));
    % Loss due to finite speed of the piston
     Wloss_rate_mechfric =  Wloss_mechfric*freq;
      Kfluid_comp=Kfluid0*(300+TKfluid)/((y(Tcomp)+TKfluid)...
      *(y(Tcomp)/300)^1.5);
    Wloss_rate_hys = ((1/32)*(2*pi*freq)*gammaa^3*(gamm...
    aa-1)*Twhtr*Pmean*Kfluid_comp).^0.5*(Vp/(2*Vtotal_ave)).^2*Ap;
    Wrate_in_actual=Wrate_ideal+Wloss_rate_pdrop-Wloss_rate_mechfric-
Wloss_rate_hys;%Actual work done in the engine
    Qreg_ideal=y(Qreg); Qrate_reg= Qreg_ideal*freq;
    Qadded = y(Qhtr); Qrate_in = Qadded*freq;% heat added in watts
    Qlost_k = y(Qk); Qrate_outk = Qlost_k*freq; % rate of heat lost
    Dspmax = max(Dsp); Dsdmax= max(Dsd);
    Tcompmax= max(DTcomp); Texpmax= max(DTexp);
```

```
% Heat     transfer rate in the cooler
htck = (0.0791*Vfluid(1)*Chcp*(Rek).^0.75)/(2*dhk*Prfluid(1));
% Heat transfer rate in the heater
htchtr = (0.0791*Vfluid(3)*Chcp*(Rehtr).^0.75)/(2*dhhtr*Prfluid(3));
% Effectiveness of the regenerator
% gedeon and wood correlation for Nusselt number of a regenerator
Nureg=(1+0.99*(Rereg*Prfluid(2)).^0.66)*(poros^1.79);
Streg=0.023*Rereg^-0.2*Prfluid(2).^-0.6;
NTUreg1=(Streg*lreg)/(1/4*dhreg);
y(Eff_reg)=NTUreg/(NTUreg+1);
DQreg1=y(Eff_reg).*DQreg;
DQreg_max=max(DQreg1);
DQreg_min=min(DQreg1);
Qrate_leak=(sum(DQleak)*timestep)/Tt;
Qrate_dissk =(sum(DQdissk)*timestep)/Tt;
Qrate_dissreg =(sum(DQdissreg)*timestep)/Tt;
Qrate_disshtr =(sum(DQdisshtr)*timestep)/Tt;
Qrate_disstotal=(sum(DQdiss_total)*timestep)/Tt;
DQout_reg=(1-y(Eff_reg))*(DQreg_max+DQreg_min);
% conduction loss from the regenerator
Qrate_outreg_cond=((2*pi*kreg*lreg)/log(drego/dregi))*(Twhtr-Twk);
Qrate_outactual=Qrate_outk-Qrate_outreg-
 % Actual heat lost from the cooler
Qrate_disstotal+Qrate_outreg_cond+Qrate_leak;
Qrate_inactual=Qrate_in+Qrate_outreg+Qrate_disstotal-Qrate_outreg_cond-
Qrate_leak;% Actual heat supplied in the heater
Eff_Stirling_ideal= Wrate_ideal./Qrate_in;%Ideal efficiency of Stirling engine
Eff_Stirling =(Wrate_in_actual)./(Qrate_inactual); % efficiency of the engine
including the losses in the engine
y(Tk) = Twk - ((Qrate_outactual)/(htck*Ask));
y(Thtr) = Twhtr - ((Qrate_inactual)/(htchtr*Ashtr));
fprintf('t = %8.3f  Wexpa = %8.3f  Wcompa =  %8.5f  Dspmax=  %8.3f  Pinmax=
%8.3f          Tcompmax          %8.3f          Texpmax          %8.3f
W\n',t,Wexpa,Wcompa,Dspmax,Pinmax,Tcompmax,Texpmax);
conv(1)=(y(Texp)-Texp0)/Texp0;conv(2)=(y(Tcomp)-
Tcomp0)/Tcomp0;conv(3)=(Pmean-Pmean0);conv(4)=(Dspmax-
Dsp0max)/Dsp0max;conv(5)=(Dsdmax-Dsd0max)/Dsd0max;
fprintf ('cycle engine performance = %8.3f/n',cycle_number);
%print the conversion criteria for each cycle
fprintf('cov(1) = %8.5f  cov(2) = %8.3f  cov(3) =  %8.3f  cov(4)=  %8.3f  cov(5)=
%8.3f  cov(6)=  %8.3f\n',cov(1),cov(2),cov(3),cov(4),cov(5),cov(6));

if(abs(cov(1))<=0.1||abs(cov(2))<=0.1||abs(cov(3))<=5000||abs(cov(4))
<=0.01||abs(cov(5))<=0.01)
   break
else
   cycle_number=cycle_number+1;
end
```

```
   end
   iteration=iteration+1;
disp('tttttttttttttttttttttttttttttttttttttttttttttttttttttttttttttttttttttttttttttttttttttttttttttttttttttttttttt')
end
yy(1)=Wrate_in_actual;
yy(2)= Qrate_inactual;
yy(3)=Eff_Stirling;
```

A.2. Function for the RK solver

```
function [t,y,dy] = rk4_Stirling(t,dt,y,freq)
%Classical fourth order Runge-Kutta method %Integrates n first order differential equations %dy(t,y) over interval t to t+dt
%Israel Urieli - Jan 21, 2002
global_file_betaStirling
Stirling_parameter
t0 = t;
y0=y;
[y,dy1] = feval('Deriv_Stirling',t,y,freq);
for j = 1:length(dy1)
 y(j) = y0(j) + 0.5*dt.*dy1(j);
end
t = t0 + 0.5*dt;
[y,dy2] = feval('Deriv_Stirling',t,y,freq);
for j = 1:length(dy1)
y(j) = y0(j) + 0.5*dt*dy2(j);
end
t = t0 + 0.5*dt;
[y,dy3]= feval('Deriv_Stirling',t,y,freq);
for j = 1:length(dy1)
y(j) = y0(j) + dt*dy3(j);
end
t = t0 + dt;
[y,dy] = feval('Deriv_Stirling',t,y,freq);
for j = 1:length(dy1)
dy(j) = (dy1(j) + 2*(dy2(j) + dy3(j)) + dy(j))/6;
y(j) = y0(j) + dt*dy(j);
end
```

A.3. Function for computing the change in the variables

```
function [y,dy]=Deriv_Stirling(t,y,freq)
%call in the global file
global_file_betaStirling
%%%%%%%%%%%%%%%%%%%%%%%%%%%%%%%%%%%%%%%%%%%%%%%%%%%%
%change in the piston and displacer displacements
theta=2*pi*freq*t;
dyxDsp=1;
```

```
dy(dyxDsp)=2*0.5*Zc*pi*freq*sin(theta-alfa); %change in the displacement of the
piston
dyxDsd=2;
dy(dyxDsd)=-2*0.5*Zc*pi*freq*sin(theta);%change in the displacement of the
displacer
%%%%%%%%%%%%%%%%%%%%%%%%%%%%%%%%%%%%%%%%%%%%%%%%%%%%%%%%%%%%%%%%%%%%%%%%%%%%
%change in the expansion and compression volumes
dyVcomp=3;
dy(dyVcomp)=0.5*Vl*(2*pi*freq)*cos(theta-alfa);%Udeh's best model recent
dyVexp=4;
dy(dyVexp)=0.5*Vl*(2*pi*freq)*cos(theta); %Udeh's best modelrecent
%%%%%%%%%%%%%%%%%%%%%%%%%%%%%%%%%%%%%%%%%%%%%%%%%%%%%%%%%%%%%%%%%%%%%%%%%%%%
%shuttle loss
Qshuttle=(0.4*Kpiston*Zc^2*Dd*(y(Texp)-y(Tcomp)))/(Dannular*Ld);
%%%%%%%%%%%%%%%%%%%%%%%%%%%%%%%%%%%%%%%%%%%%%%%%%%%%%%%%%%%%%%%%%%%%%%%%%%%%
% computing the change in the pressure of the engine (dp)
dyPin=5;
dy(dyPin)=((((Qshuttle-((Chcp/R)*y(Pin).*dy(dyVcomp))-
(Chcp*y(Tcompexp)*y(Mcompexp)))/(Chcp*y(Tcompk)))-
((Qshuttle+((Chcp/R)*y(Pin).*dy(dyVexp))-
(Chcp*y(Tcompexp)*y(Mcompexp)))/(Chcp*y(Thtrexp)))).//((y(Vcomp)/(gamma
a*y(Tcompk)))+((Vk/y(Tk))+(Vreg/y(Treg))+(Vhtr/y(Thtr)))+(y(Vexp)/(gammaa*
y(Thtrexp)))))*R;
%%%%%%%%%%%%%%%%%%%%%%%%%%%%%%%%%%%%%%%%%%%%%%%%%%%%%%%%%%%%%%%%%%%%%%%%%%%%
%change in the mass of the working fluid in the engine compartments
dyMcomp=11;
% change in the mass of the working fluid in the compression space
dy(dyMcomp)=-((Qshuttle-((Chcp/R)*y(Pin).*dy(dyVcomp))-
((Chcv/R)*y(Vcomp).*dy(dyPin))-
(Chcp*y(Tcompexp)*y(Mcompexp)))/(Chcp*y(Tcompk)))-y(Mcompexp);
dyMexp=12;
% change in the mass of the working fluid in the expansion space
dy(dyMexp)=((Qshuttle+((Chcp/R)*y(Pin).*dy(dyVexp))+((Chcv/R)*y(Vexp).*dy(
dyPin))-(Chcp*y(Tcompexp)*y(Mcompexp)))/(Chcp*y(Thtrexp)))+y(Mcompexp);
dyMk=13;
dy(dyMk)=(dy(dyPin).*Vk)./(R*y(Tk));  %change in the mass of the working fluid in
the cooler
dyMhtr=14;
%change in the mass of the working fluid in the heater
dy(dyMhtr)=(dy(dyPin).*Vhtr)./(R*y(Thtr));
dyMreg=15;
%change in the mass of the working fluid in the regenerator
dy(dyMreg)=(dy(dyPin).*Vreg)./(R*y(Treg));
%%%%%%%%%%%%%%%%%%%%%%%%%%%%%%%%%%%%%%%%%%%%%%%%%%%%%%%%%%%%%%%%%%%%%%%%%%%%

%temperature variation in the cold and hot space
dyTcomp=16;
dy(dyTcomp)=y(Tcomp)*((dy(dyPin)./y(Pin))+(dy(dyVcomp)/y(Vcomp))-
(dy(dyMcomp)/y(Mcomp)));   %change in the temperature of the cold space
```

```
dyTexp=17;
dy(dyTexp)=y(Texp)*((dy(dyPin)./y(Pin))+(dy(dyVexp)/y(Vexp))-
(dy(dyMexp)/y(Mexp)));   %change in the temperature of the hot space
% % % % %
dyQk=33;
dy(dyQk)=((Vk*dy(dyPin).*Chcv)/R)-
Chcp*(y(Tcompk)*y(Mcompk))+Chcp*(y(Tkreg)*y(Mkreg));  %heat lost from the
working fluid in the cooler
dyQreg=34;
dy(dyQreg)=((Vreg*dy(dyPin).*Chcv)/R)-
Chcp*(y(Tkreg)*y(Mkreg))+Chcp*(y(Treghtr)*y(Mreghtr));  %heat transfer in the
regenerator
dyQhtr=35;
dy(dyQhtr)=((Vhtr*dy(dyPin).*Chcv)/R)-
Chcp*(y(Treghtr)*y(Mreghtr))+Chcp*(y(Thtrexp)*y(Mhtrexp));%heat  transfer  in
the heater
% %
```

Appendix B MATLAB codes for modelling multi-carrier system

B.1. Function for the parametric analysis of multi-carrier system

```
function yy = CCHP_metrics(x)
% run Aspen model
try
  [Tfluegas,Aspen]=open_Aspen();
catch
  [Tfluegas,Aspen]=open_Aspen();
end
Twhtr= Tfluegas-20;
freq1=(25:3.33:58.33);
for m=1:length(freq1)
   for k=1:length(freq1)
       y=Stirling_model(freq1,Twhtr); %call in Stirling function
DQrate_inactual(m)=y(1);
DQrate_outactual(m)=y(2);
Aspen.Tree.FindNode("\Data\Blocks\ORCCOMB\Data\Blocks\SEHEATER\Input\D
UTY").Value= -(DQrate_inactual);
Aspen.Tree.FindNode("\Data\Blocks\ORCCOMB\Data\Blocks\SECOOLER\Input\D
UTY").Value= (DQrate_outactual);
Aspen.Tree.FindNode("\Data\Blocks\ARS\Data\Streams\1\Input\TOTFLOW\MIXE
D").Value = mflow_ref;
Aspen.Tree.FindNode("\Data\Blocks\ARS\Data\Streams\CW1\Input\TOTFLOW\MI
XED").Value = 0.015;
%              Aspen.Reinit;
pause(5);
try
   run_Aspen;
catch ME
```

```
   if ~isempty(ME.identifier)
      try
         run_Aspen;
      catch
         yy(1)=-0.61;    yy(2)=-0.40;    yy(3)=-0.33;    yy(4)=-0.36;
         Quit(Aspen);
         delete(Aspen);
         return
      end
   end
end
 if Simulation_Converg == 0 && time_aspen < 20
    Final_flue_temp =
Aspen.Tree.FindNode("\Data\Blocks\ORCCOMB\Data\Streams\FGTHTR\Output\T
EMP_OUT\MIXED").Value; %Temperature of the flue gas to stackApplication
    Heatrate_fuel =
Aspen.Tree.FindNode("\Data\Blocks\ORCCOMB\Data\Blocks\COMBUSTR\Output
\QCALC").Value;%Combustor heat duty
    Wnet_ORC =
Aspen.Tree.FindNode("\Data\Blocks\ORCCOMB\Data\Blocks\REXPAND\Output\
WNET").Value; %Net work ORC
    Heatrate_Absorber_ARS =
Aspen.Tree.FindNode("\Data\Blocks\ARS\Data\Blocks\ABSORBER\Output\QCALC
").Value;%Heat added into the ARS Absorber
    Heatrate_Evap_ARS =
Aspen.Tree.FindNode("\Data\Blocks\ARS\Data\Blocks\EVAPOR\Output\QCALC").
Value; %Refrigerating effect of ARS
    Heatrate_Boiler =
Aspen.Tree.FindNode("\Data\Blocks\ORCCOMB\Data\Blocks\HWEXCH\Output\H
X_DUTY").Value; %Heat load of  hot water heater
%                 Heatrate_EGR(m,k) =
Aspen.Tree.FindNode("\Data\Blocks\ORCCOMB\Data\Blocks\EGR\Output\HX_DU
TY").Value; %Heat added to the desorber
    Heatrate_Cond_ARS =
Aspen.Tree.FindNode("\Data\Blocks\ARS\Data\Blocks\CONDEN\Output\QCALC").
Value;%Heatrate ARS condenser
    Heatrate_Desorb_ARS =
Aspen.Tree.FindNode("\Data\Blocks\ARS\Data\Blocks\HEHOTSTR\Output\QCALC
").Value;%Heatrate ARS condenser
    Exfl_gases=
Aspen.Tree.FindNode("\Data\Blocks\ORCCOMB\Data\Streams\GASES\Output\ST
RM_UPP\EXERGYFL\MIXED\TOTAL").Value; %Exergy of flue into Stirling engine
%                 Exfl_FGTD(m,k)=
Aspen.Tree.FindNode("\Data\Blocks\ORCCOMB\Data\Streams\FGTD\Output\STR
M_UPP\EXERGYFL\MIXED\TOTAL").Value; %Exergy of flue into ARS
    Exfl_HRTT=
Aspen.Tree.FindNode("\Data\Blocks\ORCCOMB\Data\Streams\HRTT\Output\STR
M_UPP\EXERGYFL\MIXED\TOTAL").Value; %Exergy of refflow into ORC expander
```

```
    Exfl_ERTR=
Aspen.Tree.FindNode("\Data\Blocks\ORCCOMB\Data\Streams\ERTR\Output\STR
M_UPP\EXERGYFL\MIXED\TOTAL").Value; %Exergy of refflow into ORC
regenerator
    Exfl_CRTC=
Aspen.Tree.FindNode("\Data\Blocks\ORCCOMB\Data\Streams\CRTC\Output\ST
RM_UPP\EXERGYFL\MIXED\TOTAL").Value; %Exergy of refflow into ORC
condenser
    Exfl_CRTP=
Aspen.Tree.FindNode("\Data\Blocks\ORCCOMB\Data\Streams\CRTP\Output\STR
M_UPP\EXERGYFL\MIXED\TOTAL").Value; %Exergy of refflow into ORC pump
    Exfl_CRTR=
Aspen.Tree.FindNode("\Data\Blocks\ORCCOMB\Data\Streams\CRTR\Output\STR
M_UPP\EXERGYFL\MIXED\TOTAL").Value; %Exergy of refflow into ORC
Regenerator
    Exfl_HRTE=
Aspen.Tree.FindNode("\Data\Blocks\ORCCOMB\Data\Streams\HRTE\Output\STR
M_UPP\EXERGYFL\MIXED\TOTAL").Value; %Exergy of refflow into ORC evaporator
    Exfl_CWI=
Aspen.Tree.FindNode("\Data\Blocks\ORCCOMB\Data\Streams\CWI\Output\STR
M_UPP\EXERGYFL\MIXED\TOTAL").Value; %Exergy of waterflow into ORC
condenser
    Exfl_CWO=
Aspen.Tree.FindNode("\Data\Blocks\ORCCOMB\Data\Streams\CWO\Output\STR
M_UPP\EXERGYFL\MIXED\TOTAL").Value; %Exergy of waterflow into ORC
condenser
    Exfl_CWO=
Aspen.Tree.FindNode("\Data\Blocks\ORCCOMB\Data\Streams\CWO\Output\STR
M_UPP\EXERGYFL\MIXED\TOTAL").Value; %Exergy of waterflow into ORC
condenser
    Tevap =
Aspen.Tree.FindNode("\Data\Blocks\ARS\Data\Blocks\EVAPOR\Input\TEMP").Valu
e;%Temperature of the evaporator
    Thwater =
Aspen.Tree.FindNode("\Data\Blocks\ORCCOMB\Data\Streams\DHWTROUT\Outp
ut\TEMP_OUT\MIXED").Value;%Temperature of the evaporator
    Tflue =
Aspen.Tree.FindNode("\Data\Blocks\ORCCOMB\Data\Streams\GASES\Output\TE
MP_OUT\MIXED").Value; %Temperature of the flue gas into the power plant
    Tamb = Aspen.Tree.FindNode("\Data\Blocks\ORCCOMB\Data\Streams\WET-
COAL\Input\TEMP\NCPSD").Value; %Ambient temperature
 else
%        Final_flue_temp(m,k) = inf; % Its Penalized if simulation doesn't converge;
    Wnet_ORC = 0; % Its Penalized if simulation doesn't converge;
    Heatrate_fuel = 0;
    Heatrate_Absorber_ARS = 0; %Its penalised if the simulation doesn't converge;
    Heatrate_Evap_ARS = 0;%Refrigerating effect of ARS
    Heatrate_Boiler = 0; %Heat load of  hot water heater
```

```
%                 Heatrate_EGR(m,k) = 0; %Heat added to the desorber
    Heatrate_Cond_ARS = 0;    Heatrate_Desorb_ARS = 0;    Exfl_gases= 0;
    Exfl_HRTT= 0;  Exfl_ERTR= 0;  Exfl_CRTC= 0;   Exfl_CRTP= 0;
    Exfl_CRTR= 0;     Exfl_HRTE= 0;     Exfl_CWI= 0;     Exfl_CWO= 0;
    Exfl_CWO= 0;     Tevap = 0;     Tflue = 0;     Tamb = 0;
    Thwater = 0;
 end
Wrate_in_CCHP = DWrate_in_actual- Wnet_ORC;
% Qrate_in_CCHP(m,k) = Qrate_inactual- Heatrate_Desorb_ARS(k);
Qrate_in_CCHP = -(Heatrate_fuel)-Heatrate_Absorber_ARS-Heatrate_Cond_ARS;
yy(1) =
(Wrate_in_CCHP+Heatrate_Evap_ARS+Heatrate_Boiler)./(0.80*0.90*HHV_wood.*
mflow+Heatrate_Absorber_ARS+Heatrate_Cond_ARS);%Energy utilization factor
of CCHP
yy(2) = -((Wrate_in_CCHP-(Heatrate_Evap_ARS.*(1-
(Tamb./Tevap)))+((Heatrate_Boiler).*(1-
(Tamb./Thwater)))./((Qrate_in_CCHP).*(1-(Tamb./Tflue))));%exergetic
efficiency of CCHP
yy(3)=(1-
((Qrate_in_CCHP)./((Wrate_in_CCHP./0.23)+(Heatrate_Evap_ARS./(0.8*0.8))+(H
eatrate_Boiler./0.8))));%primary energy savings
yy(4)= Wrate_in_CCHP./((Qrate_in_CCHP)+(Heatrate_Desorb_ARS)-
(Heatrate_Boiler./0.9));%Fuel utilisation efficiency
yy(5)= -(Wrate_in_CCHP./((Qrate_in_CCHP)-(Heatrate_Boiler./0.9)-
(Heatrate_Evap_ARS/3.0)));
yy(6)=-(1-
((mCO2fuel.*Qrate_in_CCHP)./((mCO2mun*Wrate_in_CCHP)+((mCO2fuel*Heatr
ate_Boiler)./0.9)+((mCO2fuel*Heatrate_Evap_ARS)./3.0))));
cr(m)=Heatrate_Evap_ARS./(Heatrate_Boiler+Heatrate_Evap_ARS);
Quit(Aspen);
delete(Aspen);
pause(20);
end
EUF_CCHP = yy(1);Eff_CCHP_II = yy(2);PES_CCHP = yy(3);FUE_CCHP = yy(4);
ATE_CCHP = yy(5);CO2_ER = yy(6);freq_new=freq1';
x_plane=(21:-1:1);[freq_new,x_plane]=meshgrid(freq_new,x_plane);
figure(10)
y1=Eff_CCHP_2';
surf(freq_new,x_plane,y1)
colormap hsv;
figure(11)
y2=Eff_CCHP_II';
surf(freq_new,x_plane,y2)
colormap hsv;
figure(12)
y3=PES';
surf(freq_new,x_plane,y3)
colormap hsv;
```

```
figure(13)
y4=FUE';
surf(freq_new,x_plane,y4)
colormap hsv;
figure(14)
y5=ATE_2';
surf(freq_new,x_plane,y5)
colormap hsv;
figure(15)
y6= CO2_ER_CCHP;
surf(x_plane,freq_new,y6)
colormap hsv;
```

B.2. Function to open and run Aspen models

```
 function Aspen=open_Aspen()%function to open and run an Aspen file from
matlab
global HHV_wood mflow
try
  Aspen = actxserver('Apwn.Document.36.0'); %34.0 ---> V8.8; 35.0 ---> V9.0; and
36.0 ---> V10.0
catch
  Aspen = actxserver('Apwn.Document.36.0'); %34.0 ---> V8.8; 35.0 ---> V9.0; and
36.0 ---> V10.0
end
[stat,mess]=fileattrib; % get attributes of folder (Necessary to establish the location
of the simulation)
Simulation_Name = 'System Integration_CCHP_22_cr';% Aspeen Plus Simulation
Name
Aspen.invoke('InitFromArchive2',[mess.Name '\' Simulation_Name '.bkp']);
Aspen.Visible = 1; % 1 ---> Aspen is Visible; 0 ---> Aspen is open but not visible
Aspen.SuppressDialogs = 1; %supress file
Aspen.Tree.FindNode("\Data\Blocks\ORCCOMB\Data\Streams\WET-
COAL\Input\TOTFLOW\NCPSD").Value= mflow;
% % Aspen.Tree.FindNode("\Data\Blocks\ORCCOMB\Data\Flowsheeting
Options\Calculator\WATER\Input\FORTRAN_EXEC\#0").Value =
moisture_new(:,:,m);
Aspen.Tree.FindNode("\Data\Blocks\ORCCOMB\Data\Flowsheeting
Options\Calculator\WATER\Input\FORTRAN_EXEC\#0").Value = '      H2ODRY =
15.0';
Aspen.Tree.FindNode("\Data\Properties\Parameters\Pure
Components\HEAT\Input\VAL\HCOMB\DRY-WOOD\#0").Value =
HHV_wood*(100-15)./100;
pause(5);
Aspen.Reinit;
try
 Aspen.Engine.Run2(1); % Run the simulation
```

```
catch
 pause(5)
 Aspen.Engine.Run2(1); % Run the simulation
end
while Aspen.Engine.IsRunning == 1 % 1 --> If Aspen is running; 0 ---> If Aspen stop.
    pause(0.5);
end
% Tfluegas =
Aspen.Tree.FindNode("\Data\Blocks\ORCCOMB\Data\Streams\GASES\Output\TE
MP_OUT\MIXED").Value;
end
```

B.3. Function for parametric optimisation of CCHP

```
function [x,fval,popu,scores] = ga_optimisation()
Aeq = []; A = [];  b = [];
beq = []; lb=[25 0.0071]; ub=[58.33 0.0325];
fgoalopts = optimoptions(@fgoalattain,'UseParallel',false);
options = optimoptions('gamultiobj','UseParallel',true,'UseVectorized',false,
'ParetoFraction',0.5,'MaxGenerations',150,'PlotFcn',{@gaplotgenealogy,@gaplotscor
ediversity,@gaplotpareto,@gaplotspread,@gaplotscores},'display','iter');
optimoptions(options,'InitialPopulationMatrix',population,'InitialScoresMatrix',scor
es);
options = optimoptions(options,'HybridFcn',{@fgoalattain,fgoalopts});
fun = @CCHP_metrics;
% addAttachedFiles(pool,'Stirling_parameter.m');
[x,fval,exitflag,output,popu,scores] = gamultiobj(fun,2,A,b,Aeq,beq,lb,ub,options);
```

Appendix C MATLAB codes for HRES optimisation

C.1. Function for implementing the dispatch strategies and computing the performance indicators of the HRES

```
function yy =HRES_metrics(x)
global Demand
global PV_power2
% pv_out=PV_power;
global WT1_power
global WT2_power
PV_optconstants2;
load('data_opt','WT1_power','WT2_power','Demand')
PV_power2 = power_PV;
    % global PV_power
    WT_type = round(x(4)); %type of wind turbines
    Mana_strat= round(x(6)); % control strategy
    Bat_type = round (x(8)); % type of battery
    Num_ST = round (x(9)); % number of ST engines
```

```
x(2)=round(x(2));  x(1)=round(x(1));  x(6)=round(x(6));  x(3)=round(x(3));
kk=length(WT1_power); nn1=(kk/100); nn=round(nn1);
WT1_power1=zeros(nn,1); WT2_power1=zeros(nn,1);  Demand1=zeros(nn,1);
ii=1;
% WT2_power1=WT2_power';
for j = 1:nn
%    sum1_pv=0;
  sum2_wt1=0;   sum3_wt2=0;  sum4_dmd=0;
  for mm=ii:ii+100
%       sum1_pv=(sum1_pv + PV_power(mm,:));
      sum2_wt1=(sum2_wt1+ WT1_power(mm,:));
      sum3_wt2=(sum3_wt2+ WT2_power(mm,:));
      sum4_dmd=(sum4_dmd+ Demand(mm,:));
  end
%    PV_power1(j)=sum1_pv./100;
  WT1_power1(j)=sum2_wt1./100;
  WT2_power1(j)=sum3_wt2./100;
  Demand1(j)=sum4_dmd./100;
  ii=mm;
end
PV_power1=PV_eff*(PV_power2*4)/1000;
if WT_type==1
  WT_cost= WT1_cost;
  WT_cap=WT1_size;
  Wind_power= WT1_power1;
  x(2)=x(2);
else
  WT_cost=WT2_cost;
  WT_cap=WT2_size;
  Wind_power= WT2_power1;
  x(2)=x(3);
end
t= length (Wind_power);
PV_gen = zeros(t,1);  WT_gen = zeros(t,1);  Demand_inst = zeros(t,1);
err_power = zeros(t,1);  ST_power = zeros(t,1); buff_power = zeros(t,1);
Bat_power = zeros(t,1); dump_energy=zeros(t,1);   Bat_disch = zeros(t,1);
Bat_chg = zeros(t,1);
unmet_energy = zeros(t,1);% energy not supplied by the HRES and backups
Excess_power = zeros(t,1);
if Bat_type ==1
  Bat_cap=Bat1_cap;%capacity of battery
  SOC_batmax=x(7)*Bat_cap;%maximum state of charge of battery
  SOC_batmin=SOC_batmax*(1-Bat_DOD);%minimum state of charge of
battery
elseif Bat_type ==2
  Bat_cap=Bat2_cap;%capacity of battery
  SOC_batmax=x(7)*Bat_cap;%State of charge of battery
```

```
        SOC_batmin=SOC_batmax*(1-Bat_DOD);%minimum state of charge of
battery
      else
        Bat_cap=Bat3_cap;%capacity of battery
        SOC_batmax=x(7)*Bat_cap;%State of charge of battery
        SOC_batmin=SOC_batmax*(1-Bat_DOD);%minimum state of charge of
battery
      end
      SOC = zeros(t,1);
      j=1;
      t_stirling = 0;%hours of operation of Stirling engine in a year
      SOC(j)= SOC_batmin;
      count = 0;%count the number of start-ups of ST back-up
      buff_power(j)=ST_power(j);
      for j=1:length(PV_power1)
        PV_gen(j)=PV_power1(j)*x(1);
        WT_gen(j)= Wind_power(j)*x(2);
        Demand_inst(j)= Demand1(j);
        err_power(j)= WT_gen(j)+PV_gen(j)-Demand_inst(j);
        %%%%%% energy management strategies
        if Mana_strat == 1 % No battery with load following stirling engine
          if err_power (j)<0
           if -err_power(j)<=2*(x(5))
             ST_power(j)= -err_power(j);
           else
             ST_power(j)= 2*(x(5));
             unmet_energy(j)=(-err_power(j))-ST_power(j);
           end
          else
            ST_power(j)=0;
          end
          if err_power(j)>0
            dump_energy(j)= err_power(j);
          end
          FC_diesel(j)= 0.24*ST_power(j)+(0.084*2*x(5));
          buff_power(j+1)=ST_power(j);
        end
        if Mana_strat == 2 %Battery with Stirling load following
          %%%%%%% battery charging mode
         if err_power(j)>0 && SOC(j)< SOC_batmax
            SOC_buff= SOC(j)+ (err_power(j)/Bat_voltage);%Compute and store
the SOC at time t+1
            Bat_chg(j)=Bat_ncharge*(SOC_buff-SOC(j))*Bat_voltage;% power
stored in battery
            SOC_j=SOC(j);%store the SOC at time t
            SOC(j+1)=SOC_buff;
            buff_power=ST_power(j);
            %check if the power stored in the battery is more than the
```

```
            %maximum power of battery
             if SOC_buff > SOC_batmax
               dump_energy(j)= (SOC_buff-SOC_batmax)*Bat_voltage;
               SOC_new=SOC_batmax;
               Bat_buff = Bat_ncharge*(SOC_batmax-SOC_j)*Bat_voltage;% Actual
power that is delivered to the battery
               SOC(j+1)=SOC_new;
               Bat_chg(j)=Bat_buff;
             end
          elseif (err_power(j)>0 && (err_power(j)/Bat_voltage)>SOC_batmax)||
(err_power(j)>0 && SOC(j)>= SOC_batmax)
            dump_energy(j)= err_power(j);
            SOC(j+1)=SOC(j);
          else
           dump_energy(j)=0;
           SOC(j+1)=SOC(j);
        end
         %%%%%%%% battery discharging mode
         if err_power(j)<0 && (-err_power(j)/Bat_voltage)< SOC_batmax
           if (-err_power(j)/(Bat_ndischarge*Bat_voltage))<SOC(j)&& SOC(j) >
SOC_batmin
             SOC_buff = SOC(j)-(-err_power(j)/(Bat_voltage*Bat_ndischarge));%
discharging mode battery
             Bat_disch(j)= (SOC_buff-SOC(j))*Bat_voltage;%energy supplied by
battery
             SOC_j=SOC(j);
             SOC(j+1)= SOC_buff;
             if SOC_buff < SOC_batmin
               ST_power(j)= (SOC_batmin - SOC_buff)*Bat_voltage;% Unmet
energy supplied by the Stirling engine
               Bat_disch(j)= -((SOC_j-SOC_batmin)*Bat_voltage);%energy
supplied by battery
               SOC(j+1)= SOC_batmin;
             end
           else
             if -err_power(j)<=2*(x(5))
               ST_power(j)= -err_power(j);
             else
               ST_power(j)= 2*(x(5));
               unmet_energy(j)=(-err_power(j))-ST_power(j);
             end
             if unmet_energy(j)>0
&&(unmet_energy(j)/(Bat_ndischarge*Bat_voltage))<SOC(j)&& SOC(j) >
SOC_batmin
                SOC_buff = SOC(j)-
(unmet_energy(j)/Bat_voltage)/Bat_ndischarge; % discharging mode battery
                Bat_disch(j)= (SOC_buff-SOC(j))*Bat_voltage;%energy supplied
by battery
```

```
                    SOC_j=SOC(j);
                    SOC(j+1)= SOC_buff;
                    %check battery hasn't discharged beyond its DOD
                    if SOC_buff < SOC_batmin
                      Excess_power(j)=(SOC_batmin - SOC_buff)*Bat_voltage;%
energy not supplied by battery
                      Bat_disch(j)= -((SOC_j-SOC_batmin)*Bat_voltage);%energy
supplied by battery
                      SOC(j+1)= SOC_batmin;
                      if Excess_power(j)<0
                        unmet_energy(j)=-Excess_power(j);
                      end
                    else
                      unmet_energy(j)=0;
                    end
                end
              end
            elseif err_power(j)< 0 && (-err_power(j)/Bat_voltage)>= SOC_batmax
              if -err_power(j)<=2*(x(5))
                ST_power(j)= -err_power(j);
              else
                ST_power(j)= 2*(x(5));
                unmet_energy(j)=(-err_power(j))-ST_power(j);
              end
              if unmet_energy(j)>0
&&(unmet_energy(j)/(Bat_ndischarge*Bat_voltage))<SOC(j)&& SOC(j) >
SOC_batmin
                    SOC_buff = SOC(j)-
(unmet_energy(j)/Bat_voltage)/Bat_ndischarge;% discharging mode battery
                    Bat_disch(j)= (SOC_buff-SOC(j))*Bat_voltage;%energy supplied
by battery
                    SOC_j=SOC(j);
                    SOC(j+1)= SOC_buff;
                    %check battery hasn't discharged beyond its DOD
                    if SOC_buff < SOC_batmin
                      Excess_power(j)=(SOC_batmin - SOC_buff)*Bat_voltage;%
energy not supplied by battery
                      Bat_disch(j)= -((SOC_j-SOC_batmin)*Bat_voltage);%energy
supplied by battery
                      SOC(j+1)= SOC_batmin;
                      if Excess_power(j)<0
                        unmet_energy(j)=-Excess_power(j);
                      end
                    else
                      unmet_energy(j)=0;
                    end
               end
            else
```

```
            ST_power(j)=0;
          end
        FC_diesel(j)= 0.24*ST_power(j)+(0.084*2*x(5));
        buff_power(j+1)=ST_power(j);
        end
        if Mana_strat == 3 % No battery with circuit charging
          if err_power (j)<0
            ST_power(j) = 2*x(5);
            if ST_power(j)<(-err_power(j))
              unmet_energy(j)=(-err_power(j))-ST_power(j);
            end
          else
            ST_power(j)=0;
          end
          if ST_power(j)>-err_power(j)&& err_power(j)<0
           dump_energy(j)=ST_power(j)-(-err_power(j));
          end
          if err_power(j)>0
            dump_energy(j)= err_power(j);
          end
        FC_diesel(j)= 0.24*ST_power(j)+(0.084*2*x(5));
        buff_power(j+1)=ST_power(j);
        end
        if Mana_strat == 4 %No Battery with circuit charging with two stirling
engines
          if Num_ST==1
           if err_power(j)<0 && -err_power(j)<= (0.5*x(5))
              ST_power(j)= 0.5*x(5);%%use one ST engine
           elseif err_power(j)<0 && -err_power(j)<= (x(5))&& (-err_power(j))>
(0.5*x(5))
              ST_power(j)= x(5);%% use two ST engines
           elseif err_power(j)<0 && -err_power(j)<= (1.5*x(5))&& (-
err_power(j))> (x(5))
              ST_power(j)= 1.5*x(5);%% use three ST engines
           elseif err_power(j)<0 && (-err_power(j))> (1.5*x(5))
              ST_power(j)= 2*x(5);%% use four ST engines
           else
              ST_power(j)=0;
           end
          else
           if err_power(j)<0 && -err_power(j)<= (x(5))
              ST_power(j)= x(5);%%use one ST engine
           elseif err_power(j)<0 && -err_power(j)>(x(5))
              ST_power(j)= 2*x(5);%% use two ST engines
           else
              ST_power(j)=0;
           end
          end
```

```
          if err_power(j)<0 && -err_power(j)> ST_power(j)
             unmet_energy(j)=-(err_power(j))-ST_power(j);
          end
          if ST_power(j)>-err_power(j)&& err_power(j)<0
             dump_energy(j)=ST_power(j)-(-err_power(j));
          end
          if err_power(j)>0
            dump_energy(j)= err_power(j);
          end
         FC_diesel(j)= 0.24*ST_power(j)+(0.084*2*x(5));
         buff_power(j+1)=ST_power(j);
         end
        %%%%%%battery management strategy 5
         if Mana_strat == 5 %Battery with one Stirling circuit charging
          %%%%%%%%% battery charging mode
          if err_power(j)>0 && SOC(j)< SOC_batmax
           SOC_buff= SOC(j)+ (err_power(j)/Bat_voltage);%Compute and store the
SOC at time t+1
           Bat_chg(j)=Bat_ncharge*(SOC_buff-SOC(j))*Bat_voltage;% power stored
in battery
           SOC_j=SOC(j);%store the SOC at time t
           SOC(j+1)=SOC_buff;
           %check if the power stored in the battery is more than the
           %maximum power of battery
              if SOC_buff > SOC_batmax
                dump_energy(j)= (SOC_buff-SOC_batmax)*Bat_voltage;
                SOC_new=SOC_batmax;
                Bat_buff = Bat_ncharge*(SOC_batmax-SOC_j)*Bat_voltage;% Actual
power that is delivered to the battery
                SOC(j+1)=SOC_new;
                Bat_chg(j)=Bat_buff;
              end
            elseif (err_power(j)>0 && (err_power(j)/Bat_voltage)>SOC_batmax)||
(err_power(j)>0 && SOC(j)>= SOC_batmax)
              dump_energy(j)= err_power(j);
              SOC(j+1)=SOC(j);
            else
             dump_energy(j)=0;
             SOC(j+1)=SOC(j);
       end
          %%%%%%%%%battery discharging mode
          if err_power(j)<0 && (-err_power(j)/Bat_voltage)< SOC_batmax
            if (-err_power(j)/(Bat_ndischarge*Bat_voltage))<SOC(j)&& SOC(j) >
SOC_batmin
              SOC_buff = SOC(j)-(-err_power(j)/Bat_voltage)/Bat_ndischarge;%
discharging mode battery
              Bat_disch(j)= ((SOC_buff-SOC(j))*Bat_voltage);%energy supplied by
battery
```

```
            SOC_jj=SOC(j);%hold the value of the state of charge of battery at time
t
            SOC(j+1)= SOC_buff;
            %check if the battery has been discharged below its
            %minimum capacity
            if SOC_buff < SOC_batmin
               Excess_power(j)= (SOC_batmin - SOC_buff)*Bat_voltage;% energy
not supplied by battery
               Bat_disch(j)= -((SOC_jj-SOC_batmin)*Bat_voltage);%energy
supplied by battery
               ST_power(j)=2*x(5);
               SOC(j+1)=SOC_batmin;%update the state of charge of battery after
discharging power
               %check if the stirling has excess power to charge
               %battery
               if ST_power(j)>Excess_power(j)
                    SOC_buff= SOC(j+1)+ ((ST_power(j)-
Excess_power(j))/Bat_voltage);%Compute and store the SOC at time t+1
                    Bat_chg(j)=Bat_ncharge*(SOC_buff-SOC(j+1))*Bat_voltage;%
power stored in battery
                    SOC_j=SOC(j+1);%store the SOC at time t+1
                    SOC(j+1)=SOC_buff;
                    %check if the power now stored in the
                    %battery is more than the maximum capacity
                    %of the battery
                    if SOC_buff > SOC_batmax
                       dump_energy(j)= (SOC_buff-SOC_batmax)*Bat_voltage;
                       SOC_new=SOC_batmax;
                       Bat_buff = Bat_ncharge*(SOC_batmax-
SOC_j)*Bat_voltage;% Actual power that is delivered to the battery
                       SOC(j+1)=SOC_new;
                       Bat_chg(j)=Bat_buff;
                    end
               else
                  unmet_energy(j)=Excess_power(j)-ST_power(j);
               end
             end
          else
            ST_power(j)=2*x(5);
            if ST_power(j)<(-err_power(j))
                unmet_energy(j)=(-err_power(j))-ST_power(j);
            end
            %check if stirling has excess power
            if (ST_power(j)-(-err_power(j)))>0
               %store some of the excess in the battery
                SOC_buff= SOC(j)+ ((ST_power(j)-(-
(err_power(j))))/Bat_voltage);%Compute and store excess power into the SOC at
time t+1
```

```
                Bat_chg(j)=(Bat_ncharge*(SOC_buff-SOC(j))*Bat_voltage);%
power stored in battery
                SOC_j=SOC(j);%store the SOC at time t
                SOC(j+1)=SOC_buff;
                %ensure battery's capacity isn't exceeded
                if SOC_buff > SOC_batmax
                    dump_energy(j)= (SOC_buff-SOC_batmax)*Bat_voltage;
                    SOC_new=SOC_batmax;
                    Bat_buff = Bat_ncharge*(SOC_batmax-SOC_j)*Bat_voltage;%
Actual power that is delivered to the battery
                    SOC(j+1)=SOC_new;
                    Bat_chg(j)=Bat_buff;
                end
            else
              if unmet_energy(j)>0 &&
(unmet_energy(j)/(Bat_ndischarge*Bat_voltage))<SOC(j)&& SOC(j) >
SOC_batmin
                SOC_buff = SOC(j)-
(unmet_energy(j)/Bat_voltage)/Bat_ndischarge;% discharging mode battery
                Bat_disch(j)= (SOC_buff-SOC(j))*Bat_voltage;%energy supplied
by battery
                SOC_j=SOC(j);
                SOC(j+1)= SOC_buff;
                %check battery hasn't discharged beyond its DOD
                if SOC_buff < SOC_batmin
                  Excess_power(j)=(SOC_batmin - SOC_buff)*Bat_voltage;%
energy not supplied by battery
                  Bat_disch(j)= -((SOC_j-SOC_batmin)*Bat_voltage);%energy
supplied by battery
                  SOC(j+1)= SOC_batmin;
                  if Excess_power(j)<0
                     unmet_energy(j)=-Excess_power(j);
                  end
                else
                  unmet_energy(j)=0;
                end
              end
            end
          end
        elseif err_power(j)< 0 && (-err_power(j)/Bat_voltage)>= SOC_batmax
          ST_power(j)= 2*x(5);
          if ST_power(j)<(-err_power(j))
              unmet_energy(j)=(-err_power(j))-ST_power(j);
          end
          if ST_power(j)>(-err_power(j))
            %check if battery can accommodate some power from ST eng
            if SOC(j)< SOC_batmax
```

```
                SOC_buff= SOC(j)+ ((ST_power(j)-(-
err_power(j)))/Bat_voltage);%Compute and store the SOC at time t+1
                Bat_chg(j)=Bat_ncharge*(SOC_buff-SOC(j))*Bat_voltage;% power
stored in battery
                SOC_j=SOC(j);%store the SOC at time t
                SOC(j+1)=SOC_buff;
                % Ensure battery doesn't exceed its limit
                if SOC_buff > SOC_batmax
                    dump_energy(j)= (SOC_buff-SOC_batmax)*Bat_voltage;
                    SOC_new=SOC_batmax;
                    Bat_buff = Bat_ncharge*(SOC_batmax-SOC_j)*Bat_voltage;%
Actual power that is delivered to the battery
                    SOC(j+1)=SOC_new;
                    Bat_chg(j)=Bat_buff;
                end
            else
                dump_energy(j)= ST_power(j)- (-err_power(j));
            end
        else
            if unmet_energy(j)>0
&&(unmet_energy(j)/(Bat_ndischarge*Bat_voltage))<SOC(j)&& SOC(j) >
SOC_batmin
                SOC_buff = SOC(j)-
(unmet_energy(j)/Bat_voltage)/Bat_ndischarge;% discharging mode battery
                Bat_disch(j)= (SOC_buff-SOC(j))*Bat_voltage;%energy supplied
by battery
                SOC_j=SOC(j);
                SOC(j+1)= SOC_buff;
                %check battery hasn't discharged beyond its DOD
                if SOC_buff < SOC_batmin
                    Excess_power(j)=(SOC_batmin - SOC_buff)*Bat_voltage;%
energy not supplied by battery
                    Bat_disch(j)= -((SOC_j-SOC_batmin)*Bat_voltage);%energy
supplied by battery
                    SOC(j+1)= SOC_batmin;
                    if Excess_power(j)<0
                        unmet_energy(j)=-Excess_power(j);
                    end
                else
                    unmet_energy(j)=0;
                end
            end
        end
    else
        ST_power(j)=0;
    end
%       SOC(j+1)=SOC(j);
    FC_diesel(j)= 0.24*ST_power(j)+(0.084*2*x(5));
```

```
        buff_power(j+1)=ST_power(j);
        end
      %%%%%%%%Battery with two Stirling circuit charging
        if Mana_strat == 6 %Battery with two Stirling circuit charging
         %%%%%%%%% battery charging mode
         if err_power(j)>0 && SOC(j)< SOC_batmax
          SOC_buff= SOC(j)+ (err_power(j)/Bat_voltage);%Compute and store the
SOC at time t+1
          Bat_chg(j)=Bat_ncharge*(SOC_buff-SOC(j))*Bat_voltage;% power stored
in battery
          SOC_j=SOC(j);%store the SOC at time t
          SOC(j+1)=SOC_buff;
          %check if the power stored in the battery is more than the
          %maximum power of battery
             if SOC_buff > SOC_batmax
               dump_energy(j)= (SOC_buff-SOC_batmax)*Bat_voltage;
               SOC_new=SOC_batmax;
               Bat_buff = Bat_ncharge*(SOC_batmax-SOC_j)*Bat_voltage;% Actual
power that is delivered to the battery
               SOC(j+1)=SOC_new;
               Bat_chg(j)=Bat_buff;
             end
           elseif (err_power(j)>0 && (err_power(j)/Bat_voltage)>SOC_batmax)||
(err_power(j)>0 && SOC(j)>= SOC_batmax)
             dump_energy(j)= err_power(j);
             SOC(j+1)=SOC(j);
           else
            dump_energy(j)=0;
            SOC(j+1)=SOC(j);
          end

          %%%%%%%%%battery discharging mode
          if err_power(j)<0 && (-err_power(j)/Bat_voltage)< SOC_batmax
            if (-err_power(j)/(Bat_ndischarge*Bat_voltage))<SOC(j)&& SOC(j) >
SOC_batmin
              SOC_buff = SOC(j)-(-err_power(j)/Bat_voltage)/Bat_ndischarge;%
discharging mode battery
              Bat_disch(j)= (SOC_buff-SOC(j))*Bat_voltage;%energy supplied by
battery
              SOC_j=SOC(j);
              SOC(j+1)= SOC_buff;
              %check battery hasn't discharged beyond its DOD
              if SOC_buff < SOC_batmin
                 Excess_power(j)=(SOC_batmin - SOC_buff)*Bat_voltage;% energy
not supplied by battery
                 Bat_disch(j)= -((SOC_j-SOC_batmin)*Bat_voltage);%energy
supplied by battery
                 SOC(j+1)= SOC_batmin;
```

```
                %%%%%%%%% use stirling engines one to four to meet the
                %%%%%%%%% unmet energy by the battery
                if Num_ST==1
                  if Excess_power(j) <= (0.5*x(5))
                    ST_power(j)= 0.5*x(5);
                  elseif Excess_power(j)<= (x(5))&& Excess_power(j) > (0.5*x(5))
                    ST_power(j)= x(5);
                  elseif Excess_power(j) <= (1.5*x(5))&& Excess_power(j) > (x(5))
                    ST_power(j)= 1.5*x(5);
                  elseif Excess_power(j) > (1.5*x(5))
                    ST_power(j)= 2*x(5);
                  end
                else
                  if Excess_power(j) <= (x(5))
                    ST_power(j)= x(5);
                  elseif Excess_power(j) > (x(5))
                    ST_power(j)= 2*x(5);
                  end
                end

                if ST_power(j)< Excess_power(j)
                  unmet_energy(j)=Excess_power(j)-ST_power(j);
                end
                %check if stirling has excess power
                if ST_power(j)> Excess_power(j)
                  %store some of the excess in the battery
                   SOC_buff= SOC(j+1)+ ((ST_power(j)-
Excess_power(j))/Bat_voltage);%Compute and store the SOC at time t+1
                   Bat_chg(j)=Bat_ncharge*(SOC_buff-SOC(j+1))*Bat_voltage;%
power stored in battery
                   SOC_j=SOC(j+1);%store the SOC at time t
                   SOC(j+1)=SOC_buff;
                   %ensure battery's capacity isn't exceeded
                   if SOC_buff > SOC_batmax
                      dump_energy(j)= (SOC_buff-SOC_batmax)*Bat_voltage;
                      SOC_new=SOC_batmax;
                      Bat_buff = Bat_ncharge*(SOC_batmax-SOC_j)*Bat_voltage;%
Actual power that is delivered to the battery
                      SOC(j+1)=SOC_new;
                      Bat_chg(j)=Bat_buff;
                   end
                end
              end
            else
              if Num_ST==1
                if (-err_power(j))<= (0.5*x(5))
                  ST_power(j)= 0.5*x(5);%%use one ST engine
                elseif (-err_power(j))<= (x(5))&& (-err_power(j))> (0.5*x(5))
```

```
                ST_power(j)= x(5);%% use two ST engines
              elseif (-err_power(j))<= (1.5*x(5))&& (-err_power(j))> (x(5))
                ST_power(j)= 1.5*x(5);%% use three ST engines
              elseif (-err_power(j))> (1.5*x(5))
                ST_power(j)= 2*x(5);%% use four ST engines
              end
            else
              if (-err_power(j))<= (x(5))
                ST_power(j)= x(5);%%use one ST engine
              elseif (-err_power(j))> (x(5))
                ST_power(j)= 2*x(5);%% use four ST engines
              end
            end
             %check if stirling has excess power
             if ST_power(j)<(-err_power(j))
                  unmet_energy(j)=(-err_power(j))-ST_power(j);
             end
             if (ST_power(j)-(-err_power(j)))>0
                %store some of the excess in the battery
                 SOC_buff= SOC(j)+ ((ST_power(j)-(-
err_power(j)))/Bat_voltage);%Compute and store excess power into the SOC at
time t+1
                 Bat_chg(j)=Bat_ncharge*(SOC_buff-SOC(j))*Bat_voltage;% power
stored in battery
                 SOC_j=SOC(j);%store the SOC at time t
                 SOC(j+1)=SOC_buff;
                 %ensure battery's capacity isn't exceeded
                 if SOC_buff > SOC_batmax
                    dump_energy(j)= (SOC_buff-SOC_batmax)*Bat_voltage;
                    SOC_new=SOC_batmax;
                    Bat_buff = Bat_ncharge*(SOC_batmax-SOC_j)*Bat_voltage;%
Actual power that is delivered to the battery
                    SOC(j+1)=SOC_new;
                    Bat_chg(j)=Bat_buff;
                 end
             else
                if unmet_energy(j)>0
&&(unmet_energy(j)/(Bat_ndischarge*Bat_voltage))<SOC(j)&& SOC(j) >
SOC_batmin
                  SOC_buff = SOC(j)-
(unmet_energy(j)/Bat_voltage)/Bat_ndischarge;% discharging mode battery
                  Bat_disch(j)= (SOC_buff-SOC(j))*Bat_voltage;%energy supplied
by battery
                  SOC_j=SOC(j);
                  SOC(j+1)= SOC_buff;
                  %check battery hasn't discharged beyond its DOD
                  if SOC_buff < SOC_batmin
```

```
                    Excess_power(j)=(SOC_batmin - SOC_buff)*Bat_voltage;%
energy not supplied by battery
                    Bat_disch(j)= -((SOC_j-SOC_batmin)*Bat_voltage);%energy
supplied by battery
                    SOC(j+1)= SOC_batmin;
                    if Excess_power(j)<0
                       unmet_energy(j)=-Excess_power(j);
                    end
                  else
                    unmet_energy(j)=0;
                  end
                end
              end
            end
          elseif err_power(j)< 0 && (-err_power(j)/Bat_voltage)>= SOC_batmax
            if Num_ST==1
              if (-err_power(j))<= (0.5*x(5))
                ST_power(j)= 0.5*x(5);%%use one ST engine
              elseif (-err_power(j))<= (x(5))&& (-err_power(j))> (0.5*x(5))
                ST_power(j)= x(5);%% use two ST engines
              elseif (-err_power(j))<= (1.5*x(5))&& (-err_power(j))> (x(5))
                ST_power(j)= 1.5*x(5);%% use three ST engines
              elseif (-err_power(j))> (1.5*x(5))
                ST_power(j)= 2*x(5);%% use four ST engines
              end
            else
              if (-err_power(j))<= (x(5))
                ST_power(j)= x(5);%%use one ST engine
              elseif (-err_power(j)) > (x(5))
                ST_power(j)= 2*x(5);%% use two ST engines
              end
            end

            %% check if the energy supplied by ST is less than the diff and compute
unmet energy
            if ST_power(j)<(-err_power(j))
              unmet_energy(j)=(-err_power(j))-ST_power(j);
            end
            %%%%% check if ST contains excess energy to charge battery
            if ST_power(j)>(-err_power(j))
              %check if the battery can takeup some excess power
              if SOC(j)< SOC_batmax
                 SOC_buff= SOC(j)+ ((ST_power(j)-(-
err_power(j)))/Bat_voltage);%Compute and store the SOC at time t+1
                 Bat_chg(j)=Bat_ncharge*(SOC_buff-SOC(j))*Bat_voltage;% power
stored in battery
                 SOC_j=SOC(j);%store the SOC at time t
                 SOC(j+1)=SOC_buff;
```

```
                %ensure battery capacity is not exceeded
                if SOC_buff > SOC_batmax
                    dump_energy(j)= (SOC_buff-SOC_batmax)*Bat_voltage;
                    SOC_new=SOC_batmax;
                    Bat_buff = Bat_ncharge*(SOC_batmax-SOC_j)*Bat_voltage;%
Actual power that is delivered to the battery
                    SOC(j+1)=SOC_new;
                    Bat_chg(j)=Bat_buff;
                end
            else
                dump_energy(j)= ST_power(j)- (-err_power(j));
            end
        else
            if unmet_energy(j)>0
&&(unmet_energy(j)/(Bat_ndischarge*Bat_voltage))<SOC(j)&& SOC(j) >
SOC_batmin
                SOC_buff = SOC(j)-(unmet_energy(j)/Bat_ndischarge);%
discharging mode battery
                Bat_disch(j)= (SOC_buff-SOC(j))*Bat_voltage;%energy supplied
by battery
                SOC_j=SOC(j);
                SOC(j+1)= SOC_buff;
                %check battery hasn't discharged beyond its DOD
                if SOC_buff < SOC_batmin
                    Excess_power(j)=(SOC_batmin - SOC_buff)*Bat_voltage;%
energy not supplied by battery
                    Bat_disch(j)= -((SOC_j-SOC_batmin)*Bat_voltage);%energy
supplied by battery
                    SOC(j+1)= SOC_batmin;
                    if Excess_power(j)<0
                        unmet_energy(j)=-Excess_power(j);
                    end
                else
                    unmet_energy(j)=0;
                end
            end
        end
    else
        ST_power(j)=0;
    end
%       SOC(j+1)=SOC(j);
    FC_diesel(j)= 0.24*ST_power(j)+(0.084*2*x(5));
    buff_power(j+1)=ST_power(j);
    end
    if ST_power(j)>0
        t_stirling=t_stirling+1;
    end
    diff_ST_power=buff_power(j+1)-buff_power(j);
```

```
        if diff_ST_power==ST_power(j)&&ST_power(j)>0
           count=count+1;
        end
      end
%       gca (figure);
%    %    yz=Bat_power;
      yv=(ST_power);
      yx=(SOC./SOC_batmax);
      ynn=SOC';
      yxx = (PV_gen+WT_gen)';
      yxz=Demand_inst;
      yxv=-Bat_chg;
      yxu=-Bat_disch;
      Wind_out=Wind_power;
      demand_out=Demand1;
      PV_powertot=sum(PV_power1);
      WT_powertot=sum(Wind_out);
      Demand_tot=sum(demand_out);
      Bat_dischtot=sum(Bat_disch);
      ST_powertot=sum(ST_power);%total power produced by stirling in kWh
      FC_dieseltot=sum(FC_diesel);%total diesel fuel consumed by the engine
      mass_woodchips=3600*ST_powertot/(0.80*HHV_woodchips*eff_stirling);
%       Cost_woodchips=unitcost_diesel*FC_dieseltot; %%cost of diesel fuel
      Cost_woodchips = unitcost_woodchips*mass_woodchips;%%cost of
%       woodchips
% co2 emissions by the HRES
     yy(4)=1000*HHV_woodchips*emission_factorco2*mass_woodchips;
    Emissions_fuelco2=HHV_fuel*emission_factorco2*FC_dieseltot;
   % n2o emissions fuel
     Emissions_fueln2o=HHV_woodchips*emission_factorn2o*mass_woodchips;
%      Emissions_fueln2o=HHV_fuel*emission_factorn2o*FC_dieseltot;
      dump_energytot=sum(dump_energy);
      unmet_energytot=sum(unmet_energy);
      PV_mntcost = 0;
      WT_mntcost = 0;
      Woodchips_cost=0;
      for k = 1:Life_system
          PV_mntcost = PV_mntcost + PV_mcost*PV_powertot*x(1)
         *((1+Inf_rate)^(k)/(1+Int_rate)^(k));
        WT_mntcost = WT_mntcost + WT_mcost*WT_powertot*x(2)
        *((1+Inf_rate)^(k)/(1+Int_rate)^(k));
        Woodchips_cost = Woodchips_cost + Cost_woodchips*
        ((1+Inf_ratefuel)^(k)/(1+Int_ratefuel)^(k));
      end
      C_maintenance = PV_mntcost + WT_mntcost; %maintaenance cost of
      PV and    wind over the life of the project
      %capital recovery factor
      crf= (Int_rate*(1+Int_rate)^Life_system)/(((1+Int_rate)^Life_system)-1);
```

```
%replacement cost of diesel generator over the life of the project
%% it has been called ST to avaoid major changes to the function

ST_Nrep = round(Life_system/ST_life); % number of times battery is replaced
ST_repcost=0;%cost of replacing battery
for m = 1:ST_Nrep
   ST_repcost = ST_repcost + ST_cost*((1+Inf_rate)^(m*ST_life)
   /(1+Int_rate)^(m*ST_life));
end
ST_repcostactual = ST_repcost - ((ST_cost*(ST_life-(Life_system-
(ST_Nrep*ST_life)))/ST_life)*((1+Inf_rate)^(Life_system)/(1+Int_rate)^(Life_syst
em)));
if Mana_strat == 1 % No battery with load following
yy(1)=((crf*((PV_cost*PV_series*x(1))+(WT_cost1*WT_cap*x(2))))+(2*ST_cost*x
(5))+(C_maintenance
+(ST_mntcost*ST_powertot)+Woodchips_cost))/(Demand_tot*Life_system);
    yy(2)=(Demand_tot-(PV_powertot*(x(1))+WT_powertot*(x(2))-
ST_powertot))/Demand_tot;%loss of power supply probability
elseif Mana_strat == 2 %Battery with Stirling load following
   if Bat_type ==1
      Bat_cost = Bat1_cost;
      %net present replacement cost of battery
      Bat_Nrep = round(Life_system/Bat_life); % number of times battery is
replaced
      Bat_repcost=0;%cost of replacing battery
      for m = 1:Bat_Nrep
       Bat_repcost = Bat_repcost + Bat_cost*((1+Inf_rate)^(m*Bat_life)
    /(1+Int_rate)^(m*Bat_life));
      end
      Bat_repcostactual = Bat_repcost - ((Bat_cost*(Bat_life-(Life_system-
(Bat_Nrep*Bat_life)))/Bat_life)*((1+Inf_rate)^(Life_system)/(1+Int_rate)^(Life_sy
stem)));
   elseif Bat_type ==2
      Bat_cost = Bat2_cost;
      %net present replacement cost of battery
      Bat_Nrep = round(Life_system/Bat_life); % number of times battery is
replaced
      Bat_repcost=0;%cost of replacing battery
      for m = 1:Bat_Nrep
       Bat_repcost = Bat_repcost + Bat_cost*((1+Inf_rate)^(m*Bat_life)
    /(1+Int_rate)^(m*Bat_life));
      end
      Bat_repcostactual = Bat_repcost - ((Bat_cost*(Bat_life-(Life_system-
(Bat_Nrep*Bat_life)))/Bat_life)*((1+Inf_rate)^(Life_system)/(1+Int_rate)^(Life_sy
stem)));
   else
      Bat_cost = Bat3_cost;
      %net present replacement cost of battery
```

```
            Bat_Nrep = round(Life_system/Bat_life); % number of times battery is
replaced
            Bat_repcost=0;%cost of replacing battery
            for m = 1:Bat_Nrep
             Bat_repcost= Bat_repcost + Bat_cost*((1+Inf_rate) ^(m*Bat_life)
          /(1+Int_rate) ^(m*Bat_life));
            end
            %actual replacement cost for one battery
            Bat_repcostactual = Bat_repcost - ((Bat_cost*(Bat_life-(Life_system-
(Bat_Nrep*Bat_life)))/Bat_life)*((1+Inf_rate)^(Life_system)/(1+Int_rate)^(Life_sy
stem)));
         end
         yy(1)=((crf*((PV_cost*PV_series*x(1))+(WT_cost1*WT_cap*x(2))+
(NBat_series*Bat_cost*x(7))))+(2*ST_cost*x(5))+C_maintenance
+Woodchips_cost+(ST_mntcost*ST_powertot)+
(Bat_repcostactual*NBat_series*x(7)))/(Demand_tot*Life_system);
         yy(2)=(Demand_tot-(PV_powertot*(x(1))+WT_powertot*(x(2))-
ST_powertot-(SOC_batmax*Bat_voltage)))/Demand_tot;%loss of power supply
probability
      elseif Mana_strat == 3 % No battery with Stirling circuit charging
yy(1)=((crf*((PV_cost*PV_series*x(1))+(WT_cost1*WT_cap*x(2))))+(2*ST_cost*x
(5))+(C_maintenance
+(ST_mntcost*ST_powertot)+Woodchips_cost))/(Demand_tot*Life_system);
         yy(2)=(Demand_tot-(PV_powertot*(x(1))+WT_powertot*(x(2))-
ST_powertot))/Demand_tot;%loss of power supply probability
      elseif Mana_strat == 4 %No Battery circuit charging with two stirling engines

yy(1)=((crf*((PV_cost*PV_series*x(1))+(WT_cost1*WT_cap*x(2))))+(2*ST_cost*x
(5))+(C_maintenance
+(ST_mntcost*ST_powertot)+Woodchips_cost))/(Demand_tot*Life_system);
         yy(2)=(Demand_tot-(PV_powertot*(x(1))+WT_powertot*(x(2))-
ST_powertot))/Demand_tot;%loss of power supply probability
      else %Battery with one Stirling circuit charging
         if Bat_type ==1
            %net present replacement cost of battery
            Bat_Nrep = round(Life_system/Bat_life); % number of times battery is
replaced
            Bat_repcost=0;%cost of replacing battery
            for m = 1:Bat_Nrep
               Bat_repcost = Bat_repcost +
Bat_cost*((1+Inf_rate)^(m*Bat_life)/(1+Int_rate)^(m*Bat_life));
            end
            Bat_repcostactual = Bat_repcost - ((Bat_cost*(Bat_life-(Life_system-
(Bat_Nrep*Bat_life)))/Bat_life)*((1+Inf_rate)^(Life_system)/(1+Int_rate)^(Life_sy
stem)));
         elseif Bat_type ==2
            Bat_cost = Bat2_cost;
```

```
            Bat_Nrep = round(Life_system/Bat_life); % number of times battery is
replaced
            Bat_repcost=0;%cost of replacing battery
            for m = 1:Bat_Nrep
               Bat_repcost = Bat_repcost +
Bat_cost*((1+Inf_rate)^(m*Bat_life)/(1+Int_rate)^(m*Bat_life));
            end
            Bat_repcostactual = Bat_repcost - ((Bat_cost*(Bat_life-(Life_system-
(Bat_Nrep*Bat_life)))/Bat_life)*((1+Inf_rate)^(Life_system)/(1+Int_rate)^(Life_sy
stem)));
         else
            Bat_cost = Bat3_cost;
            Bat_Nrep = round(Life_system/Bat_life); % number of times battery is
replaced
            Bat_repcost=0;%cost of replacing battery
            for m = 1:Bat_Nrep
               Bat_repcost = Bat_repcost +
Bat_cost*((1+Inf_rate)^(m*Bat_life)/(1+Int_rate)^(m*Bat_life));
            end
            Bat_repcostactual = Bat_repcost - ((Bat_cost*(Bat_life-(Life_system-
(Bat_Nrep*Bat_life)))/Bat_life)*((1+Inf_rate)^(Life_system)/(1+Int_rate)^(Life_sy
stem)));
         end
          yy(1)=((crf*((PV_cost*PV_series*x(1))+(WT_cost1*WT_cap*x(2))+
(NBat_series*Bat_cost*x(7))))+(2*ST_cost*x(5))+C_maintenance
+Woodchips_cost+(ST_mntcost*ST_powertot)+
(Bat_repcostactual*NBat_series*x(7)))/(Demand_tot*Life_system);
yy(2) =(Demand_tot-(PV_powertot*(x(1))+WT_powertot*(x(2))-ST_powertot-
(SOC_batmax*Bat_voltage)))/Demand_tot;%loss of power supply probability
      end
      yy(3) = dump_energytot;
```

C.2. Function for multi-objective optimisation of HRES

```
function [x,fval,popu,scores] = ()
global Demand
global WT1_power
global WT2_power
global sum2
global sum22
global sum3
global PV_power2
PV_optconstants1;
simOut = sim('PV_Simulinkopt','StopTime',
'8760','SaveState','on','StateSaveName','xout',...
'SaveOutput','on','OutputSaveName','yout',...
'SaveFormat','Dataset');
```

```
outputs = simOut.get('yout');
PV_power = simOut.get('out');
WT1_power = simOut.get('out2');
WT2_power = simOut.get('out4');
Demand = simOut.get('out3');
PV_power2 = power_PV;
k=length(WT2_power);
n=(k/2400);
i=1;
% WT2_power1=WT2_power';
for j = 1:n
%    sum1=0;
   sum2=0;
   sum22=0;
   sum3=0;
%    i=j;
   for m=i:i+2399
%        sum1=(sum1 + PV_power(m,:));
       sum2=(sum2+ WT1_power(m,:));
       sum22=(sum22+ WT2_power(m,:));
       sum3=(sum3+ Demand(m,:));
   end
%    sum11(j)=sum1./100;
   sum221(j)=sum2./100;
   sum222(j)=sum22./100;
   sum33(j)=sum3./100;
   i=m;
end
sum1_=0;
for i= 768:792
 sum1_=(sum1_ + PV_power2(i,:));
% %  sum2_=(sum2_+ WT1_power(i,:));
% %  sum22_=(sum22_+ WT2_power(i,:));
% %  sum3_=(sum3_+ Demand(i,:));
end
sum11_=PV_eff*4*(sum1_/1000);
sum11=sum11_;
% sum12=sum11';
sum21=sum221';
sum211=sum222';
sum31=sum33';
%start optimisation
% IntCon=1
num_var=9;
x=ones(1,num_var);
pop_size=200;
xx=round(n);
l=zeros(xx,1);
```

```
for j=1:xx
   if j==32
      A=[-sum11 -sum211(j) 0 0 0 0 0 0;-sum11 0 -sum21(j) 0 0 0 0 0; 0 0 0 0 -1 0 0
0 0;0 0 0 0 0 0 -4.960 0 0];
      b=[-sum31(j);-sum31(j);-90;-20];
      break;
   end
end
Aeq=[];
beq=[];
lb=[1 0 0 1 60 1.6 1 1 0.6];
ub=[1200 5 8 2 120 2.4 30 3 1.4];
nonlcon=[];
fgoalopts = optimoptions(@fgoalattain,'UseParallel',true);
options =
optimoptions('gamultiobj','UseParallel',true,'PopulationSize',pop_size,'ParetoFractio
n',0.50,'UseVectorized',false,'MaxGenerations',300,'PlotFcn',{@gaplotgenealogy,@ga
plotscorediversity,@gaplotbestf,@gaplotpareto,@gaplotspread,@gaplotscores},'di
splay','iter');
options =
%optimoptions(options,'InitialPopulationMatrix',population,'InitialScoresMatrix',sco
res);
options = optimoptions(options,'HybridFcn',{@fgoalattain,fgoalopts});
fun=@PV_OBJ;
[x,fval,exitflag,output,popu,scores] =
gamultiobj(fun,9,A,b,Aeq,beq,lb,ub,nonlcon,options);
End
```

Appendix D Scoring criteria and decision matrix for TOPSIS decision making

Table D-1. Judgement criteria for the decision matrix [260].

Intensity of importance	Definition
1	Equal importance
3	Weak importance
5	Essential or strong importance
7	Demonstrated importance
9	Absolute importance
2,4,6	Intermediate values

Table D-2. Decision matrix for the TOPSIS.

	LCOE	LPSP	Dumped Power	CO_2 emissions
LCOE	1	$1/3$	$1/5$	$1/3$
LPSP	3	1	$1/2$	1
Dumped power	5	2	1	4
CO_2 emissions	3	1	$1/4$	1